

New Technologies for Urban Safety of Mega Cities in Asia

October 18-19, 2005

Singapore

-Editor-

Hisashi Kanada

ICUS, IIS

The University of Tokyo, Japan

Organised By

*Protective Technology Research Centre,
School of Civil and Environmental Engineering
Nanyang Technological University,
Singapore*

*International Center for Urban Safety Engineering (ICUS),
Institute of Industrial Science, The University of Tokyo,
Tokyo, Japan*

NEW TECHNOLOGIES FOR URBAN SAFETY OF MEGA CITIES IN ASIA

KIMIRO MEGURO
Professor, ICUS
IIS, University of Tokyo, Japan

ICUS Report No 12, FEBRUARY, 2006

PREFACE

Rapid urbanization has characterized the world's development in the last decades and it will become more dramatic in the years to come. In the beginning of the 21st Century, over 50 % of the world's total population will concentrate in urban areas, especially in Asia. More than sixty percent of the world's mega cities (more than ten million inhabitants), i.e. 14 cities among 22, are located in Asia.

Fast urban growing poses several challenges, such as land use administration, infrastructure maintenance, vulnerable building management, environment preservation, among others, for the sustainability of these emerging metropolises. Considering the increasingly important role of these urban areas and the large number of people that they concentrate, the necessity of addressing the previously mentioned issues is clear. Modern technologies such as Geographic Information Systems, Global Positioning System, Remote Sensing and satellite image analysis, computer simulations, and non traditional construction materials as well as innovative solutions combining existing and/or conventional technologies can be very useful for this purpose. Based on this understanding, the International Symposium of Urban Safety of Mega Cities in Asia has been organized every year, since 2002, in order to provide a forum for discussion among decision makers, practicing professionals, and researchers.

Following the success of previous gatherings at Bangkok, Thailand (2002), Tokyo, Japan (2003), and Agra, India (2004), the 4th International Symposium was co-organized by the Protective Technology Research Center, School of Civil and Environmental Engineering, Nanyang Technological University, Singapore and the International Center for Urban Safety Engineering, Institute of Industrial Science, The University of Tokyo, Japan. It was sponsored by the Center for Sustainable Urban Regeneration, The University of Tokyo, 21st Century Center of Excellence Program.

The objective of bringing together experts in areas of design, construction and maintenance of urban infrastructure, urban planning, disaster mitigation, and environment preservation was successfully accomplished. As on previous occasions, the symposium served to create

new and strengthen existing networks of people addressing rapid urbanization issues in the Asian region.

I hope that the present volume, which contains the papers presented during the symposium, provides valuable reference material. Finally, I would like to gratefully acknowledge the efforts of organizers, participants, and sponsors, who contributed to the success of this event.

CONTENTS

Opening Session

SECTION 1: Keynote & Plenary Papers

ROHAN KUMAR GUNARATNA

- The New Face of Al Qaeda: The Threat Four Years After 9-11 1

YOSHIFUMI YASUOKA, W. TAKEUCHI, T. NEMOTO, P. J. BARUAH
AND T. ENDO

- Satellite Observation Network for Environment and Disaster
Monitoring in Asia 3

KIMIRO MEGURO, PAOLA MAYORCA, NAVARATNARAJAH SATHIPARAN,
RAMESH GURAGAIN, NASROLLAHZADEH NESHELI

- Shaking Table Tests of 1/4 Scaled Masonry Models Retrofitted with
PP-band Meshes 9

TEDDY BOEN

- Reconstruction of Houses in Aceh Seven Months after the
Earthquake & Tsunami, December 26, 2004 19

W.C. FAN, G.F. SU

- Progress in Emergency Management Research for a Mega-city in China ... 31

PENNUNG WARNITCHAI

- Lessons Learned from the 26 December 2004 Tsunami Disaster in
Thailand 41

Technical Sessions

SECTION 2: Safety Assessment and Monitoring of Existing Infrastructure

MITSUYOSHI TSUNEKUNI, TSUGIO NISHIMURA, YOSHITAKA KATO,
TAKETO UOMOTO

- Structural Performance Monitoring of Reinforced Concrete Bridges 51

SHINICHIRO OKAZAKI, TAKETO UOMOTO

- Development of Monitoring System for RC Bridge Based on
Restoration Design Method 61

EMA KATO, ATSUSHI YOKOZAWA, YOSHIKAZU AKIRA, HIROSHI YOKOTA

- Study on Durability of RC Deck of Existing Pier 69

YOSHITAKA KATO AND NAOKI TAKESHITA

- Simulation Study on Relation Between Local Rainfall Conditions and
Amount of Moisture Supplied to Concrete 79

S FAISAL HASHMI, ONKAR DIKSHIT AND SUDHIR MISRA

- Using Digital Close Range Photogrammetry to Estimate Deflections
in a Bridge 89

PHAN HUU DUY QUOC, TOSHIHARU KISHI	
- Research on Durability Evaluation for In-Place Concrete Effect of Early Drying on the Quality of Cover Concrete	99
XIANJIE XU, RI GAO, LANCHAO JIANG, WEIGUO YANG	
- Safety Evaluation of Aged Steel Truss Bridge with Cracking Members	109
WORAKANCHANA KAWIN, KIMIRO MEGURO	
- Failure Mechanism of Shih-Kang Dam by Applied Element Method ...	119
HISASHI KANADA, YUKIHIRO ISHIKAWA, TAKETO UOMOTO	
- Utilization of Near-infrared Spectral Imaging System for Inspection of Concrete Structures	129
RAKTIPONG SAHAMITMONGKOL, TOSHIHARU KISHI	
- Internal Damage of Reinforced Concrete and Chemically Prestressed Concrete Under Uniaxial Load	139
SOMNUK TANGTERMSIRIKUL, JITTBODEE KHUNTHONGKAEW AND PITISAN KRAMMART	
- A Durability Design Concept for Concrete Structures in Thailand	147

SECTION 3: Threat Reduction and Consequence Management

DR. ALIREZA ANDALIB, DR. SHARIF MOTAWEF	
- Poverty and Disaster Threat in Mega Cities: Tehran Case Study, Iran ...	153
FANG YEA SAEN, B ARCH, MSIA	
- Planning and Design for Security	163
MIN-CHENG TENG, CHIEN-MEI LEE, KUO-SHUH FAN	
- Disaster Mitigation Assessment for Storage Tank Facility	173
MIN-CHENG TENG, SHIH-CHIEN HUANG, KUO-SHUH FAN	
- Safety Management Research of the Coach Accident	183
SHINYA KONDO, KIMIRO MEGURO	
- A Case Study of the Introduction of Disaster Management System at Islamic Republic of Iran	193
DUSHMANTA DUTTA	
- Vulnerability of Coastal Cities of Asia to Rising Sea Level: A Case Study in Bangkok	203

SECTION 4: Keynote & Plenary Papers

MIHO YOSHIMURA, KIMIRO MEGURO	
- Survey on Residents' Attitudes for Retrofitting of Existing Vulnerable Houses	213

KUMAR NEERAJ JHA, SUDHIR MISRA	
- A Case Study in Rehabilitation of a Large Industrial Structure	221
NAVARATNARAJAH SATHIPARAN, PAOLA MAYORCA, NASROLLAHZADEH NESHELI, RAMESH GURAGAIN, KIMIRO MEGURO	
- In-plane and Out-of-plane Behavior of PP-band Retrofitted Masonry Wallettes	231
MASANORI ITO, YOSHITAKA KATO, TAKETO UOMOTO	
- The Importance of Curing in Preventing the Spalling-off of Patching Repair Material.....	241
PAKAWAT SANCHAROEN, TAKETO UOMOTO	
- Allocation of Life-cycle Repairing Cost Based on Parameter Uncertainties of Deterioration Prediction Model	249
TAKETO UOMOTO	
- Importance of Maintenance of Concrete Structures for Urban Safety ...	257
 SECTION 5: Design and Assessment of Structures for Seismic, Shock and Impact Loads	
BING LI, TSO-CHIEN PAN	
- Recent Seismic Load Tests on Reinforced Concrete Beam-Column Joints at NTU, Singapore	267
XIN ZHANG AND TSO-CHIEN PAN	
- Approximation of Damage for a Reinforced Concrete Column Subjected to Intermediate Range Blast Loading	277
MEHEDI AHMED ANSARY, MD.REZAUL ISLAM	
- Seismic Microzonation of Sylhet City.....	283
BRIAN CAVILL	
- Ductal – An Ultra-high Performance Material for Resistance to Blasts ...	293
ANJAYA KUMAR PATRO AND RAVI SINHA	
- Optimal Aseismic Performance of Buildings with Friction Dampers ...	303
Y. LU, Z. WANG	
- Numerical Investigation of Structural Response to Above- Ground Explosions	313
YOSHIAKI NAKANO, HO CHOI	
- Experimental Study on Seismic Behavior and Crack Pattern of Concrete Block Infilled RC Frames	323
CHEE LEONG LIM AND TSO-CHIEN PAN	
- Simplified Methodology for Damage Assessment of 2-Storey RC Frame Subjected to Explosion-Induced Ground Motions (EIGMS)	333

HAICHENG RONG, BING LI AND TSO-CHIEN PAN	
- Effects of Exterior Cladding Panels on Responses of Multi- storey RC Frame Structures to Distant Explosions	341
SHYAM SUNDER REDDY T, RAMANCHARLA PRADEEP KUMAR	
- Earthquake Resistant Construction in the Urban Areas of Andhra Pradesh (India): Present Practices and Immediate Requirements	351
HUAN SHI, JIANG GUOPING, TAN XIANGQIAN, LIU ZHIHANG, HUANG FENGLI	
- Dynamic Response of Steel Bar in RC Under Blast Load	361
X. GU 1, Y. LU , S. GONG, Y. ZHOU	
- Statistical Study of Lethality Rate from Accidental Building Failure ...	369
YUTAKA NAKAMURA, MIKA KANEKO, HIROSHI KAMBARA, KAZUO TAMURA	
- Safety Evaluation Methodology for Building Contents Subjected to Earthquake Loading	379
MA GUOWEI, AN XINMEI, LI YONGSHENG	
- Safety Evaluation of Submerged Tunnel Against Blast Load	389
TAT-SENG LOK, CHEE-HIONG LIM	
- Full-Scale Tests of Blast Doors for Protection Against Explosion	399

SECTION 6: Environment Impact Assessment of Urbanisation

HONG CHEN, RYOZO OOKA, SHINSUKE KATO	
- Study on Optimum Design Method for Pleasant Outdoor Thermal Environment Using Genetic Algorithms (GA) and Coupled Simulation of Convection, Radiation and Conduction	409
TAKEAKI WATANABE, SHINSUKE KATO, RYOZO OOKA, TAKEO TAKAHASHI, RYOHEI KONO	
- Prediction of Pollutant Dispersion Caused by Automotive Exhaust - A Comparison Between Field Measurements and Wind Tunnel Data - ...	419
OKORO, D., IKOLO, O. A	
- Levels of Polynuclear Aromatic Hydrocarbons and Heavy Metals in Water and Sediment of Ubeji Creek, Warri River in Niger Delta Area of Nigeria	429
RYOZO OOKA, YOSHIHUMI YASUOKA, JUNICHI SUSAKI, TAKAHIRO ENDO, YOICHI KAWAMOTO, HIDENOBU NAKAI, MADOKA NAKASHIMA, REI TAKADA, MASAHIRO SETOJIMA, MANABU FUNAHASHI, KEIICHI OKADA	
- Development of New Environmental Indices for Urban Sustainability	439

JUNICHI SUSAKI, RYOZO OOKA, YOSHIHUMI YASUOKA, TAKAHIRO ENDO, YO-ICHI KAWAMOTO, HIDENOBU NAKAI, MADOKA NAKASHIMA, REI TAKADA, MASAHIRO SETOJIMA, MANABU FUNAHASHI, KEIICHI OKADA

- Extraction of Parameters from Remote Sensing Data for Environmental Indices for Urban Sustainability 447

OKORO, D., OSAKWE, J

- Environmental Impact Assessment of Heavy Metals on Fishes and Crustaceans in Ogonu Creek, Warri River in Niger Delta Area of Nigeria 457

SECTION 7: Tsunamis, Flood and Environmental Risk Assessment

TRAN THUC, NGUYEN XUAN HIEN, DANG QUANG THINH, HUYNH THI LAN HUONG

- Flood Forecast and Flood Control Structures Operation for Flood Control of Ha Noi City 465

TAWATCHAI TINGSANCHALI, AKAPOB TEERAORANIT

- Flood Control Investigation of Had Yai City, Southern Thailand 471

MASASUKE TAKASHIMA, SHUNICHI KOSHIMURA, KIMIRO MEGURO

- Development of Possible Tsunami Exposure Estimation Module for Tsunami Disaster Response 481

AKIYUKI KAWASAKI, YUICHI SATO, SATORU SADOHARA

- Creating an Integrated Water Geodatabase for Environmental Risk Management 489

NIKOLAI BOBYLEV

- Environmental Assessment of Urban Underground Infrastructure 499

ASHUTOSH KUMAR, B. RAJESH BABU, RAMANCHARLA PRADEEP KUMAR

- Interactive Structural Dynamics Learning Kit 509

SECTION 8: Advanced Technologies for Assessment of Urban Safety

KAZI REZAUL KARIM AND TSO-CHIEN PAN

- The Great Sumatra-Andaman Islands Earthquake ($M_w = 9.0$) of 26 December 2004: Potential Vulnerability of Buildings and Infrastructures in Remote Metropolitan Areas 519

ZHU QING, LI YUAN, TOR YAM KHOON

- Emergency Routing Algorithm Based on the 3D-GIS 529

TAIFENG JIANG, HONG HUANG, RYOZO OOKA	
- Application of a Coupled Simulation Method for Predicting Fire Spread in a Modeled Urban Area	539
YOICHI KAWAMOTO, RYOZO OOKA	
- Prediction of Urban Heat Island in Tokyo Metropolitan Area in 2020	549
HONG HUANG, RYOZO OOKA, SHINSUKE KATO, HONG CHEN	
- Optimal Design of Smoke Control System in Room Fire Using CFD and Genetic Algorithms	559
SHINSUKE SAWASAKI, RYOZO OOKA, TOMONORI SAKOI, KAZUYO TSUZUKI	
- Study on Thermal Evaluation of Hot Outdoor Environment Using 2-Node Model and PHS Model	569
HANSA VATHANANUKIJ	
- Geoinformatics and Public Domain System Model on Thailand Mega Prototype Safety	579
CHEN PO-HAN, FENG FENG, HSU WEN JING, DUH BEEN-LIRN	
- Path Finding in 2-Layer 1-IRS Topologies for Real-Time Evacuation Systems	585
 SECTION 9: Planning and Development of Urban Infrastructure	
KONG GUANGYA, YANG WENYI, XIAO YI, JEFFREY WANG	
- Assessment of Adverse Effects to Utilities Caused by Mass Excavation	593
YANG WENYI, KONG GUANGYA, JEFFREY WANG	
- Assessment of Building Distortion and Movement Around The Excavation Box	603
GUAN HONG TAN, YE KONG POH, MAX STRINGER, JAMES MW BROWNJOHN	
- Ubiquitous Real Time Monitoring and Alert Applied to Excavation Works	611
REIKO AMANO, HITOSHI KURIOKA, OSAMU IMAZEKI	
- Computational Fluid Dynamics Simulation of Thermal Behavior Under Working Water Screens in a Tunnel	619
CHIN-HSUN YEH, WEI-CHANG CHEN, WEN-YU JEAN, LAP-LOI CHUNG	
- Planning of Emergency Rescue Routes After Strong Earthquakes	629



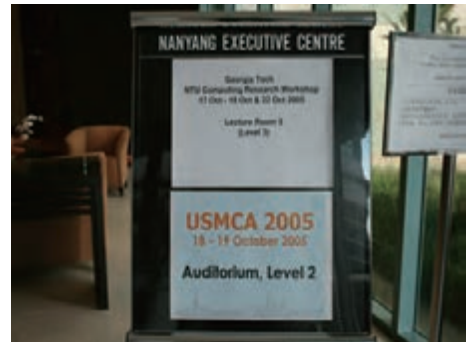
Gate of Nanyang Technological University



Symposium Venue



Entrance of Nanyang Executive Centre



Welcome Board



Reception



ICUS Corner



Auditorium



Recture Room



Opening Ceremony



John HARRISON (p.1)



Yoshifumi YASUOKA (p.3)



Kimiro MEGURO (p.9)



Teddy BOEN (p.19)



Weicheng FAN (p.31)



Pennung WARNITCHAI (p.41)



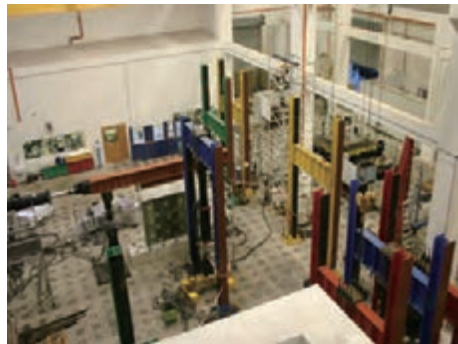
Tso-Chien PAN (p.267,277,333,341,519)



Laboratory Tour of PTRC



Shaking Table



Experiment Facility of PTRC



View from Dinner Venue



Symposium Dinner



Tat-Seng LOK (p.399)



Ceremony during Symposium Dinner



Tea Break



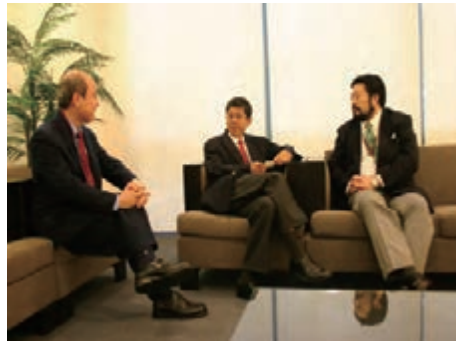
Tea Break



Lunch



Lunch



High-Level Talks



Ceremony at Plenary Speech



Channel NewsAsia



Closing Ceremony



After-Symposium Dinner



Participants Photo

Opening Session

THE NEW FACE OF AL QAEDA: THE THREAT FOUR YEARS AFTER 9-11

DR ROHAN KUMAR GUNARATNA

Head, International Centre for Political Violence and Terrorism Research
Institute of Defence and Strategic Studies, Nanyang Technological University
ISRKGunaratna@ntu.edu.sg

ABSTRACT

The terrorist threat environment has changed significantly in the past four years. First, Iraq has replaced Afghanistan as the epicentre of terrorism. Second, Al Qaeda has morphed from a group into a movement. Third, Al Qaeda has been able to influence three dozen local jihad groups to ideologically and operational emulate Al Qaeda's mandate of a global jihad.

The presentation will discuss the changing global threat environment and its implications for the Asia-Pacific. The presentation will focus on how Jemaah Islamiyah has taken over the role of Al Qaeda, both as an ideological and an operational vanguard. The presentation will conclude with an assessment of the threat to Southeast Asia by existing and emerging groups, particularly those with close links to the global jihad movement.

SATELLITE OBSERVATION NETWORK FOR ENVIRONMENT AND DISASTER MONITORING IN ASIA

Yoshifumi Yasuoka, W. Takeuchi, T. Nemoto, P. J. Baruah and T. Endo
Institute of Industrial Science, The University of Tokyo
4-6-1 Komaba, Meguro-ku, Tokyo, Japan 153-8505
Tel: +81-3-5452-6409, Fax: +81-3-5452-6408
E-mail: yyasuoka@iis.u-tokyo.ac.jp

ABSTRACT

The Institute of Industrial Science, University of Tokyo (IIS/UT) established a satellite data receiving network, SEASON (Southeast and East Asia Satellite Observation Network), for monitoring environment and disaster in Asian regions. The SEASON receives satellite data from TERRA/MODIS and AQUA/MODIS as well as NOAA/AVHRR at Tokyo (IIS/UT Campus) and at Bangkok (Asian Institute of Technology; AIT Campus). The data from two receiving stations cover Southeast and East Asian regions.

Although MODIS and AVHRR have coarse spatial resolution (MODIS; 1km, 500m and 250m, AVHRR; 1km) their frequent observation function (around twice a day at one point) enables us to monitor land/ocean surface in almost near-real time manner. Also their wide observation swath (more than 2000km) enables to observe regional to global scale phenomena such as deforestation, urbanization or land degradation. It is also expected that they may provide data for urban safety assessment in Asian mega-cities.

This presentation introduces overview of the SEASON, and demonstrates its application examples.

1. INTRODUCTION

Monitoring of environment and disaster requires the measurements of a wide variety of parameters covering physical, chemical, biological, or geographical fields. Furthermore it requires observation from local to regional/global spatial scale, and from short to long time scale. Comprehensive and efficient environment and disaster monitoring system may not be realized only with conventional ground observation methods. Remote sensing from satellite is expected to provide an effective tool for observing a wide range of environment and disaster variables from local to global scale regularly.

AVHRR on NOAA and MODIS on TERRA and AQUA are the typical earth observation sensors primarily for regional or global scale monitoring. Although their spatial resolution is coarse (MODIS; 1km, 500m and 250m,

AVHRR; 1km), their frequent observation function (around twice a day at one point) enables us to monitor land/ocean surface and atmosphere conditions in almost near-real time manner. Additionally, their wide observation swath (more than 2000km) enables to observe regional to global scale phenomena such as deforestation, desertification and urbanization. They are also expected to provide timely data for monitoring urban conditions such as urban expansion, heat island or damages due to flooding or forest fires.

The Institute of Industrial Science (IIS), the University of Tokyo (UT) has been receiving and processing satellite data from NOAA/AVHRR, TERRA/MODIS and AQUA MODIS in order to observe environmental changes and disasters in Asian regions. The IIS/UT started the reception of NOAA/AVHRR data since 1980 at Tokyo (IIS/UT Campus), and in 1997 the data receiving station of NOAA/AVHRR was deployed at Bangkok (Asian Institute of Technology; AIT Campus) in order to cover more extensive areas including Southeast Asian regions. It also started the reception of satellite data from TERRA/MODIS since 2001 and from AQUA/MODIS since 2003 both at Tokyo and at Bangkok together with NOAA/AVHRR.

The data received at AIT, Bangkok is transferred to IIS/UT within 24hours, and all data from these stations are archived in a massive data archive system at IIS/UT (600TB). All of the archived data can be accessed upon requests from users through WWW (<http://yasulab.iis.u-tokyo.ac.jp>). The IIS/UT has also been producing a variety of thematic maps for environmental and disaster monitoring including time series vegetation index maps, land and ocean surface temperature maps or forest fire maps. The system is named as SEASON (Southeast and East Asia Satellite Observation Network).

This presentation gives an overview of the SEASON and its application examples in monitoring of urban environment and disasters.

2. SYSTEM OUTLINE OF SEASON

2.1 Data Reception and Processing

Both of the satellite data receiving stations at Tokyo (IIS/UT) and at Bangkok (AIT) are equipped with L-band antenna for AVHRR HRPT signal and with X-band antenna for MODIS HRPT signal, and with data processing facilities to produce Level 1B product (geo-corrected data) for AVHRR and MODIS raw data. The data received at Bangkok is transferred to IIS/UT data archiving system via network (NECTEC and SINET) in midnight (6-7 GB/night). The system block diagram of the SEASON is illustrated in Figure 1. Satellite data coverage of two stations is illustrated in Fig. 2.

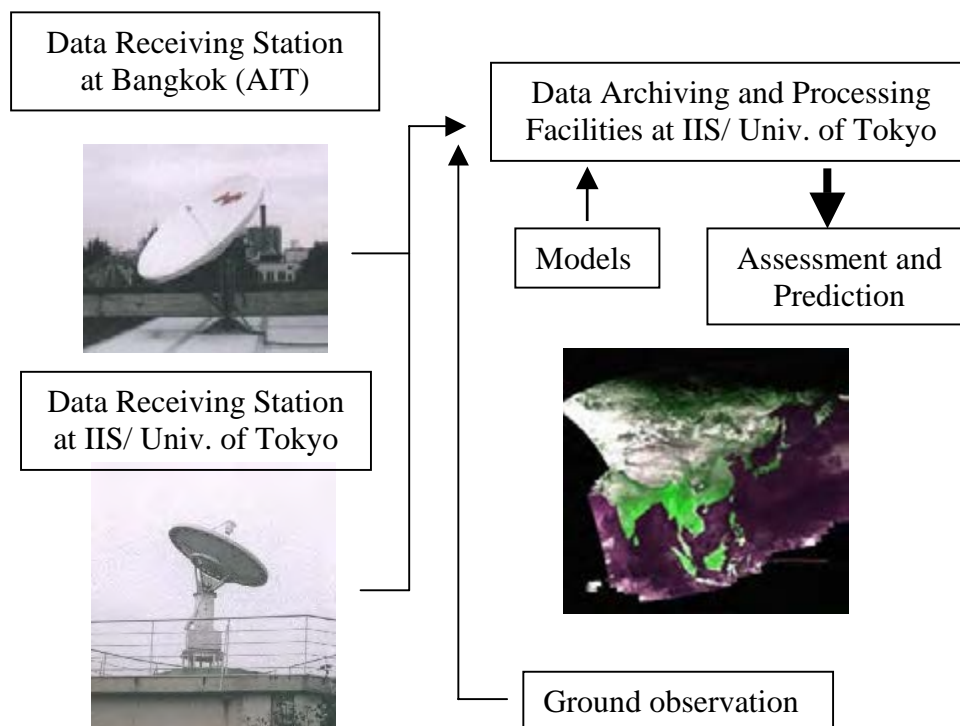


Fig. 1 System Block Diagram of SEASON

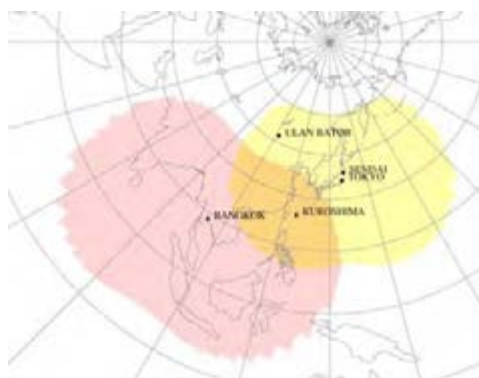


Fig. 2 Satellite data coverage of SEASON

2.2 Data Archiving and Distribution

All of the data received at Tokyo and at Bangkok have been archived at IIS/UT with a massive data archive system (600TB). So far the total data amount for AVHRR and MODIS is around 150TB. The SEASON provides all of the archived data to any users in the world free of charge through WWW (<http://yasulab.iis.u-tokyo.ac.jp>). Any user may download AVHRR and MODIS data from the ftp site by specifying satellite (AVHRR or MODIS), year/month/date, requested bands, longitude/latitude, spatial resolution (for MODIS; 250m, 500m, 1000m). The SEASON send data after geometric correction and other necessary processings.

3. TIME SERIES DATA SET FROM SEASON

Although spatial resolution of AVHRR and MODIS is coarse, periodic and frequent observation capability enables us to produce regular time series data set observing land/ocean surface or atmosphere. The SEASON has been producing time series satellite mosaic images over Asia, and a variety of thematic maps for monitoring and assessing environment and disasters. Figure 4 shows an example of time series NDVI (Normalized Difference Vegetation Index) images derived from cloud free composite AVHRR data (10 days composite; May to September, 1990). The NDVI is a satellite derived index showing how each point is covered by vegetation, and time series NDVI data may be used to assess deforestation, desertification or urbanization.

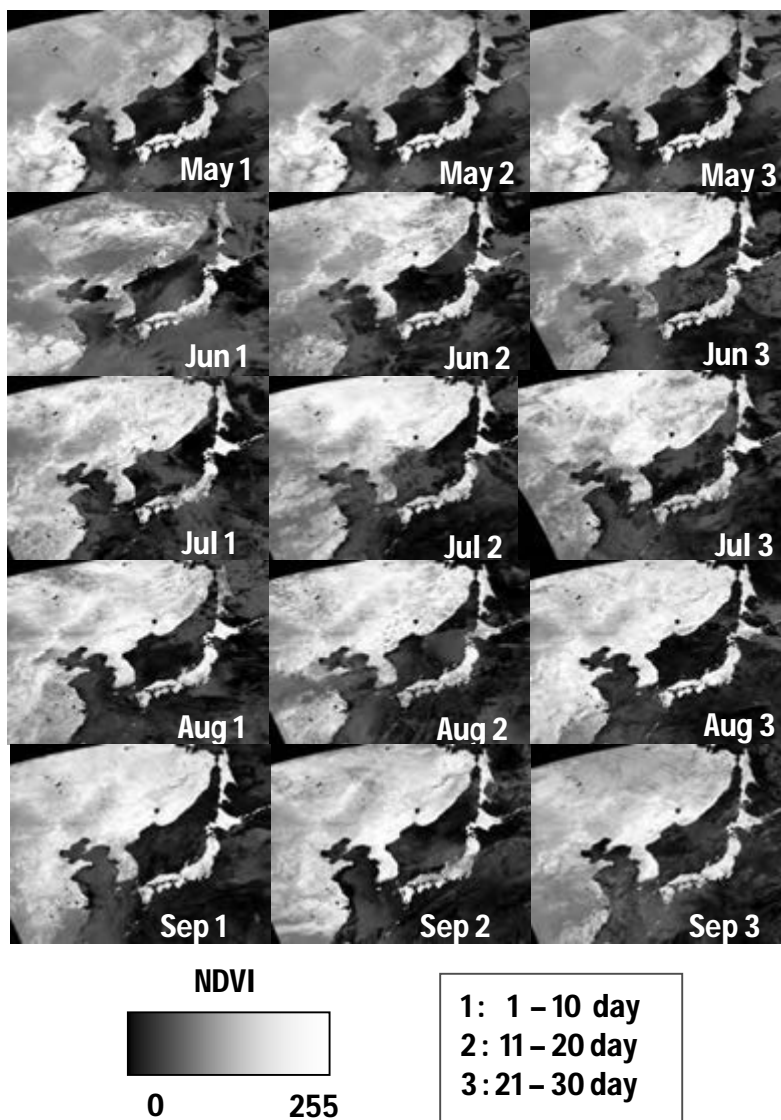


Fig. 4 Time series NDVI images (10days composite) from May to September, 1990.

Figure 5 illustrates an example of the applications of long-term NDVI data set indicating a trend of early spring with respect to vegetation green-up. In Figure 5 an inverse relationship between changes in air temperature and in the green-up day of vegetation in spring (Julian day from 1st of January) over East Asian region shown in Figure 4. The green-up day of vegetation is determined by the sharp increase in the annual NDVI pattern. Figure 5 indicates that the green-up of vegetation has been getting earlier by five days in average during these 17 years associated with temperature increase (Ooyoshi, 2002).

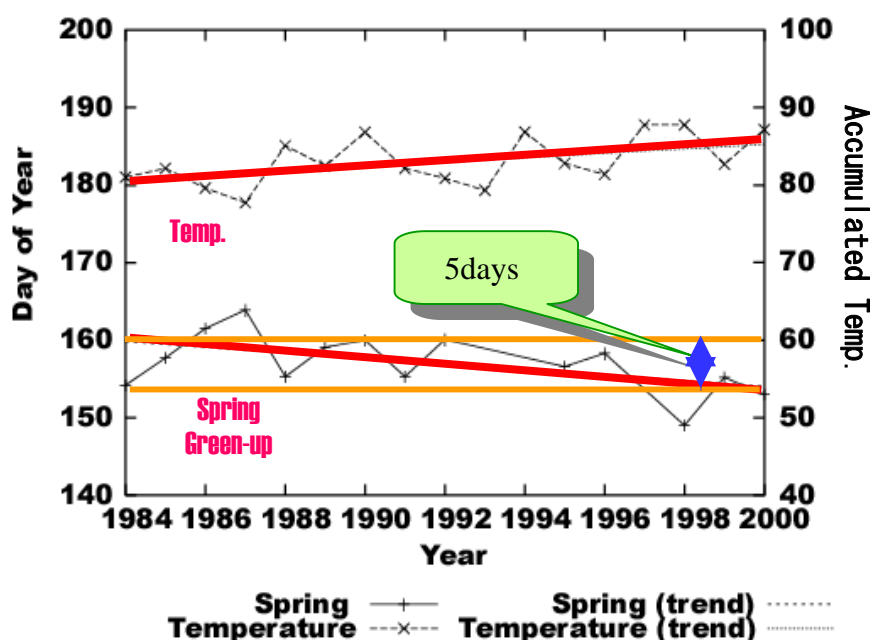


Fig. 5 Long-term trends of air temperature and the green-up in spring assessed from the NDVI data shown in Figure 4.

4. URBAN SCALE ALLICATION OF SEASON DATA SET

Monitoring of urban expansion, heat island or land cover change in and around city requires intensive spatial and geographic data. It is, however, not easy to collect spatial data over a big city area. Satellite remote sensing is one of effective tools to collect spatial data in a short period. The data from SEASON may be also applied to the monitoring of environment and disasters in urban areas.

Figure 6 shows land surface temperature distribution derived from MODIS data around Tokyo area (Fig. 6 (a)), and its temporal change in a summer season (Fig. 6 (b)). Figure 6 (b) shows that the temperature in urban area is higher than that in surrounding forest or cropland by around ten degrees, and it clearly indicates that heat island occurs in urban area (Hung, 2002).

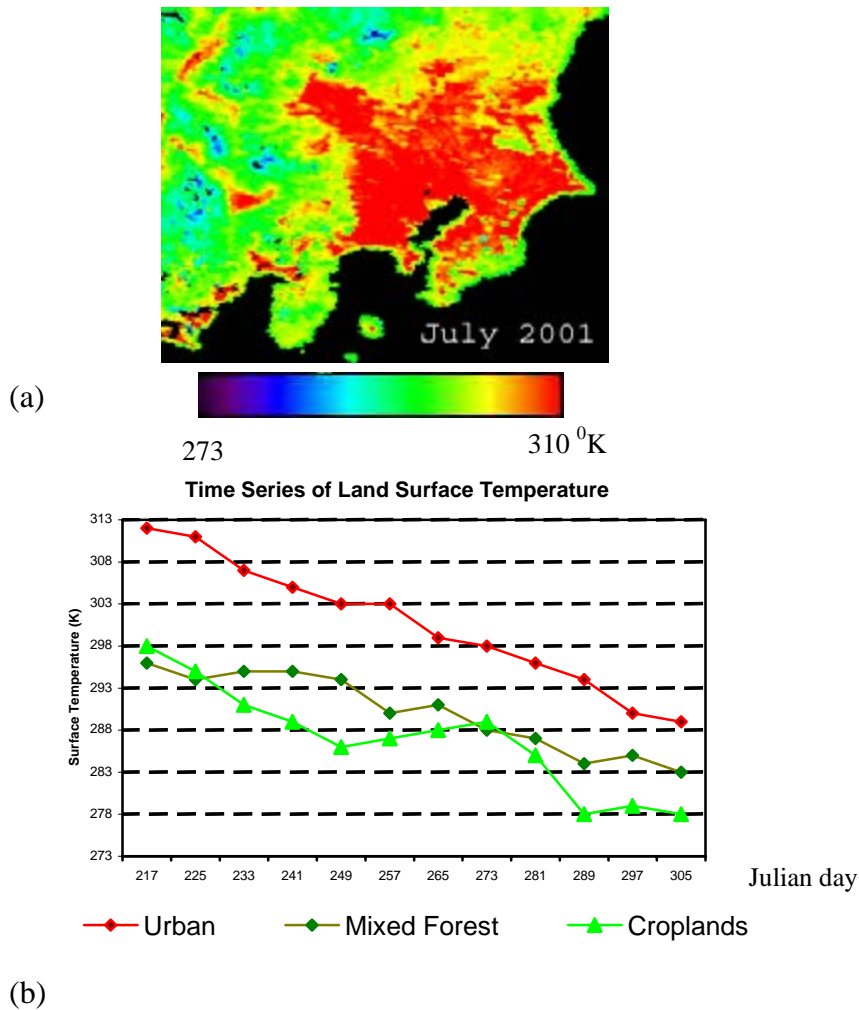


Fig. 6 Urban heat island, (a) Distribution of land surface temperature (LST) from MODIS (July, 2001), (b) Temporal change of LST in urban area, forest area and cropland area around Tokyo.

5. SUMMARIES

An Asian satellite observation network system at the IIS/UT was introduced with applications to the assessment of urban environment and disasters. Remote sensing from space is a new technology enabling us to observe a wide range of variables over extensive urban areas at a regular interval. Recent developments in remote sensing technologies have been remarkable and very rapid. It is expected to develop more practical application examples of remote sensing to urban safety management.

REFERENCES

- Hung, T., et. al. : Acquiring, Managing and Utilizing MODIS data for Research at the IIS / UT. Proc. of ACRS, 2002.
- Ooyoshi, K., et.al. : Analysis of Vegetation Phenology in East Asia, Proc. of JSPRS, Tokyo, 2004 (in Japanese with English abstract).

SHAKING TABLE TESTS OF 1/4 SCALED MASONRY MODELS RETROFITTED WITH PP-BAND MESHES

KIMIRO MEGURO

Professor, Institute of Industrial Science, The University of Tokyo, Japan
meguro@iis.u-tokyo.ac.jp

PAOLA MAYORCA

Post Doctoral Fellow, The University of Tokyo, Japan
paola@iis.u-tokyo.ac.jp

NAVARATNARAJAH SATHIPARAN

Master Degree Student, The University of Tokyo, Japan
sakthi@risk-mg.iis.u-tokyo.ac.jp

RAMESH GURAGAIN

Master Degree Student, The University of Tokyo, Japan
ramesh@risk-mg.iis.u-tokyo.ac.jp

NASROLLAHZADEH NESHELI

Post Doctoral Fellow, The University of Tokyo, Japan
nesheli@iis.u-tokyo.ac.jp

ABSTRACT

Retrofitting of low earthquake-resistant masonry structures is the key issue for earthquake disaster mitigation in developing countries as only that can reduce the probable casualty significantly. Promotion of retrofitting is possible only if the retrofitting technique considers issues of economical affordability and social acceptability together with technical feasibility. An appropriate PP-band retrofitting technique, which considers all these issues, has been developed and being studied at Meguro Laboratory, ICUS, Institute of Industrial Science, the University of Tokyo since some years.

Shaking table experiment of two masonry building models was carried out in this year to test the effectiveness of the newly developed technique. The test revealed that the technique is very effective which could enhance the seismic capacity of masonry buildings by 10 times in terms of maximum base displacement and 4 times in terms of maximum velocity. The retrofitted model survived with life safety level damage until 15 more shakings than the shaking at which the non-retrofitted building model was totally collapsed. The result suggested that the technique can enhance safety of existing masonry buildings to survive even in worst case scenario of earthquake ground motion like JMA 7. This paper describes the process and preliminary outcomes of the experiment conducted.

1. INTRODUCTION

It is seen in past and recent earthquakes that unreinforced masonry buildings, if not retrofitted, are the number one killer during earthquakes. Human

casualties due to earthquakes in 20th century are mostly due to structural damage most of which is assigned to unreinforced masonry buildings (Coburn and Spence, 2002). So, retrofitting of low earthquake-resistant masonry structures is the key issue for earthquake disaster mitigation to reduce the casualty significantly. Seismic retrofitting not only reduces the damage to buildings during earthquakes, but also the costs of rescue and first aid activities, rubble removal, temporary residence building, and permanent residence reconstruction to re-establish normal daily life (Yoshimura and Meguro, 2004).

Different masonry retrofitting techniques are available however, effective retrofitting technique should guarantee not only its efficiency in terms of improvement of the seismic resistant characteristics of the structure (strength, ductility and energy dissipation) but also locally and economically availability of material and easy-to-use method. Considering these issues of developing appropriate seismic retrofitting techniques for masonry buildings to reduce the possible number of casualties from future earthquakes in developing countries, a technically feasible and economically affordable PP-band retrofitting technique has been developed and different aspects are being studied in Meguro Laboratory, ICUS, Institute of Industrial Science, The University of Tokyo since some years (Mayorca and Meguro, 2004).

This year, shaking table experiments were carried out to understand dynamic response of buildings, propagation and distribution of crack patterns, failure behavior, and overall effectiveness of seismic retrofitting technique.

2. EXPERIMENT PROGRAM

2.1 Specimens Construction

For shaking table experiment, two models were built in the reduced scale 1:4 using the burnt bricks as masonry unit and cement, lime and sand (1:8:20) mixture as mortar. Attention has been made to make the models as true replica of brick masonry buildings in developing countries in terms of masonry strength even though the construction materials used were those available in Japan. Both the models represented a one-storey box-like building without roof. Both the buildings were of dimension 950x950x720 mm³ with wall thickness 50mm. The sizes of door and window in opposite walls were of size 243x485mm² and 325x245mm² respectively.

One of the buildings was retrofitted with PP-band mesh after construction. The geometry, construction materials and proportion, construction process and technique, cement/water ratio and other conditions that can make difference in strength of the building models were kept identical for better comparison of the effectiveness of the newly developed retrofitting technique for enhancing the seismic safety of masonry buildings. The cross-section of the band used was 6x0.24mm² and the pitch of the mess was 40mm. The retrofitting procedure is described in section 2.2. The non-retrofitted model is named as “N-B-40” and retrofitted one by “R-B-40” to use in this paper. The mechanical properties of masonry in terms of

compressive, shear and bond strength was similar to the material used for construction in both the cases (Table 1).

Table 1: Mechanical Properties of the Masonry

Property	N-B-40	R-B-40
Compressive strength (MPa)	20.96	20.30
Shear strength (MPa)	0.074	0.075
Bond strength (MPa)	0.085	0.074
Diagonal compression strength (MPa)	0.173	0.181

2.2 Retrofitting Process

Most of the residential buildings in developing countries are of non-engineered type and owner built. The case of Nepal has been taken here as an example, where more than 98 % of the buildings are constructed by the owners following the advice of local craftsmen. In both urban and rural areas the traditional craftsmen, who are not given any specific training on seismic safety and they do not have adequate access to information related to safer building practices, play the pivotal role (Dixit, 2004). So the implementation procedure for retrofitting technique for masonry buildings should be as simple as possible to be applicable for developing countries.

Installation procedure (Figure 1) for PP-band retrofitting technique is simple enough to understand and apply by the craftsmen and homeowners without any prior knowledge and expertise on earthquake engineering. Thus, it is expected to meet the very critical requirement of developing countries, the “easy-to-use” method, for promoting safer building construction.

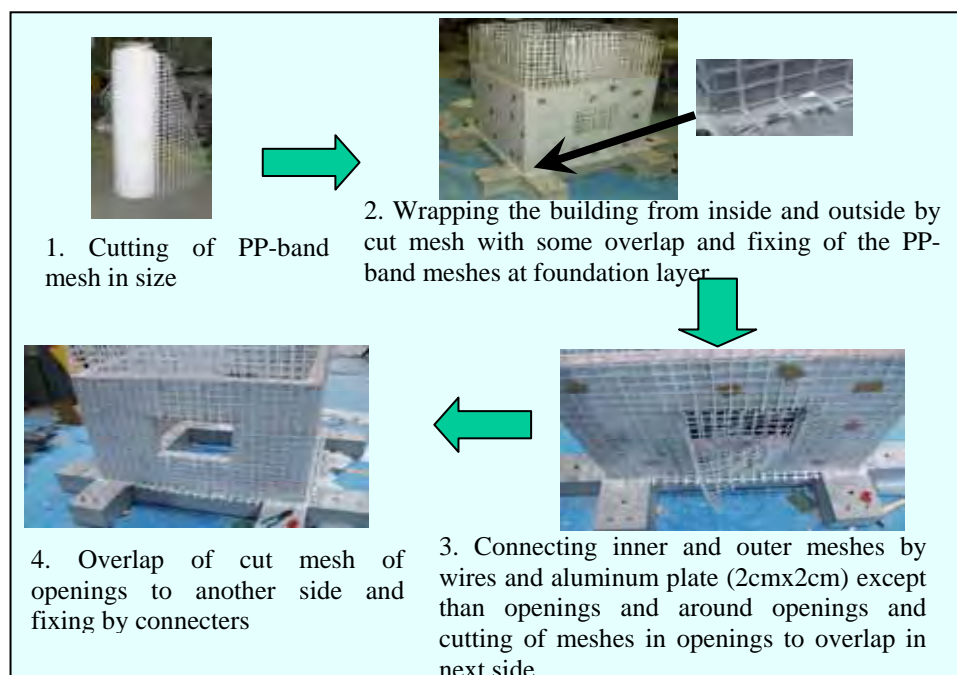


Figure 1: Retrofitting Process

2.3 Instrumentation

The tests were carried out in the shaking table facility available in the Institute of Industrial Science, the University of Tokyo. The size of the shaking table is $1.5 \times 1.5 \text{ m}^2$ and it has six degrees of freedom which operates in frequencies ranging from 0.1 to 50 Hz. It has a maximum displacement capacity of $\pm 100 \text{ mm}$ and maximum weight of the specimens that can be tested is 2 tons.

To study the global and local behavior of the buildings during shakings, accelerations and displacements at different places were measured with accelerometers and lasers, respectively. During the tests, twelve accelerometers, four with three-dimensional measurement capacity and eight with one-dimensional measurement capacity were installed. Seven lasers, four in N-S direction and three in E-W direction were used to measure displacements.

2.4 Input Motion

Simple easy-to-use sinusoidal motions of frequencies ranging from 2Hz to 35 Hz and amplitudes ranging from 0.05g to 1.4g were applied to obtain the dynamic response of both retrofitted and non-retrofitted structures. This simple input motion was applied because of its adequacy for later use in the numerical modeling. Figure 2 shows the typical shape of the applied sinusoidal wave.

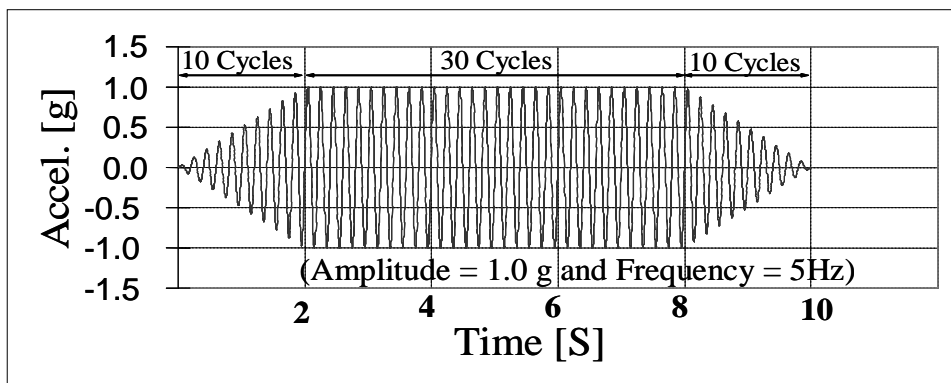


Figure 2: Typical Shape of Input Sinusoidal Motion

Loading was started with a sweep motion of amplitude 0.05g with all frequencies of 2Hz to 35Hz for identifying the dynamic properties of the models. A total of 46 runs were applied to N-B-40 while as 16 more runs were applied to R-B-40 with 62 as a final run. Sequence of loadings for each successive runs is given in Table 2. The numbers in table indicate the run numbers. General trend of loading was from high frequency to low frequency and from lower amplitude to higher amplitude. Higher frequencies motions were skipped towards the end of the runs.

Table 2: Loading Sequence

Amplitude	Frequency							
	2Hz	5 Hz	10 Hz	15 Hz	20 Hz	25 Hz	30 Hz	35 Hz
1.4 g		59	58	57				
1.2 g		56	55	54	53			
1.0 g	62	52	51	50	49			
0.8 g	61	47	44	41	38	35	32	29
0.6 g	60	46	43	40	37	34	31	28
0.4 g	48	45	42	39	36	33	30	27
0.2 g	26	25	24	23	22	21	20	19
0.1 g	18	17	16	15	14	13	12	11
0.05 g	10	09	08	07	06	05	04	03
Sweep	01, 02							

- Loading steps for both non-retrofitted and retrofitted models
- Loading steps for retrofitted model after non-retrofitted model building collapsed

3. FINDINGS

3.1 Crack Patterns and Energy Dissipation Mechanism

Initial cracks pattern in both the models, non-retrofitted and retrofitted were similar with some variation. The cracks get widened and widened in each successive loading after major cracks occurred in case of non-retrofitted model. However, more new cracks were propagated in retrofitted case.

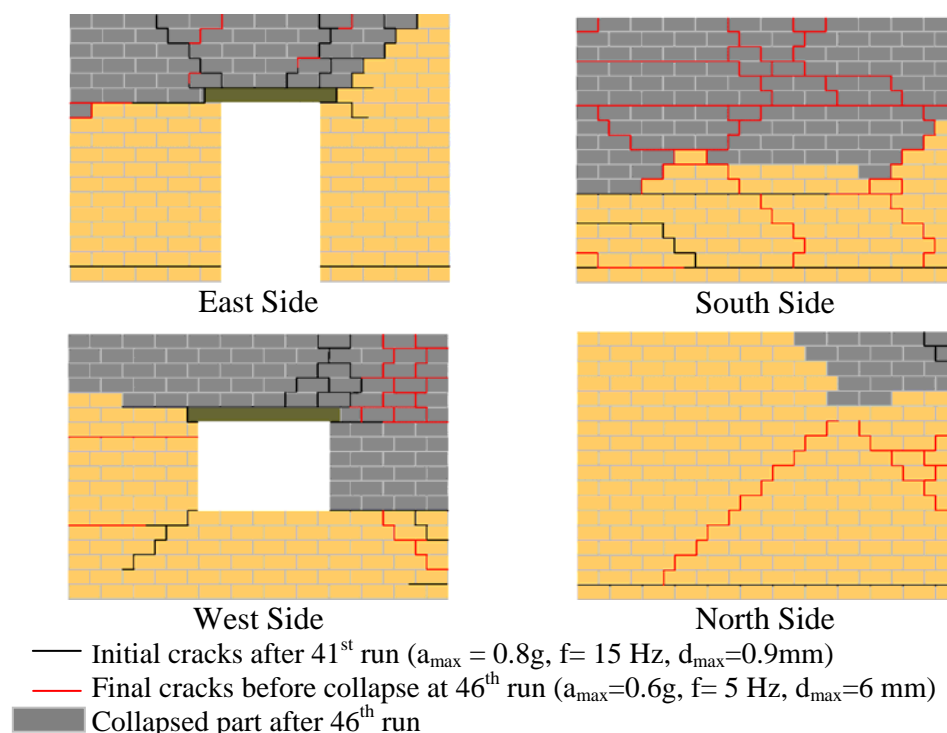


Figure 3: Crack Patterns of Non-retrofitted Building Model

Figure 3 shows the crack patterns of the non-retrofitted model while as Figure 4 is the case of retrofitted one. In case of non-retrofitted building model, cracks started from top corner of the openings in the 27th run. Horizontal cracks at base level of east and north walls were observed in the 28th run; cracks at corner of the openings propagated up to top layer of the wall, significant diagonal cracks were observed in both walls with openings and flexural crack at the bottom layer of the south side wall was also observed in the 35th run. The 44th run was the critical run to the non-retrofitted model in which, a large vertical crack was observed in top part of south side wall and was bent inside tentatively by 14 mm at the top-middle and partially separated from bottom wall. The top part of the west wall (part, above the door opening) was totally separated from the specimen and it was removed from specimen before next test run proceed. The 46th run led the non-retrofitted structure collapse.

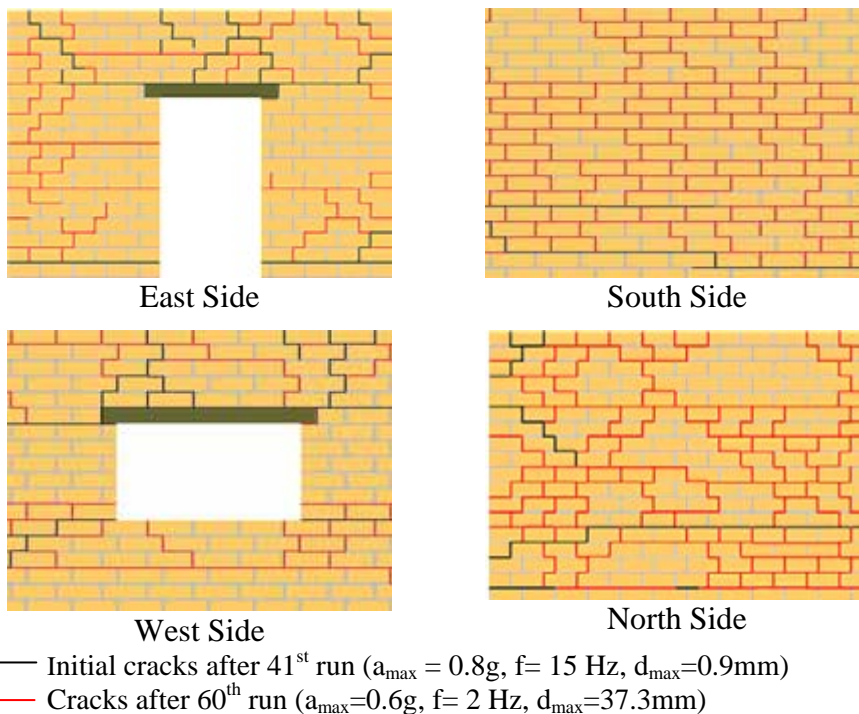


Figure 4: Cracks Pattern of Retrofitted Building Model

In case of retrofitted building model, similar cracks as non-retrofitted building was started from top corner of the opening in the 27th run. Horizontal cracks at base layer of east and south walls were observed in the 28th run, cracks propagated horizontally from top and bottom corner of the openings in the 29th run, some diagonal cracks were observed at top part of the walls with openings in the 35th run, many cracks in all four walls were observed in the 44th run, and many new cracks were observed until the 46th run. The process of widening of the cracks already occurred and propagation of new cracks was continued to 15 more times until the run 61. In later stages, there was significant permanent deformation to the structure. At the final stage of the test, by the 62nd run, with 63.4mm base

displacement, 10 times more than the input displacement applied in the 46th run and 4 times more velocity, almost all the brick joints were cracked and building had substantial permanent deformations. However, building did not loose the overall integrity and stability and collapse was prevented in such a high intensity of shaking. Thus, the PP-band retrofitting technique maintained the integrity of the structural elements preventing from separation and collapse. Further, the retrofitted model showed the better energy dissipation mechanism as many new cracks were propagated without loosing the overall integrity and stability of the structure.

3.2 Failure Behavior and Performance Evaluation

The performances of the non-retrofitted and retrofitted models are assessed based on the damage level of the buildings at different levels of shaking. Performances were evaluated in reference to three levels of performances: Immediate Occupancy, Life safety and Collapse Prevention based on damage levels described in (FEMA 356, 2000). The criteria for different performance levels in case of non-retrofitted case were taken as criteria for Unreinforced Masonry (Nonfill) Walls defined in FEMA 356, Table C1-3: Structural Performance Levels and Damage. The equivalent JMA intensities were calculated based on the input motions to the structures at different runs. Table 3 below shows the performances of non-retrofitted building models with different JMA intensities.

Table 3: Performance of Non-retrofitted Building Model in Different JMA Intensities

Acceleration (g)	Frequency (Hz)							
	2	5	10	15	20	25	30	35
1.4								
1.2								
1.0								
0.8			PC	LS	LS	LS	IO	IO
0.6		TC	LS	LS	LS	IO	IO	IO
0.4		PC	LS	LS	LS	IO	IO	IO
0.2	IO	IO	IO	IO	IO	IO	IO	IO
0.1	IO	IO	IO	IO	IO	IO	IO	IO
0.05	IO	IO	IO	IO	IO	IO	IO	IO

Index	JMA ~4	JMA 5-	JMA 5+	JMA 6-	JMA 6+	JMA 7
-------	--------	--------	--------	--------	--------	-------

IO: Immediate Occupancy
 LS: Life Safety
 CP: Collapse Prevention
 PC: Partial Collapse
 TC: Total Collapse

Partial collapse of the non-retrofitted building was occurred at the 44th run at intensity JMA~4 (Photo 1) and total collapse at the 46th run (Photo 2) at intensity JMA 5- but it should be noted that the model was already cracked in different loadings as discussed in section 3.1.



Photo 1: Partial Collapse of Non-retrofitted Building Model at the 44th run (Seismic Intensity, 4 JMA Scale)



Photo 2: Collapse of Non-retrofitted Building Model at the 46th run (Seismic Intensity, 5 JMA Scale)

The damage criteria for retrofitted building model are taken from FEMA 356, Table C1-3 for reinforced masonry walls. The drift limit criteria which are only 0.6% and 1.5% for life safety and collapse prevention level for reinforced masonry building was exceeded by the tested model retrofitted by PP-band technique. However, the overall damage level was not much as described in FEMA in relation to the drift. More drift than reinforced masonry building is logical if the characteristics of the PP-band mesh, which is many times less stiff than steel, is considered. So the drift criteria for reinforced masonry buildings could not be directly applied in this case and performance evaluation was done based on the overall damage to the structure. Table 4 below shows the performance of the retrofitted building model at different JMA intensities.

Table 4: Performance of Retrofitted Building Model with Different JMA Intensities

Acceleration (g)	Frequency (Hz)							
	2	5	10	15	20	25	30	35
1.4		LS	LS	LS				
1.2		LS	LS	LS	LS			
1.0	CP	LS	LS	LS	LS			
0.8	LS	LS	LS	IO	IO	IO	IO	IO
0.6	LS	LS	IO	IO	IO	IO	IO	IO
0.4	LS	LS	IO	IO	IO	IO	IO	IO
0.2	IO	IO	IO	IO	IO	IO	IO	IO
0.1	IO	IO	IO	IO	IO	IO	IO	IO
0.05	IO	IO	IO	IO	IO	IO	IO	IO

Index	JMA ~4	JMA 5-	JMA 5+	JMA 6-	JMA 6+	JMA 7
-------	--------	--------	--------	--------	--------	-------

IO: Immediate Occupancy
 LS: Life Safety
 CP: Collapse Prevention

PC: Partial Collapse
 TC: Total Collapse

The retrofitted building performed at life safety level of damage at 46th run at which the non-retrofitted building was collapsed. Moreover, life safety level of performance was maintained until 15 more runs after the 46th run leading to intensity JMA 6+. In the 62nd run, another JMA 6+ intensity shaking, the building got the collapse prevention level of damage, which is crushing, extensive cracking, damage around openings and corners and some fallen units according to FEMA 356 definition.

Considering the pre-damage level of building during previous loadings including very high intensity shakings it can be interpreted that the retrofitting technique can achieve reasonable safety even in worst case scenario of earthquake like JMA 7. Further, this technique may also be applicable to retrofit earthquake damaged buildings as it was effective even after masonry had severe cracks.

As the model was already considerably deformed beyond the limit of measurement system, test was stopped after the 62nd run. Photos 3 and 4 show the retrofitted building after the 46th run and at the final stage of the test after the 62nd run, respectively.



Photo 3: Retrofitted Building Model after 46th run (Seismic Intensity 5- JMA Scale)



Photo 4: Retrofitted Building Model after 62nd run (Seismic Intensity 6+ JMA Scale)

It should be noted again that this building model survived 15 more shakings in which many runs were with higher intensities than JMA 5- at which the non-retrofitted building was collapsed before reaching to the final stage at the 62nd run.

CONCLUSION

Two brick masonry building models, identical in terms of masonry strength and geometry were constructed and one model was retrofitted with an easy-to-install and economic retrofitting technique. Both models were tested on shaking table by applying similar input motions. Dynamic behaviors of the models were studied. Cracks patterns were analyzed and failure behavior and performances were evaluated. The result showed that the pp-band retrofitting technique enhanced the seismic resistance capacity of the building model significantly, specifically the life safety performance capacity of the building was enhanced from JMA~4 to JMA 6+ and collapse

prevention safety level was achieved until the final stage. From the result, it was found that this retrofitting technique can enhance safety of existing masonry buildings even in worst case scenario of earthquake ground motion like JMA 7 and thus is one of the optimum solutions for promoting safer building construction in developing countries.

REFERENCES

- Coburn, A. and Spence, R. 2002. *Earthquake Protection*. West Sussex: John Wiley & Sons Ltd.
- Yoshimura, M. and Meguro, K., 2004. Proposal of Retrofitting Promotion System for Low Earthquake-Resistant Structures in Earthquake Prone Countries. *Proceedings on 13th World Conference on Earthquake Engineering*, Vancouver, Canada.
- Paola Mayorca, P. and Meguro, K., 2004. Proposal of an Efficient Technique for Retrofitting Unreinforced Masonry Dwellings. *Proceedings on 13th World Conference on Earthquake Engineering*, Vancouver, Canada.
- Dixit, A.M., 2004. Promoting Safer Building construction in Nepal. *Proceedings on 13th World Conference on Earthquake Engineering*, Vancouver, Canada.
- FEMA 356, 2000. *Prestandard and Commentary for the Seismic Rehabilitation of Buildings*. Federal Emergency Management Agency

RECONSTRUCTION OF HOUSES IN ACEH SEVEN MONTHS AFTER THE EARTHQUAKE & TSUNAMI, DECEMBER 26, 2004

TEDDY BOEN

Senior Advisor of WSSI (World Seismic Safety Initiative)

Jakarta, Indonesia

tedboen@cbn.net.id

ABSTRACT

The Dec 26, 2004 earthquake of M 9.0 that shook Aceh and the subsequent Tsunami catastrophe was one of the worst natural disasters in modern history. The world - governments and people – responded with unprecedented generosity in solidarity with the rescue and relief efforts of the affected communities and local and national authorities. This has been very useful in reducing or mitigating the consequences of the disaster, and particularly in speeding the current recovery and reconstruction efforts. In the wake of the recovery and reconstruction of houses in Aceh, many NGOs and donors tried to re-invent the wheel in earthquake resistant houses by introducing house types that are not compatible with the local culture and also neglect social problems.

Key Words: Earthquake, Tsunami, Non-Engineered, Reconstruction, Local Culture

1. INTRODUCTION

In general, buildings can be divided into two main categories, namely engineered buildings and non-engineered buildings. Approximately 70 % of the buildings inventory in Indonesia consists of urban and rural non engineered buildings, about 20 % mid rise buildings and 10 % high-rise buildings.

Non-engineered buildings are buildings which are spontaneously and informally constructed in various countries in the traditional manner without any or little intervention by qualified architects and engineers in their design and can be divided into two main categories. The first category; dwellings (non-engineered buildings) constructed in small towns and villages are built according to tradition, their types suiting the culture and materials available in that area. This type of buildings is generally also called indigenous or vernacular buildings. Indigenous buildings are gradually fading and replaced with the second category of non-engineered buildings, namely either city type masonry construction or a combination of traditional look only (very few) but not adopting the traditional skills and crafts in detailing, material use, etc. The traditional houses generally have a good record or performance in past earthquakes.



Figure 1: Indigenous or Vernacular Houses in Aceh

However, as the economic condition is prospering, there is a strong trend towards the construction of masonry houses and measure of status is associated with the owners of such masonry houses. Such type of masonry construction has become a *new culture* all over Indonesia and from past earthquakes it is evident that provided they were built with good quality materials and good workmanship, they survived the most probable strongest earthquake in accordance with the Indonesian seismic hazard map

From documenting past earthquake damages in various areas in Indonesia over the past 30 years, it can be stated that in almost all rural as well as urban areas all over Indonesia, a good earthquake resistant design feature can be identified, namely almost all masonry buildings are built with reinforced concrete framing, consisting of the so called “practical columns and beams”. In Indonesia, the damage and collapse of the new culture “non-engineered” masonry buildings are mostly caused by the poor quality of materials and poor workmanship, resulting in, among others poor detailing, poor concrete quality, and poor brick lying.



Figure 2: “New Culture”, One or Two Story Masonry Houses

2. AREAS IN BANDA ACEH AFFECTED BY THE DEC 26, 2004 TSUNAMI

In general there are two zones affected by the tsunami, zone 1 is the coastal areas which were destructed by the tsunami forces such as battering, scouring, impact and buoyancy. In Banda Aceh this zone goes up to 3 km inland. Zone 2 was only inundated, where the tsunami force is already

reduced and only caused flooding, dumping mud and debris. This area is approximately 0.5 to 1.5 km further inland.

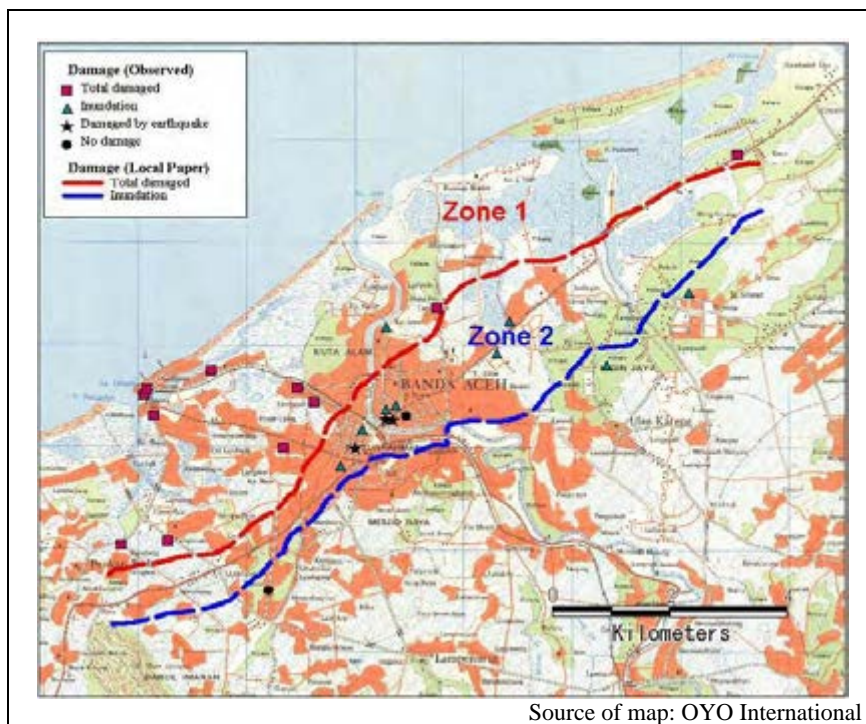


Figure 3: Damaged & Inundation Zones in Banda Aceh

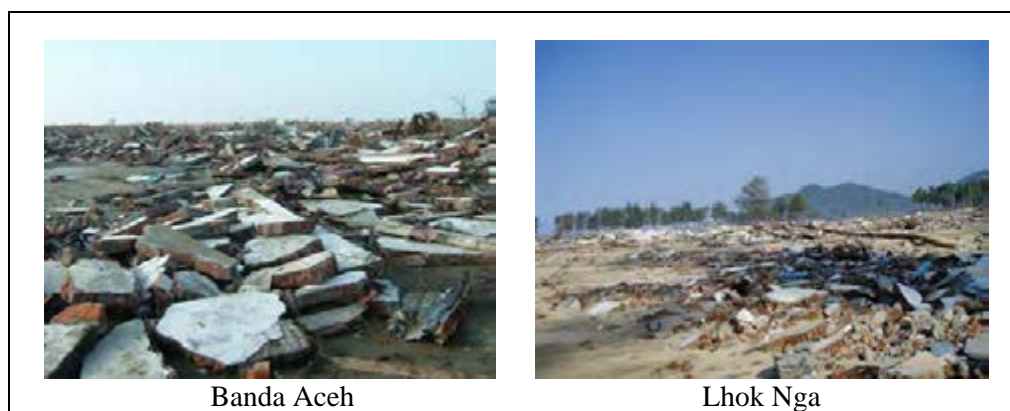


Figure 4: Settlement Destroyed in Zone 1

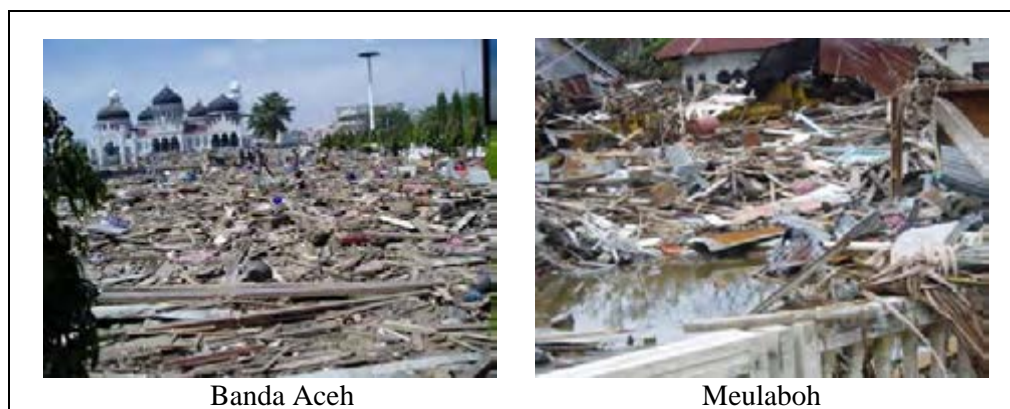


Figure 5: Wreckage and mud in Zone 2

3. NON ENGINEERED BUILDINGS IN ACEH

The majority of the buildings that collapsed in Banda Aceh city, and villages in Lhok Nga, Krueng Raya, Meulaboh city and villages along the West coast of Aceh, are non engineered buildings consisting of two types. The first type is a one or two stories buildings made of burnt brick confined masonry using sand and Portland cement mortar. The roof mostly consists of galvanized iron sheets. All those buildings used RC “practical” columns and beams as confinement. The second type is timber construction consisting of a timber frame and also timber planks walls and usually use galvanized iron sheets as roof. This is in line with the facts obtained during past earthquakes surveys in various areas all over Indonesia as mentioned in the introduction. And such timber and masonry houses are in accord with the local culture that should be rebuilt because it is sustainable. If necessary improve the quality and strength and not trying to re-invent the wheel.



Satellite Image, Source: Digital Globe

Figure 6: Banda Aceh Northern Shore One or Two Story Masonry or Timber Houses



Satellite Image, Source: Digital Globe

Figure 7: Meulaboh, One or Two Story Masonry or Timber Houses



Figure 8: One or Two Stories Masonry Buildings (First Type)



Figure 9: Timber Houses (Second Type)

Almost none of the people's housing, one to two story masonry buildings, collapsed by the Dec 26, 2004 earthquake shaking, even though some had cracks in the walls. The destruction was caused by the tsunami forces.

The ratio of those two types of structures is estimated to be 30 % to 70 %. The epicenter of the M9.0 earthquake is approximately 240 km SW of Banda Aceh, therefore the shaking was not too significant and timber as well as masonry structures were reasonably built and could withstand the M9.0 earthquake shaking.

4. RECONSTRUCTION OF HOUSES IN ACEH

As mentioned above, the coastal areas up to approximately several km inland were practically "wiped out" and buildings wrecked and disintegrated. Approximately 120,000 houses were destroyed. As is well-known, right after the Dec 26, 2004 tsunami, the world - governments and people – responded with unprecedented generosity in solidarity with the rescue and relief efforts of the affected communities and local and national authorities. Approximately \$ 7 billion has been pledged for humanitarian emergency relief and reconstruction assistance to Tsunami affected areas. This has been instrumental in reducing or mitigating the consequences of the disaster, and in boosting the current recovery and reconstruction efforts. Apart from the pledged funds from donor countries, funds in the possession of NGOs working in Aceh are estimated \$ 1 billion.

In Aceh, the government declared that the emergency response must be terminated on March 26, 2005. Subsequently all foreign armies pulled out and NGOs as well as UN agencies started activities related to the reconstruction of houses and infrastructure. Normaliter, in preparation of such reconstruction, an in-depth study must be conducted regarding available site-specific information, studying the local social, economic, and cultural constraints, and the limitations of local material as well as human resources. Such study is necessary to absorb an appreciation of the local family life as well as social life and the cultural patterns. Reconstructing destroyed settlements as is the case with Aceh in fact is a special case, different from areas with lower level of damage. In heavily damaged settlements, the social structure of the community is disrupted and many village chiefs died during the tsunami. Building in such cases is not only about the physical but also the social order of the community must be re-established. In fact, in such heavily damaged areas, it is easier to focus on repair and reactivation of the physical infrastructure and is usually the first priority for reconstruction. Also, such areas could be viewed as a site for “urban renewal”. However, due to land titles of the tsunami survivors, drawing new plans will be difficult. The National Planning Board completed the master plan for the rehabilitation and reconstruction of Aceh and Nias three months after the tsunami and the master plan introduced buffer zones for Aceh and suggested that the areas with total destruction shall not be reoccupied. If strictly followed this means an area up to approximately 2 km inland will be vacated and in Banda Aceh it covers an area of approximately 15 km². The plans prepared were not practical and lack sufficient vision. The main reason is, all planning authorities are dependent upon their architects and engineers. Architects and engineers usually work for clients in towns, they, in fact, have experience in buildings only under the peculiar conditions prevailing in towns. Therefore, the rebuilding plans were prepared without adequate site specific input and understanding of the risk, thus undermining their political acceptability. Apart from that, the plans for rebuilding were untimely, three months after the disaster. The stipulations about the buffer zones are very confusing and not rational. In the meantime, as a result, some victims returned to their lands and started rebuilding, some without any consideration of future losses.



Figure 10: People Started Rebuilding Using Salvaged Materials

Several weeks after the master plan was issued, the government activated the Aceh Rehabilitation and Reconstruction Agency (BRR). Apparently BRR took a more rational approach regarding the buffer zoning by allowing people to return to their original places and rebuild their houses on their respective original lands. However, some villages were relocated and many of the new sites do not take into account of the following; access to water, access to public services, access to public transportation, access to and integration with adjacent neighborhoods; access to religious site, recreation, etc. Most probably those sites are socially unacceptable. Post earthquake disaster relocation is frequently used but seldom studied. Appropriate planning and analysis shall be made prior to recommending implementing post earthquake disaster relocation. Post earthquake disaster relocation attempt most often cast in terms of increasing physical safety and in doing so, may have unintended consequences of increasing social disruption.

In the meantime, numerous NGOs started to “adopt” several villages to be reconstructed and started discussing with village chiefs about their intentions and some NGOs even discussed the reconstruction plan with the to be recipients. Many NGOs signed an MOU, subsequently built one or two “model houses” and put their respective banners in front of those model houses. Numerous organizations did not follow up their pledges and could not be contacted because they were no longer at the registered addresses.

In many cases, the lack of immediately available site-specific information is coupled with the influx of many so-called “experts” (local and foreign) offering an endless number of earthquake resistant building type “solutions”. Unfortunately, those “experts” lack technical capacity and a clear understanding of the local building culture and the social order of the community as well as the ability to adapt disaster resistant techniques to local styles and situations. Many NGOs ended in trying to “re-invent the wheel” by introducing house types defying the local culture. Their experts (local and foreign) tend to take into account the resources of their work environments in their respective countries; they assume the existence of the experienced building contractors and the sophisticated materials that are always used into building and they assume naturally that their client can pay for them. However, there are few NGOs that construct houses based on the prevailing culture in Aceh.



Figure 11: “Re-Invent the Wheel”: House Types Defying the Local Culture



Figure 11(cont'd): “Re-Invent the Wheel”: House Types Defying the Local Culture

There is reason to believe that several NGOs do not differentiate type of houses between immediate shelter needs (which were already built by the government); medium term / transition houses and permanent houses (which are appropriate to restore their livelihood). Most of the houses already built are of the transition type but built on permanent former lands belonging to recipients. From past experiences all over the world, such “temporary/transition” houses become permanent and the final reconstruction stage fails to materialize.

Also no phase construction which will allow phasing of occupancy is observed. Usually phase construction is adopted to construct transition houses on the site and allow early occupation while the permanent houses are being constructed.

From built houses it can also be observed that no needs assessments were performed prior to the construction of the houses. There is no differentiation made in the range of the target group among the disaster victims, whether they belong to the very low income or the moderate income group or even middle class up group. From the houses that were not destroyed it is clear that many of them belong to the middle class up group. Even BRR did not consider this social constraint and generalized the requirement for victims need and stipulate a house of 36 m² with a budget Rp. 28,000,000,-. It will be more appropriate if the requirement is the quality and not the cost.

The site developments by NGOs also do not consider roads and path, drainage systems, sanitary systems, provision for water supply and electric power as parallel activities when planning the site layout. In almost all sites that are already reconstructed so far, no clear indication can be seen regarding the planning of the infrastructure mentioned earlier and no

indication of the application of progressive occupation with a continuous upgrading of services. Only few organizations prepared layout plans that consider the long term living environment. Inappropriate layout plans could end up in creating slums long after the memory of the disaster has faded.



Figure 12: Site Developments by NGOs with no Planning of Roads and Paths, Drainage, Sanitary Systems, Provision for Water Supply and Electric Power

Most of the NGOs subcontract the construction of houses and the to be recipients were left as by standers. NGOs should in fact play a role of facilitator instead of construction agencies and direct participation of the recipients would be more appropriate.

It is also not clear which seismic standards were being adopted by some NGOs since many houses were built based on “nail and hammer” methodology without considering the slightest basic principles of carpentry. One organization built “precast” houses that consist of 1 m elements for the foundation, columns as well as beams. The joints of the elements used bolts. Such types of “precast” construction defy any established standards for earthquake resistant design of “precast” buildings.



Figure 13: Timber Beams & Columns Connection by “Nail & Hammer”

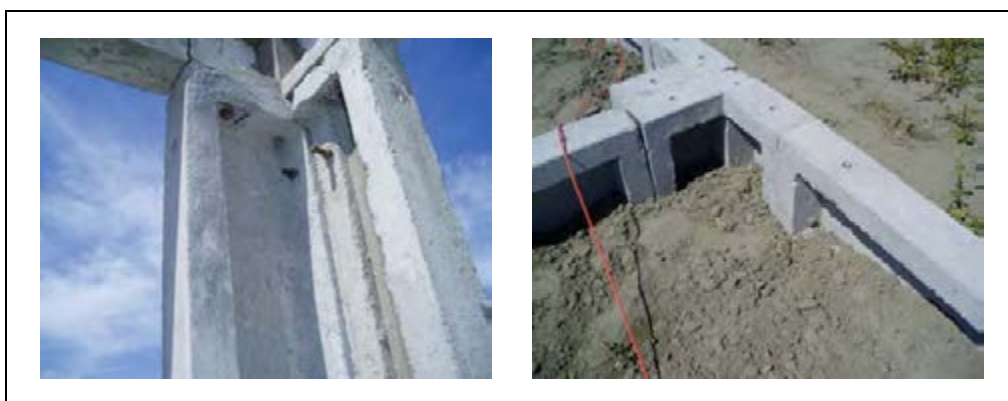


Figure 14: “Precast” Houses, Joints Using Bolts

5. CONCLUSIONS

- The houses compatible with the local culture in Aceh are one story timber houses and one or two story masonry houses.
- The main design parameter for houses is resistance to ground shaking.
- Organizations involved in the reconstruction of houses in Aceh should study past local experiences and local research in the respective field and it is not advisable to complicate the matter by trying to re-invent the wheel.
- Organizations involved in the reconstruction of houses in Aceh should act as facilitators and not as contractors or developers.

REFERENCES

- World Bank, 2005. *Rebuilding A Better Aceh & Nias. Preliminary Stocking of the Reconstruction Effort, Six Months after the Earthquake & Tsunami.*
- Directorate General of Human Settlement Ministry of Public Works, 2005. *Post Disaster Damage Assessment in Nanggroe Aceh Darussalam.*
- Boen, T., 2005. Nias / Simeulue Earthquake March 28, 2005. *EERI Journal, Vol.39.*
- Boen, T., and Jigyasu, Rohit, 2005. *Cultural Considerations for Post Disaster Reconstruction Post-Tsunami Challenges.* UNDP Conference.
- Boen, T., 2005. Sumatra Earthquake, 26 December 2004. *Special Report ICUS.*
- Boen, T., 2003. *Earthquake Resistant Design of Non-Engineered Buildings in Indonesia.* EASEC Conference, Bali.
- Boen, T., 2001. *Earthquake Resistant Design of Non Engineered Buildings in Indonesia.* EQTAP Conference, Kamakura.
- Boen, T., 2001. *Earthquake Resistant Design of Non Engineered Buildings in Indonesia.* EQTAP Conference, Bali.
- Boen, T., et.al., 2001. *Post Earthquake Disaster Relocation: Indonesia's Experience.* APEC Conference, Taiwan.
- Boen, T., 2001. *Impact of Earthquake on School Buildings in Indonesia.* EQTAP Conference, Kobe.
- Boen, T., 2000. *Disaster Mitigation of Non Engineered Buildings in Indonesia.* EQTAP Conference, Manila.
- Shah, H., and Boen, T., 1996. *Seismic Hazard Model for Indonesia.*
- Vilacis, C., and Katayama, T., 1995. *Catastrophe and National Development.*
- Boen, T., 1994. *Earthquake Hazard Mitigation in Developing Countries, the Indonesian Experience.*
- Boen, T., 1994. *Manual, Repair and Strengthening of Buildings Damaged During the Liwa (South Sumatra) Earthquake (in Indonesian).*
- Boen, Teddy, 1994. *Manual, Repair and Strengthening of Buildings Damaged During Halmahera Earthquake (in Indonesian).*
- Boen, T., 1992. *Manual, Repair and Strengthening of Buildings Damaged During the Flores Earthquake (in Indonesian).*
- Federal Emergency Management Agency, 1990. *Seismic Considerations - Elementary and Secondary Schools.* FEMA 149 / Revised May 1990.
- Arya, A.S., 1987. *Protection of Educational Buildings against Earthquakes.* UNESCO Principal Regional Office for Asia and the Pacific, Thailand.
- IAEE Committee on Non-Engineered Construction, 1986. *Guidelines for Earthquake Resistant Non-Engineered Construction.* The International Association for Earthquake Engineering.
- CIB/W-73, 1984. *Small Buildings and Community Development.* Proceedings, International Conference on Natural Hazards Mitigation Research and Practice.
- Boen, T., 1978. *Detailer's Manual for Small Buildings in Earthquake Areas.*

PROGRESS IN EMERGENCY MANAGEMENT RESEARCH FOR A MEGA-CITY IN CHINA

W.C. FAN^{1,2} G.F. SU²

State Key Laboratory of Fire Science, University of Sci. & Tech. of China¹
Center for Public Safety Research, Tsinghua University, P.R.China² 100084
wfan@tsinghua.edu.cn, sugf@tsinghua.edu.cn

ABSTRACT

The accident to the public safety of a mega-city could result in large-scale loss of life and major economic impact. In order to improve the public safety for a mega-city, a series of emergency management research is ongoing in China. The emergency management research is structured around the science, engineering, and technology that support all emergency response plan and activities. Now research progress focuses on continuously improving city-level response plan, designing the prototype of emergency response platform and putting it in practice, and developing the key technologies of emergency management activities. These research ranges are involved in the whole emergency response process, including monitoring and control, forecast and alert, command and decision-making, as well as analysis and assessment before and after the events.

Keywords: emergency, public safety, response plan, response platform, multi-scale, double nested, decision-making, alert level.

1. Introduction

Urbanization, the exodus from rural areas to cities, will be a major demographic phenomenon of the 21st century. The disasters are more destructive when they strike large cities, given the growing trend of high urban-population densities. Mega-cities, a term coined in the 1970s by the United Nations to define urban settlements of ten million inhabitants or more, are particularly at risk. Currently, 280 million people live in about 30 mega-cities across the world. This figure is expected to rise to 350 million by 2015. Several of mega-cities, such as Beijing, Shanghai, Tianjin, etc. are located in China.

Natural disasters in mega-cities are likely to cause large numbers of casualties because of the high demographic density in urban areas. Many of the casualties when a emergency event as flood, earthquake or fire - strikes a mega-city are due to the collapsing of buildings and other infrastructure which were designed for large numbers of residents. High concentrations of people and buildings mean that even moderate disasters can lead to heavy losses.

We will enhance our capabilities for responding to an emergency event all across the city. Today, many departments or agencies have little or no

capability to respond to a coupling incident with mass destruction. Even the best prepared departments do not possess adequate resources to respond to the full range of disasters we face. Many do not yet have in place mutual aid agreements to facilitate cooperation with others in time of emergency.

Emergency management activities include prevention, preparedness, response, and recovery actions. Generally speaking, the calamity incident will always happen, is impossible to totally avoid. Effective incident management begins with a host of preparedness activities in advance of any potential incident. Past experience has shown that preparedness plans are the key to providing an effective response to major incidents and natural disasters. At the same time, when the accident has already happened, the response on the basis of plan is the focus too that we pay close attention to.

2. Emergency Management Plan

The emergency management plan focuses on those activities that are directly related to an evolving incident or potential incident. Sometimes we call it emergency response plan.

The national response plan and a series of response plans for public emergency event have been studied and developed in China since 2003, and were established and issued until the beginning of 2005.

The national response plan is an all-hazards plan that provides the structure and mechanisms for national level policy and operational coordination for emergency management. It can be partially or fully implemented in the context of a threat, anticipation of a significant event, or the response to a significant event. Selective implementation through the activation of one or more of the system's components allows maximum flexibility in meeting the unique operational and information-sharing requirements of the situation at hand and enabling effective interaction between various ministries and commissions, local, and other entities.

For a mega-city, it is the most important to direct based on the emergency response plan of the city. A basic premise of the national response plan is that incidents are generally handled at the lowest jurisdictional level possible. Police, fire, public health and medical, emergency management, and other personnel are responsible for emergency management at the local level. That's to say, a city in the local area may act as a first responder and may provide direction or assistance consistent with its specific authorities and responsibilities. In the vast majority of incidents, local city resources and intercity mutual aid normally provide the first line of emergency response and incident management support.

The city-level plan for emergency response provides a framework to enable the management of cascading impacts and multiple incidents as well as the prevention of and preparation for subsequent events. Examples of emergency management plan from a city perspective include:

- Increasing citywide public awareness;
- Assessing trends that point to potential hazards;
- Elevating the city public safety advisory system alert condition and coordinating protective measures across departments;

- Increasing countermeasures such as monitoring, forecast, fighting, aid decision-making and infrastructure protection;
- Conducting public safety surveillance and assessment processes;
- Providing immediate and long-term public safety and rescue response assets;
- Providing strategies for coordination of city resources required to handle subsequent events;
- Evaluating in the aftermath of an incident;
- Enabling immediate recovery activities, as well as addressing long-term consequences in the impacted area.

3. Designing the prototype of emergency response platform

The emergency management actions range from initial notification to early coordination efforts to assess and disrupt the incident, to preparatory activation of the response plan, to deployment of city resources in support of emergency response and recovery operations. These actions do not necessarily occur in sequential order; many may be undertaken concurrently in response to single or multiple disasters or incidents. Under most situations where it is apparent that an incident may be imminent or has already occurred, assessment and pre-incident interagency coordination typically are simplified. City authority moves quickly to coordinate multiple department activities to include the following: information-sharing, integration of the resources, analysis coupling multi-disasters and forecasting, alert and decision-making, interagency course of action development, operational coordination, and other assistance as required. In order to implement the emergency management and realize the purpose to response plan, all of these need a comprehensive city system for public emergency response to bring together and make use of all necessary response resources quickly and effectively.



Fig. 1 the prototype of emergency response platform for urban region of a city



Technologies developed for a variety of purposes are often directly applicable, or quickly adaptable, for public safety needs. We are working to provide a prototype system of emergency response platform for the city public safety, based on existing technologies and developing of technology.

The safety management and emergency response platform is designed to improve the response operations more scientific, effective, and efficient. It is a centralized solution for event correlation, information sharing, resources aggregation, disaster analysis, response and investigation of emergency events with the networked matrix mode.

The response platform can quantify the risk for a study area of any size, whether for a building, region, city, or neighborhood. Using simulation and GIS technology, the public safety platform combines hazard layers with city databases, and then applies standardized loss estimation and risk assessment methodology. The platform environment allows users to create graphic presentations, helping users visualize and understand their hazard risks and solutions.

The emergency response platform gives decision-makers the tools to make better decisions. It establishes a mechanism for sharing the information all cross city including basic geographical information and public safety information, enhances the analysis of available options for rescue operation, optimizes the decision-making process, and can greatly improve the ability to select the best course of response plan.

4. Some key technologies of developing for emergency management

4.1 Exploring multi-scale disaster modeling, simulation, and forecasting in emergency response platform, building a fully integrated capability across all different disaster sectors and the key factors.

The public incidents often have double characteristics (determinacy and randomness). According to such dual law, the development trend, affecting range and probability taking place of the incident can be forecasted. Scientific decision-making must be set up on the basis of predicting the accident accurately. That is to set up the multi-scale prediction models that, say, dangerous materials leak and spread under different scene and environmental condition (wind speed, wind direction, temperature, humidity, topographical, urban buildings, etc.), and to store in the model database of the response platform. For example, when the chlorine leakage accident happens, we can obtain spot information of the accident from the monitoring system with the aid of GIS system, use the information in the public safety platform database, such as volume, pressure, physics & chemical property of this dangerous source, etc., then choose the model which accords with present terms from the model database, input the data to forecast accident and analyze its grade of risk. The results of calculation of these models, can offer scientific basis for the alert grading and rescuing. Namely, according to the predicting result and resource distribution, the response plan is selected from the plan database, to optimize decision-making, and implement it.

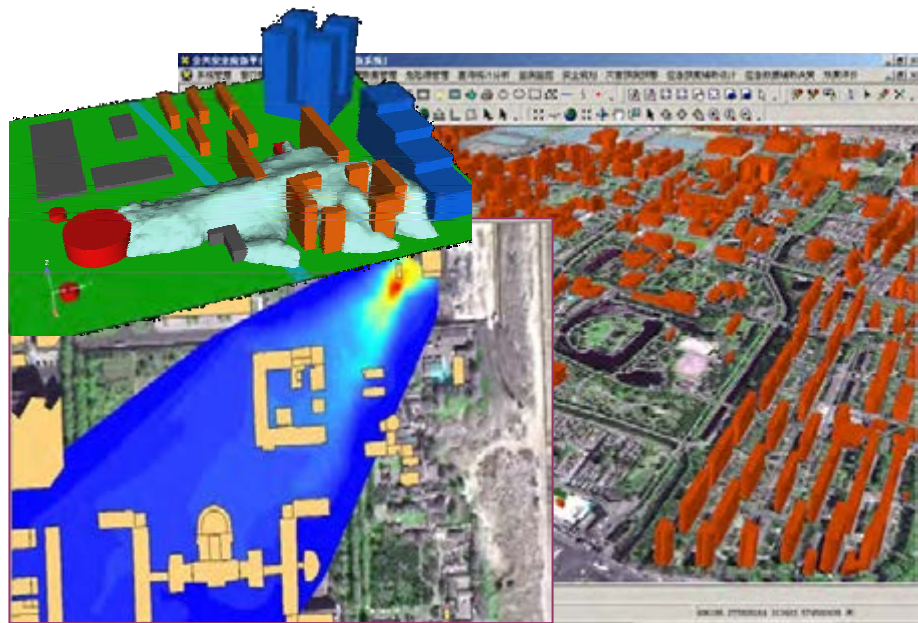


Fig. 2 the simulation of chlorine leakage accident in response platform

4.2 Advancing risk assessment and decision-making aid systems based on spatial technique, including information sharing and analysis on the critical public safety information found within massive data sets.

In order to fulfill the prediction of the public incident and decision-making, it is necessary to gain the full and accurate geographical information and public-safety related information. The city response platform have already included a large amount of relevant basic information, such as topographical data of the city, pipe network data of the urban lifeline, information of the dangerous source, key place and infrastructure, rescue force, population distribution and layout of refuge area, etc. The data involved are extensive and complicated in space distribution to meet an urgent need for public safety.

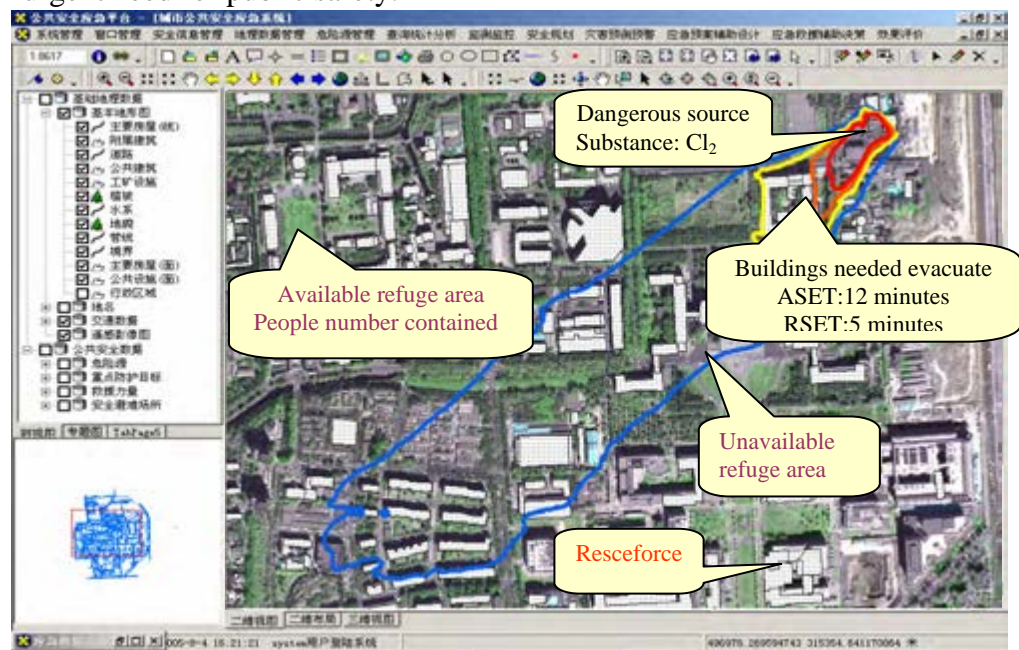


Fig. 3 the risk assessment and decision-making aid analysis

Intelligent analysis and data sharing are vital for emergency management. The intelligent capabilities of response platform support all aspects of emergency management: planning, response and recovery. The decision-making aid system is a part of response platform. Decision-making aid system adds a comprehensive set of advanced spatial modeling and analysis tools to desktop of response platform. These tools can help you predict the scope of a disaster, where the damage would be the greatest, what lives and property would be at highest risk, and where specific resources would be required.

4.3 Initiating a double nested city evacuation model considering the big region of urban and large quantity of people.

When the public incident happens suddenly, it is required to evacuate the personnel in the larger area, to choose the route evacuated safely, then to estimate out the time needed for reaching the refuge area. On the basis of GIS platform, using the information of urban area, such as kind of building, story of building, population distribution, topological structure of road network, etc., we can adopt different numerical models to simulate the evacuation of crowd inside and outside the building. Combined with the prediction of accident development and route of rescue operation, determine the range, route evacuated and tactics guided, avoid jams and blocking as much as possible, guarantee the personal security.

Considering the big region of urban and large quantity of people, a framework method of double nested city evacuation model is developed under the situation of urban fire or gas leak.



Fig. 4 the evacuation model of urban region

4.4 Establishing the method and standard of alert response level about emergency event

Based on the modern crisis management theory, considering the factors, such as casualties, property loss, environmental disruption, etc., and considering the controllability, affecting range and future development of

the incident, utilizing the method with the fuzzy neural network, we can establish the weight of each evaluation index, obtain the severity of the incident, and put forward alert response levels.

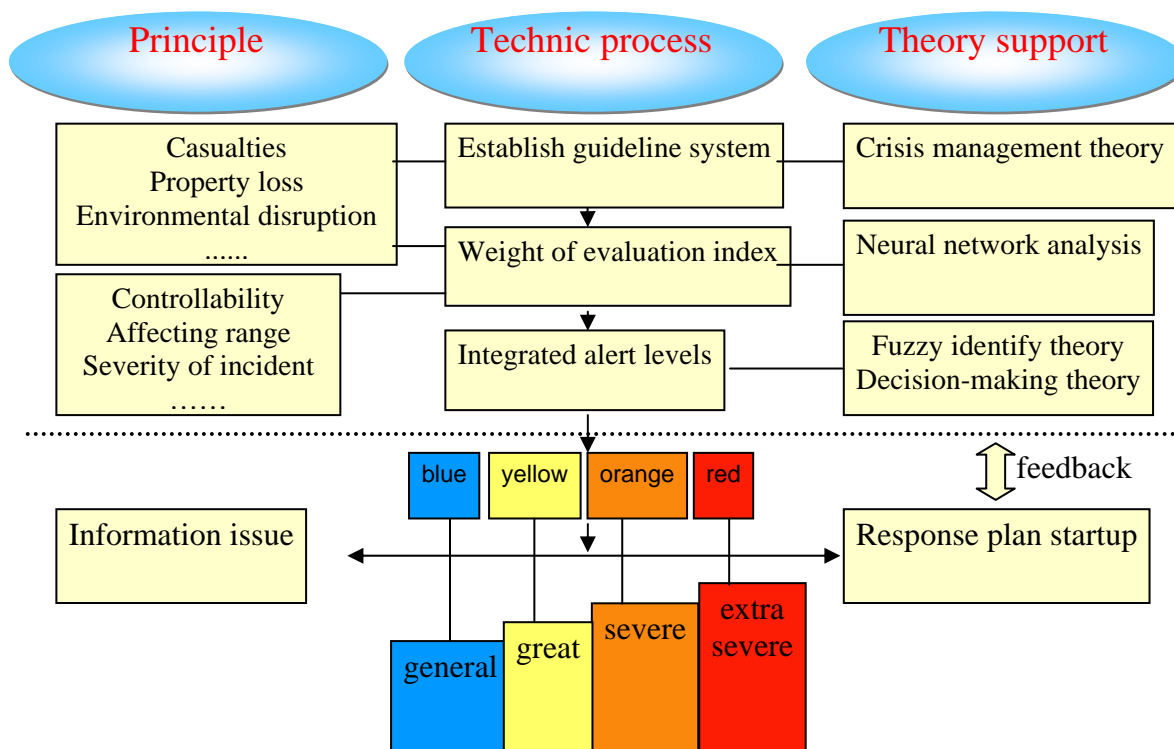


Fig. 5 the alert response level of emergency event

The level of risk of response activity is specified by building on the common colors of traffic lights that everyone understands, but adds a fourth color, orange, and changes a color, green to blue, as shown in Fig. 5. Another warning scheme used to indicate response activity is the alert levels (ONE, TWO, THREE, and FOUR). It indicates the level of hazards and degree of imminence. Alert level notifications are accompanied by brief explanatory text to clarify hazard implications as fully as possible. The actual level of event maybe is different from the alert level, the response plan should been developed that specifies the appropriate actions that should be taken when the alert level changes.

4.5 Improving the response plan, and studying the techniques that could make the response plan more active and more optimizing

The digitized plan is integrated and combined by many kinds of resources on many networks. Only a plan melts dynamically, that is could fully give play to the role of information system and public safe science and technology. Generally, that only the digitized dynamic plan can be very well realized on the emergency response platform.

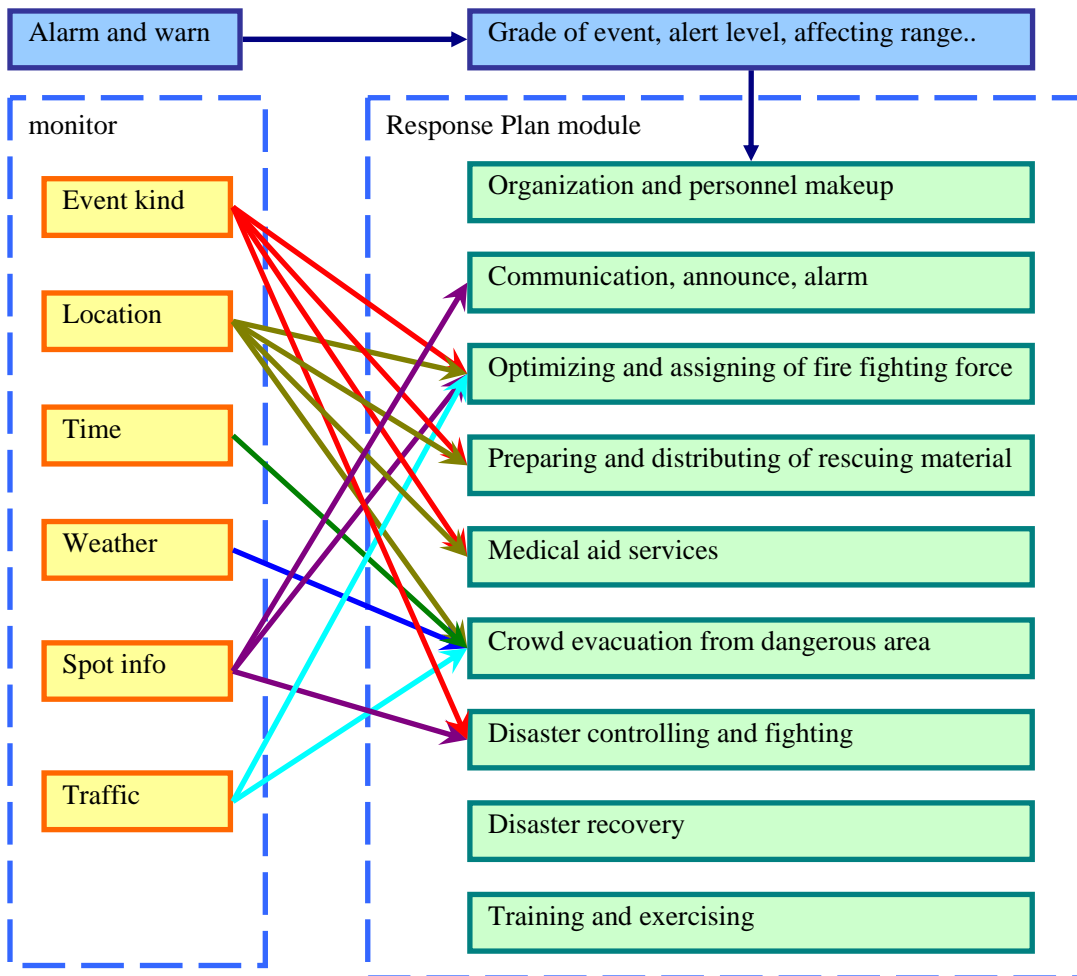


Fig. 6 the digitized and dynamical plan for emergency response

5. Conclusions

Urbanization is still fast going on in China. Many safety technologies needed for protection of a mega-city against natural disasters and man-activity related incidents. Among them emergency management technology is crucial.

The emergency management research is multi-disciplinary research area of great potential, which has drawn an increasing attentions of scientist, engineer, manager and officer with various backgrounds in China. Emergency management research should not only make cities safer, but also make our daily lives better, while protecting against the emergency events. Thus, the technologies developed for emergency response should fit well with the city planning, infrastructure and habits.

Research efforts needed of a constant examination of the city vulnerabilities, continual testing of our public safety systems, updating evaluations of the emergency response capability and its weaknesses and exercising different response actions through the research progress.

Natural disasters and man-activity related incidents are common enemy for human being. International and regional exchange and cooperation play an important role to enhance public safety research.

ACKNOWLEDGEMENTS

This paper was supported by the National 985 Project, and based on Sci.&Tech. 'Eleventh Five-Year' pre-plan (Research and demonstration of the key technologies for public emergency response).

The authors deeply appreciate the supports, and thanks for the works of Center for Public Safety Research, Tsinghua University and State Key Laboratory of Fire Science, University of Science and Technology of China.

REFERENCES

- State Council of P.R. China, 2005. National Public Emergency Response Plan.
- Fan W.C., 2004. Surveying the science and technology support of the public safety management of city from the fire science. In Ding, S.S. *Operating Mechanism for Disaster Management*. Public Saying Press, Beijing, 107~137.
- State Administration of Work Safety, 2004. The guide for working out the response plan of dangerous chemicals accident.
- Ding, S.S., 2004. *The Management of Urban Disaster*. Public Saying Press, Beijing.
- Yuan, H.Y., Su, G.F., Chen, T., Yang, R., Shen, S.F., and Fan, W.C., 2005. Research of the system of emergency response platform and plan for petrochemical industry enterprises. Seminar about precautions against disasters with the industrial safe practice in the urban, Taipei.
- Chen, T., Song, W.G., Fan W.C., and Lu, S.X., 2002. Jamming transition of pedestrian evacuating flow in crossing exit. In Huang, P., Wang, Y., Li, S., Qian, X.(eds) *Progress in Safety Science and Technology*, Vol. III, Science Press, Beijing, 507~512.
- Chen, T., Yuan, H.Y., Su, G.F., and Fan, W.C., 2004. An automatic fire searching and suppression system for large spaces, *Fire Safety of Journal*, 39(4): 297~307.

LESSONS LEARNED FROM THE 26 DECEMBER 2004 TSUNAMI DISASTER IN THAILAND

PENNUNG WARNITCHAI
Asian Institute of Technology, Thailand
Pennung@ait.ac.th

ABSTRACT

Triggered by a massive earthquake ($M_w = 9.3$) in the area off the western coast of northern Sumatra, a series of destructive tsunami waves propagated through out the Indian Ocean and devastated communities along thousands of kilometers of exposed coastline. In Thailand, all provinces facing Andaman Sea were seriously attacked by tsunami waves, where the total death toll including missing of more than 8000 was reported. An international survey team, comprising members from Thailand, Japan, and USA, spent four days from 8 to 11 January 2005 in several hard-hit areas to collect information on tsunami inundation, building damage characteristics, ground and foundation failures, and associated data from eyewitnesses and survivors. The areas investigated include Khao Lak (Phang-Nga), Phi Phi Island, and Phuket Island. Many lessons learned from this post-tsunami reconnaissance survey are briefly summarized in this paper.

1. INTRODUCTION

Triggered by a massive earthquake ($M_w = 9.3$) in the area off the western coast of northern Sumatra, a series of destructive tsunami waves propagated throughout the Indian Ocean and devastated communities along thousands of kilometers of exposed coastline. Along with Thailand, deaths by this ocean-wide tsunami have been reported in 10 other countries—Indonesia, Sri Lanka, India, Malaysia, Myanmar, Maldives, Bangladesh, Somalia, Tanzania and Kenya. The total death toll including missing is more than 280,000. It can be ranked as one of the world's most catastrophic events in recent times.

In Thailand, all provinces facing Andaman Sea were attacked by tsunami waves. The death tolls including missing in Phang-Nga, Phuket, Krabi, Ranong, Trang, and Stool provinces are, respectively, 6026, 921, 1384, 171, 6, and 6. The numbers of severely damaged buildings are, respectively, 4615, 1235, 632, 349, 165, and 57. These are statistics provided by the Department of Disaster Mitigation and Prevention, Ministry of Interior, Royal Thai Government, on 24 January 2005. Nearly half of

those confirmed dead and half of those missing were foreign tourists who were spending their holidays in the resort areas.

2. POST-TSUNAMI RECONNAISSANCE SURVEY

An international survey team, comprising members from Asian Institute of Technology, Chiba University (Japan), EDM/NIED (Japan), JICA, MCEER (USA), GISTDA (Thailand) and Thai Meteorological Department, was formed to collect information on tsunami inundation, building damage characteristics, ground and foundation failures, and associated data from eyewitnesses and survivors. The team, coordinated by myself, spent four days from 8 to 11 January 2005 in several hard-hit areas, such as Khao Lak (Phang-Nga), Phi Phi Island, and Phuket Island. Many lessons learned from this post-tsunami reconnaissance are briefly summarized in the following section. In addition, 11 hours of geo-referenced digital video footage were recorded along the survey route, and about 1,500 GPS-located digital photos were also collected by the team and were linked to satellite images (IKONOS, Quickbird). It is envisioned that these geo-referenced data will be invaluable for future research in evaluating damage from tsunami waves. Further details about these geo-referenced data and their possible applications can be found in Yamazaki (2005) and Ghosh (2005).

3. LESSONS LEARNED

Among several beaches in Phuket Island, the impact of tsunami was reported to be highest in Kamala and Patong Beaches. The maximum height of tsunami waves above the tide level at that time was about 4 to 5 meters, while the inundation depth was about 2 meters. The first sign of tsunami attack was the withdrawal of the sea. People were surprised and went to see the exposed seabed. Many of them were killed or seriously injured as the sea withdrawal was shortly followed a high tsunami wave.

At Kamala Beach, three tsunami waves struck the shore at 9.54, 10.14 and 10.57 am, respectively, and the 2nd and 3rd waves were higher than the 1st wave. The waves swept onto the land at high velocity as a sheet of water. The flow depth in Kamala beach area was about 2 meters or less, so only the first story was flooded as shown in Fig. 1. But the flow velocity was roughly estimated to be about 3 to 4 m/s or higher. Hence, a lateral hydrodynamic pressure greater than 5.0-8.0 kN/m² was exerted on buildings and obstacles by the high-velocity water. After the water has receded, a great amount of debris which was floating during the tsunami flooding finally deposited on ground (Fig. 2), and water marks could be observed on building walls. The damage seemed disproportionately severe compared with that would be expected from a normal flooding of similar height. The high hydrodynamic pressure due to high-velocity water and the collision of floating debris appeared to be the main causes of the severe damage.



Figure 1 Tsunami flooding in Kamala Beach



Figure 2 A scene in Kamala Beach after the water has receded

Tsunami wave heights at various sites shown in Fig. 3 were measured by a Japanese team led by Prof. Matsutomi (2005) and a Thai team led by Dr. Nakhorn Poovarodom of Thammasart University. The heights vary considerably from site to site, and the maximum height occurred at Khao Lak in Phang-Nga Province. This area has many luxurious hotels and was quite popular for foreign tourists, especially those from Europe.

Water marks in the form of stripped roof tiles on the 2-story building in Fig. 4 indicate that the flow depth in Khao Lak area was as high as 7 to 8 meters. The flow velocity in this area was estimated to be about 6 to 8 m/s, and hence a very high hydrodynamic pressure of about 20 to 30 kN/m² was exerted on buildings and obstacles by tsunami waves. Due to these extremely high flow depth and pressure, Khao Lak was the hardest-hit area with the largest death toll. Most of the resorts surveyed sustained heavy to complete damage. As shown in Fig. 5, a reinforced concrete building facing Kuk-kak Beach in Khao Lak was completely destroyed by tsunami impact. This is only an example of many completely damaged buildings in this area.

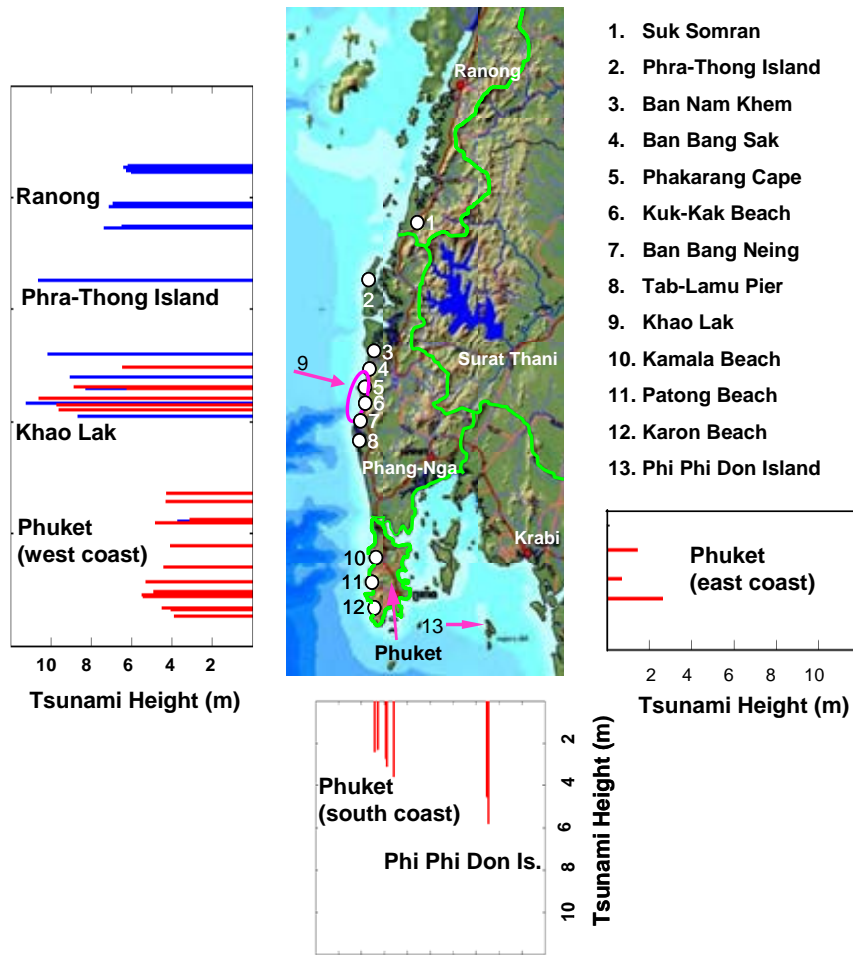


Figure 3 Tsunami wave height distribution



Figure 4 Maximum flow depth of about 7 to 8 meters in Khao Lak



Figure 5 An RC building in Khao Lak was completely destroyed



Figure 6 Breaking of masonry infill walls by wave impact in Phi Phi Island

One damage pattern commonly found in RC frame buildings is the breaking of frame-infill masonry walls (Fig. 6). These walls are generally 100 mm thick. They are much weaker than RC frame members, and they could not withstand high hydrodynamic pressure or impact of major floating debris carried by the strong current. Breaking of infill masonry walls, particularly in the first story, can be found in many sites where the flow depth was about 2 m or higher. As shown in Fig. 6 the flow height did not reach the 2nd story of a 2-story building, but it was able to demolish all infill masonry walls in the 1st story. We observed that in general RC frames in which infill walls had been completely ripped away were still in good condition—no damage or major cracks found in RC columns, beams, and beam-column joints. The breaking of infill walls seemed to help saving the RC frame structures by reducing the lateral pressure load on the structures. Therefore, to improve the safety of RC frame buildings in the tsunami affected areas, infill masonry walls in the 1st story (and the 2nd story in some areas) might be replaced by weaker (and lighter) panels that could be easily

ripped away by the water. These observation and design improvement concept are well in line with those made by several investigators of past tsunami disasters (Wiegel, 1970).



Figure 7 Floating foundations of a building in Phuket



Figure 8 Displaced buildings at Ton Sai Bay in Phi Phi Island

Another type of frequently observed damage to buildings in tsunami affected areas is the severe scouring of supporting sand underneath building spread footings, leading to foundation failure as shown in Fig. 7. This severe scouring was caused by highly turbulent and strong tsunami-induced currents. We have also found severe scouring of roads and wall foundations in many sites, particularly in beach front areas. Another type of failure associated with shallow spread footings is shown in Fig. 8. Here, several buildings at Ton Sai Bay in Phi Phi Island were floated and displaced from their original positions.

As spread footings were commonly used for low-rise buildings in Phuket and many southern provinces of Thailand, this issue was widely discussed among design engineers in several forums. Some engineers suggested that the use of spread footings for buildings in tsunami hazard areas should be forbidden, and that pile foundations should be used instead to improve the resistant to scouring, undercutting, and flotation effects.

One important feature of tsunami flooding we have learned from this survey is that strong-current tsunami waves carried with them a great amount of debris including cars and boats. Figure 9 gives us a clear idea about the extent of debris carried by tsunami waves during the tsunami flooding. We found pieces of wood, furniture parts, refrigerators, trees, metal (zinc) roof sheets, sand and mud in the debris. High-density debris in tsunami waves is certainly one of the key factors that are responsible for a large number of tsunami victims.



Figure 9 Debris deposited on a beach in Khao Lak



Figure 10 A car on the roof of a building in Phakarang Cape



Figure 11 A battleship was tossed on to the shore at Tab-lamu Pier

Many cars were rolled, pushed around, hit by floating debris, or thrown against buildings (Fig. 10) and obstacles. Many fishing boats were pushed from the shore toward the land and crashed into buildings. One patrol boat was transported into as far as 1.2 km in land at Ban Bang Neing in Khao Lak area. The largest object that was displaced by tsunami waves is a battleship of Royal Thai Navy as shown in Fig. 11. The ship was tossed on to the shore in front of a naval base at Tab-lamu pier in Phang-Nga.

While the southern and central parts of Phang-Nga have several resort hotels, the northern part is still a rural area with fishery and agricultural villages. In a populated fishery village named Ban Nam Khem, more than a thousand of residents were killed, and most RC residential buildings and masonry structures for shrimp farming suffered heavy damage. The survey team also visited one fisherman village named Ban Pak Jok in Phra-thong Island—a small island located just off the northern coast of Phang-Nga (see Fig. 3). In this village, all wooden fisherman houses and small light-frame concrete buildings were completely wiped out as shown in Fig. 12. All survivors were evacuated from the island and resettled in the northern coast of Phang-Nga.



Figure 12 Devastated fisherman houses in Phra-thong Island

We saw evidence in this village and in many other sites (such as Phakarang Cape) that wooden houses, compared with normal RC frame buildings, are much more vulnerable to tsunami impact. At sites where RC buildings were lightly or moderately damaged, wooden houses would be severely damaged or completely destroyed. The finding suggests that wood construction should be as much as possible avoided in tsunami hazard areas. In Ban Pak Jok village, only one structure was left intact: an RC water tank tower. It reminded us of a tsunami tower in Japan, in which people can easily evacuate from low-lying ground to its high-level platform during the tsunami flooding (Fig. 13). Since the whole area of Phra-thong Island is very flat and surrounded by sea, it would be very difficult to find a safe (high-level) ground for the evacuation in the next tsunami event. Hence, RC tsunami towers seem to be a practical solution in this case.



Figure 13 Water tank tower & Tsunami tower



Figure 14 Sand belt area in Phi Phi Island was attacked by tsunami waves from both side

By interviewing several eyewitnesses and survivors, the survey team learned that tsunami waves at some sites were quite complex. These sites include Phi Phi Island, which was among the worst affected areas. Looking from the tsunami source area, this island is located outside the shadow of Phuket Island, and thus was hit by large tsunami waves of about 5 to 6 m maximum height (see Fig. 3). The number of casualties in this island was 691 and that of missing was 951. Most of them were tourists and residents in a highly populated sand belt between two bays as shown in Fig. 14. The elevation of this sand belt area is only 2 to 3 m above the sea level. When the first tsunami wave attacked from Loh Dalum Bay, people were panic and they tried to escape by running to Ton Sai Bay on the other side. However, by the time they reached Ton Sai Bay, a much larger tsunami wave was also arriving in this bay and then swept across the whole sand belt area, killing a large number of people.

4. CONCLUDING REMARKS

Prior to this event, a tsunami disaster of this scale was considered by the Thai public to be impossible. This general belief was simply based on the fact that such disaster has never happened before in the history of Thailand. They also believed that the risks from other natural disasters (such as earthquakes) were also very low and limited to a small scale. Most decision makers in the government did not pay much attention to planning and preparation to mitigate the risks or supporting more scientific researches to understand the risks. The emphasis was only placed on emergency response measures. After the event, the attitude of the general public and government officials towards natural disasters has changed significantly. They are now much more interested to learn about these natural disasters and their potential impacts. They are also more ready invest their money on making and ensuring a safe environment. It seems that the Thai public has also learned a very important lesson from this tsunami disaster.

REFERENCES

- Yamazaki, F., Matsuoka, M., Warnitchai, P., Polnga, S. and Ghosh, S., 2005. Tsunami Reconnaissance Survey in Thailand Using Satellite Images and GPS, *Asian Journal of Geo-informatics*, Vol. 5, No. 2, pp. 53-61.
- Ghosh, S. et al., 2005. Post-Tsunami Urban Damage Survey in Thailand Using the VIEWS Reconnaissance System.
<http://mceer.buffalo.edu/research/tsunami/Tsunami032505.pdf>
- Matsutomi, H. et al., 2005. The December 26, 2004 Sumatra Earthquake Tsunami, Tsunami Field Survey around Phuket, Thailand.
http://www.drs.dpri.kyoto-u.ac.jp/Sumatra/Thailand/phuket_survey_e.html
- Wiegel, R. L., 1970. Chapter 11: Tsunamis. *Earthquake Engineering*, edited by Wiegel R. L., Prentice-Hall, New Jersey, USA.

Technical Sessions

STRUCTURAL PERFORMANCE MONITORING OF REINFORCED CONCRETE BRIDGES

MITSUYOSHI TSUNEKUNI¹, TSUGIO NISHIMURA²,
YOSHITAKA KATO² AND TAKETO UOMOTO²

¹Tokyo Electric Power Services Co., Ltd., Japan

²International Center for Urban Safety Engineering,
Institute of Industrial Science, University of Tokyo, Japan
tunekuni@tepsco.co.jp

ABSTRACT

In Japan, the deterioration of some concrete bridges constructed in 1960s is beginning to be detected. For the future increase of maintenance cost for deteriorated bridges, the quantitative evaluation of deterioration degree and/or soundness for structural performance, e.g. safety or serviceability performance, will become an important task. In this study, the monitoring method of soundness evaluation of the structural performance of reinforced concrete bridges is discussed through loading tests of reinforced concrete beams in laboratory and the behavior measurement of a reinforcement concrete (hereafter referred to a "RC") road bridge in situ.

For in-situ measurement of a 35-year-old RC road bridge, some sensors, i.e. optical fiber sensors and velocity meters, were mounted on the main girders. Using the data measured by these sensors, the soundness of structural performances of the bridge in terms of safety and serviceability performances were evaluated.

1. INTRODUCTION

A large number of concrete bridges were constructed since the era of high economic growth in Japan. Among about 130,000 bridges with span longer than 15m, the number of concrete bridges, e.g. reinforced concrete or pre-stressed concrete, is about 71,000 (MLIT, 2002). Due to the steady increase of old and decaying bridges in the future, the evaluation of the soundness of existing concrete bridges will be becoming an important task to decide whether a bridge is still in serviceable condition or not.

Currently, the maintenance of concrete road bridges is carried out mainly by periodic visual inspections. On the basis of the inspection results, the degree of deterioration and the main cause of deterioration are determined. In this process, however, it is difficult to evaluate the safety and serviceability performances, which are criteria mentioned in standard specification (JSCE, 2002). Therefore the measurement method related to the structural performance for RC road bridges is firstly considered through the load tests in laboratory in this study. By applying similar measurement methods, then, the evaluation of soundness of a 35-year-old RC road bridge were performed.

2. LOADING TEST OF SPECIMENS IN LABORATORY

2.1 Outline of loading test

In order to clarify the measurement method for soundness evaluation of RC road bridges in advance, the loading tests of RC beams were carried out in laboratory. Basing on results of the test, the structural behavior measurement method and soundness evaluation method were considered. The two RC beams were tested in flexure supposing the main girders of road bridges; the one was for static test and the other was for fatigue test.

Details of specimens are shown in Figure 1. The compressive strength of concrete was 30 MPa whereas the yield strength of steel was 399MPa. The beams were 3400 mm long, 200 mm wide and 300 mm thick and were simply supported over a span of 3000mm. Two 19 mm diameter steel bars were used as reinforcement. The flexural and shear reinforcement was designed to ensure flexural failure. Sixteen 10mm stirrups were placed in the beam as shear reinforcement at spacing of 200mm. There was a 40mm clear cover of concrete. The tests were carried out using a 294 kN capacity hydraulic servo actuator as shown in Figure 2. The actuator was operated under load control. Strains of reinforcement bar, concrete of extreme compressive fiber and deflections at mid-span were recorded during testing.

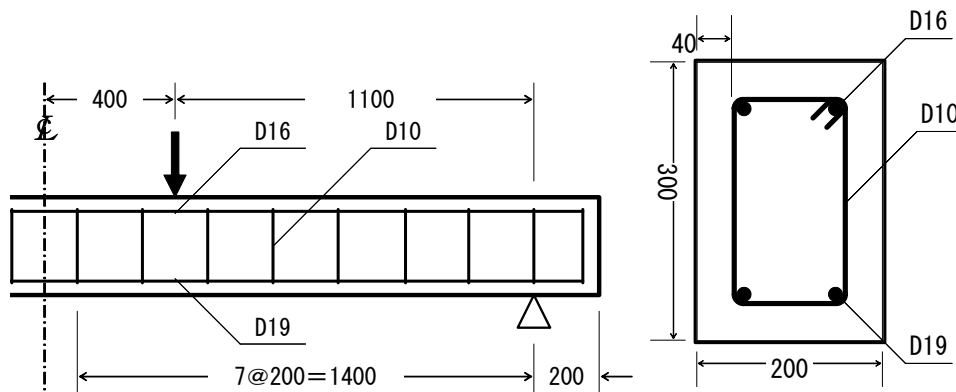


Figure 1: Details of test beam (mm)



Figure 2: Test set-up

2.2 Results of tests

2.2.1 Results from static test

The result of the static test is shown in Figure 3. This result shows that the flexural stiffness abruptly degrades after reinforcement yielding; The failure of RC beam initiated by yielding of reinforcement. That is to say, the flexural failure of main girders of RC road bridges must be check for the reinforcement yielding not for the ultimate strength in actual.

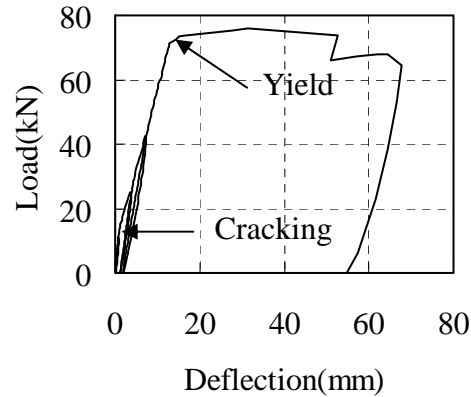


Figure3: Loads vs Deflection diagram for static loading

Even if the sectional force would be important to access the behavior, the evaluation of that for structural members, especially main girders of RC bridges, may be difficult in general. So the estimation method of the bending moment utilizing the measurement of beam was considered in the test.

The estimation of acting load on the beam was calculated using strain of extreme compressive fiber and of reinforcement bar as follows:

$$M=C \cdot y_1+T \cdot y_2 \tag{1}$$

where M: Acting bending moment

T: Resultant tensile force of the steel

C: Resultant compressive force of concrete

y_1, y_2 : Distance from the neutral axis to C and T.

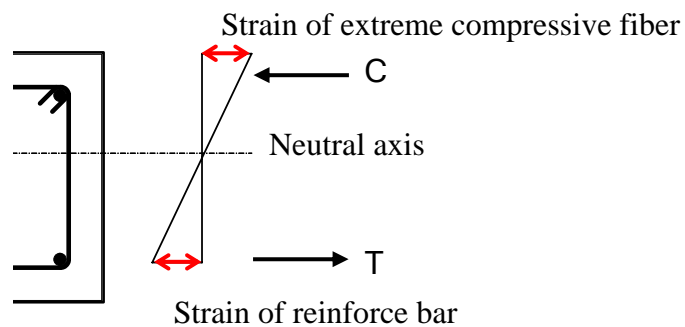


Figure4: Distribution of strain of cross section

Figure 5 shows the comparison of measured and estimated load. Though the estimation load is 1.2 times the measured one, the estimation of acting sectional force seems to be possible using the strain distribution in cross section. The cause of error in estimation seems to be the increase in strain of steel exposed to crack planes (Okamura, H. and Maekawa, K., 1991).

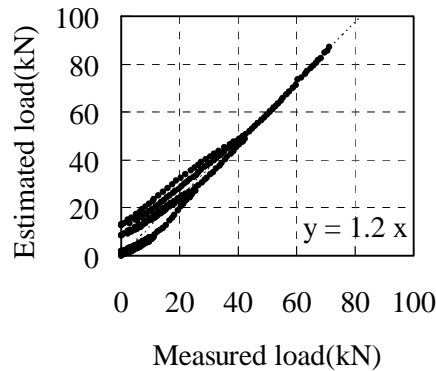


Figure5: Estimation result of applied load

2.2.2 Results from fatigue test

The fatigue test of a RC beam is tested under cycling load with constant minimum load of 20kN. In order to accelerate the damage, the test was performed while increasing the maximum load, such as 17, 37 and 60 kN. The number of cycles was 30,000 cycles for each maximum load. The test was conducted at 1 Hz.

The result is shown in Figure 6. The deflection at mid-span and load were recorded at cycle numbers of 1, 1,000, 10, 000 and 30,000 for each maximum load case. From this result, it is seemed that the deflections increase according to the increase in cycle number. Figure 7 shows the comparison the measured deflection at minimum load for each minimum load and one calculated using secant flexural stiffness between 2 to 17kN. The increase in the deflection at minimum load may be caused by concrete creep, whereas the increase in the deflection at maximum load, in other words, the degradation of flexural stiffness, may be caused by the fatigue crack extensions. The increase in deflection at minimum load can be considered as the residual deflection of the actual deflection.

The correlation of the measured deflection and the one considering cyclic creep expressed as Eq.(2) (Balaguru and Shah, 1982) is demonstrated in Figure 8. It turns out that the creep will significantly affect on the deflection. Therefore the effect of concrete creep should be taken into consideration in the soundness evaluation.

$$\epsilon_c = 129 \cdot S_m \cdot t^{1/3} + 17.8 \cdot S_m \cdot S_r \cdot N^{1/3} \quad (2)$$

where ϵ_c : the cyclic creep strain

S_m : $(\sigma_{max} + \sigma_{min}) / 2f'_c$, S_r : $(\sigma_{max} - \sigma_{min}) / f'_c$

σ_{max} , σ_{min} : the maximum and minimum

applied compressive stress in concrete

t : the time from start of loading (h), N : the number of cycles,

f'_c : the compressive strength of concrete

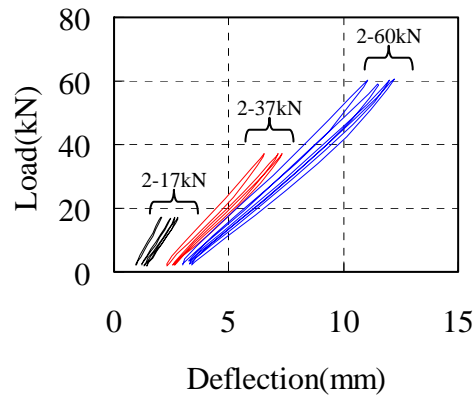


Figure6: Loads vs Deflection diagram for fatigue loading

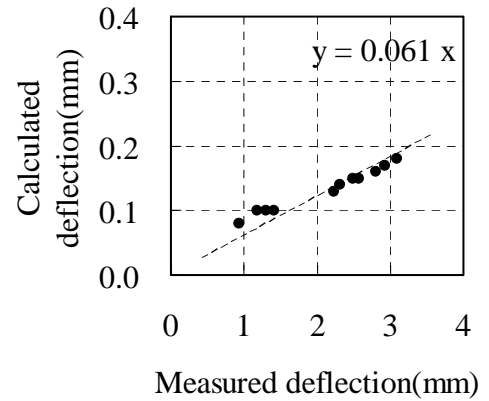


Figure7: Scatter gram of measured and calculated deflection

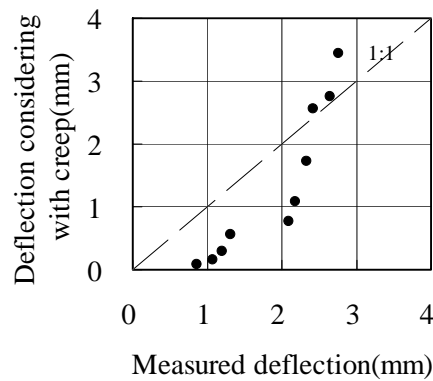


Figure8: Scatter gram of measured and deflection with creep

3. MONITORING AND SOUNDNESS EVALUATION

3.1 Monitoring concrete bridge

The pilot monitoring was carried out on a 35-year-old RC road bridge (Figure 9) from April 2004. The outline of the bridge is summarized on Table 1. Due to increasing traffic load in recent years, bending cracks occurred in each main girder, as shown in Figure 10. Then, by the use of some sensors such as optical fiber sensors and velocity meters, behaviors, i.e. the deflection and strain of main girder against vehicle loads, are measured.



Figure 9: Monitored concrete road bridge



Figure10: Cracks of a main girder

Table 1: Outline of monitoring concrete road bridge

Span	15m
Type	3 span-continuous RC T- girder bridge
Erection	1970
Traffic volume	24,000(from 8a.m.to 8 p.m.)

3.2 Applied sensor for monitoring and example of measured data

Types of sensor mounted on the bridge are listed on Table 2, and the set situation of the sensors is shown in Figures 11 and 12. These sensors are arranged on two main girders, called G7 and G5. The main girder G7 is placed in position under a up lane, and G5 is under the opposite one.

Optical fiber sensor with length of 1.5m was used for measurement of the extreme tensile fiber strain against vehicle loads. And velocity meter was utilized for estimating the deflection and vibration.

As the road bridge considered in this research is 3-span continuous bridge, the bending moment against vehicle loads has maximum value at the point of 6m from the end of girder. Sensors were firmly mounted on the main girders at this point.

Example of data measured by each sensor in October 21, 2004 is illustrated in Figure 13. The passage of a vehicle can be clearly detected at the peak point of the time history.

Table 2: Sensors applied for monitoring

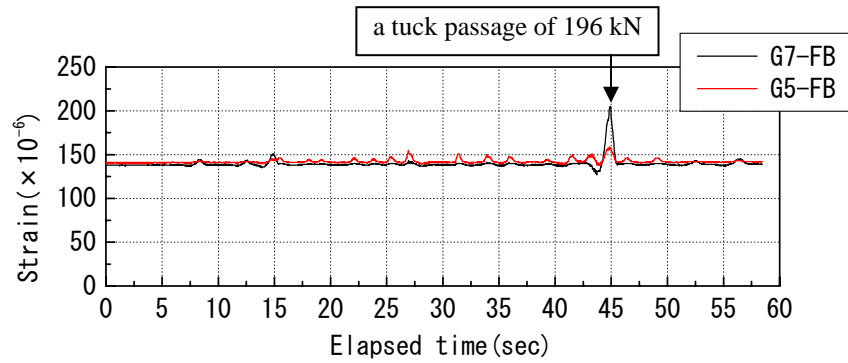
<i>Type of Sensor</i>	<i>Name</i>	<i>Sampling rate</i>
Optical fiber	G7-FB, G5-FB	100 Hz
Velocity meter	G7-V, G5-V	200 Hz



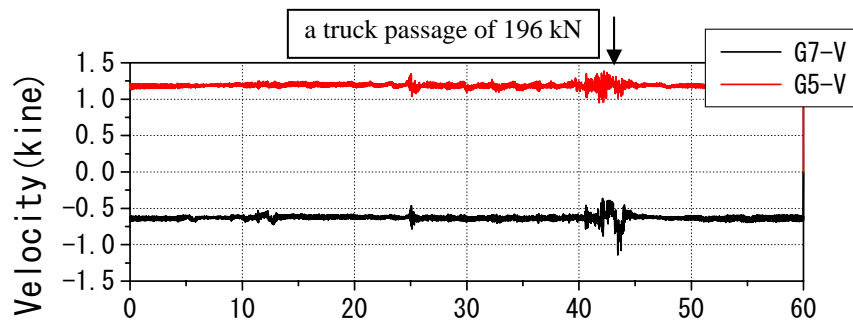
Figure 11: Optical fiber sensor



Figure 12: Velocity meter



(a) Time history of strain of extreme tensile fiber



(b) Time history of velocity

Figure 13: Example of measured data

3.3 Soundness Evaluation

3.3.1 Soundness for structural performance

In this section, the evaluation method based on measurements will be discussed. In this paper, the term of soundness means the satisfaction degree of structural performance specified in “Japan Standard Specifications for Concrete Structure” (JSCE, 2002), e.g. safety or serviceability. The soundness for each performance is quantitatively evaluated with index listed on Table 3.

By comparing bending moment induced by vehicle loads with flexural strength of main girders, the soundness in items of safety performance is evaluated. By the use of measured deflection and natural frequency against vehicle loads, the soundness for serviceability is assessed on the basis of allowable limit of vibration.

Table 3: Evaluated soundness for each structural performance

Structural Performance	Object	Indices
Safety	Main girder	Bending moment and Flexural strength
Serviceability	Superstructure	Strain of steel bar
		Deflection and Natural frequency

3.3.2 Evaluation of soundness for safety performance

(1) Evaluation based on acting bending moment

The evaluation method of the soundness regarding the safety performance is described on the basis of measured data. The flexural strength, e.g. cracking or yield moment, are calculated for the monitored cross section of main girders. The acting flexural moment can be estimated by the way as follows. Owing to the characteristic of RC members, the distance from extreme compression fiber to neutral axis is constant on condition that the flexural moment is less than the yield one. Assuming that the neutral axis may be equivalent to the height of crack propagation detected in-situ, then, the acting flexural moment can be calculated by the equation satisfying the condition of equilibrium of bending moment as follows:

$$M=C \cdot y_1+T \cdot y_2 \quad (2)$$

where M: Acting flexural moment on a cross section

T: Resultant tensile force of the steel

C: Resultant compressive force of concrete

y_1, y_2 : Distance from the neutral axis to C and T.

In Eq.(2), C and T can be evaluated on the basis of the strain distribution on the assumption that strain is proportional to the distance from neutral axis and that the strain at extreme tensile fiber is equal to the strain measured by the optical fiber sensor (Figure 14). The flexural moment was 860 kN·m for the passage of truck of 198 kN. The moment is greater than cracking moment, 331 kN, whereas less than yield moment, 3,700 kN. From the results, the monitored girders seem to be still sound condition based on the result of RC beams loading test.

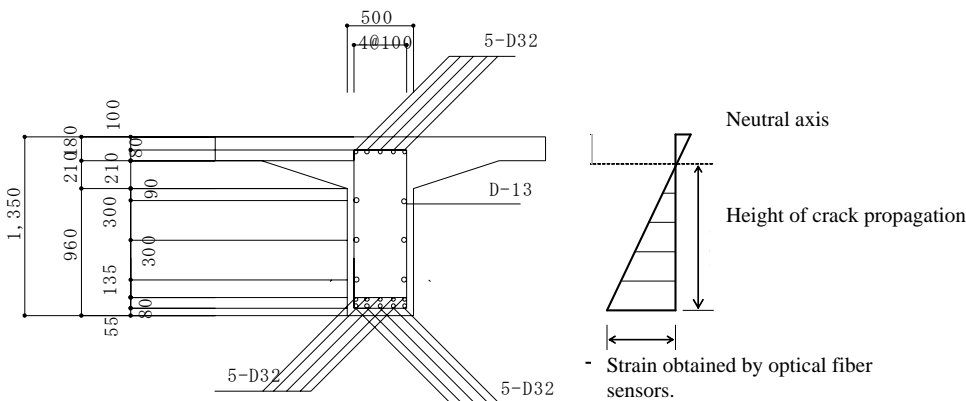


Figure 14: Cross section of main girder and distribution of strain

(2) Evaluation based on strain of reinforcement bar

The method described above is considered as the evaluation on the case in the acting load increment. By an analogy of loading test results of RC beams, it is possible that the degradation of the safety performance may

occur due to the increment in strain of the reinforcement bar by some causes, e.g. the vehicle load, concrete creep and so on.

In accordance with the standard specification (JSCE, 2002), the creep strain is 950×10^{-6} ; the strain is 2.5 times as big as the strain caused by the dead load of main girder own.

The histograms of measured strain took account of the creep strain are illustrated in Figure 15. From these observation data, the probability of exceeding the yielding strain can be thought of almost zero on assumption of logarithms distribution. Consequently the measured main girder is safety form the point of view of the strain of reinforcement bar.

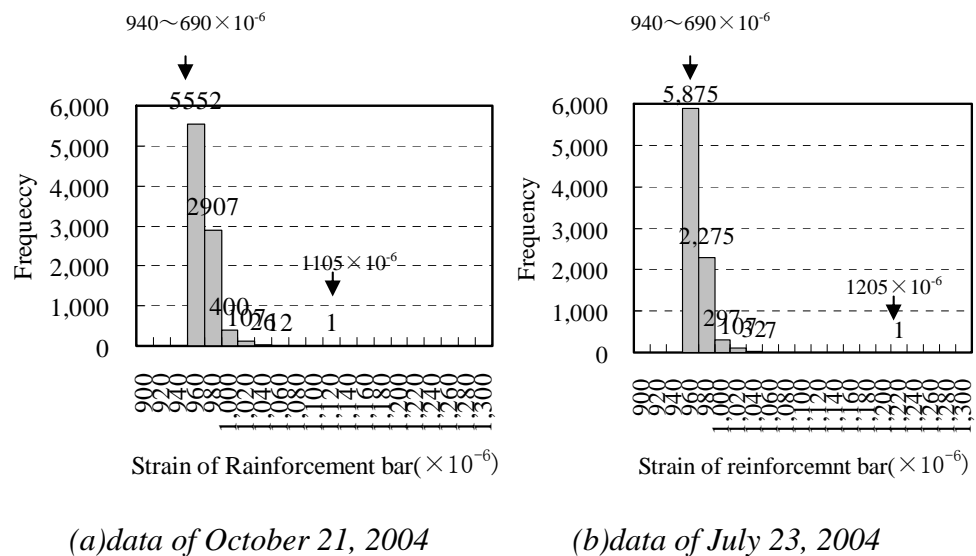


Figure 15: Frequency distribution of reinforcement steel bar

3.3.3 Evaluation of Soundness for serviceability performance

The bending cracks which occur in main girder may cause the decline of flexural stiffness. As a result, the soundness regarding serviceability performance may deteriorate. Since there are no specifications for the concrete bridge serviceability in Japan, the soundness was checked on the basis of allowable limit of vibration mentioned in standards of highway bridges of Canada in this study. The allowable limit of vibration is expressed as the relation between static deflection and natural frequency as shown in Figure 14. The static deflection of main girder is obtained by dividing the measured dynamic deflection by the impact coefficient for the considering bridge, 0.2. The dynamic deflection is obtained by the integration of velocity time history (Figure 13b); the natural frequency in flexure is attained by performing the FFT of measured velocity time history in free vibration after the vehicle passage.

The evaluation results, which are calculated by the use of the measured maximum deflection data on October 21, 2004 and January 23, 2005, are illustrated in Figure 16. Since the considering road bridge corresponds to one with frequently walker, the results shows that the considered road bridge is acceptable in serviceability.

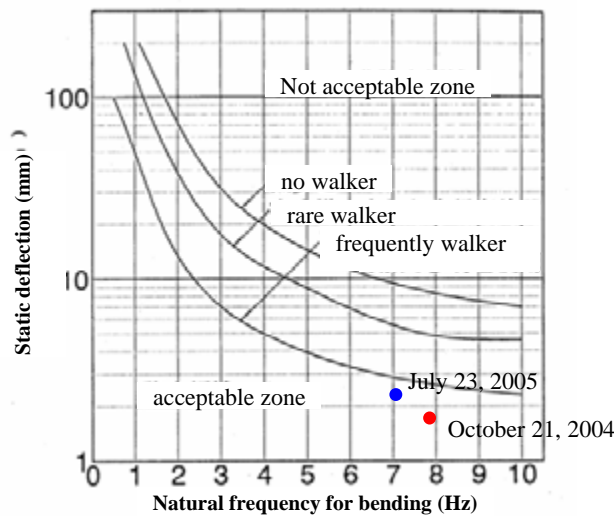


Figure 15: Frequency distribution of reinforcement steel bar against vehicle

4. CONCLUSIONS

In this paper, the measurement method for soundness evaluation is discussed through the load test of RC beams. And the pilot monitoring based on behavior measuring of RC road bridge in situ by the use of some sensors, such as optical fiber sensor and velocity meter, was performed.

The following conclusions can be drawn:

- a. Based on the result of loading tests of RC beam, the flexural stiffness degrades after reinforcement yield.
- b. The effect of concrete creep on the deflection might be taken into considering in the evaluation of safety performance from point of view of reinforcement bar safety.
- c. Obtaining the strain distribution in considered cross section utilizing optical fiber, the soundness for safety performance could be evaluated. The safety performance was assessed by comparison the flexural strength and acting flexural moment.
- d. As the result of behavior measurement utilizing the sensors, such as optical fiber to measure the extreme tensile concrete fiber and the velocity meter to measure the deflection and frequency, the soundness of structural performance, i.e. safety and serviceability performances, could be evaluated based on measurement data.

REFERENCES

- Ministry of Land, Infrastructure and Transport of Japan (MLIT), 2002. Annual statistics report of road, Japan Highway Users Conference.
- Japan Society of Civil Engineers (JSCE), 2002. Standard specification for concrete structures “Structural performance verification”, 14-16.
- Balaguru, P.N. and Shah, S.P., 1982. A method of predicting crack widths and deflection for fatigue loading. *ACI Special Publication 75-5, Detroit*, 153-175.
- Okamura, H. and Maekawa, K., 1991. Nonlinear analysis and constitutive models of reinforced concrete. Gihoudou publishing company, 44-45.

DEVELOPMENT OF MONITORING SYSTEM FOR RC BRIDGE BASED ON RESTORATION DESIGN METHOD

SHINICHIRO OKAZAKI¹
TAKETO UOMOTO²

¹Department of Civil Engineering, University of Tokyo

²International Center for Urban Safety Engineering,
Institute of Industrial Science, University of Tokyo
okazaki@iis.u-tokyo.ac.jp

ABSTRACT

There are about 670,000 road Bridges in Japan. As for these bridges, standard design code has been greatly revised in order to reflect the increase of live load and earthquake especially after Hanshin-Awaji earthquake. For example, for structures, designed followings the code used before Hanshin-Awaji earthquake may be in appropriate for seismic load. In addition, most of the bridges are inspected only by visual inspection, causing difficulty to inspect all bridges in details. Therefore it is required to build an effective and efficient maintenance system for increasing number of bridges. To maintain those old bridges, we cannot estimate the deterioration without design drawings and calculated details. However, old bridges usually don't have this information. In this case, used to restore those information can be restoration design method.

This research shows that, it can extract the bridge which has no design drawing and calculated details and estimated their structural performance every revision of design code by applying restoration design method. This result shows that the supper structure of this bridge is safe enough to be continually used, but pier does not have enough capacity for seismic wave. So it is develop a new monitoring system for pier to evaluate condition of bridges at any time by accelerometer attached t piers for measuring seismic damage, and estimating condition of the bridge.

1. INTRODUCTION

In Japan, we have a lot of highway road bridges almost 670,000. These of bridges stocks which are serviced more than 50 years are increasing greatly. So it can be said that it is necessary to construct an effective, efficient maintenance management, in order to do the priority level of the selection of the bridge for the maintenance management program more simply and objectively.

In addition, although various inspections are required when the maintenance management is actually conducted, it is necessary to know the initial condition of the structure to predict the deterioration extent. The deterioration cannot be estimated without design drawings and calculated details. However, old bridges usually do not have this information. In this



Figure 1: Focus Bridge

case, it is generally restore that information by using restoration design method.

This research shows that we can extract the bridges which have no initial design drawing and calculated details and estimate the structural performance in addition with every revision of design code by applying restoration design method. This research is also developed a new monitoring system for RC bridges to evaluate, current condition of bridges at any time by using accelerometer attached to piers for measuring seismic damage.

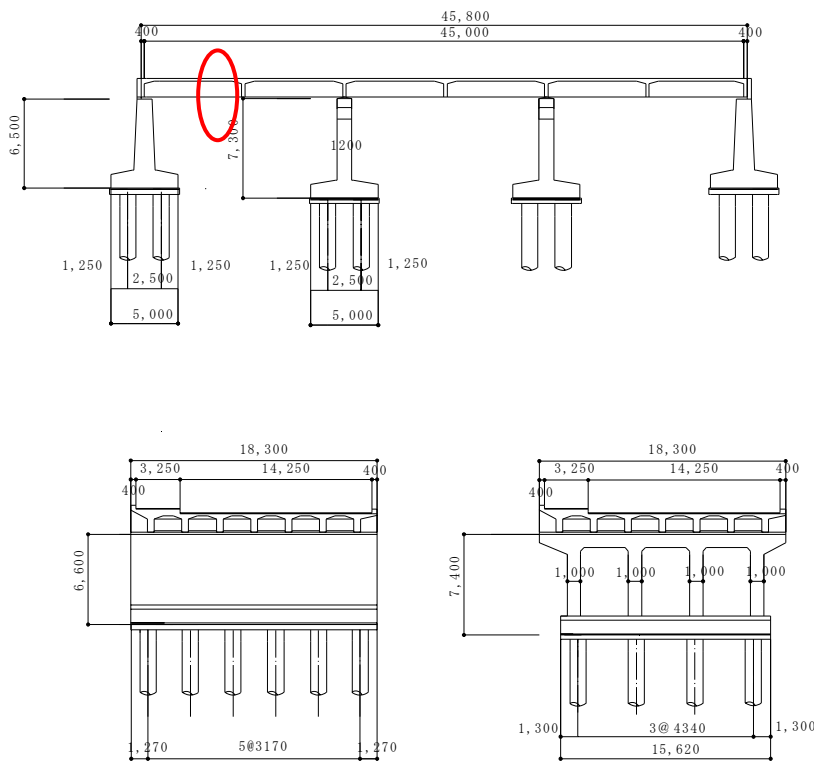


Figure2: Cross-Section of the Focus Bridge

Table 1: Major Modification of the Design Codes

	Before 1973	1973~78	1978~80	1980~90	1990~94	1994~96	1996~2002	2002~
Superstructure work	The design weight of car as live load is 20tf	-	<ul style="list-style-type: none"> Applying ultimate strength design method Minimum strength of concrete is changed 21N/mm² 	-	Changing calculation of minimum thickness of slab	The design weight of car as live load is 25tf	-	Reduced allowable tensile stress of concrete
Substructure work	-	Changing the bearing capacity formula of pile	-	-	-	-	Applying ultimate lateral strength design method for all members	-
Seismic design	Seismic force is calculated by $0.2 \times W$ (W:weight of bridge)	-	-	Applying modified seismic coefficient method	Applying ultimate lateral strength design method for pier	-	<ul style="list-style-type: none"> Applying ultimate lateral strength design method for all members Two types of design seismic wave is defined 	Two levels of seismic wave is defined

2. RESTORATION DESIGN METHOD

Restoration design method is used to restore the arrangement of restoring reinforcing bars and stress condition based on the cross-section information of a bridge (length, width of bridge and girder, pier, etc.) and the then design code.

The example bridge showing figure 2) has been from 1970, and length of bridge is 45m, width is 18.3m, type of superstructure and pier is rigid-frame structure. The road bridge specification and JSCE guidelines for concrete are based on. And there is no information about property of concrete. It is assumed that designed compressive stress of concrete is 18N/mm², and allowable compressive stress due to bending is 8N/mm². The type of steel bar is SD295, and allowable tensile stress is 140N/mm².

REVISION OF DESIGN CODE

In addition to the restoration of the design drawing and calculated details, the same information at restoring them every transition of design code, are also restored for evaluating the safety is also conducted. Table 1 shows main changes of design codes. In 1990, new seismic design method, and ultimate lateral strength design method were introduced. Then in 1996, design live load was changed to 25tf from 20tf, the value that has been used since 1973.

ABOUT EVALUATING SAFETY

When evaluating the safety, the latest code of JSCE, "JSCE guidelines for concrete, standard specifications for concrete Structures-2002 structural performance verification", was applied. For super structure work, the safety, serviceability, and fatigue were evaluated. For substructure work, we safety to seismic load was evaluated.

RESULT OF RESTORATION DESIGN METHOD

Figure 3, 4, 5 shows the results of restoration design method for the example bridge. In this case, we focus only the pier of substructure work because pier received the largest damage from seismic wave. Comparison between restored designs information and the design drawings which is available only upper structure work, show almost the same result. So this fact shows that this method has high reliability and accuracy.

Figure 3 shows that ratio of tension reinforcement of girder and slab change only 0.1% in 1994. But figure shows that ratio of tension reinforcement and hoop tie is largely changes in 1990 and 1996. For these amounts of reinforcement, are inadequate when compared to that of the latest design code. Figure 4, 5 shows that ratio of tension reinforcement and tie hoop is greatly changed at 1990 and 1996, the year of changing the design code.

At first, girder of super structure was estimated. And place which is received the largest bending moment from living load of this bridge is in the circle on Figure 2, In this case, the amount of reinforcement changes only in 1994. Figure 6 shows that the original slab's cracking moment is less than design moment of the latest design code, but yield moment is more than design moment. In figure 7 girder's clacking moment is more than design moment. So, this result shows that super structure work has enough capacity to ensure its safety all during period at all era.

And next, table 2 shows the result of comparison between the safety ratio for fatigue of the girder by the newest code, and old one. The safety rate f is calculated from the following equation (1).

$$\frac{1}{f} = \gamma_i \frac{\sigma_{rd}}{f_{rd} / \gamma_b} \quad (1)$$

(f : safety ratio for fatigue γ_i : structural analysis factor, γ_b : member factor, σ_{rd} : variable load, f_{rd} : design fatigue strength of material)

Each era of bridge also have enough safety for fatigue.

And next we estimate serviceability by displacement due to bending which is calculated by following equation (2).

$$u = \frac{1}{EI} \iint M dx dx \quad (2)$$

(u : displacement of girder, E : Young's modulus I : effective moment of transformed cross section, M : designed bending moment)

The limit displacement is not specified description on the code, so it is applied highway bridge that of Railway Bridge instead. The strictest value in this criterion is $L/1800$ (L : span of the bridge (m)), the code for the Shinkansen, super express in Japan. In this case, the limit is 8.3mm and Fig shows the calculated displacement of this bridge in case of designed load. Each era of bridge also have enough serviceability.

Next, pier is estimated. In this case, Figure 6 shows the result for verifying only the axial direction of bridge. By using the ultimate lateral strength method, verifying the proof stress of bridge at each era for seismic wave. And safety ratio of ultimate lateral strength for seismic wave is defined by followed equation (3), and makes safety fixed quantity.

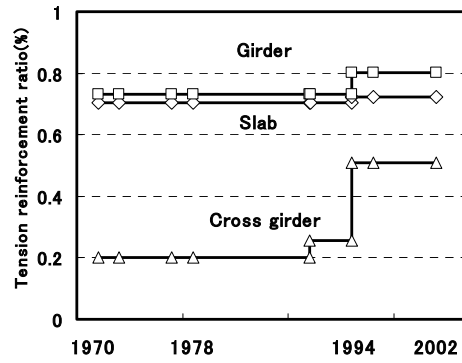


Figure3: Modification of Tension Reinforcement (Super structure)

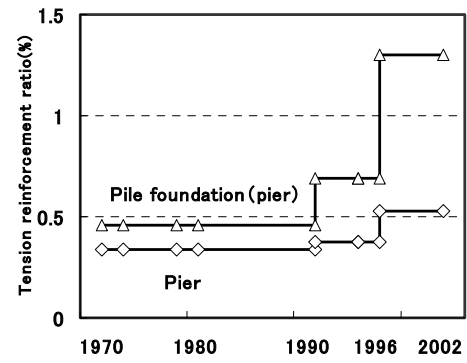


Figure4: Modification of Tension Reinforcement (Sub structure work)

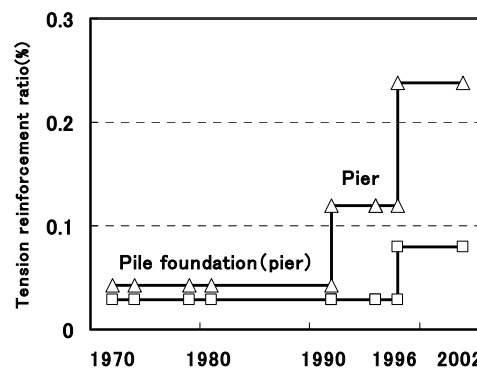


Figure5: Modification of hoop tie (substructure work)

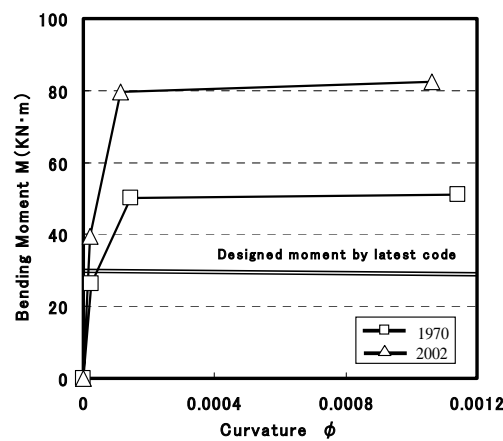


Figure6: M- φ graph of slab

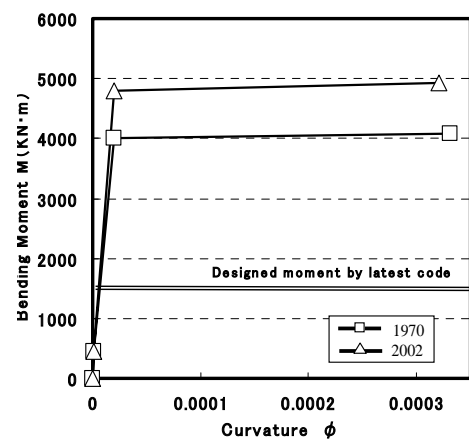


Figure7: M- φ graph of girder

Table2: Result of estimating the focus bridge at each era

	Year	Yield moment of steel (kN·m)	Ultimate moment (kN·m)	Safety ratio for fatigue of steel f	Safety ratio for fatigue of concrete f
Girder	1970	3.96×10^3	4.09×10^3	4.44	2.42
	2002	4.74×10^3	4.92×10^3	4.19	2.60
Slab	1970	50.0	51.0	1.65	1.42
	2002	79.4	82.3	2.86	1.81

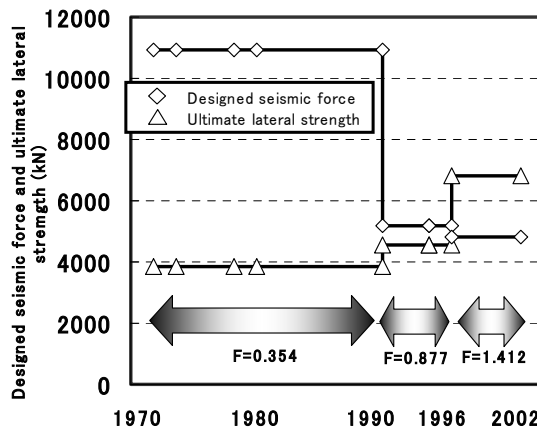


Figure8: Modification of designed seismic force and ultimate lateral strength (substructure work)

$$F = \frac{P_u}{P_q} \quad (3)$$

(P_u : ultimate lateral strength of pier, P_q : designed seismic load)

Figure 8 show that designed seismic load is decrease as proceeding era due to allowable plastic ratio is increasing and, and ultimate lateral strength is increasing because of the increasing amount of the tension reinforcement. So the safety ratio is less than 1.0 at the era of before 1996, it is suggested that they are required to reinforce.

3 MONITORING SYSTEM FOR RC BRIDGE

For maintaining concrete structures properly, it is required to estimate their condition precisely. And based on the result, it is required to plan how to repair that structure. In future, the number of aged bridge becomes rapidly increase. So it will be very difficult to conduct visual inspection on to all bridge. So it is recommended to estimate health of bridge by using network system. The outline of this system is that, the instruments which are set up on girder and pier and so on measure at and send these data to any place on the network at all time. And estimating the health by processing health of structure is estimated by processing these data.

Nowadays, RC bridges are measuring flexure and vibration of girders by any kind of instruments experimentally, but couldn't estimate structure condition because systems are not developed the systems theoretically. So we develop new system for estimating theoretically.

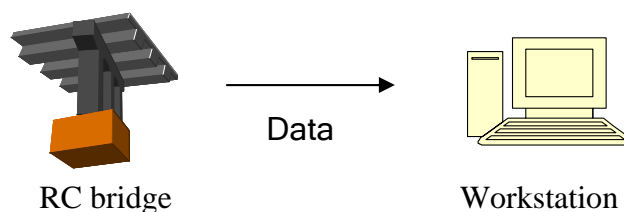


Figure8: Example of Monitoring System

3.1 DEVELOPMENT OF MONITORING SYSTEM

This system is that, measuring any data at the target bridge and saved instant data are sent by fiber optic and received and save them at workstation in IIS (Institute of Industrial Science, University of Tokyo). The results of section 2, the upper structure of this bridge is safe enough to be continually used, but pier does not have enough capacity for seismic wave. So pier is required to be monitored the damage by seismic wave at any time. For estimating the load of seismic wave and displacement of pier, two accelerometers which can measure triaxial direction are put on the top of the pier and inside the ground. In case of earthquake, the accelerometer in the ground observes seismic wave and each accelerometer start measuring the acceleration of the wave. In the next section, the method shows how to estimate the damage to pier by these data.

3.2 ESTIMATING DAMAGE TO PIER

Figure 9 shows the wave which observes in the ground at Oct 23, 2004 (Niigata Earthquake). The maximum differential displacement which is integrating this wave twice on time direction of each data is 0.078mm. By using this displacement, calculate the maximum bending moment is calculated, at the root of the pier. Figure 10 shows the model for calculating the bending moment at any place of pier on the axial direction of bridge. This model shows that displacement δ is given by load P on the top of the pier. In this case, relative displacement of the top of the pier and the ground is defined δ , the inertial force of upper structure is P, and the bending moment at root of the pier is M. Then we can calculate P and M by measured δ in case we supposed that the pier has elastic behavior (following equation (4),(5)). In addition the stiffness of member is 4 times of the stiffness of one element of pier because 4 bodies of the rigid-framed pier receive the seismic wave on axial direction of the bridge.

$$P = 3EI' \delta / L^3 \quad (4)$$

$$\begin{aligned} M &= PL \\ &= 3EI' \delta / L^2 \end{aligned} \quad (5)$$

(P: inertial force of upper structure, M: bending moment at root of pier, EI': stiffness of pier on axial direction of the bride, δ : relative displacement of the pier and the ground L: height of the pier over the ground)

Figure 11 shows calculated bending moment on the M- ϕ graph of the element of the pier. On present stage, only comparing measured moment to capacity of the pier, it has enough safety to this seismic wave. Applying this equation to the collected data into workstation, this system can evaluate the damage to the pier immediately.

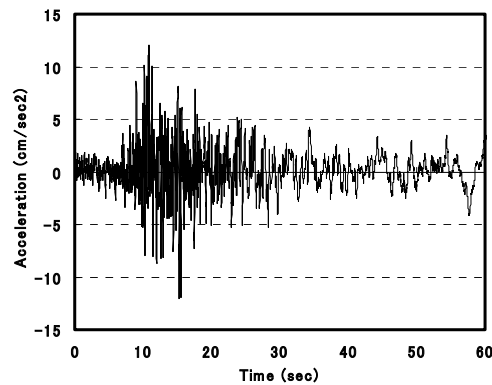


Fig9: Acceleration Data of Niigata Earthquake

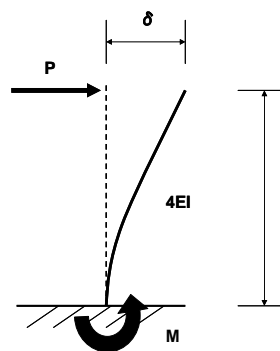


Fig10: Model for Calculating the Bending Moment

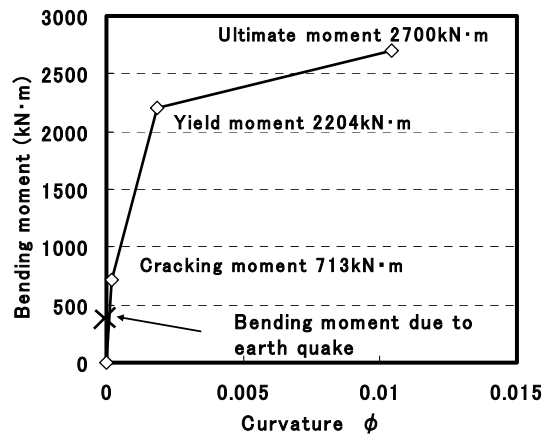


Fig11: Calculated bending moment on the $M- \phi$ graph of the element of the pier

4 CONCLUSION

The result of this research is as follows.

- (1) It is possible to restore reinforcing bar arrangement by using restoration design method
- (2) Result of restore design method by each era of changing design code shows that super structure have enough safety but pier which is before 1996 don't have enough resistance against earthquake.
- (3) By developing monitoring system, it is possible to evaluate the damage on pier by calculating the bending moment.

STUDY ON DURABILITY OF RC DECK OF EXISTING PIER

Ema Kato, Atsushi Yokozawa, Yoshikazu Akira, Hiroshi Yokota
Port and Airport Research Institute, JAPAN
katoh-e@pari.go.jp

ABSTRACT

To keep harbor structures in good condition during their service period, it is necessary to implement a well organized maintenance strategy and to conduct suitable maintenance work according to the degree of deterioration. For this purpose, it becomes very important to quantitatively evaluate the present and future structural performance of deteriorated structures.

This paper discusses the structural performance and material deterioration of reinforced concrete deck of the existing pier which has been in service for 39 years. Reinforced concrete slabs were extracted from the deck and were load tested in the laboratory. The degree of material deterioration was analyzed with the extracted slabs by measuring the mechanical properties of concrete and the degree of rebar corrosion.

1. INTRODUCTION

Reinforced concrete structures in harbors are attacked by chloride ion, which may cause deterioration of materials. As a result, corrosion of rebar embedded into concrete may induce cracks in concrete and subsequently cause spalling of cover concrete. The material deterioration, particularly corrosion of rebar decreases structural performance (Yokota et al., 1998), but the relationship between the rebar corrosion and structural performance has not been made clear.

In this study, the material deterioration and the remaining structural performance of the existing structure were experimentally investigated. Test slabs were extracted from the deck of the existing pier that has been in service for about 39 years.

2. OUTLINES OF INVESTIGATION

2.1 Test Slabs

Figure 1 shows a general cross section of the pier that has been in service for 39 years. Three test slabs were extracted from the reinforced concrete deck of the pier, shaded regions in Figure 1. The structural details of the slabs are given in Table 1. The distances from the bottom surface of the slabs to H.W.L. and L.W.L. were about 0.1 m and 2.2 m respectively; therefore, all the extracted slabs were located in the splash zone. The

deterioration grades of slabs were judged visually according to the Manual on Maintenance and Rehabilitation of Port and Harbour Structures as summarized in Table 2 (Port and Harbour Research Institute ed., 1999). Partial delamination of cover concrete was observed in slab No. 1. In slab No. 2, many cracks and delamination were observed. In slab No. 3, all the cover concrete disappeared and heavy rebar corrosion was observed. Moreover, the white products were observed around the aggregate in No.3.

Since the mechanical properties of the rebar were not stated in the design documents, tensile tests of non-corroded rebars sampled from No. 1 were conducted to examine their fundamental mechanical properties, which is summarized in Tables 3.

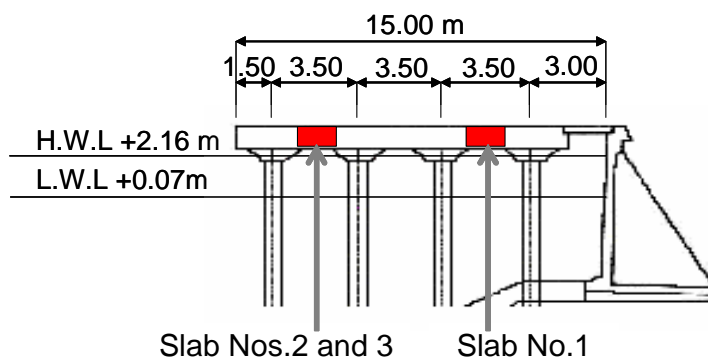


Figure 1: Outline of the pier.

Table 1: Outlines of slabs.

Slab No.		No. 1	No. 2	No. 3
Width (mm)		1513	1465	1498
Length (mm)		1518	1523	1510
Thickness of slab (mm)		269	373	309
Thickness of pavement (mm)		—	86	71
Transverse rebar	Diameter (mm)	13	13	13
	Number of upper rebar	4	4	4
	Position below the top (mm)	98	199	189
	Number of lower rebar	8	7	7
	Position below the top (mm)	215	309	306
Longitudinal rebar	Diameter	13	13	13
	Number of upper rebar	4	4	4
	Position below the top (mm)	111	205	204
	Number of lower rebar	8	8	8
	Position below the top (mm)	200	292	300
Deterioration grade		II	III	V

All rebars are a deformed bar.

Table 2: Definition of the deterioration grade.

Grade	0	I	II	III	IV	V
Rebar corrosion	No	Localized spotted rust stain	Small extent of rust stain	Much rust stain	Heavy rust stain	Large extent of rust stain
Crack	No	Only a few small cracks	Some cracks	Many cracks	Many wide cracks	—
Cover concrete	No	No	Partial delamination	Partial spalling	Spalling	Large extent of spalling

Table 3: Mechanical properties of rebar.

Yield strength	386 N/mm ²
Tensile strength	544 N/mm ²
Young's modulus	192 kN/mm ²

2.2 Investigations

2.2.1 Measurements of compressive strength and *Cl* contents

The concrete cores of 100 mm in diameter were taken from each slab after the loading test. The compressive test was conducted with these cores cut by 200 mm long. To measure the chloride ion contents in concrete, concrete samples in slabs Nos. 1 and 2 were milled into powder sample after cutting into small pieces. Then, chloride ion contents were measured with the dissolved powder samples as per the JCI Standard (Japan Concrete Institute, 1987). Then, diffusion coefficients of chloride ion in concrete were calculated according to Fick's second law of diffusion.

2.2.2 Evaluation of Rebar corrosion

After the loading test, the upper and lower longitudinal rebars in the loading span, which carried tensile force in the loading test, were taken out from the concrete and visually inspected. In slabs Nos. 1 and 2, corrosion of the upper longitudinal rebar was not observed, therefore, the weight losses of these rebars were set at 0.0 %. The weight losses of the other longitudinal rebars were measured by the following procedures: At first, the rebar was cut into 2 pieces of 100mm long each. Rebars were sand blasted to remove corrosion products and concrete sticking to the surface of rebars. Then, rebars were immersed in 10% diammonium hydrogen citrate solution to completely remove corrosion products.

2.2.3 Loading test

Figure 2 shows the test setup. Slabs were simply supported with a loading span of 1000 mm. A monotonically increased load was applied symmetrically at three points. During the test, the applied load and deflection at the supporting points and at the midspan were measured and

recorded. Because the cover concrete had already spalled in slab No.3, the supporting area of the slab was reinforced by mortar.

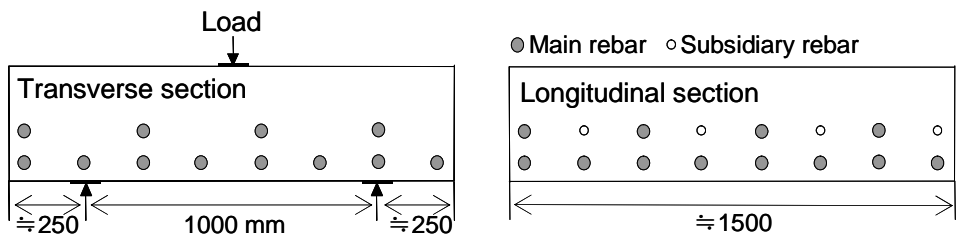


Figure 2: Test setup

3. RESULTS AND DISCUSSIONS

3.1 Material deterioration

3.1.1 Compressive strength and Young's modulus

Figure 3 shows the relationship between the compressive strength and Young's modulus of concrete of each slab. The line in this figure shows the relation for general concrete specified in the Standard Specifications for Concrete Structures (Japan Society of Civil Engineers, 2002a). If concrete is not deteriorated, experimental results are the same or slightly larger than the values indicated by the line. However, all the experimental results were smaller than those. Especially, decrease in Young's modulus and its scattering were remarkable in slab No. 3. This decrease was probably caused by the alkali silica reaction of aggregate (Kobayashi et al, 1993).

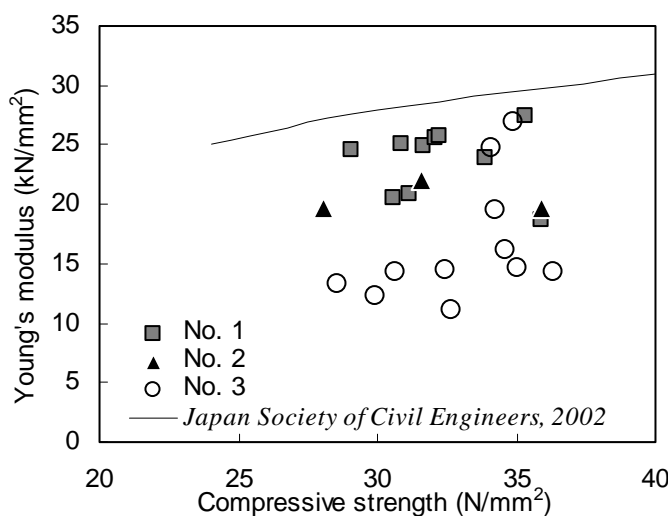


Figure 3: Compressive strength vs. Young's modulus

3.1.2 Chloride ion profiles

Figures 4 and 5 show the apparent diffusion coefficient and the surface chloride ion content of all concrete samples and results of visual inspections respectively. Though the concrete samples were extracted from non-deteriorated regions of the slab, diffusion coefficients and surface chloride ion contents varied with the extracted points.

Figure 6 shows the distribution of chloride ion contents based on the profile of normal distribution. They were measured with the concrete samples at 40 to 60 mm deep, which was in the cover concrete for the transverse rebars. The chloride ion contents in slab No. 1 were widely distributed compared with No. 2, while these averaged contents were not so different. As one of these causes, the difference in the sampling point of

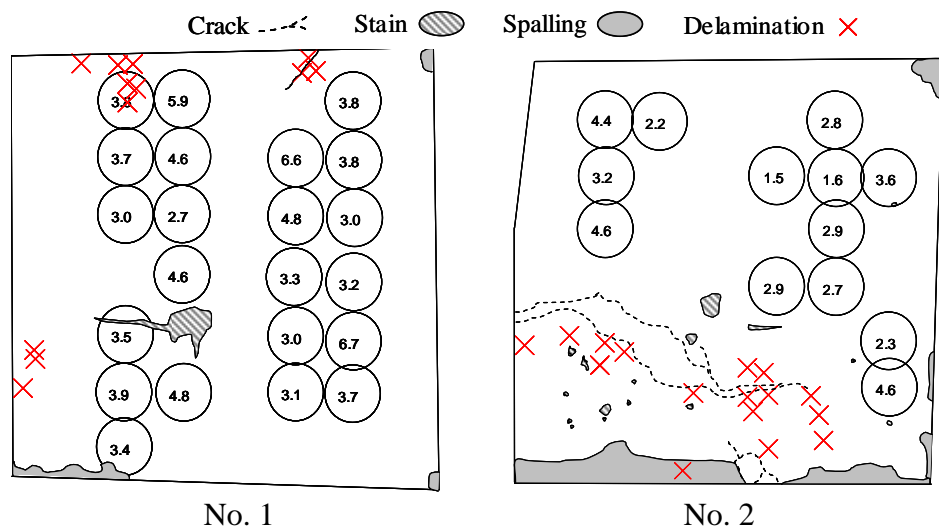


Figure 4: Distribution of apparent diffusion coefficient (cm^2/year)

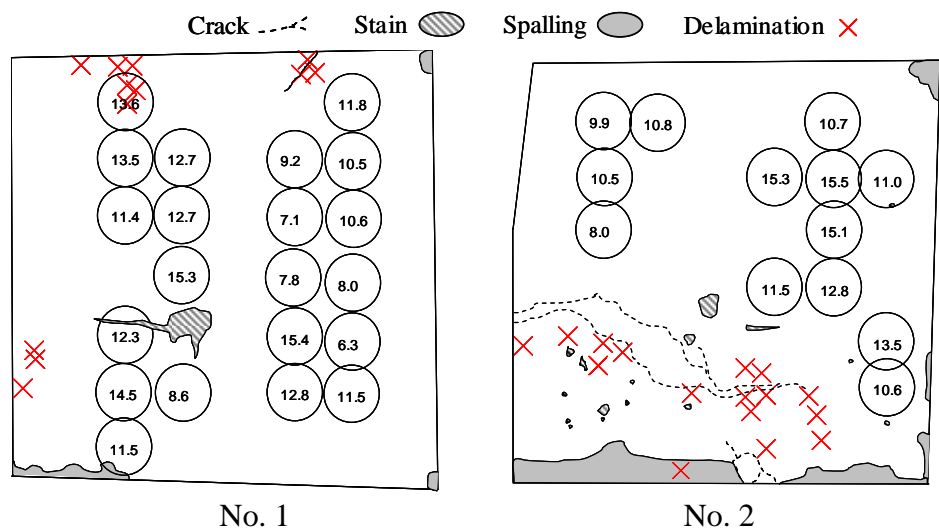


Figure 5: Distribution of surface chloride ion content (kg/m^3)

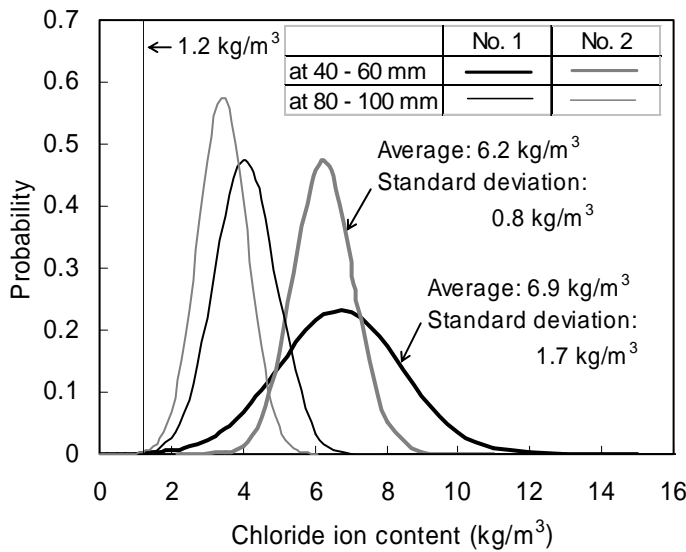


Figure 6: Distribution of Cl⁻ content

concrete was considered. Especially in slab 2, the sampling was done after obviously deteriorated parts were removed.

The measured chloride ion contents in the concrete at 80 to 100 mm deep were also plotted in the same figure. They showed less variation compared to those at 40-60 mm deep.

According to the Japan Society of Civil Engineers (2002b), the design chloride threshold value to start the rebar corrosion is set at 1.2 kg/m³. Because the chloride ion contents at the position of rebar in slabs Nos. 1 and 2 were larger than the threshold value, corrosion of the lower and the upper rebars in each slabs were considered to have already started.

According to the same standard specifications, the design chloride ion content at the position of rebar can be set at 1.3 times the calculated results with considering the dispersion. In this paper, the coefficients of variation of measured data were smaller than 0.25. Therefore, for the prediction of chloride ion content at the position of rebar, the value of 1.3 times the average data was considered to have enough accuracy.

In the investigation of existing structures in marine environment, chloride ion profile of concrete has generally been estimated according to one sampled concrete. Consideration of dispersions of material properties and environmental conditions is necessary to evaluate and to predict the present and future performance of the RC member.

3.1.2 Corrosion profiles

Figure 7 shows the frequency of weight loss of rebar in slab Nos. 2 and 3 based on the normal distribution. Rebar corrosion did not occur in slab No. 1, where the chloride ion content at the lower rebar was larger than the threshold value. In slab No.2, rebar corrosion occurred only in the delaminated and cracked areas. Because of the localized corrosion, these distributions were not considered to be suitable for the normal distribution.

Slab No. 3 had a wide distribution in weight loss of rebar ranging from 10 % to 60 %.

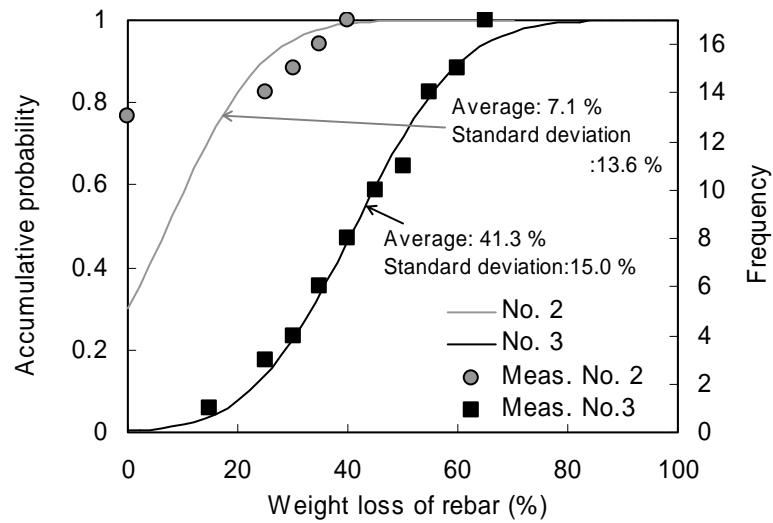


Figure 7: Probability and frequency of weight loss of rebar

3.2 Structural performance

The relationship between applied load and midspan deflection is shown in Figure 8. Because of the different positions of rebar, structural performance of each slab cannot be directly compared. However, the apparent stiffness decreased with an increase in the deterioration grade. It is considered that this is due to the corrosion cracks and deterioration of bond property between rebar and concrete (Japan Concrete Institute, 1998).

Figure 9 shows the relationship between ultimate load ratios and weight loss of rebar due to corrosion. The ultimate load ratio is defined as the ratio

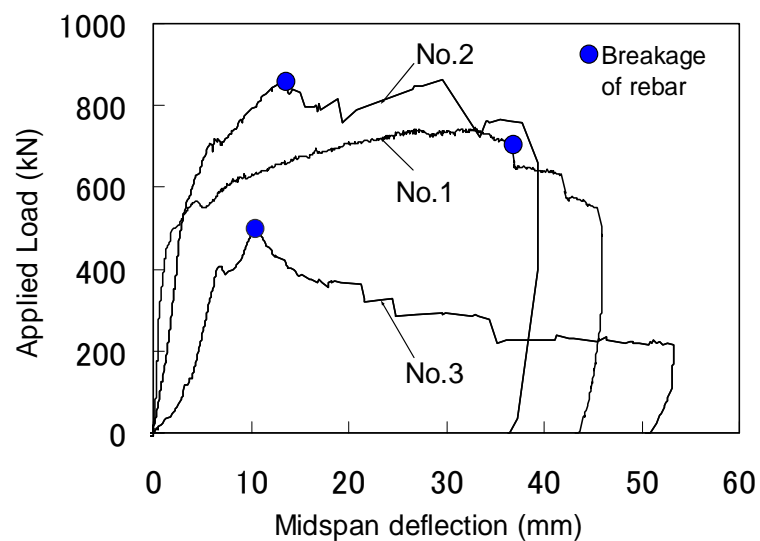


Figure 8: Applied load and midspan deflection

of the ultimate load to that of slab No.1. Those were modified with the dimension of each slab. In the same figure, the calculated ultimate load ratio taking into account the cross-sectional loss of rebars is also plotted as a broken line. The experimental ultimate load ratio of slab Nos. 2 and 3 were smaller than the calculated result. Horizontally straight lines in the same figure represent the maximum and minimum weight losses of rebar. The ultimate load ratios of the both slabs were not evaluated by the averaged weight loss of rebar. In slab No. 2, the ultimate load could be almost calculated with considering the maximum weight loss, however, that in slab No. 3 was not evaluated. Therefore, the difference between the calculated and measured ultimate loads was considered to become increase with an increase in the weight loss of rebar. Taking into account the localized corrosion, decreases in bond property and in elongation of rebar (Kobayashi, 2005) were simultaneously needed to evaluate the structural performance of heavily deteriorated RC members with good accuracy.

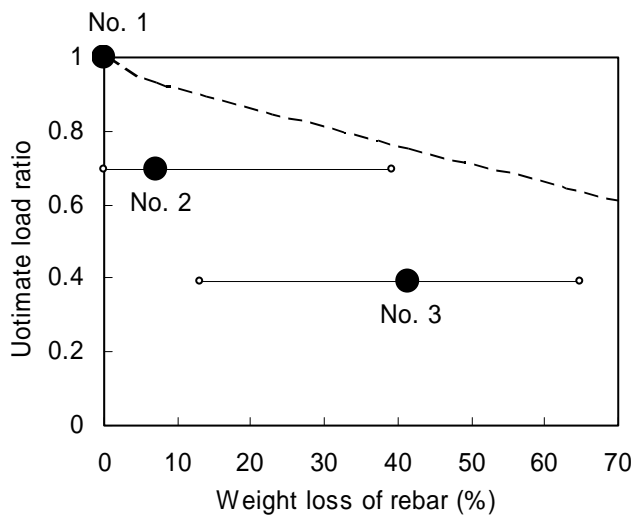


Figure 9: Weight loss vs. ultimate load ratio

4. CONCLUSIONS

In this study, the structural performance and material deterioration of a reinforced concrete deck of the existing pier that has been in service for 39 years were discussed. Influence of ASR on Young's modulus of concrete was considerably larger than that on compressive strength of concrete. The chloride ion profiles in the slabs were widely distributed; therefore, consideration of dispersions of material properties and environmental conditions was necessary to evaluate and predict the present and future durability of RC members. Moreover, the localized corrosion, the bond property and the mechanical properties of rebar were necessary to evaluate the structural performance of heavily deteriorated RC members with good accuracy.

REFERENCES

- Japan Concrete Institute, 1987. Corrosion of Concrete Structures, *Standards and Test Methods for Corrosion Protection*. (in Japanese).
- Japan Concrete Institute, 1998, Committee Report on Rehabilitation of Concrete Structures. (in Japanese)
- Japan Society of Civil Engineers, 2002a. Standard Specifications for Concrete, Structures-2002, Structural Performance Verification, JSCE Guidelines for Concrete, No.3, pp.32-33.
- Japan Society of Civil Engineers, 2002b. Standard Specifications for Concrete Structures-2002, Materials and Construction, pp.24-25. (In Japanese)
- Kobayashi, K., 2005. Experimental Study on Seismic Behaviour of RC Member Deteriorated by Chloride Induced Corrosion, *Concrete Research and Technology*, Vol. 16, No. 2, pp.49-59
- Kobayashi, K. et al., 1993, Method of Diagnosing Alkali-Silica Reaction by Compressive Loading Test, *Journal of Materials, Concrete Structures and Pavements*, Japan Society of Civil Engineers, No. 460 / V-18, pp.151-154 . (In Japanese)
- Port and Harbour Research Institute ed., 1999. Manual on Maintenance and Rehabilitation of Port and Harbour Structures, *Coastal Development Institute of Technology*, pp.91-103. (In Japanese)
- Yokota, H., Fukute, T., Hamada, T., and Akiyama, T., 1988. Structural Assessment of Deteriorated RC and PC beams Exposed to Marine Environment for More Than 20 Years, *Proceedings of the 2nd International RILEM/CSIRO/ACRA Conference*, Melbourne, pp.209-219.

SIMULATION STUDY ON RELATION BETWEEN LOCAL RAINFALL CONDITIONS AND AMOUNT OF MOISTURE SUPPLIED TO CONCRETE

YOSHITAKA KATO and NAOKI TAKESHITA
International Center for Urban Safety Engineering,
Institute of Industrial Science, University of Tokyo, Japan
katoyosh@iis.u-tokyo.ac.jp
Department of Civil Engineering, University of Tokyo

ABSTRACT

It is well known that deteriorations of concrete structures and these speeds depend on environmental conditions. There are few researches dealt with the evaluation of actual environmental impacts that can be used as boundary conditions for predicting the deteriorations progress of concrete structures though several types of simulation tools to predict the deteriorations progress of concrete structures have been developed. As a first step to address this matter, we tried to clarify the relation between the local rainfall conditions and the amount of adhering raindrops on concrete surface based on the simulation study.

The amount of adhering raindrops is necessary to predict moisture content of concrete structure appropriately. Therefore, a water absorption velocity of concrete was obtained experimentally. As a result, it was found that the water absorption velocity was quite small compared with the amount of rainfall. Therefore, the presence of adhering raindrops is important to discuss the effect of rainfall on the moisture content of concrete.

Finally, the treatment method of rainfall as boundary condition for predicting moisture content in concrete was proposed based on the analysis and experiment results. And the example of processing method of a large amount of weather data was also introduced as one example of utilization of this research result.

1. INTRODUCTION

It is well known that deteriorations of concrete structures are caused by several environmental impacts. For instance, carbon dioxides and chloride ions destroy passive state film formed on surface of reinforcing bar, as a result the reinforcing bar easily corrode with existences of water and oxygen. These deteriorations of concrete structure cause failure of concrete structure without conducting remedial measures. Proper remedial measures should be conducted based on a diagnosis result of an existing concrete

structure as well as a prediction result of a future performance of existing concrete structure before a damage of concrete structure becomes severe. To address this matter, several kinds of prediction models for deteriorations progress of concrete structures have been proposed. These proposed models can predict the deteriorations progress with certain accuracy under an applicable range of each model, especially in case of laboratory tests. However, it is usually difficult to apply these proposed models to predict the deteriorations progress of existing concrete structures because change of actual environmental conditions are larger than that of laboratory test. Environmental conditions, such as temperature, humidity, amount of supplied chloride ions and so on, are treated as boundary conditions in proposed models so that proposed model can predict the deteriorations progress of concrete structures considering actual environmental conditions. The reason why it is difficult to predict the deteriorations progress of concrete structures is that treatment methods of actual environmental conditions as boundary conditions of proposed models have not been clarified yet.

There are many environmental factors that should be considered to predict the deteriorations progress of concrete structures. Moisture affects on several kinds of deteriorations of concrete structure indirectly although moisture is not a factor to cause a deterioration of concrete structures directly. Moisture content of concrete is usually affected by rainfall and steam. The boundary condition of steam may be able to be set by using measurement results of humidity. On the other hand, the effect of rainfall on concrete surface might be complicate due to effects of rainfall, wind and structure form. Therefore, the adhering raindrop on concrete surface was simulated considering these effects. And the treatment method of rainfall as a boundary condition for predicting the moisture content of concrete was proposed based on the analysis results.

2. OUTLINE OF PREDICTION MODEL FOR AMOUNT OF ADHERING RAINDROPS ON CONCRETE SURFACE

Calculation of amount of adhering raindrops on concrete surface was conducted based on the following procedure.

- Basic input-data obtained from EA AMeDAS (Automated Meteorological Data Acquisition System) Weather Data (Akasaka 2003)
- Calculation of mean diameter of raindrops using Marshal-Palmer distribution (Marshal 1948)
- Calculation of terminal velocity of raindrops using empirical equation (Fabien 2002) based on experimental data (Gunn 1949)
- Simulation of rainfall using the finite volume method
- Calculation of amount of adhering raindrops on concrete surface from simulation result

2.1 Calculation of Raindrop Properties

Diameter, terminal velocity and density of raindrop in atmosphere are necessary to calculate the amount of adhering raindrops on concrete surface as input data-sets. Marshall and Palmer (1948) proposed probability density function of diameter distribution of raindrops per unit volume as follows (equation 1 and see Figure 1).

$$N_d = 8000 \exp(-4.1DR^{-0.21}) \quad (1)$$

where, N_d ($\text{m}^{-3}\text{mm}^{-1}$): probability density function of diameter distribution of raindrops per unit volume, D (mm): diameter of raindrops, R (mm/h): amount of rainfall per one hour.

Total number of raindrops per unit volume (K) and its weight (M) can be expressed as follows, respectively.

$$K = \int_0^{\infty} N_d dD = 1951R^{0.21} \quad (2)$$

$$M = \int_0^{\infty} \frac{1}{6} \pi D^3 N_d dD = 89R^{0.84} \quad (3)$$

Average weight of raindrops can be calculated using equation (2) and (3).

$$\frac{M}{K} = \quad (4)$$

Average diameter of raindrops (D_{ave} (mm)) can be calculated as follows with density of water ($1000\text{kg}/\text{m}^3$).

$$D_{ave} = 0.65R^{0.21} \quad (5)$$

Terminal velocity of raindrops (V (m/s)) was proposed by previous research result (Fabien 2002).

$$V = 9.4(1 - \exp(-1.57 \times 10^3 (D_{ave} \times 10^{-3})^{1.15})) \quad (6)$$

Finally, density of raindrops per unit volume (ρ_w (kg/m^3)) can be obtained using equation (7).

$$\rho_w = 2.8 \times 10^{-4} \frac{R}{V} \quad (7)$$

Figure 2 shows the relationships between raindrop properties that were obtained by the above mentioned procedure.

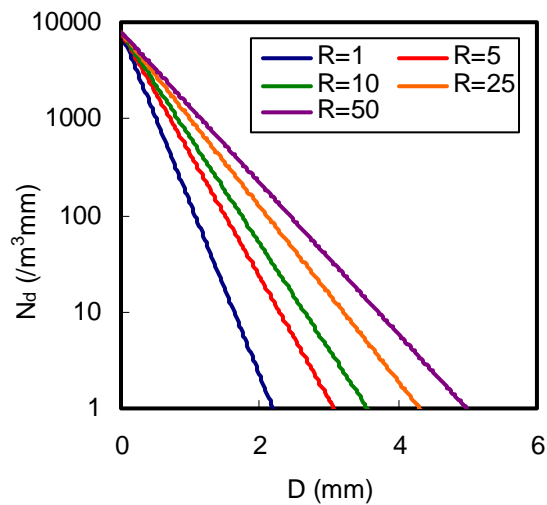


Figure 1: Marshall-Palmer probability density function

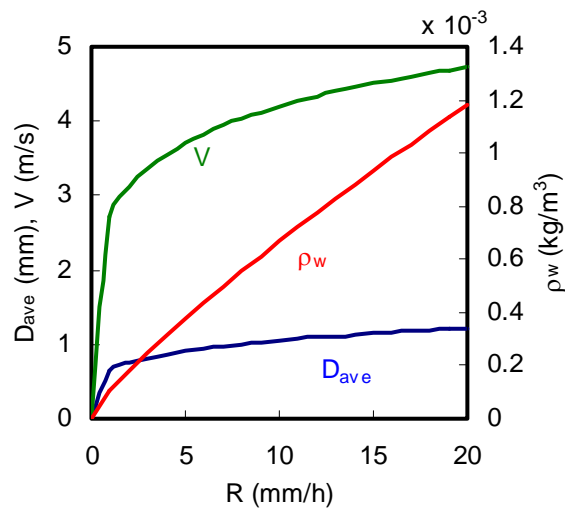


Figure 2: Relations between raindrop properties

2.2 Analysis Conditions

Simulation of rainfall was conducted using the finite volume method. It was assumed that raindrops were transported by air transportation. It is easy to simulate air transportation because air can be treated as continuous elements in this simulation. On the other hand, it is difficult and takes a long time to simulate raindrops itself because raindrops should be treated as discontinuous elements.

Structure condition of analytical object is shown in Figure 3 as a case study of this research. Analysis area is shown as the hexahedron (4 x 5 x 3) in same figure. One element of the analysis area is a cube of 0.25 in the length. In this research, a wind direction was assumed to be a transverse direction of the pier though a wind direction against structure is also very important factor to evaluate the amount of adhering raindrops on concrete surface. The effect of wind direction will be considered in our future research.

Analysis cases are shown in Table 1. These cases were determined based on the weather data measured at weather central in Tokyo. Namely, the range of analysis cases were determined based on maximum amount of rainfall (19 (mm/h)) and maximum wind velocity (8.2 (m/s)). And “1.74 (mm/h) is the ratio of total amount of rainfall of one year to total rainfall frequency of one year.

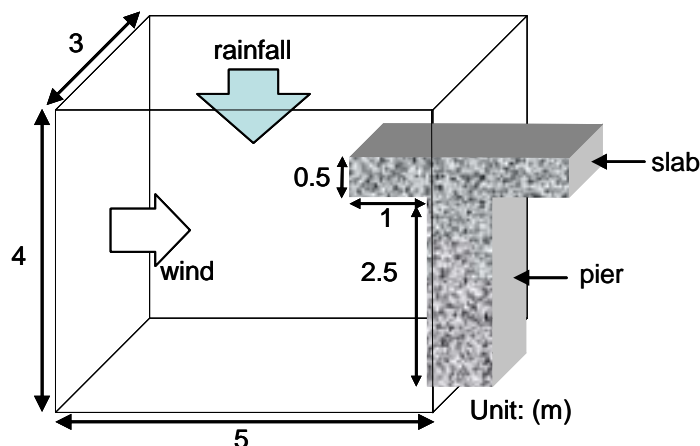


Figure 3: Analytical object

Table 1: Analysis cases

		Amount of rainfall (R) (mm/h)					
		1	1.74	3.54	7	12	20
Wind velocity (w) (m/s)	1	○	○	○	—	—	—
	2	○	○	○	—	—	—
	3	—	○	○	—	—	—
	4	—	○	○	○	○	○
	5	○	○	○	○	○	○
	7	—	○	○	○	○	○
	10	—	○	○	○	○	○

3. ANALYSIS RESULTS AND DISCUSSIONS

The amount of adhering raindrops is necessary to predict the moisture content of concrete structures appropriately so that it is important to discuss about the amount of adhering raindrops from this viewpoint. Before discussing the analysis results, a water absorption velocity of concrete was obtained experimentally because an amount of moisture penetrated into concrete is governed by the water absorption velocity of concrete.

3.1 Water absorption velocity of mortar

The water absorption velocity of concrete was obtained experimentally using mortar specimen. The reason why mortar specimen was used is to secure an accuracy of experiment with a reasonable level. The water absorption velocity was measured by an increment of specimen weight. The increment of specimen weight due to water absorption was considered to be quite small so that it was necessary to thin a thickness of specimen as much as possible. Moreover, an actual concrete surface was considered to be covered with a mortar layer.

The mix-proportion of mortar specimen was $W/C = 0.5$ and $S/C = 1.5$. Dimensions of the specimen are 60 x 60 x 5 (mm). The moisture content of

specimen is set to 0 (%) using D-dry processing. Figure 4 shows the method of supplying water to the specimen that simulated the raindrops.

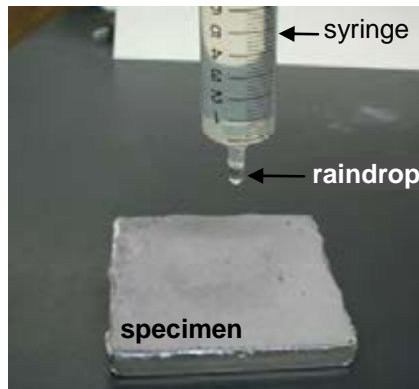


Figure 4: Experiment situation

Figure 5 shows the experiment results. It is found that the maximum water absorption velocity is around 0.6 (mm/h) and this value is quite small value for the rainfall. Therefore, it can be concluded that the presence of adhering raindrops is more important than the amount of adhering raindrops when the effect of rainfall on the moisture content of concrete is discussed.

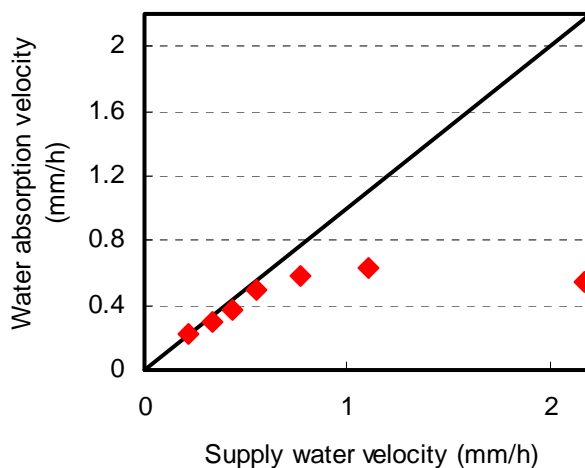


Figure 5: Water absorption capacity of mortar

3.2 Analysis results

Figure 6 shows the examples of analysis results. From these results, it can be found that there is no adhering raindrop on the concrete surface of the pier when the wind velocity (w) is small. In the case of amount of rainfall (R) = 1.74 (mm/h), raindrops never adhere to the concrete surface of the pier in that case the wind velocity = 1 and 2 (m/s). And an area of the concrete surface wet by adhering raindrops (wet area) is larger the higher velocity of wind (w). These phenomenons are caused by combination effects of rainfall, wind and structure form (slab width). The wet area can be determined using analysis results and corresponds to the relationship between the amount of rainfall (R) and the wind velocity (w).

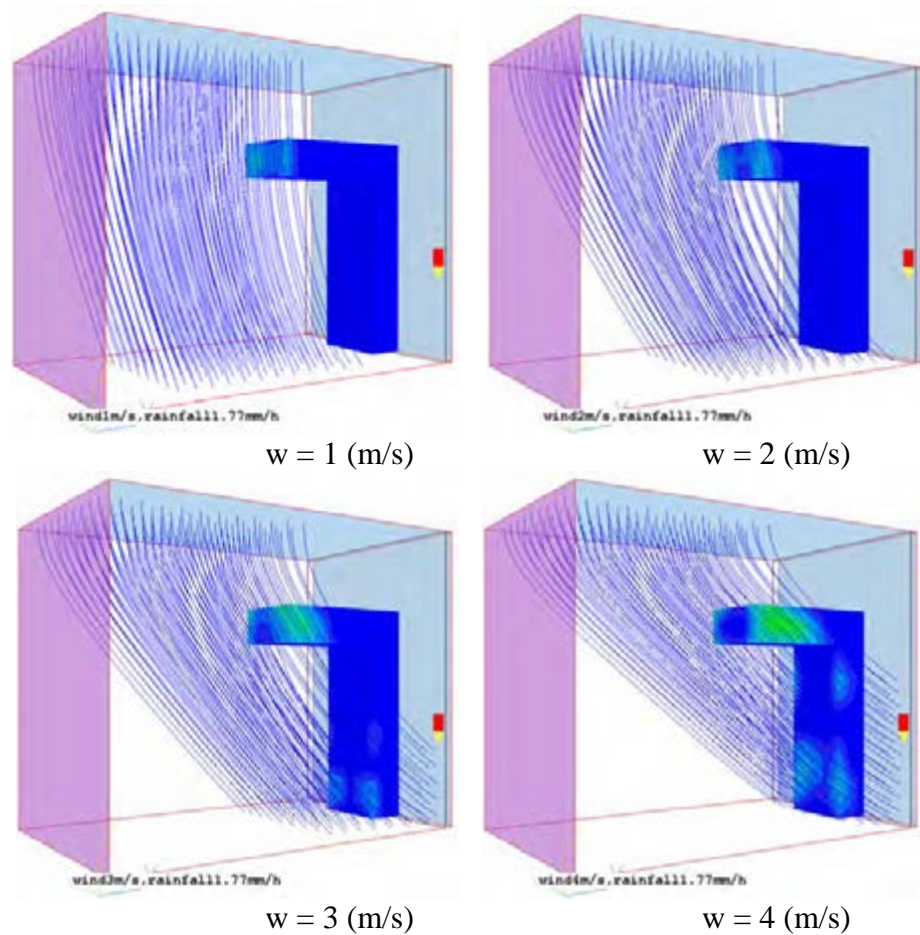


Figure 6: Examples of analysis results ($R = 1.74 \text{ (mm/h)}$)

Figure 7 shows a distance from a grand to a top of the wet area. An area below the line means the wet area, in other words, an area above the line means the dry area to which the raindrops never adhere. This relationship is naturally affected by the structure form so that this relation should be changed according to the structure form.

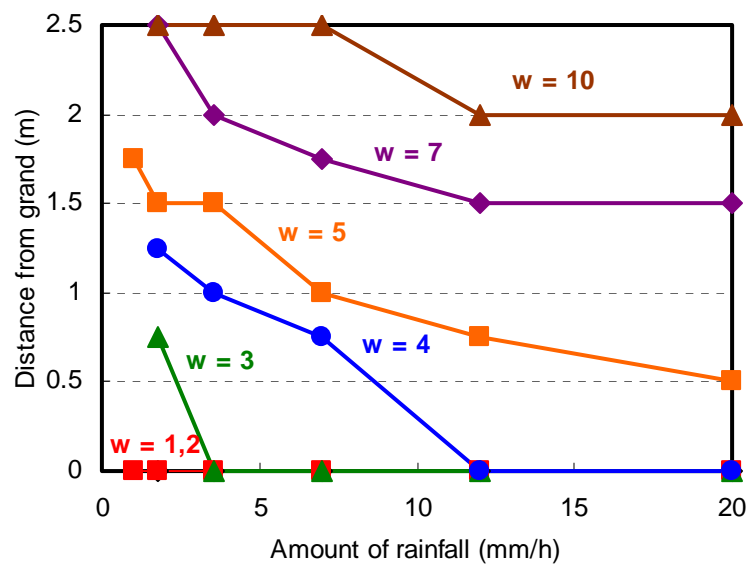


Figure 7: Calculation results of wet area

3.3 Utilization of analysis results to treat rainfall as boundary condition of concrete structure

Figure 8 shows the example of EA AMeDAS weather data. Then, how should we utilize these data as a boundary condition for predicting the moisture content in concrete.

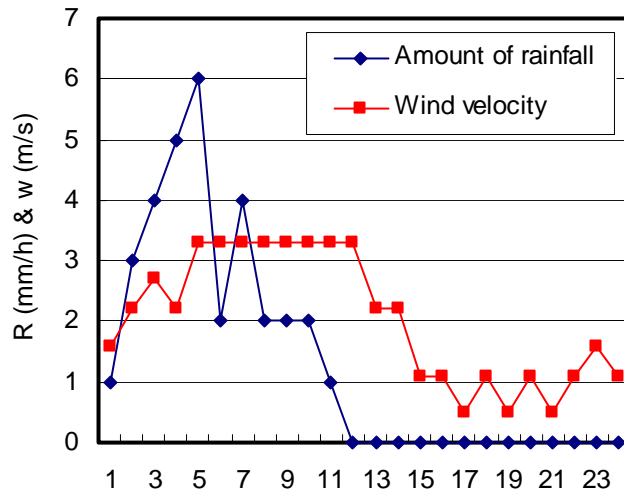


Figure 8: Example of EA AMeDAS weather data

As we already discussed, the presence of adhering raindrops is important when the effect of rainfall on the moisture content of concrete is discussed. Namely, the boundary conditions are simply divided into “Wet condition” and “Dry condition”. From this viewpoint, the boundary condition in the case of Figure 8 can be expressed as follows.

1 – 11: wet condition, 12 – 24: dry condition

However, this boundary condition may not be appropriate because the weather data does not show the presence of adhering raindrops on concrete surface. Figure 9 shows the calculation results of the distance from grand and top of the wet area that was discussed in previous section using the weather data. The boundary condition can be expressed as follows based on this calculation results.

- 1: dry
- 2-3: wet (below 0.75 (m)) dry (above 0.75 (m))
- 4: wet (below 0.5 (m)) dry (above 0.5 (m))
- 5: wet (below 0.75 (m)) dry (above 0.75 (m))
- 6: wet (below 1.25 (m)) dry (above 1.25 (m))
- 7: wet (below 1 (m)) dry (above 1 (m))
- 8-11: wet (below 1.25 (m)) dry (above 1.25 (m))
- 12-24: dry

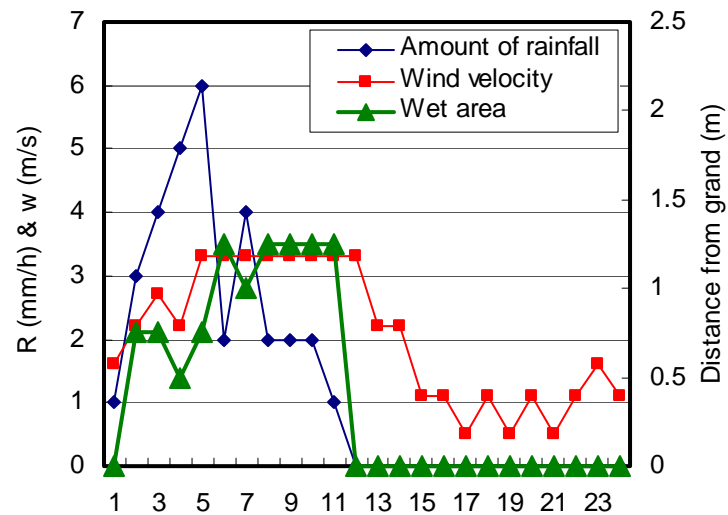


Figure 9: Calculation results of wet area using the weather data

Finally, the weather data of one year is statistically processed following the above mentioned method. The total rainfall time in one year is 500 hours according to the weather data. Figure 10 shows the relationship between the distance from grand to top of the wet area and distribution of its frequency as bar charts. It is found that the total time of wet condition is 247 hours in one year and the distance from grand to top of the wet area is almost below 1.25 (m). The boundary condition of concrete pier below 1 (m) in height is wet condition in the case that the distance from grand to top of the wet area is 1.0 (m). Therefore, the frequency of wet condition in each section can be expressed as cumulative of the distribution of frequency. The calculation result is also drawn in Figure 10 as a line chart. The boundary condition of concrete structure can be set appropriately considering the effects of rainfall, wind and structure form. And a large amount of weather data can be concisely processed using this proposed method.

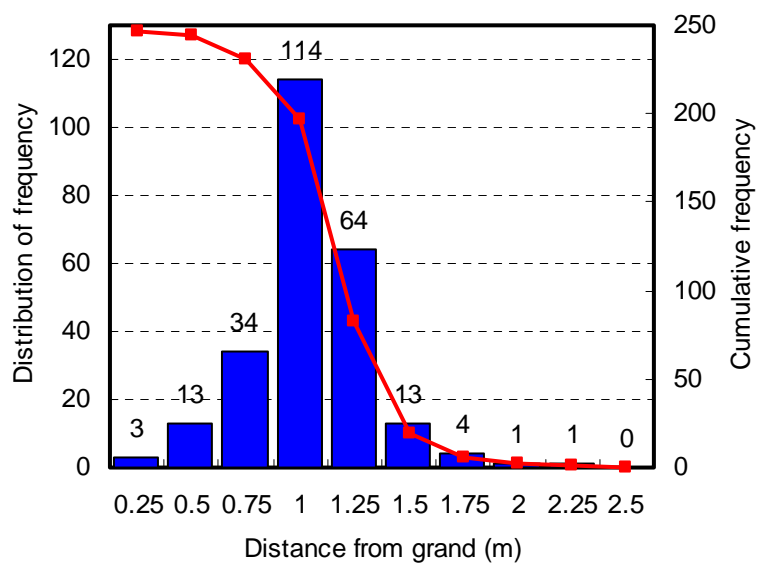


Figure 10: Relationship between wet area and frequency in one year

4. CONCLUSION

To develop treatment methods of actual environmental conditions as boundary conditions for predicting deteriorations process of concrete structures, the rainfall was selected as a first step of our research.

The amount of adhering raindrops is necessary to predict moisture content of concrete structures appropriately. The water absorption velocity of concrete was obtained experimentally because an amount of moisture penetrated into concrete is governed by the water absorption velocity of concrete. As a result, it was found that the water absorption velocity of concrete was quite small compared with the amount of rainfall. Therefore, the presence of adhering raindrops is important to discuss the effect of rainfall on the moisture content of concrete.

Finally, the treatment method of rainfall as boundary condition for predicting moisture content in concrete was proposed based on the analysis and experiment results considering the effects of rainfall, wind and structure form. And a large amount of weather data can be concisely processed using this proposed method.

REFERENCES

- Marshall, J. S. and Palme, W. M., 1948. The Distribution of Raindrops with Size. *J.Meteor*, Vol.5, 165-166.
- Gunn, R. and Kinzer, G. D., 1949. The Terminal Velocity of a Fall for Water Droplets in Stagnant Air, *J.Meteor*, Vol.6, 243-248.
- Akasaka, H. et al, 2003. Expanded AMeDAS Weather Data, Architectural Institute of Japan
- Fabien J.R. van Mook, 2002. Driving Rain on Building Envelopes. *Technische Universiteit Eindhoven*, 28-37

USING DIGITAL CLOSE RANGE PHOTOGRAMMETRY TO ESTIMATE DEFLECTIONS IN A BRIDGE

S FAISAL HASHMI¹, ONKAR DIKSHIT² AND SUDHIR MISRA³
Department of Civil Engineering
Indian Institute of Technology Kanpur, India 208 016

¹Former graduate student

²Associate Professor, onkar@iitk.ac.in

³Associate Professor, sud@iitk.ac.in

ABSTRACT

Deflections in bridges can be taken as a quantitative measure of their overall structural integrity. Whereas accurate measurement of deflection under load using conventional methods is very cumbersome, Digital Close Range Photogrammetry (DCRP) offers an easy, quick and accurate alternative. Results obtained in a study where the method was used to estimate deflections in a railway steel truss bridge are reported here.

The DCRP system is based on the principle of Direct Linear Transformation (DLT), wherein an effort is made to establish a relation between 3-D space coordinates in an object and the plane coordinates in a 2-D image, using DLT equations, whose coefficients called DLT parameters, reflect the relationship between the object space and image plane.

In the present study, 27 targets were fixed on a single 33m span of a multispans truss bridge, including 12 targets at locations not likely to be disturbed under application of load, which was done by having a goods train stop at predetermined locations on the bridge. The 3D spatial coordinates of all targets were determined using total stations, and images of the truss taken under varying load from two stations where digital cameras had been appropriately stationed. Using DLT, deflection under loading was calculated using the difference in coordinates of a given target before and after application of load. The observed deflection was found to vary between about 8.5mm to 18mm, depending on target locations. Further work on estimating the errors and accuracies is presently in progress.

1. INTRODUCTION

Deflection in bridges can be used as an indicator of its overall integrity. Conventional measurement of deflection can be carried out using dial gages, etc. but such methods require elaborate scaffolding and physically approaching the structure to record the observations. It may be noted that non-contact methods for estimation of deflections have also been

suggested in the recent past to enable better monitoring of concrete bridges (Markus and Mass, 1997; Tsakiri et al., 2004).

Now, though photogrammetry has been routinely used in several applications, rapid developments in the areas of digital photography, image processing, etc. have led to the evolution of Digital Close Range Photogrammetry, which can also be used as a simple yet effective tool for an accurate estimate of the deflections in bridges under the action of live loads. Results obtained in a study where the method was used to estimate deflections in a railway steel truss bridge are reported here. The loads on the bridge were applied by stopping a goods train at pre-determined locations on the bridge.

2. BASIC DIGITAL CLOSE RANGE PHOTOGRAMMETRY

In the recent years, DCRP has been used in diverse fields such as CAD, architecture, archaeology, medicine (Slama, 1980; Atkinson, 1996), and also in structural engineering in estimating deflections in laboratory tests, etc. (Markus and Mass, 1997, Tsakiri et al., 2004). In principle, the DCRP seeks to estimate the 3D coordinates of a point in an object using the 2D coordinates available for that point from two (or more) photographs taken from different locations (constituting a set of 'stereo images'). Thus, in simple terms, from a set of (x, y) coordinates $\{x_{ia}, y_{ia}\}$ and $\{x_{ib}, y_{ib}\}$ obtained for the point i from two images taken from locations, a and b , DCRP seeks to obtain the 3D coordinates of the i^{th} location [Abdel-Aziz and Karara, 1971, 1974; Marzan and Karara, 1975]. The method uses the principle of Direct Linear Transformation (DLT), which yields a set of collinearity equations, whose coefficients, called the DLT parameters can be defined as below (Ghosh, 1979)

$$x = \frac{L_1 X + L_2 Y + L_3 Z + L_4}{L_9 X + L_{10} Y + L_{11} Z + 1} \quad y = \frac{L_5 X + L_6 Y + L_7 Z + L_8}{L_9 X + L_{10} Y + L_{11} Z + 1}$$

In the overall setup, there are 11 unknown parameters in DLT equations (L_1 to L_{11}), which can be solved by using at least 6 known points in terms of object coordinates (X, Y, Z) and corresponding image coordinates (x, y) (Mikhail and Bethel, 2001) .

3. METHODOLOGY

A multispan railway steel truss bridge was identified for studying the possible application of DCRP in estimating deflections in field under service loads applied by the action of passing trains. The bridge consisted of several simply supported spans of 33m and all experiments were conducted on a single representative span (Span no. 4). Targets were fixed at different points of the truss in the central portion of the span and the change in their coordinates were studied under varying positions of the load, which was applied by having a goods train stop at predetermined location on the span.

3.1 The procedure adopted and targets used

The following is a summary of the procedure adopted in the study.

1. Targets are pasted at ‘positions of interest’. Targets used were O-shaped with a 100mm outer diameter as shown in Figure 1(a). This size of the targets was adopted on the basis of preliminary studies and after ensuring that the average number of pixels in each target should not be less than 64 (8×8), (Kadari, 2003; Sagar, 2004).

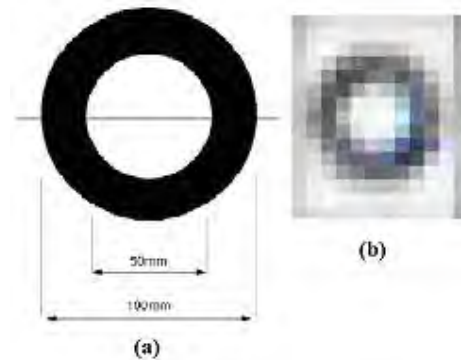


Figure 1: (a) Ring shaped target (b) Zoomed image of the same

2. A total of 27 targets were used, and were pasted at different points on the truss, piers and electric poles. Of these, 14 were pasted at locations likely to remain stationary (or their movements can be neglected), such as locations on the piers. These targets were used as reference or control points to estimate the changes in coordinates of the other ‘live’ targets, fixed on the truss.
3. 3D coordinates of at least six of the targets are determined directly using a Total Station (TS). These six points were not likely to move on account of application of load, and are referred to as *control* or *reference* points, as against others, which were ‘live’ in nature.
4. Two photographs are taken from two different camera stations to constitute a stereo pair used for computation of coordinates. It may be mentioned that the targets as they appear in a photograph were appropriately zoomed, as shown in Figure 1(b). It can be clearly seen that the edges of the ‘well-defined’ circle appear jagged, and it is not easy to uniquely identify the centre of the circle, as discussed later.
5. Using coordinates of control points measured on photograph and those by TS, a DLT model is established for both camera stations in the form of aforementioned DLT equations.
6. The model established in (4) above is used and the photo coordinates of control targets from the stereopair, the DCRP system computes 3D coordinates for all targets points. The details of the system development are available elsewhere (Hashmi, 2005).
7. Using the set of coordinates obtained without any loading as reference, the deflections under different loading conditions are calculated from the difference in corresponding values.

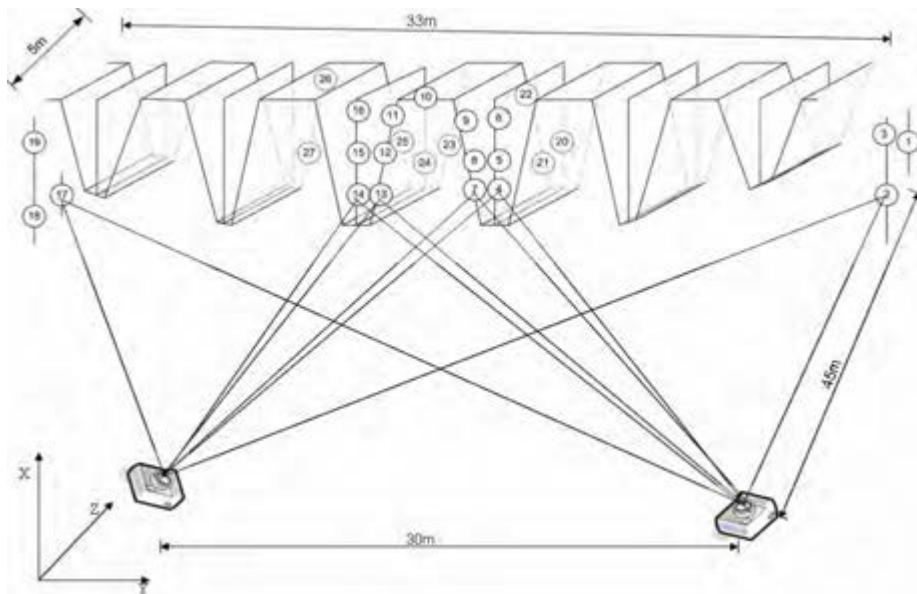


Figure 2 Experimental set up used in the field showing different targets fixed to the bridge and camera positions

3.2 Set up used at site

Figure 2 shows schematically the arrangement adopted with two camera stations separated by about 30m at a distance of approximately 45m from the bridge being used for taking appropriate photographs of targets pasted on the bridge and numbered from 1 to 27. It is clear that the study concentrated on estimating the deflection in the central part of the truss. The camera configuration indicates that the base (separation between camera stations) and distance of the target ratio (B/D ratio) used was 0.67. This low value of the ratio was due to physical inaccessibility at certain locations on site, though higher values have been clearly recommended (Kadari, 2003).

3.3 Data reduction process

Ground coordinates of all target points were measured with Trimble 5600 TS. Coloured (RGB) images were acquired using Nikon digital cameras (DX100) and were processed using Matlab 7.0 software. Only red band of all images was used for further processing to reduce memory needed in the computer, and since its use gave better visual appearance (needed as centre of target was manually picked) than the green and blue layers. Centers of targets in an image were recorded manually by zooming the image and manually clicking on the 'apparent' centre of each target.

4. OBSERVATIONS

After initial measurement of coordinates with the total station, without any load, images from the two cameras were taken in the four loading conditions (LCs) briefly described below, and illustrated in Figure 3.

- a) LC1 [Figure 3 (a)]: There is no loading on the bridge, and the data in this condition was used as a reference to determine the changes in (x, y, z) coordinates of each of the targets.
- b) LC2 [Figure 3 (b)]: In this condition, the front of the engine is at mid-span, i.e., the remaining portion of the span was not loaded, though the adjacent span (span no. 3) had wagons on it. It can be seen that in this condition, the loading is practically only on account of the engine. It may be noted that the engine is six axle (with the design load of each axle being about 18 tonnes) (Raina, 2005)

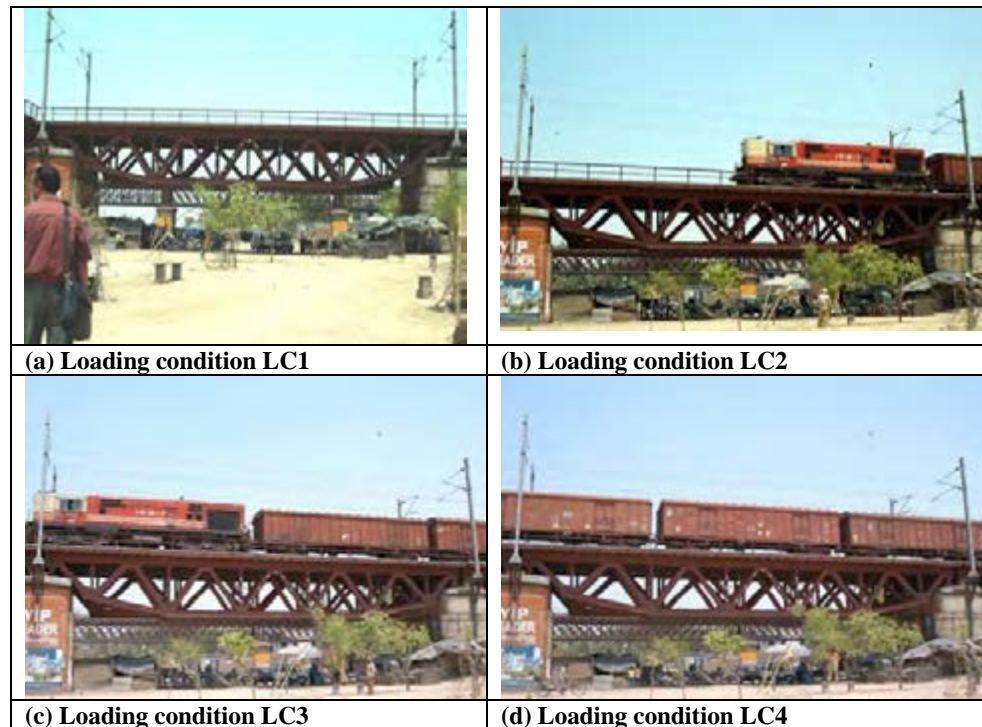


Figure 3 Loading conditions LC1, LC2, LC3 and LC4

- c) LC3 [Figure 3 (c)]: Here the whole span is loaded, though the loading is not symmetric – one half is loaded with the engine and the other one with one luggage carrying wagon (four axles, design load of 20 tonnes for each).
- d) LC4 [Figure 3 (d)]: In this condition, the engine has crossed out of the span under study (# 4), and the entire span is under the action of loads due to the wagons only, which also extend to other spans.

5. RESULTS AND DISCUSSIONS

5.1 Comparing 3D coordinates determined using DCRP and TS

As mentioned above, coordinates were determined with respect to a fixed coordinate frame using an arbitrary origin. To ensure reliability of

results, the coordinates computed by DCRP were compared with those measured using by TS, assuming the latter as the reference. The comparison was made in terms of the absolute value of difference in coordinates in the X, Y and Z direction, as computed by the two methods and recorded as ϵ_X , ϵ_Y , and ϵ_Z , which can be looked upon as the X, Y, and Z components of an *error vector*. Thus, ϵ_{X_i} for the i^{th} point was determined as $|\{X_{DCRP} - X_{TS}\}|$. Though the details are not described here, the ϵ_X , ϵ_Y , and ϵ_Z were found to vary between 0.4-4.2mm, 0.1-5.6, and 0.2-13.5mm, respectively, with their average values being 2.5mm, 3.0mm, and 7.3mm. The corresponding standard deviations (SD) for these were 1.2, 1.9, and 3.0mm (Hashmi, 2005).

This result thus established that at least in the X and Y directions, the coordinates obtained using DCRP and the TS are in reasonable agreement, though the same cannot be said for the coordinates in the Z direction (out of plane). Possible reasons for the relatively larger error in the Z direction are discussed in greater detail subsequently.

5.2 Deflection in control targets

As mentioned above, that control points are relatively fixed is an inherent assumption in DCRP, and thus an effort was made to first establish that these six targets (1, 2, 3, 17, 18 and 19) fixed on the pier and poles on the piers did not move under applied load. This was done by finding the average standard deviations in X, Y and Z coordinates (SD_X , SD_Y , and SD_Z) computed by DCRP under the different loading conditions for these points for all loading conditions. First, the standard deviation in X direction for the i^{th} target is determined from the set $\{x_{i1}, x_{i2}, x_{i3}, x_{i4}\}$, where individual values represent the X-coordinate for that target in the four loading conditions. Then, SD_X is computed by averaging individual standard deviations for the six locations. SD_Y , and SD_Z were calculated similarly. The values of SD_X , SD_Y , and SD_Z were found to be 1.19, 2.25, and 4.84mm respectively. In this case also, it can be seen that the small values of SD_X and SD_Y , validate the assumption that control points do not move appreciably under loading. The issue of the larger value obtained in the Z direction is discussed separately.

5.3 Deflection in truss

After calculating the 3D coordinates of all the targets using DCRP, the deflection vector (comprising of X, Y and Z components) for each point was calculated for the different LCs using the difference in the corresponding coordinates, with the values determined under LC1 (no load on the bridge) serving as reference in all cases. Thus, the X component of deflection at point i under loading condition 2 and 3 were calculated as $\{x_{i2} - x_{i1}\}$ and $\{x_{i3} - x_{i1}\}$, respectively. Now, the discussion here focuses on the results for targets 6, 9, 10, 11, and 16, set at the upper part of the truss (Figure 2), and a summary of the results is given in Table 1.

Table 1 Observed deflections at five representative targets under load

Point	Loading condition								
	2			3			4		
	ΔX	ΔY	ΔZ	ΔX	ΔY	ΔZ	ΔX	ΔY	ΔZ
6	5.4	10.1	16.3	11.7	-2.8	46.9	10.6	4.2	20.5
9	7.8	8.7	20.0	15.5	5.3	62.4	13.3	6.3	30.1
10	13.7	0.2	20.2	17.2	-4.6	43.8	15.6	7.2	16.8
11	8.1	-1.0	1.8	17.5	-4.3	45.7	13.1	2.2	18.7
16	9.9	5.0	10.5	17.1	-2.2	52.2	11.8	2.7	15.9

5.3.1 Deflection in the X direction

In the chosen coordinate system as shown in Figure 2, ΔX can be looked upon as ‘deflections’ under applied load, and the results given in Table 1 are plotted in Figure 4. When closely examining these deflections, it should be borne in mind that, (a) load from locomotive is transferred through six axles (three each in front and rear), (b) load in the case of wagons is transferred through four axles (two each in front and rear), (c) the loads in the wagons used is not clearly known here. However, the following observations can, nonetheless, be made.

- (a) The deflection varies between 5.4mm and 17.5mm depending upon the loading condition and the location.
- (b) Though there is an aberration at target 11, the deflection on the loaded half span in LC2 is clearly larger than that in the unloaded half.
- (c) The maximum deflections were observed in the case of LC3, as can be expected given the fact that the load is being applied through a total of 12 axles [Figure 5 (a)], and the fact that the loads transferred through the locomotive axles are likely to be higher than those from the wagons (where they are likely to vary depending upon the cargo, and the extent of loading of the wagons).
- (d) Given that the loading is most symmetric in LC4 [Figure 5 (b)], the deflections observed in that case are also balanced.

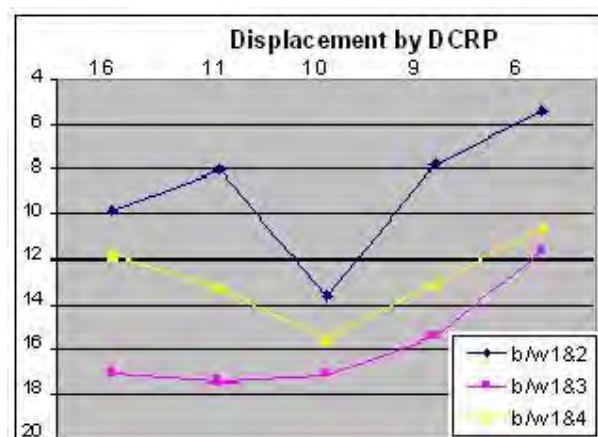


Figure 6 Displacements of points 6, 9, 10, 11, and 16 by DCRP

5.3.2 Deflection in the Y direction

It should be noted that observations here show negative values also, and are lower in magnitude compared to the deflections in the X direction. Results show that the deflection in the Y direction, also tabulated in Table 1, varies between -4.6mm and 10.1mm depending upon the loading condition and the location. In other words targets undergo some relative movement in the Y direction also as the truss deflects primarily in the X direction under application of load. Though some such movement can be expected from considerations of geometrical compatibility, an exact analysis cannot be carried out from the limited data collected during this study.

5.3.3 Deflection in the Z direction

Results from Table 1 show that observed deflections in the Z direction (out of plane deflections) are quite large, which is contrary to what should be expected – given that there was no out of plane loading. Thus, this aberration can only be attributed to different sources of errors, and the issue is discussed from that perspective in the following section.

6. ERRORS IN MEASUREMENTS

6.1 Sources of error

Precision of 3D coordinates determined by DCRP is related to a number of parameters, including the following:

- accuracy of the 3D coordinates of control points (which in the present study were determined using the total station)
- accuracy in measurement of various distances such as between two or more camera stations, camera stations and control field, etc.
- accuracy of establishing the centre of targets in photographs
- network geometry adopted for data acquisition, in terms of camera positions and the ratio of the distance between the camera to that from the objects involved (B/D ratio), etc.
- rounding-off errors of the DCRP system

It may be also mentioned that the mathematical structure of DLT equations, which forms the basis of DCRP, is such that any error in x , y coordinates (determined from an image, for example) leads to a much higher error in the computed Z direction than in the X or Y directions (Fraser, 1984). The situation deteriorates further, i.e., the errors are aggravated in case when the intersection geometry for control points is poor or these are located in a single plane (Athyala, 2003; Kadari, 2003). As mentioned above it was found in the present study, that in most of cases, the error in Z direction was nearly twice that in the X or Y direction. In fact, similar findings with higher errors in the Z direction have also been reported by Athyala (2003) and Kadari (2003) and attributed to poor B/D ratio.

6.2 Remedies

Some of the steps that can be taken to minimize errors in estimates made using DCRP can be summarized as follows

- a) Photo coordinates of targets should be determined using an average of values from repeated observations. This will reduce error on account of not being able to identify the 'true' centre. In the present research, the process (of clicking the centre of the same target) was repeated five times and the average reading was taken as the photo coordinate of the target and was used in the DLT model. The precision of picking the centre of target manually was about $1/10^{\text{th}}$ of the pixel dimension.
- b) Matrices should be appropriately scaled during transformation. This is especially important given the special structure of matrices that are formed during the processing of DLT equations
- c) Special attention should be paid to the layout and geometry used during imaging, (distance between cameras (B), their positions relative to the object, and the distance from the object (D)). It has been suggested that in order to obtain good results, the B/D ratio should be higher, as an improved convergent geometry of intersecting rays, can be achieved under these conditions (Fraser, 1992).
- d) Accuracy can be further improved by either using multiple pairs of stereo images from the two sets of cameras, or increasing the number of cameras. In the present preliminary study, where the object was to establish the applicability of the method and test the software developed, only a single set of images taken from only two cameras has been used.

7. SUMMARY AND CONCLUDING REMARKS

This research has proposed a DCRP based system for monitoring deflection of a railway bridge. The accuracy of the DCRP measurements is closely related to parameters such as the dimensions of the control field, properties of the camera used, the setup geometry used in taking images, etc. Efforts to estimate the deflections in the bridge yielded encouraging results, though efforts are needed to improve the accuracy obtained in the measurement of coordinates, deflections, etc.

It was found that the standard error in 3D coordinates calculated by DCRP in the X, Y, Z directions was 3.2, 1.6, and 5.2mm respectively, which may be considered acceptable at least in the X and Y directions. Deflection in the bridge was found to range between about 5mm to 18mm, depending on the location and loading condition.

ACKNOWLEDGEMENT

The field work reported here was carried out at a railway bridge, and the cooperation and help extended by the Indian Railways during the exercise is

gratefully acknowledged. The authors would like to specially thank Shri RK Gupta, Executive Director, Bridges & Structures, Railway Design and Standardization Organization, Lucknow, and other members of his team.

REFERENCES

- Abdel-Aziz, Y. I and Karara, H. M., 1971. Direct linear transformation from comparator coordinates into object space coordinates in close-range photogrammetry. In: *proceedings of the symposium on close-range photogrammetry*. American Society of Photogrammetry, Falls Church, VA.
- Abdel-Aziz, Y. I. and Karara, H. M., 1974. Accuracy aspects of non-metric imageries. *Photogrammetric Engineering* 40, pp. 1107-1117.
- Atkinson, K. B. (Ed.), 1996. *Close range photogrammetry and machine vision*. Engineering and Science. Whittles Publishing, Scotland, UK.
- Athyal, A. S., June 2003. *Design considerations for digital close range photogrammetric system*. Master's thesis, Civil Engineering Department, IIT Kanpur, India
- Fraser, C. S., 1984, Network design considerations for non-topographic photogrammetry, *Photogrammetric Engineering & Remote Sensing*, **50**, pp. 1115-1126.
- Fraser, C. S., 1992, Photogrammetric measurement to one part in a million, *Photogrammetric Engineering & Remote Sensing*, **58**, pp. 305-310.
- Ghosh, S. K., 1979. *Analytical Photogrammetry*. Pergamon Press Inc.
- Hashmi, S. F., 2005, *Monitoring of Engineering Structures using Digital Close Range Photogrammetry*, Master's thesis, Civil Engineering Department, IIT Kanpur, India.
- Kadari, R., 2003. *Network design of a digital close range photogrammetric system*. Master's thesis, Civil Engineering Department, IIT Kanpur, India.
- Markus, N. and Maas, H. G., 1997. Automatic deformation measurements with a digital still video camera. In: *Optical 3-D Measurement Techniques IV*. Zurich; Wichmann Verlag, pp. 266-271.
- Mikhail, E. M. and Bethel, J. S., 2001, *Introduction to Modern Photogrammetry*, John Wiley & Sons.
- Raina, S.K. 2005. Executive Director, RDSO, Indian Railways, *Personal communication*
- Sagar, S. D., 2004. *Measurement of displacement using digital close range photogrammetry*. Master's thesis, Civil Engineering Department, IIT Kanpur, India.
- Slama, C., 1980, *Manual of Photogrammetry*, American Society of Photogrammetry, Falls Church, Virginia.
- Tsakiri, M., Charalambos, I., Papanikios, P. and Kattis, M., 2004, *Load Testing Measurements for Structural Assessment using Geodetic and Photogrammetric Techniques*, 1st FIG International Symposium on Engineering Surveys for Construction Works and Structural Engineering Nottingham, United Kingdom, 28 June – 1 July, 2004.

RESEARCH ON DURABILITY EVALUATION FOR IN-PLACE CONCRETE EFFECT OF EARLY DRYING ON THE QUALITY OF COVER CONCRETE

PHAN HUU DUY QUOC
quoc@iis.u-tokyo.ac.jp

TOSHIHARU KISHI
kishi@iis.u-tokyo.ac.jp
Institute of Industrial Science,
The University of Tokyo, Japan

ABSTRACT

Commonly, the verification of concrete durability properties like carbonation rate, diffusion coefficient of chloride ions, etc, is carried out using laboratory tests on specimens cured in standard conditions. However, these tests fail to reflect the influence of actual factors, especially the construction quality, on the quality of in-place concrete. Therefore, it is desirable to select criteria in terms of measurable items for durability performance and corresponding nondestructive test methods applicable directly on existing structure. Undoubtedly, items that represent the resistance of a concrete against the ingress of deleterious substances, in either gaseous or liquid form, from surrounding environment into concrete are criteria for the durability performance of that concrete.

This research focuses on the use of nondestructive testing methods for direct measurement of transport properties of concrete, including air permeation, water absorption, which are selected as criteria for durability performance of in-place concrete. In this paper, the experimental results on the effect of early drying on concrete transport properties are reported. It was found that the effect of early drying on transport properties is very much higher than on compressive strength. This research may contribute to the improvement of construction quality, the early judgment of concrete quality as well as the prediction of service life of concrete structures.

1. INTRODUCTION

Concretes produced nowadays are quite different from the conventional one, both in good and bad aspects. As for good aspects, there have been tremendous improvements in concrete technology such as the utilization of chemical admixture (superplasticizer, air entraining agent...), industrial by-product (fly ash, silica fume...), the mechanization of concreting works (transporting concrete by pumping, compacting by vibration), the

development of advanced concretes like high performance concrete, the application of computer-aided analysis in design of structure, etc. Unfortunately, in contrast to such positive developments, there has not been remarkable improvement in controlling and evaluating the quality of concrete, especially concrete in structure (Hereafter, in-place concrete).

In many cases, in-place concrete appears to be good at the beginning but deteriorates sooner than expected, resulting in high total cost, shortening the service life and threatening the safety of users (Figure 1.) It is because the in-place concrete doesn't possess sufficient ability to withstand the given environmental conditions, such as carbonation, acid attack, salt attack, etc, like the example shown in Figure 2.

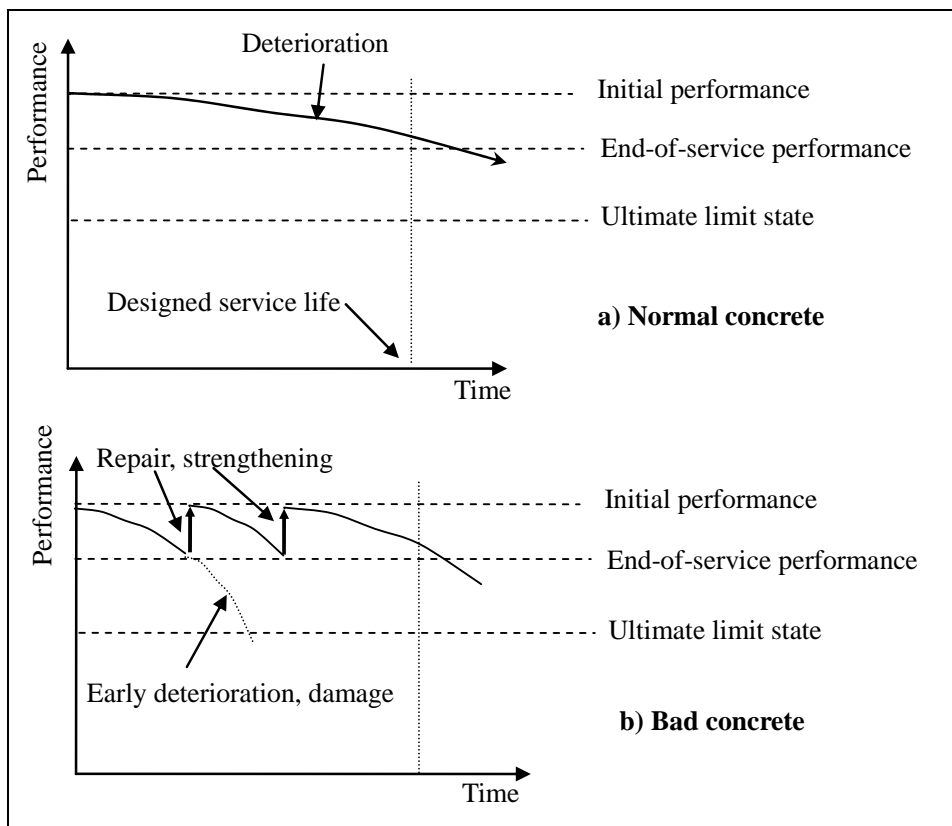


Figure 1: "Normal concrete" versus "bad concrete"



Figure 2: Corrosion of reinforcing bars due to bad cover concrete

The problems lie at the following points:

- (i) Most of the current performance verifications of concrete properties are carried out on specimens (which do not represent in-place concrete) cured under standard conditions.
- (ii) Criteria for evaluating the quality of in-place concrete are insufficient or improper. Compressive strength is nearly the only verified item.

In short, the quality of construction, the effect of environmental conditions are not properly taken into account in verification, or not suitably covered in design code.

To solve the above short-coming, it is important to identify the criteria for the durability performance of in-place concrete. In term of durability, the criteria must be those that represent the resistance of concrete against the ingress of deleterious substances, in either gaseous or liquid form, from surrounding environment into concrete.

Cover concrete, as its name implies, acts as a shield that protects the inner concrete and reinforcing bars from the attack of environmental factors. However, this important layer tends to have lower quality compared with the inner part due to various factors, such as insufficient compaction, early drying, thermal cracking, or even due to bad practices in construction like adding water, removing formwork so early, etc. (Figure 3). If cover concrete is not really a “cover”, structure will soon deteriorate.

Therefore, the objective of this research is to evaluate the transport properties of cover concrete. It has two important meanings: one is to provide necessary information for improving the quality of cover concrete, and the other is to find appropriate methods for controlling and evaluating the quality of cover concrete.

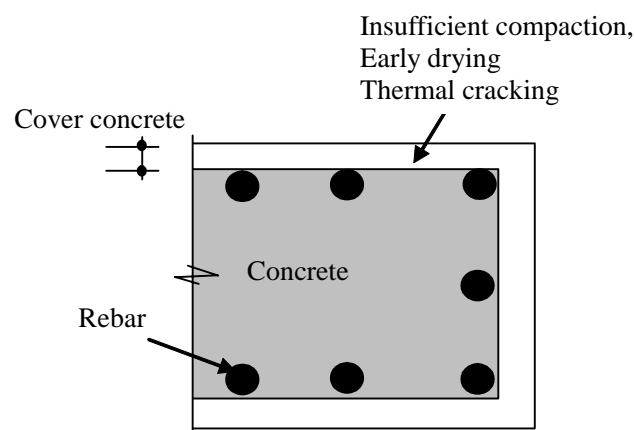


Figure 3: Cover concrete

In this research, by varying the demolding time of concrete specimen to simulate actual formwork removal time, the effect of drying on transport properties of cover concrete was investigated using simple tests. This study

is an important preparation to provide fundamental concepts and experiences for further measurement on actual concrete structure, rather than an actual investigation on in-place concrete.

2. EXPERIMENTAL OUTLINES

2.1 Materials and specimen preparation

Twelve concrete cylinders with diameter of 10cm and height of 20cm were made from concrete mixture with water-cement ratio of 0.5.

To investigate the effect of drying on the quality of cover concrete, 3 cylinders were demolded at 1, 3, 7 and 27 day-ages and immediately exposed to ambient conditions after being kept in sealed condition (no additional water is provided after mixing).. The demolding timing was varied to simulate different formwork removal time in actual structure and observe the extent of drying effect on transport properties of concrete.

The exposure started in January, which has very high humidity, so specimens are subjected to drying condition. During the exposure, specimens were kept away from the reach of rain or any kind of water.

2.2 Testing items and apparatuses

Three kinds of test were carried out on the side and the top of the exposed concrete cylinders after 8-month exposure. Air permeation, water absorption and compressive strength tests were carried out as follows:

2.2.1 Air permeation test

This testing method was firstly developed by Figg (1973) and enhanced by Kasai et. al. (1984). In this test, a cylinder hole with diameter of 10mm is drilled into the concrete specimen (Figure. 4). Then, the hole is plugged by a rubber cap. A needle is inserted through this rubber cap to bring the pressure inside the hole to a pre-decided vacuum pressure using a vacuum pump. This pressure will increase gradually because air from all directions around the hole will find their way through the pore network to fill the hole until the pressure equilibrium is reached. The rate of pressure change will be calculated as air permeation rate of concrete.

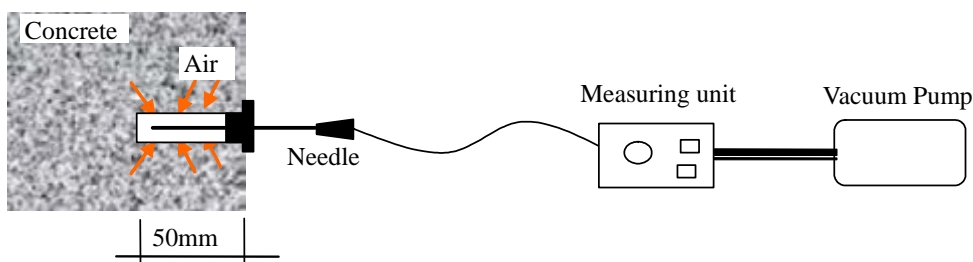


Figure 4: Air permeation test

Because the direction of air movement as well as the exact affected area in this test is unknown, the air permeation coefficient cannot be directly obtained using this test. The accuracy of this kind of measurements, factors influencing its measurement, etc, will be discussed later in this paper. It was reported that the air permeation measured using this apparatus has a good correlation with carbonation depth. Torrent (1992) reported a good correlation between air permeation coefficient and carbonation rate of concrete.

2.2.2 Water absorption test

In water absorption test, the amount of water absorbed by concrete on a unit surface area is measured using the apparatus called Porositester developed by Proceq Co. Ltd (Switzerland) (Figure 5). This apparatus has nothing special compared with common water absorption test using a tube of water, except the way of providing water source and absorption area.

In this apparatus, a “cell” is created by attaching a large rubber ring at the bottom of a steel plate. At the middle of the plate, there is a small hole through which vacuum pressure is applied to attach the plate onto the target surface by suction force.

Scaled tubes are mounted on this plate, pressed against the target surface, sealed by rubber ring and filled with water. By this way, the absorption area is kept constant through out the measurement to enable a stable and accurate measurement. The amount of absorbed water is recorded every 30 minutes up to three hours.

The advantage of this simple apparatus is that it causes no damage to the target surface. In addition, it can be operated using portable DC power supply (For example, the car battery). Different kinds of water tube are used for vertical wall (Figure 5a) and horizontal surfaces (Figure 5b).



(a) For vertical wall



(b) For horizontal surface

Figure 5: Apparatus for measuring water absorption

2.2.3 Compressive strength

Compressive strength was measured using Schmidt's hammer (Figure 6). This apparatus were selected in this study because it is a commonly used non-destructive testing method for obtaining the compressive strength of in-place concrete. In this method, an impacting force is applied on the surface of concrete. The compressive strength is calculated from the reaction of concrete surface. In addition, the compressive strength calculated from the result of Schmidt's hammer can be understood as the strength of cover concrete at the vicinity of impacting point. In this test, the specimen was kept firmly at horizontal position and 15 measuring times were applied downward on different positions on the side of the specimen.



Figure 6: Schmidt's hammer

3. EXPERIMENTAL RESULTS AND DISCUSSIONS

Experimental results show that the transport properties (air permeation, water absorption) are greatly affected by the early drying when specimens are demolded early than 1 week. Certainly, the sooner the demolding time, the worse the transport properties are. Compressive strength of concrete is relatively less influenced than transport properties.

3.1 Air permeation rate

As mentioned above, the air permeation rate is calculated from the change of air pressure in the cylinder hole and the corresponding time duration. Figure 7 shows the measured results of air permeation rate for both top and side positions of the cylinder specimens. The result indicates that the air permeation is greatly affected by the early drying. This influence is very severe if the specimen is demolded before 7 days. Compared between 1-day and 7-day demolded cases, the air permeation of the former is about twofold of air permeation of the latter. This result emphasizes the detrimental effect of early formwork removal on concrete property.

Regarding the effect of measured positions, the air permeation rate of the top surface was anticipated to be larger than that of side due to bleeding at the top surface. However, experimental result shows just a slight difference between two positions. It is attributed to the small size of cylinder specimens and the way of making this sample (compacted by rod and finished by surface tapping). For large specimens or actual structures, the difference in air permeation property between top and side may be observed.

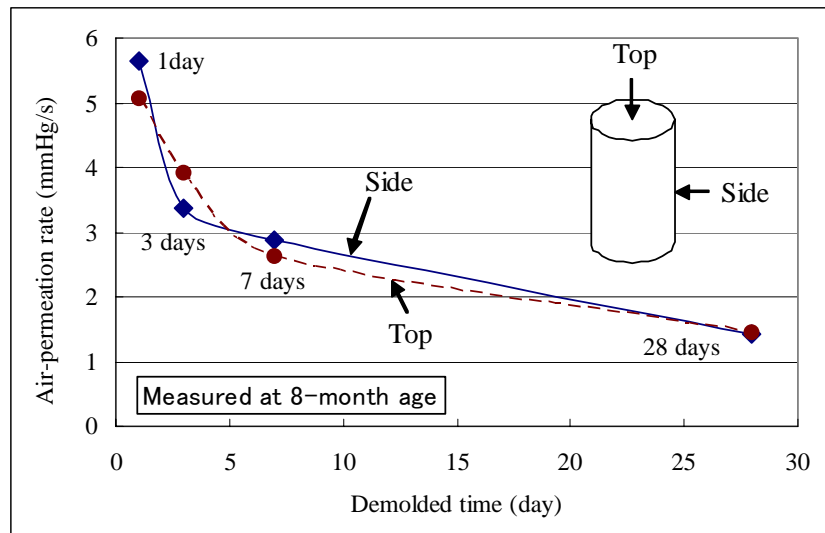


Figure 7: Variation of air-permeation rate and demolded time

3.2 Water absorption coefficient

Figure 8 shows the result of water absorption measured on specimens demolded at 1, 3, 7 and 28 days. It is clear that there is a linear relationship between the amount of absorbed water and measuring time. It means that there is steady state absorption under capillary suction. The gradients of these lines are the coefficients of water absorption for each case.

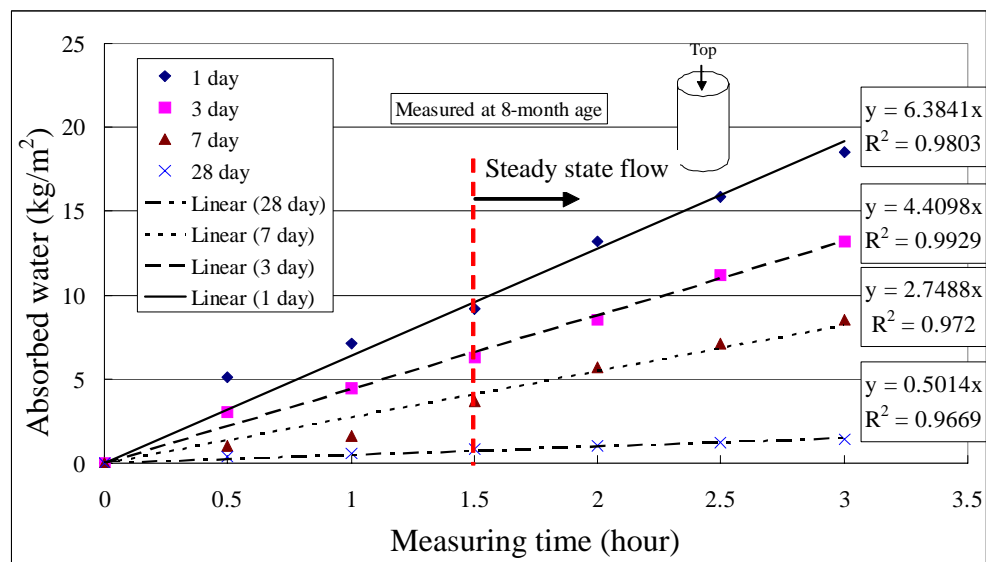


Figure 8: Water absorption measurement

The water absorption seems to reach the steady state after around 1.5 hours from the start of measurement. Therefore, it may be recommended that the time for water absorption measurement should be around 1.5 hours. Since this conclusion may be applied for other cases of water-cement ratios and curing conditions as well, though confirming experiments should be carried

out. Certainly, in order to ensure a steady state flow, the absorption area should be maintained while the water evaporation is prevented.

Plotting the coefficient of water absorption obtained from results in Figure 8 against the demolded time, one can see a similar trend with air permeation rate: the water absorption coefficient is quite sensitive to the early drying caused by early formwork removal in the first week. If demolded after one week, the effect of drying is less severe but still remarkable (Figure 9).

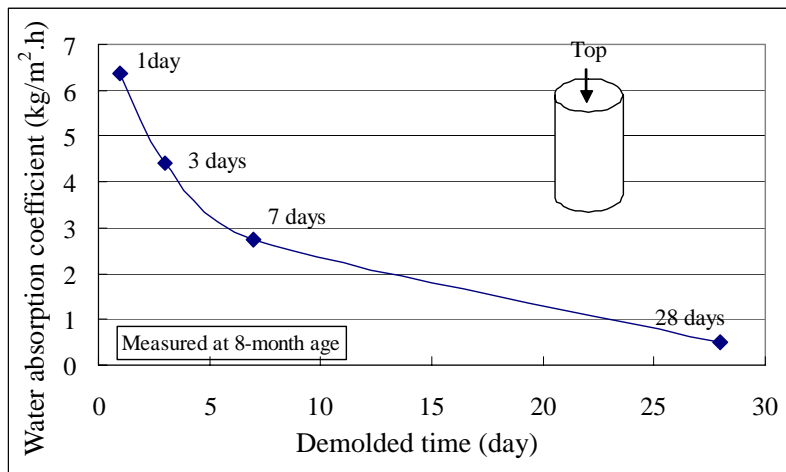


Figure 9: Variation of water absorption coefficient with demolded time

3.3 Air permeation rate versus water absorption coefficient

Figure 10 shows a relatively good correlation between air permeation rate and water absorption coefficient. This may not be a conclusion for general cases because of limited number of tests and variables in this study.

However, the result in Figure 10 is believed due to the fact that in both processes (air permeation and water absorption) transport properties are governed by the same pore network of concrete.

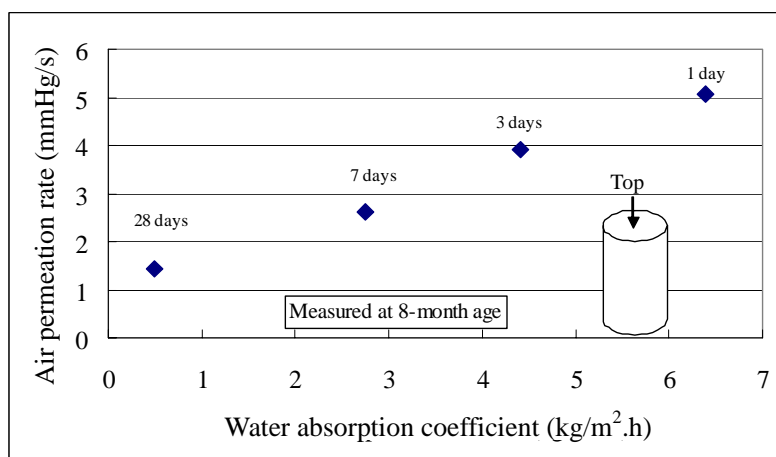


Figure 10: Air permeation rate versus water absorption coefficient

These transport properties are governed by different transport mechanisms: air permeation is a flow under applied pressure, while water absorption is a flow of water under capillary suction. The measurement of air permeation takes a few minutes, while it takes one hour and a half to obtain water permeation coefficient. Therefore, if a good correlation is obtainable, water absorption coefficient can be derived from air permeation rate.

3.4 Compressive strength

While transport properties show a high vulnerability to early drying, compressive strength of concrete was observed to be less influenced (Figure 11). Compressive strength of concrete demolded at 1 day is just 10% lower than that of concrete demolded at 28 days while the air permeation of the former is 12.4 times higher than the latter. This result indicates that strength-based evaluation of in-place concrete will not provide valuable information as long as the long term durability is concern.

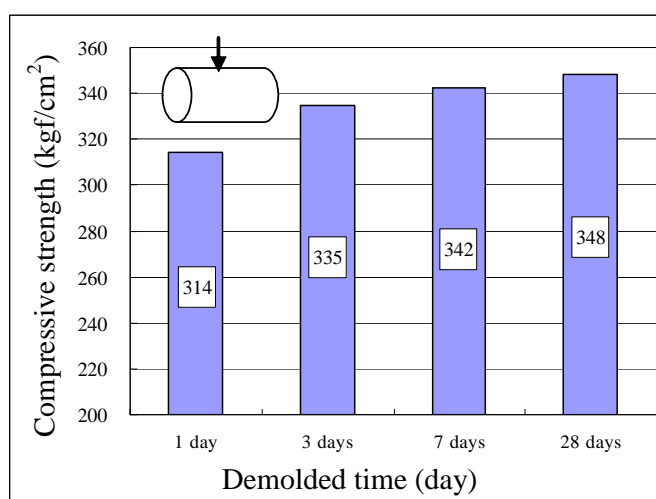


Figure 11: Compressive strength obtained by Schmidt's hammer

3.5 Factors influencing the measurement of transport properties

In this study, the measurements were carried out on specimens without any special treatment. Intentionally, it was to simulate the actual site investigation when the measurement has to be carried out at arbitrary condition. Due considerations must be given on the effect of most influential factors: temperature and moisture content of concrete.

It is reported that temperature has little influence on air permeation, but has rather remarkable influence on water absorption, mainly because the change of water viscosity with temperature. The moisture content of concrete which changes with ambient relative humidity has great influence on the transport properties as well as the their on-site measurement. Obviously, a “wet” concrete may behave as a “tight” concrete, because saturated pores will block the paths of mass transportation. Without proper consideration, over (or under) estimation result may be mistakenly obtained.

Figure 12 shows the variation of atmospheric relative humidity in Tokyo. It is easy to recognize which period in a year new concrete will be more vulnerable to drying, as well as when the measurement of transport properties of in-place concrete will end up with over/under estimated results.

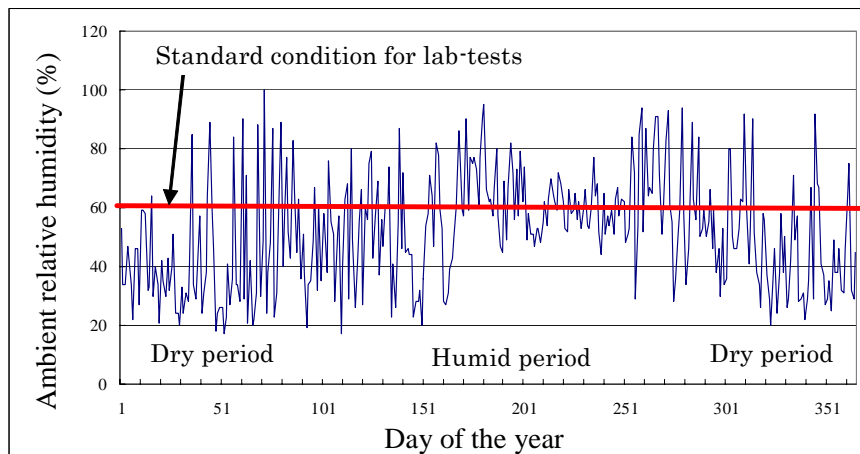


Figure 12 Variation of atmospheric relative humidity in a year (Tokyo)

5. CONCLUSIONS

- The effect of drying on transport properties of cover concrete is more remarkable than on the compressive strength. Therefore, to ensure the durability of cover concrete, transport properties have to be selected as criteria of concrete performance over time.
- It was found that steady state absorption of water can be achieved after one hour and a half. The accuracy and stability of measurement can be ensured by maintaining constant absorption area and preventing water evaporation.
- It is important to find a way to cancel out effect of moisture content and temperature on the measurement of transport properties of cover concrete.
- To evaluate the durability performance and to estimate the life span of concrete structures, more study on the relationship between transport properties (air permeation, water absorption, etc.) and durability properties (carbonation rate, chloride diffusion coefficient...) are extremely important.

REFERENCES

- Figg, J.W., 1973, *Methods of measuring the air and water permeability of concrete*, Magazine of Concrete Research, Vol. 25(85), 213-219
- Kasai, Y., Matsui, I and Nagano, M., 1984, *On-site rapid air permeability test for concrete*, ACI SP-82, 501-524
- Torrent, R. J., 1992, *A two-chamber vacuum cell for measuring the coefficient of the permeability of air of the concrete cover on site*, Vol. 25, 358-365

SAFETY EVALUATION OF AGED STEEL TRUSS BRIDGE WITH CRACKING MEMBERS

Xianjie XU Ri GAO Lanchao Jiang Weiguo Yang
School of Civil & Architecture Engineering, Beijing
Jiaotong University, Beijing, 100044, China
rigao@center.njtu.edu.cn

ABSTRACT

The safety of aged steel truss bridges, especially those with cracking members, has aroused a great deal of attention. In this paper, the application of fracture mechanics for evaluating the safety and ultimate load-carrying of the aged steel truss bridge is proposed. Three-point bending tests of three specimens for the mode-I fracture were done to get the ultimate load-carrying capacity, when specimens were destroyed. Fracture toughness K_{IC} , and the steel allowable stress $[\sigma]$ with certain crack length were formulated. Field nondestructive load test and magnetic method for measuring cracks of steel members were done. By comparing the results of the calculation and those of the field test, it is concluded that the fracture method is necessary in the safety evaluation of aged steel truss bridges with cracking members.

1. INTRODUCTION

Nowadays, many bridges that were built in the fifth decade of previous century or even earlier are still in running. And these bridges have disrepair phenomena more or less (Zheng, 2003). Therefore, the safety of these bridges becomes the matter we care.

For the steel members without cracks, it is doable that carrying through safety evaluation of steel bridge depends on the design guideline such as strength and fatigue capability that can be obtained from the current design codes. However, for the cracking members, it is necessary recurring to the theory of fracture mechanics. The allowable stress and fatigue allowable stress and other material capability can be calculated according to the stress strength factor and the doorsill value of crack extension, consequently, the safety capability of members or steel bridge can be evaluated (Xu, et al, 1994).

The Nenjiang steel bridge that locates at Qiqihaer city, Northwest of China, was built in 1935 (Gao, 2005). The whole length of the bridge is 548.1m, which consists of 6 through steel truss girders with span of 63.9m each. Figure 1 and Figure 2 show the structure of the one span of the bridge.

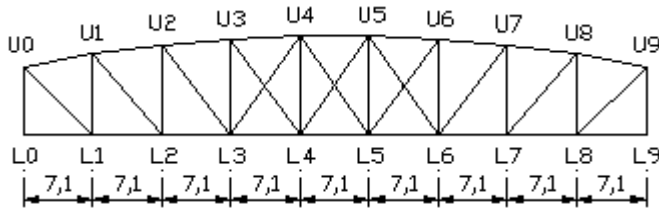


Figure 1: Front view of the bridge

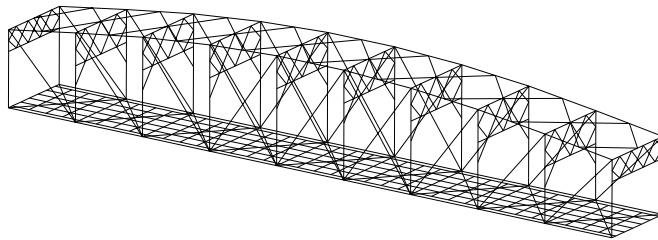


Figure 2: Structure of the bridge

The bridge was renovated technically in 1986, but the bridge appeared new damage (cracks) in some steel members. As the appearance of various problems, the security of the bridge cannot but arousing public attention. In June of 2005, field test and theoretical analysis were taken to the bridge, to evaluate the safety capability of the bridge and give disposal advice. In this paper, the safety evaluation of cracking members is analyzed mainly.

2. RESULTS OF THE NONDESTRUCTIVE TEST

According to the results of the nondestructive test taken to the main bearing members of the first truss span and some members of other truss spans of the bridge, some cracks were found in the members (Gao, 2005 and Liu, 1994). The crack length and number of the vertical and inclined web members are listed in Table 1 and Table 2 respectively.

Table 1: Crack length and number of the vertical web members

crack length(mm)	50~100	101~150	151~200	201~300	301~500
crack number(mm)	1	5	6	4	1

Table 2: Crack length and number of the inclined web members

crack length(mm)	50~100	101~150	151~200	201~300	301~500
crack number(mm)	6	2	6	-	-

Nondestructive test shows that the crack percentage of vertical web members of the bridge reaches to 63%, and the crack depth lies between 0.2mm and 2mm. The crack percentage of inclined web members reaches to 53.8%, and the crack depth of one member even reaches to 6mm. Thus, it can be considered that the crack condition of this bridge is very serious. Moreover, it shows the fundamentality of safety evaluation to cracking members of aged steel truss bridge.

3. TEST OF MATERIAL MECHANICS

Test facility: Material Test System of MTS—810.

Loading mode: Axis-pulling.

Sample dimension: 120mm×15mm×8mm, sample numbers: 9.

Test temperature: room temperature is about 25°C.

Test results are shown in Table 2-1, Table 2-2 and Table 2-3.

Table 2-1: Test result of transverse brace members

No.	Ultimate tensile strength (MPa)	Yield strength (MPa)	Elongation (%)	Reduction of area (%)
H1	506	299	33.0	36.7
H2	512	324	28.6	32.8
H3	498	308	31.8	35.3
Average	505	310	31.1	34.9

Table 2-2: Test result of inclined web members of the truss

No.	Ultimate tensile strength (MPa)	Yield strength (MPa)	Elongation (%)	Reduction of area (%)
H1	523	340	34.8	40.1
H2	531	346	32.7	39.0
H3	059	313	38.6	43.3
Average	521	333	35.4	40.8

Table 2-3: Test result of vertical web members of the truss

No.	Ultimate tensile strength (MPa)	Yield strength (MPa)	Elongation (%)	Reduction of area (%)
H1	548	317	31.0	38.2
H2	516	328	27.0	31.8
H3	500	294	28.5	36.7
Average	521	313	28.8	35.6

According to the references 5 and 6, the intensity of the steel of this bridge is between the intensity of Q235 and Q345. According to the Table 1.2.2, Table 1.2.16-2 and Table 1.2.17-2 of the reference (GB/T 700-1988, GB/T 1591-1994), the allowable stress of this steel is about 140MPa if there is no crack in the members.

4. FRACTURE TOUGHNESS AND ALLOWABLE STRESS OF CRACKING MEMBERS

To get the fracture toughness and allowable stress of cracking members, the theory of fracture mechanics is adopted in the test and calculation.

4.1 Fracture toughness and Allowable stress

For cracking members, the stress nearby the crack tip can be expressed as follows (Ding, and Sun, 1997):

$$\sigma_{ij} = \frac{K_m}{\sqrt{2\pi}} \left(r^{\frac{1}{2}} \right) f_{ij}(\theta) \tag{1}$$

where: r — the distance between stress point and crack tip;

$f_{ij}(\theta)$ — the function about the polar angle θ ;

K_m — stress strength factor $m = I, II, III$, which is shown in Figure 3.

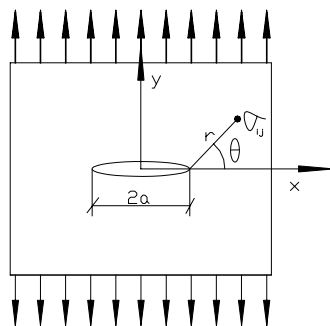


Figure 3: Stress of some point where the crack is interrupted

For the question of mode- I fracture:

$$K_I = \sigma \sqrt{\pi a} \tag{2}$$

where: σ — additional stress;

a — half length of the crack;

K_{IC} is fracture impact toughness, which is a material capability to measure crack spread resistance and can be obtained from the test. Three-point bending tests of standard samples will be taken to get the pressure P when the samples are destroyed. And the fracture toughness can be calculated from the following formula.

$$K_I = \frac{PS}{BW^{3/2}} f\left(\frac{a}{W}\right) \tag{3}$$

The standard three-point bending sample is shown in Figure 4.

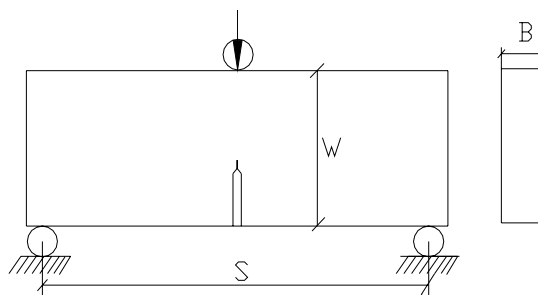


Figure 4: The standard Three-point bending test

Test facility: electronic multipurpose experiment-machine.

Loading mode: three-point bending.

Test temperature: room temperature is about 25°C.

The dimensions of three samples with the crack length a are given as follows: No.1: $B = 8\text{mm}$; $S = 64\text{mm}$; $W = 16\text{mm}$; $a = 3.6\text{mm}$;

No.2: $B = 8\text{mm}$; $S = 64\text{mm}$; $W = 16\text{mm}$; $a = 4.0\text{mm}$;

No.3: $B = 8\text{mm}$; $S = 64\text{mm}$; $W = 16\text{mm}$; $a = 4.4\text{mm}$;

The relationships between force and displacement ($P \sim \Delta$ curve) gotten from the three tests are shown in Figure 5 (Gao, 2005). Consequently, the ultimate carrying capacities described with the ultimate loads for the specimens are obtained, they are $P = 7.1\text{KN}$; $P = 6.5\text{KN}$ and $P = 12.5\text{KN}$.

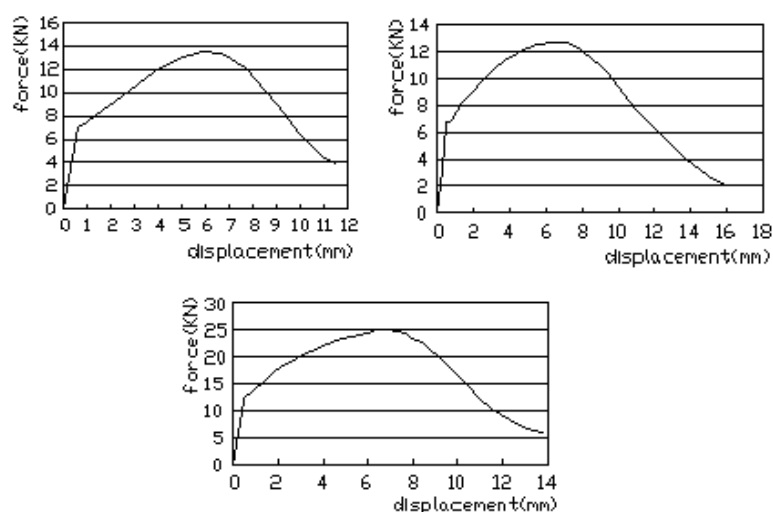


Figure 5: Relationship between force and displacement on three specimens

The factor K_{IC} can be calculated from Formula 3. They are $K_{IC} = 52.3183\text{Mpa}\sqrt{\text{m}}$; $K_{IC} = 48.3183\text{Mpa}\sqrt{\text{m}}$; $K_{IC} = 74.3183\text{Mpa}\sqrt{\text{m}}$. Herein, the minimum $K_{IC} = 48.3183\text{Mpa}\sqrt{\text{m}}$ is chosen for further discussion.

4.2 Allowable stress

Considering safety factor K , the allowable stress of the steel can be

gotten under the crack length from Formula 4.

$$[\sigma] = \frac{K_{Ic}}{K\sqrt{\pi a}} \quad (4)$$

Assuming $K = 2 (K \geq 2)$, consequently:

When crack length is 50mm, $[\sigma] = 86\text{Mpa}$;

When crack length is 100mm, $[\sigma] = 61\text{Mpa}$;

When crack length is 150mm, $[\sigma] = 50\text{Mpa}$;

When crack length is 200mm, $[\sigma] = 43\text{Mpa}$.

5. SAFETY EVALUATION OF THE STEEL TRUSS BRIDGES

For actual stress of the steel truss members, the ANSYS software and field dynamo-static test are adopted for analysis. The live-load considered in analysis and test includes auto-load, human load and wind load.

Via analysis and test, the theoretical and actual stress value of some main members can be obtained. The stress value of each case is combined and compared with the allowable stress value of members. The results are shown in Table 3-1 and Table 3-2.

Table 3-1: Results under dead load and auto-load

No.	Stress (MPa)						
	A	B	C	A+B	A+C	Allowable stress 1	Allowable stress 2
U4L5	8.67	11.97	8.00	20.64	19.97	130	50
U5L4	8.67	12.15	8.40	20.82	17.07	130	50
U4L4	12.42	9.66	4.20	22.08	16.62	145	50
U1L2	83.82	23.63	23.70	107.45	107.52	145	50
U1L1	-78.32	-22.15	-17.20	-100.47	-95.52	145	50
U0L1	81.75	19.46	14.30	101.21	96.05	145	50
L4L5	42.88	11.54	10.10	54.42	52.98	145	50
U4U5	-69.30	-19.17	-18.30	-88.47	-87.60	145	50
L0L0'	84.55	15.99	8.60	100.54	93.15	145	50
L4L5	39.73	10.34	3.20	50.07	42.93	145	50

Note: A means the calculating results under dead load, B means the calculating results under auto load, C means the testing results under auto load.

In the three tables above, U4L5、U5L4、U1L2、U0L1 are inclined web members; U4L4、U1L1 are vertical web members, and L4L5、U4U5、L0L0、L4L5 are upper chord, lower chord, cross beam and longitudinal beam respectively. Allowable stress 1 leaves cracks out of account but Allowable stress 2 takes cracks into account. Allowable stress 1 comes from the reference (JTJ 025-86, 1998), which is multiplied by the coefficient 2 in the table 3-2.

Table 3-2: Results under load case of downwind side (upwind side)

No.	Stress (MPa)						
	A	B	C (E)	D	A+B+C	A+B+D	Allowable stress 1(2)
U4L5	8.67	11.97	-0.96 (0.97)	1.31	20.98	22.92	163 (50)
U5L4	8.67	12.15	-1.43 (1.44)	1.31	20.69	22.26	163 (50)
U4L4	12.42	9.66	1.91 (-1.93)	1.30	25.29	21.45	181 (50)
U1L2	83.82	23.63	-5.05 (5.06)	7.13	109.53	119.64	181 (50)
U1L1	-78.32	-22.15	16.56 (-16.57)	-6.98	-90.89	-124.02	181(50)
U0L1	81.75	19.46	-9.29 (9.31)	7.18	99.11	117.70	181 (50)
L4L5	42.88	11.54	-5.48 (5.48)	4.52	53.46	63.23	181 (50)
U4U5	-69.30	-19.17	-3.49 (3.46)	-5.94	-97.89	-87.54	181 (50)
L0L0	84.55	15.99	12.62 (15.99)	5.19	118.35	118.35	181 (50)
L4L5	39.73	10.34	5.11 (5.11)	4.06	59.23	59.23	181 (50)

Note: A means the calculating results under dead load, B means the calculating results under auto load, C means the calculating results of downwind side under wind load, D means the calculating results under human load, E means the calculating results of upwind side under wind load.

The max stress value of each member is less than the allowable stress 1 and satisfies the requirement of the codes, which can be seen from comparison above. But about half of the members dissatisfy the requirement of steel strength if considering the cracks.

So, existence of cracks is an important factor which cannot but being considered in the evaluation of steel bridge especially aged steel bridge.

6. FATIGUE CHECKOUT OF GENERAL MEMBERS

As the members of this bridge are connected by rivets, the sort of the allowable stress is considered as D, according to the reference (JTJ 025-86, 1998). The allowable stress of the members and joint can be calculated from the formula (5) and (6).

When the max stress is tensile stress:

$$[\sigma_n] = \frac{145}{1-0.6\rho} \text{ and } \leq [\sigma] \quad (5)$$

When the max stress is compressive stress:

$$[\sigma_n] = \frac{145}{0.6-\rho} \text{ and } \leq [\sigma] \quad (6)$$

Where: $[\sigma]$ ——basic allowable stress of steel.

$$\rho = \frac{\sigma_{\min}}{\sigma_{\max}} \text{ ——ratio of stresses.}$$

To different load case, the stress of some members, such as inclined web members, will change between positive and minus, and these members should be carried out fatigue checkout. The checking stress comes from calculation results, and is shown in Table 4.

Table 4: Fatigue checkout of members

Member	Sides	ρ	σ_n (MPa)	$[\sigma_n]$ (MPa)	$\sigma_n < [\sigma_n]$
U4L5	downriver	-0.027	20.64	142.4	Yes
	upriver	-0.009	16.91	144.2	Yes
U5L4	downriver	0.007	20.82	145.0	Yes
	upriver	0.162	18.16	145.0	Yes
L0L0'	-	0.761	100.54	145.0	Yes

For the members without stress changing, their stresses do not exceed the allowable stress, and so satisfies the requirement.

7. FATIGUE CHECKOUT OF CRACKING MEMBERS

The material fatigue capability research of cracking members mainly rests with seeking the mathematical expression between the speed of crack expansion and concerned mechanics parameter, according to the theory of fracture mechanics (Ding, and Sun, 1997). If the number of stress circulation is ΔN and the crack spread is Δa , the crack expansion is $\Delta a / \Delta N$ (mm/time) at every stress circulation, which is called *crack expansion speed* and expressed by the differential coefficient da/dN in terms of limit. Commonly, the crack expansion speed can be written as formula 7 in the event of monoaxial circulation alternative stress.

$$da/dN = f(\sigma, a, C), \tag{7}$$

Where: N — stress circulation number; σ — positive stress;
 a — crack length; C — constant related with material.

According to stress intensity factor of *PARIS*, under high-cycle and identical range load, the data gained from the tests can be plotted in the reference frame of $\lg da/dN \sim \lg \Delta k_I$ after being trimmed, as shown in Figure 6. The curve is divided into three phases, and in the first phase, the range of stress intensity factor Δk_I is very low. When Δk_I is less than a certain limit value Δk_{th} , the crack doesn't expand basically, and the limit value Δk_{th} is called doorsill value of crack expansion.

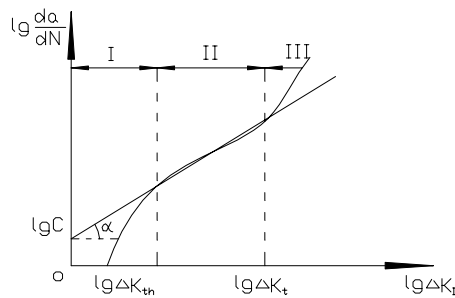


Figure 6: The curve of $\lg \frac{da}{dN} \sim \lg \Delta k_I$

Provided that the stress ratio is the ratio of the max stress of dead load and live-load to the stress of dead load, we know that, according to the reference (Liu, 1994), for the mild steel:

$$\text{When stress ratio } R = \frac{\sigma_{\min}}{\sigma_{\max}} = \frac{K_{\min}}{K_{\max}} = 0.13; \Delta k_{th} = 6.6MPa\sqrt{m};$$

$$\text{When stress ratio } R = 0.35, \Delta k_{th} = 5.2MPa\sqrt{m};$$

$$\text{When stress ratio } R = 0.49, \Delta k_{th} = 4.3MPa\sqrt{m};$$

$$\text{When stress ratio } R = 0.64, \Delta k_{th} = 3.2MPa\sqrt{m};$$

$$\text{When stress ratio } R = 0.75, \Delta k_{th} = 3.8MPa\sqrt{m}.$$

The middle value can be calculated through insertion method.

The doorsill stress value for crack not expanding can be worked out from formula 8 on condition that knowing the doorsill value of certain stress ratio.

$$[\Delta\sigma_{th}] = \frac{\Delta K_{th}}{\sqrt{\pi a}} \tag{8}$$

Where: a — half length of cracks, assuming $a = 75mm = 0.075m$ here. The checkout result is shown in Table 5.

Table 5: Fatigue checkout of cracking members

No.	Stress (MPa)						
	A	B ($\Delta\sigma$)	A+B	R=A/ (A+B)	ΔK_{th} $MPa\sqrt{m}$	Doorsill value $\Delta\sigma_{th}$ (MPa)	$\Delta\sigma \geq$ $\Delta\sigma_{th}$
U4L5	8.67	11.97	20.64	0.420	4.75	9.78	Yes
U5L4	8.67	12.15	20.82	0.416	4.80	9.95	Yes
U4L4	12.42	9.659	22.08	0.563	3.77	7.77	Yes
U1L2	83.82	23.63	107.45	0.780	3.96	8.16	Yes
U1L1	-78.32	-22.15	-100.47	0.780	3.96	8.16	Yes
U0L1	81.75	19.46	101.21	0.808	4.12	8.49	Yes
L4L5	42.88	11.54	54.42	0.788	4.00	8.24	Yes
U4U5	-69.30	-19.17	-88.47	0.783	3.98	8.20	Yes
L0L0'	84.55	15.99	100.54	0.841	4.30	8.86	Yes
L4L5	39.73	10.34	50.07	0.992	5.12	10.55	No

Note: A means the calculating results under dead load, B means the calculating results under auto load.

Through checking computations it can be found that the change of working stress of most cracking members exceeds the doorsill stress value $[\Delta\sigma_{th}]$. This means that the original crack will expand continuously and the members will come forth fatigue destroy. It can be kwon obviously that the fatigue stress of cracking members is less than that of the ordinary members, which is about tenth that of the ordinary members.

8. CONCLUSION

By the comparison above, it is concluded that crack is a very important factor steel bridge for safety evaluation. To a new steel bridge, whose members have no cracks, the allowable stress value and the fatigue allowable stress value, according to the current design codes, can be used to evaluate the safety of the steel bridge. However, for old or aged steel truss bridges, such as Nenjiang Bridge which is located at Qiqihaer city in China and has served for nearly 70 years and has been found cracks in its members, it is not suitable to evaluate the safety using allowable stress value. It is necessary to consider the influence of the cracks based on the theory of fracture mechanics, and to evaluate the safety of steel bridge after having theoretical analysis and field test.

In this paper, we analyze the safety of steel bridge only from the strength and the fatigue. As a matter of fact, safety evaluation should be taken from more aspects including deflection examination coefficient, static deflection, transverse accretion coefficient, natural period of vibration, displacement amplitude of vibration and so on.

9. REFERENCES

- Zheng, Z.X., 2003. The fatigue diagnoses and the safety evaluation system of steel bridge, *Nondestructive Testing* 5, Beijing, 9-13.
- Xu, J.M., Tu, W.D., Tang, G.Y., Lai, K.Y., Ren, Y.S., Shi, Y.J., Yang, Y.M., Li, Z.R., 1994. The natural life research of fatigue crack expansion in aged railway bridges. *Journal of the China railway society* 3. Beijing, 106-111.
- Gao, R., Jiang, L.C., and Qi, M.L., 2005. *The examination report of the Nenjiang highway steel bridge of Qiqihaer city*. 1-4. Beijing.
- Liu, B., 1994. *Measuring Technique of Experimental Fracture And Damage Mechanics*. China Machine Press, Beijing.
- Ministerial Criterion of the Ministry of Communications of the People 's Republic of China. 1998. *Design Code of Steel Structure and Timber Structure of Highway Bridges and Culverts* JTJ 025-86. China Communications Press, Beijing.
- National Criterion of the People 's Republic of China. 1994. *High Strength Low Alloy Structural Steels* GB/T 1591-1994. Standards Press of China, Beijing.
- National Criterion of the People 's Republic of China. 1988. *Carbon Structural Steel* GB/T 700-1988. Standards Press of China, Beijing.
- Ding, S.D., Sun, L.M., 1997, *Fracture Mechanics*. China Machine Press, Beijing.

FAILURE MECHANISM OF SHIH-KANG DAM BY APPLIED ELEMENT METHOD

WORAKANCHANA KAWIN

Ph.D. fellow, Institute of Industrial Science,
The University of Tokyo, Japan
kawin@risk-mg.iis.u-tokyo.ac.jp

KIMIRO MEGURO

Professor, ICUS, Institute of Industrial Science,
The University of Tokyo, Japan
meguro@iis.u-tokyo.ac.jp

ABSTRACT

The non-linear analysis of Shih-Kang dam by Applied Element Method (AEM) was carried out to study the failure mechanism. According to analysis result, Shih-Kang dam can resist a very low amount of fault induced ground rupture and deformation. The damage mechanism starts from the separation of the dam from its foundation, a crack from the top of the dam, shear cracks and compression failure. The force-deformation relationship from numerical simulation indicates the resisting force is almost diminished after shear crack on the dam body. Parametric studies including the changing dip angle of the fault, fault location were carried out. In case of the reverse fault, first, the dam separate from its foundation then follow with the shear failure of crack from the top surface. Unlike the case of reverse fault, the fault movement tends to break the dam by the tensile force. The fault location affects in the shear span length of the concrete dam which the longer shear span results in the higher resisting displacement. A redesign of Shih-Kang dam for damage prevention was proposed by placing the slip joint and reinforcement, FRP or expansive agent to control the crack width.

1. INTRODUCTION

In some of the past earthquakes, many structures have been destroyed by the fault action. Among them, one of the most spectacular events is the damage to the Shih-Kang dam in the 1999 Taiwan, Chi-Chi Earthquake. The movement of the Chelungpu fault resulted in the M7.7 earthquake and also produced a large scale ground surface rupture and deformation that damaged a lot of structures in the fault area. The Shih-Kang Dam, locating on the fault trace, was directly hit under its foundation and was severely damaged. Fortunately, there is no report on the damage from flooding after dam breaking. However, it is still questionable that if a fault movement occurs in the different dam, it may inflict the unexpected amount of damage to lives and facilities of the people living in the downstream.

Among all dams in the high seismicity region, there are few in locations where faults were not recognized or suspected to exist (Sherard et al., 1974). Some of these in the active fault zones are concrete dams which are known as low ductility material. Despite this fact, very little among them has been designed against the possible fault movement action. The slip joint of the Clyde dam (Hatton et al., 1987) is merely an example of the countermeasure. For those which were not carefully designed against fault movement, they are at risk of failure as the Shih-Kang dam if there is fault movement.

The behavior of the concrete dam under the fault rupture is not well understood since the occurrence of the event is rare. Although the Shih-Kang dam is the first case in the history, there are several cases that the fault movement break near the dam location as shown by Sherard et al (1974). The study of the concrete dam under the fault rupture has never been carried out before. Some of the closest to this study, both numerical and experimental models, has been found in the study of behavior of the soil deposit under the fault movement (Bray et al., 1994a, Bray et al., 1994b). However, the studies were mainly to predict the deformation of the ground surface, not to study the failure behavior of the structure itself.

Applied Element Method (AEM) is a numerical model for simulating the structural behavior from an elastic range to a total collapse proposed by Meguro, K., and Tagel-Din, H (1998). In AEM, a structure is modeled as an assembly of rigid elements connected together with a zero-length normal and shear springs. The major advantages of AEM are simple modeling and programming, and high accuracy of the results with relatively short CPU time. By using AEM, highly non-linear behavior, i.e. crack initiation, crack propagation, separation of the structural elements, rigid body motion of failed elements and totally collapse process of the structure can be followed with high accuracy. With these advantages, AEM will be suitable to use for analysis of the dam under the large deformation.

The first objective of this paper is to study and understand the behavior of the Shih-Kang dam under fault rupture. The second objective is to carry out the parametric study including dip angle of the fault, fault location, ground deformation shape and dam height. The last objective is to propose the redesign of Shih-Kang dam to prevent the damage due to fault movement.

2. SHIH-KANG DAM SITE CHARACTERISTIC AND GEOMETRY

Shih-Kang Dam is located on the Ta-Chia River in Taiwan. The dam sites lies over a shallow sandy and gravelly soil deposit spreading over a laminated mass of mud stone, silt stone and sand stone of Pliocene Epoch, Tertiary Period. The dam foundation was constructed on the underlying rock surface under the excavated shallow sandy and gravelly soil deposit. The dam is 25 m tall and 357 m long with 18 gates lined up, has a total

concrete bulk of 141,300 m³. Figure 1 shows the dimension of the Shih-Kang Dam.

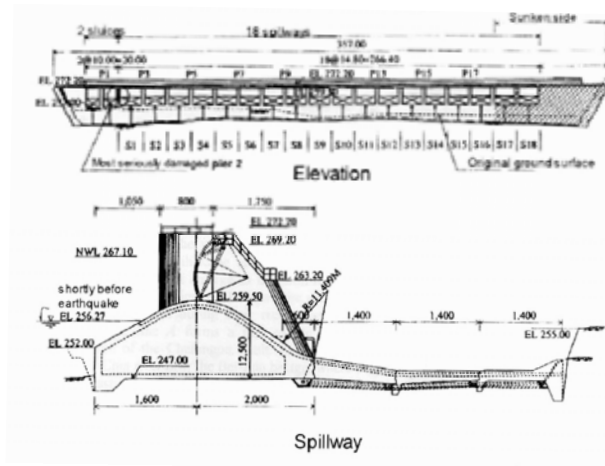


Figure 1. Shih-Kang Dam geometry (Source: Sugiyama, 2001)

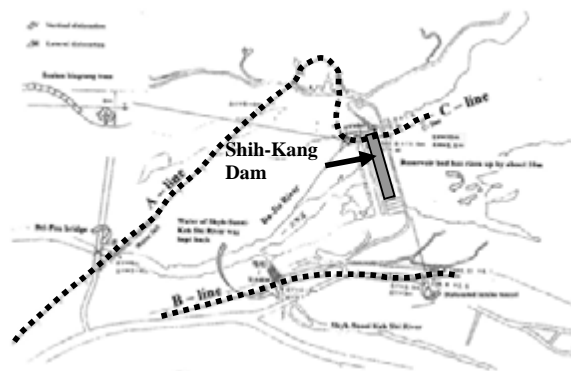


Figure 2. Shih-Kang Dam and its vicinity (Source: Konagai, 1999)

2.1 Ground surface rupture and deformation in the vicinity of the dam

The fault rupture trace in the Shih-Kang area is shown in Figure 2. Three major fault trace are composed of Line A, Line B and Line C. Line C has crossed the northern end of the Shih-Kang Dam. The different height between the two sides of line C is reported to be 10 m (Konagai et al., 1999). The line B has crossed the intake tunnel of Shih-Kang Dam. This line sheared the intake tunnel at the south of Shih-Kang Dam, completely. According to the result from the survey (Chen-Shan et. al., 2001), the ground surface of the Shih-Kang Dam has become a wavy deformation after the Chi-Chi Earthquake. It was also reported that the downstream area has been changed into bow-shape and up-lift terrain.

2.2 Reported damage in Shih-Kang Dam

The full report of Shih-Kang Dam damage can be found in reference (Sugimura et. al, 2001 and Chen-Shan et. al., 2001). To give an idea on the dam damage, the brief description is provided here. The damage in Shih-Kang Dam can be separated into two zones according to the level of damage which is the zone just above the fault and far from the fault. Figure 3 shows sketch of Shih-Kang Dam. The dam was slightly tilted spillways #15 and #16 and seriously slanting spillways #17 and #18, the latter deeply immersed in the water. The crack distribution on the spillways is shown in Figure 4. Major crack was observed between spillway #6 and #16. The diagonal cracks were found on the most damaged spillway. And transverse joints between blocks were opened in such a way that the openings on the upstream side were wider than those on the downstream side.

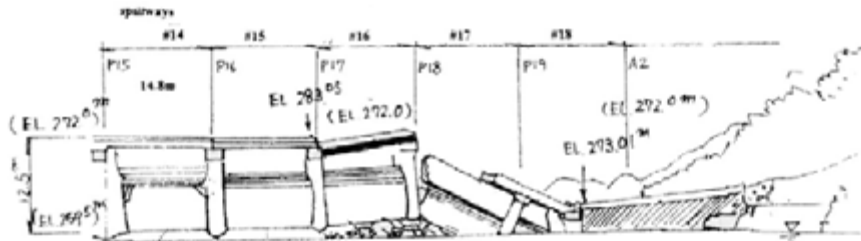


Figure 3. Sketch of damage to Shih-Kang Dam (Source: Sugiyama, 2001)

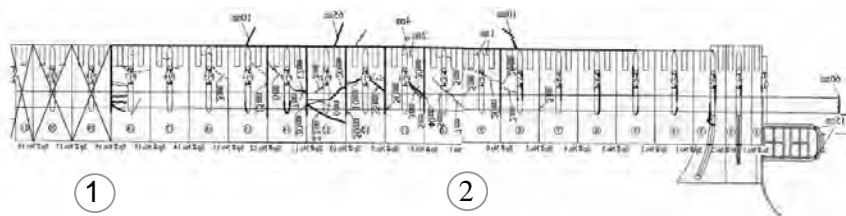


Figure 4. Sketch of actual crack pattern (Source: Konagai, 2001)

3. NUMERICAL MODEL FOR SHIH-KANG DAM

The AEM mesh representing Shih-Kang dam is shown in Figure 5. The total numbers of elements is 4578. An element size in the AEM is 1 m. The concrete thickness varies according to the depth of the dam as shown in cross-section in Figure 1. Strain energy release rate (G_{cr}) in concrete is 2×10^{-4} MN/m and Elastic modulus (E_c) is 20 GPa. The fault location is assumed at the 38 m at the bottom of the dam from the left side. The left path of the fault is fixed and the right side is the moving one.

4. NONLINEAR ANALYSIS

Concrete in Shih-Kang dam was not placed at the same time therefore there are construction joints in the dam concrete. The effect of the construction joints will be studied in future. In this study, the dam was modeled by assuming that the construction joint has no effect on the dam behavior during fault action. The input displacement in the model was chosen according to survey data (Konagai, 1999 and Chen-Shan et. al., 2001). The input displacement is composed of two parts (Figure 4). First, a shear displacement representing the reverse fault movement of dip angle approximately 20° (H:V=1:0.35) at the bottom boundary. The second input is the surface deformation along the dam foundation. This deformation was calculated from the measured deformation at the trunion girder (Chen-Shan et. al., 2001) of the dam after being damaged by assuming that there is no gap between the dam and the bed rock.

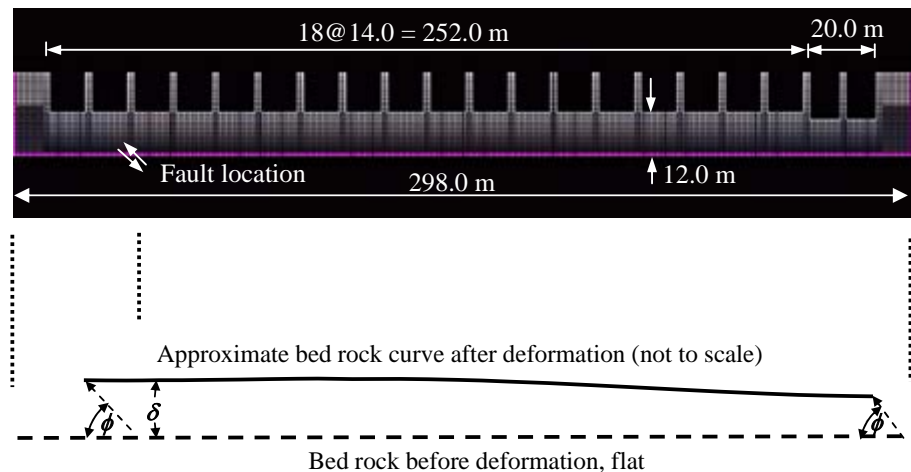
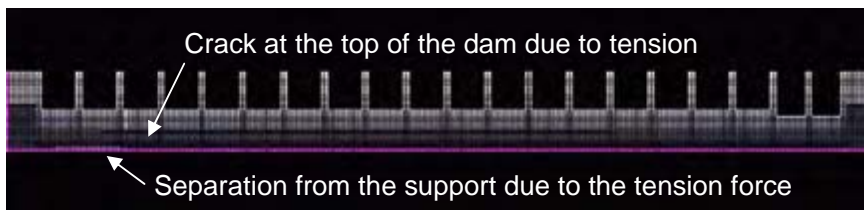


Figure 5. Shih-Kang Dam model and input ground displacement

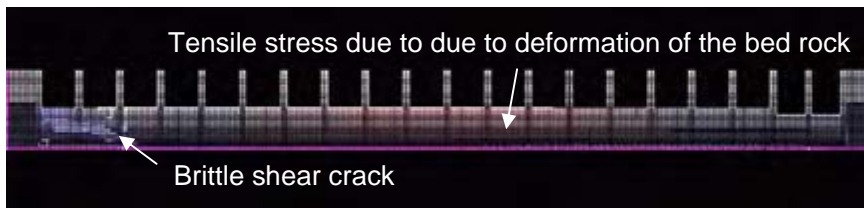
4.1 Crack patterns in spillways just above the fault

As shown in Figure 6(a), during the first 1 mm, the dam was separated from its support. At this state, in case of no special treatment in the dam, it is possible that the water will leak through this gap. At the relative vertical displacement (δ_v) between 2 sides increased to 2 mm, the crack at the top of the dam was appeared due to tension stress from bending action. This crack is also considered to be dangerous because it can cause water leakage if the crack propagates below the water level. After the $\delta_v=45$ mm, shear crack was started to propagate and the dam was found to be severely damage beyond this point (Figure 6(b)). The further increasing applied displacement will not largely increase strain energy in the dam however it will generate the crack instead until the dams from both sides are completely separated. As a result, the flooding from the reservoir is

possible at this state. At $\delta_v=150$ mm, the remaining compression struts are damaged by compression failure. At this point, the damage becomes severer (Figure 6(c)). It is noted that although the dam just above the fault becomes severely damaged, the shear transferring between each parts of the dam is still possible due to the friction of the concrete rupture under compressive force (Figure 6(d)). However, due to the damage, the ability to retain the water is totally loss and the dam is considered to be unsafe. In the far from fault zone, the flexural damage from the surface deformation can be observed at $\delta_v=75$ mm. These cracks are also able to cause the water leakage from the dam. It is important to note that although the surface deformation does not cause as high damage to the dam structure, it spread wider and has higher opportunity to damage the dam.



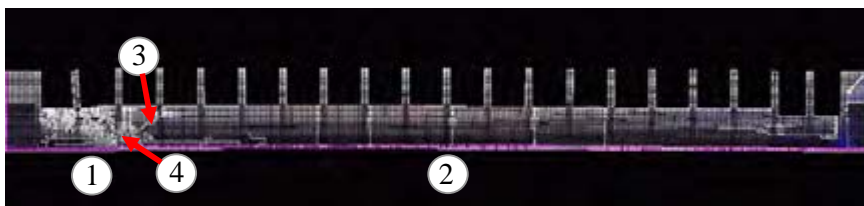
(a) $\delta= 1$ mm



(b) $\delta= 45$ mm



(c) $\delta= 150$ mm



(d) $\delta= 830$ mm

Figure 6. Crack patterns obtained by numerical simulation representing the Shih-Kang Dam

4.2 Force-displacement relationship

Figure 7 shows the force-deformation relationship of numerical model representing Shih-Kang Dam. From position 0 to 1, the behavior is linear and elastic. However, after the position 1, the stiffness of the curve drops suddenly. This coincides with the separation of the dam from its support. After the position 1, as the fault tends to lift the dam upward, the crack at the foundation propagates further into the left side of the fault. The dam will behave like a short beam under the shear action that causes the shear crack at the position 2. After shear crack, the resisting shear force is almost reduced by half however the damage area is still able to continue resisting the shear force through the compression strut until these compression struts fail by the compression stress.

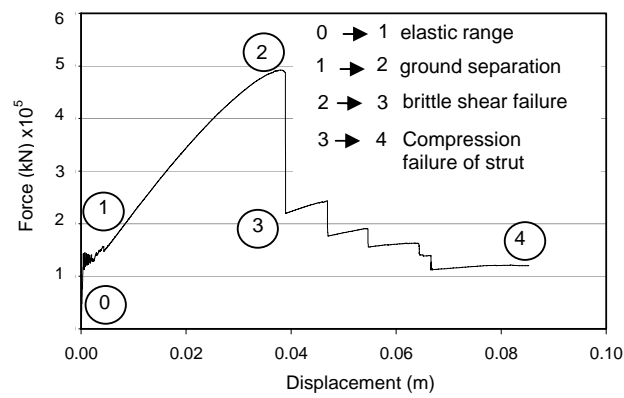


Figure 7. Vertical force-displacement relationship of the Shih-Kang Dam under 20° dip angle reverse fault

4.3 Crack pattern in the farther area from the fault

The cracks are the result of bending effect due to the curve deformation of the ground surface (Figure 5(d)). These cracks propagate from the top of the dam. As state in the previous section, this dam can also cause the water leaking and the prevention of this crack is required in order to keep the dam serviceability. By comparing the crack patterns to the investigated one, cracks from static simulation match well with the vertical crack from the investigated one; however, the diagonal crack in the area cannot be simulated. At this state, those diagonal cracks are expected to be the result of dynamic action. The displacement at the trunion girder was also compared to the measured one (Chen-Shan et. al., 2001). The comparing result shows a good agreement between observed and the measured one.

4.4 Comparison to the actual damage

Figures 4, 6 and 8 show the comparison of between real damage and crack distribution obtained by AEM. The crack distribution obtained from AEM in the zone just above the fault is very similar to actual damage in the

Shih-Kang Dam as can be seen at the locations 3 and 4 in Figure 6(d), 8(a) and 8(b), respectively. For the far from fault zone, the AEM result shows the cracks in the transverse joint between block in the same area as in the actual damage however the diagonal cracks is not exhibited. It is expected that this crack comes from the movement perpendicular to the dam axes, torsion or dynamic effect.



Figure 8. Damage to Shih-Kang dam above the fault
(Source: Jack, Yung-Wan Lien, 1999)

5. PARAMETRIC STUDY

In this section, the parameters that may affect the Shih-Kang dam behavior and damage under fault action are studied. The parameters including dip angle, fault location and the underlying bedrock are selected.

5.1 Effect of dip angle of the fault

The numerical model representing Shih-Kang Dam was subjected to fault movement with the different dip angles. The dip angle was varied from 30° , 45° , 60° , 70° (approximation of actual case) to 90° for reverse fault and 30° , 70° and 90° for the normal fault. The failure behavior of the dam in each case is explained as the followings:

5.1.1 Reverse fault

From the numerical result of the dam subjected to the reverse fault, it was observed that, regardless of the fault dip angle, the dam has the same failure pattern i.e. starting from the separating of the dam from the foundation. Then, the shear crack appears in the dam and compressive failure. With different dip angle, it was noted that shear crack occurs in the dam at smaller displacement for larger dip angle.

5.1.3 Normal fault

Unlike the case of reverse fault, normal fault causes tensile stress in the dam. This tensile stress can cause the separate of the dam from the

foundation. Because concrete is weak in tension, the dam failure at the smaller displacement compared to reverse fault case.

5.2 Effect of fault location

In this section, the effect of faulting location is studied. In the actual damage, the fault location is near to the left end of the dam. It is interesting that how the faulting location affects on the failure behavior of the dam. The numerical model representing the Shih-Kang Dam was subjected to the 70° dip angle at (a) the middle and (b) the other end of the dam. In case (a), fault was moved from the left side in the previous analysis to the center of the dam. The damage also occurred at the center of the dam at 3 mm which is the same as in the previous case. However, this crack propagated further into the left side of the fault. At the $\delta_r=6$ mm, crack started propagating from the top of the dam. At $\delta_r=310$ mm, it was found that the brittle shear failure occurred and crack passed through all section. Later, the dam was totally separated as shown in Figure 9. Comparing this to the case that the fault was applied at the left end, the dam could resist higher amount of the fault displacement (150 mm). In case (b), the same failure mechanism was observed however a slightly increasing in displacement was observed at the total separation (410 mm). However, because the shear force was transferred through the longer span, the total damage to the dam occurred at the larger deformation

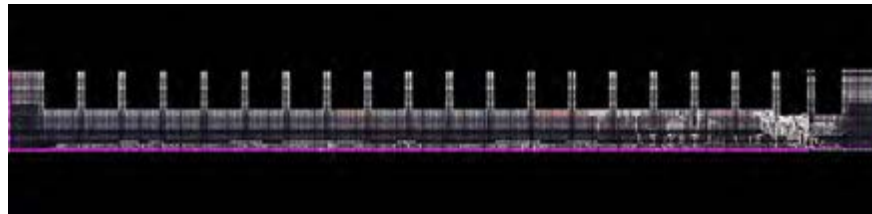


Figure 9. Crack patterns on the dam in case that fault movement Occurs at the other end of the dam

6. REDESIGN OF THE SHIH-KANG DAM TO ACCOMMODATE THE FAULT MOVEMENT

For Shih-Kang Dam to survive, it must be able to resist both surface rupture and deformation. The Shih-Kang Dam was redesigned to accommodate the 11 m of reverse fault (Figure 10). Two adjustments have been added to the previous design. First is to add slip joint in the same manner as one constructed in Clyde dam (New Zealand), to accommodate the 11 m movement and the second is to place reinforcement, FRP or expansive concrete to control the crack width of the dam.

7. CONCLUSION

The static non-linear analysis of the Shih-Kang Dam was carried out. Parametric study including dip angle of the fault, fault location were studied. Also, the redesign of Shih-Kang dam was proposed. It was found that

Concrete dam like the case of Shih-Kang Dam can resist very low amount of fault induced ground rupture and deformation. From numerical result, Shih-Kang dam damage mechanism starts from the separation of the dam from its foundation, crack from the top of the dam, shear crack and compression failure. According to the parametric study, it was found that the normal fault, if occur under the dam will damage the dam at the lower displacement than the reverse fault. Also, different fault location affects in the different shear span length. The longer the shear span's length, the more displacement the dam can resist. The proposal for the rehabilitation of Shih-Kang dam is proposed by placing the slip joint and reinforcement, FRP or expansive concrete to control the crack width of the dam. To place the slip joint, the accurate knowledge of fault characteristic in the area must be known.

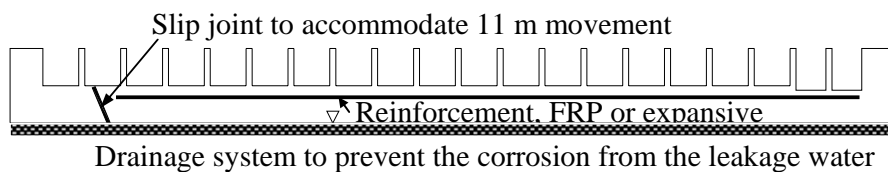


Figure 10. Redesign of Shih-Kang dam

REFERENCES

- Bray, J. D., Seed R. B. and Seed H. B. (1994a). "Earthquake Fault Rupture Propagation through Soil." *J. Geotech. Eng.*, 120(3), 543-561.
- Bray, J. D., Seed R. B. and Seed H. B. (1994b). "Analysis of Earthquake Fault Rupture Propagation through Cohesive Soil." *J. Geotech. Eng.*, 120(3), 562-580.
- Broek D. (1986) *Elementary Engineering Fracture Mechanics*, 4th Ed., Martinus Nijhoff Publishers, Boston
- Chen-Shan K., Wei-Pin, N., Yun-Jen, C., (2001). "Damage and Rehabilitation work of Shih-Kang Dam." *Seismic Fault Induced Failures*, Tokyo, Japan, 33-48
- Jack, Yung-Wan Lien (1999). *Taiwan Chi-Chi Earthquake 9.21.1999, Bird's Eye View of Cher-Lung-Pu Fault*, 1st Ed., Sino-Geotechnics Research and Development Foundation.
- Konagai, K., Miura, S., and Sugimura Y. (1999). Reconnaissance Report of the 1999 JiJi Earthquake, Taiwan (1st draft), *Japan Society of Civil Engineers*
- Meguro, K., and Tagel-Din, H. (1998). "Applied Element Simulation of RC Structures under Cyclic Loading." *J. Struct. Eng.*, 127(11), 1295-1305.
- Sherald, J. S., Cluff L. S. and Allen C. R. (1974). "Potentially Active Fault in Dam Foundations." *Géotechnique.*, 24(3), 367-428.
- Sugimura, Y., Miura, S., and Konagai, K. (2001). "Damage to Shihkang Dam Inflicted by Faulting in the September 1999 Chichi Earthquake." *Seismic Fault Induced Failures, Seismic Fault Induced Failures*, Tokyo, Japan, 143-154.

UTILIZATION OF NEAR-INFRARED SPECTRAL IMAGING SYSTEM FOR INSPECTION OF CONCRETE STRUCTURES

HISASHI KANADA¹, YUKIHIRO ISHIKAWA², TAKETO UOMOTO¹

¹International Center for Urban Safety Engineering,
Institute of Industrial Science, The University of Tokyo, Japan

²Department of Civil Engineering, Graduate School of Engineering
Shibaura Institute of Technology, Japan

kanada@iis.u-tokyo.ac.jp

ABSTRACT

Recently, the authors have developed a new non-destructive inspection method for concrete structures using near-infrared [NIR] spectroscopic technique. Near-infrared [NIR] spectroscopy had been developed in the area of food and agriculture. Electromagnetic waves are absorbed or reflected from any substance depending on the characteristics of their components. Therefore, unknown components can be estimated if its optical properties have been understood. This enables us to obtain chemical information of concrete by just sensing reflected near-infrared rays from the measuring plane.

Since typical spectrometer can measure only spectral information of one point, a new near-infrared spectral imaging system was assembled to scan a large area using equipment already available. This system consists of near-infrared irradiation equipment, imaging spectroscopy and near-infrared CCD camera. Dispersed near-infrared rays through the spectroscopy can be received in each wavelength by light-sensitive element on CCD camera. Clear spectral images can be captured due to improvement of performance. This paper describes how to obtain distribution of deleterious substances of concrete from spectral image, and introduces experimental results.

1. INTRODUCTION

The market for maintenance and repairing existing structures in Europe and America accounts for approximately 30 to 50 percent of the entire construction market. This percentage is expected to increase further in the future. In the case of social infrastructures, the inspection area is large and environmental condition or location may be tough, therefore, it often requires high labor and cost in order to inspect concrete structures. Therefore, efficient and low-cost inspection methods are required for maintenance. Many non-destructive inspection methods have recently been

developed for concrete structures. However, these methods can obtain only physical information of concrete, such as crack depth, delamination or position of reinforcement etc. near its surface. For example, delamination or loose portion of concrete can be detected by using the infrared thermography method, and the ultrasonic method is used for measurement of crack depth. Core boring or sampling may be carried out for componential analysis in order to cover the lack of chemical information.

Remote non-destructive componential analysis using spectroscopy would prove to be a powerful tool for inspectors. This enables us to scan distribution or concentration of deleterious substances two-dimensionally. Availability of this system for inspection of deteriorated concrete has been corroborated by experimental results.

2. COMPONENTIAL ANALYSES FOR INSPECTION OF CONCRETE

Considering the deterioration mechanisms of concrete, degeneration of cement hydrates or penetration of detrimental constituents are main cause except in case of fractures due to external force or use of harmful aggregates. Carbonation and chloride attack are typical deterioration causes, therefore, carbonation depth and chloride content are often measured in order to assess serviceability of concrete structures. This information can not be obtained remotely and instantly, advantages of spectroscopic technique are shown below compared to traditional methods

2.1 Traditional analytical methods for concrete components

Carbonated area can be colored by spraying phenolphthalein alcohol solution. This method is usually carried out as a simple test. EPMA analysis is performed to detect target element if necessary, in the case of carbonation, two dimensional distribution of carbon should be measured.

Chloride content in concrete is an important index indicating the status of reinforced concrete. This is measured by potentiometric titration method or fluorescent X-ray analysis. Chloride penetration area can be estimated by spraying silver nitrate solution on a concrete surface, chloride in concrete reacts with silver to produce white colored silver chloride which determines the area containing chloride. EPMA analysis can also be carried out to measure distribution of chloride. Except for spray method, these componential analyses require pretreatment, labor, time or reagent. Moreover, it is difficult to measure in the field as equipments are not designed for field use.

2.2 Advantages of near-infrared spectroscopy

Near-infrared spectroscopy has some advantages compared to traditional componential analyses. This method can measure objects directly and non-destructively without pretreatment of sample or chemical agent. Unknown components and their concentration can be estimated instantly if

their optical properties are known. This is a low-energy, pollution-free environment-friendly, cost effective inspection method which operates efficiently. Two-dimensional measurement is realized through the introduction of near-infrared spectral imaging system. Table 1 shows the comparison between near-infrared spectroscopy and traditional componential analyses.

Table 1 : Comparison between near-infrared spectroscopy and traditional componential analyses

	Traditional componential analyses	Near-infrared spectroscopy
Sampling	Destructive, chipping	Remote, non-destructive
Analyzing area	Fixed point	Two-dimensional distribution.
Duration of analysis	Long	Short
Analysis method	Different methods are required to detect target component	Multi-component simultaneous analysis
Chemical agent	Use	Nonuse
Field use	Unsuitable	Suitable
Pretreatment	Required	Not required
Equipment	Inside installation	Field use, handy type
Cost of analysis	High	Low

3. DETECTION OF DELETERIOUS SUBSTANCES BY NEAR-INFRARED SPECTROSCOPY

Causes or grades of deterioration can be estimated from presence of substances such as chloride, calcium carbonate, calcium sulfate, alkali silica gel, rust etc. on concrete surface. In this research, steel corrosion due to carbonation, chloride penetration and sulfuric acid attack were primarily focused upon, and spectrum change due to deterioration was investigated.

3.1 Near-infrared spectrum change due to deterioration of concrete

Spectrum changes of concrete due to deterioration were observed from experimental results (Kanada et al., 2004). Figure 1 shows spectrum changes due to deterioration of concrete. Increase of absorbance at 2266nm can be observed as chloride content increases. This behavior is attributed to the fact that the vibration mode of cement hydrates is changed by the action of chloride. 2266 nm can be selected as characteristic waveband to quantify chloride content of cement paste.

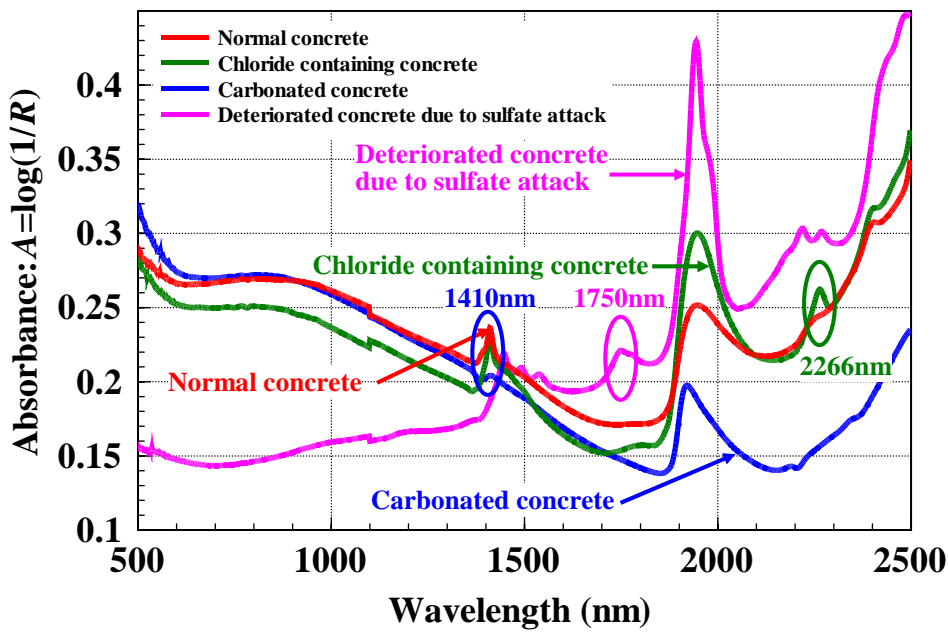


Figure 1: NIR spectrum change due to deterioration

Decrease of absorbance at 1410nm can be observed due to carbonation. Ca(OH)_2 in hydrated cement changes to CaCO_3 , therefore, absorption properties of hydroxyl (-OH) were found absent. Absorption peak at the wavelength is caused by 1st overtone spectroscopy of the hydroxyl stretch vibration in calcium hydroxide. Wavelength of 1410nm can be selected as characteristic waveband to verify carbonation.

Deterioration due to sulfuric acid is often concern for sewage treatment equipments or structures in hot-spring area. Calcium sulfate dihydrate is produced due to chemical reactions between calcium hydroxide and sulfuric acid (equation 1).



Some optical absorption peaks can be observed after deterioration due to sulfate attack and absorption peak at 1410nm was found to be absent due to neutralization. Wavelength 1750nm was selected as characteristic waveband to verify deterioration caused by sulfuric acid since compared to other peaks, it was independent and clear (F. M. Howari, et.al., 2002). Specific wavelengths were selected to detect deterioration factors (Table 2).

Table 2: Specific wavelengths to detect deleterious substances

	Wavelength	Mechanism
Chloride penetration	2266nm	Absorbance at 2266nm increases as chloride content increases.
Carbonation	1410nm	Absorbance at 1410nm decreases due to carbonation.
Sulfate attack	1750nm	Absorbance at 1750nm increases due to deterioration by sulfate attack

3.2 Introduction of near-infrared spectral imaging system

Near-infrared spectral imaging system was introduced in order to detect distribution or concentration of deterioration factors remotely. Deteriorated area can be detected to capture spectral image of specific wavelength because deleterious substance absorbs (reflects) NIR ray at the wavelength, then the area appears dark (bright). In case of chloride penetration, chloride containing cement paste absorbs NIR ray of 2266nm, so high chloride concentration area is captured as dark. Similarly, carbonated area appears bright when spectral image of 1410nm is captured, and sulfate attacked area appears dark by capturing spectral image at 1750nm.

Absorption properties at specific wavelength is in proportion to concentration of deleterious component. If its absorption properties are properly understood, concentration of target can be estimated by analyzing spectral images. 2nd derivative spectrum is commonly used for regression analysis when NIR spectrum is measured by spectrometer. Unfortunately, resolution of NIR spectrum obtained by current spectral imaging system is not high, therefore, difference spectrum is introduced to estimate concentration of target component. Figure 2 shows relationship between difference spectrum and chloride content of cement paste.

Differences of absorbance from reference (0.0kg/m^3) at 2266nm are

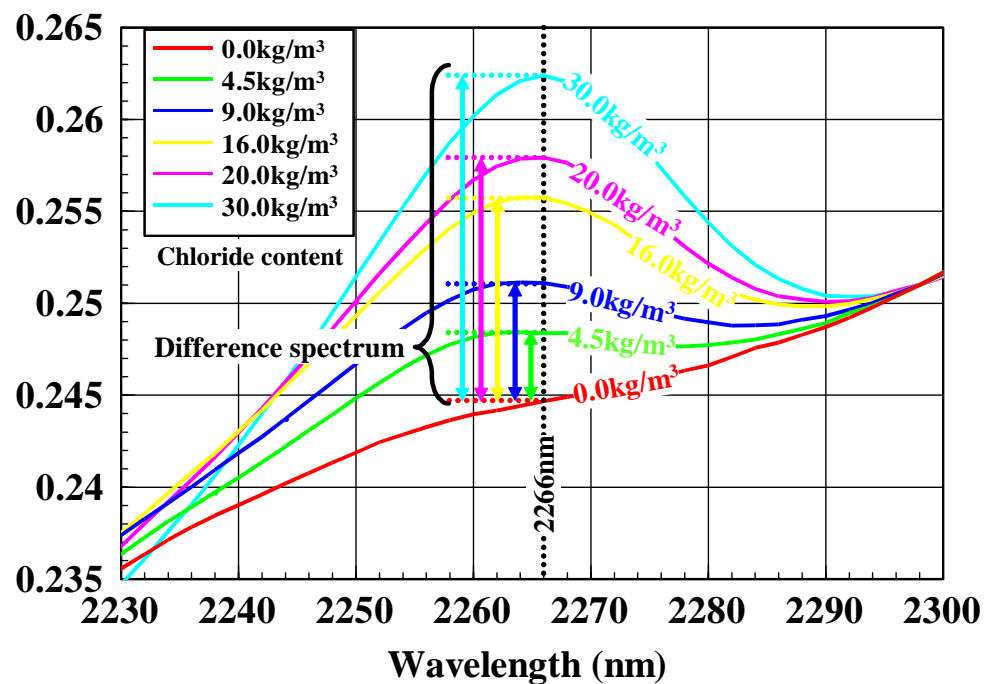


Figure 2: Difference spectrum of chloride containing cement paste

treated as difference spectrums. In case of spectrum imaging system, difference spectrum can be calculated from shading of three spectral images. Two values (wavelengths) that do not shift, even if its concentration changes, should be selected around specific wavelength. The baseline can be drawn by connecting the two selected points, length of perpendicular from the absorption peak is adopted as difference spectrum (Figure 3).

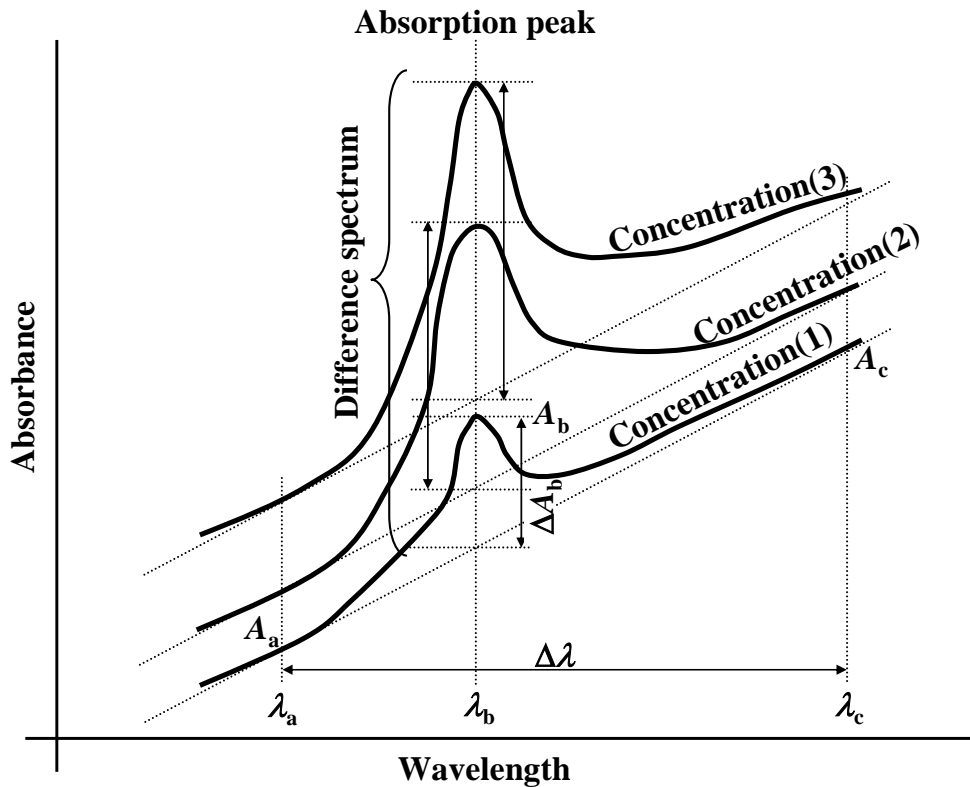


Figure 3: How to obtain difference spectrum

Difference spectrum of absorption peak: ΔA_b can be calculated from three absorbances (equation 2). Observed absorbance depends on color or roughness of measuring plane, this can remove the baseline offset and slope of the turbid interference.

$$\Delta A_b = A_b - \left(A_a + \frac{A_c - A_a}{\Delta \lambda} \times (\lambda_b - \lambda_a) \right) \quad (2)$$

3.3 Results of laboratory experiments

Laboratory experiments were carried out in order to verify the performance and availability of NIR spectral imaging system. Reflected near-infrared light from measuring plane through the spectroscope is received, and then spectral image at arbitrary wavelength can be shown. Specific examples are described follow to illustrate actual measurement.

3.3.1 Estimation of chloride content of cement paste from spectral images

Reference standard samples should be prepared in advance, concentration of unknown sample can be estimated by referring to preliminary test results. In this experiment, $\phi 5$ mm in size, of chloride containing cement paste specimens were prepared for reference. Figure 4 shows scanning of NIR spectral images of reference standard samples. Figure 5 shows chloride content and spectral image of reference standard samples. Concentration difference of chloride can not be observed from raw spectral image.

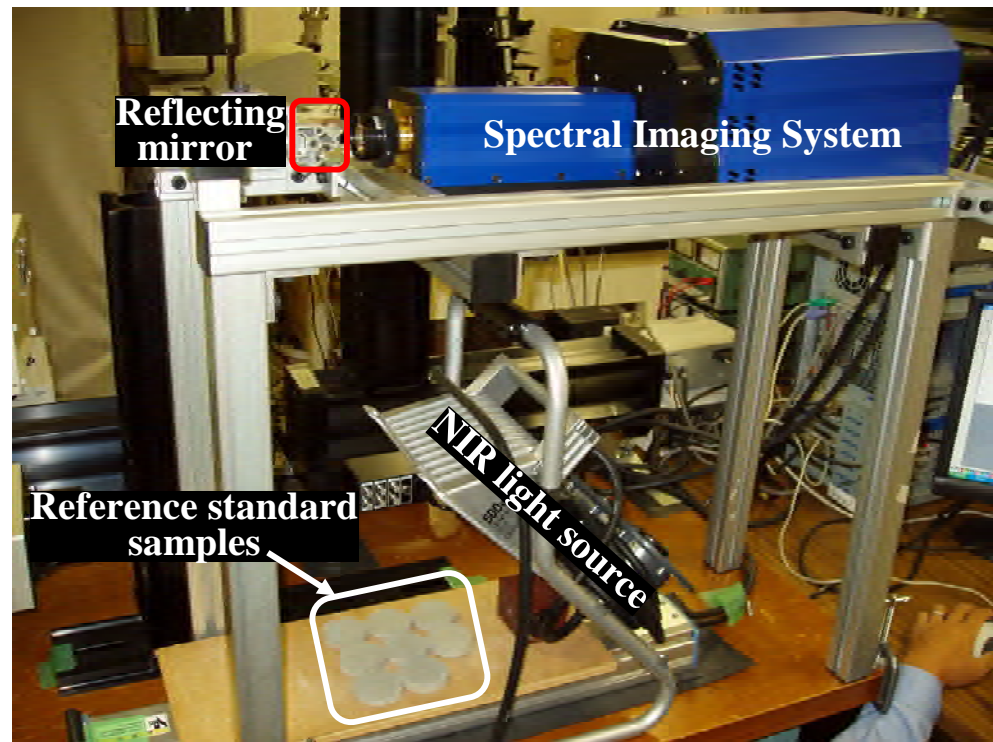


Figure 4: Actual scanning of NIR spectral images of reference standard samples

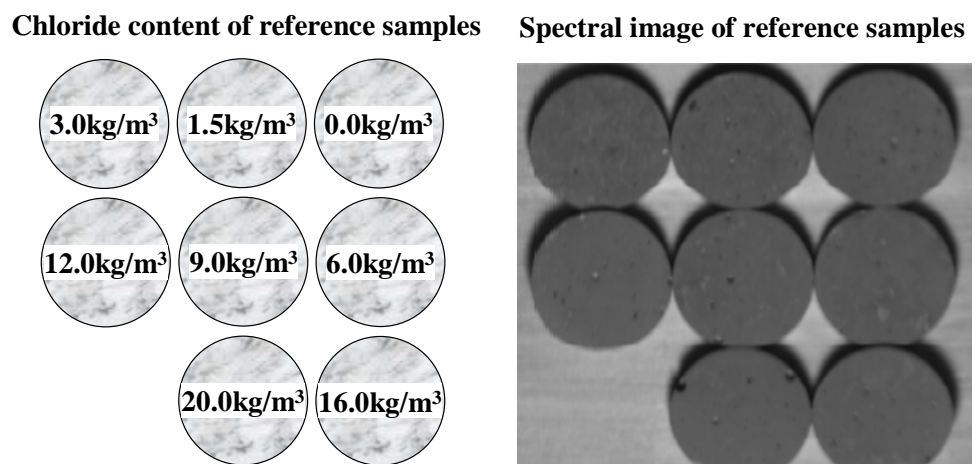


Figure 5: Chloride content of reference standard samples

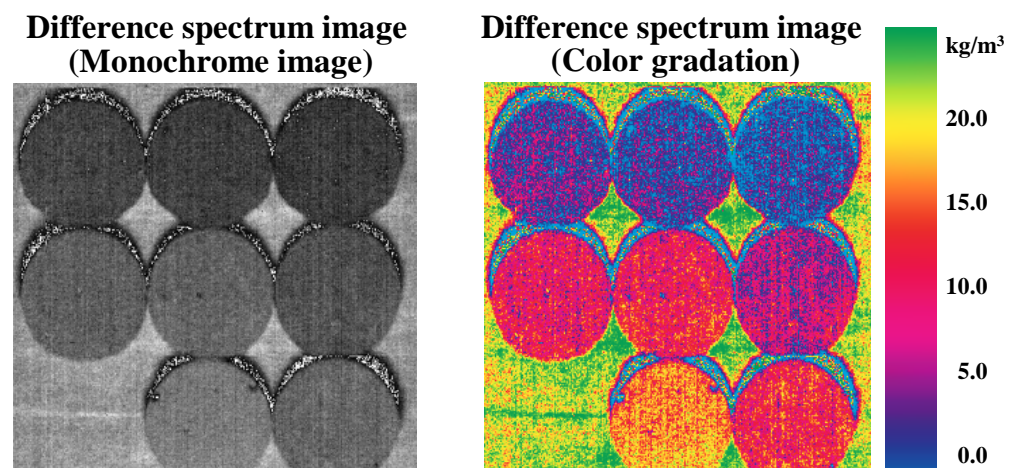


Figure 6: Difference spectrum image of reference standard samples

Difference spectrum image was introduced using the equation (2) to estimate chloride content of surface (Figure 6). The figure on the left is monochrome image of difference spectrum, black pixels indicate low concentration, gray pixels indicate high concentration. Right figure is gradation image colored concentration level, distribution can be visualized. Clear image could not be obtained due to noise, but it will be improved to increase its performance. It was confirmed that the average different spectrum of each specimen depends on chloride content from spectral analysis.

EPMA analysis is commonly applied to detect chloride penetration (Figure 7). However, processes of polishing or carbon coating are required before analysis, it takes a long time to obtain the result. NIR spectral imaging system may be used as alternative procedure of EPMA, this may be able to reduce the analysis time.

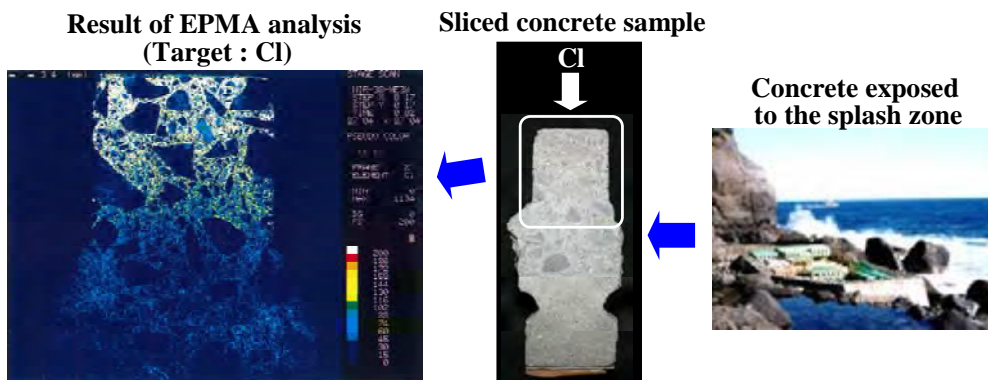


Figure 7: Result of EPMA analysis of concrete exposed to the splash zone

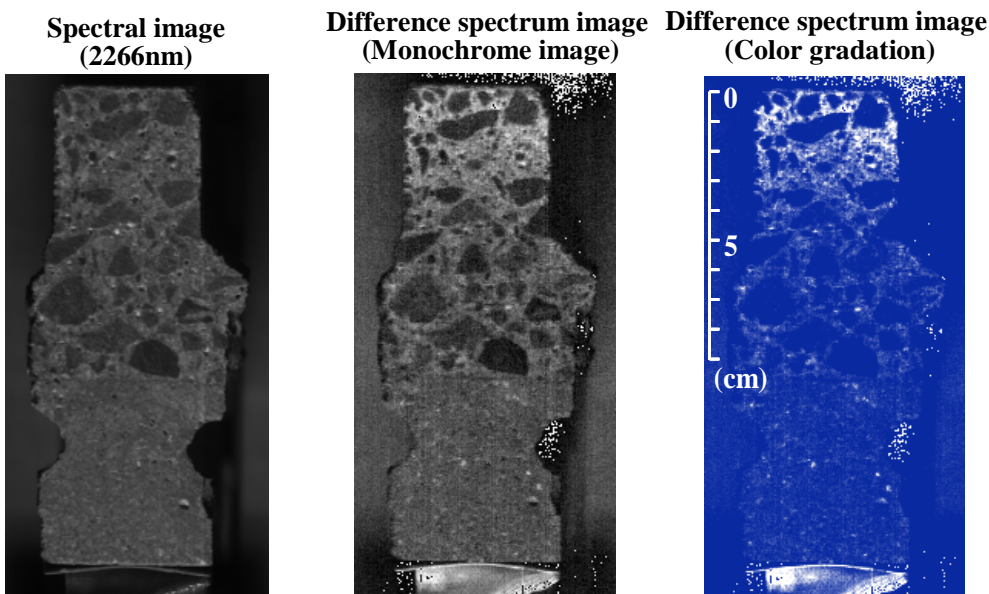


Figure :8 Difference spectrum images of sample

Figure 8 shows difference spectrum images of sliced concrete sample exposed to the splash zone. It was observed that chloride penetrated from top surface. Good agreements between penetration area detected by difference spectrum image and result of EPMA analysis were observed. Potentiometric titration method was also carried out to confirm the validity

of concentration which was estimated from spectral images. Figure 9 shows comparison of estimated chloride content from difference spectrum with results of potentiometric titration, approximate agreement can be seen.

3.3.2 Detection of deteriorated area due to sulfuric acid attack

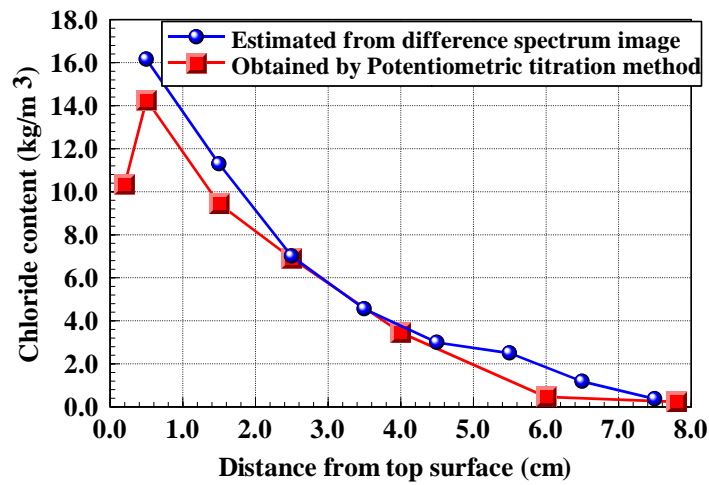


Figure :9 Comparison of chloride content obtained from difference spectrum with potentiometric titration method

Prepared two specimens (cement paste bar and mortar bar) were soaked in 10% sulfuric acid solution, calcium sulfate dihydrate was produced on surface. Deteriorated area due to sulfuric acid attack can be detected by capturing spectral image at 1750nm. Difference spectrum at 1750 nm increases as deterioration level increases as production of calcium sulfate dihydrate rises (Figure 10).

3.3.3 Application of quality control of coating agents

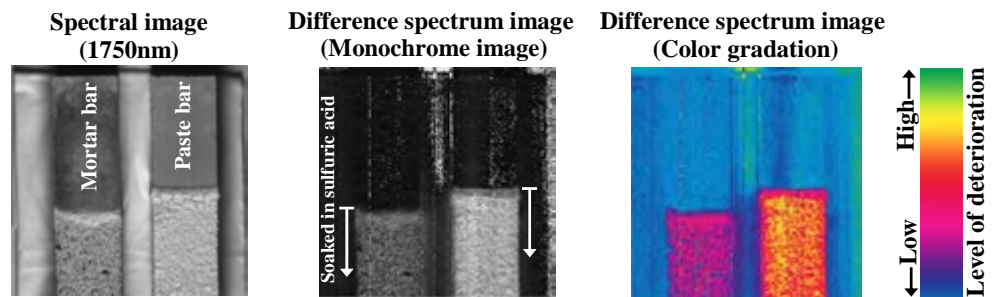


Figure :10 Detection of deteriorated area due to sulfuric acid attack

Surface coating agents are often used for the purpose of curing, but some of them are crystal-clear type, therefore it is difficult to investigate by visual check whether specified quality is achieved or not. Investigation of concentration of coating agent on concrete surface was attempted by spectral imaging system. Coating agent of water dilution type (ethylene-vinyl acetate copolymer) was adopted as sample. Diluted coating agents with water were painted on surface of mortar bar. This agent has the feature of absorption properties at 2138nm, absorption peak at the wavelength is caused by [C-H] and [C=C] stretching vibration in the agent. Quality of coating can be estimated by spectral imaging system since difference

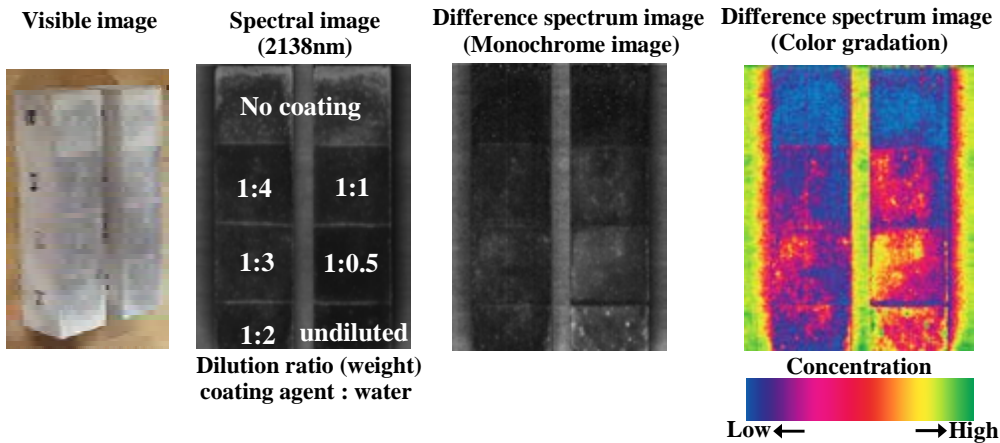


Figure 11: Quality check of coating agent by spectral imaging

spectrum depends on the concentration (Figure 11). Although volume of coating agent per area was adjusted, density could not be kept constant due uneven coating. It was confirmed that the average difference spectrum in square depended on concentration of coating agent. This technique will be utilized for inspection of finishing on concrete surface.

4. CONCLUSIONS

It has been shown that distribution of deterioration factors such as sulfuric acid attack or chloride penetration can be detected from their difference spectrum images. Compared with traditional analytical methods, the accuracy of estimated values by spectral imaging system were acceptable. If the sensitivity of light detecting element on the system is improved, noise will be reduced and stable measuring will be possible. Application of field measurement is an issue in the future

ACKNOWLEDGEMENTS

Measurement of NIR spectrum and scanning by NIR spectral imaging system were supported by Sagara lab, The University of Tokyo and JFE Techno-research Corp. EPMA analysis was carried out by Mr. Tomio Hoshino, Institute of Industrial Science, The University of Tokyo.

REFERENCES

- Hisashi Kanada, Yukihiro Ishikawa and Taketo Uomoto, 2004. *Development of New Method to Detect Deleterious Substances of Concrete Using Near-infrared Spectral Imaging System*. The First International Conference of Asian Concrete Federation
- F. M. Howari, P. C. Goodell, S. Miyamoto : *Spectral Properties of Salt Crusts Formed on Saline Soils*. Journal of Environmental Quality, 31:1453-1461, 2002.

INTERNAL DAMAGE OF REINFORCED CONCRETE AND CHEMICALLY PRESTRESSED CONCRETE UNDER UNIAXIAL LOAD

RAKTIPONG SAHAMITMONGKOL

Graduate School of Civil Engineering, the University of Tokyo, Japan
sahamit@iis.u-tokyo.ac.jp

TOSHIHARU KISHI

Institute of Industrial Science, the University of Tokyo, Japan
kishi@iis.u-tokyo.ac.jp

ABSTRACT

Deterioration of structure is a major problem in most mega cities. In several cases, the mechanical damage such as flexural cracks or splitting cracks caused by external loads can accelerate the ingress of the deteriorating substances. The chemically prestressed concrete (CPC) has been used to suppress cracking of concrete structure. The outstanding cracking resistance and structural properties of CPC have been reported in past researches. Those studies indicate that the application of CPC is one of the promising methods to control the durability and structural performance at the same time. However, the resistance to splitting cracks and internal damage has not been studied so far.

The study on the damages of RC and CPC under uniaxial loads was therefore done. The terms 'damage' includes both transverse crack, splitting crack, and internal crack (or damage condition around rebar). It is reconfirmed that CPC can reduce number of transverse cracking even when the reinforcement already yielded. The occurrence of splitting crack load is suppressed to higher load when compared with the case of RC. However, the attention should be paid to the fast growing of splitting cracks of CPC once they formed. The internal cracking condition was visually observed by injecting ink into specimens during loading and split the loaded specimens by concrete cutter. The results show that CPC can inhibit the propagation of internal cracks to surface. However, there is no clear difference in shape of internal cracks between RC and CPC.

1. INTRODUCTION

Cracking is probably the most unfavorable properties of reinforced concrete (RC). Once crack takes place in the structure, the durability and aesthetic condition can be severely downgraded. It is very difficult to completely prevent cracking in RC structure because concrete is weak under tension and cracking can be created by numerous reasons. However, it is recommended, in the limit state design, that the crack width of RC should be

limit under a certain value which is decided based on environmental condition and function of structure.

The employment of expansive concrete is one of well-known methods to improve structural performance and resolve cracking problems (Okamura, 1978). The usage of expansive concrete can be categorized broadly into the shrinkage compensating concrete, of which the expansion rate is approximately 200 μ and chemically prestressing concrete of which the expansion rate is between 200 μ and 700 μ (JSCE, 1994). The shrinkage compensating concrete is widely used to solve the cracking problem caused by volume change of concrete while the chemically prestressing concrete is used to induce the prestress in structure. However, there has been a lot of research showing the outstanding performance of chemically prestressed concrete (hereinafter, CPC) which is not explainable by the effect of prestress. A brief review on a unique performance of CPC is made in next section.

Although several properties of CPC to transverse cracking have been considerably investigated, there has been no investigation on the splitting cracks and internal damage condition of CPC. This study is thus an attempt to investigate the cracking behaviors of CPC under uniaxial load, especially the splitting crack and internal damage which is not observable externally.

2. CRACKING BEHAVIOR AND STRUCTURAL PERFORMANCE OF CHEMICALLY PRESTRESSED CONCRETE

2.1 Deformability of Restrained Expansive Concrete

When the expansive concrete is well restrained, special tensile mechanical properties can be largely evolved. The non-linear tensile properties and remarkable plasticity can be achieved. Hosoda (2001) showed these properties of restrained expansive concrete under both uniaxial tensile loading and under flexure. These properties are referred as the 'deformability' which cover the nonlinearity, plasticity, and time-dependent deformation. It was proposed that this deformability of restrained expansive concrete is a result of the uneven distribution of strain cause by the expansion of expansive additives and different rate of reaction between cement and expansive additives.

2.2 Cracking Properties of Flexural CPC Member

The superior cracking resistance of CPC under flexure has been reported (Sahamitmongkol, 2003). It was shown that CPC can increase cracking load, control crack width while reduce number of cracks at the same time. The experimental result indicates an outstanding performance of CPC to resolve cracking problem. Although the cracking resistance, which is, higher cracking load and smaller crack width of CPC, is partly increased

due to the effect of prestress, the effect of prestress can not clearly explain how CPC reduce number of cracks.

2.3 Tension Stiffening Effect of CPC

The superior tension stiffening effect of CPC was reported (Sahamitmongkol, 2004). It was shown that the abrupt reduction of average concrete strain at cracking could be prevented in CPC. This behavior identifies an ability of CPC to reduce the redistribution of CPC when cracking takes place and implies that the stress distribution of concrete in cracked portion of CPC should be different from that of RC. Outstanding performance of CPC is also observable in the post cracking condition at which the tension stiffening effect of RC is normally reduced by the deterioration of bond between reinforcing bar and surrounding concrete.

2.4 Local Bond Distribution of CPC under Tension

As the tension stiffening effect of CPC implies the different bonding properties of CPC, the strain distribution of rebar embedded in RC and CPC under uniaxial tension were measured in order to inspect the bonding properties of CPC (Sahamitmongkol, 2005). CPC show clearly different strain distribution of reinforcing bar which results in the smaller elongation. This observed bonding characteristics can be used to explain how tension stiffening effect is improved in CPC.

2.5 Influence of Internal Damage Condition on the Maximum Crack Spacing of RC

There have been some studies on the maximum crack spacing of RC. It was experimentally shown that the cover thickness and the distance between longitudinal tensile reinforcing bars are the most important factors influencing the maximum crack spacing (Kakuta, 1970). However, the relationship between maximum crack spacing and cover thickness is different for various types of reinforcing bars. The additional experimental information was shown by Goto (1980) that the shape and spacing of lug significantly affects the maximum crack spacing of RC. These studies on the maximum crack spacing indicate that the maximum crack spacing is shorter when the condition is easier for internal crack to form and propagate to the surface.

3. EXPERIMENTAL PROGRAM

Based on aforementioned reviews, it is most likely that the longer crack spacing of CPC is governed by its internal cracking condition. In order to investigate this internal cracking condition, RC and CPC prisms with different length, and size of reinforcing bar were produced. Notches were created in the specimens to control the location of transverse primary crack at different spacing. By specifying the distance between adjacent transverse cracks, the maximum crack spacing can be obtained

experimentally. The specimens were loaded under uniaxial tension and the internal damage conditions were observed by cutting specimens after loading.

3.1 Specimens

The RC and CPC prisms with different sizes of reinforcing bar and cross sectional area were produced. The reinforcing bars were located at the center of specimens. Steel plates were provided to ensure the chemical prestressing effect at the ends of all CPC specimens and C-N and D-N. The holes with a diameter of 4 mm were made at 30 mm on both side of rebar (on the direction of lugs). These holes are provided to allow the injection of red ink during loading. Table 1 is a list of all specimens and Figure 1 is the profile of specimens.

Table 1: List of specimens

Name	Type of Specimen	Type of Concrete	Rebar	Cross Sectional Area	c/d ratio
A-N	A	Normal	D29	200x200 mm ²	3.00
A-E	A	Expansive	D29	200x200 mm ²	3.00
B-N-1	B	Normal	D29	100x100 mm ²	1.25
B-N-2	B	Normal	D29	100x100 mm ²	1.25
B-E-1	B	Expansive	D29	100x100 mm ²	1.25
B-E-2	B	Expansive	D29	100x100 mm ²	1.25
C-N	C	Normal	D19 - 1	100x100 mm ²	2.12
C-E	C	Expansive	D19 - 1	100x100 mm ²	2.12
D-N	D	Normal	D19 - 2	100x100 mm ²	2.12
D-E	D	Expansive	D19 - 2	100x100 mm ²	2.12

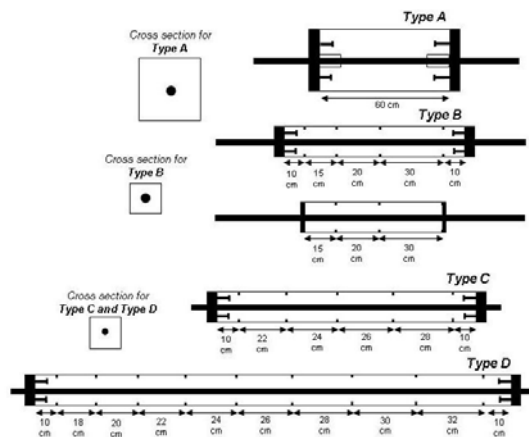


Figure 1: Profile of specimens

3.2 Materials

3.2.1 Concrete

The mix proportions of conventional concrete and expansive concrete used in this study are given in Table 2.

Table 2 Mix proportions and compressive strengths

	W/(C+E) (%)	s/a (%)	Unit Content (kg/m ³)					Strength (MPa)
			W	C	E	S	G	
NC	50	48	165	330	0	860	956	40.15
EC	50	48	164	268	60	860	956	33.97

Note: NC: normal concrete, EC: expansive concrete

3.2.1 Reinforcing bar

In this experiment, the screw shaped steel bar is used as the reinforcement. There were three types of reinforcement used in this experiment. The geometries and yielding strength of reinforcing bar are shown in Figure 2 and Table 3.

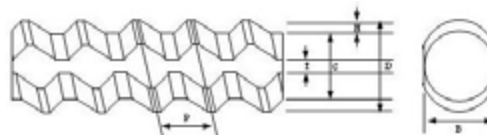


Figure 2: Shape of reinforcing bars

Table 3 Dimensions and properties of reinforcing bars

Rebar	Yielding Strength (MPa)	Cross Section					Shape of Lug		T (mm)
		Area (mm ²)	D _{avg} (mm)	D (mm)	B (mm)	C (mm)	P (mm)	H (mm)	
D29	390	642.4	28.6	32.1	26.6	27.2	12.0	2.45	11.4
D19 - 1	390	286.5	19.1	21.5	17.5	18.0	8.0	1.75	8.4
D19 - 2	700	286.5	19.1	21.5	17.5	18.0	8.0	1.75	8.4

3.3 Curing, Loading, Measurement, and Observation of Internal Damage

The specimens were kept under moist curing after the removal of formwork at 24 hours until the loading at 28 days. Before loading the red ink is injected into the holes inside specimens. The specimens were subsequently loaded monotonically under direct tension. The strains at 20 mm from both side of each notch were measured in lateral direction in order to detect the occurrence of splitting and opening of splitting cracks. After loading, the specimens were cut by diamond-sawed concrete cutter. The visual observation of internal damage condition was done. The shape of internal cracks and general damage conditions were visually compared.

4. EXPERIMENTAL RESULTS

4.1 Maximum Crack Spacing

Because the distance between adjacent notches were varied, the maximum crack spacing of each specimen can thus be determined as the maximum crack spacing in which no transverse cracking took place. Table 4 shows the maximum crack spacing obtained in this experiment. It is clear that that the crack spacing of CPC is longer than that of RC. The increment of yielding strength of reinforcing bar from 390 to 700 N/mm² slightly reduces the

maximum crack spacing. The maximum crack spacing of CPC is approximately 30% longer than that of RC in this experiment.

Table 4 Maximum Crack Spacing of specimen in series C and D

Specimens	Maximum Crack Spacing
C-N	22 cm
D-N	20 cm
C-E	28 cm
D-E	26 cm

4.2 Splitting Crack

The splitting cracks could be observed from the strain value measured in lateral direction at 20 mm from notches. The occurrence of splitting crack was attained as the point where a sudden change of strain is observable and opening rate of splitting crack were achieved from the increment of these strains.

4.2.1 Occurrence of splitting cracks

The stress of reinforcing bar when the splitting crack took place is displayed in Figure 3. The cover to diameter (c/d) ratio significantly affects the occurrence of splitting crack. It is easier for splitting cracks to form in the specimens with thinner cover. In addition, the occurrence of splitting cracks of the shorter cracked portion occurs at higher stress of reinforcing bar. It is also interesting that the stress of rebar at the occurrence of splitting cracks can be increased to almost double of that of RC when CPC is employed.

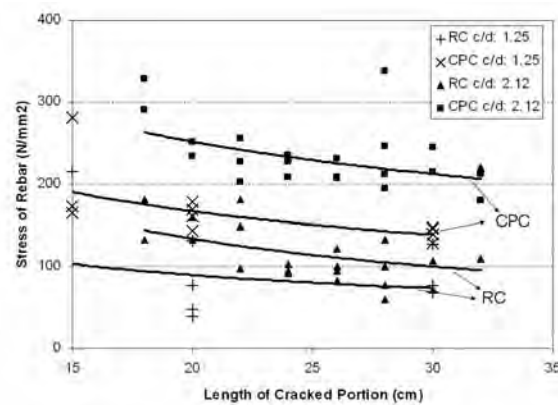


Figure 3: Shape of reinforcing bars

4.2.2 Growth of splitting cracks

The growth of splitting cracks of RC and CPC with c/d ratio of 1.25 is shown in Figure 4. As discussed in previous section, the splitting crack took place at lower load in RC; however, the splitting crack of RC grew at moderate rate. In the other hand, although the occurrence of splitting crack could be observed at higher load in CPC, its growing rate is much faster

than that of RC. This result indicates that the special attention should be paid to splitting crack of CPC once it takes place. Providing suitable transverse reinforcement should be one of the proper countermeasures on this behavior of CPC.

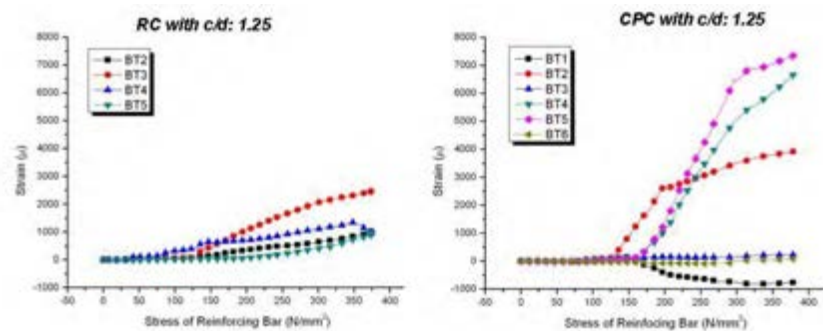


Figure 4: Opening of splitting cracks of RC and CPC with c/d of 1.25

4.3 Internal Cracking Condition

The internal damage conditions of RC and CPC are shown in Photo 1 and Photo 2, respectively. As can be easily observed, the additional transverse cracking was generated between transverse cracks formed at predetermined notched positions. The bond deterioration area can be observed from the white area in the photos. The large bond deterioration area is perceivable at the location of additional transverse crack.

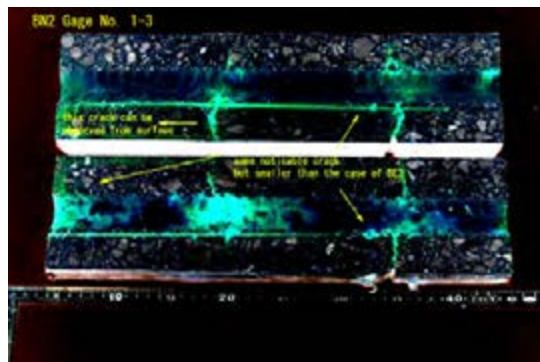


Photo 1: Internal damage condition of RC with c/d of 1.25

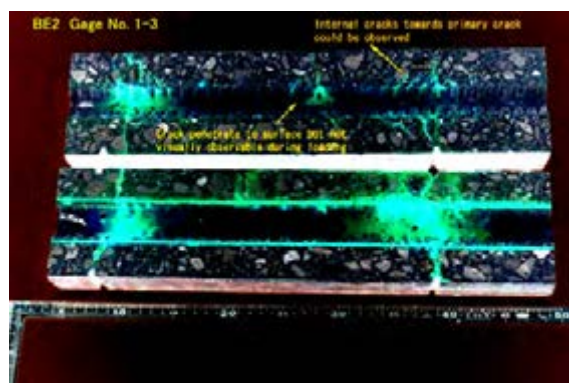


Photo 2: Internal Damage Condition of CPC with c/d of 1.25

In the case of CPC, the internal cracking could be observed between predetermined notched locations. However, this crack did not penetrate to the surface and, as the results, there is no bond deterioration area observed. Nevertheless, the large deterioration can be observed at predetermined notched location because of the occurrence of splitting crack. It is, however, important to note here that the condition illustrated by these photos is the final condition and does not give any information about the process how this damage develops. As indicated by the splitting crack in previous section, it is possible that the bond deterioration of CPC should be very small up to a certain load and increases rapidly afterwards. This behavior implies that CPC can still perform very well if applied to the suitable range of load.

5. CONCLUSION

CPC shows the notable ability to suppress the propagation of internal cracks to surface and the occurrence of splitting cracks. However, the special attention should be paid when CPC is subjected to relatively high load. The rapid damage can take place if the load is increased beyond a certain level. Providing transverse reinforcement should be an effective countermeasure to this limitation of CPC.

REFERENCES

- Okamura, H., et al., 1978. *Application of Expansive Concrete in Structural Elements*, reprinted from Journal of the Faculty of Engineering, The University of Tokyo (B), vol.34, no.3
- JSCE, 1994. *Recommendation for Practical Application of Expansive Concrete*, Concrete Library International, No. 23, pp. 5-9 (in Japanese)
- Hosoda, A., 2001. *Crack Resistance and Post Cracking Behavior of Expansive Concrete Based on Microscopic Mechanism and Application to RC members*, Doctoral Dissertation, The University of Tokyo, 2001 (in Japanese)
- Sahamitmongkol, R., and Kishi T., 2003. *The Effect of Restrained Level on Cracking Resistance for Chemically Prestressed Reinforced Concrete*, Proceedings of JCI Annual Conference, Vol. 25, No.2, pp.763-768
- Sahamitmongkol, R., and Kishi T., 2004. *Cracking and Tension-Stiffening of Chemically Prestressed Concrete under Uniaxial Tension*, Proceedings of JCI Annual Conference, Vol. 26, No.1, pp.237-242
- Sahamitmongkol, R., and Kishi T., 2005. *Bonding Characteristics of CPC and RC under Uniaxial Tension*, Proceedings of JCI Annual Conference, Vol. 27, No.1, pp.245-250
- Kakuta, Y., 1970. *Maximum Crack Width of Reinforced Concrete*, Concrete Journal, Vol.8, No.9, 1-10 (in Japanese)
- Goto, Y., and Otsuka, K., 1980. *Experimental Studies on Cracks Formed in Concrete around Deformed Tension Bars*, JSCE Journal, No.294, pp.85-100 (in Japanese)

A DURABILITY DESIGN CONCEPT FOR CONCRETE STRUCTURES IN THAILAND

SOMNUK TANGTERMSIRIKUL¹⁾, JITTBODEE KHUNTHONGKAEW¹⁾
and PITISAN KRAMMART²⁾

¹⁾ Sirindhorn International Institute of Technology, Thammasat University

²⁾ Department of Civil Engineering, Rajamangala Institute of Technology

ABSTRACT

This paper reported the concept on durability design for concrete structures in Thailand. According to the newly revised building design acts by the department of public works and city planning, long-term performances of structures such as durability must also be considered in addition to the short term mechanical properties. Concepts for durability design based on three major deterioration environments i.e. carbonation, chloride and sulfate environments are proposed as references for the revised building design acts. The concepts of design for carbonation and chloride penetration were based on test results and prediction models whereas that for sulfate resistance was mainly based on experimental results. The design concept is applicable for both cement-only and cement-fly ash concrete. Various levels of seriousness are specified for each type of environment. For carbonation, the degree of seriousness is set according to concentration of CO₂ and relative humidity of the environment whereas for chloride attack, it is set based on types of sub-environment and distance from the seashore. For sulfate attack, the degree of seriousness was set based upon the sulfate content in the environment as water-soluble sulfate content. Two different types of sulfate environments i.e. sodium and magnesium are separated due to different attacking mechanisms. Concrete mix proportion in terms of water to binder ratio and fly ash percentage, for each class of fly ash according to Thai standard, can be derived as the output of the design. This durability design concept is being processed as a part of the standard specification of the Engineering Institute of Thailand and the Thai Concrete Association.

1. INTRODUCTION

The design and construction of concrete structures in Thailand have been practiced based upon short-term properties such as slump and 28-day compressive strength (Tangtermsirikul, Kaewkhluab and Kaewmanee, 2003). Selection or specification of proper concrete for different types of severe environment is also one of the practices which has been ignored. It is evident that the previously mentioned practice can not respond to the current

needs of service-life or life-cycle design. The practice also created a lot of problems on low quality structures especially for those located in severe environments (Tangtermsirikul, 2004). Realizing this problem, the Department of Public Works and City Planning, academically supported by the Thai Concrete Association and the sub committee on Concrete and Materials of the Engineering Institute of Thailand, set up a committee to modify and renew the existing building design acts. Design of concrete structures is one part of the targeted modification. The new concept will include long-term properties into the design consideration. Durability is one of the major items to be considered in the new design acts. As reported by the first author (Tangtermsirikul, 2004), majority of cases of early deterioration of concrete structures in Thailand have been due to substandard practices in all 4 necessary stages e.g. analysis and design, material selection, construction and maintenance. This design modification is a part of the efforts to improve quality of concrete structures toward service-life based practice and is the effort in the stages of design. It is certainly that the other 3 essential stages must be improved along side with the design practice. This paper gives the explanation only on a part of the first stage (design) by only emphasizing on the durability consideration.

2. DURABILITY DESIGN CONCEPT

The revised design acts will refer to the details given in the codes or standards which are published by professional organizations like Engineering Institute of Thailand and Thai Concrete Association, etc. This causes advantage in a sense that there is no need to frequently modify the acts if the main concept of practice does not change and it is easier and faster to modify the codes or standards of the professional organizations. However, these reference codes or standards have to get approval from the Council of Engineers which is the legal body taking care of engineering professional matters of the country.

Since this is the first time of the country to consider durability in the design of concrete structures, there are still worries about understanding of practical engineers. Therefore, the committee on Concrete and Materials of the Thai Concrete Association together with the subcommittee on Concrete and Materials of the Engineering Institute of Thailand decided to launch a simple durability design concept at the first step also with the objective to educate the practical engineers. It is expected that a more complicated concept can be launched in the future. For the first simple concept, the main task is to be able to design a good concrete mix proportion and to specify materials, especially the binders, to fit each severe environment in which the structure will be located. Three types of most frequently existing severe environments, selected for the first durability design codes, are chloride, carbonation and sulfate environments. Since fly ash is currently popularly used as a cement replacing pozzolan in Thailand, the design also includes the consideration on fly ash concrete.

2.1 Design for Carbonation Resistance

In carbonation environment, the maintenance-free service life is defined as the service life until steel, nearest to the exposed concrete surface, is depassivated by carbonation. To satisfy the defined maintenance-free service life in carbonation environment, the thickness of concrete cover should be provided not smaller than the depth of carbonation during the designed maintenance-free service life.

$$C \geq X_c \quad (1)$$

where C is the thickness of concrete cover (mm) and X_c is the depth of carbonation (mm)

The carbonation depth can be estimated from

$$X_c = \alpha_1 \alpha_2 k t^{0.5} \quad (2)$$

where α_1 is the effect of rain subjection which is 1.0 for surfaces which can be wetted by rain and is 0.95 for surfaces which has no possibility to rain subjection. α_2 is the effect of severity of the environment which can be obtained from Table 1. The severity level of the carbonation environment can be specified from the average relative humidity and average CO_2 concentration of that environment as shown in Figure 1 (Tangtermsirikul and Khunthongkeaw, 2005). t is the maintenance-free service life (years). k is the carbonation coefficient which can be derived from

$$k = 1.5 k_f (w/b)^3 \quad (3)$$

where w/b is the water to binder ratio and k_f is the effect of fly ash on carbonation coefficient which can be obtained from Figure 2.

Table 1: Effect of severity of carbonation environment on carbonation depth

Level of severity of carbonation environment	α_2
Typical	0.65
Medium	0.85
Severe	1.0

2.2 Design for Sulfate Resistance

It was realized that different types of sulfate cause different mechanisms of deterioration, i.e. sodium sulfate mainly causes expansion whereas magnesium sulfate causes conversion and dissolution of calcium silicate hydrate (Krammart and Tangtermsirikul, 2004). Therefore, different recommendations are provided for proper mix proportioning of concrete in sodium and magnesium sulfates.

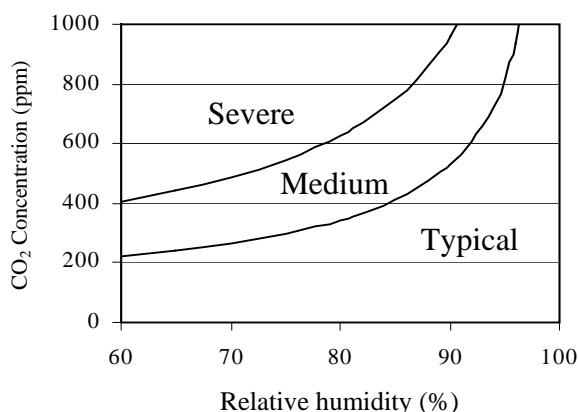


Figure 1 : Level of severity of carbonation environment

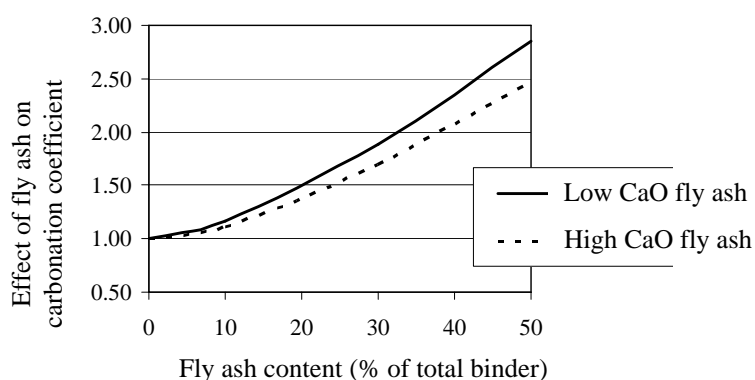


Figure 2 : Effect of type and content of fly ash on carbonation coefficient

2.2.1 Sodium Sulfate

Table 2 shows the classification of level of severity of sodium sulfate environment whereas the recommended conditions for mix proportioning of sodium sulfate resisting concrete in each severity level are given in Table 3.

Table 2 : Classification of level of severity of sodium sulfate environment

Level of severity	Concentration of sulfate (SO_4^{2-})	
	In water (ppm)	Soluble sulfate content in soil (% by weight of soil)
Low	Less than 150	Less than 0.1
Medium	150-1,500	0.1-0.2
Severe	1,500 –10,000	0.2-2.0
Very severe	Higher than 10,000	Higher than 2.0

Table 3 : Specification of sodium sulfate resisting concrete

Level of severity	Recommended binder type	Maximum w/b
Low	-	-
Medium	OPC 2 or OPC5 or OPC 1 with pozzolan	0.50
Severe	OPC5 or OPC 1 with pozzolan	0.45
Very severe	OPC 1 with pozzolan or OPC 5 with pozzolan	0.40

In case that fly ash is used to improve sodium sulfate resistance, the minimum amount of fly ash, which leads to an equivalent expansion of the fly ash concrete to that of the concrete using Type 5 cement (sulfate resisting cement), can be estimated from Figure 3.

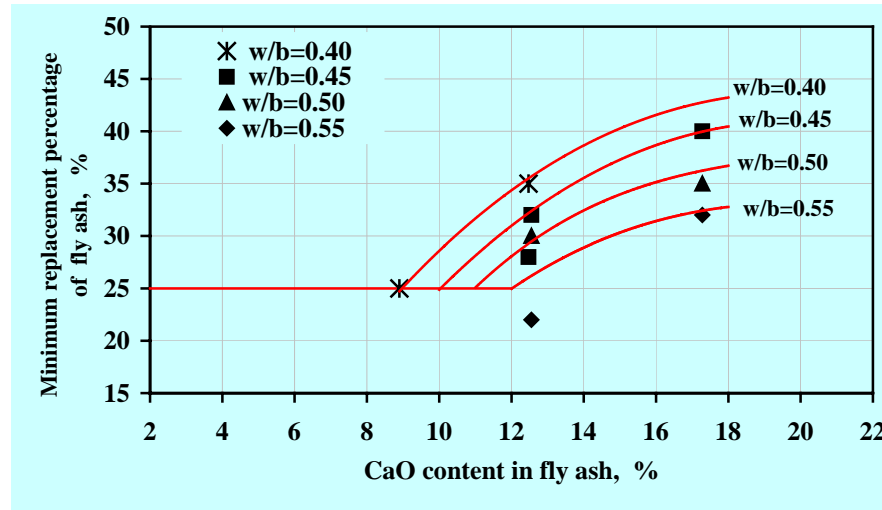


Figure 3 : Minimum fly ash replacement percentage to obtain an equivalent expansion to that of the Type 5 cement

2.2.2 Magnesium Sulfate

Table 4 shows the classification of level of severity of magnesium sulfate environment whereas the recommended conditions for mix proportioning of magnesium sulfate resisting concrete in each severity level are given in Table 5. In magnesium sulfate environment, the use of pozzolans worsens the concrete resistance, so pozzolans are not recommended for the case of magnesium sulfate [Krammart and Tangtermsirikul, 2004].

Table 4 : Classification of level of severity of sodium sulfate environment

Level of severity	Concentration of sulfate in water (ppm)
Low	Less than 300
Medium	300 – 1,000
Severe	1,000 – 3,000
Very severe	Higher than 3,000

Table 5 : Specification of sodium sulfate resisting concrete

Level of severity	Recommended binder type	Maximum w/b
Low	-	-
Medium	OPC 1 or OPC 2 or OPC 5	0.50
Severe	OPC5	0.45
Very severe	OPC 5	0.40

3. CONCLUSION

According to the revised building design acts in part of concrete structures, it is the first time in the country that the long-term performance of concrete especially durability has to be taken into consideration. The newly revised design acts make reference to codes and standards established by professional organization such as Engineering Institute of Thailand and Thai Concrete Association. The first durability design code for Thailand is being drafted by the two organizations. This paper introduces two examples of concepts for design of durable concrete in carbonation and sulfate environment. The concepts also include the design of concrete using fly ash as a cement replacing material as fly ash is currently popularly used in Thailand. It is hopefully expected that by the use of this durability design code, the newly constructed concrete structures in Thailand will have longer service life and require much less maintenance cost.

REFERENCES

- Krammasrt, P. and Tangtermsirikul, S., 2004. Expansion, strength reduction and weight loss of fly ash concrete in sulfate solution. *Asean Journal on Science and Technology for Development*. Vol.21, No.4, 373-390.
- Tangtermsirikul, S., Kaewkhluab, T. and Kaewmanee, K., 2003. Information Acquisition and Structural Health Monitoring of Bridges in Bangkok. *Proceedings of the Second International Symposium on New Technologies for Urban Safety of Mega Cities in Asia*. 30-31 October 2003, Tokyo, Japan, 133-140 (CD-ROM)
- Tangtermsirikul, S., 2004. Problems and Future Direction of Concrete Structures in Thailand : Design, Materials, Construction and Maintenance. *The 3rd International Symposium of New Technologies for Urban Safety of Mega Cities in Asia*. 18-19 October 2004, Agra, India, 177-184
- Tangtermsirikul, S. and Khunthongkeaw, J., 2005. Model for Simulating Carbonation of Fly Ash Concrete. *Proceedings of the International Workshop on Service Life of Concrete Structures – Concept and Design*. 4 February 2005, Sapporo, Japan, 41-52

POVERTY AND DISASTER THREAT IN MEGA CITIES: TEHRAN CASE STUDY, IRAN

Dr. Alireza ANDALIB (PhD Urban Planning; Islamic Azad University,
Science & Research Campus, Tehran, Iran.)

E-mail: andalib110@yahoo.com

& Dr. Sharif MOTAWEF (PhD Urban Planning; Management and Planning
Organization MPO, Tehran, Iran)

E-mail: sm_1332@yahoo.com

ABSTRACT

Rapid population growth in Asia have caused difficulties in most mega cities that some has exceeded 10 million. The rapid population growth has not given enough time to urban planners to program for securing safety of these cities, and has caused many problems. Additionally, lacks of access to resources and population density for urban infrastructures have ended into poverty, poor infrastructures and resources at the same time. These problems have been now, the most common characteristics of urban areas in most mega cities in Asia and Latin America.

Spatial structure in any Asian big city has turned these urban areas to be severely vulnerable facing disasters, such as earthquakes and floods. These are because of poverty at all levels in mega cities. Buildings, in these cases are mainly poorly structured and made of poor quality materials; so they are harshly vulnerable facing disasters. For the same reason, urban infrastructures are also vulnerable.

This paper intends to discuss some global experiences in mega cities on consequences of poverty after a disaster event. It aims to determine some relationships between poverty and people capacity in disaster response in mega cities. The case study indicates that a relationship between poverty and natural hazards' results in urban poor areas. In other words, natural hazards, such as earthquakes can cause disasters in poorly constructed areas and squatters that can not usually seen in any quality structured areas and wealthy people residential quarters.

1. INTRODUCTION

Natural hazards hit human settlements can always cause disasters. Areas affected disasters may be occupied both by rich or poor people. Hazards do not recognize poor people from wealthy. But those people usually suffer from hazards' consequences in a very different way. The wealthy people are seen in urban areas build resistant houses that can stand hazards such as earthquakes. But poor people can not do the same, so their houses are built by cheap materials and their structure can not resist hazards. Additionally, economic situations usually enable wealthy people to have savings, so they do not lose every thing by each earthquake, which poor people usually do.

Recently researches' findings show that in wealthy countries when an earthquake event happens, less building's damage and less human death occurs than if an earthquake of a similar degree happens in poor countries. So the main question here is if poverty causes disasters? We know that hazards themselves can not count as disasters unless they cause sever damage and claim lives. So the other question that: does poverty turn a hazard into a disaster?

This paper attempts to examine these subjects, in order to find answers to such questions. Using many research's results that have been done recently in Iran and else where, the paper tries to analyze any hypothesized relations, between poverty and turning hazards into disasters. Research's findings on poverty Tehran, from one side; and on earthquakes effects, on the other, have been collected and analyzed in order to examine the hypothesized relations between poverty and disaster effects.

2. THEORETICAL FRAMEWORK

2.1 Main Concepts

Systems usually need to gain their stability and settle to work in stable conditions. But natural hazards such as, earthquakes are generally disturbing these systems by causing disasters, which affect the ongoing works of these systems. When an earthquake event happens in a city, it dose not destroy buildings only, but also disturbs the entire city life and brake many existing systems. Thus, to reduce an earthquake effects, building reinforcement is not the only effort to be done, but reinforcing the other factors such as, economic and social life systems need to be considered (Motawef, 2004).

Global experiences on natural disasters indicate that in wealthy and developed countries, economic and social welfare systems are already established to deal with disaster effects. An earthquake event may severely disturb local poor community life. Poverty causes poor quality houses structure and building materials (DPCT, 1978 & Coburn, 1992). Therefore, any damage-reduction plan should deal with strengthening economy, social structure, public awareness, and management measures.

2.2 Research Objectives

The main objective of this paper is to flash light on other systems' rather than building damage, occurs because of disasters. This paper intends to project light on poverty.

2.3 Research Methods

Preparing this paper needed an expanded literature review of the most recently conducted research projects on two study subjects, particularly in Iran on Tehran. First, social research in slum and poverty, and the second, studies conducted on disaster and effects in urban areas. Many research projects have been done recently by Iranian and others, including papers provided for a national conference recently held by the Municipality of Tehran. In this paper, analytical works have been done in order to find relations between poverty and disaster effects in the poorest dwelling areas in the mega city of Tehran. This analysis has been done using the most recent analytical techniques.

3. IRAN BACKGROUND: TEHRAN CASE STUDY

3.1 Iran as an Asian Country

Iran, with more than 65 million populations is located on the west of Asia. It is also located on the Alps-Himalaya Earthquake Belt, between Turkey and Afghanistan. This was the reason of regular earthquakes, affecting almost the whole area of the country. Many major earthquakes have destroyed large parts of urban and rural areas during the last 30 years. In addition, many large cities in Iran, such as Tehran, Tabriz, Mashhad and Shiraz are located on a very earthquake-risk area. Recent earthquakes, counting, the Tabas 1979, the Manjil 1989, and the Bam 2003 earthquakes mainly affected small towns and low-population-density rural areas. However, sever destruction have been caused in these areas, and serious concern is needed to use new technology to reduce death and damage occur because of earthquake in Iran.

3.2 Tehran as a Mega City

Tehran, the Iranian Capital, is located on the southern outskirts of the Alborz Mountain Chain, on the Alps-Himalaya Earthquake Belt. The city of Tehran and its attached smaller human settlements, accommodate more than 10 millions people, on a large expanded area (figure1). It includes the city of Tehran with nearly 7 million residents, the city of Karaj with more than 1 million residents, and many other towns with more than 3 millions. Population density is very high in Tehran, including 22 districts. Some of these districts, especially district 17; are located on the southern part of Tehran, occupied by poor people.

3.3 Tehran: Population and Agglomeration

According to the 1996 population census, the total population of Tehran for its 22 districts is calculated at 6,742,165. The average population density of the entire city of Tehran is 110 persons per hectare. The average density of District 10 is 349 person/ha and 347 person/ha in District 17, where the poor people live. These two districts have the highest population density values. The density of Districts 1, 2, 3 and 4, which are located in northern Tehran and occupied by wealthy people, is shown to be between 71 person/ha and 92 person/ha.

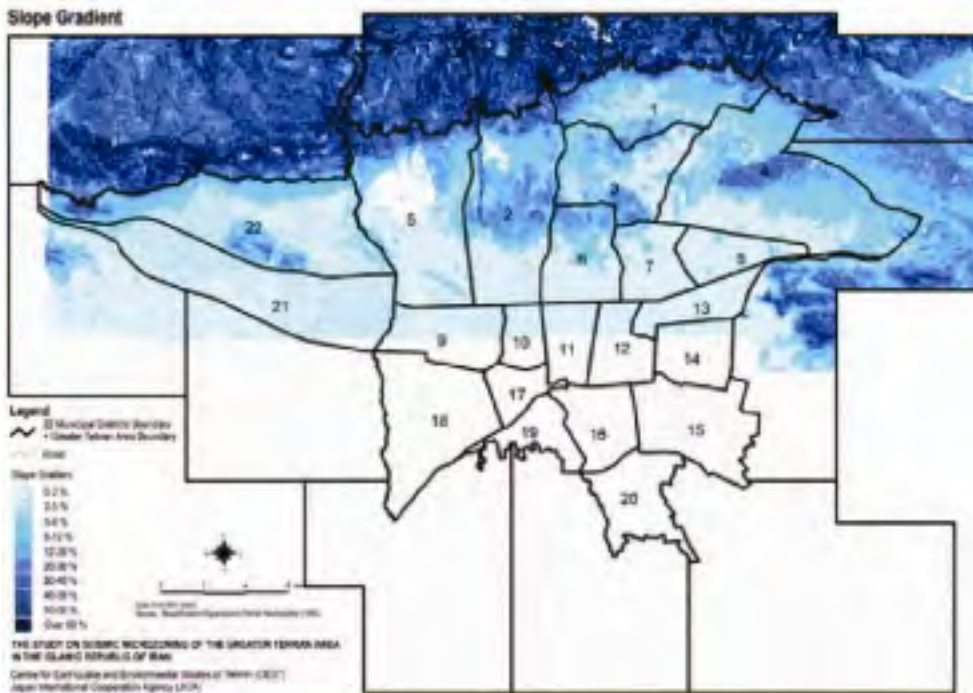


Figure (1): Map of Tehran and its 22 districts. Source: (JICA, 2000)

Building statistics were also prepared by SCI based on 1996 census data; however, census data only covers residential buildings. For 1996, the total number of residential buildings in Tehran is 1,484,138 units. Apartment houses or connected buildings should be counted as one residential building unit, from the seismic damage analysis point of view. The distribution pattern of these buildings shows the characteristics of Tehran's urban growth. Districts having more than 60 % of Steel structures plus RC structures are Districts 1, 2, 3, 4, 5, 6 and 22, where wealthy people live. On the contrary, Districts 10, 16 and 17, which are located in southern Tehran consist of less Steel and RC structures (SCI, 1997).

Districts 10, 16 and 17 have more than 70 % of traditional-type buildings. Particularly, in District 17, 90% of buildings have less than 3 stories (SCI, 1997). According to the book "Tehran – The Jewel on the Silk Road" (Taher Art & Cultural Institute, 1999), buildings in the older parts of Tehran (Districts 10, 11, 12, and their surrounding areas) were built before the 1950's (TACI, 1999).

3.4 Poverty in Tehran Urban Areas

Tehran has been highly expanded during its more than 200 year history. During the 19th century, it was growing fast, as a capital. But during the Reza Shah Era, (1925-41) a modernization period was started, and mainly concerned building urban and regional infrastructures. The main work in this regard was the establishment of the railway network of the country connecting north to south Iran via the capital Tehran. This was equal with creating new jobs that attracted rural people to migrate to Tehran. New squatters were established then (60-70 years ago) by villager migrants near the railway station in Tehran, forming Districts 15, 16 and 17. Slums were growing up on the outskirts of Tehran, mainly around the railway station, near their work places.

At the present time, these districts, especially district 17, are the most poor, with highly population and building density of Tehran. All poor residential areas have remarkable characteristics, such as high population and building density, poor building quality, and lack of urban infrastructures. All these characteristics are known with sever vulnerability to earthquake hazard.

4. NATURAL DISASTER AND EFFECTS IN TEHRAN

4.1 Earthquake Disaster

The Greater Tehran Area is located at the foot slope area of the Alborz Mountains, which form part of the Alps-Himalayan Organic Zone. This zone is one of high seismic potential with many peculiar active faults (Berberian, 1983). The urban area of Tehran has been developed on alluvial layers, accumulated on hard rock through complex geological formations. According to historical seismic data, Tehran has suffered from several strong earthquakes with return periods of 150 years (Moinfar, 1994). The city of Manjil, located 200 km north-west of Tehran, suffered from a strong earthquake in 1990, which killed approximately 14,000 people (Panah, 1993). Seismologists believe a strong earthquake will strike Tehran in the near future because the city has not experienced a disastrous earthquake since 1830. Urban development has been rapidly progressing in Tehran without the development of proper disaster prevention systems against potential earthquakes (Tavakoli, 1983). It is urgently necessary to prepare a regional/urban earthquake disaster prevention plan in order to mitigate possible seismic damages in Tehran (JICA, 2000).

4.2 Expected Earthquake and its Effects

The distribution of the active faults in Iran was investigated since 1976. Distribution of active faults in and around the city of Tehran was originally and systematically compiled in 1983 (Berberian, 1983), and then in 1998 and 1999 (Berberian, 1999). Based on these reports, the features of the main active faults in Tehran can be summarized as follows (figure 2):

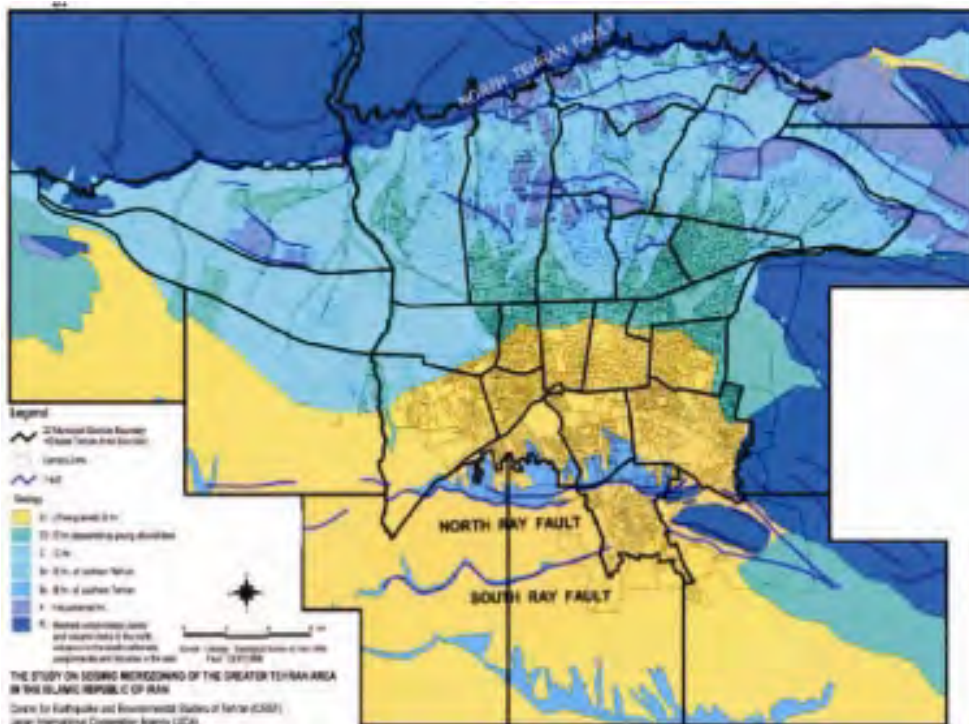


Figure (2): Map of Tehran and its major faults. Source: (JICA, 2000)

4.2.1 Mosha Fault (MF): The Mosha Fault is one of the fundamental faults of the central Alborz Mountains and is situated to the north of Tehran.

4.2.2 North Tehran Fault (NTF): The North Tehran Fault is the most prominent tectonic structure in the immediate vicinity of the city.

4.2.3 South and North Ray Faults (RF): The South and North Ray Faults are the most prominent faults in the southern plains in Tehran. These faults are distributed throughout both sides of the Ray depression.

4.3 Different Effects on Different Urban Areas

The Ray Fault Model yields the largest damages. In this case, about 380 thousand inhabitants, or about 6% of the total population will die. The casualties in District 15 will be vast because of the large number of its inhabitants. The death ratio in Districts 11 and 12 will be as high as 15 to 20% because there are many vulnerable buildings. The death ratio in the northern part of the city, i.e., in Districts 1 to 5 shall only be about 2%. In case of the NTF Model, the worst case indicates about 130 thousand fatalities, or about 2% of the total population. The death ratio in the northern part of the city, in Districts 1 to 5, shall be high, approximately 3%. The death ratio in the southern part shall be low, approximately 1%. In case of the Mosha Fault Model, the death ratio does not exceed 0.3 % of the total population of the city. The casualties in District 12 shall be vast, approximately 1.7%. This is due to the existence of many vulnerable buildings of adobe and wood and brick structure, the high damage ratio of these buildings and the low rescue ratio. Such a tendency is also observed in the case of the Floating Model. A 'full rescue' case is a case where a combination of the community rescue, emergency squads and expert operations is available. In the Ray Fault Model, human casualties are

estimated to culminate in the southern part of the city. In some census zones, the number of dead will amount to 100 or more. This area corresponds to Districts 11 and 12, where vulnerable buildings such as adobe are prevailing and emergency rescue activities are not effective for these kinds of structures (JICA. 2000).

4.4 Effects Because of Poverty

In case of the Ray Fault Model, the death ratio in several census zones in Districts 11 and 12 shall be enormous, 40% or more. In these districts, building quality because of poverty will cause severe destruction or total collapse. In the NTF Model, the high-death ratio area is limited, due to better building construction.

Because the Ray Fault Model offers the highest potential earthquake scenario that would generate the greatest damage to the city of Tehran, poor areas and squatters which are located on the southern part of Tehran may receive the highest ever destruction and human death. Most buildings of Districts 11, 12, 15, 16 and 17 are with high vulnerability and risk against earthquakes. Additionally, people live in these districts are from the lower income-groups that can not do required building reinforcements, or rebuild their houses according to date building codes. Furthermore, streets in these districts, especially in Districts 11, 12 and 17 are very narrow, that can cause difficulties for rescue operations after an earthquake. These districts, also lack urban infrastructure, or have infrastructures that are overcrowded.

In summary, the southern part of the city of Tehran will be severely damaged in the event of an earthquake caused by fault activity on the South Ray Fault (BHRC, 1990). One reason for the expected, huge seismic damage is that the southern part of Tehran is not only located close to an earthquake source, but also has many buildings that are constructed with traditional materials such as brick, masonry, wood and steel. Building structures of this area also seems to be non-resistant to strong earthquakes. Besides these conditions, the population density of the area is the highest in Tehran and even one of the highest in the world. According to the 1996 Census Data, a number of its census zones have a population density of over 500 persons per hectare and, sometimes, exceed 700 persons per hectare. Due to the combination of these physical and social conditions and the growth of population, the potential vulnerability against a strong earthquake seems to be growing every year. District 17 has been designated as the Pilot Study Area (PSA) in order to identify and collect basic information for the preparation of necessary measures to mitigate a seismic disaster.

4.5 Case Study in a Poor Area: a Pilot Study Area (PSA)

The PSA is located in the central part of District 17. As of 1996, population was 32,239 inhabitants, with a population density of 465 persons per hectare. The total number of buildings in these zones is 4,843 (figure 3).

Urbanization of this area has been progressing since the 1960, owes to the concentration of population in Tehran. Before the urbanization took place, the area had been extensively used as agricultural land. Building development in this area is mainly targeted for residential use; therefore, almost all of the buildings in this area were constructed with less than three stories.

Issues and problems for seismic disaster preparedness in the PSA are described below based on the diagnosis of the PSA from the viewpoint of mitigating a seismic disaster.

4.5.1 Building Damage

Almost all of the buildings in the PSA will be either heavily damaged or will totally collapse due to the Ray Fault Earthquake. The damage ratio for the buildings is estimated at more than 80%, according to the available damage function data.

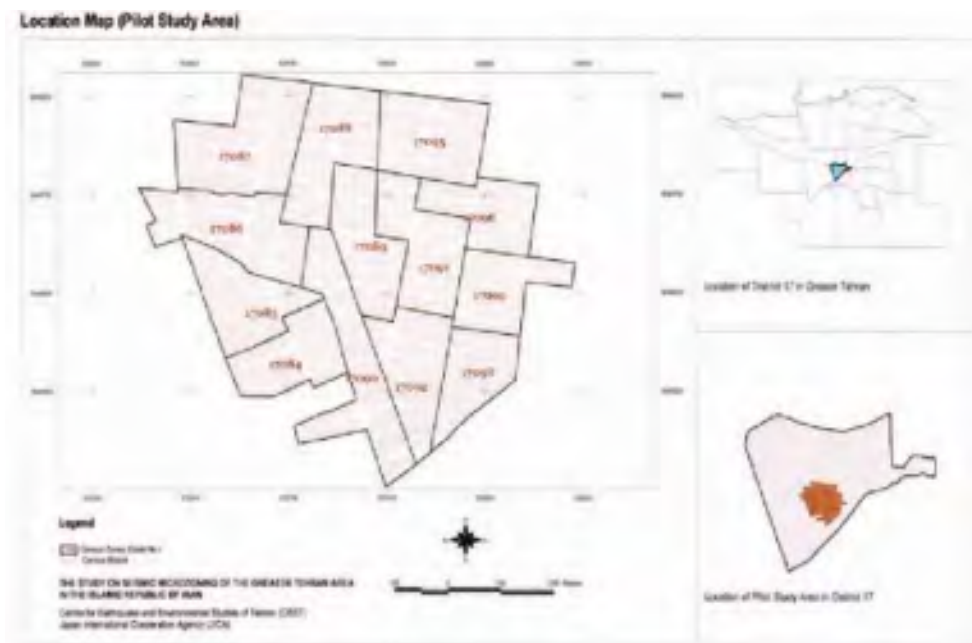


Figure (3): Map of PSA in District 17.

Source: (JICA, 2000)

4.5.2 Human Casualties

In the PSA, not only will building damage be high, but also the number of human casualties. It is estimated that 3,048 people could die out of the total 32,239 night-time population (1996 Census) of the area. If a community rescue function and related rescue operation by another organization arrive timely and work effectively, the total number of deaths will be reduced to 2,151. But narrow streets will cause problems. But there is less hope because of narrow streets.

4.5.3 Disaster Prevention Base

For quick and effective response to emergencies such as a seismic disaster, it is essential to properly equip facilities that will serve as bases that provide countermeasures for disasters. Presently, in District 17, there is

nothing being done to prepare for a seismic disaster or to take necessary countermeasures.

4.5.4 Community Organization

Community organization plays a significant role not only in first aid activities during a seismic disaster, but also for collection and dissemination of disaster information to the entire community. However, community groups have not yet been organized in the PSA. Therefore, their establishment on a housing block basis should be, at least, discussed for the mitigation of a possible disaster. General community participation in disaster mitigation should also be discussed and planned.

4.5.5 Disaster Prevention Awareness

It is necessary to raise the people's awareness on seismic disaster prevention based on proper dissemination of disaster prevention information through administrative organizations, school education and mass media. The main purpose of raising public awareness on seismic disaster prevention is to minimize human casualties as much as possible.

5. CONCLUSION

In response to the main question of this paper that if poverty causes disasters? The findings of this research shows that hazards themselves can not cause disasters unless they cause sever damage and claim lives. But it is poverty that turns a hazard into a disaster. The research findings show that in wealthy urban areas in Tehran; when an earthquake event happens, less building's damage and less human death occurs than if an earthquake of a similar degree happens in poor areas, such as District 17, south of Tehran.

Also, a clear conclusion indicates that Tehran as a mega city, and its southern districts, such as District 17 and the PSA, including its surrounding area, has indicated that the whole city and mainly poor areas have no defense system against a potential strong earthquake. In the worst case scenario, huge damage is estimated in these areas; therefore, necessary measures for seismic disaster mitigation, at least to save human lives, must be prepared as soon as possible. The following items are the main recommendations to be considered in a planned manner:

- 1) Most of the southern districts of Tehran are occupied by poor people who came to live in squatters, and very poor conditions in Tehran, seeking job during the last 60 years. Their low income level has forced them to live in poor quality and vulnerable houses against earthquakes. They should be supported.
- 2) Urban seismic disaster prevention and a risk management plan must be prepared by Tehran immediately. It is necessary to clarify the role of community in disaster prevention.
- 3) People's participation and public awareness on seismic disaster prevention should be promoted.

- 4) Basic materials explaining earthquake disaster and measures for disaster mitigation should be prepared and disseminated properly. School education for younger generations should also be promoted.
- 5) Reinforcement of residential buildings must be discussed in depth. If buildings were to be built strong enough to withstand an earthquake, then building damage could easily be minimized. However, economic conditions dictate use of the most economic and higher cost performance structures and materials for building construction
- 6) In relation to urban redevelopment, relevant institutional frameworks, such as tax incentives, low interest housing loans, and bonuses for floor to area ratio etc., should be formulated to create stronger urban structures against seismic disaster.

REFERENCES:

- BHRC, 1990, Iranian Code for Seismic Resistant Design of Buildings.
- Berberian, M. M., Ghoreishi, B., Arajang R awesh, A. Mohajer Ashjai, 1983, Seismotectonic and earthquake fault hazard investigations in the Tehran region, Geological Survey of Iran, Report No. 56.
- Berberian, M., and R. S. Yeats, 1999, Pattern of Historical Earthquake Rupture in the Iranian Plateau, Bull. Seism. Soc. Am., Vol.89, No.1.
- Coburn, A.W., R.J.S. Spence, and A. Pomonis, 1992, Factors Determining Human Casualty Levels in Earthquakes: Mortality Prediction in Building Collapse, Proc. 10th. WCEE.
- Coburn, A.W. and R.J.S. Spence, 1992, Earthquake Protection, John Wiley.
- Disaster Prevention Council of the Tokyo Metropolitan Area, 1978, Report on the Earthquake Damage Estimation of Central Area in Tokyo.
- Japan International Cooperation Agency (JICA) 2000, The Study on Seismic Micro zoning of the Greater Tehran Area in the Islamic Republic of Iran: Final Report & Main Report; Pacific Consultants International; OYO Corporation; November 2000.
- Moinfar, A.A., Mahdavian, A. and Maleky, E., 1994, Historical and Instrumental Data Collection of Iran, Iranian cultural fairs institute.
- Motawef, Sharif, 2005 "Earthquake, Damage and Reconstruction of Bam"; paper presented in the International Conference on Bam Earthquake, held by the Housing Foundation of Iran in Bam: May 2005.
- Panah et. al. 1993, Case Study 1, Landslide Hazard Zonation Study in Affected Area by Manjil Earthquake, 1990, Manual for Zonation on Seismic Geotechnical Hazards, Technical Committee for Earthquake Geotechnical Engineering, TC4, International Society of Soil Mechanics and Foundation Engineering, 1993.
- Statistic Center of Iran (SCI) 1997, Results of The 1996 Population and Housing General Census; SCI, Tehran, Iran.
- Taher Art & Cultural Institute (TACI) 1999; "Tehran – The Jewel on the Silk Road" (Taher Art & Cultural Institute, 1999), Tehran, Iran.
- Tavakoli Behrooz, B. and S. Tavakoli, 1983, Estimating the Vulnerability and Loss Functions of Residential Buildings, Journal of the International Society for the Prevention and Mitigation of Natural Hazards, Vol.7 No.2.

PLANNING AND DESIGN FOR SECURITY

FANG YEA SAEN

B Arch, MSIA

Vice President, Security Division

CPG Consultants Pte Ltd, 238B Thomson Road

#15-00 Tower B Novena Square Singapore 307685

fang.yea.saen@cpgcorp.com.sg

ABSTRACT

Acts of terrorism in the last decade have prompted governments and corporations to respond with urgent security reviews and protective measures for their infrastructures and buildings in an unprecedented manner. The leading example without dispute is the United States. Countries in this region are also grappling with the issue of terrorism and the appropriate level of protection to ensure that business and life go on as usual.

On the one hand, there may be inaction born out of a sense of helplessness or apathy. On the other hand, hasty measures may be taken creating other problems like a fortress environment. There is hence a call for balance, ie for an agenda where additional security requirements are met without sacrificing other considerations.

This paper advocates a holistic approach in achieving this balance. It is also a systematic approach, considering steps like

Security concept plan

Risk assessment – threats, vulnerabilities, asset protection

Master planning for security

Building design for security

Security system, technology and engineering

Security management and business continuity issues.

This paper also stresses the need to work with all stakeholders for the holistic approach to work. Because explosions from improvised explosive devices (IEDs) are such a current and real threat, the security planning and design process has to deal with this in a pragmatic way in order for a balanced outcome to happen.

The paper also covers the benefits of the holistic approach to security planning and design and ends with a conclusion that not only is this holistic approach necessary, but that enhanced security and protective features will increasingly become part of the building design and design process from now on.

1. INTRODUCTION

With the end of the cold war, it was optimistically thought that world peace would reign. Unfortunately terrorism and the threat of terrorism are increasingly seen as part of the modern global city life. Interestingly, Britain had experienced this to some extent with their earlier bombings by the IRA and had built up a certain response and resilience to this. However transnational terrorist threats are new to many countries, including the US.

At the same time, the world is seeing greater concentration of people in the big cities, where economic opportunities and the buzz of urban life draw people like bees to honey. With such concentration comes vulnerability to lives and safety, something which terrorists recognise. The power to disrupt life and business through an incident which is magnified by the publicity of the international media is a potent tool increasingly being exploited.

Recent acts of terrorism have prompted government with responses from greater surveillance, intelligence work to hardening of infrastructure and key assets. Such calls are percolating down to 'softer' buildings like commercial and civic buildings as terrorists are seen to shift to easier targets. Governments are also calling upon corporations and owners to view the cost of security upgrading not as an extra cost but as a necessary cost of doing business. Individuals are also asked to report suspicious behaviour and bear with inconvenience as the price to pay for greater security.

However there may be a sense of helplessness born out of lack of knowledge or a limited budget in a competitive business environment. It could also be apathy resting on the assumption that attacks will not happen in one's backyard or that governments have the direct and full responsibility to protect citizens against acts of terrorism.

On the other hand, protective measures may be taken hastily, leading to other problems like creating a suffocating and defensive fortress environment, witness what is happening in Washington DC and the associated public debate.

There is hence a call for a balance between security and openness and accessibility. For what attraction is city living when it begins to feel more like a prison?

The **holistic approach** starts with an understanding of what the government is committed to do and going on to realistically assessing the risks pertinent to an organization, in a particular country and at a specific period of time and lastly, considering the range of factors and solutions that relate to security. This is to enable a cost-effective and sustainable strategy to be implemented to enhance security. The holistic approach will hence become the critical context for the application of specific protective measures.

2. THE HOLISTIC APPROACH

2.1 Elements of the holistic approach

What are the elements of this holistic approach? They are -

- Security concept plan
- Risk assessment - threats, vulnerability, asset protection
- Master planning for security
- Building design for security
- Security system, technology and engineering
- Security management and business continuity issues.

2.2 Security concept plan

The security concept plan is an overall strategy which considers the range of factors, weighs their relative significance, evaluates a panoply of solutions and proposes an integrated, effective and sustainable plan for security. It balances and mediates the different and possible conflicting requirements, like security versus openness, security versus cost or security versus fire safety. For example in prison design, security and normal fire escape provisions are contradictory requirements. Such contradictions and the ensuring trade-offs and creative solutions to resolve them are true of other building types. Overall, the security planning and design process seeks to deliver peace of mind, safety and protection of assets.

2.3 Risk assessment

Risk assessment should be a systematic process. It is a key step as it is about framing the right question even before one searches for the right answers. AS/NZS 4360 standard on Risk Management is a good guide and can be applied to the security planning and design process.

A necessary step in risk assessment is to identify the possible **threats** jointly with the stakeholders. One has to remember that threats evolve to elude new surveillance and protective measures taken. Hence such risk assessment will need to be reviewed on a regular basis so that security and protective measures remain relevant.

With global warming and recent natural disasters, people are also increasingly concerned over environmental hazards as the impact far exceeds even terrorist incidents. Though this is not covered in this paper, it would be good to bear this in mind, especially in locations where environmental hazards become relevant – see Figure 1.

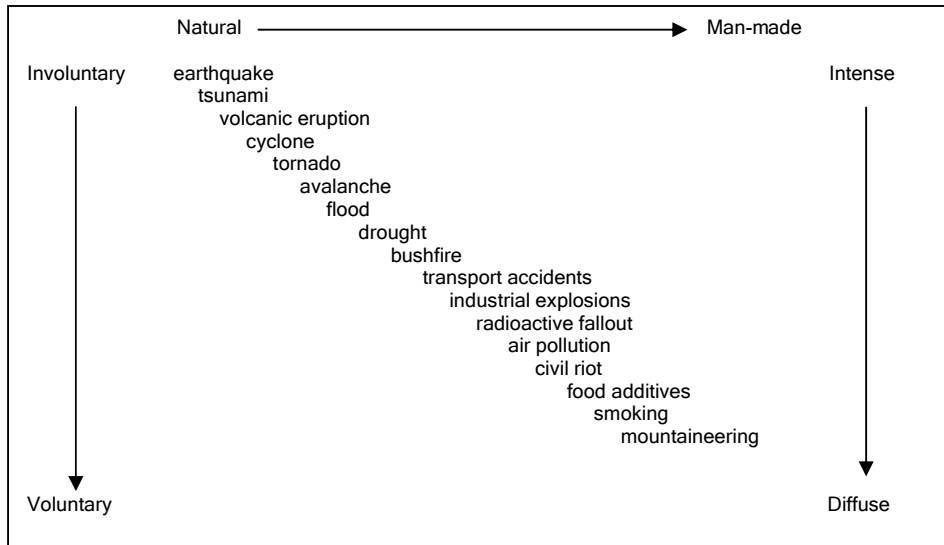


Figure 1. *Spectrum of environmental hazards (Keith Smith, Environmental Hazards)*

Another consideration in the risk assessment stage is the **vulnerabilities** of a building and an organization. Are there potentially single points of failure, eg power supply to the whole building which is accessible by the public? Are there other Achilles' heels? Are key staff located together?

Another consideration is the identification of the organisation's key **assets**? Cash is commonly perceived as assets to be protected. But from an organisation's viewpoint, assets include other things like data, information, art pieces, money, horses, VIPs, computer systems, even prisoners (for whose health and safety the prison service is responsible while under custody), 24x7 capability residing in certain key equipment and key staff, etc.

To each of these threats and vulnerabilities, consequences of the loss or damage of the assets and probability of the occurrence can be factored in, giving in an approximate way –

Overall risk assessment = threat/vulnerability x consequence x probability.

The next step is the treatment of the risks - see Figure 2. Various options should be considered and evaluated. This fits very well into the holistic approach advocated in this paper. Can part of the risk be covered by guard service? What about insurance? Is the mirror site for a data centre adequate in covering the risk? Or does the potential bad publicity and subsequent exposure to further attacks necessitate stronger protective measures? This risk treatment process is also a risk allocation process, calling upon different measures to do what they are each best in.

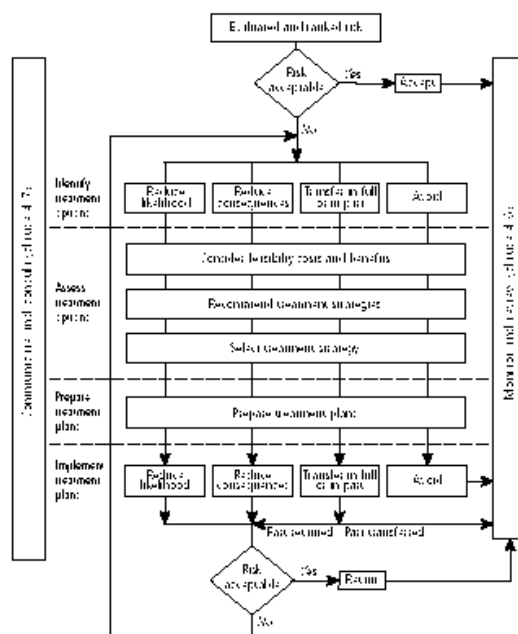


Figure 2. Risk treatment process chart from AS/NZS 4360

2.4 Master planning for security

Master or site planning for security considers the city or site layout issues which impact security.

Figure 3 is a typical ‘onion’ security ring concept, providing layers of defence to a building and asset with a single access control point. In an army camp or prison complex, the two outer layers would be typically barbed wire fence with no vegetation in between for unobstructed CCTV monitoring. The fences would normally be equipped with an FIDS (fence intrusion detection system). However not all developments need this or can look like this. In a creative way and going along this holistic approach, one can consider how other measures can constitute layers of defence. One layer could be a guard tour circuit, though there will be ‘holes’ because the guard will be moving around. Or a layer could be invisible infra-red beams which when broken signify an intrusion. The general aim at the master planning for security is to create security through deterrence, detection, delay and a credible response against potential incidents.

At the master or site planning level, it may be necessary to check that views of key operations or access by VIPs cannot be easily overlooked by potential perpetrators who may be planning an attack. Similarly, location of critical infrastructural facilities like power stations or sub-stations may be done to avoid vulnerability to attacks which can potentially incapacitate a whole township.

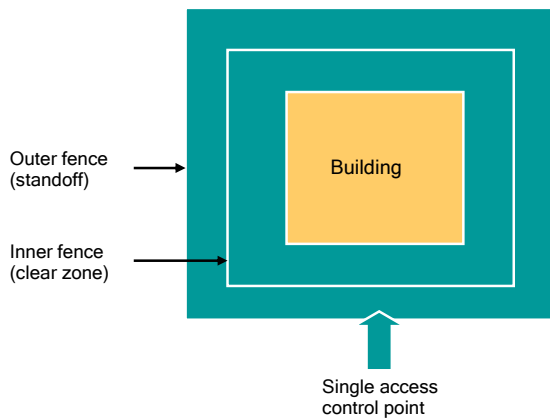


Figure 3. Example of 'Onion' security layers of protection

2.5 Building design for security

Building design for security looks at aspects of the building layout and design to create greater security. For example, can zoning be done to group similar functional spaces not only for greater work efficiency but also to avoid security conflicts?

A popular approach is Crime Prevention Through Environmental Design or CPTED for short. This looks at low-tech, soft approaches in design to creating greater security. For example, can the kitchen of houses be designed to overlook a common area, as this 'natural surveillance' contributes to security?

In terms of building services, it may be necessary for the sake of security to route them in such a way that there are no single points of failure, though it may mean the overall system is less efficient from an engineering viewpoint.

Building owners will increasingly be looking at facilities with more effective mail room design and entry control facilities, as these are the frontline checks against illegal access, weapons, contraband goods and possible IEDs. Such facilities will increasingly be incorporated in the building designs and workflow patterns.

2.6 Security system, technology and engineering

In a typical situation, a security consultant is engaged when the building design is decided and he is asked to put in the security systems. In the holistic approach, this is seen as wrong approach as security flaws are embedded in an architectural layout and design and extensive security systems are then called upon to overcome these. Hence an understanding of security system, technology and engineering should be factored in the master planning and building layout.

CCTVs have become a pervasive element. They have proven useful for the authorities analysing records to apprehend culprits, even if the CCTVs were not a sufficient deterrent in the first place. While there are still concerns of privacy (of Big Brother), terrorism will inadvertently lend greater force for CCTVs to be accepted as a feature of city life, witness the case in London.

There is a plethora of security systems and new ones are coming out by the week. Biometrics, anti-ram bollards, crash barriers, access control, turnstiles, under-vehicle scanners, x-ray machines, gamma scanners, metal detectors, etc, are just some examples of technology used in homeland security. This paper is not going to run through each of these, except to mention the point that there should be an understanding of how the systems impact the functioning of a building, whether they can be used in a sustained manner and how they can be less intrusive.

As metal detectors and x-ray machines become more pervasive, the public will begin to feel the inconvenience of airport security even for prosaic access to normal buildings and complexes. Hence there is scope to make measures less intrusive. For example, can checks on identity, weapons, bombs, etc all be done through an all-in security portal? The greatest challenge will be in places where the public will be in greatest numbers like shopping centres, checkpoints and mass rapid transit systems.

2.7 Security management and business continuity issues

It is helpful for designers and engineering experts to be familiar with aspects of security management and business continuity to see how they contribute to security. By doing so and recognising the respective advantages in delivering security, then it would be natural to ask security management and emergency preparedness to cover that part of security where they are strongest in. For example, guards can pick up suspicious behaviour through CCTV or actual sighting, where no CCTV intelligence or analytical programme is able to do so cost-effectively at the moment. Secondly since it is impossible to prevent an incident from happening by systems and building design, it is critical to get ready emergency preparedness to address the residual risks.

It has been well documented that in neighbourhoods where windows are broken but are not quickly repaired, that these attract more broken windows. But where broken windows and graffiti are quickly addressed, this communicates to potential perpetrators that here is a community where people care and are willing to take remedial action, possibly even to apprehend the perpetrators.

Under this topic, one would also attempt to understand guard service and associated building design implications. For example providing even basic facilities like toilets in guard house so that the guards need not be absent from their post for too long and create vulnerable gaps would be something that is consistent with this holistic approach.

3 STAKEHOLDERS

In planning and design for security, an important consideration is identifying the key stakeholders and dealing with their concerns. Too often this process is not thoroughly carried out with the inputs of some stakeholders coming late in a project and becoming difficult to accommodate. For example, if the security intelligence part is not fully addressed, then the solution may not have been calibrated to the appropriate threat level. Or if the customers' viewpoints are not fully factored in, then the security measure may not be user-friendly. Stakeholders can be the property owners, the facility managing agent, the guard service company, the customers, general public, security agency, the government, investors, etc.

Often the client may be represented by a few parties. There is one watching the budget and one directly responsible for the business operations and yet one more directly responsible for security. Hence not only must the interests be identified, but also the possible conflicts. A key thing is also making the stakeholders see that there are other stakeholders and requirements in order to prepare them for a balanced outcome with tradeoffs.

4 DEALING WITH BLAST THREATS

This is put as a separate section as it is a key concern in the current security milieu and will dominate security agenda. For a start, all know that they do not want to retreat to or create a bunker solution, which a military or law enforcement facility can do and sometimes do to create a deterrent effect. A typical military solution like narrow windows is not appropriate in a civilian building as most users value views and daylight and sense of connectedness to the outside environment.

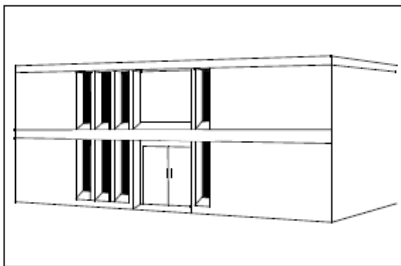


Figure 4. Example of narrow windows from Field Manual FM 3-19.30 Physical Security which may be applicable to military installations but may not be acceptable in civilian buildings

However when one understands that in most cases, just as in fire fighting response, the key protection is lives and secondarily property. With this understanding, it becomes more pragmatic to allow glazing to flex and crack with the blast, absorbing the blast energy but with fragments not flying beyond a certain distance and hurting people. GSA has a glazing

performance condition which helps in calibrating the level of protection at the façade glazing and allowing protection in a pragmatic way – refer to Figure 5.

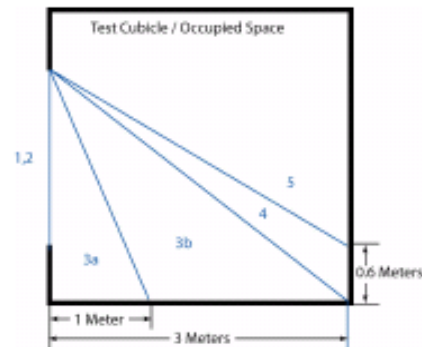


Figure 5. Glazing performance condition for blast as given by General Services Administration (GSA)

In the US, standoffs are typically specified as protection against car bombs. In critical buildings, visitor parking is even not allowed in basement parking centres. Standoffs of 30m are not unusual, enforceable by bollards. However in urban areas, such compliance is difficult given the limited land and high land prices. For example in Singapore, land may cost the equivalent of \$9,000 per m². If the standoff can be reduced, then the saving in cost of land can be thrown into protective measures like column or façade strengthening. However this trade-off does not happen, if the client is not convinced of the threat in the first place, which a systematic risk assessment can address.

5 BENEFITS OF HOLISTIC APPROACH

In the holistic approach, no single measure is expected to provide the security. For example, if the building design was leaned upon to provide all the security – then a fortress design is the logical outcome. However if security is to be contributed by a combination of design, systems, guard service, law enforcement, citizen vigilance, etc, then a building can afford to be more open, more accessible, ie create the balance.

The holistic approach would also be more cost-effective, as security systems and measures will not become white elephants if they go against the natural workflows of corporations. The holistic approach would also be exploiting the relative strengths of different measures.

The holistic approach gives the client and the consultants the flexibility and creativity to deliver security as they have a wider range of options to consider.

6 CONCLUSION

Up to now, we have looked at how security planning and design can be and should be a holistic process. And how judgment calls are made in this process to mediate among the various considerations, so that no single measure should be asked to carry the burden of security. This understanding will enable all stakeholders to agree to trade-offs and to a common strategy for security.

Whereas current security initiative centres on retrofitting of existing buildings, it is envisaged that in future, the norm will be for buildings to incorporate enhanced security features as part of the overall building planning and design process, in recognition that terrorist threats are here to stay.

“The terrorist is as much concerned with how many are killed as how many are frightened.” (quote from the Economist)

Lastly, in this holistic equation advocated, the final judgment call will be with the public who will be asked to bounce back from any security incident, not to be cowed, but to declare that life will go on and then there will be greater vigilance against future events.

REFERENCES

- Australian Standards / New Zealand Standards. *AS/NZS 4360 Risk Management*.
- Betts, Curt P., 2005. *Guidance for Security Engineering*. ASCE 2005, US Department of Defense
- Building and Construction Authority, Singapore, January 2005. *Enhancing Building Security*
- Crowe, Timothy D. 2000. *Crime Prevention Through Environmental Design: Applications of Architectural Design and Space Management Concepts (2nd Edition)*
- Department of Defense, 8 October 2003. *UFC 4-010-01, DoD Minimum Antiterrorism Standards for Buildings*
- Department of the Army Headquarters, Washington DC, January 2001. *FM 3-19.30 Physical Security*
- FEMA, Dec 2003. *FEMA 427 - Primer for Design of Commercial Buildings to Mitigate Terrorist Attacks*
- National Security Coordination Centre (Singapore), 2004. *The Fight Against Terror – Singapore’s National Security Strategy*
- Smith, Keith, November 2000. *Environmental Hazards: Assessing Risk and Reducing Disaster*. Routledge, New York

DISASTER MITIGATION ASSESSMENT FOR STORAGE TANK FACILITY

Min-Cheng Teng¹ Chien-Mei Lee² Kuo-Shuh Fan³

¹Senior Assistant Research, National Sci & Tech. Center for Disaster Reduction, Taipei, Taiwan, Email: jack@ncdr.nat.gov.tw

²Research Assistant, National Sci & Tech. Center for Disaster Reduction, Taipei, Taiwan, Email: cmlee@ncdr.nat.gov.tw

³Associate Professor, National Kaohsiung First Univ. of Sci & Tech., Kaohsiung, Taiwan, Email: ksfan@ccms.nkfust.edu.tw

ABSTRACT

In recent years, manufacturing industries in Taiwan develop vigorously. Otherwise, the chemical process update continually. However, the complicated factors of caused the loss of property and the threat of environmental pollution. Besides, the factory owner the capacity for awareness of industrial safety and accident prevention is weak. For all of process equipments, the storage equipments are one of factors which is easy to neglect caused storage tank accidents by man-made. In the other hand, natural disasters such as earthquake and lightning, also be the reason of accident.

A storage tank without any mitigations strategy typically causes severe damage and other economic loss, such as by earthquake damage, fire, exploding pollution of surrounding areas, chemicals to leak, during disaster occurrence. The main failure mechanisms of tanks are as follows. (1) Buckling of the shell. (2) Damage to the roof. (3) Differential settlement or failure of the foundation soils. (4) Fire. (5) Explosion. (6) Contents to leak, etc. The research context to classify storage tank accidents in Taiwan, fire accident is in 30%, 20% in explosion accident and 20% in chemical leak release accidents. Moreover, the inappropriate process and lack of profession are the main causes of the accident.

In this study, a series of shaking table tests has been conducted to assess the feasibility of seismic base isolation for liquid-filled storage tanks experimentally for reduction natural disaster. The friction pendulum bearings (FPS) are considered as the dynamic characteristics of an FPS-isolated tank remain unchanged regardless of the storage level. Effectiveness of FPS for seismic isolation of storage tanks is confirmed. This research also combines interpretations of the Council of Labor Affairs and National Fire Agency, Ministry of the Interior regulations, summaries of state and local regulatory requirements. This study is designed to assist in the development of a comprehensive compliance and management program for oil storage tanks. Moreover, study man-made disaster after discussed domestic regulation, the research would give the advice about measures of

disaster mitigations and emergency response plan that would be the reference for industries in order to develop the capacities of storage tank accident mitigation.

1. INTRODUCTION

Large storage tanks are vital for industrial purposes and daily life. A storage tank without any mitigations strategy typically causes severe damage and other economic loss, such as by earthquake damage, fire, exploding pollution of surrounding areas, chemical to leak, during disaster occurrence. The main failure mechanisms of tanks are as follows. (1) Buckling of the shell. (2) Damage to the roof. (3) Differential settlement or failure of the foundation soils. (4) Fire. (5) Explosion, etc. The vulnerability of tanks to ground motion has been demonstrated recently in Chi-Chi earthquake (1999) of Taiwan, and numerous other major earthquakes worldwide. For example, The 1964 earthquake in Niigata, Japan caused extensive damage to two oil refineries ; the 1964 Prince William Sound earthquake in Alaska caused the failure of several oil storage tanks and fires ; the 1971 San Fernando earthquake in California led to the failure of many water tanks both above-ground and in-ground, and the failure of oil storage tanks in the 1978 Sendai earthquake of Japan polluted a local waterway ; On July 17, 2001, an explosion occurred at the Motiva Enterprises LLC Delaware City Refinery (DCR) in Delaware City, U.S.A.(CSB,2002). A work crew had been repairing a catwalk above a sulfuric acid storage tank farm when a spark from their hot work ignited flammable vapors in one of the tanks. This tank had holes in its roof and shell due to corrosion. The tank collapsed, and one the contract workers was killed; eight others were injured. A significant volume of sulfuric acid (H_2SO_4) was released to Delaware River, resulting in significant damage to aquatic life. and environment ; There was a terrible explosion at the resined plant in Taoyuan City, Taiwan, on October 7, 1996, with extraordinary or improper operate procedure of neutralization tank. The tank and plant collapsed, and nine workers were died; forty eight persons were injured.

Earthquakes may induce substantial hydrodynamic pressures on the shell wall of storage tanks, and the overturning moment caused by the lateral pressures could result in excessive compressive stresses at the bottom of one side of the tank, and hence, dynamic buckling of the shell wall (Jia:1989, Liu:1989). Damage to storage tanks not only instantly disrupts essential infrastructure but can also cause fires or environmental contamination when flammable materials or hazardous chemicals leak.

Although seismic isolation has been recognized as a promising alternative to protecting structures against earthquakes, engineering research and practices on seismic isolation of storage tanks remains limited. Unlike most structures (such as buildings or bridges), the weight of storage tanks varies in time because of variable liquid storage level, and they may contain low-temperature (e.g. LNG) or corrosive substances. Being made of stainless steel, FPS bearings are also resistant to chemicals, fires, temperature extremes, and adverse environmental exposure. Given the

above advantages, FPS seismic bearings are better for industrial tank applications.

Wang, Teng and Chung (2001) devised a hybrid structural-hydrodynamic model and solution algorithm, which permitted simple, accurate and efficient assessment of the seismic response of rigid cylindrical storage tanks in the context of seismic isolation. As a further step towards this study, a series of shaking table tests is conducted using a model tank consisting of stainless steel and acrylic. The 0.01m thick acrylic shell enables the sloshing response of the liquid to be observed during the tests. The tank is isolated using four friction pendulum seismic bearings fabricated by local workshop. The El Centro, Hachinohe and Kobe earthquakes of various intensities were adopted as inputs for the experiments and various storage levels of the liquid were considered. Experimental results show evident reductions in dynamic pressure on the shell wall of the tank consistently while isolated. The effectiveness of the friction pendulum bearings in the protection of storage tanks against earthquakes was verified. Moreover, numerical simulations carried out using the hybrid structural-hydrodynamic model previously devised (Wang, Teng, Chung, 2001) agree very well with the corresponding test results, indicating adequacy of the analytical model.

2. METHODOLOGY FOR EARTHQUAKE NATURAL DISASTER

2.1 Analytical Modelling

A rigid, circular cylindrical tank defined by a cylindrical coordinate system, with r , θ and z denoting, respectively the radial, circumferential, and axial coordinates, is filled with liquid to a storage level H , as illustrated in Fig. 1. The liquid with density ρ , is assumed to be incompressible, irrotational and inviscid. Under horizontal earthquake ground acceleration, $\ddot{x}_g(t)$, in the direction $\theta = 0$, the velocity potential function, $\varphi(r, \theta, z, t)$, of the liquid flow within the tank satisfies the Laplace's equation as

$$\frac{\partial^2 \varphi}{\partial r^2} + \frac{1}{r} \frac{\partial \varphi}{\partial r} + \frac{1}{r^2} \frac{\partial^2 \varphi}{\partial \theta^2} + \frac{\partial^2 \varphi}{\partial z^2} = 0 \quad (1)$$

The solution of Eqn. (1) can be conveniently expressed by superpositioning two components as

$$\varphi(r, \theta, z, t) = \varphi_1(r, \theta, z, t) + \varphi_2(r, \theta, z, t) \quad (2)$$

where φ_1 is associated with the portion of the liquid that varies in synchronization with the rigid tank, and φ_2 is associated with the hydrodynamic motion of the liquid relative to the tank.

The hydrodynamic system (2) can be revised for each mode as an analogy of a single-degree-of-freedom base-excited spring-mass system as

$$m_j \ddot{\bar{D}}_j(t) + k_j \bar{D}_j(t) = -m_j \ddot{x}_g(t) \quad j = 1, \dots, \infty \quad (3)$$

where and By considering only the first N modes, the hydrodynamic system due to ground excitations can be concisely expressed as

$$\mathbf{M}_s \ddot{\bar{\mathbf{D}}}(t) + \mathbf{K}_s \bar{\mathbf{D}}(t) = -\mathbf{M}_s \mathbf{1} \ddot{x}_g \quad (4)$$

where

$\mathbf{1}$ denotes the $N \times 1$ uniform vector with all its entries being 1.

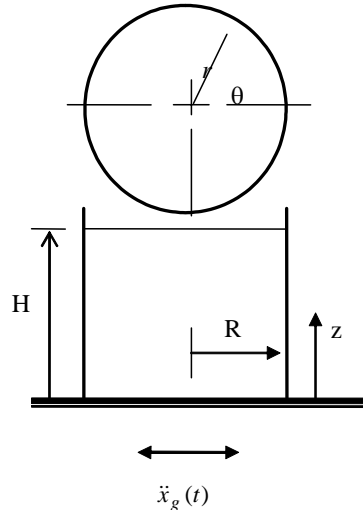


Figure 1: Configuration of the Cylindrical Tank

2.2 Hybrid Structural-hydrodynamic Systems of Base-Isolated Rigid Tanks

When friction pendulum bearings are installed beneath its base for seismic isolation, the rigid tank and the liquid it contains will slide together during earthquakes (Fig.2). The kinetic energy (T) and the potential energy (V) of the hybrid structural-hydrodynamic system are defined, respectively, as

$$T = \left[\dot{\bar{\mathbf{D}}} + \mathbf{1}(\dot{x}_b + \dot{x}_g) \right]^T \mathbf{M}_s \left[\dot{\bar{\mathbf{D}}} + \mathbf{1}(\dot{x}_b + \dot{x}_g) \right] + \frac{1}{2} m_b (\dot{x}_b + \dot{x}_g)^2 \quad (5)$$

$$V = \frac{1}{2} \bar{\mathbf{D}}^T \mathbf{K}_s \bar{\mathbf{D}} + m_t g R_{FPS} (1 - \cos \gamma) \cong \frac{1}{2} \bar{\mathbf{D}}^T \mathbf{K}_s \bar{\mathbf{D}} + \frac{1}{2} \frac{m_t}{R_{FPS}} x_b^2 \quad (6)$$

where x_b and \dot{x}_b are, respectively, the sliding displacement and sliding velocity of the base (relative to the ground); m_b is the effective mass of the tank, including the mass of the tank itself and the equivalent impulsive mass (m_0) of the liquid; $m_t = \sum_{j=1}^N m_j + m_b$

is the total mass of the hybrid system; R_{FPS} is the radius of curvature of the sliding surface and $\gamma \cong x_b / R_{FPS}$ is the sliding angle around the center of curvature as depicted in Fig. 2. Considering

the friction force, $f(t)$, between the sliding interfaces of the bearing as a non-conservative force, the equation of motion of the hybrid system can be derived by applying the Lagrange's equation as

$$\mathbf{M}\ddot{\mathbf{x}}(t) + \mathbf{K}\mathbf{x}(t) = -\mathbf{E}\ddot{x}_g(t) + \mathbf{B}f(t) \quad (7)$$

where

$\mathbf{x}(t) = \begin{pmatrix} \bar{\mathbf{D}}(t) \\ x_b(t) \end{pmatrix}$ is the displacement vector; $\mathbf{M} = \begin{bmatrix} \mathbf{M}_s & \mathbf{M}_s \mathbf{1} \\ \mathbf{1}^T \mathbf{M}_s & \mathbf{1}^T \mathbf{M}_s \mathbf{1} + m_b \end{bmatrix}$ is the mass

matrix; $\mathbf{K} = \begin{bmatrix} \mathbf{K}_s & \mathbf{0} \\ \mathbf{0} & \frac{m_t g}{R} \end{bmatrix}$ is the stiffness matrix; $\mathbf{E} = \begin{pmatrix} \mathbf{M}_s \mathbf{1} \\ \mathbf{1}^T \mathbf{M}_s \mathbf{1} + m_b \end{pmatrix}$ is the

location matrix of the earthquake load, and $\mathbf{B} = \begin{pmatrix} \mathbf{0} \\ 1 \end{pmatrix}$ is the location matrix of

the friction force.

The hybrid structural-hydrodynamic system (7) is highly nonlinear because of friction. A numerical procedure based on the concept of shear balance at the sliding interfaces (Veletsos:1995, Shivakumar:1995) is developed in the following section to solve this nonlinear dynamic problem.

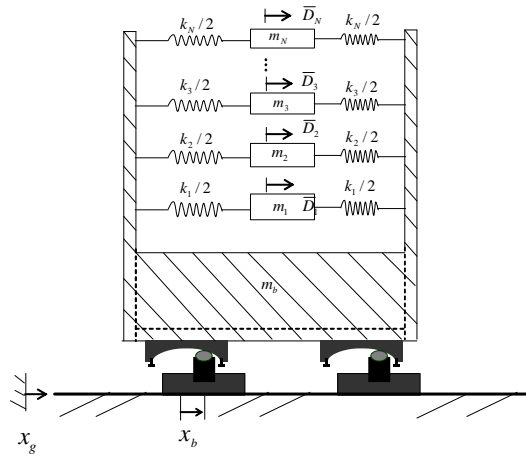


Figure 2: Tank Isolated with Friction Pendulum Bearings

2.3 Experiment Model

The cylindrical model tank with a radius (R) of 1.36m, and a height of 2m is illustrated in Figure 3 for side view. The capacity of the model tank is 3 tons as filled up with water. The design was restricted to an ultimate shake table capacity of 10 tons payload and plan dimensions. The main body of the storage tank consists of stainless steel and acrylic. Below the height of 0.8m is stainless steel of 0.003m-thick, and above 0.8m to the top is acrylic shell of 0.01m- thick. The acrylic shell enables the sloshing response of the

liquid to be observed during the tests. The base frame of the tank is welded together with H-beams (H250*250*9*14) and a steel plate (2m*1.8m*0.01m). The H-beams are reinforced with stiffeners. The total weight of the tank is 0.916 tons when empty. The tank is considered rigid. Figure 3 shows the model tank that has been readily installed on the shaking table for testing.

The tank, without seismic isolation, is estimated to have a maximum base shear of 11.84 kN and a maximum overturning moment of 10.42 kN – m, through preliminary numerical simulations, under the excitation of El Centro earthquake with its PGA scaled up to 0.7g. The weight of the tank is 0.916 tons as empty and 27.89 kN in full storage (H=1.8m). A safety factor of 2 is considered in the design.

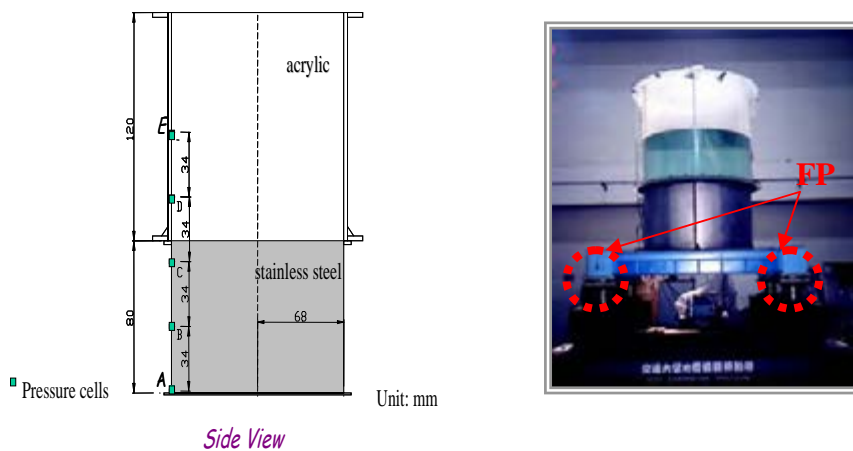


Figure 3: Storage Tank Model on Shaking Table

3. METHODOLOGY FOR MAN-MADE DISASTER

3.1 Man-Made Disaster Regulations Discussion

As discuss to storage tank safety management must keep the regulations of Council of Labor Affairs, Taiwan R.O.C and National Fire Agency, Ministry of the Interior. National Fire Protection Association (NFPA) and American Petroleum Institute (API) U.S.A is the most popular for protected storage tanks ; For example, NFPA 30 - Flammable and Combustible Liquids Code is the industry's most trusted and complete source for safety rules concerning flammable and combustible liquids. The purpose of NFPA 30 code shall be to provide reasonable requirements for the safe storage and handling of flammable and combustible liquids. Furthermore, the API 650 is the welded steel tanks for oil storage standard code that is designed to provide the petroleum industry with tanks of adequate safety and reasonable economy for use in the storage of petroleum, petroleum products, and other liquid products commonly handled and stored by the various branches of the petroleum industry.

Industrial Technology Research Institute (ITRI) Significant Accident Data Base was collected the accident cases of storage tank from 1982 to 2003(ITRI Web Site). Accident was classified according to cause type, fire

accident has 39 percent accident cases, explosion has 37 percent and leak of chemical is 24 percent as figure 4 shown.

Figure 5 indicates the fire accident was classified according to cause. In the Fig 5 unknown, inappropriate operation and inappropriate design had observably main risk source with storage tank. Moreover, in Figure 6 integrated fire, explosion and leak of chemical accident have the similar result to Figure 5.

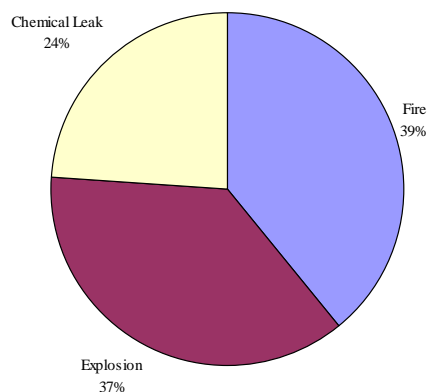


Figure 4: Tank accidents were classified according to type

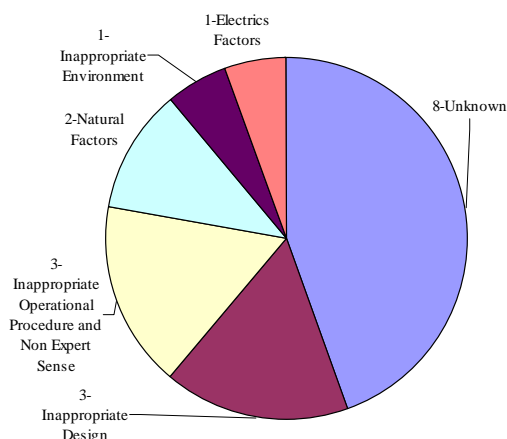


Figure 5: Fire accidents were classified according to cause

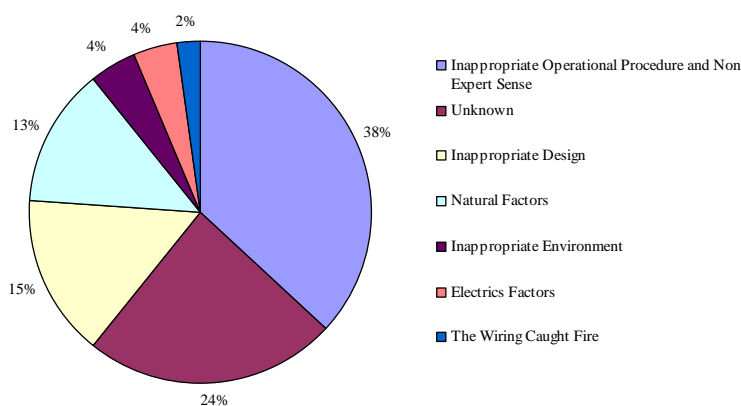


Figure 6: Integrated fire, explosion and leak of chemical accident were classified according to cause

3.2 Emergency Response Planning for Fire Protection

The typical announced flow chart as shown in Figure 7. For example, National Fire Agency, Ministry of the Interior is the primary public management organization for disaster rescue.

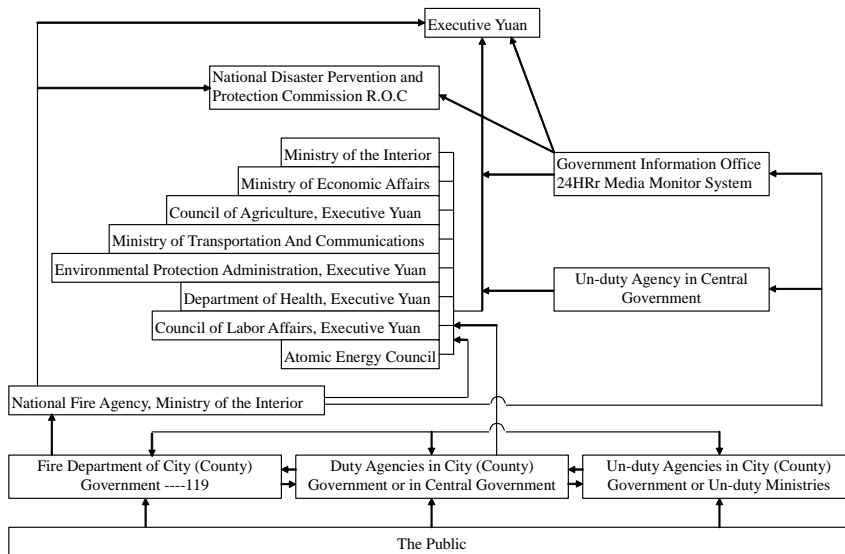


Figure 7: Fire Disaster Announced Flow chart

4. DISCUSSION

Figure 8 indicates the experimental and numerical dynamic pressure $w/$ and w/o isolation under El Centro $PGA=0.7g$. Results are indicated the dynamic pressure in the storage tank had observably reduction with FPS isolation. For example, in Figure 8 the peak dynamic pressure without seismic isolation (broken line) of pressure cell denoted as A is 4.31 kN/m^2 and using FPS (solid line) the peak dynamic pressure dropped into 1.66 kN/m^2 the reduction ratio has a 61 percent; moreover the dynamic pressure of pressure cell denoted as E the reduction ratio even has a 56 percent. Summary, another test cases effectiveness of friction pendulum bearings seismic isolation of the model tank are presented in Table 1.

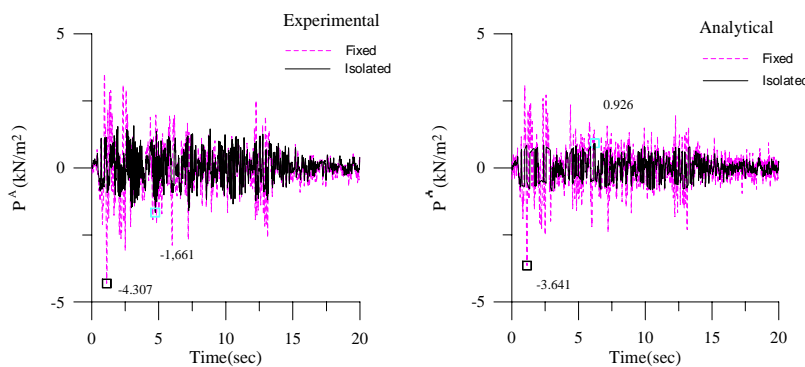


Figure 8: Dynamic Pressure Near Bottom of Tank (El Centro Earthquake, PGA=0.7g, H=1.80m)

Table 2 indicates the percentage seismic effectiveness of peak dynamic pressure remains constant change when we adjust the earthquake intensity from 0.34g to 0.7g (H=1.8m) under El Centro earthquake excitation. In Tab. 2 seismic effectiveness of peak dynamic pressure gradually rose from 28% to 65%.

Table1: Effects of Isolation to Dynamic pressure

H=1.8m	El Centro PGA=0.7g			Hachinohe PGA=1.0g			Kobe PGA=1.0g		
	W/o isolation (kN/m ²)	Isolation (kN/m ²)	Redu (%)	W/o isolation (kN/m ²)	Isolation (kN/m ²)	Redu (%)	W/o isolation (kN/m ²)	Isolation (kN/m ²)	Red (%)
A	4.31	1.66	61	8.29	2.62	68	9.6	2.42	75
B	3.99	1.47	63	7.72	2.22	71	9.33	2.17	77
C	4.00	1.41	65	7.94	2.23	72	9.06	2.16	76
D	3.81	1.45	62	7.80	2.48	68	8.95	2.25	75
E	3.29	1.46	56	6.69	2.22	67	7.01	1.72	75

Table2: Effects of Earthquake Intensity to Isolation (El Centro)

P. Cell	PGA=0.34g			PGA=0.5g			PGA=0.7g		
	W/o isolation (kN/m ²)	Isolation (kN/m ²)	Redu (%)	W/o isolation (kN/m ²)	Isolation (kN/m ²)	Redu (%)	W/o isolation (kN/m ²)	Isolation (kN/m ²)	Red (%)
A	2.53	1.21	52	4.28	1.69	61	4.31	1.66	61
B	2.34	1.13	52	3.97	1.59	60	3.99	1.47	63
C	2.35	1.08	54	3.98	1.48	63	4.00	1.41	65
D	2.24	1.18	47	3.79	1.49	61	3.81	1.45	62
E	1.93	1.38	28	3.27	1.35	59	3.29	1.46	56

5. CONCLUSIONS AND RECOMMENDATION

This study has explored the feasibility of using friction pendulum bearings for seismic isolation of rigid storage tanks by the scope of natural disaster. The dynamic analysis of rigid tanks implemented with sliding-type isolation systems is a highly nonlinear problem due to the presence of frictions. An analytical model for seismically isolated cylindrical storage tanks has been derived and a solution algorithm developed, to assess the

structural-hydrodynamic characteristics of such hybrid systems. Based on the simulation results, it can be concluded that:

1. Seismic isolation of tank using FPS can effectively reduce the impulsive dynamic pressure of the liquid.
2. Control efficiency increases with earthquake intensity.
3. Numerical simulation closely predicts the test results.
4. Fire, explosion and chemical leak is the main accidents were classified according to cause type.
5. Unknown, inappropriate operation and inappropriate design had main risk source with storage tank fire accident.

REFERENCES

- Jia, ZH. and Ketter, RL. Experimental study of “elephant foot budge” instability of thin-walled metal tanks. Technical Report NCEER-89-004, SUNY/Buffalo, New York, 1989.
- Liu, WK. and Uras, RA. Transient failure analysis of liquid-filled shells, part I: theory. *Nuclear Engineering and Design*. 1989; 117: 107-139.
- Liu, WK. and Uras, RA. Transient failure analysis of liquid-filled shells, part II: applications. *Nuclear Engineering and Design*. 1989; 117: 141-157.
- Wang, Y.P., Teng, M.C., and Chung K.W., “Seismic isolation of rigid cylindrical tanks using friction pendulum bearings,” *Earthquake Engng. Struct. Dyn.*, Vol.30, No.7, 2001, pp. 1083-1099.
- Wang, Y.P., Teng, M.C., and Chung K.W., “Experimental Study of Seismic Isolation of Rigid Cylindrical Tanks Using Friction Pendulum Bearings,” *Proceedings of the Workshop on Diagnosis, Analysis and Control of Vibration and Noise, Shanghai, 2001*, pp.26-28.
- Veletsos, AS. and Shivakumar, P. Hydrodynamic effect in rigid tanks containing layered liquids. *Earthquake Engng Struct. Dyn.* 1995; 24, 835-860.
- Shivakumar, P. and Veletsos, AS. Dynamic response of rigid tanks with inhomogeneous liquids. *Earthquake Engng Struct. Dyn.* 1995; 24, 991-1015.
- INVESTIGATION REPORT U.S. CHEMICAL SAFETY AND HAZARD INVESTIGATION BOARD (CSB) REPORT, NO. 2001-05-I-DE, OCTOBER, 2002.
- Industrial Technology Research Institute (ITRI) Significant Accident Data Base, Web Site : <http://w3.itri.org.tw/accident/>.

SAFETY MANAGEMENT RESEARCH OF THE COACH ACCIDENT

Min-Cheng Teng¹ Shih-Chien Huang² Kuo-Shuh Fan³

¹Senior Assistant Research, National Sci & Tech. Center for Disaster Reduction, Taipei, Taiwan, Email: jack@ncdr.nat.gov.tw

²Research Assistant, National Sci & Tech. Center for Disaster Reduction, Taipei, Taiwan, Email: schuang@ncdr.nat.gov.tw

³Associate Professor, National Kaohsiung First Univ. of Sci & Tech., Kaohsiung, Taiwan, Email: ksfan@ccms.nkfust.edu.tw

ABSTRACT

Coach travel, because of their convenience and mobility, has become one of the main transportation means on the road for tourism. Safety is the foremost concern and demand for travelers using this mode of transportation. Numerous major coach-involved traffic accidents worldwide have resulted in a high number of fatalities and injuries. As demonstrated recently on October 14, 2003 in Taiwan, a coach accident resulted in 4 deaths and 13 injured. Therefore, the developing of accident analysis and safety management laws review for coach is imperative in Taiwan. Accident analysis and safety management are the major topics addressed in this paper. We apply GIS (Geological Information System) software to build a system for the coach analysis. In this system, we use space analysis, property query to sift through the crash/accident data to obtain a coherent trend pattern for further studies. The purpose of this paper is also to consider imperfections in correlative laws and frame. GIS-Based Accident System have four properties to describe the characteristics of a coach accident: (1) occurred time: about year, month, day; (2) damage: dead, wounded, coach damage; (3) road fragment; (4) results of accident.

The major safety issues discussed in this study are potential for coach accident as a result of the transportation disaster injuries mitigation. Assessment of accident investigation, safety recommendation to the Directorate General of Highway, MOTC in Taiwan. In addition, safety management research will help to increase the capability of traffic accident reduction

1. INTRODUCTION

The vigorous development and growth of the Tourism industry in Taiwan has fueled a growing demand for an efficient method of ferrying increasing number of passengers from one destination to another. As a result, the coach bus, because of its high passenger handling capacity, has become the favored mode of transport throughout the internal highway

routes. However, as a result, this has also led to numerous accidents involving coach buses resulting in large numbers of dead, wounded and wreckages. According to the Ministry of Communications report, coach traffic accident cases and number of injured people compared from January to August 1993 with 1992, both rose by 11.9% and 11.3% respectively. Over the years, there has been much emphasis placed on studies of traffic accident disaster early warning and prevention measures conducted for times of natural disasters. There has however been a lack of studies for such measures conducted for non nature-related disaster, such as in this case of coach-related accidents. Thus, the case analysis of the accident and safety management of system of taking necessary precautions against coach disaster and should be strengthened further achieve that end.

2. PRESENT SITUATION DESCRIBING

According to the Department of Statistics, Ministry of Transportation and Communications database, the vehicle registration of tour buses increased from 21,598 in 1995 to 26,545 in 2005. That shows a steady growth of nearly a thousand vehicles annually as Figure 1 indicated.

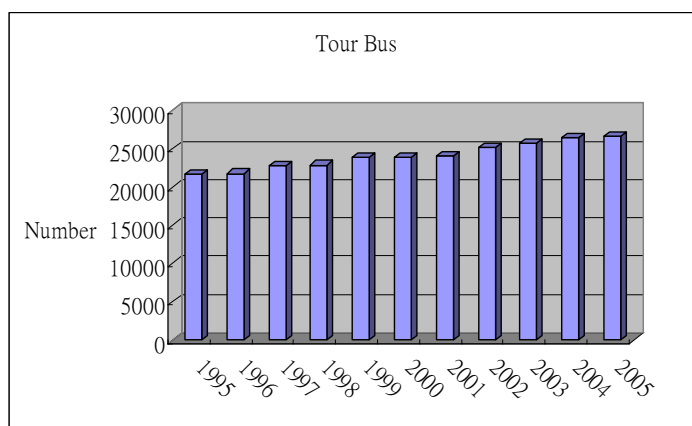


Figure 1: The Vehicle Registration of Tour Bus

According to the Department of Statistics, Ministry of Transportation and Communications database of May, 2005 (as shown in Tab. 1), the number of tour buses that are more than 10 years old exceeds 30%. That figure exceeds 60% for tour buses more than 5 years old. Older vehicles typically require more maintenance to keep them in operation amidst a higher rate of depreciation as well. They may not be inadequate to meet the rigorous demands of tourists seeking more modern, faster, more efficient, comfortable and especially safer means of coach transportation. Therefore the vehicle industry should encourage the vehicle operators to be proactive in adopting a strategy of safety improving, thus promoting higher passenger traffic safety quality.

Table1: Vehicle Car Age Statistical

Age(year)	Number of Tour Bus			Percent(%)	Accumulated Percent(%)
	Private	Business	Subtotal		
< 1	16	206	222	0.84	0.84
1 ~ 3	126	3853	3979	15.00	15.83
3 ~ 5	129	4348	4477	16.87	32.70
5 ~ 7	238	2801	3039	11.45	44.16
7 ~ 10	383	5756	6139	23.14	67.29
> 10	1110	7569	8679	32.71	100.00
Total	2002	24533	26535		

3. METHODOLOGY

A major task in the methodology was helping to formulate a new framework for coach accident data collection, referencing and analysis. The coach accident data collection and statistical methods used to perform accident analysis. The method of analysis reporting will rely on the inherent capabilities of the fundamental software platform used in architecture, the GIS platform. GIS map can not only display traffic accident casualty rates in different countries, it can also isolate the figures to coach-related accidents only and how they compare in dangerous sections of the highway. In addition, we can also discuss the coach safety management from a regulation point of view. This paper reviews and summarizes current coach accident safety management methods in highway adopted by transportation departments. Furthermore, we can investigate the effectiveness of past safety improvement strategies with the newly developed system.

3.1 Comparative Method of Literature

This research approach, primarily studies the written historical information of the report that records in order to observe the foundation, for example: The record file of the organ, survey report, statistical analysis, etc., Summary of the content and classification after collecting relevant report, newspaper and a periodicals, etc.

The information in this text collects will include: (1) Government's materials; (2) special book; (3) periodical article; (4) an academic dissertation; (5) others (news report, network information, etc.).

3.2 Data Collection and Analysis

49 coach accidents data were collected from May 5th, 2002 to June 3rd, 2005, which are sourced from the media and newspaper. In May 2005, the website of Directorate General of Highways, Ministry of Transportation and Communications (MOTC) in Taiwan has indicated there are potentially 49 coach-dangerous sections on the highway.

Upon the completion of material collection, the total display is obtained in the GIS platform. An attribute table is then generated, also performed directly in the GIS platform, and then mapped directly on the

GIS map to give the coach accident and dangerous section of highway map. The GIS map can display the accident casualty figures in these different locations, isolate them further to coach accident-related incidents, and compare them accordingly.

4. DISCUSSION

4.1 Accident Data Compared with Dangerous Section

The highway coach accident material comprised of 45 cases between May 5, 2002 and June 3, 2005, which resulted in a total of 52 deaths and 617 wounded. These coach accidents caused serious damage as well. The following serve as examples: a truck crashed into two coaches and one automobile that caused 5 deaths and 21 wounded in national highway on November 1, 2002; the coach accident that occurred in Taitung Country on October 16, 2003, caused 5 deaths and 12 wounded; another coach that was carrying tour group from Hong Kong, turned over at the mountain area causing 5 deaths and 32 wounded in October 18, 2004.

Figure 2 shows the accident data compared with dangerous section for different counties. What has to be noticed is 11 locations in Tainan County, 9 locations in Taipei County, 8 locations in Chiayi County for dangerous of highway. Further analysis of coach accident, the highest numbers of incidents were in Taipei County (8) and Nantou County (8), followed by Miaoli County (4).

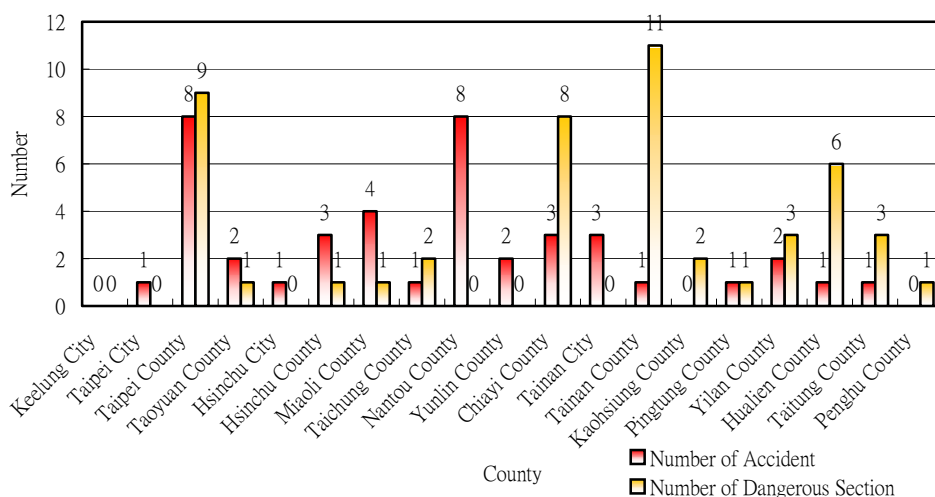


Figure2: Number of Coach Accidental Section Compare With Dangerous Section in Each County

4.2 The Coach Accident and Dangerous Section on GIS Map

The major goal of this paper is the development of a GIS-based system of highway accident analysis for coach that can provide an insight into the highway safety and coach travel as well as contributing date,

damage and description of accident at any location. Figure 3 and figure 4 indicate the coach accidental and dangerous sections that were plotted in a geological information system (GIS). Figure 3 shows most of the coach dangerous sections were in Taipei County, followed by Chiayi County and Tainan County. Relatively, figure 4 shows most of coach accidents were in Taipei County, followed by Nantou County, Miaoli County.



Figure3: The GIS map of dangerous sections in Taiwan

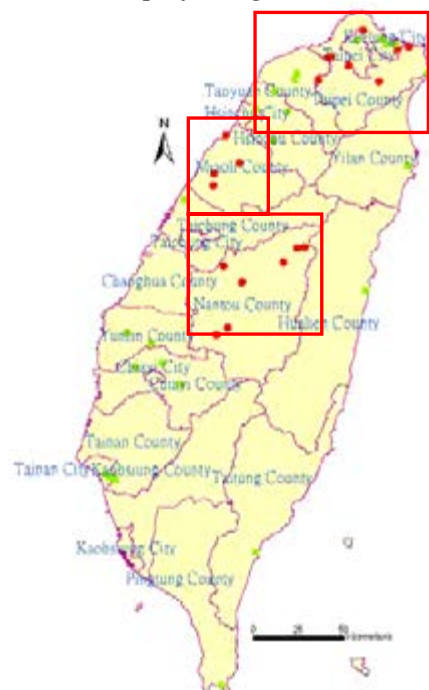


Figure4: The GIS map of coach accidental sections in Taiwan

The damage of the accidents based on GIS map is as shown in Figure 5. As the diagram indicates from accident damage information transferred from the statistical data to the GIS map. The most casualties were in Taipei County.

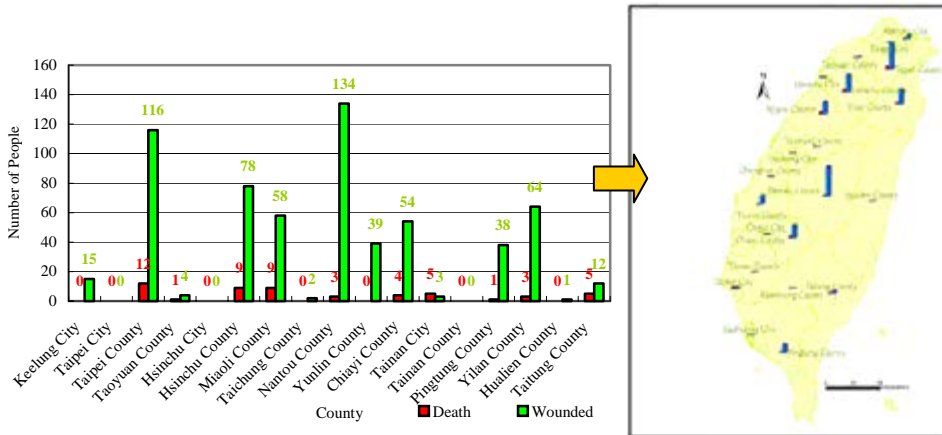


Figure5: GIS map of coach accident damage

Directed to highest coach accidental and dangerous sections was analysis of Taipei County, Tainan County, Chiayi County, Nantou County, Miaoli County.

The dangerous and accidental sections of Taipei County are presented in Figure 6. It must be noted that the dangerous section 5 is near the coach accidental section 4. In addition to coach accidental section 4, other accidents mostly occurred in tourist spots that caused serious damage of up to 12 deaths and 116 wounded in the past. Comparatively, in the coach dangerous sections, we should not overlook the sharp turn(s) that is(are) inherent in the mountain region as well.

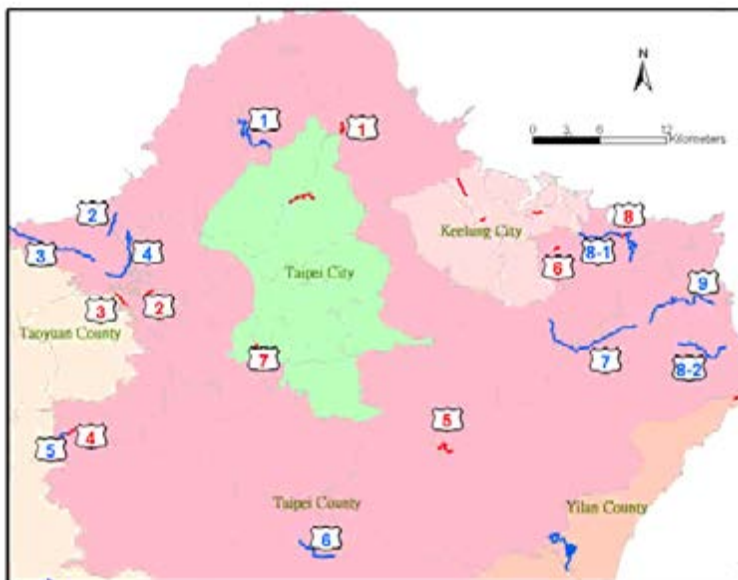


Figure6: The GIS map of coach dangerous and accidental sections in Taipei County

Figure 7 shows there were 8 coach related accidents in Nantou County highway that caused 3 deaths and 134 wounded. The location of the accidents was concentrated on the mountain region road area where 3 incidents had occurred in coach accidental sections 1 to 3, separately. However, the coach accidental sections 1 to 3 are in the same highway. That proved this highway was a highest risk area for transportation by coach. Comparatively, for coach dangerous sections there aren't any other in Nantou County.

Figure 8 indicates there are 4 coach transportation related incidents in Miaoli County highway that caused 9 deaths and 58 wounded of which three of the incidents occurred on the national freeway. However, the location of the coach dangerous section is only in section 1.



Figure7: The GIS map of coach dangerous and accidental sections in Nantou County

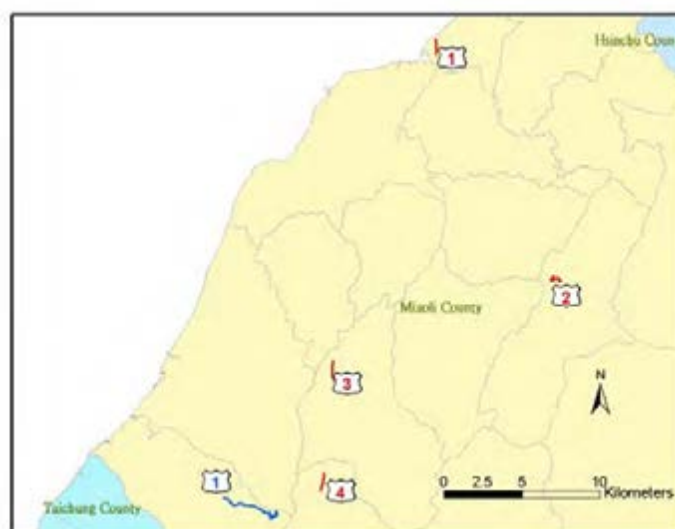


Figure8: The GIS map of coach dangerous and accidental sections in Miaoli County

The coach accidental sections were not tallied with dangerous sections in these counties. Figure 9 shows the 8 coach dangerous sections were not correspond with coach accidental sections in Figure 10 shown 11 coach dangerous sections, however only one coach accident section in national freeway in Tainan County.

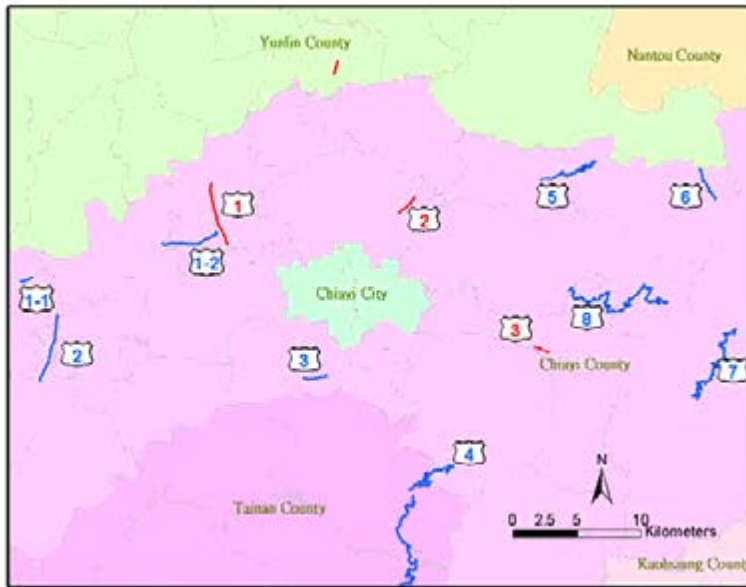


Figure9: The GIS map of coach dangerous and accidental sections in Chiayi County



Figure10: The GIS map of coach dangerous and accidental sections in Tainan County

Analyzing highway accident data is crucial to understanding safety trends, designing strategies to combat safety problems, and evaluating impact on safety measurements. Particularly, the proportion of coach accident was highest in national freeway (24%) totally 11 out of all 45 coach accident cases. Figure11 shows the coach accident map of national freeway that caused 11 deaths and 123 wounded and most of the accidents occurred in the northern part of the Taiwan.

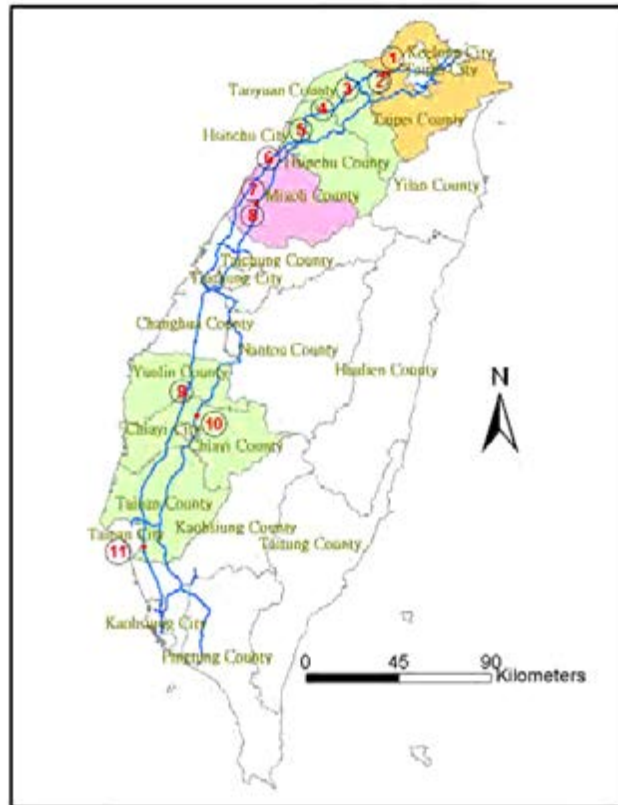


Figure11: The GIS map of coach accident in National Freeway

4.3 Regulations Discussion

As discuss to coach safety management must keep the domestic regulations of Council of Labor Affairs, Taiwan R.O.C and Ministry of Transportation and Communications (MOTC). For example, MOTC issued “Directions for the Safety Type Approval and Conformity of Production of Motor Vehicles”. The vehicle safety type approval shall follow the principle of whole vehicle inspection and testing items, the vehicle type variation and safety factors, etc., to select proper type and spec. of the whole vehicle for inspection and testing in accordance with the Attachment of Directions. This research also combines interpretations of the United Nation Economic Commission for Europe (UN/ECE), Federal Motor Vehicle Safety Standards in U.S.A. (FMVSS), Safety Regulations for Road Vehicle IN Japan, (SRRV) ; summaries of state and local regulatory requirements about vehicle inspection and testing items.

5. CONCLUSION

- (1) Implement a common direction for ECE regulations and consolidating them with the domestic regulations to achieve a world-class vehicle safety management system.
- (2) GIS map can display the differences in accident casualty figures in the different counties, group them directly by coach accident section and compared them to dangerous sections of the highway. This GIS map can provide for reference of government in setting more safety regulations.
- (3) Every county can mark the dangerous road sections with a sign to provide advanced warning to the coaches. An alternate, safer route can also be suggested. These measures can prevent many future accidents from happening .
- (4) The proportion of coach accident was highest in national freeway (24%) totally 11 out of all 45 coach accident cases. Therefore, the government can review the characteristics and road environment for these coach accident road sections, and act accordingly to prevent more accidents as well.

REFERENCES

- Directions for the Safety Type Approval and Conformity of Production of Motor Vehicles, Ministry of Transportation and Communications, 2004.
- Collision of a Greyhound Lines, Inc. Motorcoach and Delcar Trucking Truck Tractor-Semitrailer Loraine, Texas, Transportation Safety Board (NTSB) Highway Accident Report, NO:PB2002-916201, 2003.
- Motorcoach Run-Off-The-Road Accident Tallulah, Louisiana, National Transportation Safety Board (NTSB) Report, No: PB2005-916201, 2003.
- Regulation No 39 of the Economic Commission for Europe of the United Nations (UN/ECE) —Uniform provisions concerning the approval of vehicles with regard to the speedometer equipment including its installation, Official Journal of the European Union, 2003.
- Directorate General of Highways, Ministry of Transportation And Communications, http://www.thb.gov.tw/c_bus/c_bus.htm
- Department of Statistics, Ministry of Transportation And Communications, <http://www.motc.gov.tw/hypage.cgi?HYPAGE=stat.asp>
- Institute of Transportation, Ministry of Transportation And Communications, <http://www.iot.gov.tw>
- National Police Agency, Ministry of the Interior, <http://www.npa.gov.tw/>
- Search for News of TVBS-NEWS Website, http://www.tvbs.com.tw/news/news_search.asp?p=1

A CASE STUDY OF THE INTRODUCTION OF DISASTER MANAGEMENT SYSTEM AT ISLAMIC REPUBLIC OF IRAN

Shinya KONDO

Institute of Industrial Science, The University of Tokyo, Japan
(Present: Disaster Center and Human Renovation Institution, Kobe, Japan)
kondo@risk-mg.iis.u-tokyo.ac.jp

Kimiro MEGURO

Professor, International Center for Urban Safety,
Institute of Industrial Science, The University of Tokyo, Japan
meguro@iis.u-tokyo.ac.jp

ABSTRACT

For realization of efficient disaster countermeasures, it is important to prepare an environment in which people can analyze/assess past disaster responses, sort out potential problems, and discuss countermeasures for them. Therefore authors proposed a New Style Disaster Management System for developing this environment.

At Islamic Republic of Iran, people have suffered severe damage due to many strong earthquakes. For example, over 26 thousand persons were killed and 30 thousands injured by Bam earthquake 2003. Seismologists believe a strong earthquake will strike Tehran. According to the damage estimation, casualty can reach 380 thousands, and over 50 % of building is collapsed in Greater Tehran City in the worst scenario. As a result, it is necessary to get lessons from past disaster to shape and pass down them to other people and to create an environment for the implementation of disaster countermeasures.

In this study, the authors propose the flowchart of the introduction of customized Disaster Management System and introduce Disaster Management System to the organization which plans disaster reduction at Islamic Republic of Iran using this flowchart. At first, the system that people in charge can analyze/assess and draft/update disaster management manual by themselves was installed at Greater Tehran Gas Company. Then the disaster information database about disaster response in Bam earthquake 2003 was constructed at Iranian Red Crescent Society.

1. INTRODUCTION

Ideal disaster management measures are conducted in the following balanced countermeasures: “Disaster Mitigation”, “Preparedness / Disaster Response” and “Optimum Recovery / Reconstruction Plan” (Figure 1). “Disaster Mitigation” means efforts to prevent hazard from becoming a disaster. “Preparedness / Disaster Response” means proper measures to

prevent the disaster from affecting widely. “Optimum Recovery / Reconstruction Plan” means recovery and reconstruction from disaster promptly to reduce its effects to a minimum. Comprehensive disaster management will not improve without user’s imagination of the real situation in disaster clearly or the implementation of these three measures.

Same as before, we should prepare the environment people can make disaster management manual by themselves. The process of making disaster management manual consists of 6 stages like Figure 2. First stage is “Imagining real situations in disaster”. Second stage is “Analysis of present disaster reduction”. Third stage is “Reviewing disaster measures”. Forth stage is “Concretization of disaster measures”. Fifth stage is “Implementation or learning disaster measures”. And the last stage is “Evaluation of method and results of each stage”.

Based on these points, the authors proposed Disaster Management System which supports people to make disaster management manual as the process above. This system consists of several systems, for example, “New Style Management Manual” (Kondo and Meguro, 2001) is the basis of Disaster Management System and supports the stage “Analysis of present disaster reduction”. This system has three features, “Analysis and Assessment of existing manuals”, “Independent edition by each purpose/user”, and “Drafting and Updating of manual”. And “New Style Information Database” (Kondo and Meguro, 2002) supports the stage “Imagining real situations in disaster”. This database consists of newspaper, reconnaissance reports, and reports on past disaster. With features, “Analysis and Assessment of existing manuals” and “Independent edition by each purpose/user”, this system can provide information such that people can imagine real situation in disaster. Moreover, the system can accumulate and share lessons learned from analyzing information about past disasters.

At Islamic Republic of Iran (Iran), people have suffered severe damage due to many strong earthquakes. For example, Bam earthquake 2003 killed over 26 thousand persons and injured over 30 thousand persons. Seismologists believe there is possibility that a strong earthquake will strike Tehran. According to the damage estimation, casualty distributes 380 thousands, and over 50 % of building will be collapsed in Greater Tehran City in the worst scenario. Based on these points, it is necessary to get lessons learned at past disaster into shape and pass down them to other people and to create an environment for the implementation of the disaster countermeasures.

In this study, the authors propose the flowchart for introducing customized Disaster Management System to the organization, and try to introduce some features of this system to the organization planning disaster reduction at Islamic Republic of Iran. At first, the system “New Style Management Manual” was applied to Greater Tehran Gas Company (GTGC). And “New Style Disaster Information Database” about disaster response in Bam earthquake 2003 was constructed at Iranian Red Crescent Society (IRCS).

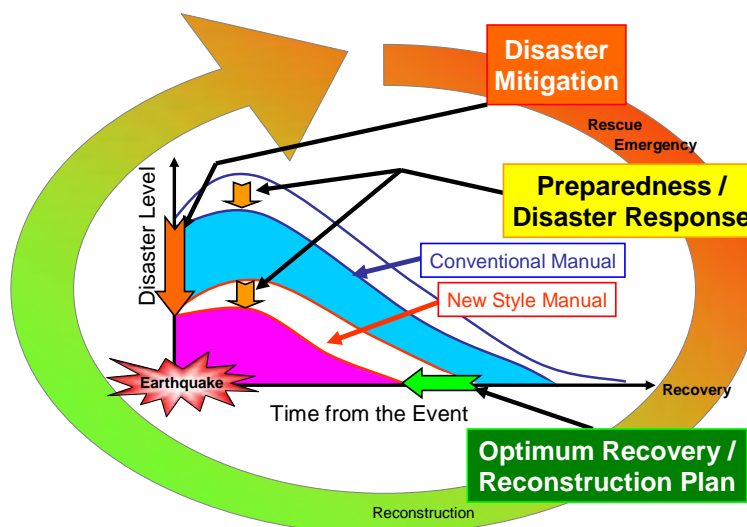


Figure 1: Difference in the effects of disaster reduction capability between conventional type and new type of disaster management manual

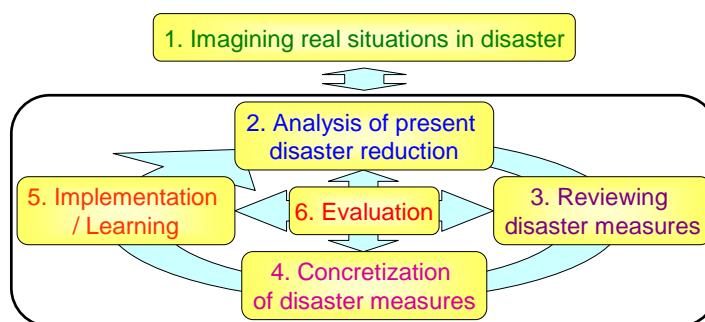


Figure 2: The process of making disaster management manual

2. OUTLINE OF PROPOSED SYSTEM

2.1 Analysis and Assessment of existing manuals

“Analysis and Assessment of existing manuals” makes people to understand the relation between each works from indexes set at each measure easier. Therefore it becomes easier to analyze contents of present manual rationally/objectively from various points of view. Figure 3 presents an example of analysis and assessment of the disaster management manual of a big city in the Tokyo metropolitan region. The x-axis is “Time to start from an event”. The y-axis represents different “Responsible organization”. The z-axis is “Amount of the work” to be done. From the x-axis, we can see actions are not well pointed out after 6-24 hours and four days. Also from the y-axis, it can be seen that amount of work is not balanced among organizations.

2.2 Independent edition by each purpose / user

“Independent edition by each purpose / user” is to pick information of the latest disaster and to understand the user’s need, directly by accessing

the manual. Users can choose necessary conditions from indexes set at previous section “Organization of the Manual” excluding “Work loads”, picking up necessary items from whole manual, so they can get idea about their own role, during a disaster. Figure 4 shows the application of this feature in the existing government disaster management manual as presented in Figure 3. This figure shows that how a General Manager, (normally mayor or governor) of an organization can select his own responsibility just by clicking a button on his position.

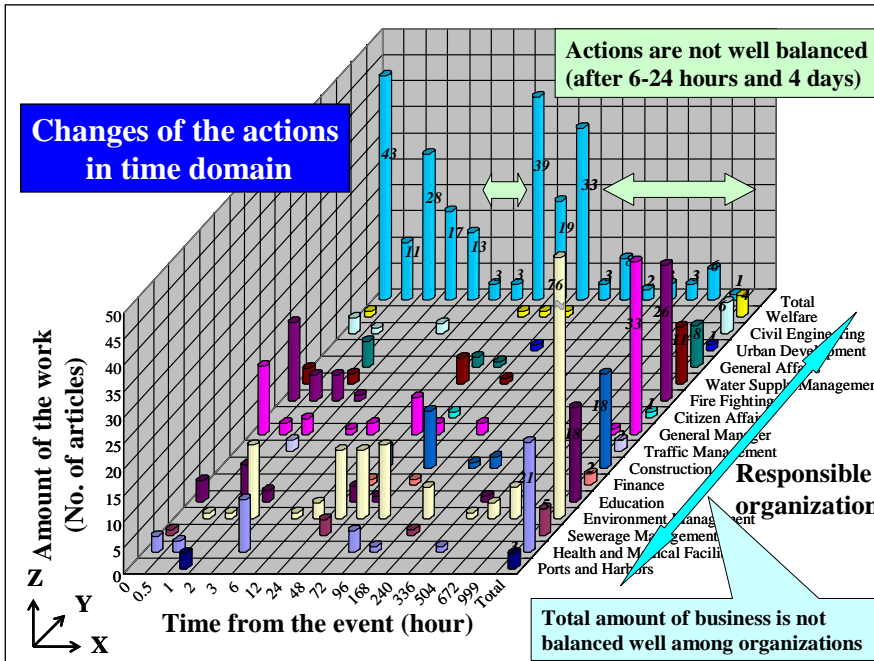


Figure 3: Analysis and Assessment of existing manuals

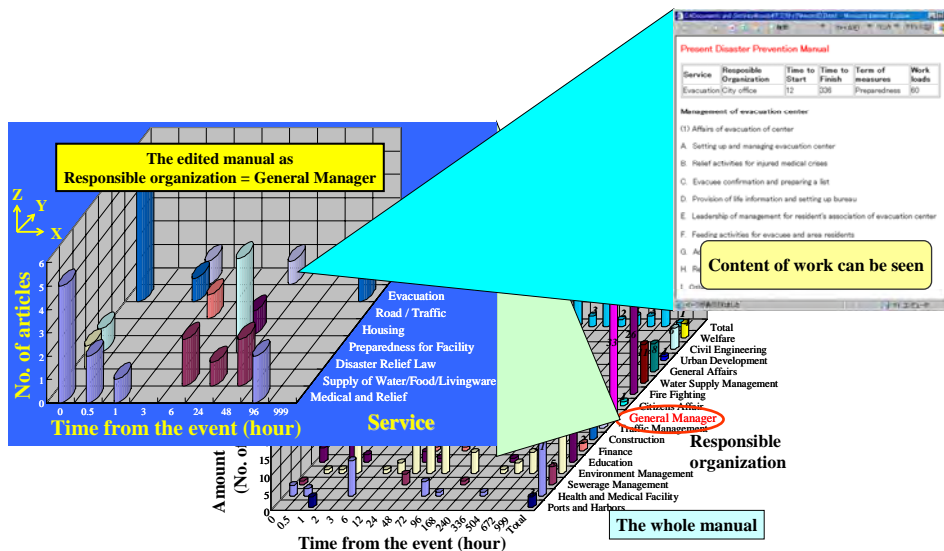


Figure 4: Independent edition by each purpose / user

3. OUTLINE OF FLOWCHART TO INTRODUCE

In this study, the authors introduced Disaster Management System to the organization at Iran followed the flowchart. Figure 5 is the flowchart for introduction of system to the organization. Content of each work is included below.

3.1 Checking the length to introduce

For introducing proposed system to the organization, people should check the length that expert can work on-site. So, the schedule and function to install can be decided. At GTGC and IRCS, each length that the authors could work to install is shown in Table 1.

3.2 Grasp of characteristics of the region

People should grasp characteristics of the region, for installing system adapting to the organization. At this stage, people studied damage estimation (JICA, CEST 2000) at Tehran city.

3.3 Setting up project team

People should set up project team with members of the organization for installing and managing proposed system by themselves. Members of project team consist of expert, facilitator, database creator, and interpreter (Farsi to English).

3.4 Grasp of characteristics of the organization

At this stage, people should know structure of the unit of the organization. So members of the organization were recruited to the project team. The authors could grasp characteristics of the organization from them.

3.5 Decision the data for database

Project team selected data for making database by database creator. At GTGC, existent disaster management manual was used. Based on Disaster Information Database at IRCS, facilitator could ask people who are responded for Bam earthquake to make database.

3.6 Making database

The authors asked database creator to put 7 indexes in Farsi to each measure, “Responsible organization”, “Service contents”, “Term of measures (relatively)”, “Time to start and finish measures from an event (absolutely)”, and “Work loads (man x day)”. So it is easy for people to imagine situation after disaster happened. Picture 1 shows the people during making database at IRCS.

3.7 Checking the network

Checking the network is very important because proposed system uses Web application. But network at Iran was poorer than at Japan. Then project team decided to install proposed system to each PC.

3.8 Installing the system

Expert installed proposed system with a policy decided at pre-step. Expert installed proposed system as shown Table 2.

3.9 Working out the bugs

After installing the system, project team should find out the bugs of system. They should fix bugs if found. During this time, one bug was found. Farsi was displayed from left to right (Usually right to left) on screen.

3.10 Evaluation the system

After pre-step, project team asks members of the organization to evaluate installed system. If some problem is pointed out, they feed back to the system. During this time, they asked boss and several directors at GTGC, and some researcher to study about disaster response at IRCS. In each situation, installed system got high evaluation.

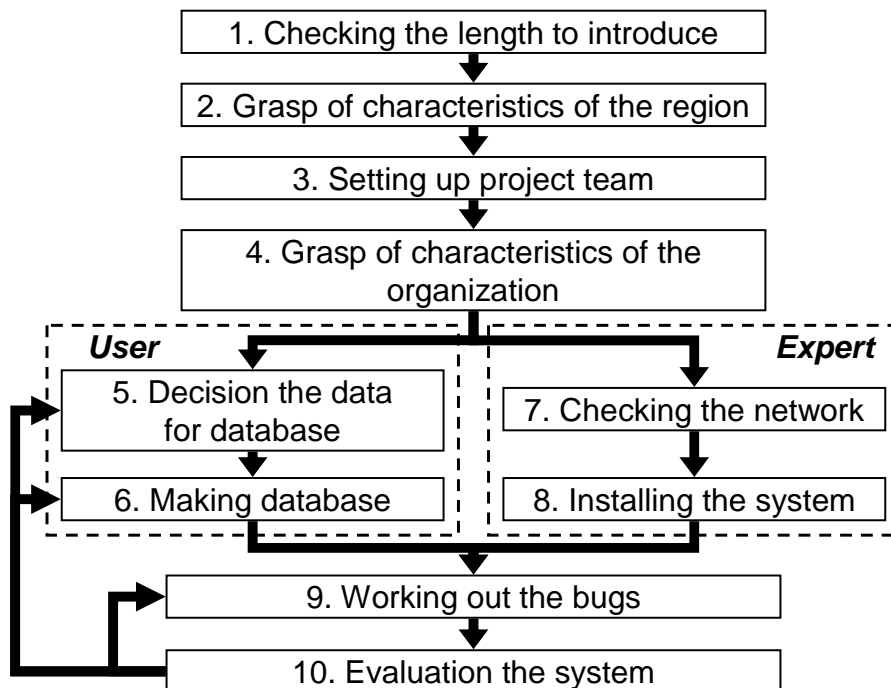
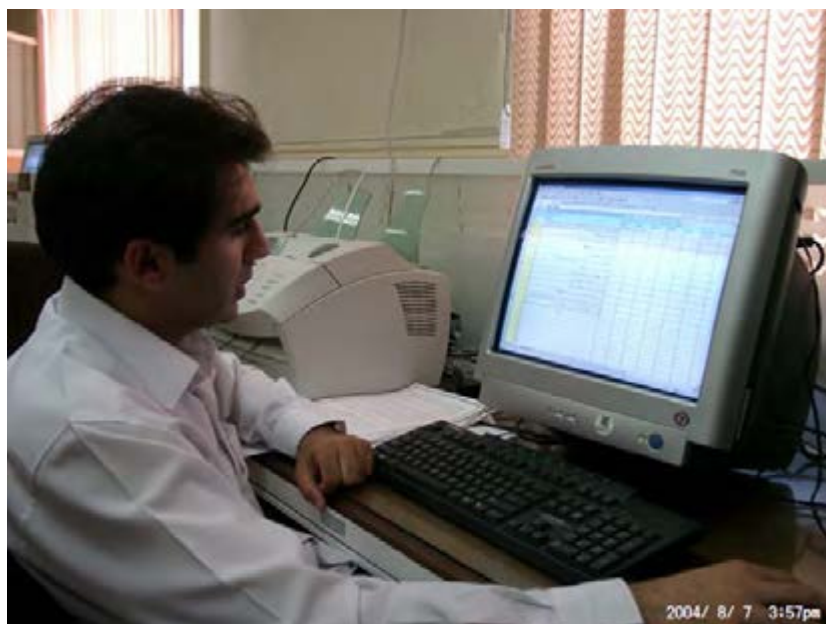


Figure 5: Flowchart for introduction of system

Table 1: The length to install proposed system.

Organization	Date	Length
GTGC	27 th , June – 6 th , July, 2004	9days
IRCS	7 th , August – 14 th , August, 2004	8days



Picture 1: People making database

Table 2: Environment of proposed system.

Function	Software
OS	Windows XP
Server	Apache
DBMS	MySQL
Server-side Script	PHP

4. RESULT OF INTRODUCTION

Figure 6 shows a result of analysis GTGC Disaster Management Manual. The x-axis is “Responsible Organization”. The y-axis is “Time from the event”. The z-axis is “Work loads”. The right side of window shows name of responsible organization corresponding to the number on the x-axis. From this figure, we can see that all sections will start all works after 1 hour to 2 months from the event. This result shows database creator has a shortage of imagination for disaster situation. So, the environment members can imagine real situation should be prepared.

Figure 7 shows the example at using Disaster Information Database of disaster response of IRCS in Bam earthquake. The x-axis is “Responsible Organization”. The y-axis is “Time from the event”. The z-axis is “Work loads”. With this system, people can imagine real situation in disaster easier. Therefore this system prepares environment for members to pick out lessons.

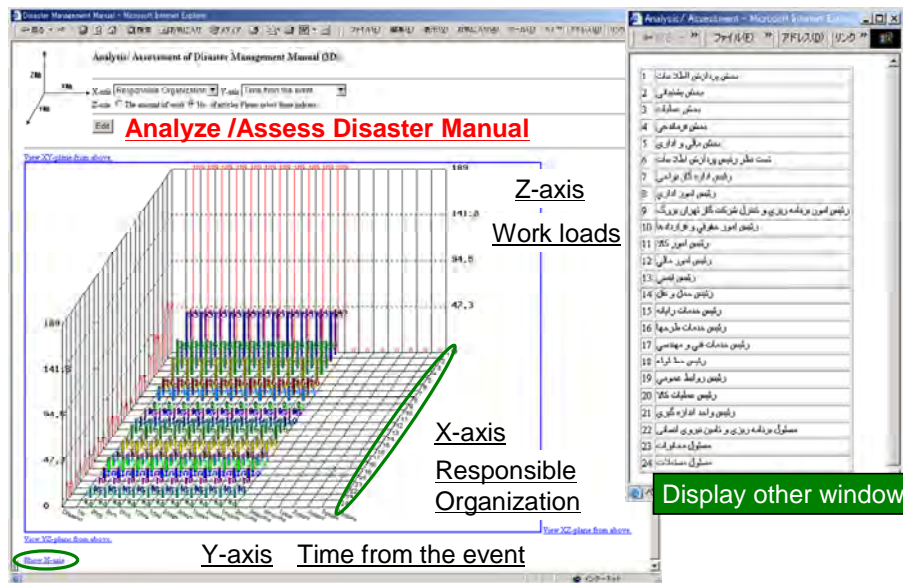


Figure 6: Result of analysis GTGC Disaster Management Manual

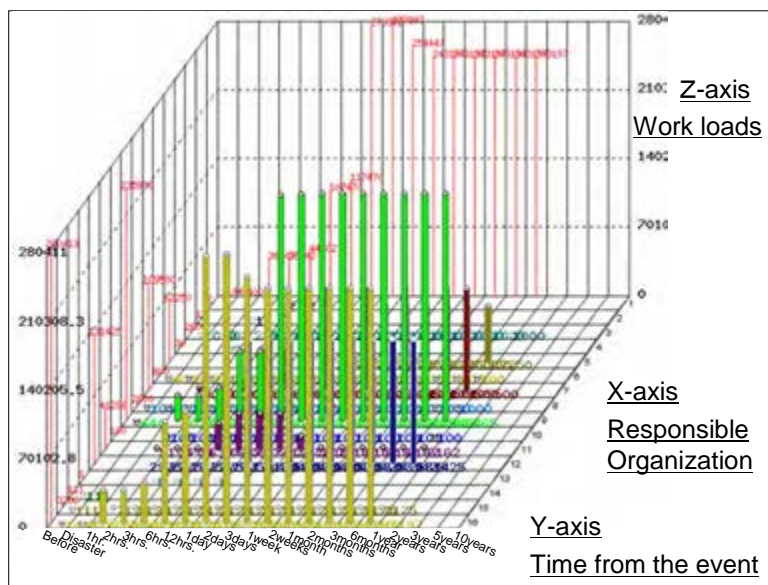


Figure 7: The example to use Disaster Information Database of disaster response of IRCS in Bam earthquake

5. CONCLUSION

In this study, the authors proposed the flowchart for introducing customized Disaster Management System to the organization. Moreover, the authors tried to introduce some features of this system to the organization which plan disaster reduction at Islamic Republic of Iran. At first, the system “New Style Management Manual” was applied to Greater Tehran Gas Company (GTGC). “New Style Disaster Information Database” about disaster response in Bam earthquake 2003 was constructed at Iranian Red

Crescent Society (IRCS). With this system, these organizations can create the environment that people can make disaster management manual by themselves. And they can improve earthquake disaster reduction.

REFERENCES

- Kondo, S., Hamada, S., and Meguro, K., 2001, *Proposal of New Style Disaster Manual for Implementation of Efficient Disaster Countermeasures*, 26th JSCE Earthquake Engineering Symposium, pp.1481-1484.
- Meguro, K., 2001, *Dynamic Evaluation Model for Large Earthquake Disaster*, Journal of Geography, Vol. 110, No. 6 (979).
- Kondo, S., Meguro, K., 2002, *Development of New Style Disaster Information Database for Implementation of Efficient Disaster Countermeasures*, No.4, Journal of Social Safety Science, Institute of Social Safety Science, Japan, pp.261-266.
- Japan international cooperation Agency (JICA), Center for earthquake and environmental studies of Tehran (CEST), and Tehran Municipality, 2000. *THE STUDY ON SEISMIC MICROZONING OF THE GREATER TEHRAN AREA IN THE ISLAMIC REPUBLIC OF IRAN*

VULNERABILITY OF COASTAL CITIES OF ASIA TO RISING SEA LEVEL: A CASE STUDY IN BANGKOK

DUSHMANTA DUTTA

School of Applied Sciences and Engineering,

Monash University, Australia

dushmanta.dutta@sci.monash.edu.au

ABSTRACT

The paper presents the outcomes of a case study conducted to analyze the flood characteristics in Bangkok under sea level rising scenarios. A physically based distributed hydrological model, which combines surface and river flow, was adopted to simulate the flood scenarios due to different magnitudes of sea level rising. The input rainfalls and the upstream boundary conditions of a worst flood event of 1995 were considered as the baseline for the modeling based on the available records of rainfall and water level datasets of the last three decades. The study was aimed to capture a macro picture of floods to present an overview of severity of flood situations under climate change conditions.

1. INTRODUCTION

The 20th century was the warmest the world has seen in 1,800 years. A warming climate leads to changes in many aspects of climate system and earth environment including precipitation, wind pattern, the frequency and severity of extreme weather events and rise of sea level. Based on a study of 2001, the Intergovernmental Panel on Climate Change (IPCC) has predicted that the global mean sea level (msl) may rise as much as 88 cm by the end of the 21st century. Approximately 20% of the global population lives within 30 km of coastal areas and the number is expected to become double by 2025 (Cohen et al., 1997). The sea level rise will have wide ranging effects on coastal population and ecosystem, such as saline water intrusion, erosion of shorelines, amplified intensity and frequency of coastal flood inundation, etc.

The socio-economic impacts of climate change in the coastal cities of Asia will be enormous due to the rapid urbanization and high population growth. The combined effects of potential sea level rise and extreme rainfall events triggered by climate change may lead to catastrophic flood disasters in many of the coastal cities of Asia, which are located in the low-lying floodplains of major rivers. So far only a few studies have been conducted in this direction and a very few countries have prepared long-term plans to deal with these problems. It is important to assess the impacts of mean sea level rise on flooding in coastal cities and prepare long-term plans for risk management (Dam, 2003).

A study that was conducted to analyze the socio-economic impacts of floods in several large coastal cities of Asia under projected climatic and socio-economic scenarios using a distributed hydrological model and an

agent based land use change model. The paper presents the outcomes of a case study which was conducted to analyze the flood characteristics in Bangkok under sea level rising scenarios. A physically based distributed hydrological model, which combines surface and river flow, was adopted to simulate the flood scenarios due to different magnitudes of sea level rising. Input rainfalls and upstream boundary conditions of a worst flood period were considered based on the records of the last three decades as the baseline for modeling. The study was aimed to capture a macro picture of flooding to present an overview of severity of flood situation utilizing surface elevation of 1km resolution and without going into micro details of urban topography and drainage.

2. STUDY AREA

Bangkok, the capital city of Thailand, is one of the major cities in Asia and a regional hub. It is located on the lower flat basin of the Chao Phraya River, which is originated in the northern most part of Thailand and discharges to the Gulf of Thailand after flowing approximate 900 km (Fig. 1). The catchment area is 157,925km², which covers about 30% of Thailand's land area. The average annual discharge of the Chao Phraya Basin is about 770 m³/s with a peak of 4,560 m³/s recorded in 1995 (Thammasittirong, 1999).

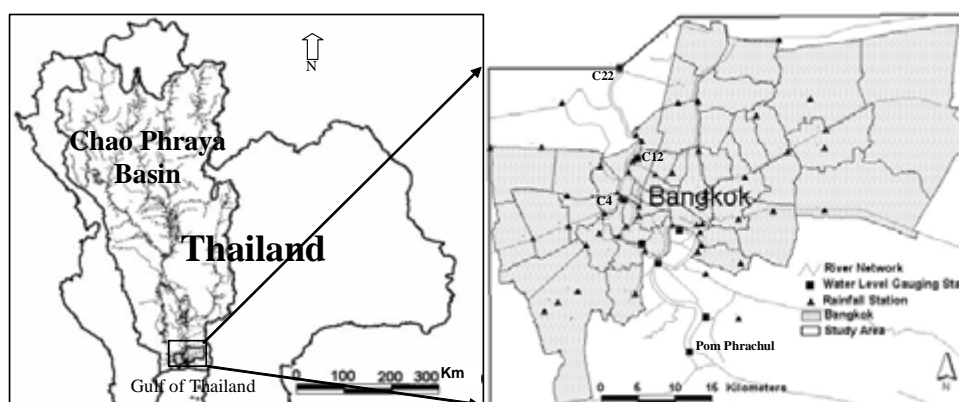


Figure 1. Location of the study area

Floods, mainly caused by upstream inflow and high intensity rainfalls, are the most frequent natural disasters in Bangkok. It affects a large number of populations and causes huge economic damage every year. Due to its low elevations, ranging from 0m to 4m above msl, tidal effect is prominent in the Chao Phraya river upto several kilometers inside Bangkok and that attributes significantly to floods. There are usually two high tides and two low tides per day in Gulf of Thailand, but these are often asymmetrical with amplitude of 1-2m. The daily variation of tides is normally from -0.5 m to 1.5 m with a peak of 2.5 m recorded in 1995.

3. METHODOLOGY

The surface and river components of the IISDHM, a physically based distributed hydrological model (Jha, et al, 1997, Dutta et al., 2000), were used for flood inundation simulation. In this model, 1D Saint-Venant's equations of continuity and momentum equations are used for river network flow simulation and 2D form of the equations for surface flow routing. The exchange of flow between the channel network and flood plains is simulated using the floodplain compartment concept (Dutta, et al., 1997).

3.1 Model Setup

The model setup for this case study was done with 1km spatial resolution and 1hour temporal resolutions. Elevation data was obtained from HYDRO1K DEM of USGS and landuse data from the USGS global landuse database. Surface roughness coefficients for different grids were assigned based on the landuse types. For river network, only the main stream of the Chao Phraya river was considered with the hydrological gauging station C22 as the upstream boundary and Pom Phrachul as the downstream boundary (Figure 1). River cross section data, hourly rainfall data in the 4 gauging stations within the study area, hourly water level data for upstream and downstream boundary stations were obtained from various local sources including the Bangkok Metropolitan Administration (BMA), Royal Irrigation Department (RID) and the Port of Thailand Authority.

3.2 Model Calibration and Verification

The model was calibrated and verified two selected flood events of 1995. The calibrated parameters were Manning's roughness in the river and runoff coefficient. Calibration and verification was performed using the observed water level data for the C12 and C4 water level gauging stations in the Chao Phraya River (Figure 1). Figures 2 and 3 show the observed hourly water level data for the upstream and downstream boundary stations and the average hourly rainfall in the study area for the period of calibration and verification of the model.

The calibrated value of runoff coefficient was 0.4 and Manning's roughness for river was 0.04. Figures 4 and 5 show the comparison of simulated and observed water levels at C12 and C4 stations during the period of verification. As can be seen from Fig. 4, the simulated water level agrees well with the observed water levels at C12 for the peak and pattern of flow. However there are some overestimations of the simulated water level at C4. The simulated maximum surface inundation during the period of verification for the flood event of 1995 is shown Figure 6. It shows that surface inundation was highest at the lowest part of the study area. Inundation height in most of the areas was within 1m, as mentioned in several reports on the 1995 floods. However, in absence of any ground actual flood inundation map, simulated results could not be verified.

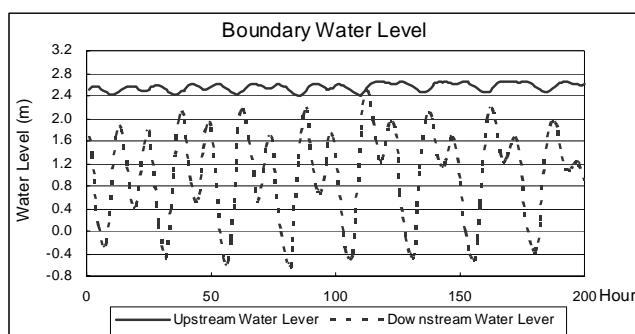


Figure 2. Input hourly boundary water levels at u/s and d/s (from October 23rd to 31st, 1995)

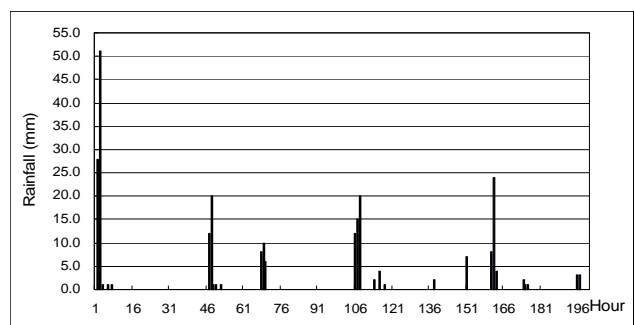


Figure 3. Input hourly average rainfall data (from August 4th to 13th, 1995)

4. IMPACTS OF SEA LEVEL RISING ON FLOODS

For analyzing the impacts of sea level rising on floods in Bangkok, two scenarios are considered, one for 50cm rising of the highest recorded period of sea level based on the past 20 years record and another is 100cm rising. These are close to the highest level of prediction of global average sea level rise in different SRES Scenarios in IPCC study as shown in Figure 7. This is close to the scenario of the highest value predicted by IPCC as 88 cm by the end of the 21st century (Watson, 2001). The hourly time series of water level of floods in 1995 is used as upstream boundary condition and hourly time series of sea level as the downstream boundary condition. The boundary condition data was selected from 23-31 October 1995, the highest water level duration recorded in 1995. Hourly rainfall data was taken for the higher rainfall duration of 1995 floods that is from 4-13 August.

The simulated maximum flood inundation maps for the two selected scenarios of sea level rising are shown in Figures 8 and 9. The simulated results show that almost 55% of the study area will be affected by flood if mean sea level rises by 50 cm and 72% area will be affected if mean sea level rises by 100 cm. Table 1 shows the possible areas of inundation under different flood depths as compared to the 1995 floods, which shows that overall inundation in the study area will be increased by 16% due to 50cm rise of sea level and 34% due to 100cm rise. Similarly, the inundation heights will increase significantly in many locations as shown in Figure 10 for the location a (Pak Num) (Figure 9). These results show there will be serious effects of sea level rising in flooding conditions in Bangkok city and that will in turn lead to high socio-economic consequences.

Table 1. Flood inundation areas in different scenarios

Flood depth in cm	Simulated flood Area in km ² (in %)		
	Floods in 1995	Sea level rise 50cm	Sea level rise 100cm
10-20	987 (29.6)	1025 (30.9)	891 (26.8)
21-50	188 (5.6)	593 (17.8)	1,219 (36.6)
51-100	37 (1.1)	141 (4.2)	189 (5.7)
101-150	37 (1.1)	1 (0.1)	43 (1.3)
151-200	24 (0.7)	43 (1.3)	9 (0.3)
201-250	6 (0.2)	22 (0.7)	51 (1.5)
251-300	0 (0.0)	5 (0.2)	9 (0.3)
301-350	0 (0.0)	0 (0.0)	1 (0.2)
Total	1,279 (38)	1,830 (54)	2,412 (72)

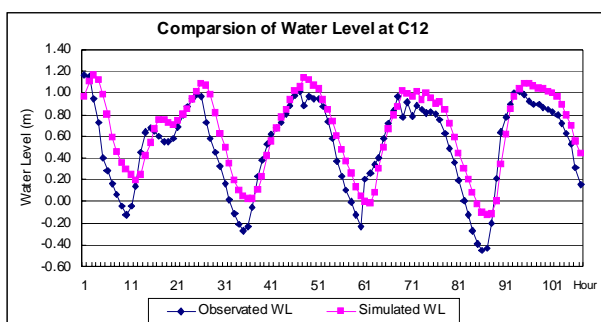


Figure 4. Comparison of simulated and observed water level at station C12

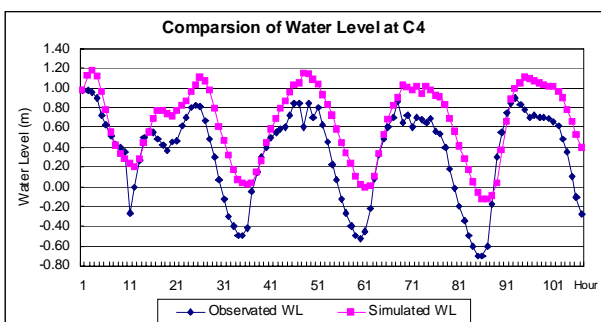


Figure 5. Comparison of simulated and observed water level at station C4

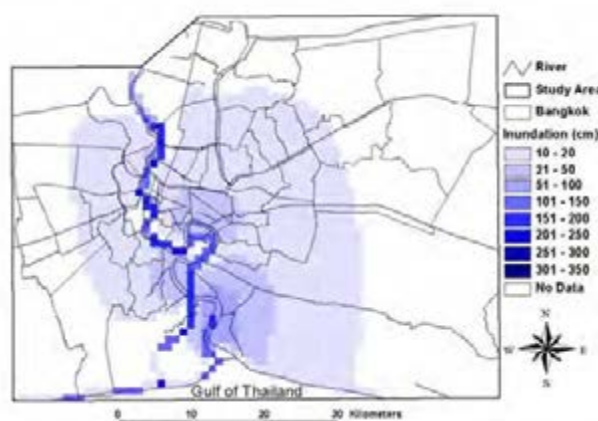


Figure 6. Simulated maximum flood inundation in 1995

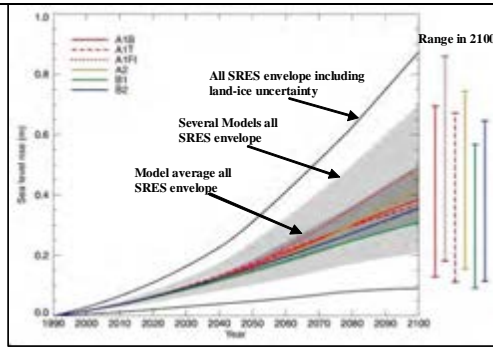


Figure 7. Global average sea level rise (1990-2100) (Church et al, 2001)

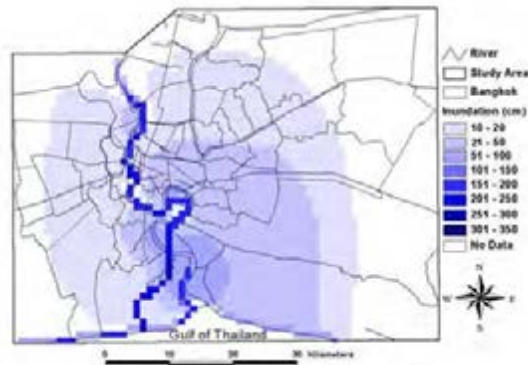


Figure 8. Simulated flood inundation map due to sea level rising to 50cm

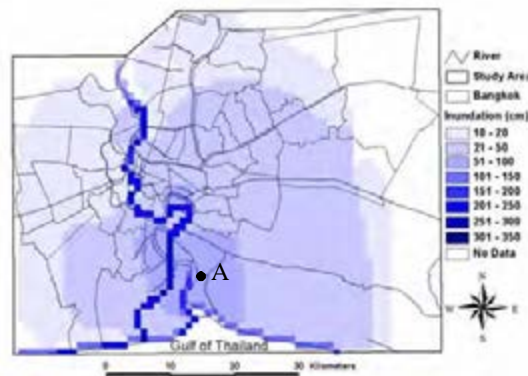


Figure 9. Simulated flood inundation map due to sea level rising to 100cm

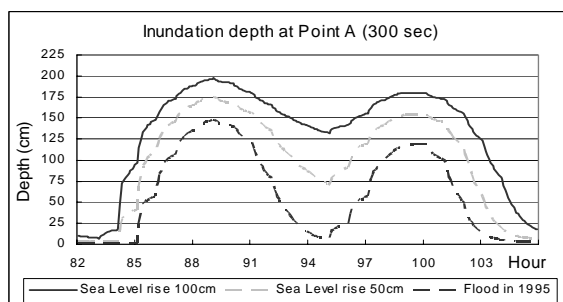


Figure 10. Comparisons of temporal inundation depth variation at Point A between simulated floods in 1995 and floods due to sea level rise by 50 cm and 100 cm

5. ASSESSEMENT OF SOCIO ECONOMIC IMPACTS AND VULNERABILITY

For the assessment of socio-economic impacts of floods, three main socio-economic aspects were considered, they were population, buildings and transportation infrastructure. The existing data and information for three

categories for 2000 were collected at the district levels. The spatial simulation of the future population and urbanization was carried out based on the IPCC SRES B1 Scenario using the AGENT-LUC model (Rajan and Shibasaki, 2000). The maximum population density was designed as 20,000Km⁻². The projected urbanization and population of future scenarios are shown in Figures 11 and 12.

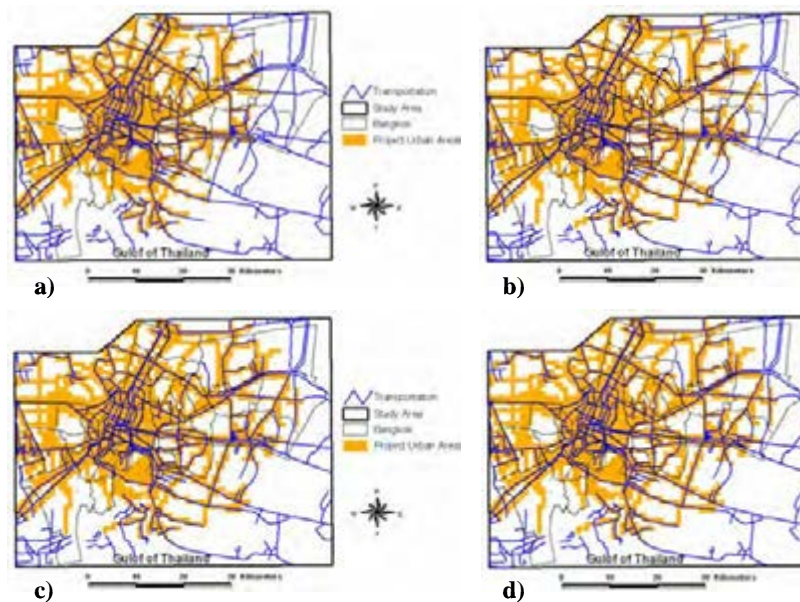


Figure 11. Projected urban area of study area in: a) 2025, b) 2050, c) 2075 and d) 2100

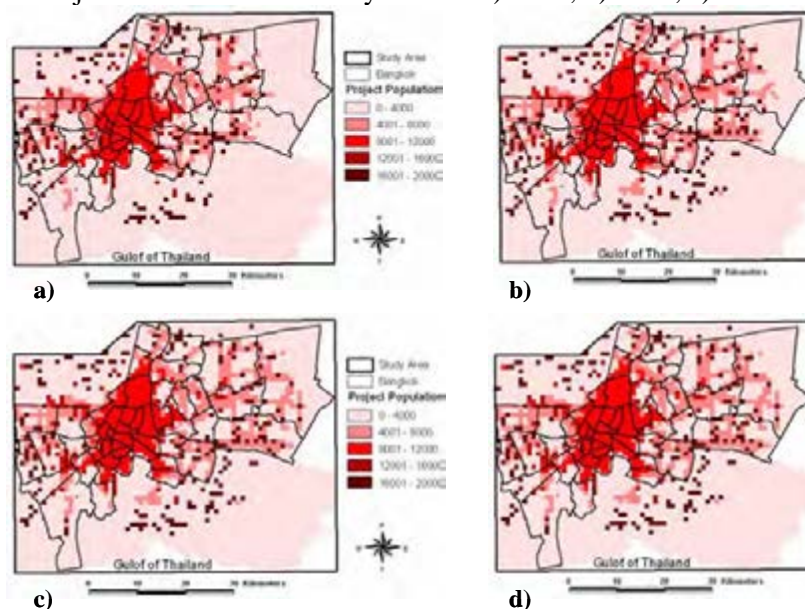


Figure 12. Projected population growth in the study area in: a) 2025, b) 2050, c) 2075 and d) 2100

Flood simulation was carried out by the hydrological model for four scenarios of mean sea level rise in the high predicted levels by IPCC for 2025, 2050, 2075 and 2100 for socio-economic impact analysis. A set of qualitative indices were developed for flood impact estimation for the three

selected categories based on the outcomes of a questionnaire survey conducted among some affected people of the study area in the recent past. Using these indices, outcomes of flood inundations for the projected mean sea level rises and growth of populations, urban buildings and road networks for the selected years, flood impacts for these three sectors were estimated.

Table 2 presents the flood impact indices for buildings. The estimated flood impacts on buildings for the selected years are presented in Table 3. It is observed that the number of affected of buildings in the ‘less impact’ class increases by 1.5 times in 75 years period from 2025 to 2100. Similarly, the number of affected of buildings in ‘moderate impact’ class increases by 30% in 75 yrs period from 2025 to 2100. The increase is not only resulted by the expansion of flood inundation area but also by the growth of urbanization. The flood impact indices for population and number of flood affected people under different categories for the selected years are presented in Tables 4 and 5. Table 5 shows that the number of affected of people in all the three categories will increase significantly during 75 years period from 2025-2100.

Table 2. Flood impact indices of buildings

Depth of flood (m)	Duration of flood (day)				
	< 1	1-2	3-4	5-7	> 7
< 0.1	A	A	A	A	A
0.10-0.60	B	B	B	B	B
0.60-1.00	B	C	C	C	C
1.00-3.50	C	C	C	D	D
> 3.50	D	D	D	D	D

A: No impact, B: Less impact, C: Moderate Impact, D: High Impact, E: Highest Impact

Table 3. Summary of the affected buildings

Impact Index	No. of affected buildings in study area			
	2025	2050	2075	2100
Less	1,145,980	1,451,322	1,629,826	1,791,502
Moderate	82,008	97,071	105,328	110,577

Table 4. Flood Risk Indices of population

Depth of flood (m)	Duration of flood (day)				
	< 1	1-2	3-4	5-7	> 7
< 0.1	A	A	A	A	A
0.10-0.60	B	B	C	C	C
0.60-1.00	C	C	C	C	D
1.00-3.50	E	E	E	E	E
> 3.50	E	E	E	E	E

A: No impact, B: Less impact, C: Moderate Impact, D: High Impact, E: Highest Impact

The flood impact indices for road and length of affected road lengths in the study area during the selected years are presented in Tables 6 and 7. It can be observed that total affected of road in scenario 2100 is much higher than the total affected road length in 2025 which may be attributed to larger flood inundation area in 2100 compared to 2025. The flood impact indices for railways and affected lengths of railway in the study area are presented in Tables 8 and 9. It can be observed that total affected lengths of railway in

future scenarios increases significantly, while the affected railway length under high impact category remains constant.

Table 5. Summary of the affected population

Impact Index	No. of affected population in study area			
	2025	2050	2075	2100
Less	5,720,020	6,804,316	7,632,711	8,969,668
Moderate	134,405	227,777	340,657	446,810
Highest	293,047	311,898	312,903	329,816

Table 6. Flood Risk Indices of road

Depth of flood (m)	Duration of flood (day)				
	< 1	1-2	3-4	5-7	> 7
< 0.1	A	A	A	A	A
0.10-0.60	B	B	B	B	B
0.60-1.00	C	C	C	C	C
1.00-3.50	C	C	C	D	D
> 3.50	C	C	D	D	D

A: No impact, B: Less impact, C: Moderate Impact, D: High Impact, E: Highest Impact

Table 7. Summary of the affected road

Impact Index	Length of affected road in study area (m)			
	2025	2050	2075	2100
Less	569,742	624,118	695,961	837,332
Moderate	65,522	80,041	110,741	133,836

Table 8. Flood Risk Indices of railway

Depth of flood (m)	Duration of flood (day)				
	< 1	1-2	3-4	5-7	> 7
< 0.1	A	A	A	A	A
0.10-0.60	B	B	B	C	C
0.60-1.00	C	C	C	D	D
1.00-3.50	D	D	D	D	D
> 3.50	D	D	D	D	D

A: No impact, B: Less impact, C: Moderate Impact, D: High Impact, E: Highest Impact

Table 9. Summary of the affected railway

Impact Index	Length of affected railway in study area (m)			
	2025	2050	2075	2100
Less	89,050	95,627	105,913	122,016
Moderate	-	-	-	966
High	1,430	1,430	1,430	1,430

6. CONCLUSIONS

The simulated outcomes of the flood model show that almost 55% of the Bangkok City will be affected by floods if mean sea level rises by 50 cm and 72% will be affected if mean sea level rises by 100 cm, which are higher by 16% and 34% respectively as compared to the simulated inundated areas due to the 1995 floods and that will lead to adverse impacts on socio-economic sectors. The outcomes of social-economic impacts

analysis show that number of flood affected buildings and population and road lengths will be rapidly increased due to possible sea level rise from 2025 to 2100.

The outcomes present a macro picture of floods and its socio-economic impacts in the Bangkok City under mean sea level rise scenarios in the 21st Century. Although the severity of the flood magnitudes simulated by the hydrological model is overestimated to a certain extent due to non-inclusion of the existing structural flood control measures such as the east and west dyke systems, retaining walls, pumping stations, diversion canals and the micro details of the topography in the modeling, nevertheless, the model outcomes present a clear picture of potential risk of severe floods and its impacts due to the predicted mean sea level rising in the Bangkok city.

Acknowledgement

The authors gratefully acknowledge the financial supports obtained from the APN Project Grant 2004-CB01-NSY for conducting this study.

References

- Cohen, J.E., Small C., Mellinger A., Gallup J. and J. Sachs (1997). Estimates of Coastal Populations, *Science*, Vol. 278, pp 1211- 1212.
- Dam Jan C. van (2003). Impacts of Climate Change and Climate Variability on Hydrological Regimes, 1st edition, Cambridge University Press.
- Dutta D., Herath S. and Musiaka K. (1997). Distributed Hydrological Model For Flood Inundation Simulation, *Annual Journal of Hydraulic Engineering, JSCE*, Vol. 43, pp 25-30.
- Dutta, D., Herath, S. and Musiaka, K. (2000). Flood inundation simulation in a river basin using a physically based distributed hydrologic model. *Hydrological Processes* 14: 497-519.
- Jha, R., Hearth S. and Musiaka K. (1997). Development of IIS Distributed Hydrological Model (IISDHM) and its application in Chao Phraya River Basin, Thailand, *Annual Journal of Hydraulic Engineering, JSCE*, Vol. 41, pp 227-232.
- Rajan, K.S. and Shibazaki, R. (2000). Land Use/Cover Change and Water Resources – Experiences from AGENT-LUC Model, *Proceedings of the APFRIEND Workshop on Mekong Basin Studies, INCEDE Report 19*, University of Tokyo, Japan, pp. 1-16.
- Thammasittirong (1999). *Operational Flood Forecasting for Chao Phraya River Basin*, Thesis WM-99-23, AIT, Thailand,
- Waston, R.T. (2001). Climate Change 2001, *Six conference of Parties to the United Nations Framework Convention on Climate Change*.

SURVEY ON RESIDENTS' ATTITUDES FOR RETROFITTING OF EXISTING VULNERABLE HOUSES

Miho YOSHIMURA

International Center for Urban Safety Engineering
Institute of Industrial Science, The University of Tokyo, Japan
yosimura@iis.u-tokyo.ac.jp

Kimiro MEGURO

International Center for Urban Safety Engineering
Institute of Industrial Science, The University of Tokyo, Japan
meguro@iis.u-tokyo.ac.jp

ABSTRACT

From recent damaging earthquakes, it is clearly found that retrofitting of low earthquake-resistant houses is the key issue for earthquake disaster reduction. However, the homeowners possess various reasons not to retrofit their houses. In this research, a questionnaire survey was conducted to homeowners in Japan in order to find more effective strategies for promotion of retrofitting vulnerable houses based on residents' needs. The main factors that encourage or discourage homeowners to retrofit their houses were identified. Moreover, their anxiety for uncertainty of building strength after retrofitting and the activities of dishonest contractors were also pointed out. Finally, based on the homeowners' attitudes, some suggestions were presented to improve the current strategies for promotion of retrofitting vulnerable houses.

1. INTRODUCTION

Even if a very good disaster response system and/or disaster recovery and reconstruction plan is available, it is impossible to reduce earthquake damage without implementing proper mitigation techniques. The 1995 Kobe earthquake caused 6,433 dead and 43,792 injured people. It is reported that 87% of people were killed in their own homes due to the collapse of the structure or the falling furniture, as the occurrence time of the earthquake was early in the morning, 5:46 am. Considering this fact, the only way to save these lives was to increase the strength of their residences by retrofitting or rebuilding them before the event.

Based on the actual earthquake damage, the structural seismic design code has been revised several times in Japan. The final (before the Kobe Earthquake) code revision was done in 1981. The structures that were constructed using this code performed well even under the strong ground motion of the Kobe earthquake as shown in Figure 1. However, there are many vulnerable ones among the structures constructed before the 1981

code revision. According to the Ministry of Land, Infrastructure and Transport Government of Japan, the number of vulnerable timber single-family houses are estimated to be 10 million in total 11.5 million houses constructed before 1981. In spite that these structures need to be retrofitted before the next big event occurs in order to reduce the earthquake damage, retrofiting activities are not carried out widely especially for private houses. Some municipalities or local governments have conducted systems to promote retrofiting activities such as, the assistance system, and the low interest loan for seismic evaluation or retrofiting of structures. However, the homeowners possess various reasons not to retrofit their houses. Unfortunately, so far, there is no municipality in which the retrofiting activities have been successfully carried out in Japan.

In this research, a questionnaire survey was conducted to homeowners in Japan in order to find more effective strategies for promotion of retrofiting existing vulnerable houses based on residents' needs. The main factors that encourage or discourage homeowners to retrofit their houses were identified. Moreover, their anxiety for retrofiting work was analyzed. Finally, based on the homeowners' attitudes, some suggestions are discussed to improve the current strategies for promotion of retrofiting existing vulnerable houses.

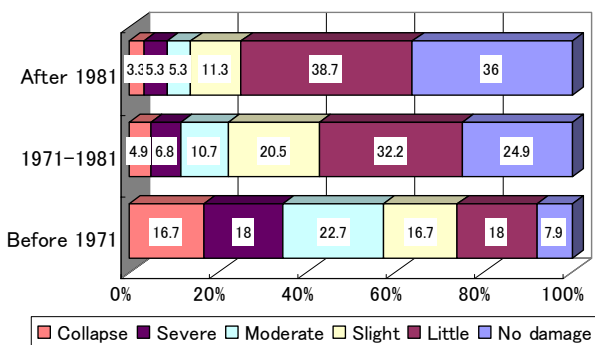


Figure 1: Damage ratio of pre-code and current-code structures

Table 1: Estimated number of vulnerable pre-code houses

Number (Million)	Houses (including all the construction type)	Timber single-family houses
Total number	46.9	24.5
Number of houses constructed before 1981	17.6	11.5
Number of vulnerable houses constructed before 1981	11.7	10.0

2. OUTLINE OF THE QUESTIONNAIRE SURVEY

A questionnaire survey was conducted for the head of a household (or, the spouse of the head of a household) of 30-69 years old who lived in the owner-occupied house in Tokyo Metropolitan region, by the internet survey form. Investigation periods were December 17-23, 2004, and it got the answer of 2,604. The number of respondents was classified by the construction year of their houses in Figure 2. The rate of the respondents who live in the pre-code houses was 17.1%. Considering that the rate of pre-code houses is 50.7% according to the national statistics of building stocks, the observed rate of pre-code houses was smaller than

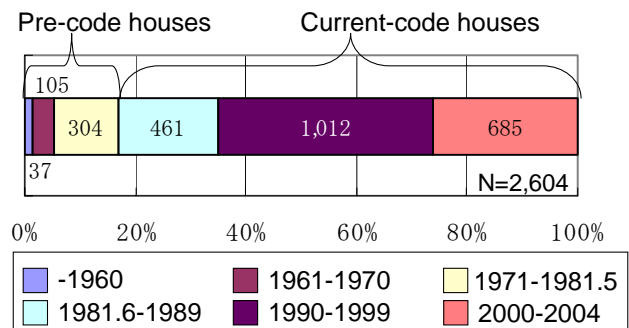


Figure 2: Number of respondents classified by construction year of their houses

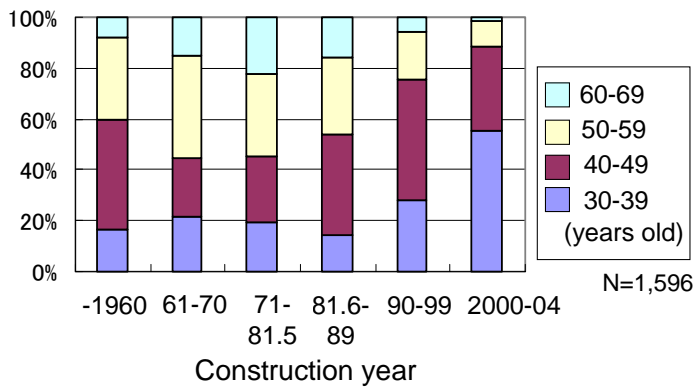


Figure3: Number of respondents classified by their age and construction years of the houses

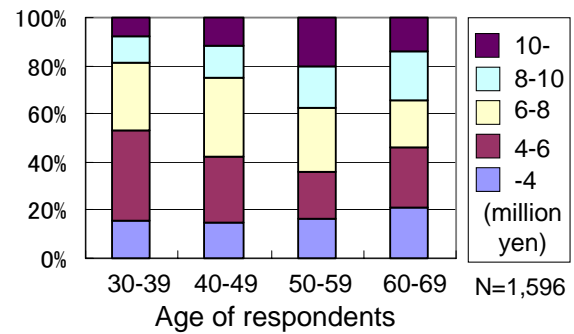


Figure4: Number of respondents classified by annual incomes levels

the real situation because the survey was done using an internet environment. The 1,596 respondents who lived in the timber single-family houses were selected among total 2,604. The relation between the age of these respondents and the construction year of their houses was shown in Figure 3. The respondents of 50-59 years old had highest annual incomes as described in Figure 4.

3. HOMEOWNERS' WISHES TO RETROFIT THEIR HOUSES

First, homeowners' earthquake risk perception was observed. Figure 5 is the expectations of the earthquake occurrence of the 1995 Kobe Earthquake level classified by the constructions year of their houses. Any statistically significant difference wasn't seen in each construction year. Figure 6 shows the expectations of structural damage to the houses when a great earthquake of the 1995 Kobe Earthquake level occurred. Homeowners expected severer damage as their houses became old. More than 50% of homeowners answered severe damage to their houses in case of the houses constructed before 1970.

Then, homeowners' wishes to retrofit their pre-code houses were investigated by five steps of "I strongly wish, I wish, I don't wish, I never wish to retrofit my house, I have already retrofitted my house". Regardless of the construction year of houses, the rate of homeowners who "strongly wish or wish" to retrofit their houses was about 35% as shown in figure 7.

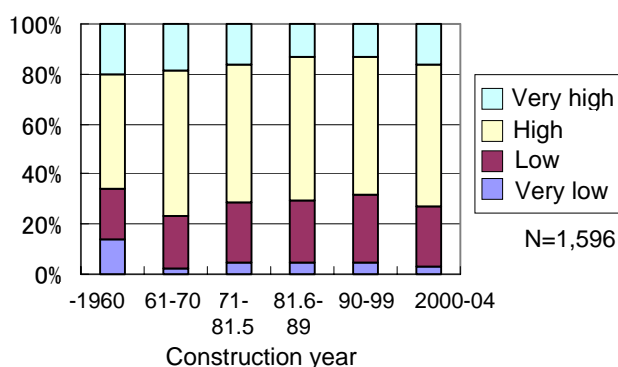


Figure5: Expectation of earthquake occurrence classified by construction year

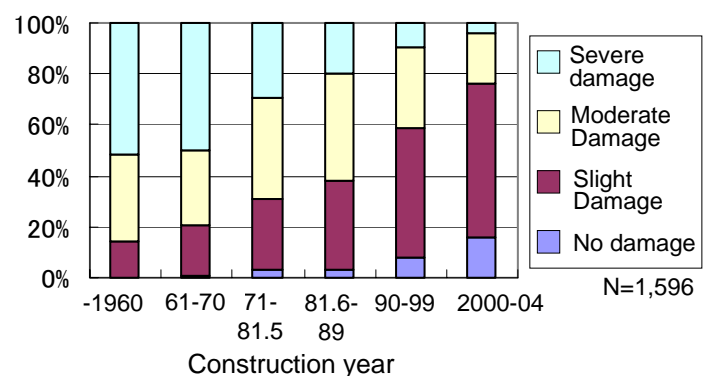


Figure6: Expectation of structural damage to the houses by construction year

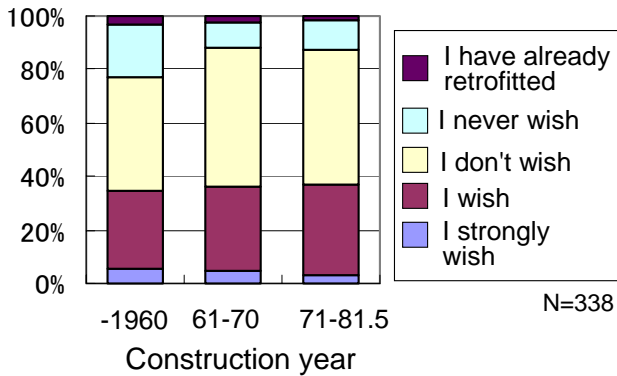


Figure7: Homeowners' wishes to retrofit pre-code houses

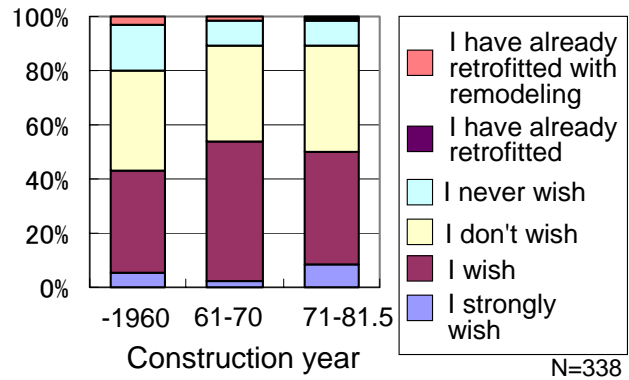


Figure8: Homeowners' wishes to retrofit pre-code houses in case of low retrofitting cost

Usually, the cost of retrofitting is remarkably reduced (to the 1/2-1/3 price) if retrofitting and remodeling is done at the same time, because it doesn't require the cost for restoring the interior. As the next question, we asked whether they wish to retrofit their houses in case that low- cost retrofitting techniques (1/2-1/3 of current price) are available. Compared with figure 7, the homeowners who wish to retrofit increased respectively by 9% 17% 13% in each construction year. It was confirmed that high cost was one factor that discourages retrofitting for the homeowners who changed their attitudes in case of low retrofitting cost. On the other hand, the rate of the homeowners who never wish to retrofit was almost same between figures 7 and 8. It means that these homeowners didn't wish to retrofit due to some reasons except for economical problems.

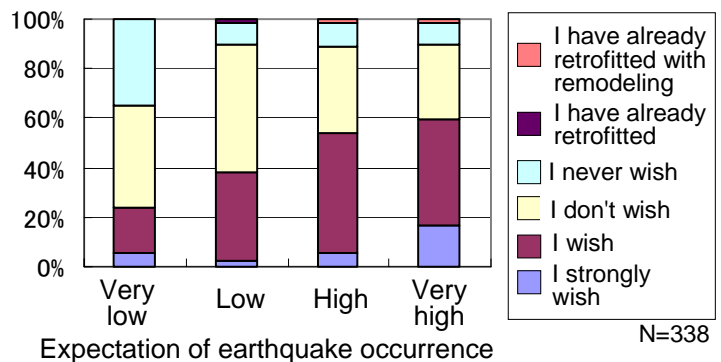


Figure9: Relations between homeowners' expectation of earthquake occurrence and their wishes to retrofit pre-code houses

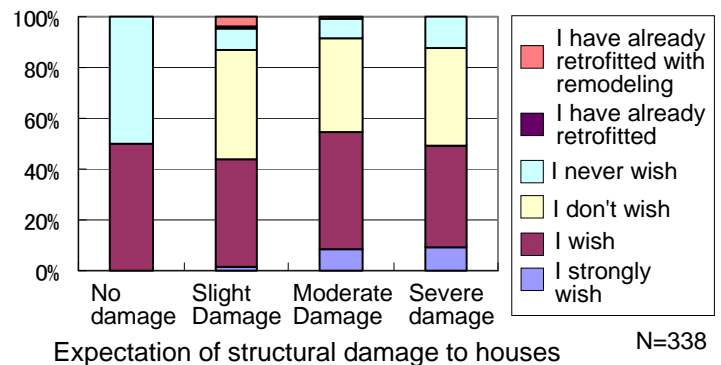


Figure10: Relations between homeowners' expectation of structural damage and their wishes to retrofit pre-code houses

Figure 9 is the relation between homeowners' expectation of earthquake occurrence and their wishes to retrofit pre-code houses. As the homeowners recognized high risk of a huge earthquake, their wishes to retrofit increased. The relation between homeowners' expectation of structural damage in case of a huge earthquake and their wishes to retrofit pre-code houses was also analyzed in figure 10. It was observed that about 50% of homeowners don't wish to retrofit their pre-code houses due to some other reasons even if they expect severe damage to their houses in case of a huge earthquake.

4. MAIN FACTORS THAT ENCOURAGE OR DISCOURAGE HOMEOWNERS TO RETROFIT THEIR HOUSES

In the previous chapter, we observed that various reasons may affect the decision-making of homeowners to retrofit their pre-code houses. Here, main factors that encourage or discourage homeowners to retrofit the pre-code houses were discussed. First, various reasons that may affect the decision-making to retrofit their pre-code houses were shown to respondents and they answered their attitudes to each reason by three steps of "I strongly agree, I agree, I don't agree to the reason". Then, the difference of the rate of "I strongly agree" for each reason was calculated among the homeowners who consent or oppose to retrofitting in figure 8. Obtained difference is regarded as an index that shows how much each reason affects decision-making of retrofitting. If this become plus value, the reason is classified to be a factor that encourage retrofitting. If it is minus, the reason becomes a factor that discourages retrofitting.

Both factors were described in figures 11 and 12. The main factors that encourage homeowners to retrofit their houses were identified as the wishes for saving their families and properties, and the fears of a sudden earthquake. The biggest factor that influences the homeowners not to decide retrofitting was their hesitation between retrofitting and rebuilding. The pre-code houses were built more than 24 years ago. Considering that average lifespan of a timber house in Japan is 26 years, it is reasonable that the decision-making between retrofitting and rebuilding become a big problem. Other negative factors were found as follows: lack of money, fears of being disturbed, optimism for earthquake disaster, to give off their fighting attitudes against earthquake disaster and confidence in building strength. The ratio of confidence in building strength was only 4% among the total factors that discourage retrofitting. The respondents had severer economical, physical, mental problems compared with the problems in perception of structural damage risk.

We confirmed that the reasons why homeowners don't wishes to retrofitting their vulnerable houses are very complex. This fact implies a combination of the strategies for improving all the factors that discourage retrofitting is necessary.

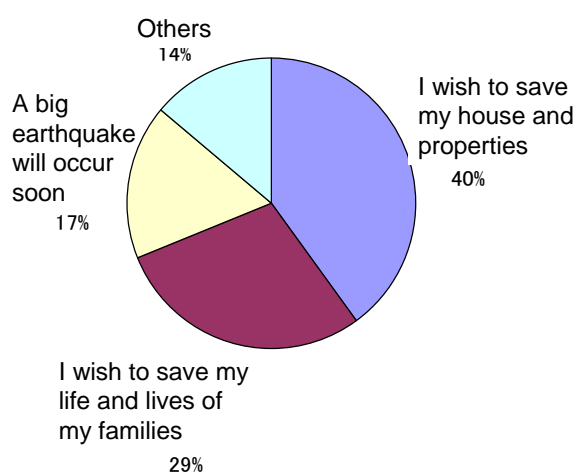


Figure 11: Main factors that encourage homeowners to retrofit their houses

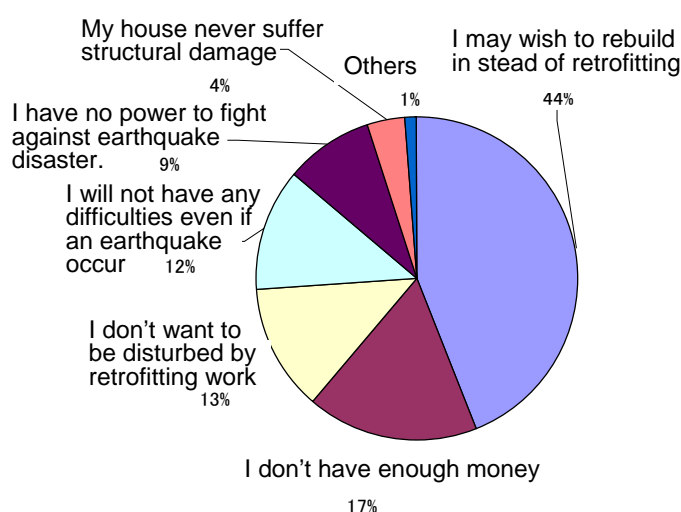


Figure 12: Main factors that discourage homeowners to retrofit their houses

5. HOMEOWNERS' ANXIETY ON RETROFITTING OF THEIR HOUSES

Moreover, the homeowners who wished to retrofit their pre-code houses were asked about their anxieties on retrofitting work. The rate of the homeowners who didn't have any anxieties was around 15% among total respondents as shown in figure 13. The biggest anxiety was "My house may suffer structural damage if it is retrofitted". When answers are seen by the age of respondents, the rate of the homeowners who feared it increased up to about 65% in case of the respondents of 50-59 and 60-69 years old. Another big anxiety related to technologies was "Seismic diagnosis may not be trustworthy". In order to lesson these anxieties, developing safer retrofitting techniques and proving the safety of retrofitted houses to homeowners through experiments, demonstration, and simulations are very important.

Several anxieties for the existence of dishonest contractors were also observed. Many homeowners felt fear such as "The contractor may do unreliable work", "The contractor may charge unreasonable retrofitting cost". These fears were stronger especially in young homeowners as shown in figure 13. On the other hand, these fears were relatively weak in elder homeowners. Recently in Japan, a lot of crimes that dishonest contractors deceive elder homeowners into retrofitting their houses at unreasonably expensive cost were reported. The carelessness for the existence of dishonest contractors in elder homeowners observed in figure 14 may be one reason of these crimes. As a result, it was verified that raising homeowners' knowledge regarding retrofitting cost and techniques was important in order to help their distinguishing dishonest contractors. Constructing a database of retrofitting works including the detail information such as average costs and characteristics of construction may be useful for this.

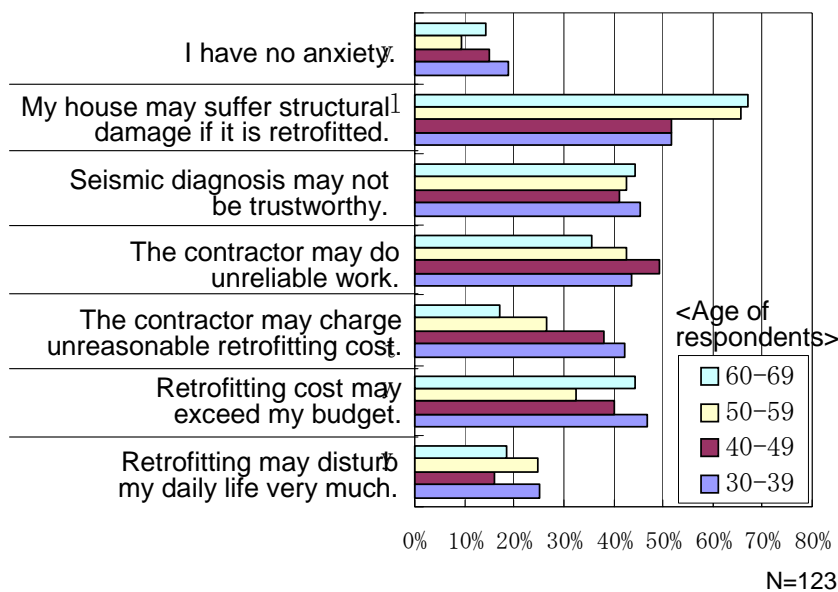


Figure 13: Homeowners' anxieties on retrofitting their houses

6. HOMEOWNERS' ATTITUDES TOWARD INCENTIVE SYSTEMS FOR RETROFITTING THEIR HOUSES

Finally, homeowners' attitudes toward the governmental systems that give incentives to retrofitting vulnerable houses were discussed. As the incentive systems, six typical incentive systems were selected. Providing free seismic diagnosis using simple flowchart, financial assistance to seismic diagnosis by special engineers, financial assistance to retrofitting work, recommendation of honest contractors were currently put into practice in some municipalities in Japan. In addition, two newly-proposed systems, "A system for providing non-financial incentive by retrofitting assurance" and "tax exemption", were also taken into consideration. "A system for providing non-financial incentive by retrofitting assurance" is a new idea proposed by authors for promoting retrofitting. The concept is illustrated in figure 14. Under this system, the government bears a portion of the building repair and reconstruction expenses if retrofitting is implemented by the owner following the guidelines before an earthquake and in spite of this the structure is damaged. It has a great merit that the government does not need to prepare huge budget before the disaster compared with the current financial assistance system. Authors proved from simulations in the previous researches that the earthquake damage and the governmental cost burden after the earthquake can be reduced with this system even if the government provides incentive money described in figure 14.

The rate who answered that each incentive system is effective was shown by the age of respondents in figure 15. As a result, the homeowners of the 50-59 years old thought little of financial assistance to seismic diagnosis and retrofitting, compared with the system for recommendation of honest contractors and free seismic diagnosis using simple flowchart. They might not be strongly attracted to financial assistances due to their high income. On the other hand, the homeowner at the 60-69 years old thought highly of all the incentive systems except for recommendation of honest contractors. The reasons for this was analyzed to be their low income, high fear in insufficient structural strength after retrofitting and carelessness for unreliable contractors as shown in figures 4 and 13.

These generation gaps of favorite retrofitting incentives suggests that the strategies for providing suitable incentives for retrofitting considering differences in homeowners needs is very useful for promoting retrofitting houses.

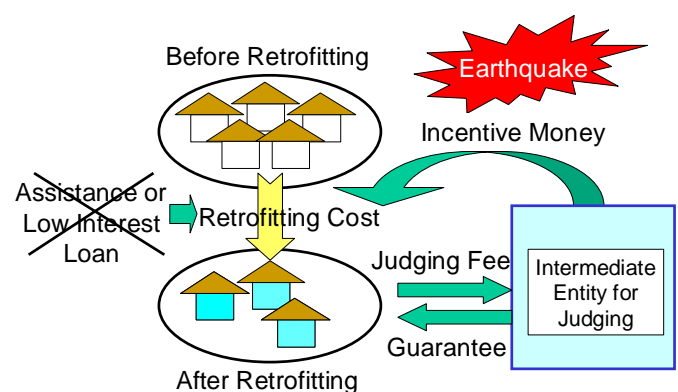


Figure14: Concept of a system for providing non-financial incentive by retrofitting assurance

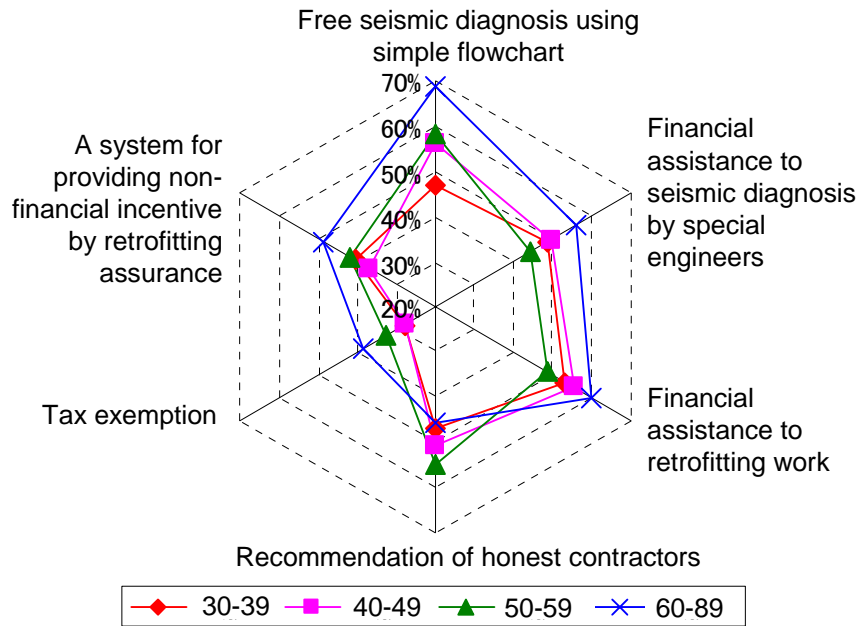


Figure 15: Homeowners' attitudes toward incentive systems for retrofitting their houses classified by their age

6. CONCLUSION

In this research, a questionnaire survey was conducted to homeowners in Japan in order to find more effective strategies for promotion of retrofitting of existing vulnerable houses based on residents' needs. First, homeowners' wishes to retrofit their pre-code houses were analyzed considering their earthquake risk perception, their economical and social situation. Next, the main factors that encourage or discourage homeowners to retrofit their houses were identified. Moreover, their anxieties for uncertainty of building strength after retrofitting and the activities of dishonest contractors were also pointed out. Finally, homeowners' attitudes toward the governmental systems that give incentives to retrofitting vulnerable houses were discussed. The differences in favorite incentive systems by generations were observed. As a result, the importance in developing suitable strategies of improving incentive system considering these differences was suggested.

REFERENCES

- Kobe City, 1996. *Hanshin-Awaji Earthquake Disaster –Record of Kobe City*, Japan.
- The Ministry of Land, Infrastructure and Transport Government of Japan, 2005. A proposal for promoting disaster mitigation countermeasures for structures. <http://www.kenchiku-bosai.or.jp/topics/050610a.pdf>, Japan
- YOSHIMURA, M., and MEGURO, K., 2003. Proposal of Retrofitting Promotion System (RPS) for Low Earthquake-resistant Structures in Shizuoka Prefecture, Japan, *7th US/Japan Workshop on Urban Earthquake Hazard Reduction*, Hawaii, USA.

A CASE STUDY IN REHABILITATION OF A LARGE INDUSTRIAL STRUCTURE

KUMAR NEERAJ JHA* and SUDHIR MISRA#,

* Visiting Faculty, Dept of CE, IIT Delhi, New Delhi, India 110 016*,

Associate Professor, Dept of CE, IIT Kanpur Kanpur, India 208 016

*knjha@civil.iitd.ac.in #sud@iitk.ac.in

ABSTRACT

Modernization of old industrial structures often needs to be undertaken in urban or semi urban environments, imposing restrictions on the methods of demolition and construction that can be used, and quite different methodologies need to be adopted in these cases compared to those used in new construction.

This paper describes the rehabilitation of an old industrial shed measuring about 66m x 286 m made with brick masonry walls varying between 500 to 700mm, with a 400mm thick masonry arch slab made with surki chuna (lime). The shed was replaced with a shell structure resting on RC columns, with precast prestressed concrete girders and folded roof. The job required working while the plant was running, which posed a lot of challenges and called for specialized design and construction methods, and planning of all activities to the last detail.

The existing masonry walls were underpinned, and the footings for new columns were laid. After the columns were raised to the required height, the concrete girders and folded roof elements were placed in position at a height greater than the existing roof. The wall elements were also precast. The existing roof, etc. were then demolished in parts with appropriate arrangements to safeguard the equipment, etc. The challenging work was completed using innovative construction methods based on sound engineering practice without damage to equipment or injury to plant workers.

1. INTRODUCTION

This case study for rehabilitation of an industrial structure carried out in an urban environment, keeping the plant in operation all the time, refers to a project located in a small town in the state of Uttar Pradesh in northern India. The value was of the project to the contractor was INR 96 million, not including the cost of cement and steel, which were supplied by the owners (at their cost). The project was initially scheduled for completion in 25 months, though it took much longer as additional works were taken up in the course of the work, and finally completed in March 1999.

The basic objective of the project was to modernize the existing factory building and fully automate the manufacturing unit. It may be noted that the building had been apparently built more than 150 years ago, and some of the bricks found during the dismantling bore marking of manufacture in 1835. The building comprised of different units such as godowns for tobacco leaf, primary manufacturing and secondary process departments, shipping department and warehouses. The unit was used for production of cigarettes (daily production worth INR 30 million) and required dust free environment. Thus, the work needed to be executed without affecting the production line. The owners had hired an independent architectural and structural consultant who provided the basic layout and structural drawings, and the detailed work was carried out by the contractors. Though ‘*as-existing*’ drawings were prepared, changes in structural design and layout were necessitated during the execution of the project, keeping in view the process and plant layout requirements and the existing plant and equipment.

2. EXISTING AND PROPOSED STRUCTURE

Figure 1 shows a typical section and plan of the old building, which was developing cracks at several locations. It was made of thick brick walls with surkhi lime and arch roof slab of total span 6m. The arches were supported on 300 mm diameter 25mm thick cast iron columns.

It may be noted that the height of the building was only 3.6m, which could not accommodate the new equipment to be installed. Hence the new design envisaged RC column beam construction with a folded plate roof, with the roof level raised to 10.2m. The plan of the new design is given in **Figure 2**, and it be seen that the building was planned in 13 grids (1 to 13, @ 22m) in one direction and 4 grids (A to D, @ 21m) in other direction. At the junction of these grids, cast *in situ* RC columns predominantly of H shape and square shapes depending on the functional requirement were provided.

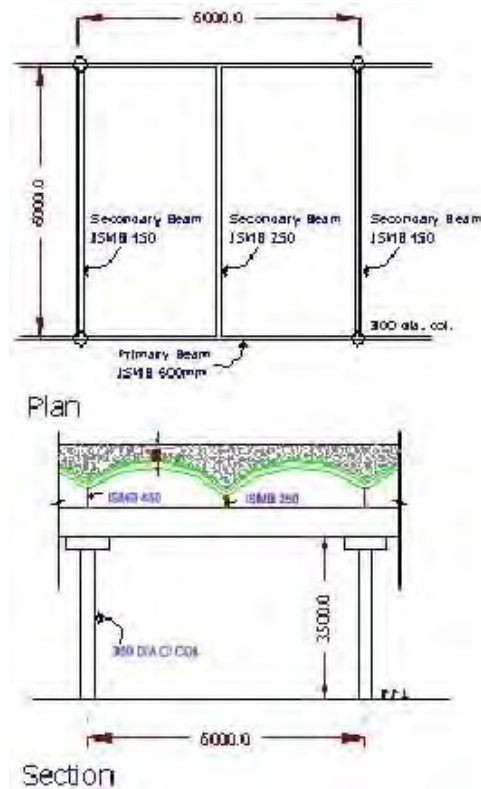


Fig 1: Plan and section of existing building

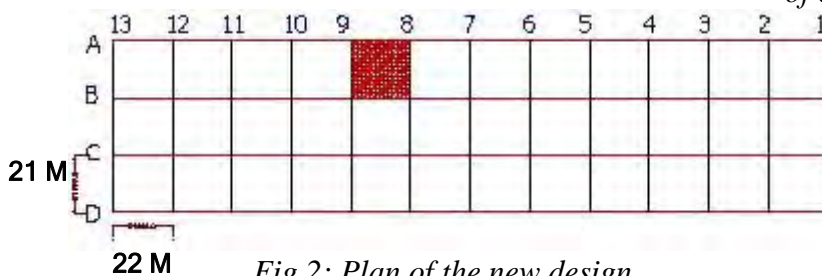


Fig 2: Plan of the new design

Prestressed concrete girders rested on the column in A-D grid direction supporting the folded roof plates. Precast wall panels were also provided for the exterior of the building.

3. CHALLENGES IN CONSTRUCTION

Space constraint

The layout of the new building, prepared in accordance with the present day byelaws specified by the local regulating authority, keeping in mind the need to preserve and if possible increase the floor space available, led to serious space constraint, e.g. the space between edges of a new column and the face of the old external wall was hardly 50 mm.

Another issue related to constrained space for construction activity was that the entire area was not handed over to the contractor at once, and hence construction had to be carried out in a phased manner. In fact, certain areas had to be completed in all respects, and handed back to the owner before fresh areas could be released. Thus, the construction work started along the panels ABCD from Grid 8 and proceeded towards Grid 13 in the first phase and then moved again from Grid 8 towards Grid 1.

Material Storage and Movement

Since production could not be stopped in situ concrete work was avoided to the extent possible, and in cases where precasting was not feasible special arrangements for construction materials and transportation of concrete, etc. had to be made. For example, inside the building, use of any motorized construction equipment was not permitted due to the likely effect of emitted gases on the quality of cigarettes produced, and therefore, concrete and other materials were shifted using horse carts. This also helped in cases where special precautions had to be taken to protect manual labour, e.g. areas with tobacco dust, etc. where the number of men deployed could thus be substantially reduced.

Safety

Special barricades were constructed with locking arrangement around footings of the new RC columns during construction. All workmen and staff were equipped with personal protective gear such as safety helmets, safety belts fall arrester, etc. Fire extinguishers were positioned at all vulnerable points, and welders used asbestos fire clothes to prevent fire related accidents. An appropriate system was developed to allow operations such as welding or gas cutting in the plant area, through special permits from the safety division of the operating plant, and properly visible signs were erected when the work was in progress.

4. CONSTRUCTION SEQUENCE

At peak mobilization, the contractor engaged 36 staff consisting of managers, senior engineers, engineers, supervisors, and foremen and about 450 site workmen. As far as equipment is concerned, gantry cranes of different capacities such as 5 tonnes, 10 tonnes, and 100 tonnes, launching girders of about 66m length in two pieces, mobile crane, trailers, pre-stressing devices, concreting equipments, and equipment for steam curing, were mobilized. In order to arrive at the suitable construction sequences apart from established practices, of formwork design, precasting, and erection, (e.g. Peurifoy 1964, Harris 1989, Andres and Smith 1998), input from the owner's departments were taken into account. Frequent brainstorming sessions were held with all engineers involved to improve efficiency of construction.

Underpinning of interior column

First of all a footing for the new column was laid out on the floor. The supporting schemes for transferring the existing load on to the existing floor, is outlined in **Figure 3**, and basically consisted of the following steps: Two steel beam sections (ISMB 600 or ISMB 300 depending on the loads) were buried in the floor, such that their top was flush with the existing floor level so as not to impede production. Two trestles (made with angle section kept at four corners and braced) were kept on the ISMBs buried earlier. Now loads from the top beams were transferred to the trestle using appropriate packing and jack system at the top.

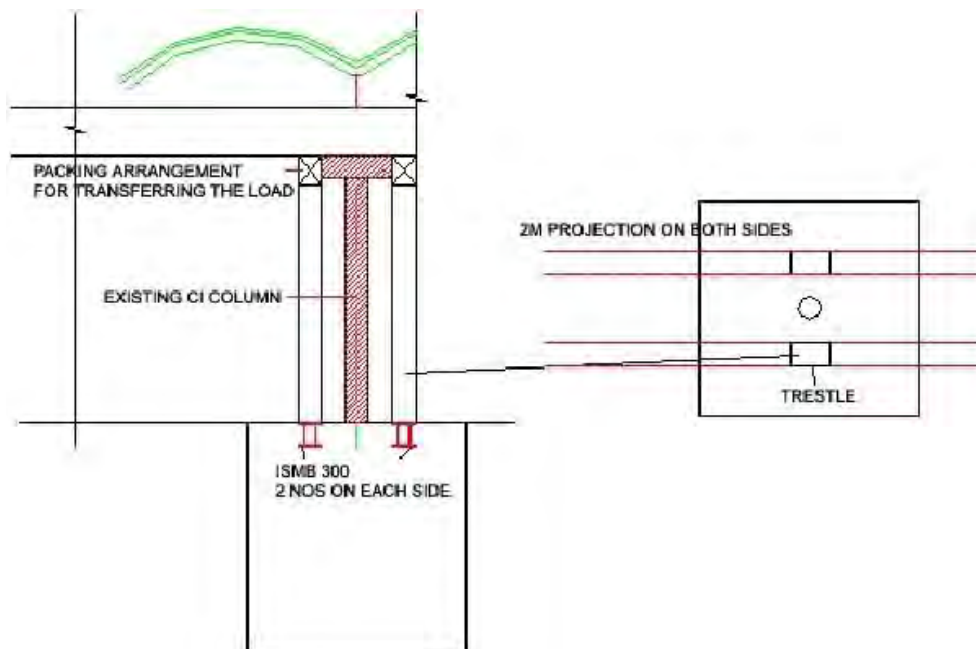


Fig 3: Underpinning arrangement for interior columns

Thus, the load was completely taken off the old columns, which could be removed, and work for the footings of the new column taken up. The depth of excavation for the new footings varied between 3m to 3.3 m. Since the soil was sandy, all sides had to be supported using shoring with the help

of planks and steel channel sections. The bottom was then compacted and new footing was cast *in-situ*. Reinforcement was tied for columns and first column lift of 2.4m height (to the bottom of 900mm deep plinth beam (whose top was flush with the floor level) was cast by leaving dowels for plinth beams. These dowels were coated with cement slurry and wrapped in plastic sheets and finally buried to be taken later for construction. Subsequently the other two lifts were also cast, to take the columns to a height just below the existing ceiling level. When it came to fourth lift the existing roof was carefully punctured at the locations of the new columns, and columns cast up to the required height (8m from existing floor level). After holes were made in the existing roof, care was taken to ensure that dust etc. from the outside did not enter the plant through these holes. Once the column casting at one location was complete, the damaged floor in this area was repaired and was handed over to client temporarily. This cycle from underpinning to temporary handover took about 20 days. It may be mentioned, that special care had to be taken to minimize generation of dust during demolition and construction and the debris from old footings, etc. were removed and disposed outside the building manually.

Underpinning for exterior column/wall

It may be noted that the new design provided for RC columns and shear walls at some grid locations to take care of earthquake loads, for the exterior columns. At the outset, footings were laid out on the floor and outside the building. The scheme used for supporting existing loads, is given in **Figure 4**. All walls were punctured at floor level and steel beams were inserted at 2m c/c due to the heavy loads on the columns. Then a notch of about 230mm was made along the length of the wall to accommodate another steel beam perpendicular to the beams laid earlier. It may be noted that the existing walls were more than 500mm thick. Similarly to the other side of the wall another notch was cut and a second beam inserted. Packing wherever required was done. Now, in this configuration, the loads from the walls were transferred to the beams, which in turn were transferring to the floor, and the footings of wall and columns of the existing structure could be dismantled. Construction of the new footing, columns and shear walls was carried out in a manner similar to that outlined for interior columns above, and the cycle time from underpinning to temporary handover was 35 days.

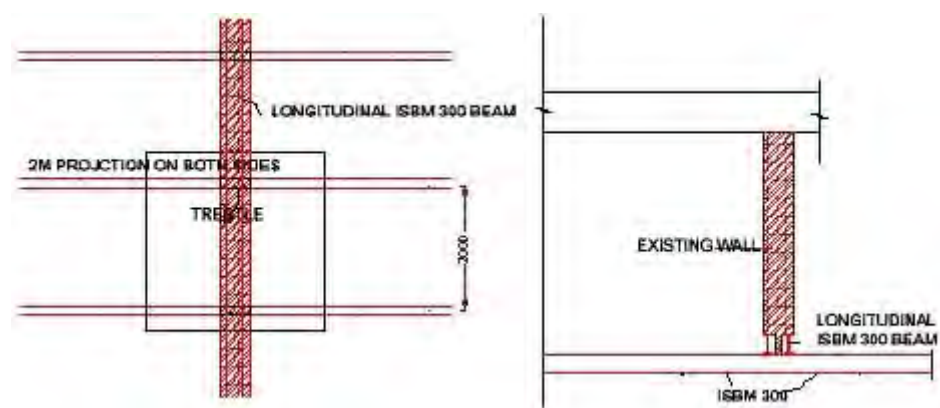


Fig 4: Underpinning arrangement for Exterior columns and wall

After 28 days of casting of in-situ columns, these were ready for receiving precast elements such as Y-girder, folded plates and wall panels. The precasting details of these elements are given below.

Precasting operations

As mentioned earlier three broad types of elements – girders and folded plates for the roof, and the wall panels, were precast, and Table 1 gives a brief summary of the operation and a more detailed discussion is given in the following paragraphs. A casting yard complete with facilities for steam curing, etc. was setup close to the site, and appropriate arrangements made for transportation and storage of elements.

Table 1: Details of precast elements

Element	Wt (t)	Numbers	Molds prepared	Remarks
Y-girder (20.7m long)	50	52	Six plywood and timber moulds	Normal curing, prestressing was carried out at the age of 28 days after casting.
Folded plates	15	432	Two steel moulds	Steam curing adopted
Wall panel	4 to 9.55	282	One each of all the types of negative mould	Normal curing

Y-girder and wall panels: The Y-girders were cast and prestressed in the casting yard. The shape of the wall panels was such that the contractor had to use a *negative* mould for their casting. Now, for making this mould, angle frames, brickwork enclosing the waste-fill, and plain concrete was used to get the desired profile of the wall panel. Once the mould was ready the reinforcements were tied and wall panels were cast. These were water cured subsequently and shifted to the stacking yard from where they were shifted again to the erection location.

Folded plates: A typical cross section of the folded plates is shown in **Figure 5**, and it can be seen that, precasting of folded plates was carried out in two stages. In the first stage after cleaning the moulds, and tying of reinforcement for two flaps, concrete was cast. Now, these flaps were lifted after 3 hours of concreting and aligned as required. In the second stage the diaphragm and bottom portion of the folded plates were cast.

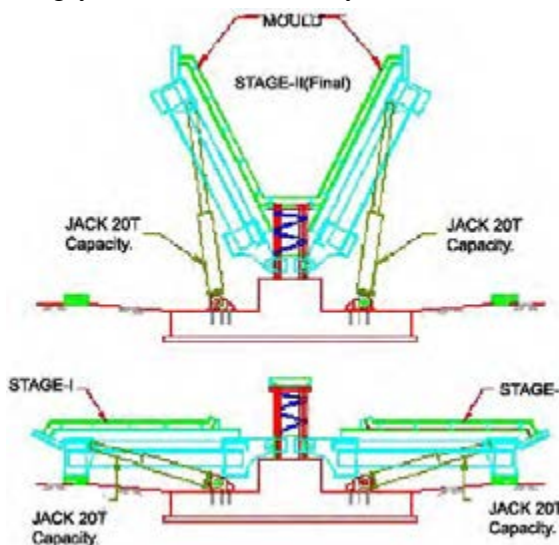


Fig 5: Folded plate casting

These elements were then steam cured and shifted from the casting yard to the stacking yard where they were further water cured for the required duration.

5. ERECTION AND JOINTING SCHEME

It may be mentioned here that before erection of precast elements, plinth beams were cast by exposing the dowels left earlier in a phase wise manner without disrupting the production. The following paragraphs describe the erection and assembly of the precast elements.

5.1 Y-girders

A typical erection sequence is shown in **Figure 6**. It may be noted that while the erection work for the girder is being carried out at a level of 8m, the roof of the existing building can be clearly seen in the photograph. Temporary brackets were fixed on both sides of the columns already cast upto their full height. The launching girder was then erected on these brackets. The plan was drawn up to cover the entire distance of the grid ABCD (66m) in a single effort – this was accomplished by erecting the launching girder in two pieces of 33m each on either side of the column.

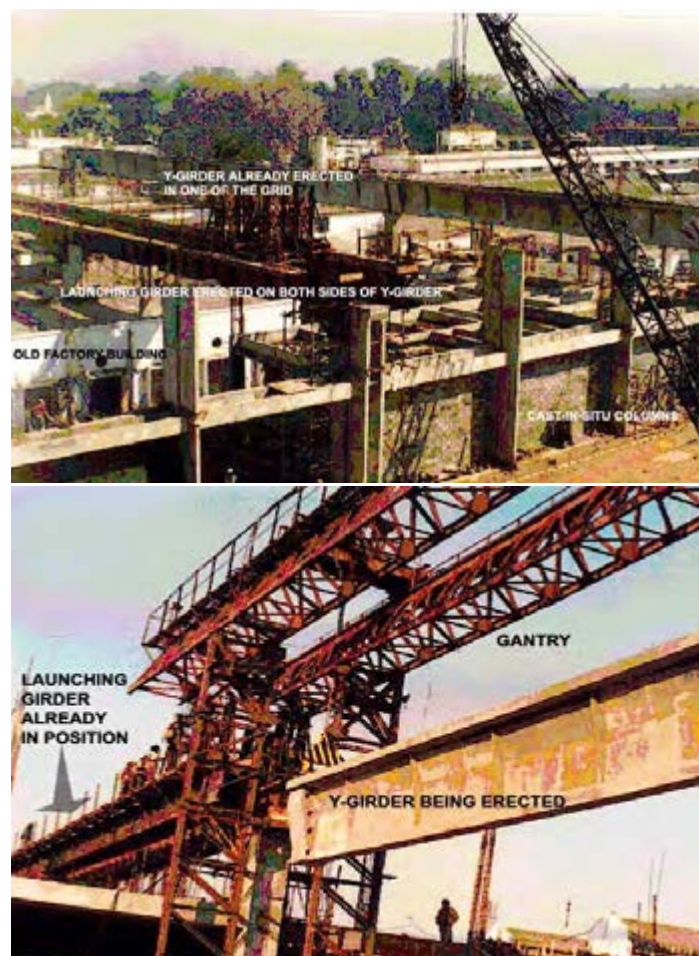


Fig 6: Photographs showing erection of Y-girder

After the erection of launching girder, Y-girders kept in the casting yard were lifted from gantry through two lifting nodes. The girder was shifted to the point when one of its ends reaches the extreme point of the gantry. At this point the load is transferred to the RC column, while making one node of gantry free and holding the other end of the girder by the second node of the gantry. Now the front moving end of the girder is kept on the trolley provided with the launching girder and the load from girder on to the RC column is released. At this time one end of the Y girder is supported through one trolley provided with the launching girder and the other end is still supported through the gantry. The girder is pushed further till the back end of the girder is near the extreme of the gantry. At this time the back portion of girder is kept on the cast in situ column and the node of the gantry is released. The back end of the girder is now kept on the second trolley and loads from column released. The Y girder now rests on both the trolleys provided with the launching girder. The trolleys are moved till the Y-girder reaches its exact location, when the trolleys are removed. This process is repeated for all the grids.

The gap between the end diaphragms of two Y-girders was kept at about 300mm. A total of 18 numbers (9 numbers on each side of the diaphragm) high tension bolts of 25mm diameter were inserted in the pockets left in the diaphragm while casting earlier. Reinforcements as per design were tied in the 300 mm gap portion and concrete was poured. Finally the pockets were grouted with non shrink grout materials.

5.2 Folded plates

The erection of folded plate elements as shown in **Figure 7**, was carried out in two stages. In the first stage, Hilman rollers were fixed to the folded plate element before loading them on to the trailer, which was hauled



Fig 7: Erection of folded plate element

to the erection location. Here, a 955A-LC crane was positioned depending on the requirement, and the folded plate element was lifted from the trailer and transferred to the Y girder. In the second stage the folded plate element was hauled to the precise location, where it was jacked up by about 25mm to facilitate removal of Hilman rollers. Finally the folded plate element was lowered on the Y girder. This process was repeated for all the elements. It may be noticed from Figure 7 that openings have been provided in the roof elements to provide north lighting. The openings were provided with glass plates leading to substantial saving in lighting within the building

It may be noted that after erection, there was a gap of about 25 mm between two folded plate elements. This gap was filled with thermocol, which also acted as a bottom shuttering, on top of which reinforcements were laid (10mm dia at 150 centre to centre) and concrete was poured in the designed profile. Once the concrete was set the thermocol pieces were removed and sealants applied from inside in the gap. This helped to seal any leakage of water from the folded plate joints.

5.3 Wall Panel

Wall panels were shifted from the casting yard to a location near the erection site, and cranes were used to lift them and appropriately align them at a desired location, and the joints were finally grouted.

6. DISMANTLING OF EXISTING ROOFS AND FINAL WORKS

The roof of the old factory (seen in Figure 6) was dismantled in phases after the roofing of the new structure had been completed as discussed above, in accordance with a carefully drawn up schedule. As a typical example, the dismantling of a typical area (hatched in Figure 1) is briefly explained here. The area was barricaded first and covered with plastic sheets all around to prevent dust and debris passing into neighboring areas. The roof was dismantled using compressors and impact hammers. At this stage, the ISMB packing and jacks used for transferring the load during construction (Figure 3) were also removed. In the final stage, the new RC flooring was laid using the bricks from the dismantling in the base course, which carried a 100mm PCC and 100mm RC layer on top.

7. CONCLUDING REMARKS

An effort has been made in this paper, to present the challenges of renovating an old industrial structure, without shutting down the plant for civil works. The paper described how use of locally available and appropriate technology can be used to accomplish the task in a time bound and professional manner. The project combined a judicious use of cast *in situ* concrete and precast concrete elements, and host of tailor made technologies such as use of horse driven buggies for concrete transportation,

underpinning arrangement for wall and column, use of launching girders for erecting Y-girder etc.

ACKNOWLEDGEMENT

The authors wish to express their sincere thanks to the staff of the contracting organization for providing various inputs for this paper. The support received from Mr. R.N.Gaur, Mr. Ramji, and Mr. H. Chauhan is especially acknowledged.

REFERENCES

1. Andres, C. K., Smith, R. C. (1998). *Principles and Practices of Heavy Construction*. Fifth Edition, Prentice-Hall, Inc.
2. Harris, F. (1989). *Modern construction equipment and methods*, Longman Scientific and Technical, England.
3. Peurifoy, R.C. (1964). *Formwork for Concrete Structures*, McGraw-Hill Book Company.

IN-PLANE AND OUT-OF-PLANE BEHAVIOR OF PP-BAND RETROFITTED MASONRY WALLETES

NAVARATNARAJAH SATHIPARAN

Master Course Student, The University of Tokyo, Japan
sakthi@risk-mg.iis.u-tokyo.ac.jp

PAOLA MAYORCA

Post Doctoral Fellow, The University of Tokyo, Japan
paola@iis.u-tokyo.ac.jp

NASROLLAHZADEH NESHELI

Post Doctoral Fellow, The University of Tokyo, Japan
nesheli@iis.u-tokyo.ac.jp

RAMESH GURAGAIN

Master Course student, The University of Tokyo, Japan
ramesh@risk-mg.iis.u-tokyo.ac.jp

KIMIRO MEGURO

Professor, ICUS, Institute of Industrial Science, The University of Tokyo,
Japan
meguro@iis.u-tokyo.ac.jp

ABSTRACT

Unreinforced masonry is one of the most used construction materials in the world. It is also unfortunately, the most vulnerable during earthquakes. This combined with the widespread use of masonry in earthquake prone regions of the world has resulted in a large number of casualties due to the collapse of this type of structures. Several methods have been proposed to improve strength, ductility and energy dissipation capability of masonry structures. However, in developing countries, retrofitting masonry structures should be economic, should be retrofitting material accessible and should be local available workmanship used. Also simple construction procedure is needed. Considering these points, a new retrofitting technique has been proposed based on the use of polypropylene bands (PP-bands), which are commonly utilized for packing. This material is available at a very low price even in remote areas of the world.

To evaluate the beneficial effects of the proposed PP-band mesh retrofitting method, diagonal compression tests and out-of-plane tests were carried out on masonry wallettes with and without retrofitting. In diagonal compression tests, the masonry wallettes were retrofitted with meshes whose borders were connected with either epoxy or just by overlapping to evaluate whether the connection type influences the retrofitting performance.

From both tests results, which are highlighted in the paper, it could be seen that PP-band retrofitted masonry wallettes had larger residual strength after the first crack in both in-plane and out-of-plane loading. It was clear that PP-band mesh retrofitting improved the overall stability and ductility of the structure.

1. INTRODUCTION

In order to verify the suitability of the proposed retrofitting technique, an experimental program was designed and executed. A real scale model test makes possible to obtain data similar to real structures. However, it requires large size testing facilities and large amount research funds, so it is difficult to execute parametric tests by using full scaled models. Recently, structural tests of scaled models become well-known as the overall behavior of the system can be also understood from scaled model. In this experimental program $\frac{1}{4}$ scale model was used to investigate the static and seismic behavior of masonry walls.

Diagonal compression tests and out-of-plane tests were carried out on masonry wall specimens with and without retrofitting for both burned and unburned bricks to evaluate the beneficial effects of the proposed PP-band mesh retrofitting method. In addition to these, efficiency of different meshes orientations was also examined. The test results are reported in this paper.

2. AXIAL TENSILE TEST OF POLYPROPYLENE BANDS

Preliminary testing of the PP-band was carried out to check its deformational properties and strength. To determine the modulus of elasticity and ultimate strain, 3 bands were tested under uni-axial tensile test. The test was carried out under displacement control method. The results are shown in Figure 1. To calculate the stress in the band, its nominal cross section $15.5 \times 0.6 \text{mm}^2$ was used.

All of the bands exhibited a large deformation capacity, with more than 13% axial strain. The stress-strain curve is fairly bilinear with an initial and residual modulus of elasticity of 3200MPa and 1000MPa, respectively. Given its large deformation capacity, it is expected that it will contribute to improve the structure ductility.

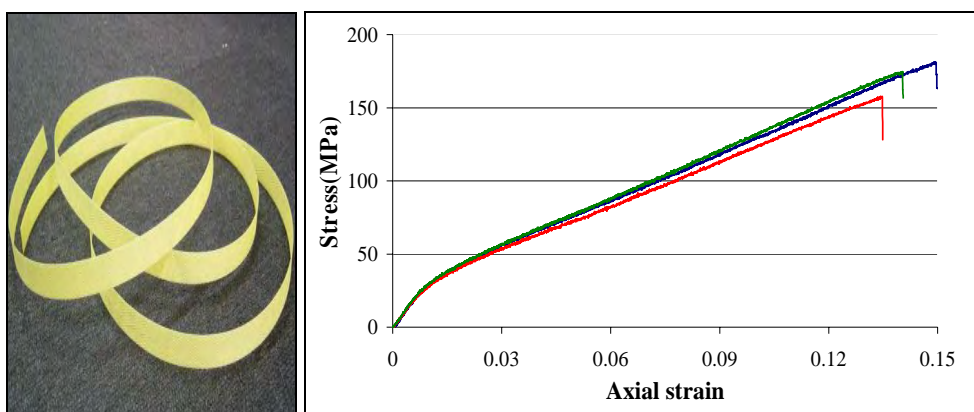


Figure 1: (a) Polypropylene band used for retrofitting (left)
(b) Behavior of PP-band under tension (right)

3. DIAGONAL COMPRESSION TEST

To evaluate the beneficial effects of proposed PP-band mesh reinforcement method, diagonal compression tests were carried out on masonry wallettes with and without retrofitting for both burned and unburned units. The wallette dimensions were $292.5 \times 290 \times 50 \text{ mm}^3$ for burned and $275 \times 275 \times 50 \text{ mm}^3$ for unburned unit and consisted of 7 brick row of 3.5 brick each. The mortar joint thickness was 5mm for both cases. Cement/Water ratios equal 0.14 and 0.33 were used for burned and unburned brick, respectively.

To observe the efficiency of different mesh orientations, two types of PP-band mesh arrangement were considered.

Type-1: PP-band mesh oriented parallel to the masonry joints.

Type-2: PP-band mesh oriented 45° from the masonry joints.

Both had mesh pitch equal to 40mm. A total of 4 wire connectors were used to attach the mesh with the masonry.

The specimens were named according to the following convention: **A-T-O** in which **A** is **B**: Burned or **U**: Unburned; **T** is **NR**: Non-retrofitted, **RE**: Retrofitted by PP-band meshes whose borders were connected with epoxy and wire connectors or **RO**: Retrofitted by just overlapping of PP-band meshes and wire connectors; and **O** is **1**: PP-band mesh oriented parallel to the masonry joints or **2**: PP-band mesh oriented 45° from the masonry joints.

Specimens were tested 28 days after construction under displacement control. The loading rate was 0.3mm/min and 2mm/min for the non-retrofitted and retrofitted cases, respectively. The retrofitted wallettes were applied 50mm vertical displacement. Average measured mechanical properties of the masonry at the time of testing are shown in Table 1. Direct Compression, direct shear and bond tests carried out to obtaining these characteristic properties were similar to that shown in Figure 2.

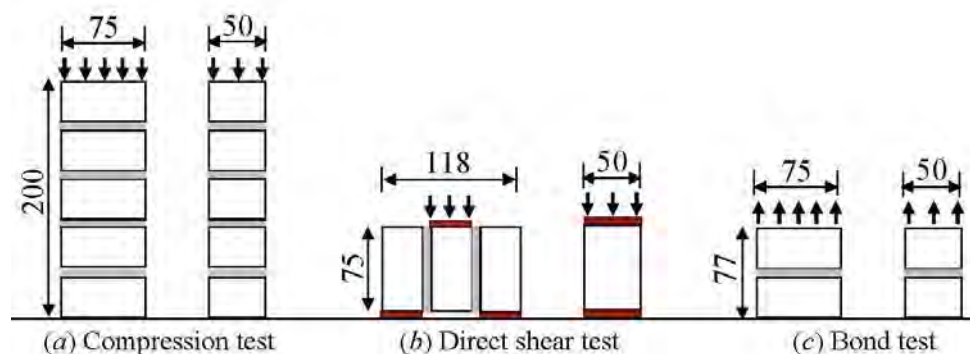


Figure 2: Layout of specimens used for direct compression, direct shear and bond test (unit:mm)

Table 1: Mechanical properties of masonry

	Burned Brick	Unburned brick
Compressive strength (MPa)	21.78	4.45
Shear strength (MPa)	0.075	0.006
Bond strength (MPa)	0.055	0.006

3.1 Behavior of retrofitted masonry

Initially retrofitting was done with PP-band meshes whose borders were connected with epoxy and wire connectors, in order to evaluate the beneficial effects of the proposed PP-band mesh reinforcement method. In the following sections, a brief discussion of diagonal compression test results of burned and unburned unit specimens is presented.

3.1.1 Behavior of burned brick specimens

Figure 3 shows the non-retrofitted and retrofitted specimens at the end of the test, which corresponded to vertical deformations equal to 0.71mm and 50mm, respectively. In the non-retrofitted case, the specimens split in two pieces after the first diagonal crack occurred and no residual strength was left. In the retrofitted case, on the other hand, diagonal cracks appear progressively, each new crack followed by a strength drop. Although the PP-band mesh influence was not observed before the first cracking, after it, each strength drop was quickly regained due to the PP-band mesh effect. Although at the end of the test almost all the mortar joints were cracked, the retrofitted wallettes did not lose stability.

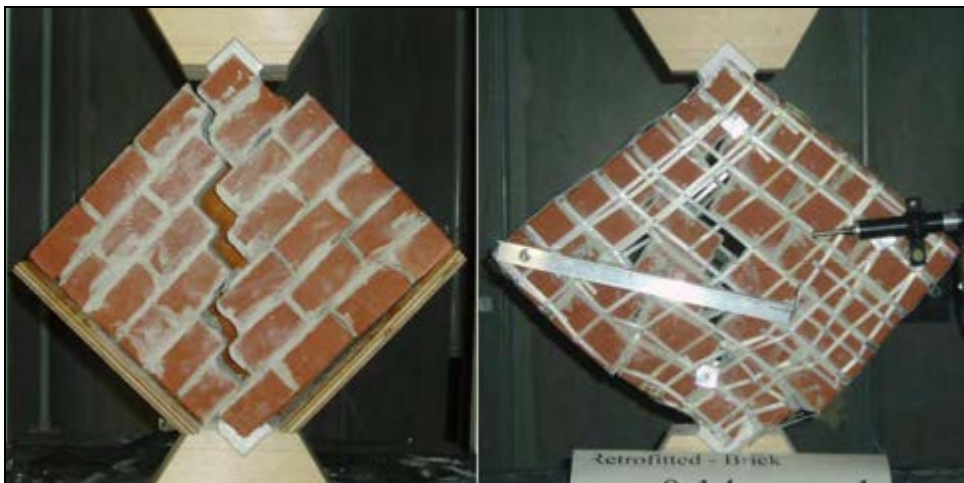


Figure 3: Failure patterns of brick masonry wallettes with and without retrofitting by PP-band mesh.

Figure 4 shows the diagonal compression strength variation with vertical deformation for the non-retrofitted and retrofitted specimens. In the non-retrofitted case, the average initial strength was 1.5kN and there was no residual strength after the first crack. However, in the retrofitted case, although the initial cracking was followed by a sharp drop, at least 50% of the peak strength remained. Subsequent drops were associated with new cracks like the one observed at the deformation of 4mm. After this, the strength was regained by readjusting and packing by PP-band mesh. When the strength exceeded 3.0kN individual PP-bands started to fail. However, this did not reduce considerably strength of the specimen, because stresses redistributed to other PP-bands. The specimen quickly recovered its strength. The final strength of the specimen was equal to 3.0kN relatively higher than initial strength of 1.5kN.

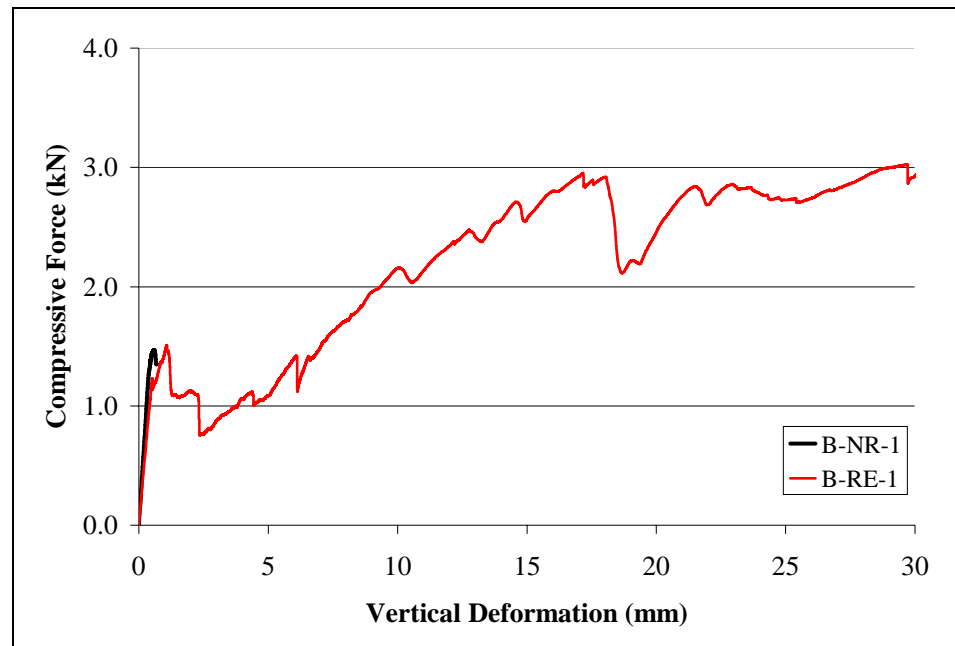


Figure 4: Force vs. vertical deformation for burned brick masonry wall specimen with and without retrofitting.

3.1.2 Behavior of unburned brick specimens

Figure 5 shows the diagonal compression strength variation with vertical deformation for the non-retrofitted and retrofitted specimens.

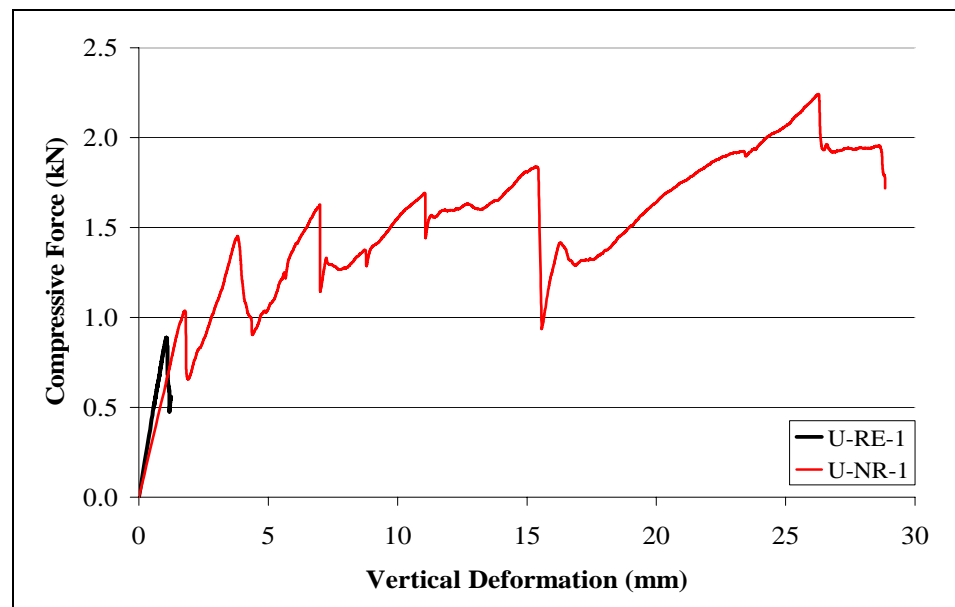


Figure 5: Force vs. vertical deformation for unburned brick masonry wall specimen with and without retrofitting.

In the non-retrofitted case, the initial strength was 0.89kN and there was no residual strength after the first crack. In the retrofitted case, although the initial cracking was followed by a sharp drop, at least 70 % of the peak

strength remained. As expected, the initial strength of unburned brick specimens was relatively lower than that of the burned brick one.

3.2 Efficiency of mesh orientation

Figure 6 compares the diagonal compression strength of retrofitted masonry wallettes with different mesh orientation:

Type 1 is PP-band mesh oriented parallel to the masonry joints.

Type 2 is PP-band mesh oriented 45° from the masonry joints.

Generally Type 2 mesh provided larger strength than Type 1 mesh arrangement. This was expected because the confining effect on the masonry wall is larger in the former case. Cracks become gradually wider as the vertical deformation increased. In this condition, the reinforcement oriented perpendicular to the crack, i.e. Type 2 worked under optimum conditions. The results of B-RE-1 and B-RE-2 were compared; the maximum strength difference was 30% at a vertical deformation of 17 mm. Although the mesh Type 1 did not fully use the mesh capacity, it improved the wallette behavior to a degree which can be considered enough for the purpose of earthquake damage mitigation. In addition to this, the mesh Type 1 is easier to manufacture and install. Therefore, it was selected as the proper solution for retrofitting.

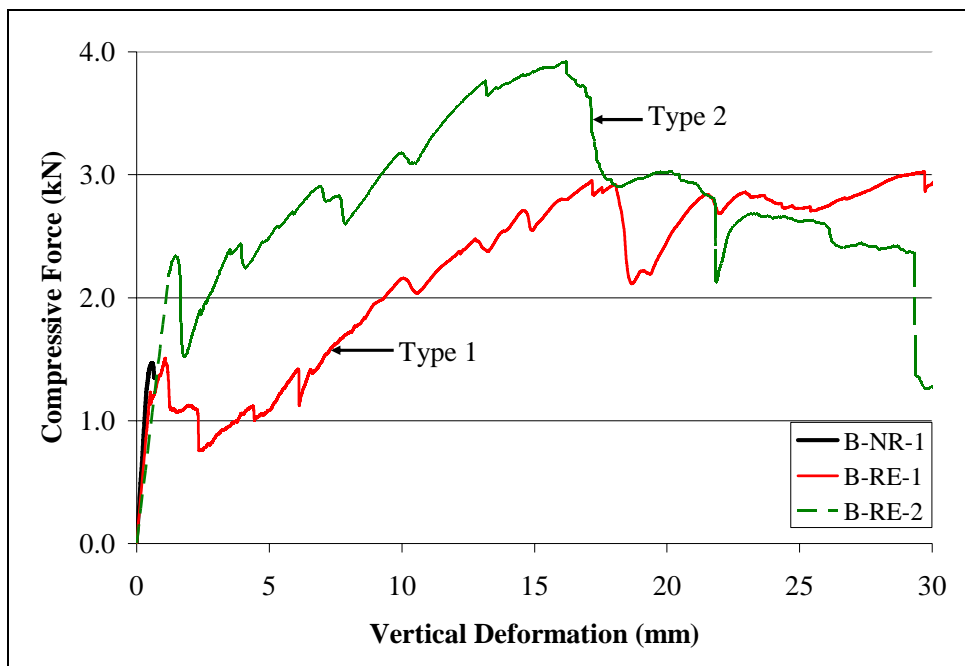


Figure 6: Comparison between masonry wallettes retrofitted by different orientation meshes:

Type 1 is PP-band mesh oriented parallel to the masonry joints.

Type 2 is PP-band mesh oriented 45° from the masonry joints.

3.3 Effect of mesh edge connection

Figure 7 shows comparison of the diagonal compression behavior of retrofitted masonry wallettes with mesh whose borders were connected with epoxy and retrofitted by just overlapping of PP-band meshes for burned masonry wallettes.

In case of burned masonry wallettes, within the 10mm vertical deformation, similar performance was observed in both cases. However at larger vertical deformation, because of PP-band slip was observed along the specimen borders, compression strength of wallettes without epoxy was considerably reduced. Also it could be observed that close to the connectors there was almost no mesh slip, ie the connectors could effectively attach two meshes. On the other hand, the bands located far from the connectors experienced considerable slip. This was not observed in the meshes connected with epoxy. As mentioned before for vertical deformation smaller than 10mm, which corresponds to 15 times the working strain, the behavior of both edge connections was almost the same.

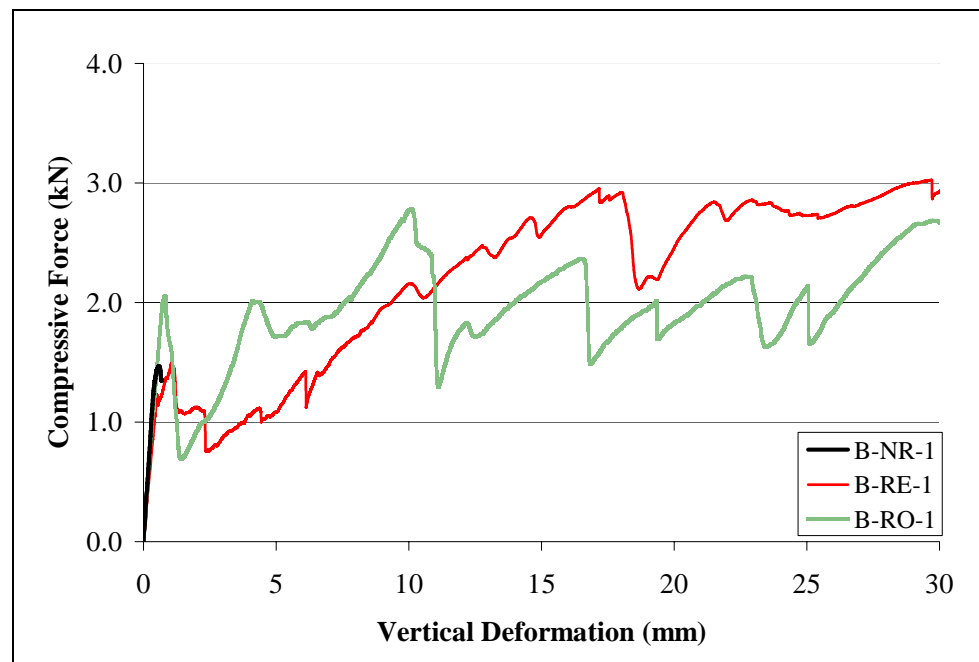


Figure 7: Behavior of masonry wallettes with mesh edges fully or partially connected

4. OUT-OF-PLANE TEST

Out-of-plane tests were carried out, in order to investigate the PP-band mesh effectiveness in walls exhibiting arching action. The nominal dimensions of these walls were 475mm by 235mm; their thickness was 50mm. The PP-band mesh edges were partially connected, i.e. no epoxy was utilized. A total of 6 wire connectors were used to attach the meshes with masonry wallettes. Considering the stability of the specimens, Cement/Water ratios equal 0.25 and 0.45 were used for burned and unburned brick, respectively.

Bond tests were performed to characterize the engineering properties of the material used in the investigation. The average tensile strength of

burned brick and unburned brick masonry obtained from bond test were 0.162MPa and 0.006MPa, respectively.

The specimens were named according to the following convention: **M-T** in which **M** is **B**: Burned or **U**: Unburned; **T** is **NR**: Non-retrofitted or **RO**: Retrofitted by overlapping of PP-band meshes and wire connectors.

Specimens were tested 28 days after construction under displacement control. The wallettes were simply supported with a 440mm span. Steel rods were used to support the wallettes at the two ends. The masonry wallettes were tested under a line load which was applied by a 20mm diameter steel rod at the mid-span of the wallettes. The loading rate was 0.05mm/min for the non-retrofitted case. For the retrofitted case, it was also 0.05mm/min for the first 30mm vertical deflection, and then it was increased to 2mm/min for the remaining test period. The retrofitted wallettes were applied up to 70mm vertical displacement. The test setup is shown in Figure 8.

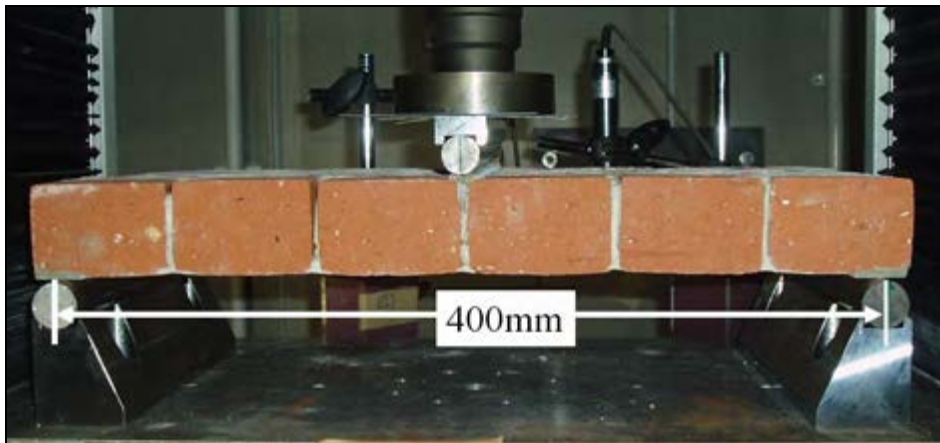


Figure 8: Out-of-plane test setup

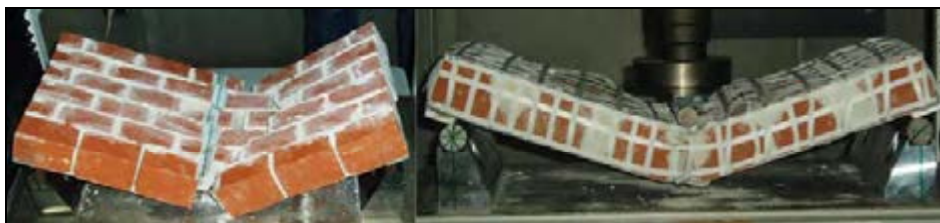


Figure 9: Failure patterns of brick masonry wallettes with and without retrofitting by PP-band mesh.

Figure 9 shows the non-retrofitted and retrofitted masonry wallettes at the end of the test, which corresponded to a mid-span net deformation equal to 2.8mm and 70.0mm, respectively. In the non-retrofitted case, the specimens split in two pieces just after the first crack occurred at mid-span, and no residual strength was left. In the retrofitted case, on the other hand, although PP-band mesh influence was not observed before the first cracking, after it, strength was regained progressively due to the PP-band mesh effect.

Figure 10 shows the out-of-plane load variation in terms of net vertical deformation for the non-retrofitted and retrofitted wallettes in the

mid-span. For burned brick, in the non-retrofitted case, the initial strength was 0.63 kN and there was some residual strength remaining for further small amount of deformation after the first crack. This behavior was observed due interlocking between bricks and also the application of load under displacement control method. In the retrofitted case, although the initial cracking was followed by a sharp drop, nearly 45% of the peak strength remained.

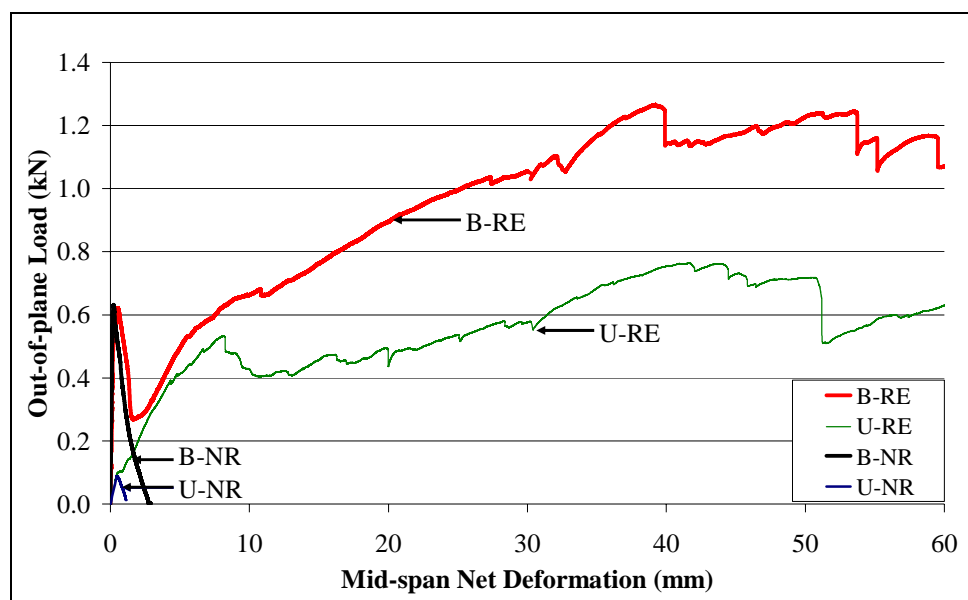


Figure 10: Out-of-plane load variation in terms of net vertical deformation

As expected, the initial strength of the burned brick was relatively higher than that of unburned brick. Even higher cement/water ratio was used for unburned brick, the poor bonding between mortar and unburned brick led to separation along the brick and mortar. On the other hand, in the burned brick case, failure occurred within the mortar. This behavior highly influenced the initial strength of the specimens.

After the initial drop in strength, the mesh presence positively influenced the wallette behavior. Both types of retrofitted brick wallettes showed similar behavior in strength up to a vertical deformation equal to 8mm. At the point, brick crushing was observed in the unburned brick case. Due to that, the overall strength of the unburned brick wallettes was considerably smaller than that of burned brick wallettes. There after, if two types of bricks are compared, almost 40% difference in strength was observed.

5. CONCLUSIONS

This paper discusses the results of a series of diagonal compression tests and out-of-plane tests that were carried out using non-retrofitted and retrofitted wallettes by PP-band meshes.

The diagonal compression tests showed that:

- (1) When appropriately set, no epoxy failure was observed before 2.9kN.
- (2) In the retrofitted case, larger residual strength after the formation of the first diagonal shear cracks was observed. Furthermore, as deformation increased, the wallette achieved higher strength than the initial cracking strength.
- (3) Mesh Type 1, in which PP band mesh is oriented parallel to the masonry joints, improved the wallette behavior to a degree which can be considered enough for the purpose of earthquake damage mitigation. In addition to this, Type 1 is easier to manufacture and install. Therefore, we consider mesh Type 1 is better for retrofitting.
- (4) For vertical deformation smaller than 10mm, similar performance between wallettes, with mesh edges fully and partially connected was observed.

The out-of-plane tests showed that;

- (1) In out-of-plane tests, the mesh effect was not observed before the wall cracking. After cracking, the mesh presence positively influenced the wallette behavior.
- (2) The retrofitted wallettes achieved strengths 2 times greater and deformations 60 times larger than the non-retrofitted wallettes.
- (3) Although the overall strength of burned retrofitted wallettes was higher than that of the unburned ones, the ratio maximum strength/cracking strength in the latter was larger.

Considering the overall performance of the specimens, it can be concluded that PP-band meshes can effectively increase the seismic capacity of masonry houses.

REFERENCE

- Sathiparan, N., 2005. *Experimental Study of Retrofit of Masonry Buildings by PP-band Mesh*, M.Eng. Dissertation, The University of Tokyo, Japan.
- Mayorca, P., 2003. *Strengthening of Unreinforced Masonry Structures in earthquake Prone Regions*, Ph.D. Dissertation, The University of Tokyo, Japan.
- Galati, N., Tumialan, J.G., Nanni, A., Tegola, A.La., *Influence of Arching Mechanism in Masonry Walls Strengthening with FRP Laminates*, The University of Missouri, Rolla, Italy.
- ASTM, E72, 1997. *Standard Test Methods of Conducting Strength Tests of Panels for Building Construction*, American Society for Testing and Materials, Philadelphia, Pa.

THE IMPORTANCE OF CURING IN PREVENTING THE SPALLING-OFF OF PATCHING REPAIR MATERIAL

MASANORI ITO¹, YOSHITAKA KATO²
TAKETO UOMOTO²

1: Research center, Tokyu Construction Co. Ltd.,
2: ICUS, Institute of Industrial Science, Tokyo University
itou.AI9184@tokyu-cnst.co.jp

ABSTRACT

The use of polymer cement mortar (hereafter, PCM) to repair deteriorated concrete structure has recently become more and more popular, especially in restoring the damaged cross-section. In this process, the curing after patching is important for the performance over time of PCM. This research studied the basic properties, such as compressive strength, bond strength, and carbonation resistance, of repair material applied by wet-spraying process and exposed to drying condition right after its application. Experimental result shows that the durability of PCM is less affected by drying environment than that of common mortar. However, it was confirmed that microstructure tends to be worsened by drying at the early age. Therefore, it is important to ensure an appropriate curing condition right after applying repair material, as long as the long term performance is concerned.

1. INTRODUCTION

In Japan, the economy grew rapidly in the period 1960~1980. Many structures, such as buildings, bridges, were built during this period. In this period limited knowledge about durability. As a result, these infrastructures rapidly deteriorated and appropriate maintenance will be necessary in future. Figure 1 shows the prediction of future investment in construction field of Japan. As can be seen in this figure, the maintenance expense will be higher than that of new investments in the future. The purpose of the maintenance is to maintain the existing structure in service as long as possible.

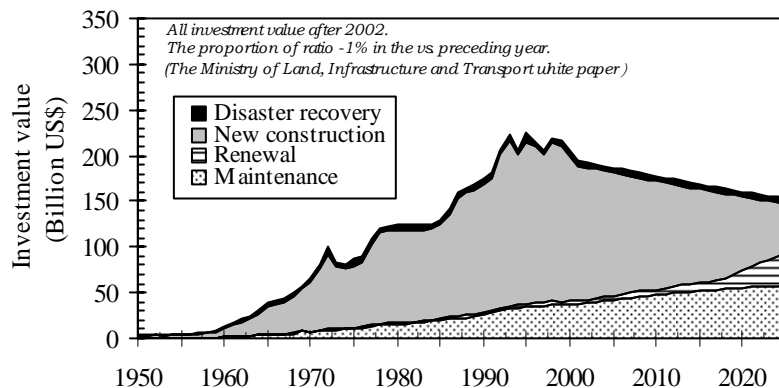


Figure1: The investment in construction amount in Japan.

Reinforced concrete structures deteriorated by various factors, such as carbonation, salt attack, alkali-aggregate reaction, etc., need to be repaired and strengthened. The use of PCM to repair deteriorated concrete structure has recently become more and more popular, especially in restoring the damaged cross-section. Technical report of patching recommends the use of high quality PCM for repair. However, satisfactory performance is not always obtained in field works, because of various environmental effects. Figure 2 shows the spalling-off of patching repair material due to re-deterioration of reinforced beam after repair. In this process, the curing is important for the performance of PCM. This research was study about basic properties, such as compressive strength, bond strength, and carbonation resistance of repair material applied by wet process and exposed to early drying condition. The evaluation of these basic properties is carried out from micro structure point of view.

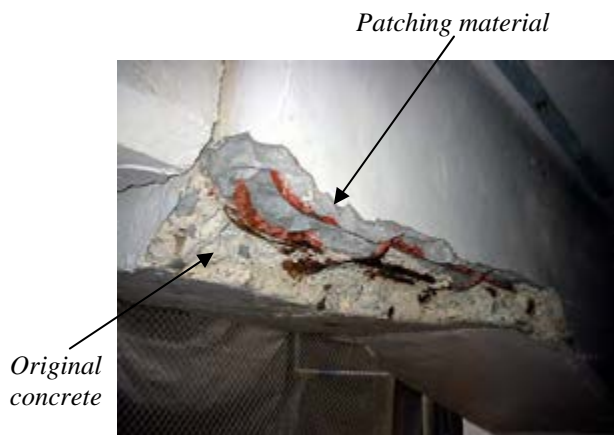


Figure2: Re-deterioration of concrete bridge

2. Experiment procedure

2.1 Materials and Mix proportions

In this research, two kinds of mortars were tested. One is the PCM, and the other is normal cement mortar (hereafter NCM). Ordinary portland cement and crushed sand with particle size smaller than 2.5mm were used. The polymer is redispersible polymer powders whose components are copolymer resins such as Vinyl acetate/VeoVa/Acrylic, and physical properties are shown in Table 1. Chemical admixtures including Powdery superplasticizer and antifoaming agent were also used. Table 2 gives the mix proportions of PCM and NCM. The polymer to cement ratio for PCM was 5%, and W/C was 38% for both PCM and NCM. Materials and mix proportions were decided referring to the commonly-used mixture in actual patching work. The flowability of the PCM was adjusted so as to obtain a 20mm layer of repair material, when spraying to the wall.

Table 1: Properties of polymer

Type	Color	Solid Content (%)	Bulk density (g/l)	Particle size (%)*
Vinyl acetate/ VeoVa/Acrylic	White powder	99±1	450±100	<3%

*: Particle diameter > 315 μ m

Table 2: Mix proportion

No	W/C (%)	P/C (%)	S/C	C (kg/m ³)	SP* (C×%)	AA** (C×%)
NCM	38.0	0.0	2.0	614	0.08	0.2
PCM		5.0	1.9			

*: SP- Superplasticizer, **: AA-Antifoaming agent

2.2 Test Specimen

The mixture was mixed for 5 minutes. PCM specimen was made by wet-mix spraying. Spraying conditions were as follows: spraying quantity - 0.1m³/h, spraying air pressure - 0.7MPa, aperture diameter of the nozzle tip - 8mm. The NCM specimen was made by applying repair material using a trowel.

2.3 Environmental condition

Table 3 gives the environmental conditions of this study. The sealing condition is to prevent the evaporation of the moisture from the specimen. The wind velocity, in the windy condition, was set at 2m/sec on the basis of two data: the wind velocity measurement data in the subway passage and the average wind velocity data of Tokyo obtained by Meteorological Agency. The drying condition was set as intermediate one of above conditions. The sheet was made to be the sealing condition only for first 2 days, and it was exposed in the wind environment afterwards. Evaporation rate of the water in wind environment were 10 times of dry environment. Figure 3 shows the experimental setup to simulate the windy condition.

Table 3: Environmental conditions

Condition	Content
Room temperature:	20°C
Relative Humidity:	60%
Seal	Use the vinyl bag
Dry	Wind Velocity: 0.0m/s, Er*: 0.017kg/m ² /h
Windy	Wind Velocity: 2.0m/s, Er*: 0.160kg/m ² /h
Sheet	Seal by plastic sheet for 2days → Windy

*:Er - Evaporation rate

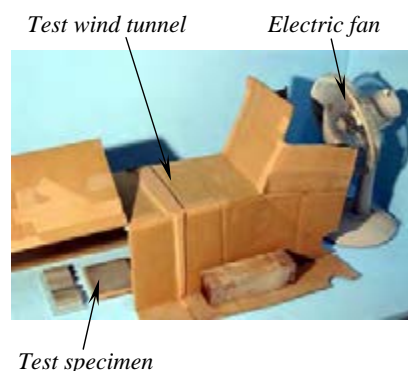


Figure3: Windy condition

2.4 Test Method

2.4.1 Moisture loss quantity test

The effect of different environmental conditions on the quantity of the moisture loss was examined. The size of the test specimen was exposed as 130x130x20mm in spraying/trowel applied each condition immediately. The measurement of the mass change was carried out by 28days.

2.4.2 Measurement of micro-pore size distribution

After the Moisture loss quantity test specimen was coarsely ground, and a large amount of acetone was added to stop hydration reaction of cement. The test sample (2.0~5.0mm) was dried by vacuum drying at room temperature. The micro-pore size distribution was measured using a mercury porosimeter (Micromeritics Autopore III 9400). In addition, 100x100x200mm test specimen was also produced by cutting initial specimen in order to evaluate to which extent the effect of the environment has reached form surface.

2.4.3 Compressive strength test

In this study, compressive strength was measured with 20x20x80mm test specimen. Though the specimen size is smaller than standard one (40x40x160mm), the result will surely exhibit similar tendency.

2.4.4 Bond strength test

Bond strength measurement was carried out in accordance with JIS A 1171(Test methods for polymer-modified mortar) at 28days. The basic mortar plate was 70x70x20mm, and test specimen was 40x40x10mm by the spraying/trowel applied on the top.

2.4.5 Accelerated carbonation test

Manufacture methods of this test specimen were as follows: Firstly, 300x300x60mm flat plates produced in the spraying or trowel applied were exposed to different conditions. At 28-day age, the cores(ϕ 50x60mm) were collected, and their sides were covered with epoxy resin in order to allow carbonation just from the surface. Accelerated carbonation conditions were as follows : CO₂ concentration-10%, temperature-20°C, relative humidity-60%. After 28days, an alcoholic solution of phenolphthalein was sprayed onto the cut surface of specimens, and the depth of uncolored portion was measured.

3. Test Result

Figure 4 shows the relationship between the time and the mass reduction. In the sealed condition, the mass change for 28 days was not measured. In windy and dry conditions, the moisture began to immediately evaporate, after it was exposed. First 1day mass reduction was 85% in about 1 month. The mass reduction increases, when the drying condition is severer. PCM has less on the decreased quantity, compared with NCM. The mass reduction was little for the case in which specimens were covered by Sheet.

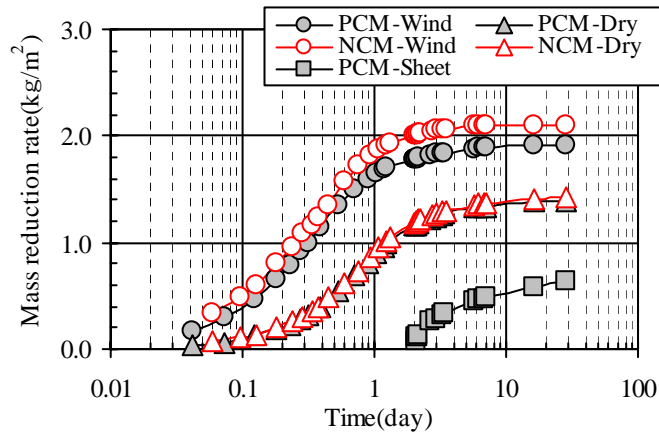


Figure4: Result of mass reduction rate

Figure 5 shows the measured result of micro pore size distribution. When drying condition become severe, the hydration reaction of the cement is inhibited due to lack of water, and consequently, the micro-pore structure is coarsened. The gel pore (<0.01mm) decreases at severer drying condition (order of drying intensity: sealed → dry → windy). In all drying conditions, the volume of gel pore in PCM is larger than that of NCM, while the volume of pore greater than 1 μ m is smaller than that of NCM. It means that the PCM is denser than that of NCM. This may be attributed to the existence of polymer in PCM. The result in this figure also shows that the same micro structure with sealed condition can be obtained by covering mortar with plastic sheet during the first two days.

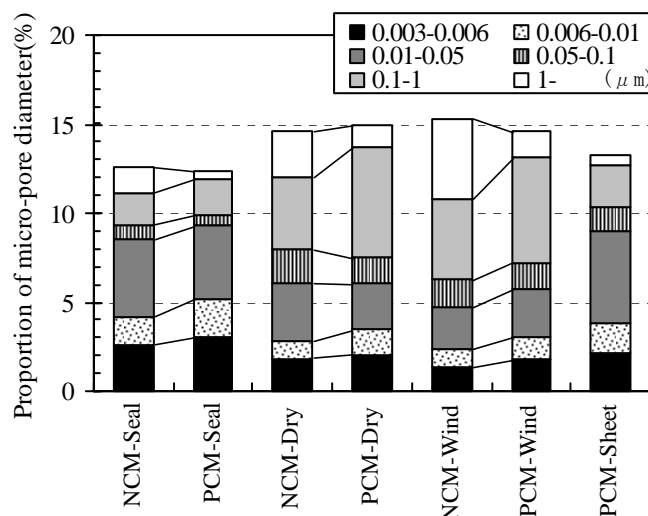


Figure5: Result of measurement of micro- pore size distribution (Effect of the environmental condition)

Figure 6 - (1) (2) shows also the measurement result of micro-pore size distribution.

This is to confirm the effect of drying at different depth from exposed surface. From the figure, the PCM was affected by the wind up to about 20mm from the surface. However, NCM received the effect of the wind deeply, and the micro-pore structure coarsened to 50mm depth from the surface.

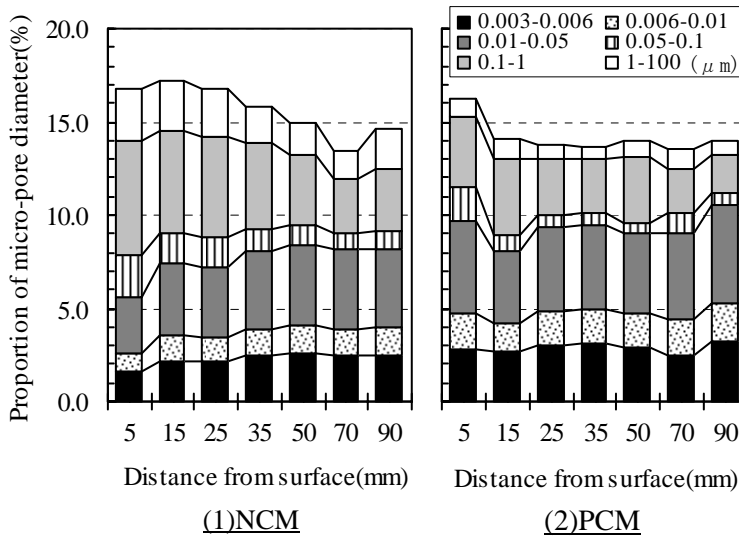


Figure6: Result of Measurement of micro- pore size distribution (Effect on the depth direction for windy condition)

Figure 7 shows the relationship between evaporation rate and compressive strength.

The compressive strength tends to be lower, at lower evaporation rate. However, there is no clear difference between PCM and NCM. Similarly, the strength of PCM covered with plastic sheet just rises slightly.

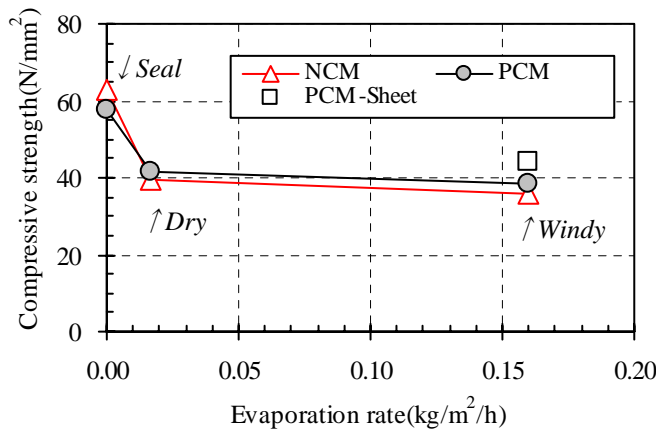


Figure7: Relationship between compressive strength and evaporation velocity

Figure 8 shows the relationship between evaporation rate and the bond strength.

Similar to compressive strength, the bond strength tends to be lower at higher evaporation rate. However, the difference in bond strength is quite remarkable compared with the result of compressive strength. The use of PCM helps minimize the loss of bond strength due to windy condition. In addition, the bond strength of PCM can be almost maintained just by covering repair material with plastic sheet in two days.

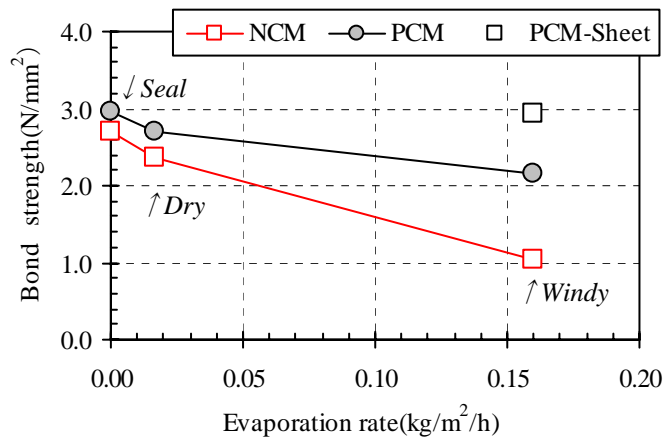


Figure8: Relationship between bond strength and evaporation velocity

Figure 9 shows the relationship between evaporation rate and the carbonation depth.

In case of NCM, the carbonation depth increases at higher evaporation rate. However, the progress of the carbonation was suppressed in PCM compared with NCM in the windy condition. This is the same tendency in the bond strength (Figure 8). By the use of the polymer, the mortar is dense, and therefore, it is considered that the penetration of CO₂ was suppressed.

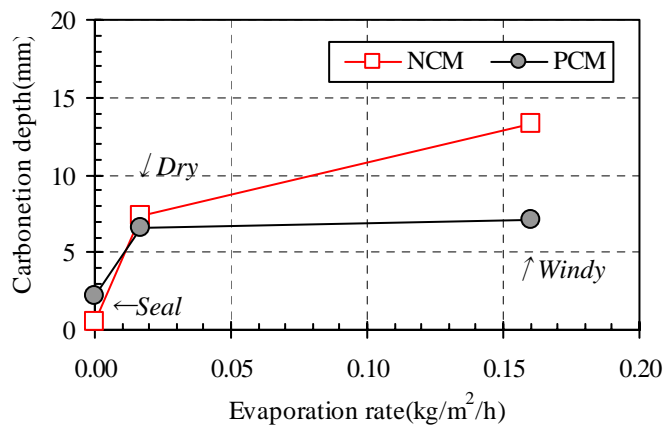


Figure9: Relationship between carbonation depth and evaporation velocity

4. Conclusions

The patching repair materials may re-deteriorate faster than anticipated. This may become a serious problem, for future management of

infrastructures. The re-deterioration may be caused by macro-cell corrosion and diffusion of chloride, etc. In addition, patching material is directly affected by the environment, since patching method is carried out without using formwork.

This research studied the basic properties of repair material applied by wet process and exposed to early drying condition. The evaluation of the basic properties carried out from micro structure point of view yielded the following conclusions:

In the environment which receives the rapid drying, the performance deterioration can be suppressed by the addition of the polymer. The same micro structure with sealed condition can be obtained by covering mortar with plastic sheet during the first two days. It is considered that the establishment of a more efficient maintenance of infrastructures becomes possible, when the research on the durability of such repairing materials is advanced.

(Figure 10-12 shows the situation of the patching by the spraying.)



Figure10:
Deteriorated part



Figure11: Spraying situation



Figure12: Situation after patching

REFERENCES

1. Japan Society of Civil Engineers, Standard Specifications for Concrete Structures – 2005, Materials and construction, 2005. (in Japanese)
2. American Concrete Institute ACI506R-90, Guide to Shotcrete, 1995.
3. American Concrete Institute ACI506.2-95, Specification for shotcrete, 1995.
4. Chandra, S., and Ohama, Y., Polymer in Concrete, CRC Press, Inc., 1994.
5. Ohama, Y., and Sato, Y., “Relation between chemical properties and durability of surface layer of polymer cement mortar”, The Society of Materials Science, Japan, Vol.39, 1990, pp.340-342. (in Japanese)
6. Ito, M., and Uomoto, T., “Evaluation of the spray repair material under wind environment”, Proceeding of the Japan Concrete Institute, Vol.27, 2005. (in Japanese)

ALLOCATION OF LIFE-CYCLE REPAIRING COST BASED ON PARAMETER UNCERTAINTIES OF DETERIORATION PREDICTION MODEL

PAKAWAT SANCHAROEN

Graduate school, Department of Civil Engineering,

The University of Tokyo, Japan

pakawat@iis.u-tokyo.ac.jp

TAKETO UOMOTO

Institute of Industrial Science, The University of Tokyo, Japan

uomoto@iis.u-tokyo.ac.jp

ABSTRACT

Repair and maintenance of deteriorated reinforced concrete structure will become the major task of construction industry in the near future. It is difficult for a decision maker to evaluate the expected life cycle or annual R&M cost and select the optimal solutions. Decision makers have to use many deterioration prediction models to create the R&M program. Parameters used in those models are decided and assumed to be constant values. In reality, there are some uncertainties in those parameters due to many reasons. This paper proposes the method to determine the expected probability and cost of R&M by considering parameters uncertainties of the prediction model. From the result, R&M program is able to be planned based on the expected repair probability as well as required total and annual resources can be allocated. Finally, example of selection of repairing options is given to illustrate the application of this approach to optimize the R&M program.

1. INTRODUCTION

The repair and maintenance (R&M) program of the structure is truly the important issue in order to maintain structure performance above the acceptable level throughout its service life. In 2002, Japan allocated approximately 13.5 trillion yen, which is 21.5% of the total construction budget, to the repair and maintenance projects. The ratio of maintenance budget to the overall construction budget is expected to continue increasing in the future because of increasing number of aging structures. In the near future, R&M will become the major task has to be concerned instead of new construction project.

Due to the limited resources and budget but large number of aging structures, R&M program has to be effectively planned. Usually, structure has to be periodically inspected and evaluated its condition. Decision of required action has to be made based on evaluated condition. One method is

using deterioration diagnosis software (Yokosawa et al., 2005) developed to assist a decision making about deterioration mechanism and condition of structure without opinion of expert. Another method is using prediction of the deterioration which has to be conducted based on many assumed parameters to schedule the required actions in the future such as repairing. However, there are many uncertainties associated with those assumed parameters used in the prediction model due to many reasons relating since in the beginning of the construction such as material properties, workmanship, structural dimensions, and environmental conditions. As a result, prediction cannot accurately simulate the real condition. Therefore, the supposed application time of the required actions have to be represented by the probability distribution instead of the deterministic value.

In this paper, the method to evaluate the expected probability of required R&M at certain time is discussed. Event tree analysis is used to facilitate the determination of all possible sequences of R&M and their expected probability during the service life. The ultimate objective of this study is to optimize the life cycle cost of R&M program from many alternative strategies. Therefore, method to calculate the expected life cycle cost of R&M is also proposed. Effect of time-value of money is considered in term of discount rate. Total and annual required resources can be allocated to the specify structure or group of structures based on the expected cost. Finally, example of selection the optimal repairing method is given based on the minimum expected life cycle cost.

2. DETERIORATION PREDICTION MODEL

In this paper, example of structural deterioration due to steel corrosion due to chloride attack is considered. Fick's second law is used to predict chloride diffusion into the concrete as shown in Equation (1). There are 3 uncertainties considered in this prediction model including surface chloride content, covering depth, and chloride diffusion coefficient. Moreover, uncertainty of the threshold chloride content is also considered in order to determine the corrosion initiation time. Examples of the results of their random variable parameters observed by other researchers are shown in Table 1.

$$C(x,t) = C_s \left(1 - \operatorname{erf} \frac{x}{2\sqrt{D_{cl} \cdot t}} \right) \quad (1)$$

where $C(x,t)$ = chloride content (% by weight of concrete) at depth x (cm) and time t (year), C_s = chloride content at the concrete surface (% by weight of concrete), D_{cl} = chloride diffusion coefficient (cm^2/year)

Monte Carlo simulation (Fishman, 1995), using generated random numbers and probability statistics sampling of uncertainties variables to provide approximate solution to a variety of mathematical problems, based on sample size of 10,000 is used to determine distribution of corrosion initiation time, when chloride content at steel level exceed the threshold chloride content, based on those four variables. The simulated result is shown in Fig. 1. For example, probability that corrosion initiation time is 5 years is 0.1390. Corrosion cracking is assumed to occur 10 years after corrosion was initiated. Then, crack repairing has to be suddenly conducted.

In the future, uncertainties of prediction of the corrosion cracking time have to be considered similar to that of prediction of corrosion initiation time.

Table 1: Random variables of model parameters

Variable	Mean	Coefficient of variation
Covering depth, x	3.81 cm	0.05
Chloride diffusion coefficient, D_{cl}	1.29 cm ² /year	0.10
Surface chloride content, C_s	0.20% by weight of concrete	0.10
Threshold chloride content, C_{lim}	0.025% by weight of concrete	0.10

Note: All variables are assumed to have lognormal probability distributions.

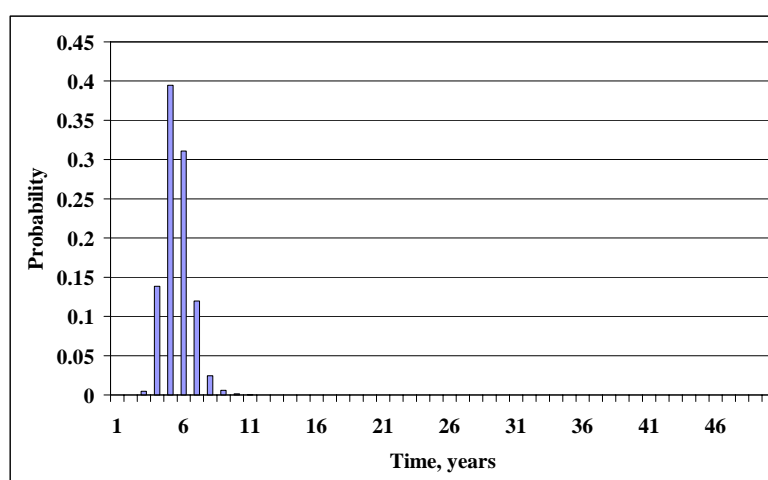


Figure 1: Distribution of corrosion initiation time

3. PROBABILITY DISTRIBUTION OF REPAIRING TIME

Probability distribution of the first repairing time is assumed to be 10 years after corrosion was initiated as shown in Fig.2. Although, a deterioration mechanism of repaired structure is different from the original one, it is firstly assumed that they are the same. Therefore, the distribution of subsequent repairing time is same to that of the first repairing time as shown in Fig.2. Except, time is relative time counted after the previous repairing was conducted instead of finishing of construction. In the future, further study on deterioration mechanism of repaired structure has to be considered.

Event tree analysis is used to determine all possible repairing events based on criteria that crack occurred during the service life has to be repaired. Table 2 shows an example of event tree analysis of possible repairing events during the service life. Based on relative time scale of subsequent repairing, absolute repairing time of each repairing can be calculated. Probability of each possible event is also calculated and shown. Both of absolute time and probability will be used to calculate the present value of repairing cost. For example, in the first event, maximum of 3 repairing have to be conducted. All of them are conducted 13 years after the

previous one. Based on distribution of repairing time, probability of repairing time at 13 years is 0.0004. Therefore, probability of the first event can be calculated as $(0.0045 \times 0.0045 \times 0.0045)$. Please be noted that events that repairing sequence cannot be implemented during the service life are not considered such as the third repairing is conducted at the year 51st.

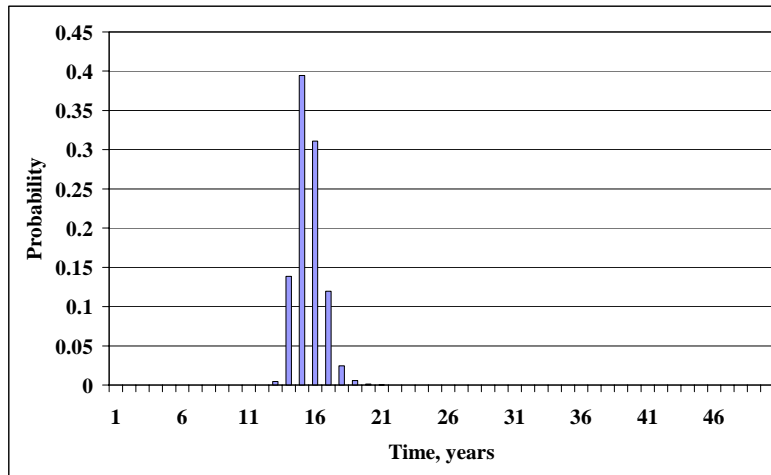


Figure 2: Distribution of repairing time

Table 2: Example of event tree analysis of repairing event

Relative time after the previous repairing			Year of the last repair	Event probability, $P_{r,j,t}$
First repair	Second repair	Third repair		
13	13	13	39	$(0.0045)^3 = 9.11 \times 10^{-8}$
13	13	14	40	$(0.0045)^2(0.1386) = 2.81 \times 10^{-6}$
13	13	15	41	7.99×10^{-6}
13	13	16	42	6.29×10^{-6}
13	13	17	43	2.42×10^{-6}
13	13	18	44	4.92×10^{-7}
.
.
.
19	-	-	19	6.00×10^{-3}
20	-	-	20	1.20×10^{-3}
21	-	-	21	4.00×10^{-4}

Probabilities of repairing i^{th} at time t can be obtained by adding the probabilities of all events repaired maximum i^{th} time and the absolute year of last repair is at the time t as shown in Equation (2). For example, there is only one event that the 3th repairing is conducted at year 39th. Therefore, its probability is equal to the probability of that event. Results of each repairing are shown in Figure 3. Finally, summation of probability of all repairing expected to be conducted at each year calculated by Equation (3) is shown in Figure 4. It should be noted that there is no cost overlapping of different

repairing observed in this example. However, if distribution of repairing time is wider, overlapping can be observed.

$$P_{r_i,t} = \sum_{j=1}^n P_{r_j,t} \quad ; \text{ if } t = t_1 + \dots + t_i \quad (2)$$

$$P_{r,t} = \sum_{i=1}^n P_{r_i,t} \quad (3)$$

where $P_{r_i,t}$ = probability of repairing i^{th} at time t , $P_{r_j,t}$ = probability of event j which the last repairing is the i^{th} at time t , $P_{r,t}$ = probability of all repairing at time t .

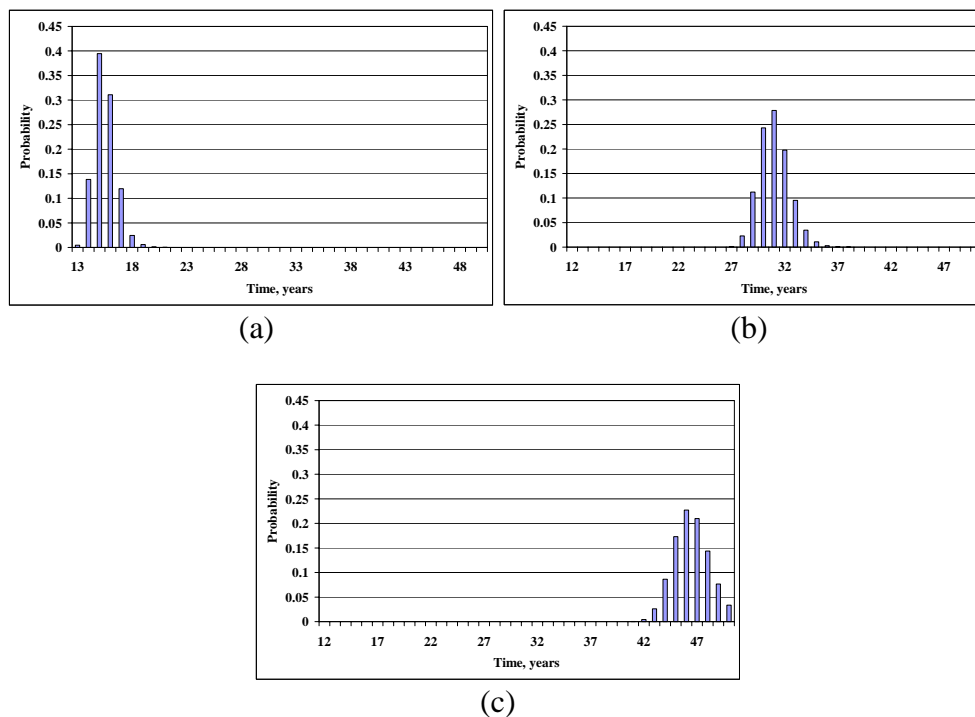


Figure 3: Expected probability of (a) 1st, (b) 2nd, (c) 3rd repairing

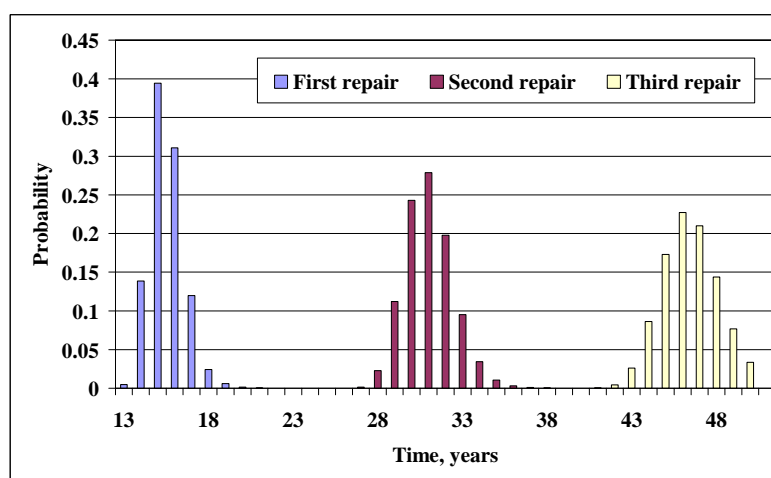


Figure 4: Probability of all repairing

4. EXPECTED REPAIRING COST

The expected repairing cost at each year is calculated based on present value as shown in Equation (4). The year structure is firstly serviced is assumed as the base year of discounting.

$$E[C_{r_i,t}] = \frac{C_{r_i}}{(1 + \nu)^{t_i}} \cdot p_{i,t} \tag{4}$$

where $E[C_{r_i,t}]$ = expected present value of repair i^{th} at time t , C_{r_i} = undiscounted cost of repair i^{th} , ν = discount rate, and $p_{i,t}$ = probability of repair i^{th} at time t . It is assumed that undiscounted repairing cost is same for all sequences repairing and equal to 100. Official discount rate, 0.1% (Bank of Japan, 2001), and assumed higher discount rate, 0.5%, are considered. Figure 5 shows the present value of repairing cost at each year during the service life of structure. From this result, resources can be annually allocated to the structure or group of structures based on the expected probability of repairing to be occurred at the certain year.

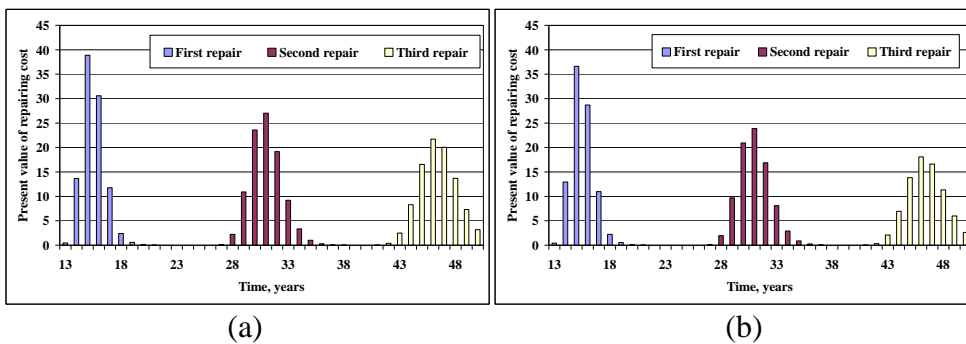


Figure 5: Present value of annual repairing cost at discount rate (a) 0.01%, (b) 0.05%

Cumulative expected life cycle repairing cost of R&M program is shown in Figure 6. Due to the effect of discount rate and the events that are not considered due to they cannot be implemented during the service life, total expected life cycle cost is less than the total of assumed total cost of three repairing, 300. From this result, the total expected life cycle cost of R&M can be estimated.

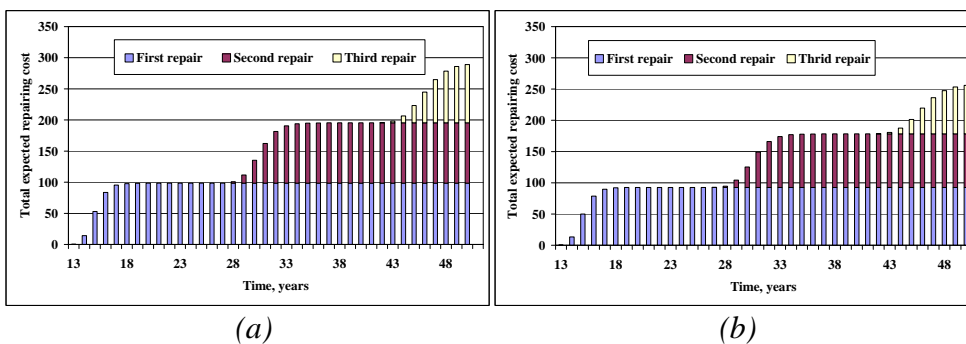


Figure 6: Present value of cumulative expected repairing cost at discount rate (a) 0.01%, (b) 0.05%

5. SELECTION OF REPAIRING METHODS

Many structure repairing methods are available in the market with different cost and performance. Decision makers have to choose the most suitable option based on an objective and many constrains. This study used minimum expected life cycle cost as an objective. Assumed performance and cost of three repairing methods is shown in Table 3. Chloride diffusion coefficient and coefficient of variation is used to indicate the performance of repairing system. Lower chloride diffusion coefficient and low coefficient of variation indicate higher performance and also higher cost. Others random variables are shown in Table 1.

Table 3: Assumed performance and cost of repairing options

Repairing	Mean	Coefficient of variation	Cost
A	1.29 cm ² /year	0.10	100
B	0.645 cm ² /year	0.10	150
C	1.29 cm ² /year	0.05	150

Figure 7 shows expected probability of all repairing at each time of repairing B and C. When compared to that of repairing A as shown in Figure 4, mainly only the first and second repairing has a high probability to be conducted due to lower chloride diffusion coefficient of repairing B. In contrast, lower coefficient of variation of the repairing C has small effect on the expected probability of repairing.

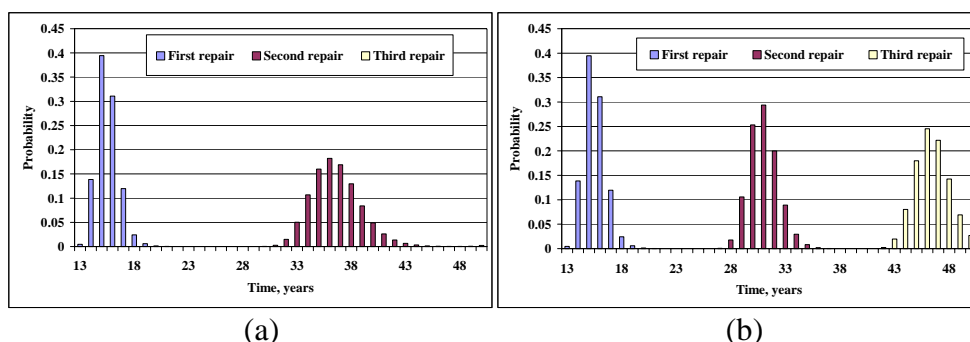


Figure 7: Expected probability of all repairing (a) A, (b) B

Comparison of total expected life cycle repairing cost by three options is shown in Figure 8. It is clearly shown that the higher performance of repairing B lower the total repairing cost. In contrast, repairing cost of option C is the highest. Based on assumed conditions, repairing B is the optimum method because of the lowest life cycle cost and satisfying assumed acceptable structural performance during the service life. In the future, more complete information of assumed variables is required in order to accurately select the optimum R&M program.

6. CONCLUSIONS

Methods to evaluate the expected probability of required R&M at each year during the service life and the present value of expected life cycle R&M cost of deteriorating structure were presented.

Due to uncertainties of parameters used in the deterioration prediction model, predicted time to conduct R&M is represented by the probability distribution instead of deterministic value. Expected cost is calculated based on obtained expected probability and discount rate. Total and annual resources can be allocated to structure or group of structure based on expected total life cycle cost and expected annual cost, respectively.

This approach is a part of the effort to determine the most optimal life cycle R&M cost for deteriorated reinforced concrete structure. However, further study about acceptable structural performance and database of R&M are being conducted.

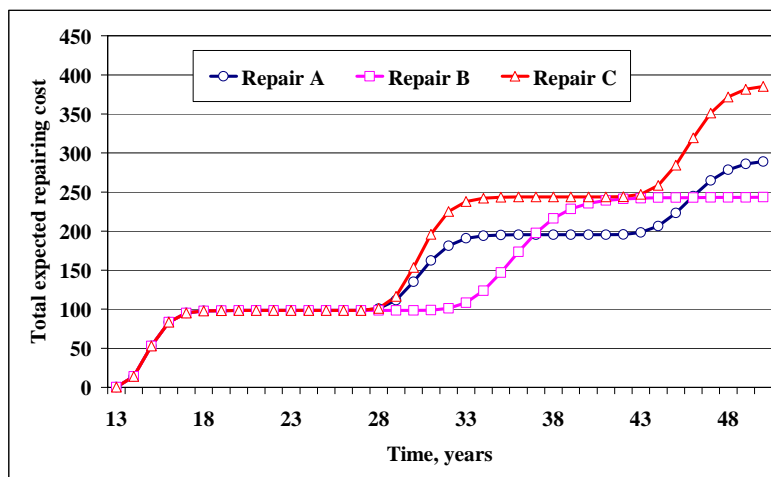


Figure 8: Comparison of total expected repairing cost

REFERENCES

- Bank of Japan, 2001. *Figures at a Glance*. Available online at <http://www.boj.or.jp/en/rate.htm> (August/2005)
- Enright, M. P., and Frangopol, D. M., 1999. Condition Prediction of Deteriorating Concrete Bridges Using Bayesian Updating. *Journal of Structural Engineering* 125(10), 1118-1125.
- Fishman, G. S., 1995. *Monte Carlo: concepts, algorithms, and applications*. Springer, New York.
- Yokosawa, Y., Sato, T., Kato, Y., and Uomoto, T., 2005. Report on Tamagawa Bridge Investigations by Using Inspection Software for Concrete Structures. *Proceedings of the Annual Convention of Japan Concrete Institute*, Nagoya, Japan.

IMPORTANCE OF MAINTENANCE OF CONCRETE STRUCTURES FOR URBAN SAFETY

TAKETO UOMOTO

ICUS, Institute of Industrial Science, University of Tokyo, Japan
uomoto@iis.u-tokyo.ac.jp

ABSTRACT

The maintenance of concrete structures is essential and important to maintain the safety of urban area. Most of the political, economical and educational activities are done in urban area. If any accident or hazard occurs, the effect is tremendous. Concrete structures are durable and people easily forget about the durability aspects of concrete structures. It is very important for both the owners and engineers to recognize how important it is to maintain concrete structures to keep the people safe in urban area. Before any accident of hazards happens, we should keep eyes to the maintenance of concrete structures. This paper describes what we are doing in Japan to maintain the existing concrete structures.

1. INTRODUCTION

Up till now in Japan, the economic growth was rapid in the period of 1960 ~ 1980. More than 100million cubic meters of concrete were used to construct the structures such as buildings, bridges, tunnels, dams, etc. to support the activities of Japanese people. As a result, these infrastructures rapidly reached 50 years in service, and due to deterioration of the structures, maintenance of these structures has become a major interest among the owners and the civil engineers.

On the other hands, population of Japan will reduce from now on because of fewer babies in a family approximately 1.2 children per one family. Although high technologies have been developed in recent years, it is sure that fewer engineers have to take care of the huge amount of structures from now on, which has never experienced in the past. Due to reduction in the economical growth, the budget for both construction and maintenance will be reduced in the future. The maintenance of existing structures must be done with the following conditions: 1) rapid increasing of the amount of existing structures reaching to the age of 50 years, 2) less amount of engineers to maintain the structures, 3) less amount of budget can be used to maintain the structures. .

Although there are many hazards in each country, concrete structures are expected to be safe for long period of time. Main hazards for the structures in Japan are as follows:

- 1) Earthquake and volcanic action
- 2) Landslide and flood
- 3) Typhoons and strong wind
- 4) Fire and Thunder
- 5) Accidents
- 6) Terrorism

If the structure is deteriorated before the hazards, the structure may easily collapse and difficult to maintain the safety of the people. The Photograph 1 shows an example of a collapsed pier during Hanshin Awaji Great Earthquake. As shown in the photo, the pier was deteriorated to large extent due to alkali aggregate reaction. Concrete is cracked severely and is just like a bundle of concrete blocks.



Photograph 1: Collapsed reinforced concrete pier affected by alkali aggregate reaction

In order to keep the safety of urban area, it is important to study and investigate not only on hazards but also on durability aspects of existing structures. Even a small amount of concrete spalling may cause traffic accidents to large extent as we experienced in Sanyo-Shinkansen in 1999.

Considering these situations now, this paper explains what is happening now in Japan and how we are dealing with the problems through researches and engineering.

2. SITUATION NOW IN JAPAN

The Figure 1 shows the estimated amount of concrete consumed in construction since 1945. As can be seen from the figure, within 25 years only 2 billion cubic meters of concrete were used until 1970. After that more than 8 billion cubic meters of concrete were used within 30 years. This shows that the existing structures being used for 50 years in service was less than 10% of the total amount of existing structures at the beginning

of the 21st century. One can imagine how the number of old structures used for more than 50 years will rapidly increase from now on.

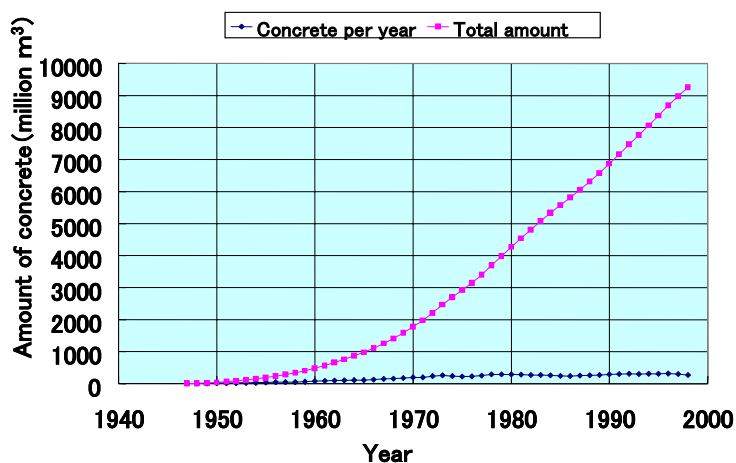


Figure 1: Estimated amount of concrete consumption in Japan

The percentage of number of civil structures being already repaired is shown in Figure 2a. The data of the buildings are shown in Figure 2b. The figure 2a shows that although the reason of repair is not the same, the percentage of repaired civil structures increases with years in service. Approximately 50 % of the structures are repaired after being used for about 60 years. The reasons for the repair are mainly due to deterioration or defects after being used.

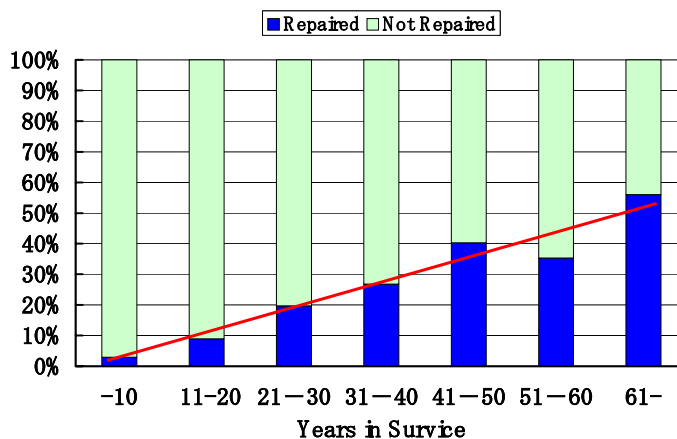


Figure 2a: Percentage of repaired civil structures after being used

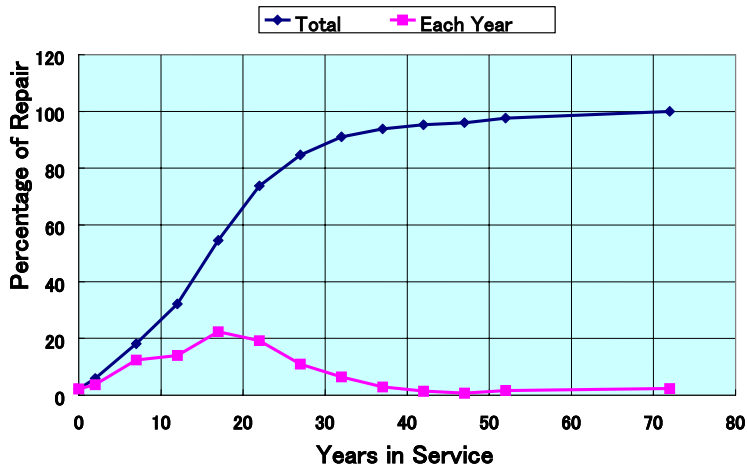


Figure 2b: Percentage of repaired houses and buildings

Compared to civil structures, 50% of houses and buildings are repaired after 17 years in service. It does not mean that houses and buildings are not durable. The repair of houses and buildings may be done because of defects or introduction of new facilities for the benefit of the user; not always due to deterioration.

3. GENERAL MAINTENANCE METHODS BEING USED UP TILL NOW (Uomoto and Misra, 2001)

The maintenance of concrete structures has been done mostly by the owners of the structures. In case of public structures, the ministries, etc. maintain the structure after the structures are completed. For the time being, the methods for the maintenance differ according to the owners of the structures. Although there are some differences, the main concept of the maintenance can be summarized as follows:

- 1) Periodic inspection and evaluation of deterioration degree
- 2) Detailed inspection and decision making
- 3) Repairing and strengthening of deteriorated structures

For periodic inspections, the inspectors inspect the structures visually, sometimes with the help of binoculars and hammers, once a year or once in several years according to the importance and time after the structure is completed. The inspectors are mostly trained engineers with experiences. The detailed inspection is done when the estimated degree of deterioration exceeds certain limit, or when some new phenomenon is found during the periodic inspection. The detailed inspection is done by visual inspections with the aid of non-destructive tests or taking core samples out from the inspected structure. The purpose of the inspection is to decide the cause of the deterioration and also to evaluate whether repair and/or strengthening is needed or not.

To repair or strengthen the existing structures, it is important to design and select sufficient methods and materials. The most popular repair method for corrosion of steel bars due to carbonation is to eliminate the carbonated concrete and replace it by new concrete and apply coatings with and without FRP sheets. But in case of steel corrosion due to chlorides from the surrounding environment, the highly chloride concentrated portion of concrete are taken out, anti-corrosive treatment is applied to the surface of the bar, and polymer cement mortar is generally used to repair the concrete before coating the concrete surface.

4. NEW STANDARD SPECIFICATIONS OF JSCE

After the investigations of many deteriorated concrete structures, the importance of durability was fully recognized by the civil engineers. To deal with the problem not only JSCE, AIJ, and JCI recommending methods to deal with the problems but also the Ministries, and other authorities started to propose practical counter measures to cope with the situation. As a result, a large amount of researches has been done related to the durability of concrete structures including non-destructive inspection methods.

Among these authorities, the Concrete Committee of JSCE, the leading committee in the field of concrete in Japan, has published new “Standard Specifications for Concrete Structures” in the years 2000, 2001 and 2002 to deal with the problems of durability (JSCE, 2000a, 2000b and 2001). The concept written in the specifications will surely be adopted by other institutions.

The main proposals of the “Standard Specifications” are the following two items:

- 1) Propose a new method to design and construct new concrete structures that can be used for specified lifetime without large amount of maintenance cost.
- 2) Propose an effective and economical system to maintain existing concrete structures with small number of engineers and workers.

To deal with the problems for the items 1) and 2), the following two Specifications are published: 1) The Standard Specification for Construction Works of Concrete Structures, Jan. 2000 (JSCE, 2000a) and 2) The Standard Specification for Maintenance of Concrete Structures, Jan. 2001 (JSCE, 2001). The concepts of the new Standard Specifications are briefly explained in the following chapters.

4.1 Durability design of concrete structures for new structures

Performance-based durability design was introduced to “Standard Specification of Concrete Structures” by the Concrete Committee of JSCE in the year 2000 (JSCE, 2000). Although durability of concrete structures was considered important in the previous specifications, performance-based design method was not used. The previous specifications described the

importance of durability by proposing that the concrete structures are durable for a long time when specified materials, mixes, covers, etc. are used. But these specifications did not mention about the duration of service time, etc.

The proposed performance-based new durability design can be summarized as follows:

The concrete structure must be quantitatively checked whether the structure possesses required performance within the designed period.

- 1) The degree of deterioration of the structure in service on specified cause must be specified.
- 2) To maintain the structure above the specified degree of deterioration, the required performance must be specified.

To examine the performance on durability, a kind of limit state design scheme was introduced for the durability of concrete structures. The equation can be written as shown in Equation (1):

$$\gamma_i \cdot A_d / A_{\text{lim}} \leq 1.0 \quad (1)$$

A_d : designed performance of the structure at specified time considering the specified deterioration cause

A_{lim} : limit of the performance of the structure

γ_i : coefficient of the structure considering the importance, etc.

Generally, deterioration items to be examined are the following items, but in some cases other causes, such as fatigue loading, must be examined.

- 1) Corrosion of steel bars due to carbonation of concrete
- 2) Corrosion of steel bars due to chloride penetration into concrete
- 3) Deterioration of concrete due to freezing and thawing
- 4) Deterioration of concrete due to chemical attack
- 5) Deterioration of concrete due to alkali-aggregate reaction
- 6) Water-tightness of concrete
- 7) Deterioration of concrete due to fire

The Figure 3 shows an example of the calculated result for minimum cover thickness to prevent carbonation induced corrosion at different years of service for OPC concrete and BFSC concrete. As shown in the figure, the cover thickness required changes according to the type of cement to be used, water-cement ratio of concrete, years of service and exposed condition (wet or dry) of the structure to be constructed. When the structure is designed for long period of time, the cover thickness may become too large, and it is recommended to use other countermeasures such as Epoxy-coated bars.

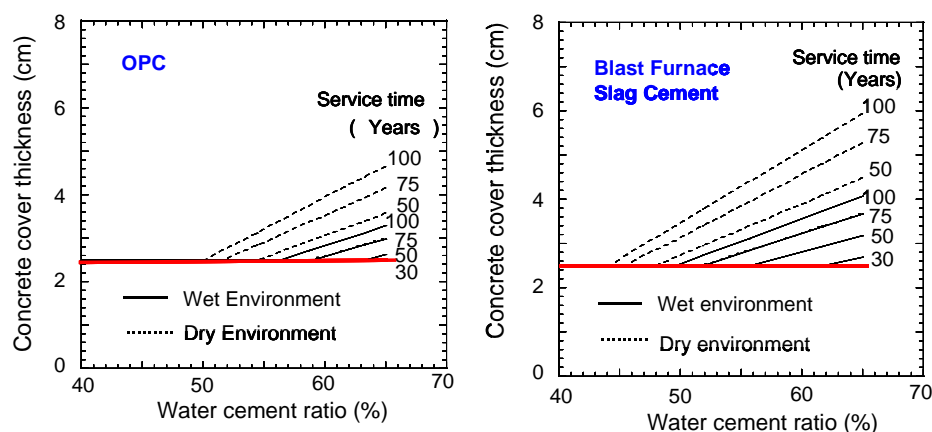


Figure 3: Calculated results of concrete cover according to JSCE Standard Specification (JSCE, 2000a)

4.2 Methods of maintenance newly proposed by JSCE (JSCE, 2001)

The methods used in the new Standard Specification are basically the same as the conventional method. The differences are that the new method requires to maintain the structure within their required performances throughout their service life. The principles of the standard are listed below:

- 1) To maintain a structure, performances required for the structure must be clearly defined.
- 2) The performances required for general structures are “safety”, “serviceability”, “hazards to the public”, “aesthetics and landscape” and “durability”.
- 3) Structures must be maintained according to the designated maintenance category by formulating a maintenance program to retain the performances within the specified tolerances throughout their service life. And the system for maintenance includes adequate “initial inspection”, “deterioration prediction”, “inspection”, “assessment/judgment”, “remedial measures”, and “record”.

The details of maintenance works are as follows:

- (1) Structures must be maintained according to a designated maintenance category by formulating a maintenance program to retain the performance within the specified tolerances throughout their service life. And maintenance system includes adequate “initial inspection”, “deterioration prediction”, “inspection”, “assessment/judgment”, “remedial action”, and “record”.
- (2) To maintain a structure, in addition to the assessment and evaluation at the time of inspection, assessment and evaluation must be made throughout the service life of the structure based on prediction of deterioration.
- (3) To predict the deterioration, required performances of the structure must be clearly defined, and also the design service life must be made clear.
- (4) The records on design, construction, initial inspection, deterioration prediction, periodical inspection, assessment and/or evaluation, and remedial actions must be kept throughout the service life.

One of the difficulties is how to predict the degree of deterioration at the end of their service life. There are several researches being done to predict the deterioration in numerical manner (JSCE, 2000b). In the published Standards, several numerical prediction methods are introduced as references for structures suffering cyclic fatigue loads, carbonation induced corrosion and chloride induced corrosion. In case of cyclic fatigue, S-N curves are used to predict the service life. In case of carbonation induced and chloride induced corrosion of steel bars, diffusion equations for carbon dioxide and chloride are used to predict the degree of corrosion. Using these prediction methods, deterioration degree can be estimated to certain degree. (See Figure 4) But for other deterioration problems, which has not been studied numerically, a quantitative model has not been proposed yet. To deal with the problem, a qualitative method “Grading method” is introduced in the Standard.

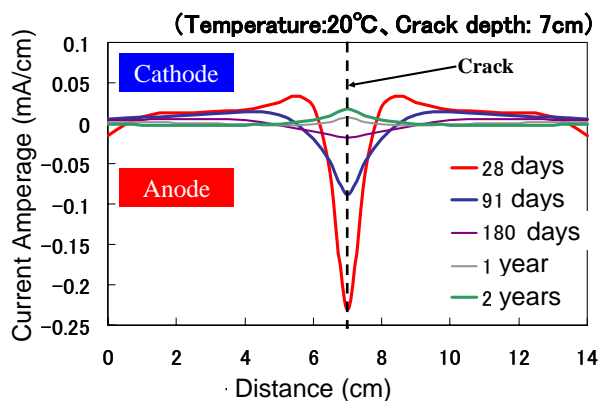


Figure 4: Quantitative prediction of corrosion in marine environment with cracks (Tsukahara et al., 2000)

5. PROBLEMS IN ACTUAL EXISTING STRUCTURES

When a civil engineer is asked by the owner to check the safety of an old existing structure, one of the largest problems is that there are neither drawings nor construction records of the structure available. No problem may occur in case of important facilities, which is maintained with great care. But in case of normal structures, the owners do not know the importance of these documents.

To deal with the problem, NDI is not enough. Fortunately, our structures are not too old, and they are mostly designed and constructed by the method specified by JSCE, AIJ or other associations. Considering these, the only way is to re-design the structure again using the methodologies used at the time of construction. Figure 5 shows an example of re-designed bridge pier constructed about 35 years ago. From the figure, it is much easier for a civil engineer to check the safety of the structure under several hazards. It will become more important for the owners and engineers to keep these documents throughout the service life of a structure.

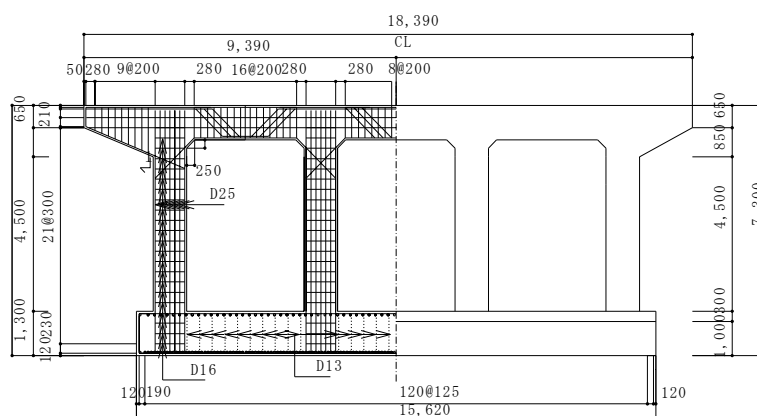


Figure 5: Re-designed reinforced concrete pier of a bridge (Okazaki, 2005)

6. CONCLUDING REMARKS

Engineering is not always complete, and further research works are needed. To sustain existing structures, durability of the structure is important. One good method is to construct durable structures, but for the existing structures maintenance is the only way to deal with the problem. Although concrete committee of JSCE has set up a good system for maintenance of existing concrete structures, there are still many things to be done: not only researches but also education to the students and engineers about durability and maintenance. I hope this paper may become a help to the concrete engineers of the world who are trying to design, construct and maintain concrete structures.

REFERENCES

- JSCE, 2000a. *The Standard Specification for Construction Works of Concrete Structures*. (in Japanese)
- JSCE, 2000b. References for “The Standard Specification for Construction Works of Concrete Structures”. (in Japanese)
- JSCE, 2001. *The Standard Specification for Maintenance of Concrete Structures*. (in Japanese)
- Okazaki, S., 2005. *Development of monitoring system for RC bridge based on restoration design method*. Thesis submitted to the University of Tokyo for Master of Engineering degree.
- Tsukahara, E., Koyama, R., Hoshino, T., and Uomoto T., 2000. Estimation Method of Corroded Portion of Reinforcing Steel Bar by Natural Potential Measurement. *Non-destructive Testing in Civil Engineering 2000*, Elsevier.
- Uomoto, T., and Misra S., 2001. Role of Engineers to Improve Quality of Concrete Structures. *Proceedings of EASEC-8*, Singapore.

RECENT SEISMIC LOAD TESTS ON REINFORCED CONCRETE BEAM-COLUMN JOINTS AT NTU, SINGAPORE

Bing Li and Tso-Chien Pan
Protective Technology Research Centre, School of Civil and Environmental
Engineering, Nanyang Technological University, Singapore
cbli@ntu.edu.sg

ABSTRACT

Current seismic provisions for determining the amount of transverse reinforcement in beam-column joints vary from one code to another. Moreover, the seismic provisions in current codes were developed for the most severe earthquake effects. There is a lack of an accepted designed method for determining the amount of lateral steel in areas of low to moderate seismicity where the ductility demand may be lower than that in areas of high seismic activity. This paper will provide an overview of simulated seismic loads tests conducted on reinforced concrete beam-column joint subassemblages at Nanyang Technological University (NTU) during recent years. Research conducted at NTU is aimed at examining the ductility and behaviour of moment-resisting frame with limit ductility in order to develop detailing guide lines for areas of low to moderate to seismicity.

1. INTRODUCTION

There are a large number of moment resisting frames built for residential and commercial purposes in Singapore and Malaysia. The current building code used is mainly based on the British Standard: the BS 8110, which has no provision for seismic loading. Hence, almost all these frames are built without seismic consideration in design and detailing, for example, no joint reinforcement in the joint cores. However recent studies have shown that although Singapore is located in a low seismicity region and there has never been any earthquake damage to the country, the seismic hazard potential in Singapore should not be ignored. This makes it necessary to study the performance of these moment resisting frames under possible earthquake conditions, and as a critical part of such frames, the non-seismically detailed beam-wide column joints deserve more attention.

This paper provides an overview of simulated seismic loads tests conducted on reinforced concrete beam-column joint subassemblages at NTU. These investigations have attempted to gain a better understanding of the general behaviour of these joints when subjected to lateral loads.

2. TESTS ON LIGHTLY REINFORCED BEAM-COLUMN JOINTS

A large number of buildings are designed as gravity-load-designed or lightly reinforced concrete structures in Singapore and Malaysia, therefore, they are constructed with reinforced concrete moment resisting frames having little or no transverse reinforcement in the joint zone. Problems have been encountered when assessing the seismic behaviour of the joints in these buildings. This is due mainly to the absence of a theoretical basis for evaluating the joint behaviour that is supported by comprehensive test data. Modern design codes are also of little assistance for assessing these joints as they are based on tests of the joints with adequate joint transverse reinforcement. Quasi-static cyclic loading tests have recently been conducted on four reinforced concrete beam-column joint subassemblages with or without a floor slab for examining the influence of regional beam-column joints to the overall behaviour of the buildings in low to moderate seismicity area and providing useful insights without going into the principle of full ductile design (Li, Pan and Pan 2003). Four specimens designated as AS1, AS2, AL1 and AL2, were built and tested (see Figures 1, 2). They were selected from an existent building, which was designed in accordance with BS 8110. Among these, AL1 and AL2 were represented connections collected from a weak direction frame and a strong direction frame, respectively. AS1 and AS2 were the joints with a floor slab. Reinforcing detailing of AS1 and AS2 were the same as those of AL1 and AL2 with exception that a one-meter width slab and transverse beams were added.

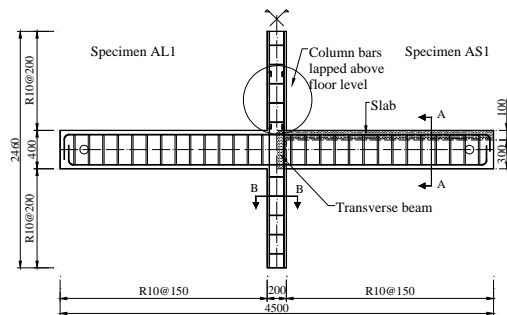


Figure 1 Dimensions and reinforcing details of AL1 and AS1

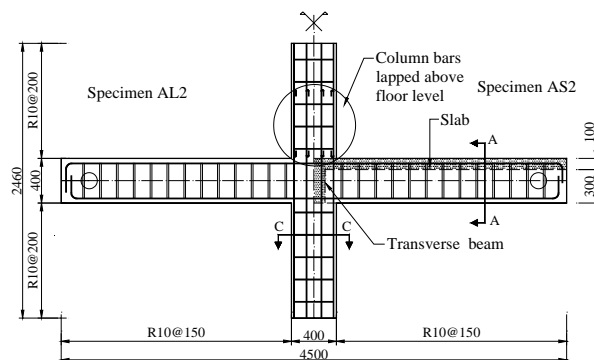


Figure 2 Dimensions and reinforcing details of AL2 and AS2



Figure 3 Test set-up

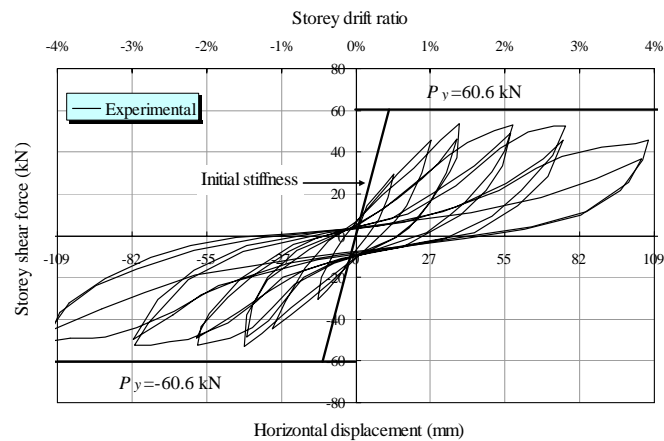


Figure 4 Storey shear force versus horizontal displacement for AL1

The storey shear force versus horizontal displacement relationship for AL1 is shown in Figure 4. The theoretical capacity was not reached until the end of the test with the maximum capacity being obtained at a displacement of 37 mm corresponding to a storey drift ratio of 1.4%. Compared with the predicted yield displacement of AL1, this displacement was much large, which was about three times that of the first yield displacement of 12.5 mm predicted through the theoretical approach. The maximum capacities of AL1 were 53 kN in both loading directions. After the loading to a storey drift ratio of 1.5%, the hysteretic loops pinched significantly due to the severe bond deterioration along the beam and column bars as well as the joint diagonal tension cracking. Consequently, the extensive of joint diagonal tension cracks caused the severe strength and stiffness degradation. At the end of the test, the residual load-carrying capacity of the specimen was about 37 kN in either loading direction and therefore, the behaviour of the test specimen was dominated by the response of the most damaged beam-column joint. Figure 5 illustrates the storey shear force versus horizontal displacement relationship for AS1. Also shown are the theoretical capacities of the test unit. Solid lines present the theoretical capacities without consideration of the presence of the slab while dash lines are the theoretical capacities assuming that all the beam longitudinal bars and slab bars yielded simultaneously. In other words, it is assumed that slab bars within the whole

slab width will effectively participate in resisting the lateral loading. The first yield displacement of AS1 occurred at a displacement of 19.6 mm corresponding to the storey drift ratio of 0.6% in the positive loading direction. At this moment, the specimen also reached its theoretical capacity, which occurred earlier than that of a 1% storey drift ratio in the negative direction. The maximum capacities were obtained at storey drift ratios of 2% and 1.5%, which were 80 kN in the positive and 70 kN in the negative loading directions indicating that the specimen took over-strength factors at 27% and 11%, respectively. If compared with AL1, the maximum capacities of AS1 were 51% and 32% higher than those of AL1 in the same loading directions. It was evident that the participation of a slab enhanced the moment resisting capacity of the specimen, but the slab bars were not fully effective to resist bending moments and therefore, the specimen didn't reach the theoretical capacity with considering the slab effect in both loading directions. In the first loading cycle to a storey drift ratio of 3.0%, the recorded storey shear force dropped to the theoretical level and the hysteretic loop showed apparent pinching.

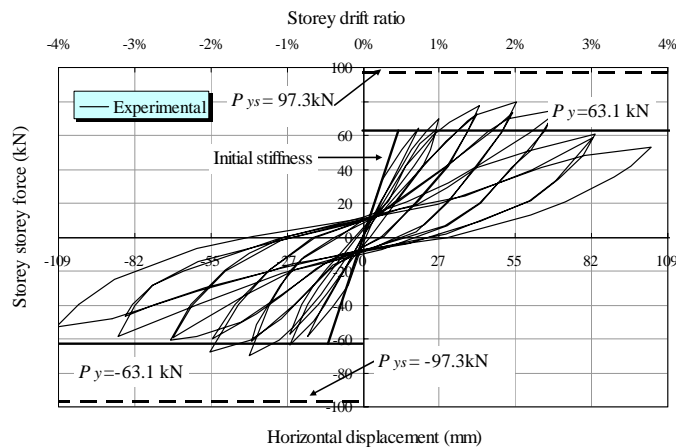


Figure 5 Storey shear force versus horizontal displacement for AS1

Figure 6 illustrates the storey shear force versus horizontal displacement relationship for AL2. The obtained yield displacement was 21 mm corresponding to the storey drift ratio of 0.8%. This was about three times that of the predicted yield displacement of 6.75 mm. At this moment, the specimen reached its theoretical capacity of 63.9 in either loading direction. The maximum capacities were obtained at a storey drift ratio of 1.5%, which were 82 kN in the positive and 75 kN in the negative loading directions indicating that the specimen took over-strength factors at 28% and 17%, respectively. From the drift ratio of 1.5%, significant pinching was observed in the hysteretic loops and, in the repeated cycle, the specimen started to lose its load-carrying capacity at 11.9% and subsequently, strength and stiffness degradation was evidently. At the second cycle of the loading run to a drift ratio of 3.0%, the specimen lost its load-carrying capacity at 20% indicating that the specimen failed at this stage. At the first semi-cycle of a 3.8% storey drift ratio, the load-carrying capacity suddenly dropped to 42 kN and so for the reasons of safety, the test was withheld at this moment.

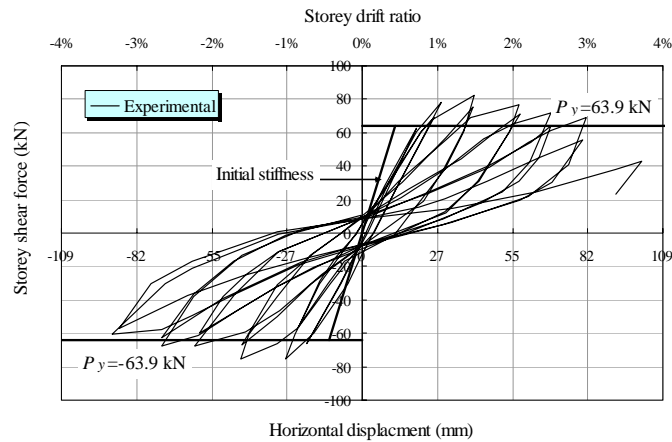


Figure 6 Storey shear force versus horizontal displacement for AL2

Figure 7 illustrates the storey shear force versus horizontal displacement relationship for AS2. The first yield displacement was 14 mm; corresponding to a storey drift ratio of 0.6%. This was about two times that of the predicated yield displacement of 6.54. At this moment, the specimen reached its theoretical capacity of 66.7 kN in either loading direction. The maximum capacities were obtained at a storey drift ratio of 2.0%, which were 98 kN in the positive and 83 kN in the negative loading directions indicating that the specimen took over-strength factors at 47% and 24%, respectively. If compared with AL2, the maximum capacities of AS2 were 19% and 11% higher than those of AL2 in the same loading directions. Subsequently, AS2 lost its load-carrying capacity progressively until the theoretical value was reached. Limited pinching was observed after the second cycle of a storey drift ratio of 1.5%. After the second cycle of a storey drift ratio of 2.0% up until the end of the test, pinching and stiffness degradation were obvious.

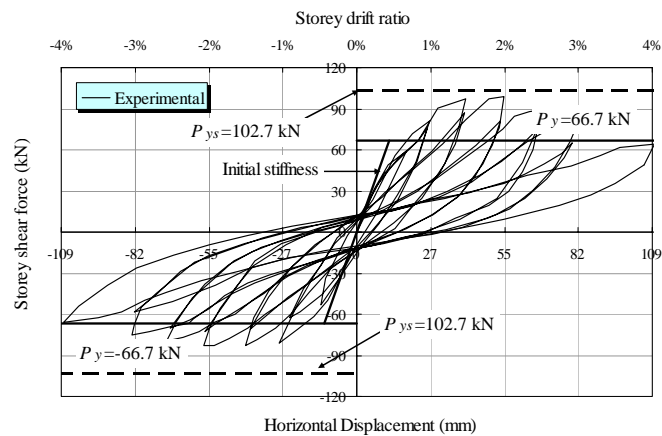


Figure 7 Storey shear force versus horizontal displacement for AS2

As expected, specimens with a slab showed a higher strength than specimens without a slab. The presence of a floor slab affects the behaviour of joints in two ways: It increases the flexural capacity of the main beams; and it imposes torsional moment on the transverse beams that affect the

confinement of the joint. This phenomenon was observed in load-deflection, moment-rotation and strain distribution. The measurement of strain distribution along the longitudinal reinforcement showed that beam reinforcement of all specimens experienced yield at a ductility level of 1.0. However, the peak magnitude of beam bar strain of those specimens with a slab was reduced. This could be attributed to the decrease in the curvature due to the slab participation. The tensile stress of the slab reinforcement outside the column cores was transferred by means of torsion moment of transverse beam. Therefore, slab participation could also be verified by the developing of torsional moment. In addition to strength, the stiffness is also an important measurement of the performance of joints. Excessive shear deformation in the joints or the loss of anchorage of the beam longitudinal reinforcement was reflected in the rapid degradation of the stiffness. When the main beam longitudinal reinforcement yielded, the stiffness decreased rapidly. Up to a drift ratio of 2%, the specimens maintained their initial stiffness; however, beyond the 2% drift ratio, the loss of stiffness varied with the type of specimen. Those specimens without a slab experienced significant losses of stiffness. In all specimens, the hysteresis loops became increasingly pinched after the second loading cycle. This is attributed mainly to the opening and closing of flexural cracks. Other factor such as shear deformation of the joint and the slippage of beam and column bars through the joint also contribute to the loss of stiffness and hence, the pinching of the loops.

3. TESTS ON BEAM-WIDE COLUMN JOINTS

Reinforced concrete structures consisting of wall-like wide column elements are very common in regions of low to moderate seismicity, and are the predominant structural system in Singapore and Malaysia. The wide-column frames are quite stiff in one direction and flexible in the other, and usually they are designed according to BS 8110 without the consideration of seismic loading. Beam-column joint regions in such frames are of special interest because they are usually non-seismically detailed and their joint dimensions are quite unusual. The lack of seismic reinforcing details is in sharp contrast to those used in modern seismic design. Therefore, it is of concern that the strength, ductility, and energy dissipation capacity of these beam-wide column joints may not be adequate to sustain earthquake-induced loads due to the lack of seismic reinforcement details in this type of joints. Proposed seismic assessment methods and approaches were obtained purely from tests on normal types of beam-column joints, which differ largely from the beam-wide column joints in terms of joint dimensions. Since joint dimensions have been found to have a great influence on the seismic behaviour of joints, the previous findings for normal types of beam-column joints may not be applicable to beam-wide column joints. NTU began a laboratory investigation of beam-wide column joints in 2000 (Li, Wu and Pan 2002). Four joint subassemblages have been tested subjected to quasi-static lateral cyclic-loading to determine design details necessary for RC wide column frames that will resist moderate earthquake without significant loss of

strength. Specimens were tested as shown in Figures 8 and 9.

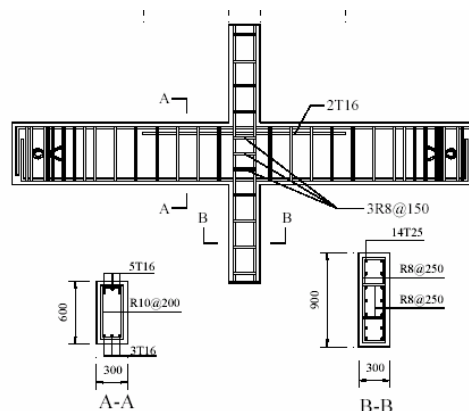


Figure 8 Dimensions and reinforcing details of M1

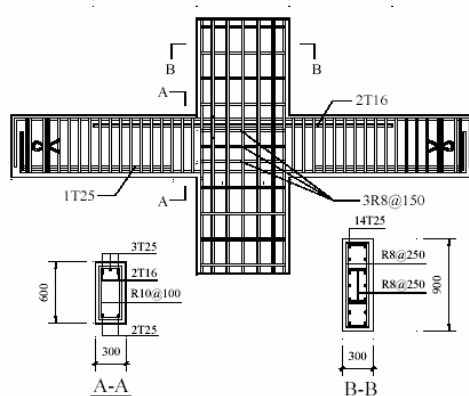


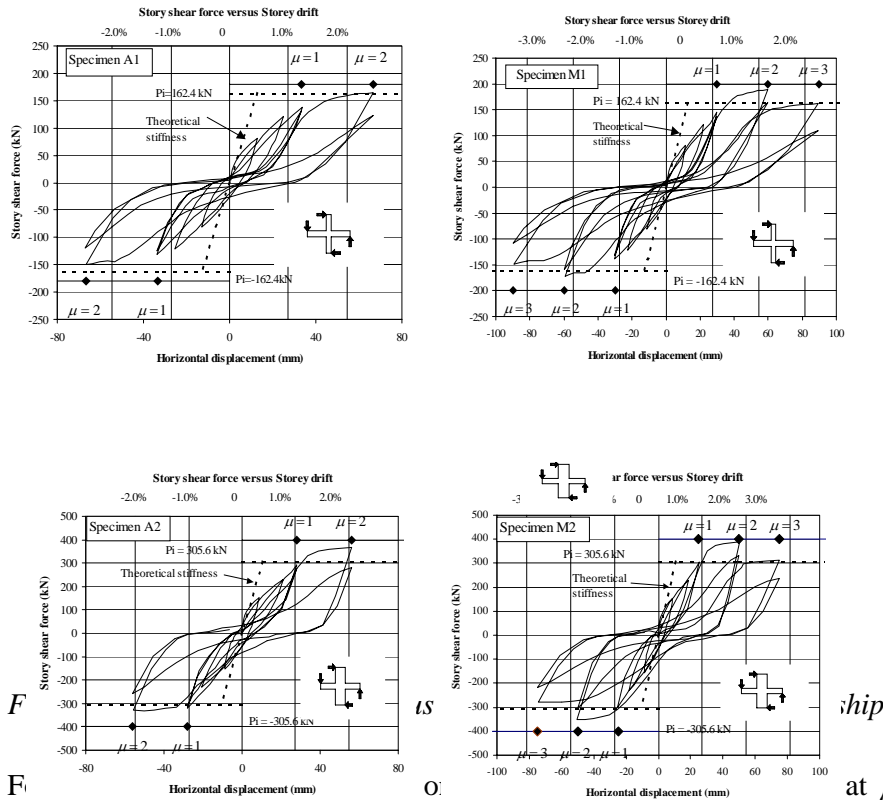
Figure 9 Dimensions and reinforcing details of M2



Figure 10 Test set-up

The as-built specimen A1 failed at displacement ductility factor μ_{Δ} of 2 or at story drift ratio of 2.4%, while the modified M1 failed at $\mu_{\Delta} = 3$ or at story drift ratio of 3.3%. By comparing the storey shear forces of A1 and M1 (see Figure 11), it can be seen that both specimens reached their ideal horizontal strength in the first cycle with $\mu_{\Delta} = 2$. However, in the second cycle with $\mu_{\Delta} = 2$, the horizontal strength of A1 dropped significantly, and

the specimen failed at this stage. For M1, the significant drop in horizontal strength occurred in the second cycle with $\mu_{\Delta} = 3$.



at $\mu_{\Delta} = 2$ or at story drift ratio of 2.04%, while the modified one M2 failed at $\mu_{\Delta} = 3$ or at story drift ratio of 2.7%. By comparing the storey shear forces of the two specimens (see Figure 11), it can be seen that both A2 and M2 reached their ideal horizontal strength in the first cycle with $\mu_{\Delta} = 2$. In the second cycle with $\mu_{\Delta} = 2$, the horizontal strength of A2 dropped significantly and the specimen finally failed at this stage. However, M2 did not suffer a significant drop of horizontal strength until the second cycle of $\mu_{\Delta} = 3$. The initial stiffness of A1 and M1 obtained from the tests were 4.82 kN/mm and 5.4 kN/mm, respectively. That was equal to 38% and 42% of the theoretical stiffness. The low stiffness was due to the early diagonal cracking within the joint core region, and the bond deterioration along the beam and column main bars. The modification of the reinforcing details in M1 did not show any significant effect on the initial stiffness, because the initial stiffness depends mainly on the column and beam section properties, which were kept unchanged for two specimens. The initial stiffness of A2 and M2 obtained from tests were 10.98 kN/mm and 12.44 kN/mm, respectively, which were equal to 38% and 45% of the theoretical stiffness. The low stiffness was due to the early diagonal cracking within the joint core region. The modification of reinforcing details in M2 did not show any obvious effect upon the initial stiffness, and was also found to have negligible effects

upon the stiffness degradation of the specimens. The stiffness of the two specimens degraded at about the same rate through the whole test.

For oblong joints A1 and M1, a maximum nominal horizontal shear stress in the joint core of $0.84\sqrt{f'_c}$ or $0.15 f'_c$ was obtained in the first positive cycle of loading to a displacement ductility factor of 2, and 3, respectively. While for the wall-like column joints A2 and M2, the maximum nominal horizontal shear stress obtained in the joint core was $0.61\sqrt{f'_c}$ or $0.11 f'_c$, which occurred in the first positive cycle of loading to $\mu_\Delta = 2$, and 3, respectively. Based on the experimental results, it was found that the maximum joint shear stresses occurred in the two oblong joints A1 and M1, and that the two wall-like column joints A2 and M2, were same. However, M1 and M2 achieved higher ductility levels than A1 and A2. The reason for such improvement may be due to the presence of joint transverse reinforcement in M1 and M2. In A1 and A2, there was no joint transverse reinforcement provided in the joint core. The joint transverse reinforcement in M1 and M2 helped the joints share a part of the total joint shear force. Thus it prevented the diagonal compression strut being overloaded at an earlier ductility stage, and the specimens survived until the higher displacement ductility levels.

The joint shear deformation was also measured during the testing of A2 and M2. For A2, the joint deformation contributed 10% to 16.5% towards the total horizontal displacement, while for M2 joint deformation contributed 13% to 24% towards the total horizontal displacement. The increased contribution of the joint deformation towards the total horizontal displacement of M2 could also be attributed to the presence of joint transverse reinforcement. In M2, the presence of the joint transverse reinforcement formed a relatively flexible truss mechanism other than the relatively stiff diagonal compression strut. Thus a part of the joint shear force in M2 was transferred by the relatively flexible truss mechanism rather than purely by the relatively stiff diagonal compression strut. The relatively flexible joint core thus allowed the increase of the joint deformation to occur in M2.

4. SUMMARIES

This paper has summarized simulated seismic loads tests conducted on reinforced concrete beam-column joint subassemblages at NTU. Based on experimental studies conducted at NTU, the following conclusions can be made:

For the lightly RC beam-column joint subassemblages, the maximum nominal horizontal joint shear stress of the subassemblages exceeded the limits either required by ACI 318 or NZS 3101 and therefore, the joint failure mechanism could be expected in the test subassemblages. To fulfill the reinforcing details for limited ductile frame structures, beam-column joint must be suitable reinforced to ensure joint shear mechanism. Limited joint reinforcement can improve the individual joint region. However it is

not enough to improve the overall performance of test specimen and whole buildings in terms of strength, stiffness and ductility. The presence of a slab increased both the strength and stiffness of subassemblages. It was also found that the development of an effective slab width is related to the flexural strength ratio, and the global displacement demand. The transverse beams were most effective in confining the joint before experiencing torsional cracks. However once the transverse beams reached their torsional cracking strength, their ability to confine the joint diminished.

For non-seismically detailed oblong joint and wall-like column joint, the maximum nominal horizontal shear stress in the joint core is $0.15 f'_c$ and $0.11 f'_c$, respectively. Both the joints failed at $\mu_\Delta = 2$. While for the two modified oblong joint and wall-like column joint, which contains 15% and 24% of joint horizontal transverse reinforcement required by NZS 3101, respectively, the joint shear forces are the same as those of the as-built specimens. However, due to the presence of the joint transverse reinforcement, both specimens achieved $\mu_\Delta = 3$. And more energy was dissipated in the modified joints, observed from the hysteresis loops of the specimens. For wall-like column joints of limited ductility frames having joint shear stress ratio (v_{jh} / f'_c) less than 0.15, the column depth is so large that even when the large diameter beam bars are used, the ratio of beam bar diameter to column depth can still satisfy the strict requirement given by NZS 3101. For oblong joints of limited ductility frames having joint shear stress ratio (v_{jh} / f'_c) less than 0.2, the improvement of the behaviour of this kind of joints cannot depend on the restriction of beam bar diameters rather than increasing the joint transverse reinforcement. A minimum amount of horizontal joint reinforcement of $V_{sh} / V_{jh} = 0.35$ is sufficient.

REFERENCES

- Li B, Wu YM and Pan T-C., 2002, *Seismic Behaviour of Non-Seismically Detailed Interior Beam-Wide Column Joints - Part I: Experimental Results*. ACI Journal, Vol. 99, Nov –Dec 2002.
- Li B, Wu YM and Pan T-C., 2003 *Seismic Behaviour of Non-Seismically Detailed Interior Beam-Wide Column Joints - Part II: Discussion and Theoretical Comparisons*. ACI Journal Vol.100, Jan–Feb 2003
- Li B, Pan T-C and Tan HY.,2002, *Earthquake Resistance of Lightly Reinforced Concrete Interior Beam-Column Joints Including a Floor Slab* – Paper 157, 12th European Conference on Earthquake Engineering"

APPROXIMATION OF DAMAGE FOR A REINFORCED CONCRETE COLUMN SUBJECTED TO INTERMEDIATE RANGE BLAST LOADING

XIN ZHANG AND TSO-CHIEN PAN

Protective Technology Research Centre, School of Civil and Environmental Engineering, Nanyang Technological University, Singapore
cxzhang@ntu.edu.sg

ABSTRACT

This paper presents response results for a supporting reinforced concrete (RC) column of a building subjected to an intermediate range, blast loading. The response results are based on finite element (FE) model, material-level modeling is applied and the material nonlinearity was considered. Anisotropic material model is used for the degradation of concrete strength. The damage of the column is evaluated for the duration where the RC column is subjected to the blast load. During the loading duration, the surface of the column subjected to blast loading is in a state of compression as it deforms. As the column springs back, the compression state of this column surface reverses its stress state to tension, leading to material failure.

1.0 INTRODUCTION

Current security issues emphasize the need of the analysis of residential / commercial buildings under blast loading. The blast effect of an explosion is in the form of a shock wave composed of a high-intensity shock front, which expands outward from the surface of the explosive into the surrounding air. As the wave expands, it decays in strength, lengthens in duration, and decreases in velocity. When the explosion originates at a large scaled range and the structure is small compared to the dimension of the blast wave front, the structure will be loaded in a manner that leads to global deformation, i.e. all the elements provide some degree of resistance to the loading. If the explosion is sufficiently close to the building, the blast loading on the structural surface will be very uneven. In this case, the structural response is characterized by local failure of some of the structural components in the first place and may evolve to the progressive collapse of the entire building later in a much slower time scale. At an intermediate scaled range, both global and localized response can be expected. In the evaluation of progressive collapse, the damage of the columns is usually the controlling factors. Therefore, it is necessary to estimate the damage of columns subjected to blast loading.

For a residential/commercial building, the explosion events are usually confined by the city environment, i.e. street width, parking lots, etc. An intermediate range of 10 m standoff distance of the charge is quite representatively a conservative estimation for most significant car bombings. Small explosion events are likely to be closer but less significant. Therefore, in this paper, a surface explosion of one-ton TNT equivalence at a 10 m standoff distance is considered for a typical building RC column. The objective is to understand the building column behavior under this loading condition.

2.0 THE COLUMN

The dimensions of the column shown in Figure 1 are 1.5 m by 0.5 m, whereby the wider dimension is exposed to the explosive. In the 10 m standoff case, its response may be computed by using only half of its domain due to the symmetry. Therefore, symmetrical boundary conditions are to be applied on the center vertical plane parallel to the direction of the blast wave propagation. As shown in Figure 1, the left plot shows the elevation of a 5 m high target column with its upper and lower ends fixed. The fixed-end boundary conditions are as approximated because restraint on this column provided by other part of the structure may be relatively weak considering the dimension of the column itself. The right plot shows the meshed half section of the column with symmetrical boundary being applied on the right hand side border.

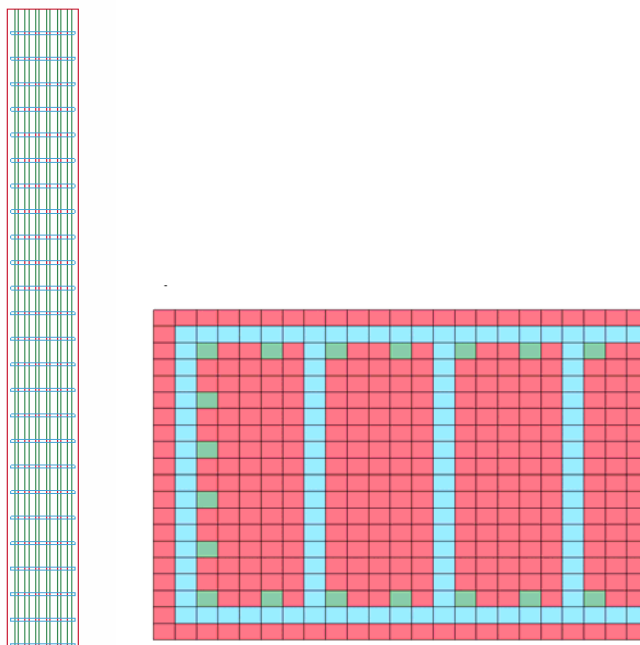


Figure 1 FE model of the column

3.0 MATERIAL-LEVEL MODEL

Concrete is a brittle material, which exhibits distributed damage and degradation of the mechanical properties with increase loading. The phenomenological response of plain concrete subject to predominantly tensile stresses is characterized a rather linear ascending branch of the stress-displacement curve. The linear ascending branch is typically followed by a progressively decreasing residual strength resulting in the formulation of macro-defects in the form of discrete cracks. When unloaded in the post-peak regime, non-recoverable deformations as well as a degradation of the stiffness of the unloading branch are observed. From a micro-structural point of view, the degradation progress of the elastic module, commonly referred to as damage, is the result of the growth and coalescence of the existing micro-cracks micro-voids along the interface of the cement paste and the aggregates. The deterioration process prevents a complete closure of micro-cracks during unloading. As a consequence, permanent strains develop. On the phenomenological level, this effect is often modeled by means of classical plasticity theory. Depending on the level of the hydrostatic stress, a rather gradual transition from highly localized fracture under tension to distributed micro-structural deterioration leading to a rather ductile material behavior when subjected to tri-axial compress is observed.

Continuum damage mechanics is concerned with the modeling of micro-structural degradation processes on a phenomenological level. The bulk of existing continuum damage approaches is concerned with isotropic damage evolution, leading to a degradation of Young's modulus as a function of a scalar damage parameter by exploiting the notion of effective stress. In contrast to the assumption of isotropy, the formation of cracks in concrete induces a directional bias to the material properties. In the formulations based on the concept of micro-plane anisotropic damage is attributed to the reduction of the stress bearing area fraction, associated with the respective micro-crack orientation.

In the literatures available, there are many constitutive models for concrete such as Meschke et al (1997), Govindjee et al (1995) and others. In this study, the concrete model used in the modeling of the building is an anisotropic brittle damage model developed by Govindjee et al (1995). Each steel rebar is modeled as a single layer of solid elements. The steel reinforcement loops are also modeled in the same way. In order to simplify the modeling, the diameters of the loops were enlarged while the Young's modulus of steel is reduced accordingly.

4.0 NUMERICAL RESULTS

The CONWEP loading is applied to the front surface of the column. The side and back surfaces, which are the surfaces not directly exposed to the loading front, are considered as free from loading. In this case, the nature of the blast loading may be slightly overestimated.

The response of the column is then determined for the FE model with the aid of the analytical software LS-DYNA (2003). The numerical results of the column response when subjected to a one-ton explosive at a 10 m standoff distance are shown in Figure 2. The assumed fixed-end boundary conditions would lead to induced column reaction forces at the supports being larger than more flexible boundary conditions. However, the column damage as determined based on the assumed fixed-end boundary conditions while being an overestimate, provides engineering conservatism.

In reality, the loss of the supporting capacity of a column may occur in two stages. The concrete material may first be partly damaged by the blast loading directly. During the first stage (i.e. loading duration), the column may still stand although it has been changed in terms of material status and geometry with some percentage of supporting capacity left. During the second stage (i.e. ensuing duration), the gravity loading of the upper storeys are activated, and the column may experience further material failure from either axial compression or column buckling. The second stage is considered to be a much slower process compared to the first stage. The current analysis is concentrated on the first stage of the damage process (i.e. loading duration).

The evolution process of the damages in the column is shown in Figure 2. It is one half of the column. The surface with black dots is the symmetrical plane. These dots are the intersections of the loops with this plane. The plots in the left side of Figure 2 show the front surface and the symmetrical plane, while those in the right side of Figure 2 show the back surface and the symmetrical plane. The color map shows the damage level of the concrete. It can be seen that the concrete is damaged first in the tensioned part of the column, making an arc-shaped damage zone. As the deformed column springs back, the compression zone reverses its stress state to that of tension, and thus becomes damaged. It is noted that the damage model for the concrete material is directional. The damage in one direction may not suggest the same level of damage in other directions. A full damage function has not been currently defined and this requires further research. Therefore, the assessment of the residual axial load resistant capacity needs to be further investigated.

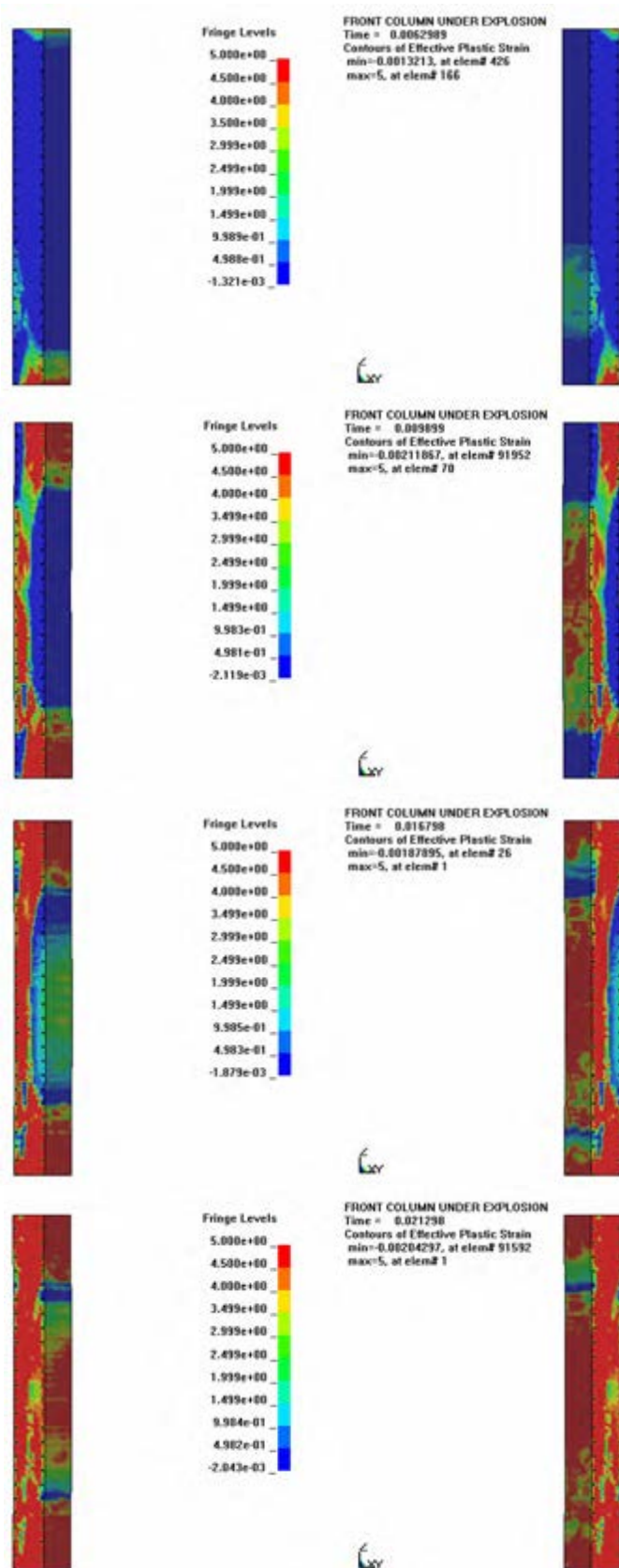


Figure 2 Concrete cracking in the column

5.0 CONCLUSIONS

The response of a RC column is computed by using anisotropic concrete model. The damage level is evaluated based on the numerical results. The blast loading considered is an intermediate range case of a one-ton TNT equivalence at a 10 m standoff distance. For the RC column, the boundary conditions are assumed to be fixed at the supports, which provide engineering conservatism. The focus of the numerical investigation is on the column response during the loading duration. The numerical results show that during the loading duration, the surface of the column subjected to blast loading is in a state of compression as it deforms. As the column springs back, the compression state of this column surface reverses its stress state to tension, leading to material failure. Such a local material failure may compromise the residual axial load capacity, whereby the extent requires further investigation.

REFERENCES

- Govindjee, S., Kay, G.J., and Simo J., 1995. Anisotropic Modeling and numerical simulation of brittle damage in concrete. *International Journal for Numerical Methods in Engineering* 38, 3611-3633.
- LS-DYNA manual, 2003. LSTC
- Meschke, G., Lackner, R., Mang, A., 1997. An isotropic elastoplastic damage model for plain concrete. *International Journal for Numerical Methods in Engineering* 42, 703-727.
- U.S. Department of the Army. 1990. *Structures to Resist the Effects of Accidental Explosions*. Army TM 5-1300. Navy NAVFAC P-397, AFR 88-22. Washington, D.C.: Departments of the Army, Navy, and Air Force.

SEISMIC MICROZONATION OF SYLHET CITY

MEHEDI AHMED ANSARY AND MD.REZAUL ISLAM
Department of Civil Engg., BUET, Bangladesh
ansary@ce.buet.ac.bd

ABSTRACT

Seismic microzonation maps can play a significant role in mitigating the consequences of earthquakes. Geographic information system (GIS) provides an ideal environment for compiling and integrating regional databases of spatial geologic and geotechnical information for developing seismic microzonation. The main aim of this study is to develop seismic microzonation map for Sylhet City based on reflection of ground shaking and the secondary site attributes such as soil amplification, liquefaction and landslide.

For microzonation purpose 167 boreholes with SPT data were collected from different relevant organizations. To verify those data nine boreholes up to a depth of 30m were carried out. Intensity values obtained for different events were calibrated against attenuation laws to check the applicability for study area. Vibration characteristics at diverse points of the study area were estimated by employing one dimensional wave propagation program SHAKE. The liquefaction resistance factor and the resulting liquefaction potential were estimated by a method suggested by Seed et al. The program used for landslide hazard analysis is XSTABL, which is a fully integrated slope stability analysis program, which evaluate the factor of safety for a layered slope using the simplified Bishop Method. The quantification of the secondary site effects and the weighting scheme for combining the various seismic hazards is heuristic, based on judgment and expert opinion. The final combined hazard is computed as a weighted sum of the various hazards.

1. INTRODUCTION

In accordance with chronological data, northeastern district, mostly, Sylhet, Mymensingh and Rangpur, experienced earthquakes at regular intervals that have instigated bulky destruction in the earlier period. Seismic hazard due to local site effects such as soil amplification, liquefaction, and landslide can be anticipated by combining the available soil parameter data with the current hazard models or by making use of existing maps showing estimated levels of these collateral hazards. Regional seismic hazard and risk analysis is used not only for estimation of potential damage and loss to existing facilities, but also for planning locations and construction of future facilities and for analyzing and comparing the regional effects of various

retrofit schemes. The GIS-based analysis is useful to engineers, planners, emergency personnel, government officials, and anyone else who may be concerned with the potential consequences of seismic activity in a given region. The results of a regional seismic hazard and risk analysis are usually presented in the form of microzone maps that serve as an effective means of conveying information from the scientific community to the professional community of decision makers involved in hazard and risk mitigation.

2. ADMINISTRATIVE BOUNDARY OF SYLHET CITY CORPORATION

Sylhet Municipality was established in 1878. During 1991, area of Sylhet Municipality was 10.49 sq.km and other urban area was 43.92 sq.km. Sylhet Municipality had 5 wards until 1991; in 1996 it had 13 wards. Recently, the Municipality is upgraded to City Corporation with 27 Wards and 210 Mahallas. Ward map was collected from Sylhet City Corporation where total area was divided in to 13 wards .The Sylhet City Corporation authority did not prepare an updated map. So it was decided to prepare an updated ward map for this study. For this purpose, GPS value of different fringes site and core sites of the study area were collected. The existing city corporation map was scanned and converted into digital map. Using this digital map and 2001 Mauza data as well as consultation with the Sylhet City Corporation officials, a map containing 27 wards was developed. From updated map it was found that existing area of municipality is 26.50 km². Figure 1 shows the updated ward map of Sylhet City Corporation

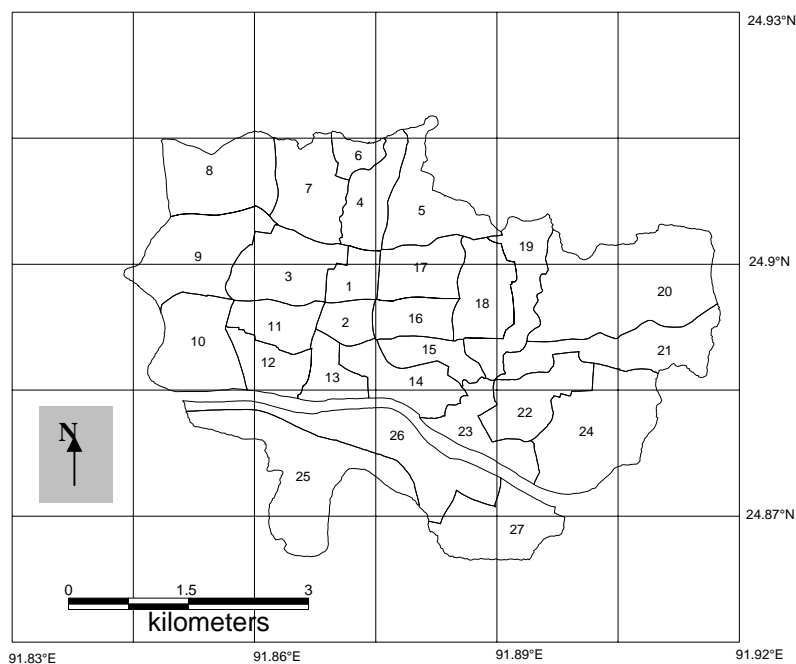


Figure 1: Updated ward map of Sylhet City Corporation

3. REGIONAL TECTONICS

In accordance with Molnar and Tapponnier (1975), for the past 40 million years the Indian subcontinent has been pushing northward against the Eurasian plate at a rate of 5 cm/year, giving rise to the severest earthquakes and most diverse land forms. Bilham et al. (2001) has pointed out that there is high possibility that a large earthquake will occur around the Himalayan region based on the difference between energy accumulations in this region. There is a seismic gap that is accumulating stress, and that a large earthquake may occur someday when the stress is relieved. The major earthquakes that have affected Sylhet since the middle of the last century is presented in Table 1.

Table 1: Some historical earthquakes around Sylhet.

Name of Earthquake	Fault	Magnitude	EMS Intensity	Distance (Km)	Focal Depth (Km)
1869 Cachar Earthquake	Tripura	7.5	VIII	92	56
1885 Bengal Earthquake	Bogura	7.0	V	234	72
1897 Great Indian Earthquake	Assam	8.1	IX	151	60
1918 Srimangal Earthquake	Sub-Dauki	7.6	IX	71	14

4. SOIL DATA

Necessary soil data was collected from different relevant sources of Sylhet City and accumulated in Microsoft Excel. For assessment of landslide potential Geological Map and Aerial Photograph is essential, however; these are not available. A total of 167 boreholes with SPT data were collected from different organizations and used to study site amplification and soil liquefaction potential characteristics of municipality area. Among these data, 9 boreholes with SPT-N data up to a depth of 100 ft. were directly collected by BUET for checking the authenticity of other collected data. The representative available boring is up to a depth of 50 ft.

5. LANDSLIDE ESTIMATION DATA

The eroded hills are mostly formed by the hill ranges and hillocks (locally called tila) appearing in the north east and south of Greater Sylhet and surrounding the Sylhet town. These hill ranges attain a low elevation and have a gentle slope. Hillocks are scattered in Sylhet City. Hillocks of fringe area have moderate slope and possess nice vegetation, so less probable of slope failure. In the core area, tilas possess slopes about right angles due to rapid urbanization associated with hill cutting. These areas are more vulnerable to landslide.

6. ASSESSMENT OF SEISMIC HAZARD

In the regional seismic loss estimation analysis it is considered necessary to determine the bedrock motion in the region. The most common method involves the use of an empirical attenuation relationship. These relationships communicate a given ground motion parameter in a region as function of the size and location of an earthquake event. Applying statistical regression analyses to recorded data, numerous relationships had been developed in the past. Often these relationships are developed with different functional forms and with different definitions of ground motion, magnitude, distance, and site conditions. To pick the most apposite attenuation law for predicting rock motions, 1885 Bengal earthquake, 1897 Great Indian earthquake and 1918 Srimangal earthquake are considered. The requirements for selecting the attenuation law are as follows:

- (i) Applicable to the ground condition of engineering bedrock in this study ($V_s=250\text{m/s}$).
- (ii) Able to explain the observed or analyzed earthquake motion of 1885 Bengal earthquake, 1897 Great Indian Earthquake and 1918 Srimangal earthquake.

In this study, the engineering bedrock is assumed to be the layer at which the shear wave velocity (V_s) exceeds 250 m/s, which exist almost 30 m deep from the surface of the study area. In this study, shear wave velocity is expected by using equation of Tamura and Yamazaki (2002). Distance versus PGA values for earthquakes is plotted on log-log paper. From isoseismal maps, the epicentral distances of different locations and their intensities are found. These intensities are converted into PGA by Trifunac and Brady (1975) equation (1) and were plotted on preceding figures.

$$\log(\text{PGA}) = 0.014 + 0.3(\text{MMI}) \quad (1)$$

From Figure 2, it is found that McGuire (1978) equations follow the PGA trend of study area. Finally, 1918 Srimangal Earthquake as the scenario event, PGA value 0.18g at bedrock level for study area was selected.

7. SITE AMPLIFICATION ANALYSIS

It is well known that the surface ground motion of earthquakes is heavily influenced by the subsurface ground condition, especially in areas covered by thick sediments. It is important to evaluate the difference in subsurface amplification site by site to know the distribution of earthquake motion across a wide area. Vibration characteristics at different points of the study area were estimated by employing one dimensional wave propagation program SHAKE. An estimation of the fundamental frequency and the maximum value of the amplification are obtained at each site. Figure 3 shows the map of fundamental frequencies of Sylhet City. Figure 4 shows map of amplification at fundamental frequencies of Sylhet City.

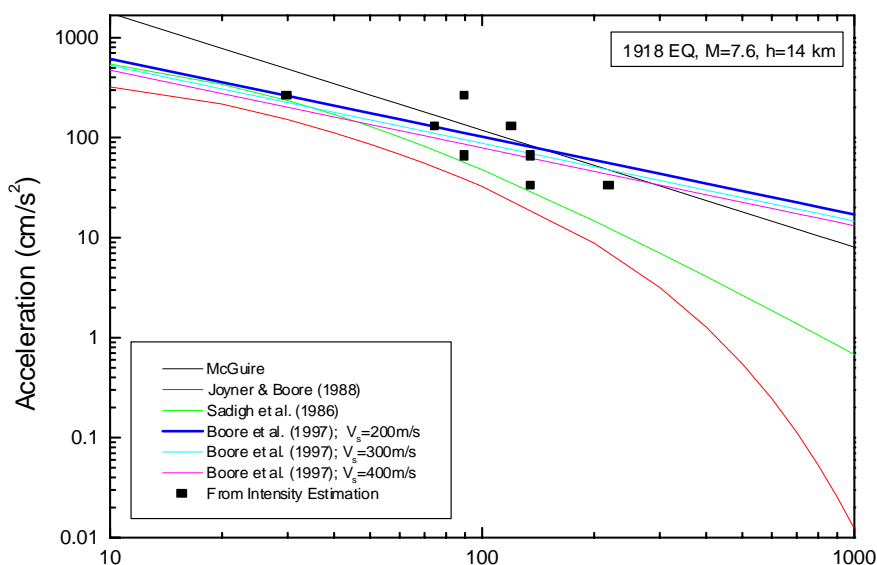


Figure 2: Distance versus PGA values based on different attenuation laws for 1918 Srimangal Earthquake

8. LIQUEFACTION ANALYSIS

The ground water level changes with the season, namely the level is low in the dry season and high in the rainy season. Based on the data on ground water level by Bangladesh Water Development Board, the groundwater distribution in the dry season and the rainy season was

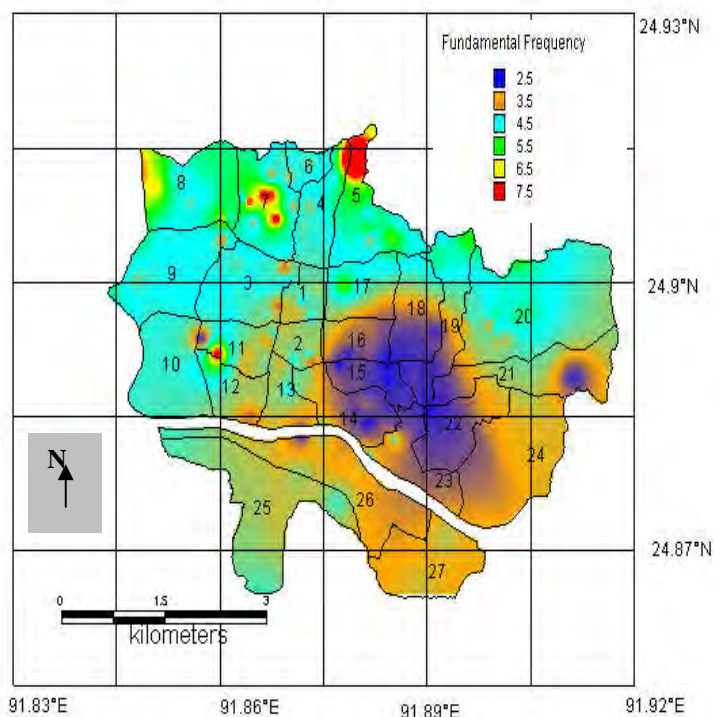


Figure 3: Fundamental frequencies at Sylhet City

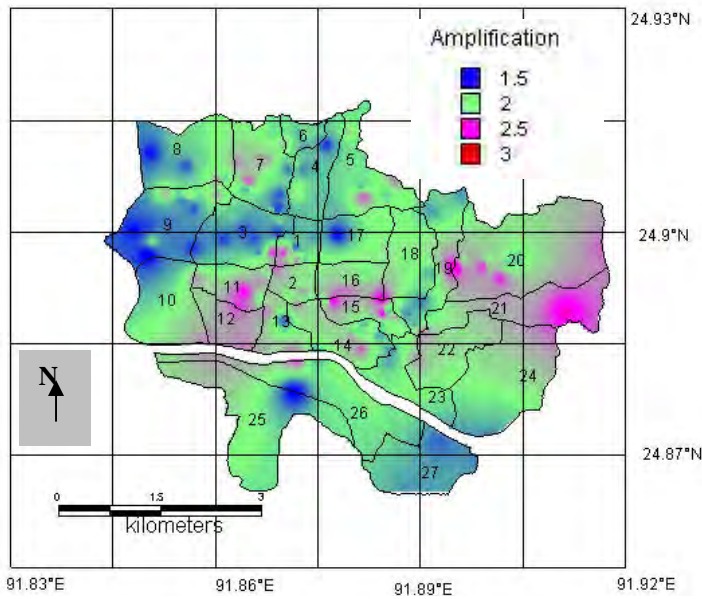


Figure 4: Amplification at fundamental frequencies at Sylhet City

estimated. The F_L method defines that ground water level to be considered as less than 10m from the ground surface. The liquefaction resistance factor, F_L , for the top 20 m of soil, and the resulting liquefaction potential, P_L for the 167 sites were estimated. Result of Liquefaction potential was presented in Figure 5 which shows that 3.35 Km² area have low and very low Liquefaction potential, 13.70 Km² area have moderate liquefaction potential and 10 Km² area have high liquefaction potential. More than one thirds (37%) area will be affected rigorously by liquefaction if Srimongal Earthquake (1918) occurs again with same magnitude and same epicentral distance.

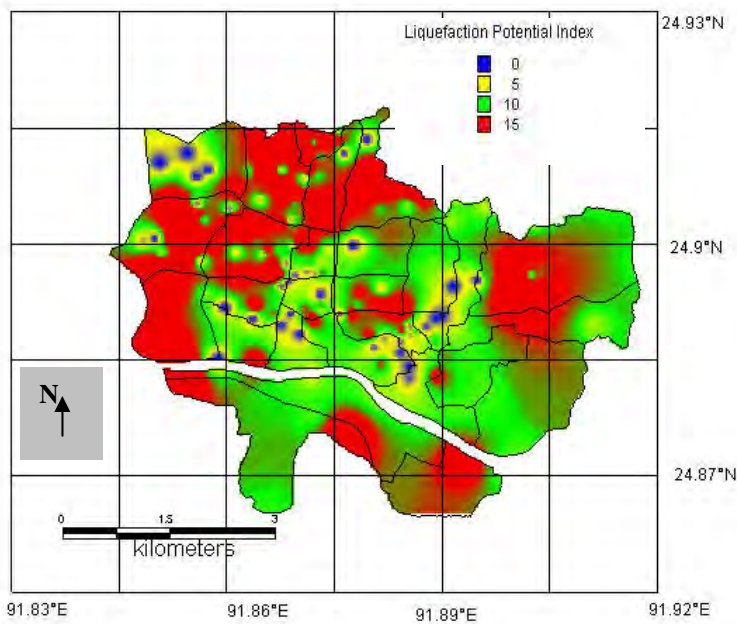


Figure 5: Map showing Microzonation based on liquefaction potential index

9. LANDSLIDE POTENTIAL ANALYSIS

Most of the recent researches in this field have focused on determining the critical level of a given ground motion parameter that will trigger landslide. The program used for stability analysis is XSTABL, which is a fully integrated slope stability analysis program. XSTABL performs two dimensional limit equilibrium and analysis to evaluate the factor of safety for a layered slope using the simplified Bishop Method. Based on the static FS, the critical acceleration to begin the process of slope failure, a_c , is computed as

$$a_c = (FS-1) g \sin\theta \quad (2)$$

Where

θ = The slope angle

FS=the factor of safety determined from a static slope stability analysis

g = the acceleration of gravity

These a_c values are judged against to the regional estimates of surface peak ground acceleration to give a prediction for the incidence of damaging earthquake-induced landslides in the area. There have been very few implementations of quantitative landslide hazard models in the GIS environment instead, a qualitative approach utilizing regional maps showing relative susceptibility of landslides in various geologic deposits will be used to depicted earthquake-induced landslide hazard. Figure 6 shows landslide potential in Sylhet City.

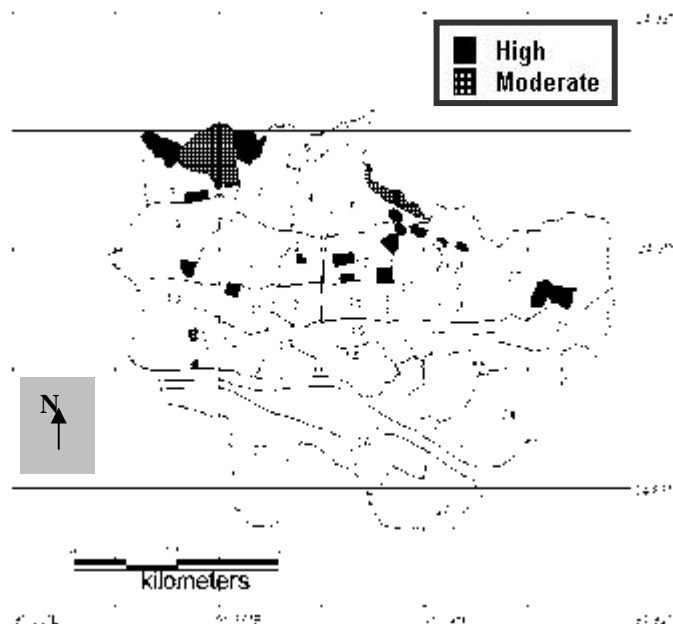


Figure 6: Map showing landslide potential in Sylhet City

10. INTEGRATION OF SITE EFFECTS IN THE GIS ENVIRONMENT

Every analysis region is different; therefore the quantification of the secondary site effects and the weighting scheme for combining the various seismic hazards is heuristic, based on judgment and expert opinion about the influence of local site conditions in the region and the exactness of the available geologic and geotechnical information. However countries like Japan and the United States have long histories on instrumental seismicity and numerous models have been projected there to correlate the various hazard. However that is not the circumstances in Bangladesh. Heuristic rules for quantification and combination were used which were developed by Stephanie and Kiremidjian (1994).

The bedrock-level ground shaking in the region was ascertained. The shaking was depicted in terms of peak ground motion values. The regional distribution of bedrock-level shaking was estimated as 0.18g. Bedrock level PGA was measured as constant since the study area was relatively small. A map showing the distribution of the surface-level ground shaking in the region was developed first, which is, produced just simple multiplication of the PGA at bedrock level with amplification factor shown in Figure 4.

It is decided that the final combined seismic hazard would be quantified in terms of Modified Marcelli Intensity (MMI). There are several relationships for converting PGA to MMI. The equation used here is developed by Trifunac and Brady (1975). The following heuristic rules are used to quantify the seismic hazard attributable to liquefaction:

For regions with liquefiable soils with high liquefaction potential

$$MMI_{LIQ} = MMI_{GS} + 2$$

For regions with liquefiable soils with moderate liquefaction potential

$$MMI_{LIQ} = MMI_{GS} + 1 \text{ and otherwise:}$$

$$MMI_{LIQ} = 0$$

To quantify the seismic hazard due to landslide (MMI_{LAN}), the following heuristic rules are used. For region designated as "high"

$$MMI_{LAN} = MMI_{GS} + 2$$

For region designated as "moderate"

$$MMI_{LAN} = MMI_{GS} + 1 \text{ and otherwise}$$

$$MMI_{LAN} = 0$$

The rules for combining the assorted hazards are based on expert opinion (after Stephanie and Kiremidjian, 1994) about the comparative precision of the hazard information and the behavior of the local geology. For this study, four potential combinations were considered and their assumed weights are shown in Table 2. The final combined hazard (MMI_F) is computed as a weighted sum of the various hazards. By over-laying the regional maps for each hazard as shown in Figures 3 to 6 in GIS environment, Sylhet City area is separated into 13 different affected areas.

Figure 7 shows the regional distribution of the final combined seismic hazard (MMI_F).

Table 2: Quantification rules for seismic hazard (after Stephanie and Kiremidjian, 1994).

Rule	Possible hazards	Weighting scheme for Final combined hazard (MMI_F)
(a)	Ground shaking	$MMI_F = MMI_{GS}$
(b)	Ground shaking + Liquefaction	$MMI_F = .55 MMI_{GS} + .45 MMI_{LIQ} + .5$
(c)	Ground shaking+ Landslide	$MMI_F = .65 MMI_{GS} + .35 MMI_{LAN} + .5$
(d)	Ground shaking +Liquefaction+ Landslide	$MMI_F = .40 MMI_{GS} + .35 MMI_{LIQ} + .25 MMI_{LAN} + 1$

Notes:

1. MMI_F = Final Combined Hazard
2. MMI_{GS} = Ground Shaking Hazard
3. MMI_{LIQ} =Liquefaction Hazard

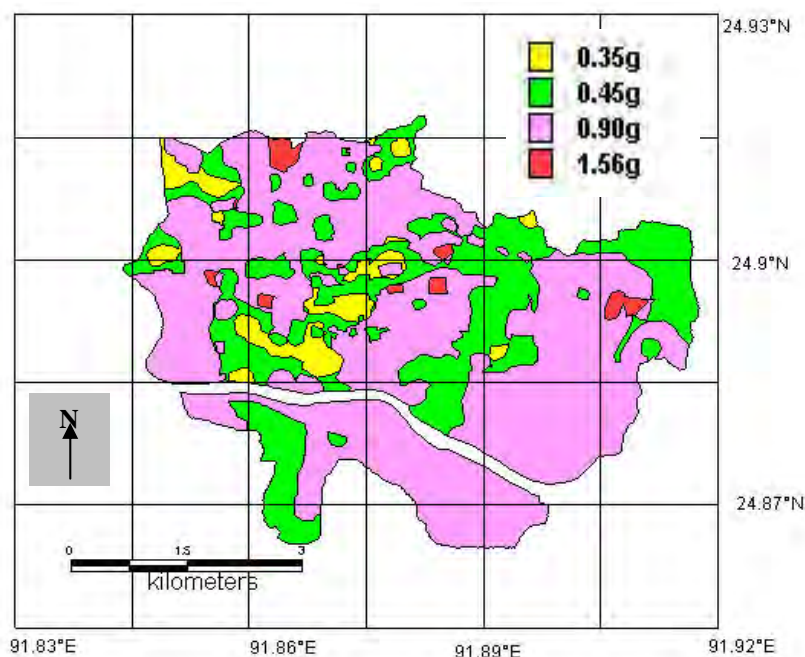


Figure 7: Map showing regional distribution of combined seismic peak ground acceleration in Sylhet City

11. CONCLUSIONS

Geographic information system is used to carry out regional seismic microzonation for Sylhet city where reflection of ground shaking and the secondary site attributes of soil amplification, liquefaction and landslide are included. The method to combine the different hazards is based on a weighted average approach. The GIS-based analysis is useful to engineers, planners, emergency personnel, government officials, and anyone else who may be concerned with the potential consequences of seismic activity in a given region. The results of this study are presented in the form of

microzone maps that serve as an effective means of transferring information from the scientific community to the professional community of decision makers involved in hazard and risk mitigation.

REFERENCES

- Bolt, B. A., 1987. *Site-specific study of seismic intensity and ground motion parameters for proposed Jamuna river bridge, Bangladesh*. Report on Jamuna bridge study.
- Boore, D., Joyner, W. and Fumal, T. E., 1997. Equation for estimating horizontal response spectra and peak acceleration from Western North American Earthquakes: A summary of recent work. *Seismological Research Letter*, Volume 68, No. 1, pp. 128-153.
- Grunthal, G., 1998. *European Macro Seismic Scale*. Luxembourg: Cahiers due Center European de Geodynamics et de Seismology, Volume 15.
- McGuire, R., 1978. Seismic ground motion parameters relations. *Journal of Geotechnical Division, ASCE*, Volume 104, pp. 461 – 490.
- Islam, M. R., 2005. *Seismic Loss Estimation for Sylhet City*. M.Sc Engg. Thesis, Dept of Civil Engineering, BUET, Dhaka
- Molnar, P. and Tapponier, P., 1975. Cenozoic tectonics of Asia, effects of a continental collision. *Science*, Volume 189(8), pp. 419-426.
- Oldham, R. D., 1899. Report on the Srimangal Earthquake of 12th June 1918. *Memoir of Geological Survey of India*, Volume 29, pp. 1-349.
- Rodríguez, C. E., Bommer, J. J. and Chandler, R. J., 1999. Earthquake-induced landslides: 1980–1997. *Soil Dynamics and Earthquake Engineering*, Volume 18, pp. 325–346.
- King, S. A. and Kiremidjian, A. S., 1994. *Regional Seismic Hazard and Risk Analysis through Geographic Information System*. PhD Thesis, Stanford University.
- Seed, H. B., Idriss, I. M. and Arango, I., 1983. Evaluation of liquefaction potential using field performance data. *Journal of Geotechnical Engineering Division, ASCE*, Volume 109, No. 3, pp. 458-482.
- Sharfuddin, M., 2001. *Earthquake Hazard Analysis for Bangladesh*. M.Sc. Engg. Thesis, BUET, Dhaka.
- Tamura, I. and Yamazaki, F., 2002. Estimation of S-wave velocity based on geological survey data for K-NET and Yokohama seismometer network. *Journal of Structural Mechanics and Earthquake Engineering*, No. 696, Vol. I-58, 237-248 (in Japanese).
- Trifunac, M. D. and Brady, A. G., 1975. A study of the duration of strong earthquake ground motions. *Bulletin of Seismological Society of America*, Volume 65, pp. 581-626.

DUCTAL[®] - AN ULTRA-HIGH PERFORMANCE MATERIAL FOR RESISTANCE TO BLASTS

BRIAN CAVILL
VSL Australia Pty Ltd, Sydney, NSW, Australia
bcavill@vslsyd.aust.com

ABSTRACT

Reactive Powder Concrete (RPC) is a cementitious material consisting of cement, sand, silica fume, silica flour, superplasticiser, water and high strength steel fibres. The material was developed by Bouygues, the parent company of VSL, and is marketed under the brand name of Ductal[®]. Production in Australia commenced in early 2003.

Ductal is almost self placing, has a compressive strength of 150-200 MPa and a flexural strength of 30-40 MPa. In structural applications, Ductal is generally used without any passive reinforcement. Very fine high strength steel fibres are able to withstand secondary tensile stresses. Prestressing counterbalances the main tensile stresses due to bending.

The durability properties of Ductal and its resistance to aggressive agents are orders of magnitude better than conventional high performance concrete. The design life in a marine environment exceeds 500 years.

The unique characteristics of Ductal, including exceptionally high energy absorption capacity and resistance to fragmentation, make it an ideal material for panels and components that may be affected by explosives, impact or shock loads. The flexural toughness is greater than 200 times that of conventional fibre reinforced concrete. In May 2004 a total of 7 Ductal panels were tested in two large explosive trials performed at Woomera in South Australia. The panels performed remarkably well, showing extremely high ductility and no fragmentation.

Ductal blast resistant panels have demonstrated very high resistance to the impact caused by blast produced fragments. In simulated fragment projectile tests 100mm thick Ductal panels have easily withstood impacts with energy equivalent to double that produced by mortar fragments.

In June 2005 the first Ductal panels manufactured to provide resistance to blast were supplied to the Australian Government and installed on an Australian Government building in a hazardous international location.

This paper will give a summary of the properties of Ductal, and provide details on the blast testing and projectile impact testing carried out on Ductal panels.

1. PROPERTIES OF DUCTAL FOR DESIGN

Production of Ductal commenced in Australia in January 2003. The development and testing of the production mix used were performed at the University of New South Wales (UNSW), and are reported in detail in Reference 2.

Table 1 lists the properties of Ductal used in design. Figure 1 shows a typical stress-strain response of a compression test with 100mm diameter by 200mm long cylinders and the stress-deflection response for a typical four-point flexure test with 100×100×500mm prisms.

Table 1: Design Properties

Property	Standard	Heat Treated Ductal ¹
Fluidity	ASTM C230	Between 190 and 250mm after 20 drops
Compressive strength	AS 1012.9	$f_{c, nm} = 160$ MPa
Flexural Tension Modulus of Rupture	AS 1012.11	$f_{ct, nm} = 24$ MPa
Flexural Tension First cracking	AS 1012.11	$f_{ct, nm} = 20$ MPa
Modulus of Elasticity	AS 1012.17	47 GPa
Shrinkage	AS 1012.13	< 500 μ strain after 56 days 0 after heat treatment
Density		2,450 kg/m ³

Table 2: Durability Properties

Durability Indicator	Value	Ductal ² compared to High Performance Concrete
Total porosity	2-6%	1.4 to 1.5 of HPC
Microporosity (>10 μ m)	< 1%	1.10 to 1.30 of HPC
Permeability (air)	2.5×10^{-18} m ²	1.50 of HPC
Water absorption	< 0.2 kg/m ²	1.50 of HPC
Chloride ions diffusion	0.02×10^{-12} m ² .s	1.50 of HPC
Electrical resistance (excl. fibre)	1.13×10^3 k Ω .cm	12 to 17 times HPC
Electrical resistance (incl. fibre)	137 k Ω .cm	1.5 to 2 times HPC
Abrasion resistance coefficient	1.3	2 to 3 times HPC
Fatigue, impact and blast resistance	-	Far superior to HPC

Heat treatment consists of curing in steam at a temperature of 90°C for a period of 48 hours after demoulding. This results in rapid strength gain and substantially reduced creep, and causes almost all the shrinkage to occur during the period of the heat treatment. The strength of heat treated Ductal is

15% greater than non-heat treated, and durability properties are also improved. The use of heat treatment is optional and depends on the application. Table 2 lists the durability properties of Ductal in general compared with high performance concrete. The extremely high resistance to the penetration of aggressive agents, due to the absence of capillary porosity, corresponds to excellent durability characteristics.

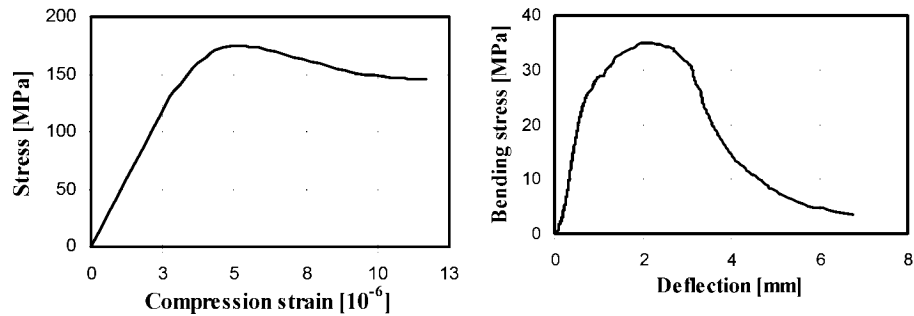


Figure 1 : Typical force deformation response of Ductal[®] in compression and flexure (tension)

While the ultra-high strength of Ductal puts it outside the direct provisions of national design standards, a Design Guide has been prepared by UNSW to be in accordance with the intent of the Australian standards. This Guide is based on extensive testing in France and at the University of New South Wales. Details are given in Reference 1.

A prestressed beam or slab made from Ductal has between 35-45% of the volume of a conventional prestressed beam or slab. The depth is approximately the same as a conventional prestressed member in order to provide stiffness for deflection control.

Flexural strength for large span beams and slabs is achieved through prestressing in combination with the high compressive strength of Ductal. Short span beams and slabs generally need no reinforcement. Shear strength is provided by the tensile strength of Ductal. No additional shear reinforcement is required. The compression stresses due to the prestress add to the material tensile strength to counter the principal tensile stresses.

Ductal is basically self-placing. External vibration is used to give the final compaction. The plant for the mixing of Ductal in Australia and the forms for the precasting were initially set-up at the University of NSW in Sydney and were relocated to the VSL factory in Melbourne in January 2004.

Ductal has been used worldwide to manufacture precast elements for very thin (20mm) fascia panels, sound absorption panels, pedestrian bridges with spans up to 120m and other innovative architectural and structural applications.

2. PROTECTIVE PANELS RESEARCH & DEVELOPMENT

Concrete panels (slabs and walls) are very important in protecting buildings against the extreme loading conditions caused by blast, shock and

impact. The high energy absorption capacity of Ductal was known from static strength tests, however the performance of Ductal elements under severe impulsive loading had not been investigated. The flexural toughness measured as the area under the flexural stress/strain curve (Figure 1) is greater than 200 times that of conventional fibre reinforced concrete.

2.1 Blast Testing at Woomera, May 2004

In a joint project between VSL Australia Pty Ltd and the Advanced Protective Technologies for Engineering Structures (APTES), University of Melbourne, Ductal panels were tested under extreme explosions at blast trials performed at Woomera in South Australia in May 2004. The Woomera trial had two separate blasts equivalent to six (6) tonnes of TNT. Each detonation consisted of a bare charge of 5 Tonnes of Hexolite – RDX/TNT (60:40).

A total of seven Ductal panels were tested located at 30m, 40m and 50m from the blast. The panels had a span of 2m and were 1m wide, with a thickness of 50mm, 75mm and 100mm. Five of the panels contained pre-tensioning strands and the other two were unreinforced.

The test data and observations showed that the panels performed remarkably well, with extremely high ductility and no fragmentation. The stressed panels were able to absorb substantial energy through their ability to sustain considerable deflection up to span/28 without fracture. The fact that the Ductal panels displayed no fragmentation in any of the tests, even at fracture, is a major advantage compared to conventional concrete. Fragmentation poses great danger to both people and infrastructure. Table 3 lists the main observations together with the calculated reflective blast pressures (P_{calc}).

Table 3 : Main observations

Panel type	D	P_{calc}	Main observations
Stressed 100mm	30m	2000	Virtually undamaged, no permanent deflection, no fragmentation.
Stressed 100mm	40m	800	Basically undamaged, no permanent deflection, no fragmentation.
Stressed 75mm	40m	800	Intact, cracked with small permanent deflection, no fragmentation.
Stressed 50mm	50m	420	Intact, shallow crack, no permanent deflection, no fragmentation.
Unreinforced 50mm	50m	420	Fractured, no fragmentation
Stressed 75mm	30m	2000	Fractured, no fragmentation
Unreinforced 100mm	40m	800	Fractured, no fragmentation

The series of photos in Figure 2 show; a typical 2 × 1m panel being installed into a concrete test frame; the test panels before a blast; one of the two blasts; the crater caused by a blast and two of the panels after being subjected to extreme blast loading.

The 100mm thick stressed panel at $D = 30m$ after the blast is shown in Figure 2 bottom left. The panel had deflected inwards 50mm, then outwards 37mm and come to rest with no permanent deflection. The panel was basically undamaged. The 50mm thick stressed panel at $D = 50m$ after the blast, also shown in Figure 2 (bottom right), withstood significant deflection and had no permanent deflection. The panel was basically intact, and had a shallow crack on the front face.



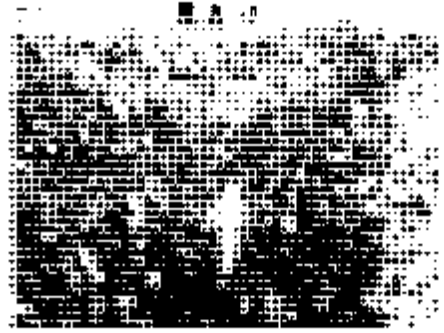
Installing panels into concrete frames



Panels ready for blast



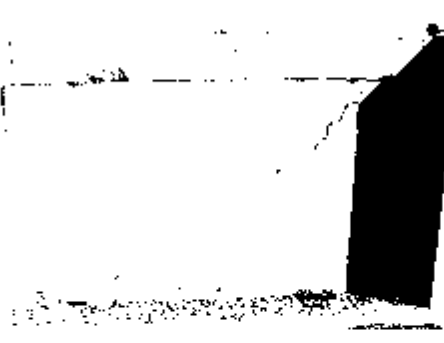
Blast, equivalent to 6t of TNT



Crater caused by the blast



*100mm panel at $D=30m$ after the blast: undamaged
The blast resulted in an average reflected impulse at the panel surface of 3771 kPa.msec with a reflected pressure of 1513 kPa.*



50mm panel at $D=50m$ after the blast, shallow crack, no spalling or fragmentation

Figure 2 : Protective panel tests, Woomera 2004

2.2 Constitutive Model for Ductal at High Loading Rates

The response of concrete to very high strain rates need to be known in order to properly design structures subjected to blast or impact effects. At these high strain rates, the strength of concrete can increase significantly. The response for Ductal was determined by a series of impact tests carried out using the Split Hopkinson Pressure bar (SHPB) setup on large-diameter test cylinders. A range of loading rates and hydrostatic pressures were used. Fig. 3 shows the stress-strain curves at different strain rates of 50mm diameter RPC (Ductal) cylinders. It can be seen that the compressive strength increases up to 1.5 times at the strain rate of about 267.4/sec. This corresponds to a strength Dynamic Increase Factor (DIF) of 1.5. Table 4 summarises the test results of 3 RPC specimens. It was found that RPC is less rate sensitive compared to both NSC and HSC (Ngo 2005).

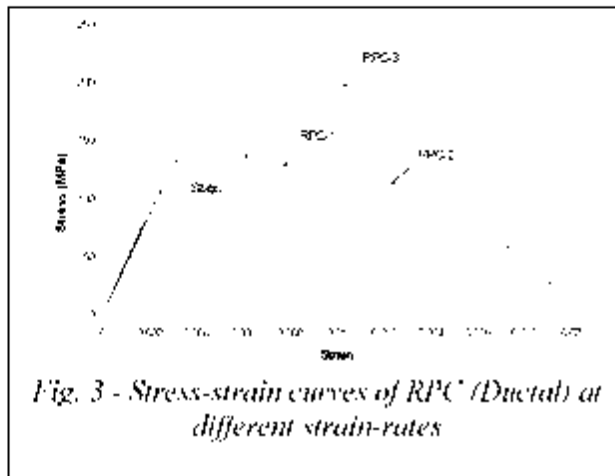


Fig. 3 - Stress-strain curves of RPC (Ductal) at different strain-rates

Concrete Specimen	Impact Velocity (m/s)	Average Strain Rate (1/sec)	Ultimate Strength (MPa)	DIF
Static Test	-	-	159.8	-
RPC-1	11.6	80.7	187.2	1.17
RPC-2	16	187.5	226.1	1.41
RPC-3	20	267.4	240.9	1.5

Table 4
Dynamic Compressive Strength of RPC (Ductal)

Based on the results of the experimental program using the Hopkinson Bar apparatus and through a rigorous calibration process, a new strain-rate dependent constitutive model has been proposed for concrete under dynamic

load. The model can take into account the strain-rate effect by incorporating multiplying factors for increases in the peak stress and strain at peak strength. This model is applicable to concrete strengths varying from 32 MPa to 160MPa with a strain rate up to 300 s⁻¹. A detailed report is given in Reference 4.

The results of the trials demonstrated the suitability of Ductal for blast resistance and confirmed the design methods. The unique characteristics of Ductal, including exceptionally high energy absorption capacity and resistance to fragmentation, make it an ideal material for panels and components that may be affected by explosives, impact or shock loads.

2.3 Fragment Impact Simulation Tests

On June 9, 2005, two 100mm thick Ductal blast resistant panel pieces were subjected to simulated fragment projectile (SFP) loading. Tests were carried out at a NATA approved projectile testing lab in Melbourne. Test pieces were sourced from the production of high-performance blast resistant Ductal panels. The pieces had a thickness of 100mm and were reinforced with high strength steel strands. They were cut from a single larger panel. In accordance with Australian Standard AS 2343 (1997), all test pieces had a plan dimension of 420 x 420mm.

During production of the project panels, Ductal cylinders and prism were tested and strength results of approximately 170 MPa in compression and 30 MPa in tension (flexural) recorded.

Testing procedure followed AS 2343 and consisted of firing projectiles at the target piece with an intended speed. Each test piece was mounted in a frame and a witness (paper) card was placed behind it to record fragmentation impacts. The test was considered to be passed if no fragment penetrated through the witness card.

Two types of steel projectiles were used, 50 caliber (13mm diameter) and 20mm diameter. The projectiles were fired at the test panels with different target speeds. The projectiles are shown in Figure 4.

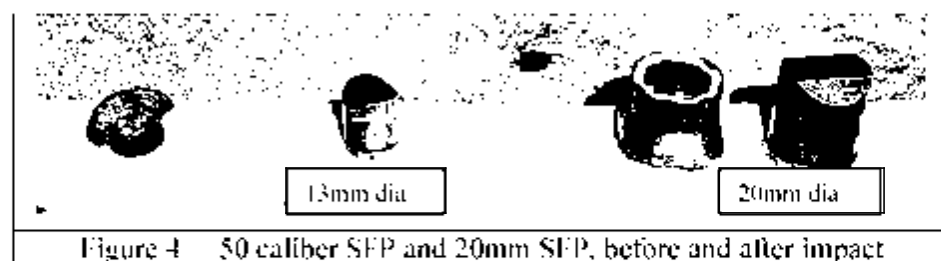


Figure 4 50 caliber SFP and 20mm SFP, before and after impact

The tests were the first of their type to be undertaken using Ductal high performance blast protection panels. The results of these simulated fragment projectile tests show that a specifically designed 100mm thick Ductal blast resistant panel will withstand a 50 caliber SFP at speeds up to 1164m/s and 20mm SFP up to 821 m/s without fragmentation on the non-impact side. The test pieces after impact are shown in Figure 5 and the details are given in Table 5.



Panel 1, with impacts from 50 caliber SFP at 715 m/s and 1164 m/s.



Panel 2, with impact from 20mm SFP at 821 m/s. The crater has a depth of 25mm

Figure 5 : Test pieces after impact

Table 5 : Observations

<p><u>Panel 1</u> 50 Caliber SFP at 715 m/s</p>	<ul style="list-style-type: none"> ▪ SFP did not cause spalling of the panel on the non-impact face ▪ No micro cracking observed behind impact ▪ Panel passed impact test successfully
<p><u>Panel 1</u> 50 Caliber SFP at 1164 m/s</p>	<ul style="list-style-type: none"> ▪ SFP did not cause spalling of the panel on the non-impact face ▪ Micro cracking observed behind impact ▪ Impact crater larger diameter and depth than in shot 1 ▪ Panel passed impact test successfully
<p><u>Panel 2</u> 20mm SFP at 821 m/s</p>	<ul style="list-style-type: none"> ▪ SFP did not cause spalling of the panel on the non-impact face ▪ Cracking observed behind impact but no spalling ▪ Panel passed impact test successfully

In comparison with standard mortar fragments the results compare favourably with impact data for 81mm Mortar, general purpose (GP) and US 4.2 inch Mortar fragments. The impact of the projectiles that caused no spalling on the non-impact face and repelled the fragment (20mm at 821m/s), are at least a magnitude of almost two greater than the impact data for the mortars. Refer to Table 6. The results clearly show the effectiveness of Ductal panels of 100mm thickness, against mortar and similar blast produced fragments.

Table 6 : Projectile (SFP)

Projectile	Weight		Velocity		Impact Energy	
	grains	grams	feet/s	m/s	ft.lbs	kJ
81mm mortar	30	1.9	6338	1932	2675	3.63
US 4.2 inch mortar	96	6.2	5551	1692	6703	9.10
81 mm GP mortar	435	28.2	9091	2772	7887	10.69
50 caliber SFP	207	13.4	3815	1164	6693	9.07
20mm SFP	830	53.8	2693	821	13363	18.12

2.4 Close Charge Tests

In July 2005 two Ductal panels were tested with close charges of TNT. All the panels had a plan dimension of 1m x 1m. One panel was 100mm thick and the other was 150mm thick. The panels were manufactured at the VSL Ductal factory in Melbourne. The tests were performed at a laboratory in England.

All panels were reinforced with high strength steel strands. The 100mm panel was subjected to a 3kg blast at 1.0m and the 150mm thick panel had a 3kg blast at 0.5m from the face of the panel.

The two panels performed very well under the very severe loading with only minor hairline cracks appearing on the back face.

2.5 Ballistic Tests

In September 2005 three 100mm thick Ductal panels were tested for resistance to attack by NATO standard 7.62/9.3g full metal case bullets.

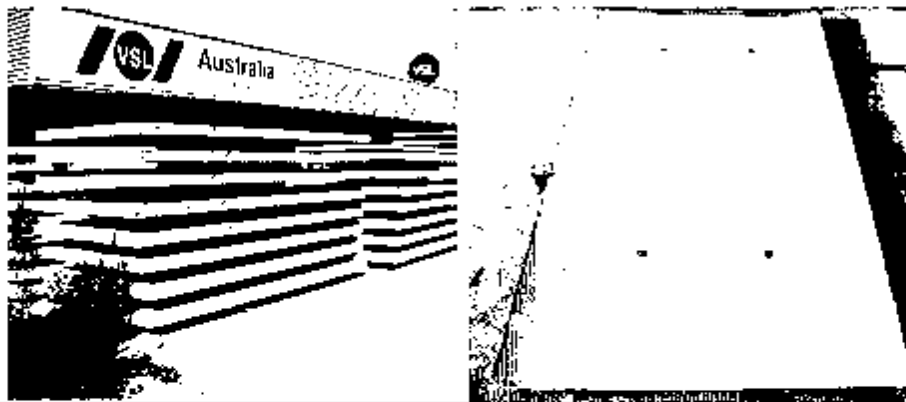
The tests were performed in accordance with AS/NZS 2343 : 1997. All panels easily passed the test and achieved an R2 rating

3. FIRST PROJECT

Panels for the first structure to utilise Ductal to provide resistance to blasts were manufactured in March/April 2005 at the VSL plant in Melbourne. The client was the Department of Foreign Affairs and Trade of the Australian Government.

The panels are up to 4.5m long x 2.0m wide x 100mm thick. They are being used to provide blast resistance to an existing building in a very hazardous international location. The panels were installed on site in July.

Photos of the panels prior to shipment from the VSL factory are shown in Figure 6. Photos of the installed panels are not available for publication due to security reasons.



Precast Ductal[®] blast resistant panels at the factory in Melbourne, prior to shipment to site.

The panels are typically 3.4m long x 2.0m wide x 100mm thick.

Figure 6

4. CONCLUSIONS

Ductal is a unique material. The ultra high strength enables structural and architectural products to be lighter, thinner and stronger than conventional. The extremely high durability gives it a design life in aggressive environments that can be measured in hundreds of years.

The exceptionally high energy absorption capacity and resistance to fragmentation, make it an ideal material for panels and components that may be affected by explosives, impact or shock loads.

The tests have confirmed that Ductal is a very effective material for blast resistance. Panels can be much thinner than those made from conventional concrete, and the risk of injury or damage caused by concrete debris is eliminated or minimised.

REFERENCES

1. Gilbert, N. Gowripalan and B. Cavill. "On the Design of Precast, Prestressed Reactive Powder Concrete (Ductal[®]) Girders", *Austrroads 4th Bridge Conference*, Adelaide, November 2000.
2. N. Gowripalan, R. Watters, I. Gilbert and B. Cavill. "Reactive Powder Concrete (Ductal[®]) for Precast Structural Concrete – Research and Development in Australia", *21st Biennial Conference of the CIA*, Brisbane, July 2003.
3. B. Cavill and G. Chirgwin. "The World's First RPC (Ductal[®]) Road Bridge at Shepherds Creek, NSW", *Austrroads 5th Bridge Conference*, Hobart, May 2004.
4. T. Ngo, P. Mendis, N. Lam and B. Cavill. "Performance of Ultra-High Strength Concrete Panels subjected to Blast Loading", *The 2005 Science, Engineering and Technology Summit*, Canberra, July 2005.

OPTIMAL ASEISMIC PERFORMANCE OF BUILDINGS WITH FRICTION DAMPERS

SANJAYA KUMAR PATRO and RAVI SINHA
Department of Civil Engineering
Indian Institute of Technology Bombay, India
sanjay@civil.iitb.ac.in, rsinha@civil.iitb.ac.in

ABSTRACT

Friction-based passive energy dissipation devices (or dampers) are known to be very effective for controlling the seismic response of multistory buildings. These devices can be used for the design of new buildings as well as to retrofit existing buildings. The locations and properties of friction devices are typically decided based on numerical modeling wherein the sliding friction is modeled with Coulomb friction having a constant coefficient of friction. However, the basic laws for sliding materials and experimental investigations show strongly non-linear relationship between friction and sliding velocity, which includes stiction and Stribeck effects. These effects may be significant and can not be ignored while simulating the seismic response of structures with friction-based dampers.

This paper analytically investigates the optimal seismic performance of frame buildings with friction-based energy dissipation devices. Nonlinear response-history analysis has been carried out considering realistic sliding friction models. The performance has been evaluated using several different response parameters. Different performance indices have been used to evaluate the performance of the building due to different earthquake ground motions. The results show that the conventional approach may significantly overestimate the performance of friction dampers. It is also concluded that optimal design of dampers can only be carried out using comprehensive friction models.

1. INTRODUCTION

In recent years, significant efforts have been undertaken to develop the use of energy dissipation or supplemental damping for aseismic design of buildings. A number of these devices have been installed in buildings throughout world (Constantinou et al., 1998). The presence of the energy dissipation devices can dissipate a significant proportion of the input seismic energy during building motion, thereby reducing the energy that needs to be dissipated by the structure through inelastic deformations. Among the energy dissipation devices, friction devices have proved to be very efficient

in dissipating larger amount of energy than the other methods that involve yielding of steel plates, viscoelastic materials and viscous materials.

The dependence of friction coefficient on slip velocity, normal load, and history of motion has received considerable attention in the recent past (Armstrong-Helouvry, 1991; Feeny et al., 1998; and Berger, 2002). These and other investigations show that the coefficient of friction at stick stage is higher than the coefficient of friction at sliding stage, which leads to stick-slip and Stribeck effect or other unstable oscillations in the response behavior of structures. However, the prevalent practice to determine the location of friction devices and the optimal slip load within building frame are based on Coulomb friction model. The stiction and Stribeck effects may lead to significant changes in their design parameters.

In this paper, the response of generalized MDOF frame building with friction device when subjected to various earthquake excitations has been considered. The paper discusses the following aspects: (i) Performance indices considering different response parameters, (ii) Optimal slip-load corresponding to each performance index, and (iii) Importance of stick-slip and Stribeck effects.

2. DRY FRICTION MODELS

The following two models have been considered in the investigation of response behavior of frame structure with friction device (Fig. 1), where F is the friction force and \dot{u} is the relative velocity.

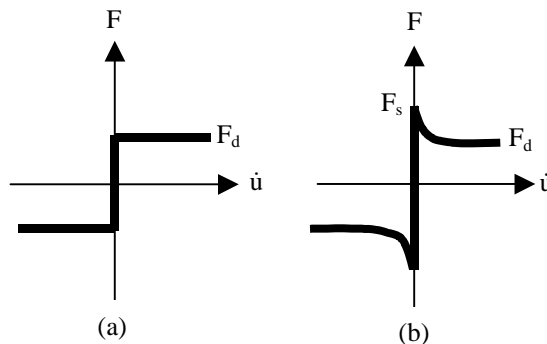


Figure 1: Dry friction models

2.1 Coulomb Friction Model (Model FM1)

This is the most frequently used model, proposed over 200 years ago and is represented in Fig. 1(a). In this model, the coefficient of friction remains constant and the friction force is expressed as

$$F = \mu F_N \operatorname{sgn}(\dot{u}) \quad (1)$$

where F_N is the normal load (controllable prestressing force) on the sliding surface, F is the frictional resistance that is same for both stick and sliding stages, μ is the coefficient of sliding friction, \dot{u} is relative sliding velocity, and $\text{sgn}(\dot{u})$ is the signum function that assumes a value of +1 for positive sliding velocity and -1 for negative sliding velocity.

2.2 Comprehensive Friction Model (Model FM2)

It has been observed through various experimental studies that friction force does not remain constant throughout the sliding phase. The frictional resistance on dry surface, modeled with reference to experimental and theoretical investigation by Wang and Shieh, (1991) shows that the friction force during sliding, F , obeys the following exponential law:

$$F = \left(F_d + (F_s - F_d) \exp\left(-\left|\frac{\dot{u}}{\dot{u}_s}\right|\right) \right) \text{sgn}(\dot{u})$$

$$F_d = \mu_d F_N$$

$$F_s = \mu_s F_N$$
(2)

The empirical parameter \dot{u}_s is known as Stribeck velocity. The Stribeck velocity depends on response memory (history of response), material properties and surface finish.

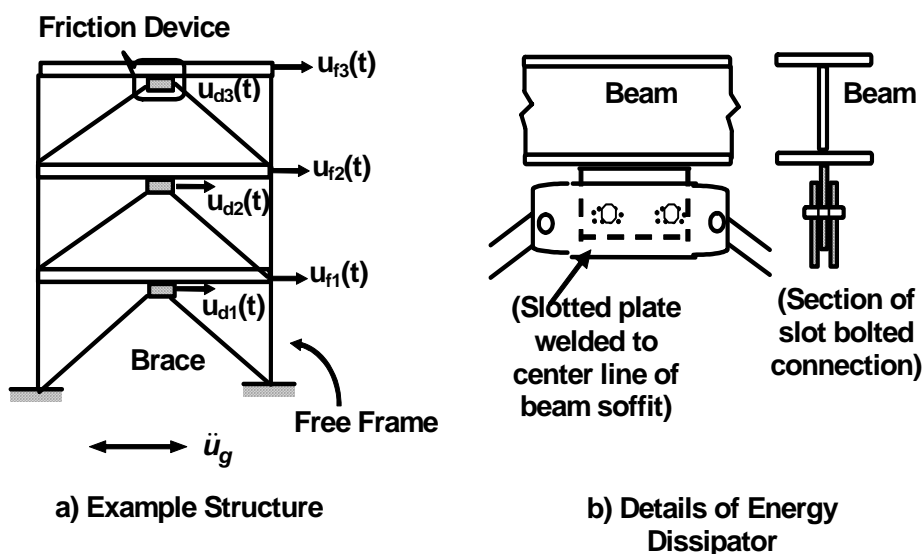


Figure 2: Schematic diagram of three-story frame structure with friction dissipater (Levy et al. (2001))

3. MATHEMATICAL FORMULATION

The mathematical formulation of multi-degree-of-freedom (MDOF) braced frame structure with friction slider on the top of chevron brace system shown in Fig. 2 has been presented below. The dynamic model of the

structure is considered as a symmetric two dimensional (2-D) shear building. In this formulation structure without brace is denoted as free frame structure (subscript f) and brace along with device is denoted as dissipater system (subscript d). Two lumped mass models, one for free frame structure and another with dissipater system represent the dynamic behavior of the structure. Two degrees-of-freedom per floor, corresponding to the horizontal displacement of the floor mass in the direction of excitation and the dissipater system, respectively, have been shown in Fig. 2(a). The sliding plate of the dissipater system is welded to the centerline of beam soffit in the vertical plane as shown in Fig. 2(b). The sliding plate having slotted holes is sandwiched between two clamping plates. Clamping plates are connected to the sliding plate through prestressing bolts. The prestressing bolts fixed in the slotted holes provide normal force to the sliding system, and the arrangement ensures that the normal force is relatively independent of the beam loads.

The motion of the structure consists of two phases: (1) non-sliding or stick phase when the stick frictional resistance (\mathbf{F}_{st}) between structure and device is not overcome, and (2) sliding or slip phase in which sliding frictional resistance (\mathbf{F}_{sl}) opposite to the relative velocity between floor and dissipater activates. This will activate when the relative motion across the sliding surface takes place. The overall response consists of a series of non-sliding and sliding phases on each story. Through the entire solution process, the equations of motion are split in two subsets with sub-indexes st (stick phase/ non-sliding phase) and sl (sliding phase). The number of active degree of freedom ranges between N_f (number of floors) and $N_f + N_d$ (number of floors + number of dissipaters). If the total number of non-sliding floors are called n_{st} and total number of sliding floors n_{sl} , thus at any instant $N_f = n_{st} + n_{sl}$. If the dissipaters are placed on all the floors, the total degrees of freedom will be $2N_f$. The generalized governing equation of motion in matrix form for $2N_f$ degree of freedom can be given as:

$$\mathbf{M}\ddot{\mathbf{u}}_{st+sl} + \mathbf{C}\dot{\mathbf{u}}_{st+sl} + \mathbf{K}\mathbf{u}_{st+sl} = -\mathbf{M}\mathbf{r}\ddot{u}_g - \mathbf{F}_{f+sl} \quad (3)$$

where

$$\ddot{\mathbf{u}}_{f,st} = \ddot{\mathbf{u}}_{d,st}, \dot{\mathbf{u}}_{f,st} = \dot{\mathbf{u}}_{d,st}, \text{ and } \mathbf{u}_{f,st} - \mathbf{u}_{d,st} = \text{constant} \quad (4)$$

and the matrices are given as:

$$\mathbf{M} = \begin{bmatrix} \mathbf{M}_f & \mathbf{0} \\ \mathbf{0} & \mathbf{M}_d \end{bmatrix}, \mathbf{C} = \begin{bmatrix} \mathbf{C}_f + \mathbf{C}_{d2} & \mathbf{C}_{d3} \\ (\mathbf{C}_{d3})^T & \mathbf{C}_{d1} \end{bmatrix}, \mathbf{K} = \begin{bmatrix} \mathbf{K}_f + \mathbf{K}_{d2} & \mathbf{K}_{d3} \\ (\mathbf{K}_{d3})^T & \mathbf{K}_{d1} \end{bmatrix}, \quad (5)$$

$$\mathbf{u}_{st+sl} = \begin{Bmatrix} \mathbf{u}_{f,st+sl} \\ \mathbf{u}_{d,st+sl} \end{Bmatrix}, \mathbf{r} = \begin{Bmatrix} \mathbf{r}_f \\ \mathbf{r}_d \end{Bmatrix}, \mathbf{F} = \begin{Bmatrix} +\mathbf{F}_{f+sl} \\ -\mathbf{F}_{f+sl} \end{Bmatrix}, \mathbf{r}_f = \mathbf{1}, \mathbf{r}_d = \mathbf{1}$$

in which

$$\begin{aligned}
 \mathbf{C}_{d1} &= \begin{bmatrix} c_{d1} & 0 & 0 \\ 0 & \ddots & 0 \\ 0 & 0 & c_{dN_d} \end{bmatrix}, \mathbf{C}_{d2} = \begin{bmatrix} c_{d2} & 0 & 0 \\ 0 & c_{dN_d} & 0 \\ 0 & 0 & 0 \end{bmatrix}, \mathbf{C}_{d3} = \begin{bmatrix} 0 & -c_{d2} & 0 \\ 0 & 0 & -c_{dN_d} \\ 0 & 0 & 0 \end{bmatrix}, \\
 \mathbf{K}_{d1} &= \begin{bmatrix} k_{d1} & 0 & 0 \\ 0 & \ddots & 0 \\ 0 & 0 & k_{dN_d} \end{bmatrix}, \mathbf{K}_{d2} = \begin{bmatrix} k_{d2} & 0 & 0 \\ 0 & k_{dN_d} & 0 \\ 0 & 0 & 0 \end{bmatrix}, \mathbf{K}_{d3} = \begin{bmatrix} 0 & -k_{d2} & 0 \\ 0 & 0 & -k_{dN_d} \\ 0 & 0 & 0 \end{bmatrix} \quad (6)
 \end{aligned}$$

In the above equations, \mathbf{M}_f , \mathbf{C}_f , and \mathbf{K}_f are the $N_f \times N_f$ mass, damping and stiffness matrices of the free frame structure excluding the bracing members, \mathbf{M}_d , \mathbf{C}_{d1} , \mathbf{C}_{d2} , \mathbf{C}_{d3} , \mathbf{K}_{d1} , \mathbf{K}_{d2} and \mathbf{K}_{d3} are $N_d \times N_d$ mass, damping and stiffness matrices of the dissipaters, \mathbf{r} is the force influence vector of structure with dissipater, and \ddot{u}_g is the ground acceleration. \mathbf{M}_d is $N_d \times N_d$ diagonal mass matrix of dissipaters. The degrees of freedom are the relative horizontal displacement of the each floors (\mathbf{u}_f) and relative horizontal displacement of each dissipater (\mathbf{u}_d) with respect to the base. The over dots represent derivative with respect to time.

In Eq. (3) stick or non-sliding phase ensures that the friction forces satisfy the equation,

$$|\mathbf{F}_{f,st}| < \mathbf{F}_{st} \quad (7)$$

where,

$$\begin{aligned}
 \mathbf{F}_{f,st} &= \mathbf{M}_{f,st} \mathbf{u}_{f,st+sl} + \mathbf{M}_{f,st} \mathbf{r}_f \ddot{u}_g + (\mathbf{C}_{f,st} + \mathbf{C}_{d2,st}) \dot{\mathbf{u}}_{f,st+sl} \\
 &+ \mathbf{C}_{d3,st} \dot{\mathbf{u}}_{d,st+sl} + (\mathbf{K}_{f,st} + \mathbf{K}_{d2,st}) \mathbf{u}_{f,st+sl} + \mathbf{K}_{d3,st} \mathbf{u}_{d,st+sl}
 \end{aligned} \quad (8)$$

and $\mathbf{F}_{f,st}$ is the unbalanced frictional resistance vector at stick stage. When the inequality in the above Eq. (7) is not satisfied for any dissipater, that dissipater enters into the sliding phase. Then subscript *sl* activates in the corresponding sliding degree-of-freedom at the floor level.

The maximum frictional resistance at stick stage (\mathbf{F}_{st}) and frictional resistance at sliding stage (\mathbf{F}_{sl}) for different friction models are given in Eq. (1) and Eq. (2). The direction of sliding is governed by the signum function and can be expressed as:

$$\text{sgn}(\dot{\mathbf{u}}_f - \dot{\mathbf{u}}_d) = -\frac{\mathbf{F}_{f,st,max}}{|\mathbf{F}_{f,st,max}|} \quad (9)$$

Before the application of base excitation, the structure is at rest. Therefore, the response of the structure always starts in stick phase. This phase of response continues until the unbalanced frictional resistance

exceeds the maximum frictional resistance at stick stage at the corresponding degree of freedom level. It is important to note that the degrees of freedom n_{st} and n_{sl} belonging to the sticking and sliding conditions at each floor vary continuously through the motion. When the relative sliding velocity ($\dot{\mathbf{u}}_f - \dot{\mathbf{u}}_d$) during motion becomes zero or changes its sign, then the structure may enter to stick phase/non-sliding phase corresponding to that dissipater level. It may reverse its direction of sliding or have a momentary halt and continue in the same direction. The status of motion during transition phase can be evaluated by checking the validity of Eq. (7) and then solving the appropriate equations of stick (subscript st) or sliding (subscript sl) during the next time-step.

4. PERFORMANCE INDICES

The response of a MDOF building includes a large number of response quantities. In order to evaluate the optimal performance of the buildings with energy dissipaters, the three indices given below have evaluated. The maximum response from all floors has been considered for their evaluation. The response quantities are normalized with respect to the corresponding maximum response of the free frame and the braced frame for the same base excitation. The index value close to zero indicates excellent performance of the energy dissipater while values close to 1 indicate ineffectiveness of the system.

(i) Drift and acceleration ratio (DAR): This ratio has been defined as (Moreschi, 2000),

$$DARF \text{ or } (DARB) = \frac{1}{2} \left(\frac{\text{Max. storey drift of str with device}}{\text{Max story drift of free or (braced) frame}} + \frac{\text{Max. Abs. Acc. of str with device}}{\text{Max. Abs. Acc. of free or (braced) frame}} \right) \quad (10)$$

It is noted that this information gives equal weight to the deformation and acceleration related responses. If required then different weights can also be assigned.

(ii) Base shear ratio (BSR): This ratio has been defined as

$$BSRF \text{ or } (BSRB) = \frac{\text{Max shear of the frame str with dissipator}}{\text{Max base shear of the free or (braced) frame str}} \quad (11)$$

(iii) Relative performance index (RPI): This ratio has been defined as (Filiatrault and Cherry, 1990),

$$RPIF \text{ or } (RPIB) = \frac{1}{2} \left(\frac{SEA}{ASEF \text{ or } (ASEB)} + \frac{SEM}{SEMF \text{ or } (SEMB)} \right) \quad (12)$$

where SEA = strain energy area, is the area under the strain-energy time history for the system with dissipaters, $ASEF$ = strain energy area for free frame structure, $ASEB$ = strain energy area for braced frame structure, SEM = maximum strain energy for the system with dissipaters, $SEMF$ = maximum strain energy for the free frame, and $SEMB$ = maximum strain energy for the braced frame. If $RPIF$ or $RPIB$ is close to 1, then the response corresponds to the behaviour of a free or braced frame structure, respectively. If $RPIF$ or $RPIB$ < 1, the response of the system with dissipaters is smaller than the response of free or braced frame structure.

5. BEHAVIOR OF EXAMPLE BUILDING

5.1 Description of example structure

A three story steel frame (Fig. 2(a)) structure with friction-based supplemental system has been considered for evaluating the optimal performance. The structural damping ratios of free-frame and of the brace are taken as 2% and 0%, respectively. The structure has the following properties (Levy et al. 2001):

Story mass: $m_{f1} = m_{f2} = m_{f3} = 200.4$ kg ,

Story stiffness: $k_{f1} = k_{f2} = k_{f3} = 11946.6$ N/m ,

Dissipater mass: $m_{d1} = m_{d2} = m_{d3} = 0.1$ kg ,

Dissipater stiffness: $k_{d1} = 80623.0$ N/m, $k_{d2} = 64192.0$ N/m,
 $k_{d3} = 37234.0$ N/m .

The coefficient of friction has been considered for steel on steel slider (slideaway) in accordance with Bilkay and Anlagan (2004). Based to their investigation the following friction parameters have considered: Minimum coefficient of sliding friction (sliding stage, μ_d) = 0.16, Maximum coefficient of sliding friction (stick stage, μ_s) = 0.29, and Stribeck velocity $v_s = 0.025$ m/s.

In this investigation, the time-history responses of the example structure have been evaluated for an ensemble of nine earthquake records (Patro, 2005). The ground motions chosen in this study cover a wide variety of earthquakes having different peak ground accelerations (PGA), frequency content and duration. Three time histories have been selected for each of soft soil (FSR), alluvium soil (FMR) and hard soil (LHR).

5.2 Optimum prestressing force

The performance indices discussed above have been evaluated for the selected ensemble of time history. The performance indices have been normalized with the maximum corresponding response of free frame (Fig. 3(a-c)) and braced frame structure (Fig. 3(d-f)), respectively. It can be observed that selection of optimal response varies from index to index.

However, depending upon the relationship between the different performance functions, the optimal design for one performance objective may also be reasonably near optimal for other performance indices.

Optimum structural performance has been found for a prestressing force of 1500-2500 N if the RPIF/RPIB is to be minimized, and 500-1000 N if the DARF/DARB is to be minimized when the comprehensive friction model (Model FM2) is used. The performance indices for prestressing force $F_N = 767$ N, which corresponds to optimal DARF/DARB response, is also shown in Fig. 3. It can be observed that other than LHR2 and LHR3 base excitations, the prestressing force $F_N = 767$ N gives near-optimal response for other base excitations with reference to free-frame structure. Similarly other than FSR1 and LHR3 base excitations, the prestressing force of $F_N = 767$ N effectively reduces the response for other base excitations with reference to braced frame structure. It has also been observed that other than few ground records optimal performance indices closely match with the indices corresponding to predicted optimum prestressing force (767 N). This indicates that robust design of structures can be carried out by considering a single performance index only.

5.3 Base shear response

The typical time-history response of base shear of example structure subjected to FMR3 base excitation is shown in Fig. 4. This responses are shown for free frame, braced frame, structure with dissipater modeled using Coulomb friction model (Model FM1), and structure with dissipater modeled using comprehensive friction model (Model FM2). As expected, significant reduction of base shear can be observed for structure with dissipaters when compared to free frame and braced frame structures. The results also clearly show that when the dissipater is modeled using Model FM2, the response has significant high-frequency components, which are not captured when using Model FM1. This illustrates the importance of including stiction and Stribeck effects in the friction model. It is also seen that the use of Model FM1 predicts lower maximum base shear compared to the use of Model FM2, indicating the possibility of over-estimating the effectiveness of the dissipaters when only simple friction model is used.

6. DISCUSSIONS AND CONCLUSIONS

The paper discusses the importance of realistic friction model for optimal aseismic design of buildings with friction dampers. It is seen that the breakaway and Stribeck effects may significantly influence the performance of the building. It is also found that optimal aseismic design may be feasible by only considering the Drift and Acceleration Ratio index for determining the optimal prestressing force.

Based on the investigations presented in this paper, the following main conclusions can be drawn:

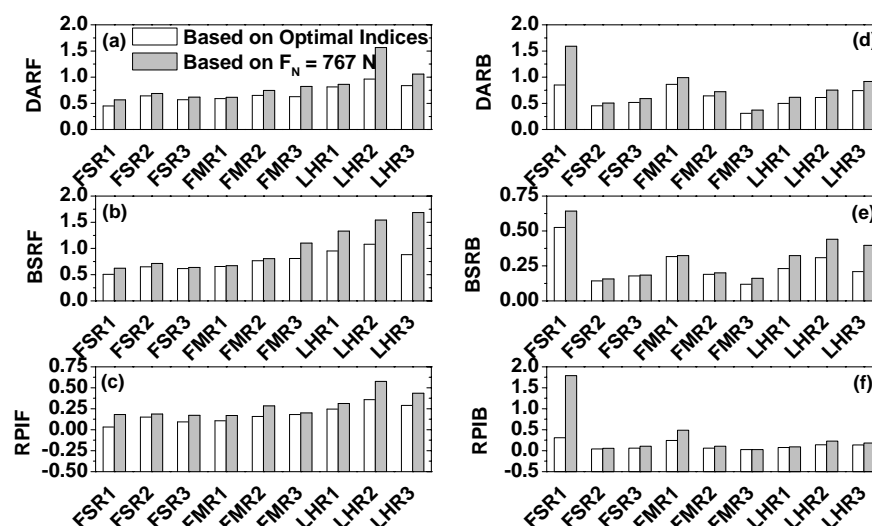


Figure 3: Optimal performance indices considering comprehensive friction model (Model FM2) subjected to ensembles of ground motions

1. Most structures with friction-based energy dissipation systems are designed based on Coulomb friction; however behavior of actual friction is more complex and includes stiction and Stribeck effect. The consideration of these effects results in much higher structure response.
2. Optimal prestressing force is closely related to the characteristics of ground motion and the performance index of interest. However, Drift and Acceleration Ratio index can be used for near-optimal design of the structure.

REFERENCES

- Armstrong-Helouvry, B., 1991. *Control of machines with friction*. Kluwer Academic Publishers, Boston.
- Berger, E. J., 2002. Friction modeling for dynamic system simulation. *Applied Mechanics Review* 55, 535-577.
- Bilkay, O., and Anlagan, O., 2004. Computer simulation of stick-slip motion in machine tool slideways. *Tribology International* 37, 347-351.
- Constantinou, M. C., Soong, T. T., and Dargush G. F., 1998. *Passive energy dissipation systems for structural design and retrofit*, MCEER Report, University at Buffalo, Buffalo, NY.
- Feeny, B., Guran, A., Hinrichs, N., and Popp, K., 1998. A historical review on dry friction and stick-slip phenomena. *Applied Mechanics Review* 51, 321-341.
- Filiatrault, A., and Cherry, S., 1990. Seismic design spectra for friction-damped structures. *ASCE Journal of Structural Engineering* 116, 1334-1355.

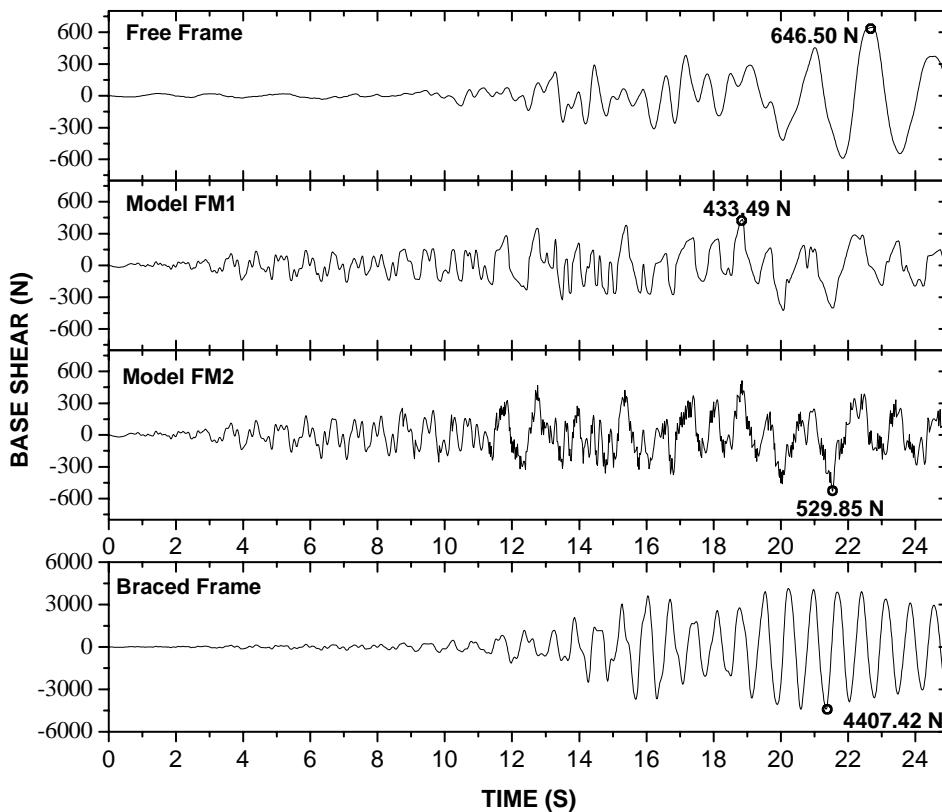


Figure 4: Base shear time-history response of example structure subjected to Landers (1992) ground motion (FMR3) for optimal prestressing force of 767 N (PGA = 0.283g)

- Levy, R., Marianchik, E., Rutenberg, A., and Segal, F., 2001. A simple approach to the seismic design of friction damped braced medium-rise frames. *Engineering Structures* 23, 250-259.
- Moreschi, L. M., 2000. *Seismic design of energy dissipation systems for optimal structural performance*, Ph.D. Thesis, Virginia Polytechnic Institute and State University, Blacksburg, Virginia.
- Patro, S. K., 2005. *Presynopsis Seminar Report*, Indian Institute of Technology Bombay, India.
- Wang, J. H., and Shieh, W. L., 1991. The influence of a variable friction coefficient on the dynamic behavior of a blade with a friction damper. *Journal of Sound and Vibration* 149, 137-145.

NUMERICAL INVESTIGATION OF STRUCTURAL RESPONSE TO ABOVE-GROUND EXPLOSIONS

Y. LU^{1*}, Z. WANG²

¹ Protective Technology Research Centre, Nanyang Technological University, Singapore

² School of Mechatronic Engineering, Beijing Institute of Technology, Beijing, China

*Email: cylu@ntu.edu.sg

ABSTRACT

In this study the response of building structures to above-ground explosion is investigated using coupled numerical analysis. The emphasis is placed on the response characteristics, looking into the concentration of localized damage and the global structural dynamic response, rather than the detailed damage processes. The computational domain encompasses the surrounding air and soil medium, thus allowing also for an evaluation of the significance of the explosion-induced ground motion in the overall structural effects. A multi-storey reinforced concrete frame is used as an example to illustrate the general structural effects. Results show that under a typical above-ground explosion scenario, the critical structural damage is dominated by air pressure, whereas the ground shock could induce additional vibration but its structural effect is relatively insignificant. The distribution of structural damage appears to be governed by member level effects, especially on the front side of the structure.

1. INTRODUCTION

When assessing the threat of explosion on a building structure, it is necessary to evaluate the structural effects of the blast loading. As a matter of fact, the response of building structures to nearby explosions is complicated by the drastic spatial and time variation of the blast loads. Therefore, a clear understanding of the response characteristics is required before any simplified approach may be adopted. For this purpose, coupled numerical simulation is deemed to be an appropriate tool.

The present study adopts the fully coupled numerical simulation approach so that the interactions between layers of different nature involved in the processes can be better preserved. The computational domain encompasses the structure, the surrounding air, the charge, as well as a sufficient layer of soil medium so that the explosion-induced ground vibration effect can also be included for evaluation. The focus is placed on the distinctive characteristics of the structural effects under nearby above-

ground explosions, looking into the relative importance of localized damage and the global dynamic response in the structural behaviour. Besides, the significance of the above-ground explosion induced ground vibration in the structural response will also be examined and discussed. The models for the constituent materials are carefully selected and validated, and a newly developed three-phase soil model for high dynamic loading is employed. As an example, a generic multi-storey reinforced concrete frame is selected to illustrate the characteristics of the structural effects and the dominant mechanisms governing the damage to the structural system.

2. COUPLED MODEL AND MATERIAL DESCRIPTIONS

A general configuration of building structures subjected to an above-ground explosion is depicted in Figure 1, in which the structure, air, soil medium and the charge are represented respectively using the corresponding material models. The algorithm of coupling the computational fluid dynamics and computational structural dynamics is adopted to facilitate the interaction between the air shock wave, the structure, and the ground.

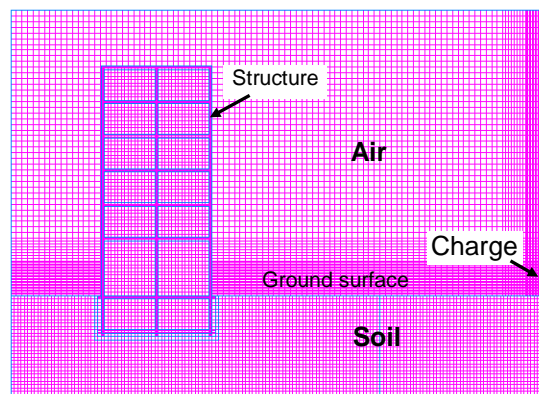


Figure 1: Schematic of a generic coupled model

For the modeling of concrete, the RHT model (Riedel et al., 1999) is adopted. The RHT model contains many features that are necessary to describe a brittle material, namely pressure hardening, strain hardening, strain rate hardening, third invariant dependence for compressive and tensile meridians, and cumulative damage (strain softening). As shown in Figure 2, the material model uses three strength surfaces: an elastic limit surface, a failure surface and a remaining strength surface for the crushed material. The failure surface Y is defined as

$$Y_{fail} = Y_{TXC(p)} \cdot R_{3(\theta)} \cdot F_{RATE(\dot{\epsilon})} \quad (1)$$

where $Y_{TXC} = f_c [A(p^* - p_{spall}^* F_{RATE(\dot{\epsilon})})^N]$, f_c = compressive strength, A = failure surface constant, N = failure surface exponent, p^* = pressure

$$f_c \cdot p_{spall}^* \cdot p^* (f_t / f_c) \cdot F_{RATE(\dot{\epsilon})}$$

$R_3(\theta)$ defines the third invariant dependency of the model as a function of the second and third stress invariants and a meridian ratio.

The elastic limit surface is scaled from the failure surface,

$$Y_{elastic} = Y_{fail} \cdot F_{elastic} \cdot F_{CAP(p)} \quad (2)$$

where $F_{elastic}$ = ratio of the elastic strength to failure strength, $F_{CAP(p)}$ is a function that limits the elastic deviatoric stresses under hydrostatic compression, and it varies in the range of (0,1). Linear hardening is used prior to the peak load. For the residual strength,

$$Y_{residual}^* = B^* \cdot p^{*M} \quad (3)$$

where B = residual failure surface constant, M = residual failure surface exponent.

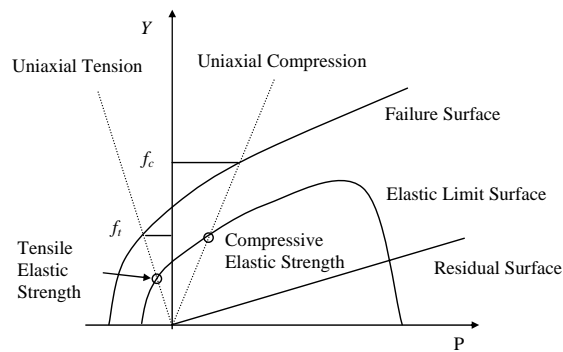


Figure 2: RHT Concrete strength model

The damage in concrete is accumulated via

$$D = \sum \frac{\Delta \varepsilon_{pl}}{\varepsilon_p^{failure}}, \quad \varepsilon_p^{failure} = D_1 (p^* - p_{spall}^*)^{D_2} \geq \varepsilon_f^{\min} \quad (4)$$

where D_1 and D_2 = damage constants, ε_f^{\min} = minimum strain to reach failure. The post-damage failure surface is then interpolated via

$$Y_{fracture}^* = (1 - D)Y_{failure}^* + DY_{residual}^* \quad (5)$$

For the reinforcing steel, the John-Cook model (Meyes, 1994) is adopted.

For an appropriate modeling of the behaviour of soil under severe explosion loading, a numerical three-phase soil model developed recently by the authors (Wang et al., 2004) is adopted in the full coupled analysis in

this study. This model extends from a classical concept (Henrych, 1975) in describing the soil as an assemblage of solid particles that form a skeleton with their voids filled by water and air. The model formulation can be roughly divided into two main parts; the equation of state and the strength model. Satisfying the continuity requirements, it follows

$$\frac{\Delta V}{V_0} = \frac{\Delta V_w}{V_0} + \frac{\Delta V_g}{V_0} + \frac{\Delta V_s}{V_0} \quad (6)$$

where V = volume of a soil element, V_0 = initial total volume of the element, V_w = volume of water, V_g and V_s = volumes of air and soil particles, respectively.

The pressure load causes deformation in each phase, as well as friction between the solid particles and deformation of the bond between the solid particles. The friction force and the force due to the bond are all exerted on the solid phase. Satisfying the equilibrium leads to an incremental form of the equation of state for the multi-phase soil, in which the contributions from the constituent phases can be obtained from their independent equations of state or stress-strain relationship.

To include the effect of hydrostatic stress on the shearing resistance of the soil, the modified von Mises' yield criterion (Drucker and Prager, 1952) is adopted, as follows,

$$f = \sqrt{J_2} - \alpha I_1 - k = 0 \quad (7)$$

where α and k = material constants related to the frictional and cohesive strengths of the material, respectively; I_1, J_2 = first and deviatoric stress invariant, respectively. This yield function is further modified to take into account the strain rate, as

$$f = \sqrt{J_2} - (\alpha I_1 - k) \left(1 + \beta \ln \frac{\dot{\epsilon}_{eff}}{\dot{\epsilon}_0}\right) = 0 \quad (8)$$

where $\dot{\epsilon}_0$ = reference effective strain rate, β = slope of the strength against the logarithm of strain rate curve, $\dot{\epsilon}_{eff}$ = effective strain rate.

The Jones-Wilkens-Lee (JWL) equation of state (Lee et al., 1968) is adopted to model the pressure generated by the expansion of the detonation product of the chemical explosive in the simulation, as follows

$$P = C_1 \left(1 - \frac{\omega}{R_1 v}\right) \exp(-r_1 v) + C_2 \left(1 - \frac{\omega}{R_2 v}\right) \exp(-r_2 v) + \frac{\omega e}{v} \quad (9)$$

where v = specific volume, e = specific energy. $C_1, R_1, C_2, R_2, \omega$ are constants.

3. NUMERICAL ANALYSIS AND DISCUSSION OF RESULTS

3.1 General

For the analysis to characterize the structural effects from an above-ground explosion, a generic multi-storey reinforced concrete frame is chosen. The frame has a total above-ground height of 20 m (six storeys), a total width of 10m, and a basement height of 3m (1 storey). The reinforced concrete beam and columns are assumed to have a uniform cross-sectional depth of 400mm. The concrete has the following properties: compressive strength = 30 MPa, tensile strength = 3 MPa, Young's modulus = 26 GPa. A gross reinforcement volumetric ratio of 2% is assumed. The reinforcing steel has yield strength of 460 MPa.

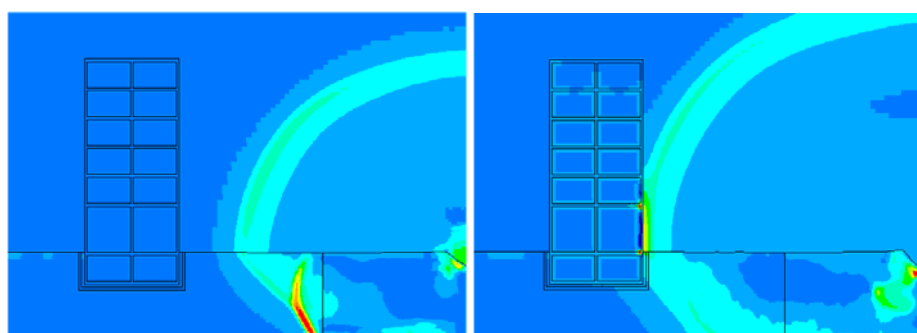


Figure 3: Computed blast wave propagation

The explosion scenario is designed such that both local and entire structural system response can be represented to allow for a comprehensive evaluation of the response characteristics. Thus, a charge of 1000 kg TNT (equivalent) is selected, representing a major incident. The stand-off distance is 30m measuring from the front face of the structure, giving a scaled standoff distance equal to $3\text{m/kg}^{1/3}$. Based on the associated analysis, a nearer standoff distance would generally result in more concentrated local damage. The detonation centre is assumed to be 1m above the ground surface. The numerical calculation is carried out using hydrocode Autodyn (Autodyn 1997) with necessary user defined subroutines.

Figure 3 depicts the contours of the pressure at two time instants. These graphs show clearly the propagation of the shock wave in air as well as in the soil. The incident and reflected waves can also be clearly observed.

3.2 Air blast load and stress wave in soil

Figure 4 shows the blast overpressure on the front face of the structure. As expected, the peak overpressure tends to decrease gradually at higher positions on the front face. At the same time, the arrival time of the shock front gradually delays as the height increases. The shape of the pressure curves and main pulse duration do not exhibit sensible difference among different target points.

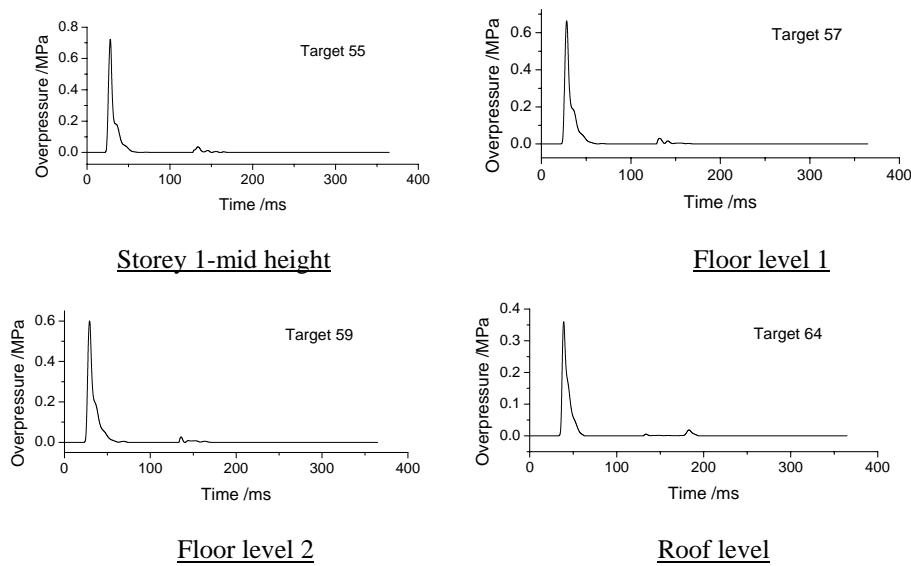


Figure 4: Blast pressure load on the front face of structure

In order to measure the stress wave in the soil, several target points are arranged inside the soil. Typical recorded soil pressure curves are plotted in Figure 5. As can be seen, the pressure in the soil also attenuates rapidly with the increase of the distance from the charge location. Near the charge the pressure exhibits extremely high value. In fact, as can be seen from the contours shown in Figure 3, a half-spherical crater of radius about 2m is created beneath the point of detonation.

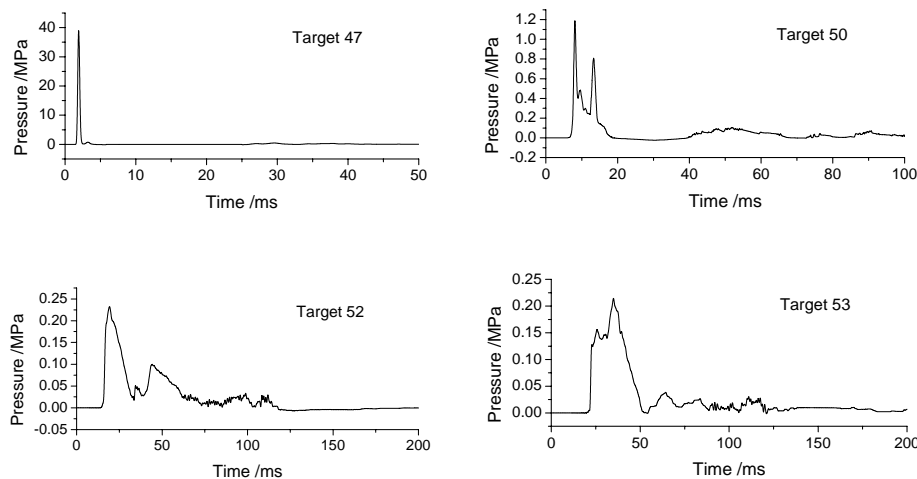


Figure 5: Stress wave propagation inside soil

3.3 Structural responses

Figure 6 shows the damage contours of the entire structure. Severe damage is observed to occur mainly in the elements on the front face of the

structure, due apparently to the strike of direct air shock wave. The remaining part of the structure exhibit more or less a uniform distribution of damage among different elements and it is generally minor. This indicates that the global dynamic response plays a relatively insignificant role as compared to the direct shock effect on the front face of the structure.

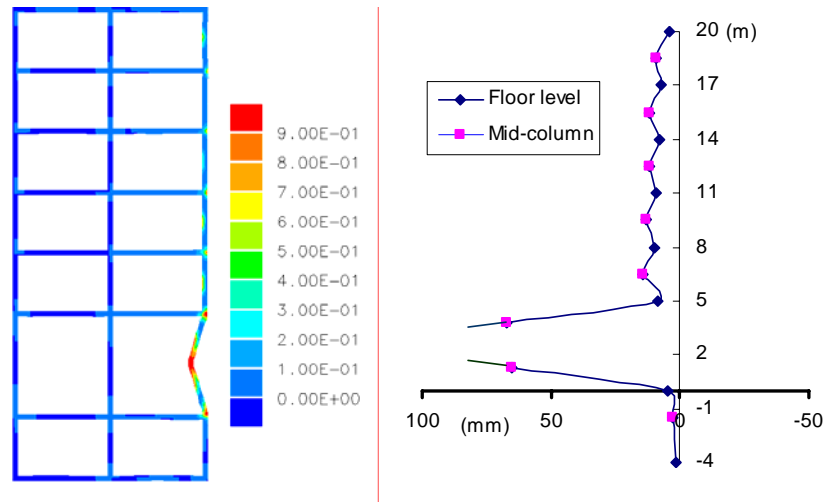


Figure 6: Damage contours and front face displacement profile

The damage to the front face elements shows a distinctive pattern. Within each storey, the severest damage is concentrated at both ends of the element on the outer side and around the middle portion on the inner side. For the particular example structure herein, the first storey column experiences disproportionately severer damage than columns in other storeys on the front face, due apparently to the relatively weaker resistance of the column because of its longer length, as well as the relatively higher loading at the first storey level.

To further illustrate the dynamic response of the structural system, the vibration histories at target points all over the structure are recorded. Figure 7 plots the horizontal velocity histories at typical target points. The highest velocity of about 6 m/s occurs at the first storey column on the front face (target 5), followed by the second storey column (about 1.7m/s, at target 8). The maximum velocity at the joint locations is generally on a lower order of about 0.5m/s, including that at the interior joints (e.g., target 21).

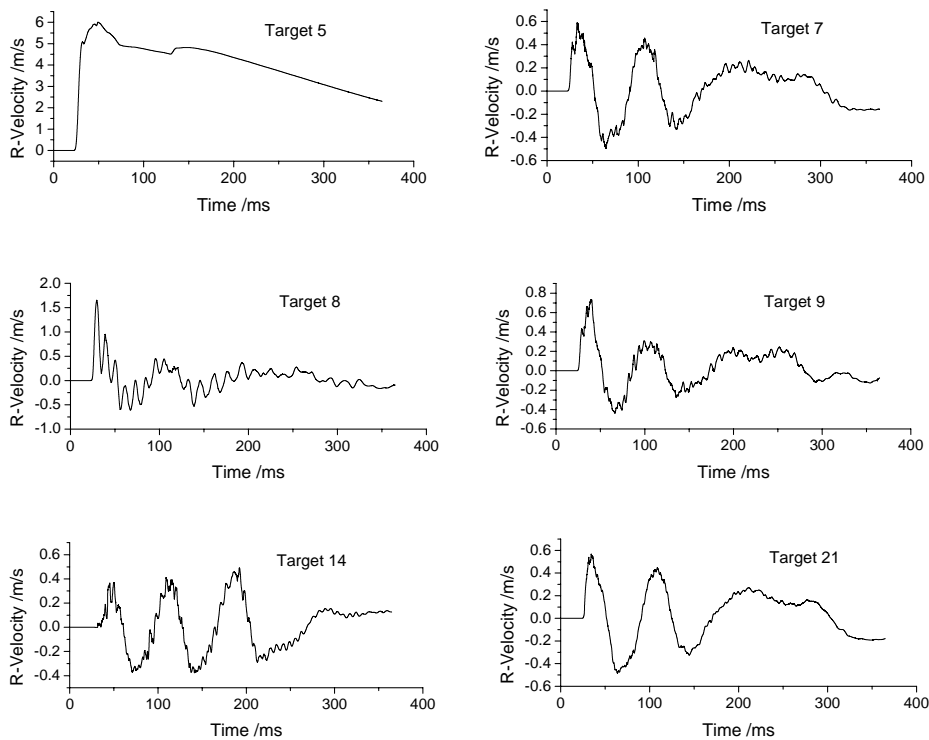


Figure 7: Horizontal velocity time histories at targets on structure

The displacement profile of the front face elements is also shown in Figure 6. The concentration of damage in the first storey column, as well as the significant element (column) level responses within each storey as evidenced in the damage contours is clearly observed. On the contrary, the global response as represented by the drifts at the floor (or joint) locations is relatively insignificant. In fact, the maximum relative drift between adjacent floors is no more than 10mm, or 0.3~0.4% of the respective storey height.

3.4 Significance of ground shock effect

The response of the structure described above is the results of a combined effect of the air shock wave and the ground vibration. In order to shed light on the extent to which the explosion induced ground vibration affects the damage and vibration response of the structure, two additional analyses are performed using the coupled model for separate air overpressure and ground vibration effects, respectively. In the analysis for the air overpressure effect only, an artificial rigid barrier is placed in front of the basement in the soil to block the propagation of the stress wave in the soil towards the structure base. Likewise, for the other case a rigid barrier is placed in front of the main structure to block the propagation of the air shock wave towards the structure so that only the ground vibration is effective.

Figure 8 shows a comparison of the damage contours for the structure separately under the air shock wave and ground shock effect. It can be clearly observed that the damage of the structure is almost entirely

attributable to the air shock wave effect, while the damage due to the ground vibration effect is practically negligible. The above trend is also evident from the comparison of the velocity responses at typical target points (not shown here). While the velocity response of the frame appears to be almost identical under combined loading or air shock only, the velocity response under the ground vibration alone is generally of one order of magnitude lower.

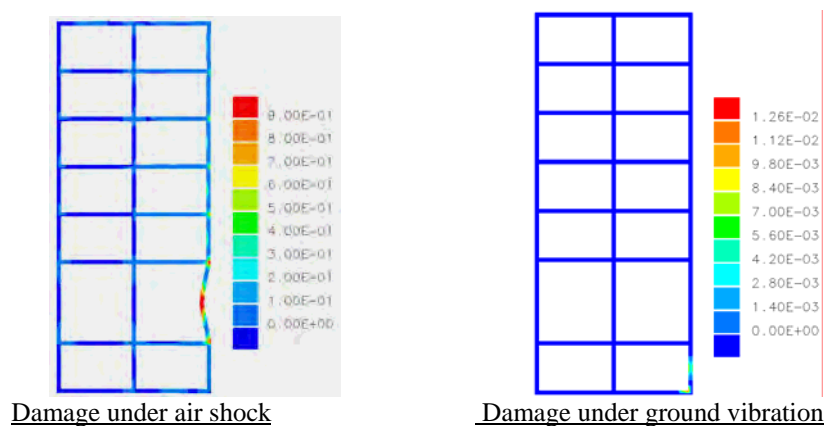


Figure 8: Damage due to separate air blast or ground vibration

4. CONCLUSIONS

Based on the analysis using coupled numerical model, the following conclusions may be drawn concerning the characteristics of a multi-storey frame structure subjected to a typical above-ground explosion: 1) The damage to the building frame primarily occurs in the elements on the front face, due to the effect of the direct air shock wave. The global dynamic response of the system is relatively insignificant concerning the structural damage. 2) For the typical explosion scenario under consideration, the structural damage and the critical vibration responses appear to be dominated by the air shock loading, while the explosion-induced ground vibration effects are limited to a certain degree of additional vibrations. 3) It should be mentioned that the present study concerns the direct blast effect. Once the residual state of the structure from the direct blast load is determined, the analysis of the post-blast process can proceed using a suitable analysis means.

REFERENCES

- AUTODYN Theory Manual, 1997, revision 3.0, Century Dynamics, San Ramon, California.
- Drucker, D.C., and Prager, W., 1952. Soil Mechanics and Plastic Analysis or Limit Design. *Q. Appl. Math* 10(2), 157-164.
- Henrych, J., 1979. *The Dynamics of Explosions and Its Use*. Elsevier, Amsterdam.

- Lee, E. L., Hornig, H. C., Kury, J. W., 1968. Adiabatic expansion of high explosive detonation products. *UCRL-50422*, Lawrence Radiation Laboratory, University of California.
- Meyers, M. A., 1994. *Dynamic Behavior of Materials*. John Wiley & Sons, New York.
- Riedel, W., Thoma, K., and Hiermaier, S., 1999. Numerical analysis using a new macroscopic concrete model for hydrocodes. Proceedings of 9th International Symposium on Interaction of the Effects of Munitions with Structures, Berlin, Germany, 315-322.
- Wang, Z., Hao, H. and Lu, Y., 2004. The three-phase soil model for simulating stress wave propagation due to blast loading. *International Journal for Numerical and Analytical Methods in Geomechanics* 28, 33-56.
- Wang, Z., Lu, Y., Hao, H. and Chong, K., 2004. A full coupled numerical analysis approach for buried structures subjected to subsurface blast. *Computers and Structures* 83(4-5), 339-356.

EXPERIMENTAL STUDY ON SEISMIC BEHAVIOR AND CRACK PATTERN OF CONCRETE BLOCK INFILLED RC FRAMES

YOSHIAKI NAKANO

Institute of Industrial Science, The University of Tokyo, Tokyo, Japan
iisnak@iis.u-tokyo.ac.jp

HO CHOI

Graduate School of Engineering, The University of Tokyo, Tokyo, Japan
choiho@iis.u-tokyo.ac.jp

ABSTRACT

In this study, concrete block infilled reinforced concrete frames for school buildings in Korea are tested under cyclic loadings, and a simplified model is proposed to investigate the relationship between residual crack widths in concrete block wall and frame's residual deformations. Although the measured crack widths in concrete block walls are much smaller than the residual deformations, a simplified model proposed in this paper considering flexural and shear deformation distribution of columns can rationally reproduce the measured crack widths. The relationship between crack widths in concrete block wall and frame's residual deformations is further investigated and their ratio is found to lie approximately in the range of 0.2 to 0.3. This result implies that the residual deformation of frames can be estimated from crack widths in concrete block wall.

1. INTRODUCTION

After an earthquake, the major concerns to damaged buildings are their safety/risk to aftershocks, quantitative damage assessment to evaluate their residual seismic capacity and to identify necessary actions on the damaged buildings. Post-event damage evaluation is therefore essential for quick recovery of damaged communities as well as pre-event seismic evaluation and strengthening of vulnerable buildings. Few investigations on unreinforced masonry walls, however, have been made to quantitatively identify their damage level and criteria to judge necessary actions for their continued use, repair and rehabilitation although their damage has been often found in the past damaging earthquakes.

In this study, concrete block (CB) infilled RC frames for school buildings in Korea, where CB walls are typically unreinforced, are experimentally investigated to develop pre- and post-earthquake seismic evaluation method. In the tests, full-scale, one-bay, single-story specimens having different axial loads in columns and different opening configurations in walls are tested under cyclic loadings, and the contribution of CB walls to

overall behaviors is examined. Furthermore, crack patterns and widths in walls and frames which may be of great significance for post-event damage assessment are carefully observed, and the measured results in CB wall are compared to those estimated by a simplified model proposed in this paper.

2. OUTLINE OF EXPERIMENT

2.1 Test Specimen

Figure 1 shows a standard design for Korean school buildings in the 1980s (The Ministry of Construction and Transportation, 2002). As can be found in this figure, CB walls are commonly used as partition walls or exterior walls in Korean school buildings. In this study, 4 specimens representing a first or fourth story of 4 story RC school buildings are tested under cyclic loadings. They are infilled wall type 1 (IW1) assuming a first story, infilled wall type 2 (IW2) assuming a fourth story, and wing wall type (WW) and partial height wall type (PW) both having an opening in the wall. The axial force applied in each column is 720 kN (4 N/mm^2) for specimens IW1, WW, and PW while 180 kN (1 N/mm^2) for IW2.

The design details of specimen IW1 are shown in Figure 2. Since seismic design provisions for buildings were introduced in 1988 in Korea, the model structures studied herein are not designed to seismic loads. Therefore, they have (1) large spacing of hoops (300 mm) and (2) 90-degree hooks at both ends of hoops as shown in the figure. Specimens IW1, WW,

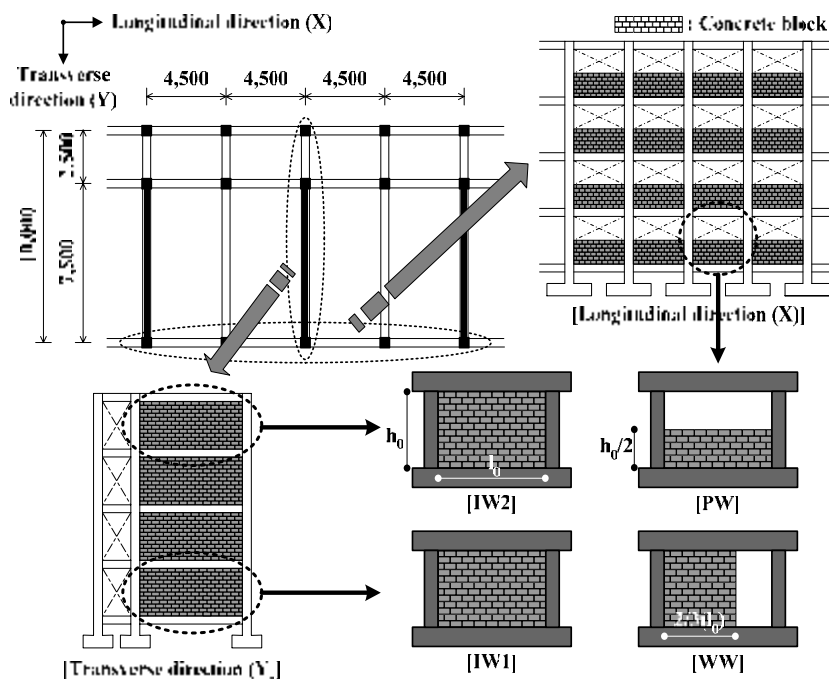


Figure 1: Standard design of Korean school buildings in the 1980s and specimen configuration

and PW have the identical re-bar arrangement in columns but different wall arrangement, while IW2 has fewer re-bars than other 3 specimens. Concrete block units are laid in the RC frame after concrete is hardened.

2.2 Test Setup and Test Program

Figure 3 and Photo 1 show the elevation view of the loading system. Cyclic lateral loads are applied to each specimen through a loading beam tightly fastened to the specimen. Figure 4 shows the loading history, where a peak drift angle R is defined as “lateral deformation (δ_p) / column height (=2,400 mm)”. As shown in the figure, peak drift angles of 0.1, 0.2, .0.4, 0.67, 1.0, and 2.0% are planned and 2.5 cycles for each peak drift are imposed to eliminate one-sided progressive failure (unsymmetric failure pattern in positive or negative loadings). It should also be noted that 0.4% loading is imposed after 1.0% to investigate the effect of small amplitude loading after large deformation (i.e., aftershocks). After severe damage is found, the specimen is pushed over to collapse. A constant axial load of 1,440 kN (720 kN for each column) is applied to specimens IW1, WW and PW while 360 kN (180 kN for each) to specimen IW2.

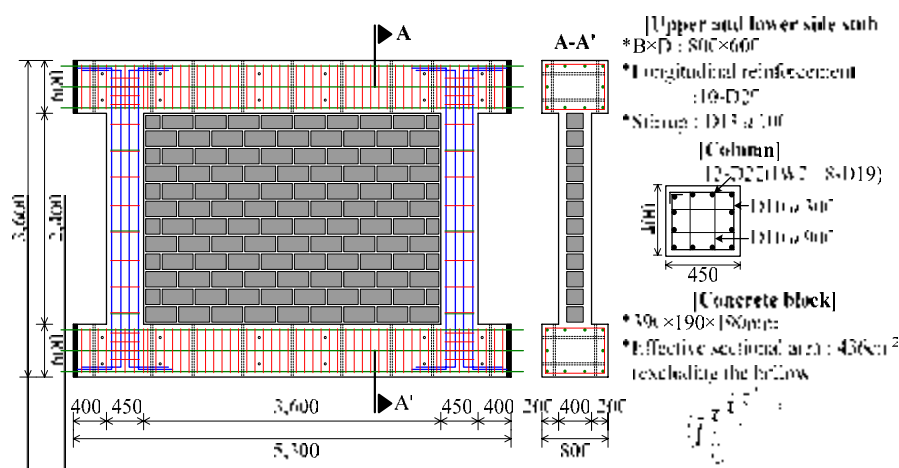


Figure 2: Detail of specimen (IW1)

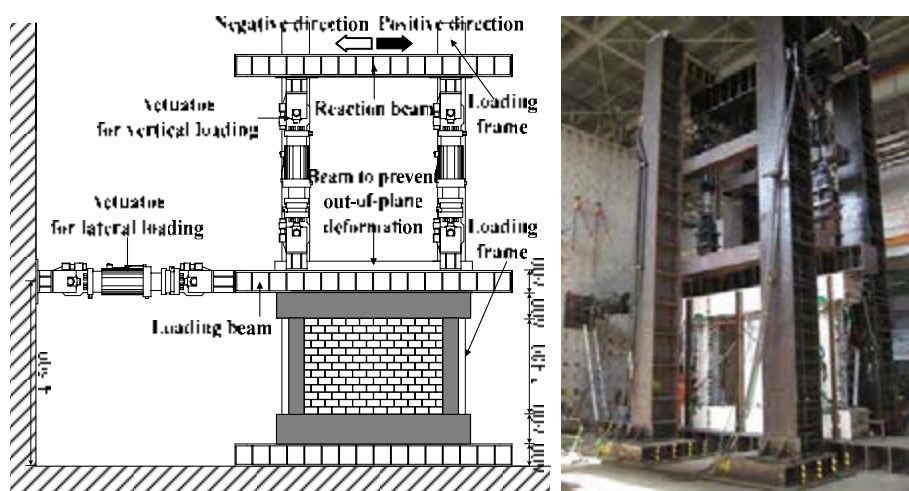


Figure 3: Test setup

Photo 1: General view of test setup

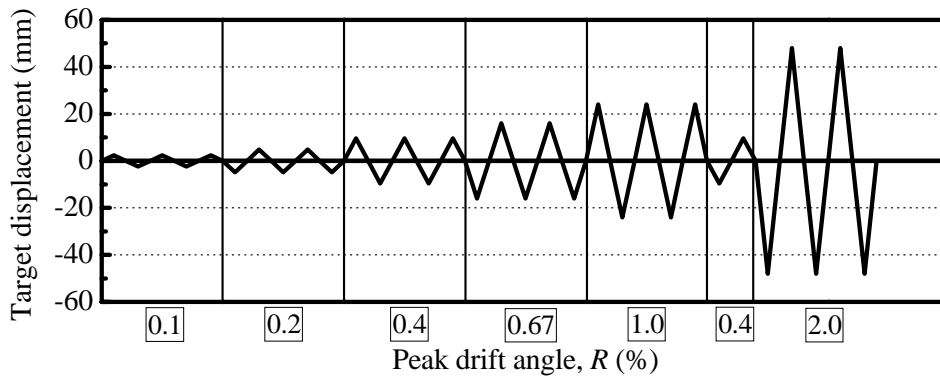


Figure 4: Loading history

3. CRACK WIDTHS AND RESPONSE OF SPECIMENS

3.1 Measurement of Crack Width

Cracks in members after an earthquake are visible and essential evidence of damage that can be found at the building site, and they often provide valuable information regarding the response that the building has experienced and its residual capacity. To investigate the relationship between crack width and residual capacity, crack widths in RC columns and CB walls are carefully measured at peak loads and unloaded stages. Figure 5 shows the measurement points in columns and walls made in this study.

The widths of flexural and shear cracks observed at the top and bottom of each column are visually measured with crack scales. Since crack widths are not necessarily uniform along the crack, its major width which is deemed to be largest along a crack is measured. It should also be noted that the width perpendicular to the crack is measured.

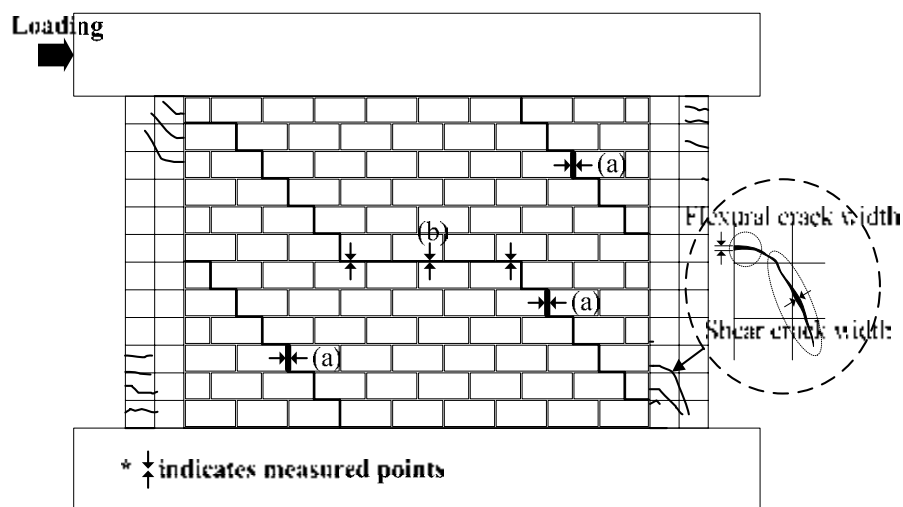


Figure 5: Schematic illustration of crack pattern and measured points

All visible cracks in the head joints found in stair-stepped diagonal cracks running through the CB wall are also measured to record the lateral dislocation of CB units (see Figure 5(a)) while several cracks in the bed joints of one continued crack are measured to investigate a rotational behavior of wall (see Figure 5(b)). In the following sections, crack widths measured in the head joints of CB walls of specimens IW1 and IW2 are investigated to understand the relationship between observed cracks and frame's behavior.

3.2 Residual Crack Width in CB Wall

The residual deformation (δ_0), total residual crack width ($\Sigma_{\max} W_0$) measured in CB wall, and their ratio [$\Sigma_{\max} W_0 / \delta_0$] at unloaded stages after each first cycle in the positive domain are plotted for specimens IW1 and IW2 with respect to the peak drift angle in Figure 6. In this figure, $_{\max} W_0$ is defined as the maximum residual crack width, as is shown (a) in Figure 5, in the head joints of a continued stair-stepped diagonal crack. When the CB wall has more than one major stair-stepped diagonal crack, $_{\max} W_0$ can be found along each continued crack and the sum of $_{\max} W_0$ ($= \Sigma_{\max} W_0$) is then calculated. The ratio [$\Sigma_{\max} W_0 / \delta_0$] of specimen IW1 differs from that of IW2 over the peak drift angle R smaller than 0.2% and larger than 1.5%. The results can be attributed to the following observations.

- (1) The ratio tends to be dependent on crack inspectors especially when the deformation is small (i.e., $R \leq 0.2\%$) since the observed crack widths are around 0.1mm which would be the limit for visual inspections. The calculated ratio is therefore sensitive to the measurement error and may not be consistent in the small drift range along different specimens.
- (2) The crack widths in CB wall significantly increases after $R = 1.4\%$ in IW1 due to extensive shear cracks in columns, while IW2 performs well even in such a large deformation. The ratio is therefore higher in IW1 than in IW2.

It should also be noted that the ratio [$\Sigma_{\max} W_0 / \delta_0$] is approximately in the range of 0.2 to 0.3 over the peak drift angle larger than 0.2 % and much smaller than 1.0. The reason can be found in the following section.

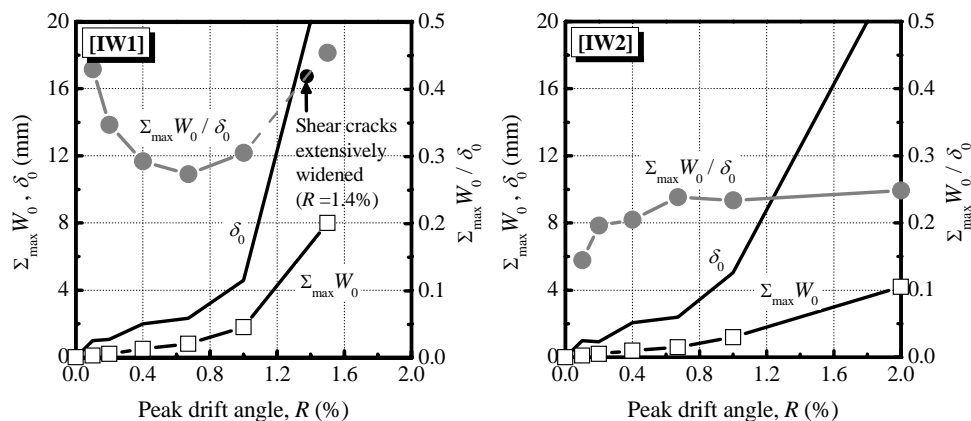


Figure 6: δ_0 , $\Sigma_{\max} W_0$ and [$\Sigma_{\max} W_0 / \delta_0$] (CB wall) vs. peak drift angle R

3.3 Estimation of Measured Crack Width in CB Wall by Simplified Model

(1) General assumptions

In order to investigate the crack development mechanism and to estimate the crack width in CB wall, the following assumptions are made.

- 1) The residual deformation (δ_0) of frame can be approximated by the sum of residual flexural deformation (δ_{f0}) and residual shear deformation (δ_{s0}) of column as shown in Figures 7(a) and (b). (i.e., $\delta_0 = \delta_{f0} + \delta_{s0}$)
- 2) Cracks in head joints of CB wall result from the discrepancy of deformation distribution along its height in each column.

If each column has an identical anti-symmetrical flexural deformation and distribution as shown in Figure 7(a), no discrepancy should be found in the CB wall's clear span length l_{0i} along column height (i.e., $l_{01} \approx l_{02} \approx l_{03}$). Since a similar flexural deformation distribution is observed in each column during tests, no major cracks due to flexural deformation are expected.

The shear deformation distribution along its height in each column, however, is not obviously identical as shown in Figure 7(b), since the deformation due to shear cracks concentrates on the bottom of compression column and the top of tensile column resulting from a compressive strut action as can be found in specimens IW1 and IW2 (see Figure 8). This may cause the discrepancy of lateral deformation distribution in CB wall along

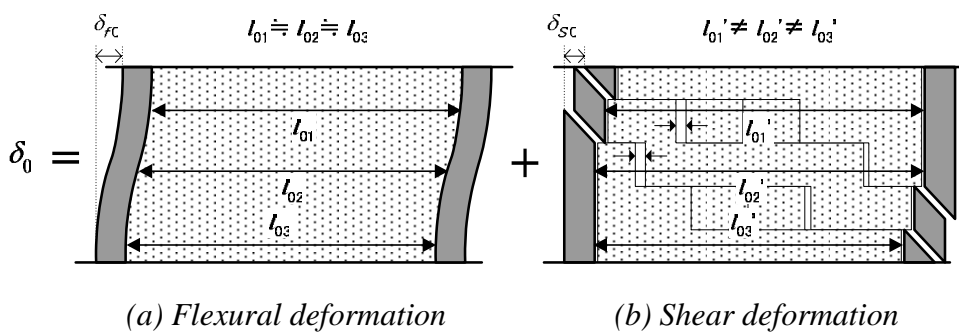


Figure 7: Deformation of column and CB wall

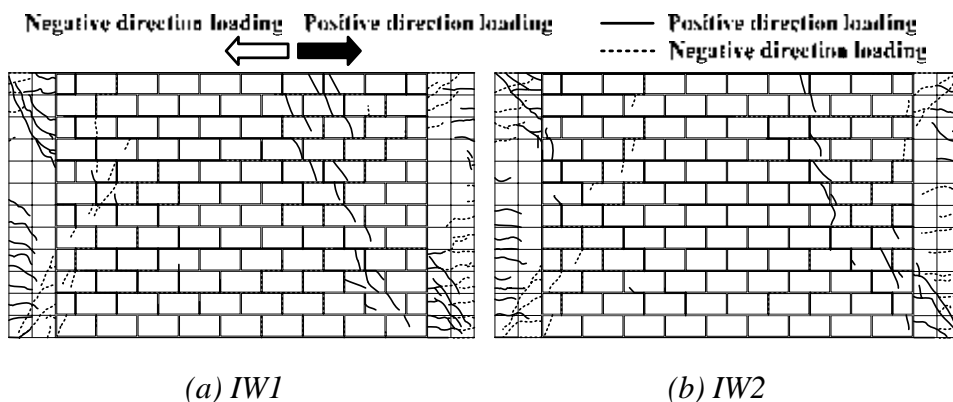


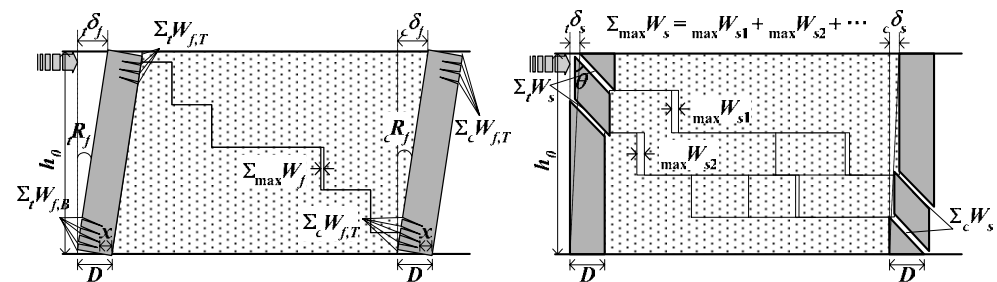
Figure 8: Cracks in RC columns and CB wall at the 1st cycle with peak drift angle of +1.0%

column height (i.e., $l_{01}' \neq l_{02}' \neq l_{03}'$). The maximum discrepancy, which may be simply expressed by the residual shear deformation (δ_{s0}) as shown in Figure 7(b), then needs to be consistent with crack widths in head joints resulting in high correlation between the residual shear deformation (δ_{s0}) and total crack width in CB wall ($\Sigma_{\max} W_0$).

Bearing in mind that the flexural deformation may highly contribute to the overall deformation of long columns but that the flexural deformation, as is described earlier, may not cause major cracks in head joints, the ratio $[\Sigma_{\max} W_0 / \delta_0]$ can be expected to be small as demonstrated in Figure 6. Based on studies by Maeda et al.(2000), AIJ Guidelines define the relationship between residual crack width and residual deformation for RC members (AIJ, 2004). However, few researches on the relationship for RC frames and/or CB wall infilled frames have been yet made to date. It is therefore of great interest and significance to investigate the applicability of analogous relationship to CB wall infilled frames. In the subsequent discussions, a simplified model considering the discrepancy of flexural and shear deformation distribution is proposed to estimate the crack width in CB wall, and the correlation between measured and estimated results is discussed.

(2) Crack width due to flexural deformation

Figure 9 shows the outline of the simplified model studied herein. The flexural deformation, ${}_t\delta_f$ and ${}_c\delta_f$, of each column can be approximated using the average total flexural crack width at the top and bottom of column as shown in equations (1) and (2) (AIJ, 2004), where “t” and “c” denote “tension side” and “compression side”, respectively. The maximum discrepancy between two columns due to flexural deformation distribution, which causes minor cracks in head joints as discussed earlier, is assumed herein to develop in the mid-height of column ($h_0/2$) as shown in equation (3).



(a) Flexural deformation

(b) Shear deformation

Figure 9: Simplified model of column and CB wall

$${}_t\delta_f = {}_tR_f \cdot h_0 = \frac{1}{D-x} \cdot \left(\frac{\Sigma_t W_{f,T} + \Sigma_t W_{f,B}}{2} \right) \cdot h_0 \quad (1)$$

$${}_c\delta_f = {}_cR_f \cdot h_0 = \frac{1}{D-x} \cdot \left(\frac{\Sigma_c W_{f,T} + \Sigma_c W_{f,B}}{2} \right) \cdot h_0 \quad (2)$$

$$\Sigma_{\max} W_f = \left(\frac{\Sigma_c W_{f,B} - \Sigma_t W_{f,B}}{D-x} \right) \cdot \frac{h_0}{2} \quad (3)$$

where,

- ${}_t\delta_f, {}_c\delta_f$: flexural deformation of tension and compression side column, respectively (see Figure 9(a))
- ${}_tR_f, {}_cR_f$: flexural rotation angle of tension and compression side column, respectively (see Figure 9(a))
- $\Sigma_t W_{f,T}, \Sigma_t W_{f,B}$: total flexural crack width of top and bottom in tension column, respectively (measured)
- $\Sigma_c W_{f,T}, \Sigma_c W_{f,B}$: total flexural crack width of top and bottom in compression column, respectively (measured)
- D : column depth (=450 mm)
- x : distance from extreme compression fiber to neutral axis ($0.2D$ (= 90 mm) is assumed herein)
- h_0 : column clear height (= 2,400 mm)
- $\Sigma_{\max} W_f$: total crack width in CB wall due to the discrepancy of flexural deformation distribution

(3) Crack width due to shear deformation

The shear deformation, ${}_t\delta_s$ and ${}_c\delta_s$, of two RC columns can be approximated based on the measured total shear crack width of each column as shown in equations (4) and (5) (AIJ, 2004). The total crack width in CB wall due to different shear deformation distribution between tension and compression side column can be estimated using the average total shear crack width as shown in equation (6).

$${}_t\delta_s = \Sigma_t W_s \cdot \cos \theta \tag{4}$$

$${}_c\delta_s = \Sigma_c W_s \cdot \cos \theta \tag{5}$$

$$\Sigma_{\max} W_s = \frac{{}_c\delta_s + {}_t\delta_s}{2} \left(= \frac{(\Sigma_c W_s + \Sigma_t W_s) \cdot \cos \theta}{2} \right) \tag{6}$$

where,

- ${}_t\delta_s, {}_c\delta_s$: shear deformation of tension and compression side column, respectively (see Figure 9(b))
- $\Sigma_t W_s, \Sigma_c W_s$: total shear crack width of tension and compression side column, respectively (measured)
- θ : angle between shear crack and vertical direction of column (45-degree angle is assumed herein)
- $\Sigma_{\max} W_s$: total crack width in CB wall due to the shear deformation distribution

(4) Total crack width in CB wall

As shown in equation (7), the total crack width in CB wall, $\Sigma_{\max} W$, can be calculated using crack widths defined in equations (3) and (6).

$$\Sigma_{\max} W = \Sigma_{\max} W_f + \Sigma_{\max} W_s = \left(\frac{\Sigma_c W_{f,B} - \Sigma_t W_{f,B}}{D - x} \right) \cdot \frac{h_0}{2} + \frac{(\Sigma_c W_s + \Sigma_t W_s) \cdot \cos \theta}{2} \tag{7}$$

Figure 10 shows the residual deformation δ_0 and δ_{f0} with respect to the peak drift angle, where δ_{f0} is assumed to be the average of ${}_t\delta_f$ and ${}_c\delta_f$ at

unloaded stages derived from equations (1) and (2). Since major wide cracks are selectively measured after 1.0 % drift, δ_{f0} is plotted up to 1.0 %. As is anticipated in 3.3 (1), δ_{f0} mainly contributes to the overall residual deformation δ_0 . It is also interesting to point out that the ratio of crack widths $\Sigma_{\max} W_{f0}$ to δ_{f0} is relatively small, which is consistent with the results shown in Figure 6. This is mainly because the flexural deformation distribution along their height of two boundary columns does not differ much (i.e., $l_{01} \approx l_{02} \approx l_{03}$) and therefore leads to minor cracks in head joints.

Figure 11 shows the estimated crack widths in CB wall at unloaded stages obtained from equation (7) together with measured results. The estimated results (shown in circle : -○-) slightly overestimate the measured results (shown in square : -□-) since all cracks developed in CB wall are not perfectly measured during tests. The estimated results, however, generally compare well with the measured results and the proposed model shown in Figure 9 successfully explains the crack development mechanism of CB wall studied herein. This result implies that the residual deformation δ_0 of frames as well as RC members can be estimated from crack widths $\Sigma_{\max} W_0$

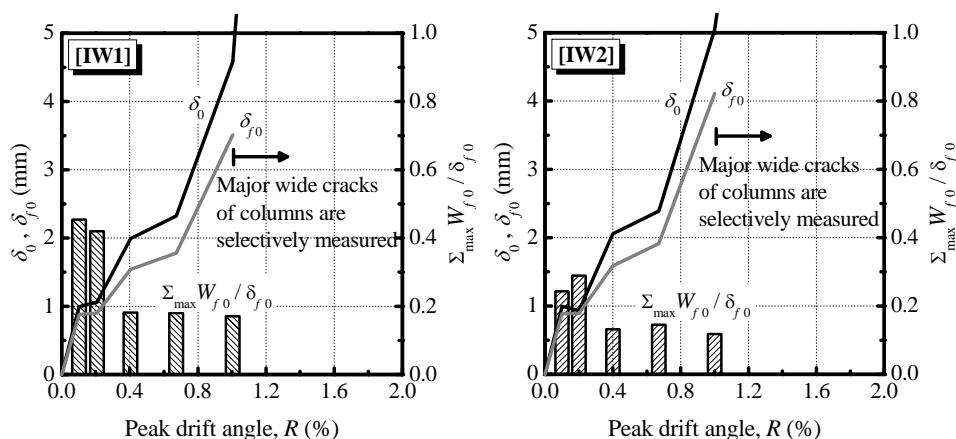


Figure 10: δ_0 , δ_{f0} and $[\Sigma_{\max} W_{f0} / \delta_{f0}]$ vs. peak drift angle R

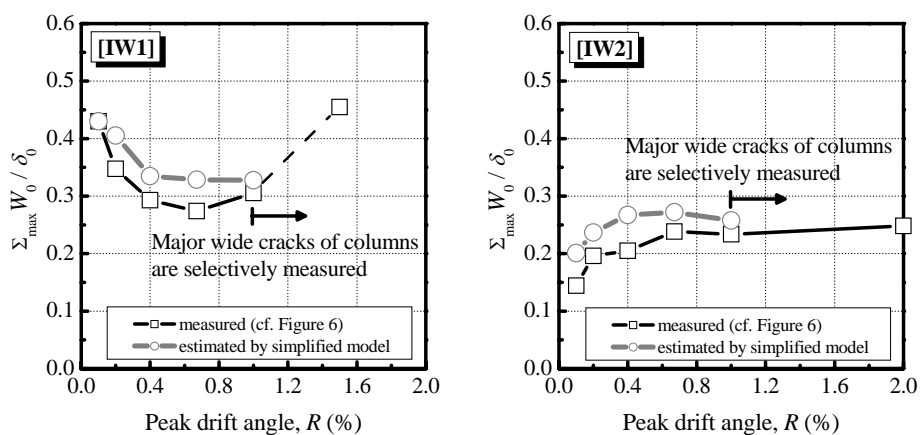


Figure 11: $[\Sigma_{\max} W_0 / \delta_0]$ vs. peak drift angle R (in positive loading)

observed in CB wall based on the ratio $[\Sigma_{\max} W_0 / \delta_0]$. The residual seismic capacity, therefore, could be evaluated through previously estimated δ_0 if the typical hysteretic characteristics of CB wall infilled frame are given.

4. CONCLUSIONS

Concrete block (CB) infilled RC frames for school buildings in Korea are tested under cyclic loadings, and a simplified model is proposed to investigate the relationship between residual crack widths in CB wall and residual deformation. The results can be summarized as follows.

- (1) The measured ratio $[\Sigma_{\max} W_0 / \delta_0]$ for specimens IW1 and IW2 lies approximately in the range of 0.2 to 0.3 before the specimen extensively fails in shear.
- (2) Although the ratio above is much smaller than 1.0, a simplified model proposed in this paper considering flexural and shear deformation distribution of columns can rationally reproduce the measured results.
- (3) The results described above imply that the residual deformation δ_0 of frames can be estimated from crack widths $\Sigma_{\max} W_0$ observed in CB wall based on the ratio $[\Sigma_{\max} W_0 / \delta_0]$. The residual seismic capacity, therefore, could be evaluated through previously estimated δ_0 if the typical hysteretic characteristics of CB wall infilled frame are given.

ACKNOWLEDGMENT

The research reported herein was performed in cooperation with Professor Waon-Ho Yi of the Kwangwoon University and Dr. Sang-Hoon Oh of RIST (Research Institute of Industrial Science and Technology) in Korea. The authors express their deepest gratitude to all these supports without which the test could not be accomplished.

REFERENCES

- The Ministry of Construction and Transportation, 2002. A study on the seismic evaluation and retrofit of low-rise RC buildings in Korea. pp. 113-155.
- Masaki Maeda, Masahiro Bunno and Masayuki Nagata, 2000. A study on the damage level estimation of RC buildings based on residual seismic capacity of members. *Proceedings of the Japan Concrete Institute*, Vol. 22, No. 3, pp. 1447-1452.
- AIJ(Architectural Institute of Japan), 2004. Guidelines for performance evaluation of earthquake resistant reinforced concrete buildings (Draft) pp. 155-161.

SIMPLIFIED METHODOLOGY FOR DAMAGE ASSESSMENT OF 2-STOREY RC FRAME SUBJECTED TO EXPLOSION-INDUCED GROUND MOTIONS (EIGMS)

CHEE LEONG LIM AND TSO-CHIEN PAN

Protective Technology Research Centre, School of Civil and Environmental Engineering, Nanyang Technological University, Singapore
cheeleong@ntu.edu.sg

ABSTRACT

Explosion-induced ground motions (EIGMs) have large amplitudes and high frequency contents, occurring within a short duration. EIGM characteristics can be segmented into two parts: the major shock duration (Phase 1) and the ensuing duration (Phase 2). When subjected to EIGMs, the structure experiences small structural deformations and large induced shear forces during the loading duration (Phase 1). After the loading duration, larger structural displacements are experienced in Phase 2. Due to the high frequency contents of EIGMs, the response analysis of Phase 1 requires a sufficient number of elements, in order to capture the local mode response. In the case of a multi-storey reinforced concrete (RC) frame, the computational effort would be large. In this paper, a simplified damage assessment method is proposed, whereby the damage assessment of multi-storey RC frame can be approximated by this simplified methodology. This methodology is for approximating the damage assessment of a multi-storey RC frame during Phase 1, by performing the damage assessment of a base column of the RC frame with simplified fixed-fixed boundary conditions. Also, this simplified methodology considers the strength enhancement due to strain rate effects. The damage assessment results of the simplified structural-level model of the simplified fixed-fixed column were determined. The results from the simplified methodology were compared with the results from a material-level model of a 2-storey RC frame. It is shown that the both results are comparable and that the simplified methodology may be able to approximate the damage of a multi-storey RC frame during the Phase 1 response, when subjected to an EIGM.

1.0 INTRODUCTION

Growing populations, industrial development and commercial development has pushed closer the supply and the demand of land. Thus, ongoing defence strategies of each country, underground space has been developed for ammunition storage. These underground ammunition storages pose a threat to structures in the vicinity of an accidental or intentional

detonation. When there is such a detonation, explosions-induced ground motions (EIGMs) are generated. These ground motions propagate through the soil or rock medium and may cause damage to the structures above and around the detonation source. The difference between earthquakes and EIGMs lies in their magnitudes, durations and predominant frequencies. EIGMs occur within shorter durations (in the order of microseconds) than earthquakes and so their frequency content is also higher than earthquakes (Lu et al, 2001; Pan et al, 2004). The acceleration amplitudes of EIGMs can be in the range of 80 to 150 g, which is larger than earthquakes (Lu et al, 2001; Pan et al, 2004).

Structural response to EIGMs can be segmented into two parts: the major shock duration (Phase 1) and the ensuing duration (Phase 2). It was shown that the high frequency nature of an EIGM led to a large shear force with small structural displacement during Phase 1, followed by significant structural displacement during Phase 2 (Pan et al, 2004). Thus, for a reinforced concrete (RC) structure designed for resistance to EIGM, it should possess toughness for the large induced shear forces during Phase 1; it should however also possess ductility for Phase 2 response where the structural displacements are significantly larger. Other researchers have performed numerical analyses of multi-storey RC frames subjected to simulated EIGMs. For a 2-storey RC frame, Lu et al (2001) noted that the mass of the second-storey filtered significant amounts of high-frequency input of energy as the stress waves propagate along the column, during Phase 1 response. This is because the presence of concentrated masses can act as frequency filters by blocking high-frequency components of waves. Thus, the masses reduce the inertia action of EIGMs on upper storey levels during Phase 1 response.

Frames have global mode(s) associated with the floor(s) where the mass is lumped. There are also local modes associated with the degrees of freedom at intermediate points accounting for the distributed masses of beams, columns and slabs. When frames are subjected to high-frequency ground motions, the local modes display significant response (Lu et al, 2001; Pan et al, 2004). Thus, in the response analysis of frames subjected to EIGMs, inclusion of the higher-frequency local modes within the analytical model leads to a significant increase in computational effort.

It has been hypothesized that the strength of a material increases with the strain rate (Malvern, 1951). For concrete and steel reinforcement bars, the hypothesized strength-enhancement effect due to higher strain rates has been demonstrated (CEB, 1993; Malvar, 1998). The strength-enhancement due to strain rate effects is normally shown as a dynamic increase factor (DIF), which is a ratio of the dynamic strength to the static strength. For this paper, the damage assessment shall consider the strength-enhancement due to strain rate effects.

For a material-level model of a 2-storey RC frame, the damage assessment of the RC frame to a simulated EIGM was determined (Pan et al, 2004). Figure 1 shows the 2-storey RC frame. The dimensions for the RC

column are 300 mm × 230 mm × 3,300 mm. For this RC column, the steel reinforcement is as follows: 6 longitudinal steel bars of 19 mm diameter and 10 mm diameter double-legged lateral ties at 100 mm spacing. The following concrete properties are assumed: concrete unit weight = 24 kN/m³; concrete compressive strength = 30 MPa; concrete elastic modulus = 26 GPa. For the steel reinforcing bars, the following properties are assumed: steel yield strength = 410 Mpa and steel elastic modulus = 200 GPa. Figure 2 shows the acceleration time history of the simulated EIGM. The ground shock is a simulated EIGM at 50 m from the source of detonation whereby the explosion is 250 ton of TNT with a loading density of 10 kg/m³. The horizontal component of the simulated EIGM at 50 m from source, has the following properties: peak ground acceleration (PGA) = 123 g; peak ground velocity (PGV) = 0.91 m/s; and a dominant frequency band between 95 Hz and 260 Hz (Zhou et al 2002; Pan et al, 2004). Figure 3 shows the damage assessment results based on the material-level model of the 2-storey RC frame (Pan et al, 2004). A parametric study was undertaken whereby a family of EIGMs was generated by scaling the PGA, PGV and dominant frequency. The scaled EIGMs were used as the input ground motions for the material-based model of the 2-storey RC frame. Representative PGAs and PGVs were taken as the mean of the horizontal PGA and mean of the horizontal PGVs, respectively. Also, the principal frequency was determined as the average of the two frequencies corresponding to the acceleration Fourier spectra, at half of the peak spectral acceleration. Figure 3 shows the types of failure mechanisms that were considered for the damage assessment, in terms of PGV and PGA of the EIGM, which would result in each failure mechanism. The two failure mechanisms considered were diagonal shear failure and flexural failure. However, the damage results were not analyzed for the chronology of flexural and shear failure (region B in Figure 3). For the material-based model of the 2-storey RC frame, there was no explicit consideration of the strength-enhancement due to strain rate effects.

In this paper, a simplified methodology is proposed as an approximation for the damage assessment of a multi-storey RC frame, during the Phase 1 response. The simplification in this methodology involves performing the damage assessment based on a structural-level model of a single column, representative of the base column of a multi-storey RC frame. The boundary conditions of the single column are assumed to be fixed at the top and bottom (fixed-fixed). The reason for such a simplification is due to how the mass of the second storey level has been shown to filter the propagation of the stress waves during Phase 1 response. Also, the strength-enhancement due to strain rate effects is explicitly considered in this simplified methodology. This simplified methodology is applied on the 2-storey frame used by Pan et al (2004) and the damage assessment results are compared with those obtained by the material-based modeling of the same 2-storey RC frame. The purpose is to compare the damage assessment obtained based on a structural-level model of a fixed-fixed column, with those obtained by the more refined material-based model of a 2-storey RC frame (Pan et. a., 2004). If the damage assessment results from the two types of model be comparable, the simplified methodology

with its gross assumptions may serve as an approximation for the damage assessment of multi-storey RC frames subjected to EIGMs, with a much reduced computational effort.

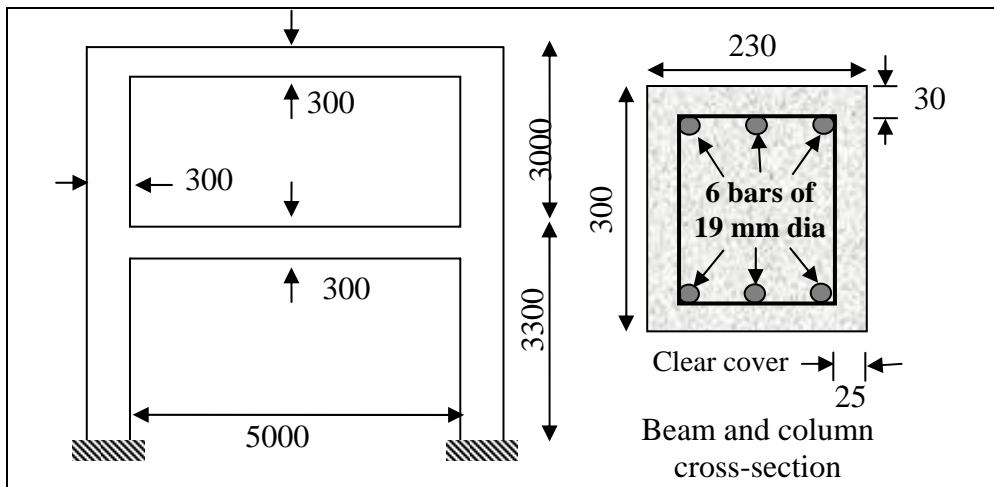


Figure 1: 2-Storey RC frame

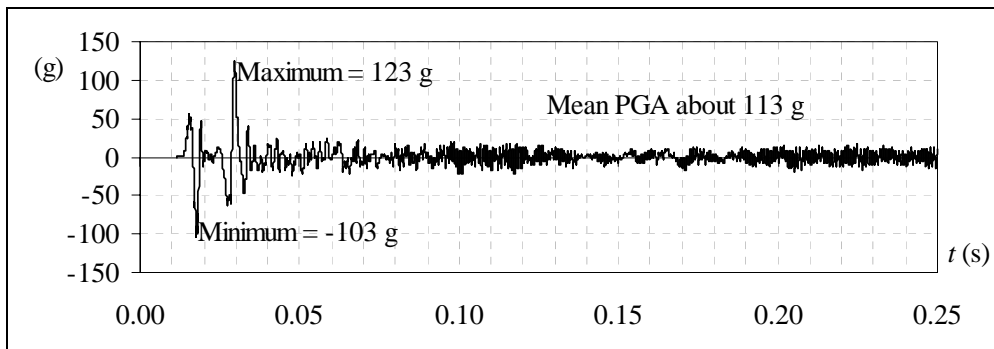


Figure 2: Simulated EIGM at 50 m from explosion
(Zhou et al, 2002; Pan et al, 2004)

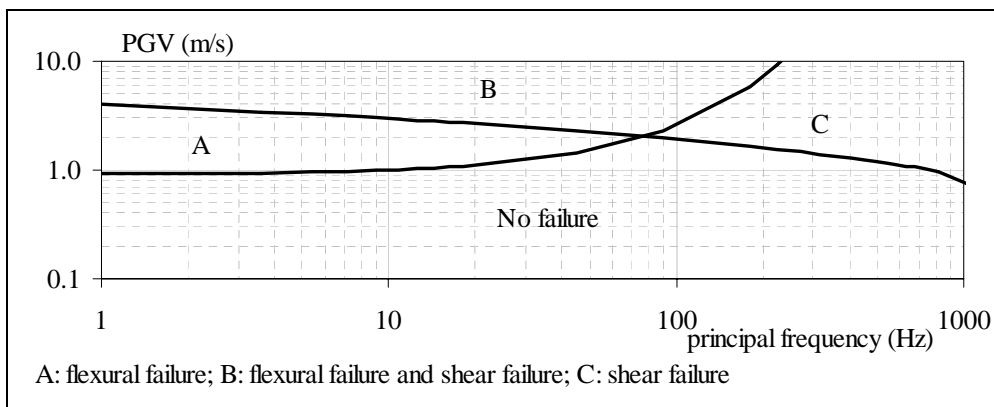


Figure 3: Failure mechanisms determined by material-based model
of 2-Storey RC frame

2.0 PROPOSED DAMAGE ASSESSMENT FOR PHASE 1

For the proposed simplified methodology, the following failure mechanisms are considered: (a) direct shear failure defined as when the induced shear force exceeding the direct shear failure strength capacity; (b) diagonal shear failure defined as when the induced shear force exceeding the diagonal shear strength capacity; and (c) flexural failure defined as when the induced bending moment exceeding the yielding moment, of the RC section. For the direct shear failure and diagonal shear failure, the strength enhancement effect due to strain rate effect is considered by using the DIF formulation by CEB (1993). For the direct shear strength capacity, the predictive equation by K&C (1973) is used. For the diagonal shear strength capacity, the predictive equation by Priestley et al (1994) is used. However, no strength-enhancement due to strain rate effects was considered for the flexural failure. This exception is because flexural responses normally occur at lower frequency ranges than shear responses.

For the column subjected to EIGM, the shear characteristic (i.e. the distinction between a diagonal shear behavior and a direct shear behavior experienced by the column), is determined based on the research by Li and Jones (2000). Li and Jones (2000) made a distinction between the occurrence of a direct shear and diagonal shear behavior, which was described in the extent of the formation of a shear hinge. Shear hinge occurs when there is a dominant zone of shear deformation. For a rectangular cross-section, the extent to the formation of shear hinges is recast as a dimensionless parameter, as follows (Equation 1):

$$\text{Direct shear: } M/(QH) \leq 0.433 \quad (1a)$$

$$\text{Diagonal shear: } M/(QH) > 0.433 \quad (1b)$$

where M is the induced bending moment; Q is the induced shear force; and H is the thickness of the beam.

For the response during Phase 1, a strength-based damage index is proposed. The proposed damage index is designed for a toughness test. Thus, no attempts shall be made to add the independent contributions to the damage from the effects of shear force and bending moment. That is, the damage index shall be taken as the maximum of two ratios, each of which is the ratio of the induced shear force or bending moment to the respective strength capacity. For an instant in time t , the propose damage index for Phase 1 is as follows:

$$\text{Damage Index} = \text{Max} \left(\frac{Q}{Q_c}, \frac{M}{M_c} \right) \quad (2)$$

where Q and M are the induced shear force and induced bending moment at time t , respectively; M_c = currently taken as the yielding moment capacity without strength-enhancement effect; Q_c = shear strength capacity including strength-enhancement effect adopting formulations by K&C (1973) and Priestley et al (1994), where the choice of shear strength capacity to be used

depend on the behavior as defined by Equation 1. When the proposed damage index exceeds one, failure is deemed to have occurred.

Furthermore, the base column of the 2-storey RC frame (Figure 1) was represented as a structural-level model. The based column was modeled with fixed boundary conditions at the top and bottom supports. Also, the base column was discretized as 19 finite, Timoshenko beam-column elements. The modal frequencies of the column ranged from the first modal frequency of 89 Hz to as high as 1.7 MHz for higher modes. The numerical analysis adopted for the response analysis of Phase 1, was elastic. Similar to the scaling of the EIGMs adopted by Pan et al (2004), a family of horizontal EIGMs was generated by scaling the simulated EIGM as shown in Figure 2. Here, the vertical ground motion of the EIGM was not considered.

3.0 DAMAGE ASSESSMENT USING SIMPLIFIED METHODOLOGY

The damage assessment results from the parametric study of using many scaled EIGMs are consolidated and presented in a similar manner as that of Figure 3. The damage assessment results from the proposed are compared to those obtained from the material-based model of the 2-storey RC frame.

The parametric study results for the damage assessment of the fixed-fixed column are shown in Figure 4. From Figure 4, the following observations can be made:

- The general trends presented in both damage assessment methods show that when the PPV of an EIGM is larger than 2 m/s, as the principal frequency is increased, there will be a transition from flexural failure to shear failure.
- However, a distinction is made between diagonal shear failure and direct shear failure when using the proposed damage assessment method.
- For EIGMs of a given PPV, a high principal frequency is required for direct shear failure as compared.
- It can be seen that the damage assessment using a fixed-fixed column can produce a similar map of failure modes for a multi-storey RC frame. The lower bound of failure modes, which represents the EIGMs that do not cause failure, is similar by both damage assessment methods. However, the proposed simplified method required less computational effort than that by Pan et al (2004).

It has been shown that the proposed simplified method produced similar failure maps of a 2-storey RC frame as compared to those produced by Pan et al (2004). Furthermore, the simplified method made a distinction between diagonal shear failure and flexural failure when subjected to certain EIGMs. Lastly, the proposed simplified method requires less computational effort than that the damage assessment method by Pan et al (2004).

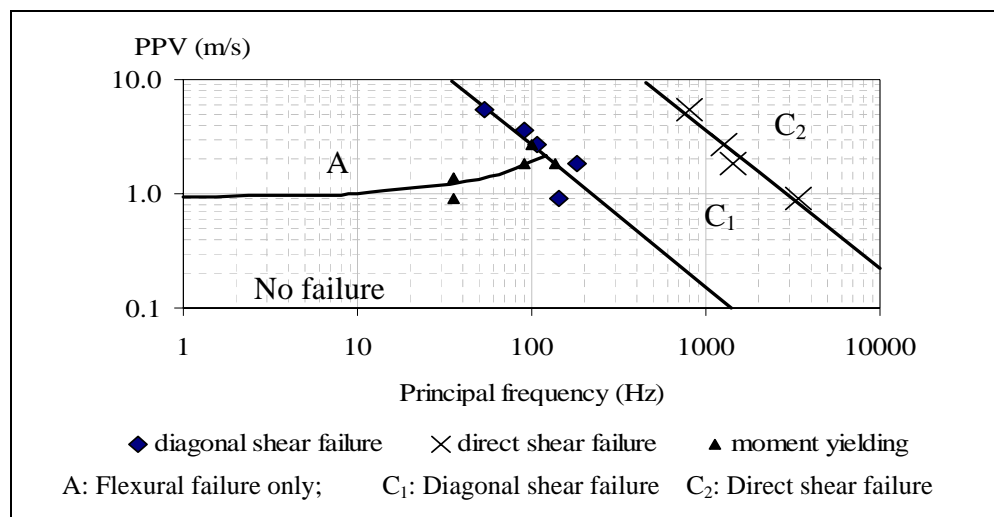


Figure 4: Failure modes determined by fixed-fixed column

4.0 CONCLUSION

A damage assessment for the shear force in Phase 1 was proposed for structures subjected to EIGM. This proposed damage assessment considered strength-enhancement due to strain rate effects. Also, the proposed method allows one to perform a toughness test of the structure during Phase 1.

A simplification was proposed for the damage assessment of RC frames when subjected to EIGMs. The simplification involves studying the damage on the base column where large forces are induced during Phase 1. This proposed simplification and the associated damage assessment of the base column were based on structural-level modeling of the base column, with fixed boundary conditions at the top and bottom. The damage results from the simplified structural-level model of a fixed-fixed column were similar with those obtained from a material-level model. The simplified method although with its gross assumptions, has its merits in that it provides an approximation of the damage, with less computational effort.

REFERENCE

- Lu, Y., Hao, H., Ma, G.W., and Zhou, Y.X., 2001. Simulation of structural response under high-frequency ground excitation, *Earthquake Engineering and Structural Dynamics*, Vol 30, 307-325.
- Pan T.-C., Dhakal R.P., and Lim C.L., 2004. Damage assessment of reinforced concrete building frames subjected to explosion induced ground motions, *Final Report*, PTRC-CSE/LEO/98.02, Protective Technology Research Centre, School of Civil and Environmental Engineering. Singapore: Nanyang Technological University.
- Wu C., Lu Y., and Hao H., 2002. Parametric calculations of underground explosion induced stress wave propagation and ground shock prediction, *Technical Report*, PTRC-CSE/DSTA/2000.02, Protective

- Technology Research Centre, School of Civil and Environmental Engineering, Singapore: Nanyang Technological University.
- Malvern, L.E., 1951. The propagation of longitudinal waves of plastic deformation in a bar of material exhibiting a strain-rate effect. *Journal of Applied Mechanics*, Transactions of ASME, Vol 18, 203–208.
- Comité Euro-International du Béton (CEB), 1993. *CEB-FIP Model Code 1990*, Redwood Books, Trowbridge, Wiltshire, UK.
- Malvar, L.J., 1998. Review of static and dynamic properties of steel reinforcing bars. *ACI Materials Journal* 95, 609-616.
- Karagozian, and Case (K&C), 1973. Construction Joint Test Program. *Final Report to Space and Missile Systems Organization*, Norton AFB, Contract F04701-72-C-0358, Glendale, CA.
- Priestley M.N.J., Verma R., and Xiao Y., 1994. Seismic shear strength of reinforced concrete columns. *Journal of Structural Engineering*, ASCE, Vol 120, 2310-2329.
- Li, Q.M., and Jones, N., 2000. Formation of a shear localization in structural elements under transverse dynamic loads. *International Journal of Solids and Structures*, Vol 37, 6683-6704.

EFFECTS OF EXTERIOR CLADDING PANELS ON RESPONSES OF MULTI-STOREY RC FRAME STRUCTURES TO DISTANT EXPLOSIONS

Haicheng Rong, Bing Li and Tso-Chien Pan
Protective Technology Research Centre, School of Civil and Environmental
Engineering, Nanyang Technological University, Singapore
cbli@ntu.edu.sg

ABSTRACT

Responses of multi-storey reinforced concrete frame structures with and without exterior cladding panels subjected to blast loadings from distant intense surface explosions are studied with the program ABAQUS. The finite element models involved are then verified by comparing the numerically results of a reinforced concrete beam and slab under blast loadings with available experimental data. Analytical results indicate that due to the variation of the blast forces received, the dynamic responses are much more severe for the frame structure with exterior cladding panels than the one without exterior wall panels under the same blast condition. The whole dynamic response process of the frame structure with exterior cladding panels can be approximately divided into two stages with the localized responses of the blast-loaded members critical in the initial stage and with the increase in time, the structural global response dominant at a later stage.

1. INTRODUCTION

The behaviour of civilian reinforced concrete structures under blast conditions has become of a major concern to structural engineers due to the recent surge in explosive events worldwide. After the trigger of a blast, a blast wave including a high-pressure shock front is formed which expands outward from the centre of detonation. As the blast wave strikes a building, the analysis of overpressure and drag force of the blast wave load on the structure, the interaction between which is extremely complicated. However, considering the relative distance of the detonation centre with the target structure as well as the size of the structure itself, two classes of blast wave-structure interaction can be generally identified as shown in Figure 1. The first one is the interaction of a blast wave produced by the detonation of a smaller charge loading a target structure at a short standoff distance, which is typical for most terrorist attacks such as car bombings. The second one is the interaction of a blast wave on a relatively distant structure as might be present due to an accidental severe surface explosion of petroleum refineries, chemical plants and ammunition storage areas, or nuclear devices of substantial yields.

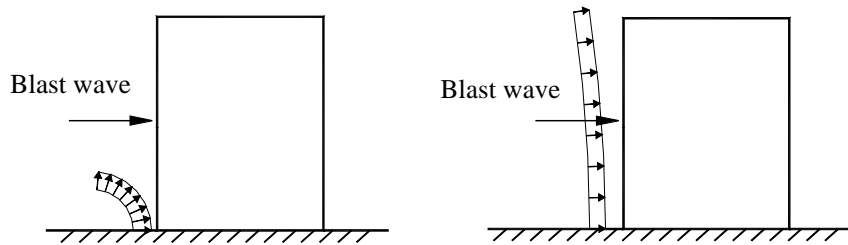


Figure 1 Two classes of blast wave-structure interaction

The profiles of blast loadings on the structure tend to be different within these two classes of blast wave-structure interaction. In the first class, the blast pressures are produced locally to individual structural members and the members are likely to be loaded sequentially. By comparison, in the second class of blast wave-structure interaction, the target structure is engulfed due to the diffraction of the blast wave and a normal squashing force will be applied to every exposed surface. Many explosion tests and numerical analyses have been carried out on the behaviours of structures in the first class of blast wave-structure interaction where the blast pressures are applied locally to individual structural members resulting in the possibility of an excessive local failure of several critical structural members and further the progressive collapse noticeable in a non-redundant structure. However little research has been devoted to behaviours of civilian structures and their possible failure mechanisms in the second class of blast wave-structure interaction and the available literature is also very limited. This paper aims to study the structural behaviours in the second class of blast wave-structure interaction especially for multi-storey reinforced concrete frame structures which are mostly common to the civilian buildings. The findings from this study are used to reach conclusions and recommendations in the blast resistant design concerning explosive safety for civilian reinforced concrete frame structures.

2. BLAST LOADINGS

Determination of the exact blast loadings of a distant explosion on the front, top and the sides, and the rear faces of the closed target is almost unrealistic considering the complicated process of the interaction of the blast wave with the concerned target. In order to reduce the complex problem of blast loadings to reasonable terms, a computational procedure is recommended in TM5-855-1 (1986) based on two assumptions that (a) the target is generally rectangular in shape, and (b) the object being loaded is in the region of the Mach reflection. These two assumptions are rational for the derivation of the blast loadings on rectangular targets in a relatively large standoff blast environment. The simplified loading configurations on various faces are shown in Figure 2 whose parameter can be calculated with the equations listed in TM5-855-1 for a closed rectangular aboveground target, i.e. a column, a beam, or a closed structure.

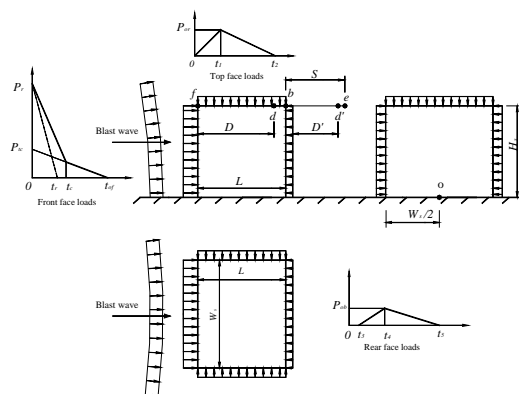


Figure 2 Blast loadings on a simply closed rectangular target

The computation of the blast loadings on a frame structure is relatively more complicated than that plotted in Figure 2 since the whole structure could not be arbitrarily taken as a closed rectangular target. The loading profiles applied to the frame structure are dependent on the out-of-plane strength and stiffness of exterior cladding panels due to the direct action of blast loadings on them, as well as their connection with the frame members of beams and columns. In this study, two extreme cases are considered that

- The exterior cladding panels are constructed with the material of reinforced concrete with significant strength and stiffness.
- there is no exterior cladding panels for the frame structure (bare frame structure);

In the case of frame structure with exterior cladding panels made of reinforced concrete, the cladding panels possess the significant out-of-plane strength, stiffness and strong connection with other frame members. As the blast wave hits the outer surfaces of the structure (outer surfaces of exterior cladding panels, exterior beams and columns), the blast wave can not go into the building and the blast loadings on the cladding panels would be transferred to the primary frames in terms of reaction forces. These transferred reaction forces together with the blast loadings acting directly on the outer surfaces of the exterior beams and columns will produce dynamic responses of the structure. Therefore, it is reasonable to treat the whole structure as a closed target, based on which the blast forces upon the front, roof and rear faces are computed.

As for the second case, the blast wave front would enter the building producing a high pressure on the rear faces of the columns. Figure 2 can not be directly used for computing the blast loadings on a bare frame structure since the whole structure can not be taken as a closed rectangular target. However, the shock wave front in the distant surface explosion condition is essentially parallel to the front faces of the blast-loaded columns. By taking each column as a closed rectangular target, the blast forces on the front and rear faces of the columns could be evaluated according to Figure 2 where the parameters (L , W_s and H_s) are equal to those of each column. The blast loadings on both side faces of each column are identical as well as on the top and bottom surfaces of each slab leading to a zero resultant force due to

the blast wave approximates to a planar wave, and therefore they are not taken into account in the analysis

In addition to blast overpressure effects, intense surface explosions produce ground shocks as results of the directly induced ground motion propagating through the soil or rock, which might affect structural responses. However considering the fact that the target to be studied is located at a large standoff distance relative to the source of explosion, the magnitude of the ground shock has been greatly diminished and the arrival time of the shocks to the structures is different from that of blast wave. Therefore the direct ground shocks are ignored in this analysis.

3. DESIGN OF THE TARGET FRAME STRUCTURE

To study the dynamic behaviours of frame structures under the distant blast conditions, a three-dimensional six-storey reinforced concrete frame structure is designed according to BS 8110. The loads involved in the design include the dead loads (5.0 kPa), the super imposed dead loads (1.0 kPa), the live loads (4.0 kPa), and the wind loads calculated in accordance with the BS 6399 code by taking the wind speed to be 30 m/sec. The layout of the structure and the reinforcement details of structural members are shown in Figure 3.

A blast wave produced by the detonations equivalent to a 50 ton TNT at the ground level with a standoff distance of 100 m is considered in the study. In these blast conditions where the standoff distance is significantly larger than the size of the target structure, the blast wave can be reasonably modeled with a planar wave as displayed in Figure 3. The wave engulfs the whole structure producing blast pressures on exposed surfaces of the structure uniformly distributed not only along the width of the structure but also along the height. Due to the symmetry of both the configuration of the target structure and the blast pressure distributions on it, a three-dimensional sub-frame including a planar frame and half of adjacent components is modelled to simulate the whole structural dynamic responses.

Two numerical examples are performed for the six-storey frame structure in order to incorporate the effects of exterior cladding panels on the structural blast responses. In the first example, the exterior cladding panels are assumed made of reinforced concrete with sufficiently out-of-plane strength and stiffness to prevent the blast waves from entering the building, therefore the modelling of the structural responses have to include the exterior cladding panels (whose reinforcement arrangements are found in Figure 3c), together with the floor slabs, beams and columns. In the second example, the structure is built without exterior cladding panels. As discussed previously, the frame structure in such a situation can be assumed to be a bare frame against the blast loadings, accordingly only the beams, columns and floor slabs are modelled for the numerical simulations.

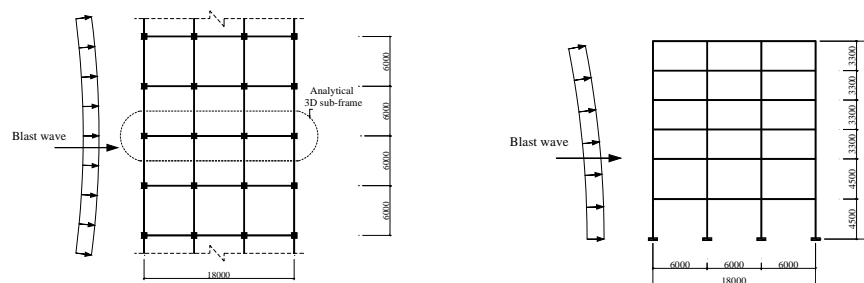


Figure 3 Details of the target six-storey frame structure

4. FINITE ELEMENT MODELS

The three-dimensional six-storey sub-frame structures are modelled to perform the numerical simulations of the structural dynamic responses under the concerned blast conditions by utilizing the program ABAQUS (2004). The finite element models consist of the structural modelling, material modelling of concrete and reinforcement, the analysis steps and loads, and the integration methods.

4.1 Structural modelling

Two types of structural members are included in the sub-frames, namely the frame members composed of beams and columns, and the planar members including exterior cladding panels and floor slabs. In order to obtain more accurate simulations of the structural responses in blast conditions, three-dimensional continuum solid elements should be employed in modelling these structural members. However it involves considerably greater computational efforts due to the complicated nonlinear behaviours of the concrete and reinforcement as well as the extremely large size of the finite element model. For simplicity, Timoshenko beam elements for modelling frame beams and columns, together with shell elements for exterior cladding panels and floor slabs are adopted. Reinforcement in the concrete modelled by means of rebars, which are one-dimensional strain theory elements (rods) defined singly or embedded in oriented surfaces. Each rebar is placed at its corresponding location for the beam elements while the layers of rebar are defined for the shell elements with the needed data-input of rebar's area, location, and the space length.

4.2 Material modelling

The dynamic responses of reinforced concrete structures under blast conditions are dependent on the material properties of the concrete and reinforcement. To obtain valid numerical simulations of the dynamic responses of the structures, the accurate modelling of the material properties becomes essential. In the finite element analysis, the material behaviours of the concrete, reinforcing bars and the bondages between them should be taken into account. It is presumed that the bars are perfectly bonded with concrete. Although it will impose some errors, it is the only practical solution for the numerical simulations of the responses of reinforced concrete structural systems, considering the unmanageable size of the computational work and the lack of reliable data on this topic in blast environments. The stiffness used in the analysis for unloaded

concrete in tension and compression is also given in Figure 4. When the cracked concrete is unloaded, the secant unloading modulus is utilized as stiffness so that the strain across the crack is reduced linearly to zero as the stress approaches zero. If the load is removed at some point after inelastic straining has occurred for the concrete in compression, the unloading response is softer than the initial elastic response, but this effect is ignored in this model. Thus initial elastic stiffness is used when the concrete in compression is unloaded.

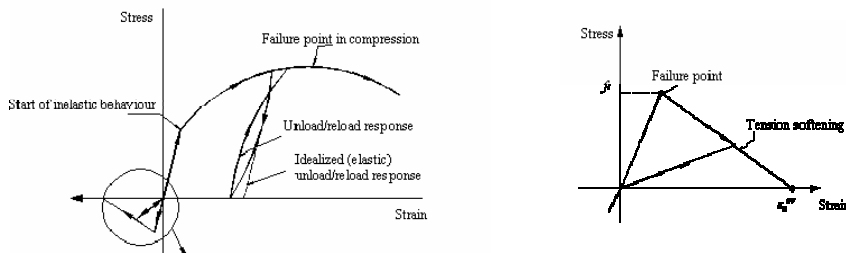


Figure 4 Concrete modelling

The von-Mises yield criterion is used to describe the constitutive behaviour of the reinforcement. The stress-strain relationship of reinforcement is modelled with an elasto-plastic curve. The strain hardening of reinforcement is not considered in this analysis since it is hard to define under the blast conditions in the case of lacking enough experimental data. The ultimate strain value is often not reported in current literatures due to the difficulty of determining exactly when the peak stress occurs as well as the confusion between ultimate strain and rupture strain. In order to consider the fact that under higher loading rates both concrete and reinforcement exhibit increased strengths, a dynamic increase factor (DIF), the ratio of the dynamic to static strength, is employed in this analysis. The expressions by Malvar and Crawford (1998) are utilized which are derived from a literature review of the extensive test data about the effects of strain rate on the strength of concrete and reinforcement. To integrate the DIF expressions into the analysis, the user subroutine USDFLD is used which allows the user to define the field variable at a material point as a function of any of available material point quantities. Thus by taking the strain rate as a field variable, the strain rate-dependent material properties can be introduced in the analysis.

4.3 Application of loads and analysis procedure

In the simulation of the structural blast responses, two steps of analyses are carried out according to different loading stages. Before the occurrence of an explosion, the service loads have been already imposed on the structure. The intensity and distribution of the stresses and strains induced by the service loads will influence the structural behaviours under blast conditions. Thus nonlinear static analysis is performed priorly for the three-dimensional sub-frame structure under service loads. The loads involved in this step include the live loads, the dead loads and the super imposed dead loads. The second step is the dynamic response simulation of frame structures loaded by blast pressures where the nonlinear dynamic analysis is performed. The functions of blast

pressures on the structures which are necessary in this step are discussed for the bare frame structure and the frame with exterior cladding panels, respectively, as follows.

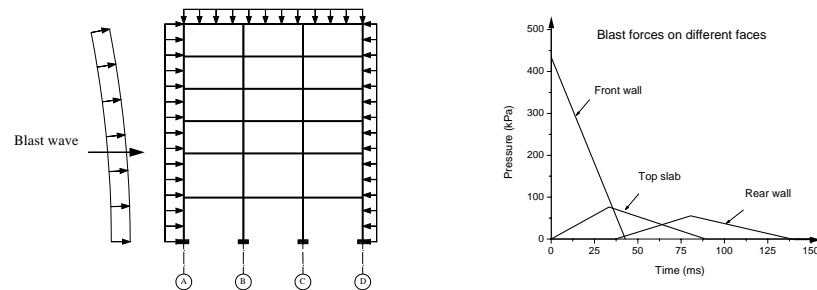


Figure 5 Blast loadings on the frame structure with exterior cladding panels

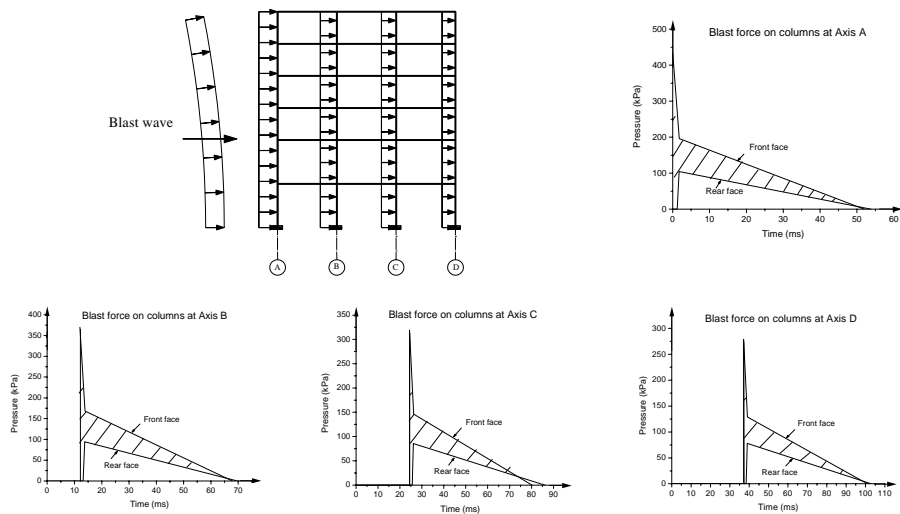


Figure 6 Blast loadings on the bare frame structure

For the frame structure with reinforced concrete exterior cladding panels, by taking the whole structure as a closed rectangular target, the blast force functions on the front, top and rear surfaces are evaluated as demonstrated in Figure 5. In this case, while the reflected pressure dominates in the blast loadings on the front cladding panels, the blast pressures composed of the incident overpressure and dynamic pressure dominate on the top and rear surface. As for as the bare frame structure, the planar wave enters the structure loading each exposed columns, thus by taking each column as a closed rectangular target, the functions of blast forces on its front and rear faces are obtained and the results under the blast condition mentioned above are shown in Figure 6 where the shadow area stands for the net blast pressure on each column.

5. VERIFICATION OF FINITE ELEMENT MODELS

The verification of the finite element models as mentioned above is carried out by implementing it into the analysis of a simply supported beam subjected

to blast loadings tested by Seabold (1967) and a square slab, clamped and longitudinally restrained along all edges exposed to uniform lateral pressure tested by Keennan (1969). The computed and experimental results for the beam and the slab are compared in Figure 7. It can be seen that the analytical results agree well with the experimental response. Therefore the numerical model has the ability to simulate the failure process of concrete and reinforcement, which are thus integrated into the nonlinear analysis of the blast-loaded six-storey frame structure.

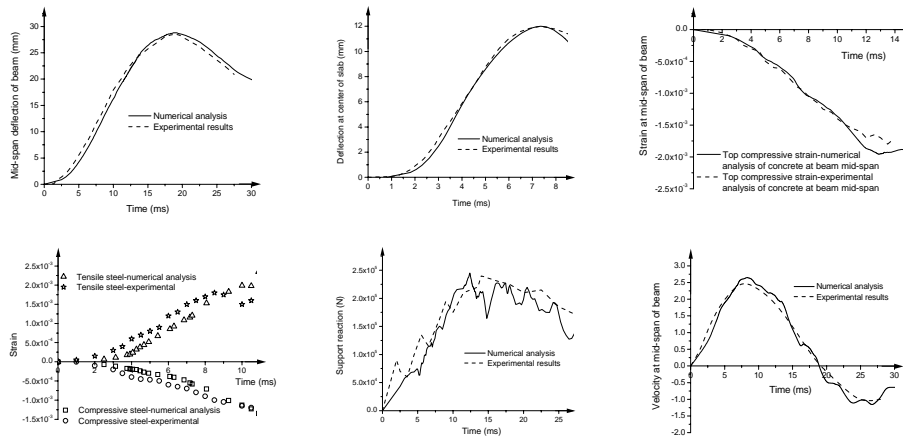


Figure 7 Comparison of experimental data with analytical results

6. NUMERICAL EXAMPLES

6.1 Example I— Frame structure with exterior cladding panels

A more detailed description of the structure responses and its damage propagation with time are shown in Figure 8. A flexural plastic hinge is assumed to initiate when the longitudinal tensile reinforcement first yields at a point along the beam element and the hinge will continue to spread over a continuous portion of the beam. Thus the occurrence time of the hinge corresponds with the first appearance of plastic strain of reinforcement whose variation with time can be found from the numerical analysis in ABAQUS (2004). It is obvious that the structural responses can be divided into two responses stages. The difference between the time of forming this damage mechanism on the front columns and top-storey beams is caused by the difference of the time when the peak blast pressures acting on them is reached. As for the other frame members, almost no plastic deformation is present.

At a later stage, the structural dynamic response is in a mode where the global response of the structural system as a whole dominates; hence the distribution of damage as well as its propagation with time is in a different manner with those at the initial stage. As shown in Figure 8, plastic hinges are formed firstly on both end sections of the first-storey columns at a time

of about 60 ms as the inter-storey drift within this storey increases. Later, damage spreads upward with more plastic hinges successively formed on those connected cross sections around the joints located in the first and second floor levels. Since the plastic hinges formed at this stage are caused by large global sideways responses, they appear only at the end sections of structural members.

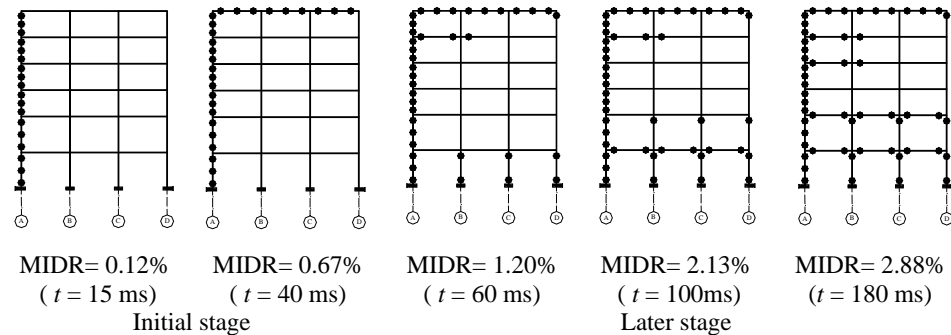


Figure 8 Plastic hinge propagation with time (Example I)

6.2 Example II — Bare frame structure

The numerical simulation results of the energy responses for the six-storey bare frame structure under the concerned blast condition are presented in Figure 10. It can be seen that due to the absence of the exterior cladding panels, this bare frame will experience a much slighter dynamic responses when compared with the first case study. Therefore much less damage is induced as shown in Figure 9 where only a small magnitude of 1.0 kNm of plastic energy appears on the floor slabs. As for the frame members (columns and beams) there is no plastic deformation on them.

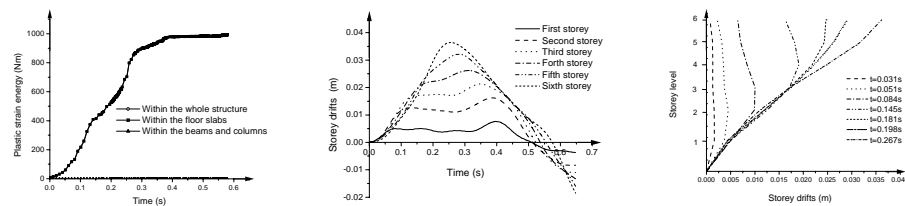


Figure 9 Responses of bare frame structure (Example II)

The responses of structural storey drift demonstrate that the maximum inter-storey drift, which happens to the second-storey level, is only about 9.5 mm equivalent to a MIDR of 0.21%. The MIDRs within other storey levels are smaller than this value and thus there is no global damage to the structure under this blast condition. In addition, from the storey drift contours at different time stations shown in Figure 9, it is obvious that the maximum storey drift occurs firstly at the first storey whereas with the lengthening of time it will move upwardly to the second storey and third storey until it is present on the top storey in sequence. Thus a transverse wave is formed in the frame structure.

7. SUMMARIES

Based on the analytical results, the following conclusions can be drawn regarding dynamic responses and damage distributions of a six-storey reinforced concrete frame structure with or without exterior cladding panels under distant blast conditions:

1. The responses of the frame structure with reinforced concrete exterior wall panels can be approximately divided into two stages; localized responses of the blast-loaded members are critical in the initial response stage while the global responses of the structural system dominate at a later stage. In addition, the flexural responses play a more important role in the plastic deformation of frame beams and columns in comparison to their respective shear responses.
2. In the identical blast situation, the existence of reinforced concrete exterior cladding panels produces more severe dynamic responses than those of the bare frame structure. Due to the diffraction of the blast waves around the columns, reflected pressure will quickly reduce to zero for the bare frame structure and only the drag forces associated with the dynamic pressure are critical in the net blast loadings on the structure. However the exterior cladding panels cause the structure to be loaded with reflected blast pressure, overpressure, and dynamic pressure, thus the blast forces received by the frame structure with cladding panels are much greater. To dissipate the work produced by such a large blast force, some plastic deformation would appear to the structure producing damage to some extent as expected in the numerical studies.

REFERENCES

- TM 5-855-1.,1999 *Fundamental of protective design for conventional weapons*. United States Department of the Army, Washington D. C.
- ABAQUS. 2004 ABAQUS/Standard user's manual. HKS, Inc.
- Malvar L.J. and Crawford J.E. 1998 *Dynamic increase factors for concrete*. Twenty-Eighth DDESB Seminar, Orlando, FL. 1998.
- Malvar L.J. and Crawford J.E.,1998 *Dynamic increase factors for steel reinforcing bar*. Twenty-Eighth DDESB Seminar, Orlando, FL.
- Seabold R. H., 1967 *Dynamic shear strength of reinforced concrete beams*, part II. Naval Civil Engineering Laboratory, Port Hueneme, California.
- Keenan, W. A.,1969 *Strength and behaviour of restrained reinforced concrete slabs under static and dynamic loadings*, Technical Report R-621, Y-F008-08-02-123, DASA-RSS3318, Naval Civil Engineering Laboratory, California.

EARTHQUAKE RESISTANT CONSTRUCTION IN THE URBAN AREAS OF ANDHRA PRADESH (INDIA): PRESENT PRACTICES AND IMMEDIATE REQUIREMENTS

SHYAM SUNDER REDDY T.¹ AND RAMANCHARLA PRADEEP KUMAR²

1. Ph.D. Student, Computer Aided Structural Engineering, International Institute of Information Technology Hyderabad, Hyderabad – 500 019, India.
2. Assistant. Professor, Earthquake Engineering Research Centre, International Institute of Information Technology Hyderabad, Hyderabad – 500 019, INDIA
e-mail: ramancharla@iiit.ac.in

ABSTRACT

According to seismic Zone map of India given in IS 1893-2002 (Criteria for earthquake resistant design of structure), 34% of Andhra Pradesh (AP) falls in zone III which is having the possibility of earthquakes up to intensity VII (MSK) or more. Active zones in the state are the Eastern Ghat belt and Godavari Valley. Recorded seismic history of AP shows that the state has experienced earthquake of magnitude up to 5.7 on the Richter scale i.e., Vizianagaram (M5.5 1917, Ongole (M5.4, 1967) and Badrachalam (M5.7 1969). Though not much of damage occurred due to these events, the earthquake in Killari (M6.3 1993) brought to the forefront the possibility of high risk to urban areas of AP, where building construction activity is growing at phenomenal rate. And also according to IS 1893-2002 the state is in the proximity of zone III areas of Maharashtra, Orissa, Tamilnadu and Karnataka apart from being near to Andaman & Nicobar Islands which fall in zone V.

Major urban centers of the state with mushrooming apartments and commercial complexes are Hyderabad (Zone II) with population over 6.0 million, Visakapatnam (zone II) with population of over 2.0 million and Vijayawada (zone III) with population over 1.8 million. Other important towns which fall in zone III are Tirupati, Nellore and Cuddapah. As there is great demand for parking in urban areas, existing building bylaws allow stilt and upper floors to be used as parking. Also the existing practice is extension of building all around on cantilevers beyond the column line, supporting upper floors on floating columns. Such practices lead to serious consequences in the event earthquake. However the existing rules do not have any methodology to check the plan and structural design/detailing while approving building permission. Authors study the existing construction practices in major cities of AP considering seismic hazard levels and suggest necessary changes in building bylaws, planning regulations, structural design/detailing and construction practices.

1. EARTHQUAKE SCENARIO OF URBAN AREAS IN ANDHRA PRADESH

1.1 Earthquake concerns of the state

Andhra Pradesh, one of the major states of INDIA is located in central part of Peninsular Indian Shield. Though Peninsular Region considered to be stable has been experiencing major damaging Earthquakes for the last few decades. As the Indian plate hitting against the mass of the Eurasian plate, which is situated in the north, inter plate movement occurring in weak planes along existing faults in peninsular region lead to earthquakes. The recent Lathur Earthquake of 1993 and Jabalpur earthquake of 1997 have proven that the faults in peninsular region are active and causing earthquakes.

The other major concern for Andhra Pradesh is its long coast line along Indian Ocean (Bay of Bengal) which has very active faults. The recent Tsunami which hit south Indian coastal areas and southeast Asia caused due to earthquake of magnitude 8.9 in Indonesia (26 December 2004) and the following earthquake in Andaman and Nicobar Islands brings out the interface activity of Indian plate and Burma plate.

1.2 Active Faults in AP

The main tectonically active zones in the state are Eastern Ghat belt and Godavary river valley. The Gundlakamma Fault which extends in a NW-SE direction front near Ongole on the coast running inland for about 100km and kaddam Fault which runs in parts on northern Andhra Pradesh are known active faults. Several minor faults zones also exist near Hyderabad, Chitoor, Venukonda, Vizianagaram and Vishakapatnam. However it must be noted that proximity to fault does not imply higher hazard. Factors such as subsurface geology and the construction practices define the level of hazard.

1.3 Significant Earthquakes

Vizianagaram earthquake of 1917 (M 5.5), Ongole earthquake of 1967 (M 5.4) connected with Eastern Ghat and Badrachalam earthquake of 13 April 1969 (M 5.7 and Intensity VII) connected to Godavary valley are the significant earthquakes recorded. Most of the other recorded earthquakes in the state are of small category. Ongole town with population of 1.5 lakh has 14 number of recorded earthquakes in the last 200 years out of which 12 is recorded between 1950 to 2000 period. The largest recorded magnitude was M5.4 in 1967.

1.4 Growing Urban Centres and recorded earthquakes.

As per the 2001 census the AP state has a population of 75.73 million in which 27.08% are living in urban areas. There are total of 210 towns in which 98 towns are having population of more than 50,000 and half of them have a population of one lakh and above. The major fast

growing urban agglomeration areas in the state are covered under Urban Development Authorities jurisdiction. Each of the Urban Development Authorities has Municipalities and Grampanchayats within. Table 1 lists Urban Development Authorities in the state

Table 1: Urban Development Authorities in the state

Sl. No	Authority	Area (km ²)	Population (million)	Seismic zone
1	Hyderabad Urban Development Authority (HUDA)	1864	6.5	II
2	Vijayawada Guntur Mangalagir and Tenali Urban Development Authority(VGTMUDA)	1550	1.8	III
3	Vishkapatnam Urban Development Authority(VUDA)	1721	2.1	II
4	Thirupati Urban Development Authority(TUDA)	848	0.75	III
5	Kakatiya Urban Development Authority(KUDA)	663	0.6	II

All the Above Development Authority Areas are developing very fast and as the land prices are constantly increasing, people are opting more for apartments. Due to high demand of parking areas in residential and commercial areas, multilevel parking floors area proposed above ground level which acts like soft floors. This trend is more in HUDA area followed by VUDA, VGTM and TUDA. Apart from the above urban areas, many other towns in AP are adopting soft floor multi storied structures.

Many of the towns in the state have number of recorded earthquakes in the last 200 years (records available from 1800 onwards). However the major urban centers having more than 2 earthquake incidents in the last 200 years are Hyderabad, Visakapatnam, Guntur, Nellore, Vizianagaram, Ongole, Kothagudam, Badrachalam and Venukonda.

1.5 Seismic Hazard Zones

As per IS 1893-2002, India is divided into four seismic zones i.e., zone II to zone V (see figure 1). The state of Andhra Pradesh lies in seismic zones II and III. Major towns/districts in zone III are Vijayawada, Guntur, Nellore, Warngal, Rajamundry, Chitoor, Badrachalam, Ongole Cudappah, Kakinada, and Khammam (see figure 2). It may be seen from the map that many urban areas are falling in zone III. Almost 11 districts of the state are partially or fully in zone III. Districts that lie in the Godavari and Krishna river valleys, including the Godavari-Krishna delta region lie in Zone II. The city of Hyderabad lies in Zone II. Figure 3 shows the earthquake occurrences in the state of AP. From the figure, it can be seen that the seismicity of Ongole region is high compared to other areas.

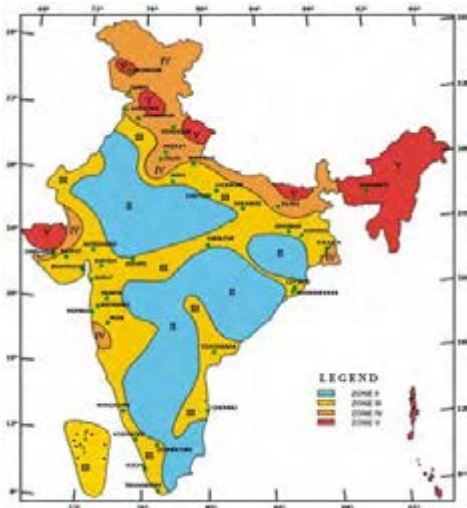


Figure 1: Seismic zone map of India



Figure 2: Zone map of AP



Figure 3: Seismicity of Andhra Pradesh

2: PRESENT CONSTRUCTION SCENARIO IN ANDHRA PRADESH

2.1 Apartment Buildings all around

Apartments and commercial complexes of more than 3 floors have become a common place in all big and small towns in the state. Due to convenience of use and driving advantage, the parking floor is build as stilt floor at ground level without any walls. The concept of apartment complexes was initially started in 1980 in Hyderabad as an affordable alternative solution by Andhra Pradesh Housing Board (APHB). Due to high demand for such housing units called flats, private builders started building the complexes and by 1990, the city of Hyderabad has changed its skyline with apartment buildings everywhere. Slowly the other cities Vishakhapatnam, Vijayawada and Tirupathi followed. The culture of apartments has spread to other cities like Kakinada, Guntur, Khammum,

Tanuku, Miryalaguda, Warangal etc. Today in 2005 one can find Apartment complexes of 3 to five floors in all district centers and in many small towns.

Ten acres and above apartment Towns can be seen in and around Hyderabad with individual blocks of ten floors and above having two or more parking floors above ground. As land prices are continuously raising, apartment complexes of twenty floors and above are being planned and AP State Govt has already proposed new building rules to accommodate such buildings.

2.2 Need for stilt parking floors (soft floor)

All the apartment complexes built initially by APHB had no covered parking provision. However, the entire scene of construction changed and parking floor became an essential need. As people started liking parking at ground level, stilt parking became a standard and government changed its building rules. Figure 4 and 5 shows typical open ground storey buildings in Hyderabad and Vijayawada. As per the existing building rules, for complexes proposed in less than 1000 m² only stilt floor is allowed. No brick walls are allowed in parking floors. Stilt floors act as soft floors causing heavy damages during earthquake (see figure 6) unless they are designed with utmost care.



Figure 4: Parking floors



Figure 5: Open ground storey

2.3 Cantilever Projections and floating columns

To maximize built up area while keeping set backs intact, the most ingenious method adopted by the builder is to project the building on cantilever up to 2.5 to 3 m from first floor. Most of the times, the projected area is covered into rooms and floating columns are raised from first floor. Cantilevers and floating columns would create an adverse stress in the structure and lead to collapse.

Figures 7 shows typical cantilever projections adopted in a building constructed recently. Figure 8 shows the floating columns being constructed in a structure.



Figure 6: Collapse of open ground storey structure during Bhuj Earthquake



Figure 7: Cantilever beams of 2.5 m



Figure 8: Floating columns raised from first floor on both sides

2.4 Code provisions and practices in construction detailing:

Indian Standard codes published by Bureau of Indian standards are very comprehensive and they are being revised regularly. The most important codes governing RC structure design and ductile detailing for the structural safety and durability of buildings are the following.

- a) IS 456:2000 Code of Practice for Plain and Reinforced Concrete.
- b) IS 1893 (Part 1):2002 Criteria for Earthquake Design of Structures, general provisions and Buildings.
- c) IS 13920:1993 Ductile Detailing of Reinforced Concrete Structures Subjected to Seismic forces- Code of Practice.
- d) IS 4326: 1993 Earthquake Resistant Design and Construction of Buildings – Code of Practice
- e) SP- 34: 1987 Handbook on Concrete Reinforcement and Detailing, BIS

Apart from the above there are number of other important IS Codes for structural safety, such as Pile Foundations, Retaining Walls, Steel Structures, Loading, , Material Testing, Fire safety etc.

The most important ductile detailing and other reinforcement provisions in the codes are hardly enforced in the present construction practices in the state. The following are the important wrong Practices which need immediate attention by all concerned in the industry.

- **Development Length which is most important for reinforcement to attain its strength is the most neglected in execution.** Top and Bottom reinforcement at ends in beams are hardly provided with the required development length.
- **Proper Placement of Steel is most important for strength and durability which is hardly taken care on sites.** Steel cover in slab for cranked top steel is never maintained properly and most of the times it is moved down below neutral axis while concreting.
- **Transfers Reinforcement in Columns, Special Confining stirrups (in Columns, Joints and Foundations), Spacing of Hoops in Beams and hook bends in stirrups are grossly neglected**
- **Verticality of the Column in each floor and from floor to floor is invariably not maintained.**
- **Concrete Preparation, Column Marking in each floor, Curing and Shuttering are other important Contraction activities where known errors are always continued.**
- **Important Detailing Provisions of the Codes IS 1392:1993, SP 34 (S&T):1987 which are neglected are illustrated in images 3.1 to 3.7.**

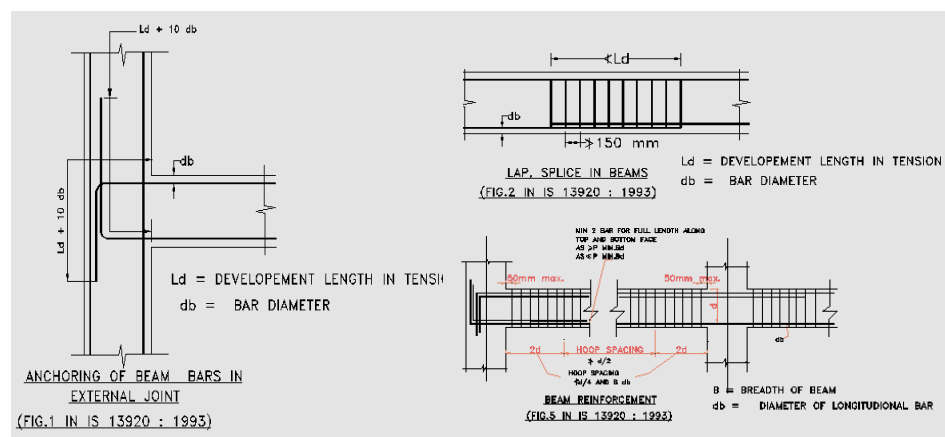


Figure 9: Detailing provisions in IS 13920

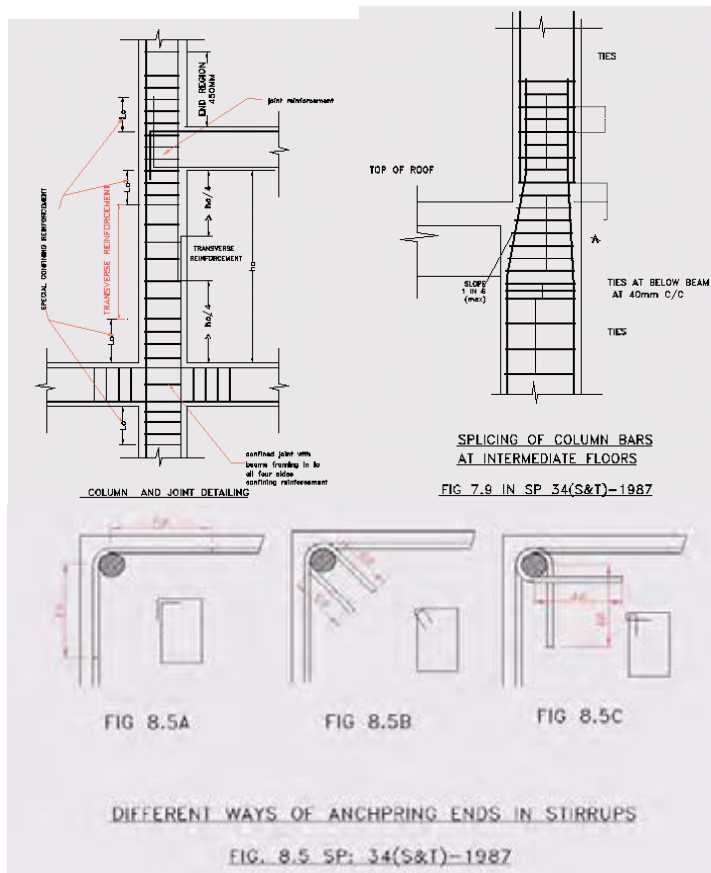


Figure 10: Detailing provision of column in IS 13920

3. BUILDING RULES AND URBAN PLANNING ISSUES

3.1 Building Control Rules

Municipal Administration and Urban Development (MAUD) department of the state government brings out Govt. Go's concerned with municipalities and all towns. The present building rules are governed by the following important G.Os.

- a) G.O. Ms. No 423 and M.A. dated: 31st July 1998: This G.O specifies permissible F.A.R (Floor Area Ratio) and set back rules for various land uses and road widths. It also specifies other building requirements such as parking, common areas, permissible balcony projections and other special regulations.
- b) G.O.Ms.No.483, M.A. dated 29th august 1998: This G.O specifies certain relaxations to building and zoning regulations it also gives extra F.A.R for road widening cases.

- c) G.O.Ms.No 528, M.A dated 25th September 1998: This G.O specifies land development/layout regulations.
- d) G.O.Ms.No 541, M.A dated 17th November 2000: This G.O specifies procedure for obtaining permission and fixes construction responsibilities.

3.2 Government and Public Concern for the Rules.

Apart from the above G.Os, there are number of other relevant G.Os, acts and policies that govern building industry in the state. Urban Land Ceiling Act, Tourism policy, Industrial policy, land acquisition act, Regularization act, special G.Os. And also court judgments do control the building process.

In all the above G.Os an attempt is made to regulate building constructions with reference to architectural and planning issues. However, there are no special regulations for safety of the buildings against earthquakes. Neither the master plan nor the zonal development plan of any city/region in the state has any proposals to safeguard buildings against earthquakes. It would be of great help if land use and planning proposals incorporate the regional seismic demands and safeguards.

As the profit is the prime *motto* of a builder, he finds a number of ingenious methods to circumvent the rules. As he employs the professionals whose prime concern is to serve the client, they also some time become instrumental in building for the worst.

However after the Bhuj Earthquake of 2001, there is a positive change among all to improve the safety of the buildings. AP state Govt Revenue and Relief Department has prepared a manual of "Earthquake Contingency Plan" in 2002 which attempts to identify the vulnerable urban and regional areas of different districts and proposes an auction plan for earthquake preparedness and immediate rescue/relief measures. Though the attempt is very much appreciable, no concrete steps are proposed in terms of building construction regulations.

Government of India, Ministry of Home Affairs through its National Disaster Management Division has constituted an expert committee which prepared a report in September 2004 proposing Model Building Bye - Laws, amendments to Town and Country Planning Act and Zoning Regulations for hazard safety. The Recommendations of the committee are widely circulated to all concerned state and central government departments and other professional institutions for discussions and opinions. The attempt by Central Government is very much appreciated and the recommendations proposed are more of legislative in nature.

4. CONCLUSIONS

During discussions with state Govt. officers in municipality and other planning departments it is found that they are equally concerned with the earthquake safety but they are not well equipped with the knowledge and the required technical, political and administrative support is lacking. Apart from the officers, Builders, Architects, Engineers and Town Planners have to acquire the subject knowledge of earthquake forces and methodology to build earthquake resistant buildings. Without the active support of all people involved with construction, no Govt. rules can be successfully implemented. Hence Awareness among all sections of the society should be cultivated to mitigate earthquake risk.

As there are well defined building Bylaws for architectural and planning controls, there should be well defined regulatory controls for Building Construction. Though IS codes are very comprehensive, a mechanism is required for strict practicing of the same by all sections. While Preparing Master plan and Zonal Development Plan for any urban area, comprehensive hazard mitigation plan and its effective implementation methodology should be given due importance.

Government should bring out rules so as to encourage basement and cellar (below ground) parking floors. In case parking is provided at stilt floor, it should have sufficient lateral rigidity and the same should be ensured by providing RC/brick walls. The existing structures in all urban areas should be examined and strengthening measures should be taken up wherever required.

REFERENCES

- P.R.Reddy and G K.Chandrakala, 2004, *Sesmicity in around Ongole, Andhra Pradesh- an appraisal. J. Ind. Geophysics. Union (April 2004) vol 8 No2 143-146.*
- Chndra, U., 1977, *Earthquakes of Peninsular India _ A Seismotectonic study, Bulletin of the Seismological Society of America, Vol67 No5 1387-1413.*
- IS 1893 (Part 1): 2002 *Indian Standard Criteria for Earthquake Resistant Design of Structures Part 1 General Provisions and Buildings (Fifth Revision).*
- IS 13920:1993 *Ductile Detailing of Reinforced Concrete Structures Subjected to Seismic forces- Code of Practice.*
- SP- 34: 1987 *Handbook on Concrete Reinforcement and Detailing, BIS*

DYNAMIC RESPONSE OF STEEL BAR IN RC UNDER BLAST LOAD

HUAN SHI¹, JIANG GUOPING¹,

TAN XIANGQIAN¹, LIU ZHIHANG¹, HUANG FENGLI²

1 Earthquake Engineering Research Center, Guangzhou University, China.

E-mail: huanshi@gzhu.edu.cn

2 National Key Laboratory of Explosion Science, Beijing Institute of
Technology, China.

Abstract

For evaluation and designing the blast resistant capability of important buildings, there is need to make investigation for dynamic response of steel bar in reinforced concrete (RC) under blast shock wave load. In this paper, the dynamic response of several reinforcing steel bar in RC, excited by some given shock wave, is theoretically analyzed and numerically simulated to investigate its movement and the damage evolution processes. It has been found in the research that: When loaded by a longitudinal shock wave, the steel bar can be brought a longitudinal relative movement in RC, and a crash zone formed around the steel bar at the same time; When loaded by a transverse shock wave, some local breaks are formed between the steel bar and concrete; The thickness and the longitudinal length of the damage zone above-mentioned are determined by the strength and the acting time of shock wave respectively.

1. INTRODUCTION

Blast is a calamity phenomena which has terribly strong destruction. It can be classified into physical, chemical and nuclear blast. In view of blast befallen frequently in nature, industry and our daily life, and which is a main attack way for the war and terrorism, the probability for the important building attacked by a blast is bigger than which fall across an intensity earthquake. The effect of blast shock wave on buildings is different from seismic in mechanics. Blast shock wave is provided with high peak pressure, short acting time, great strain rate and rapid transmit velocity. Concrete is widely used in civil buildings and ground or underground works. Recently, the constitutive relationship of reinforced concrete (RC) has been widely researched by many scientists, such as, Johnson-Cook's model for the fracture damage of RC^[1], Ottosen's model engaged to describe the shock loading process of RC^[2], Chen's continuum damage model for dynamic characteristics of RC^[3], The modified continuum damage model^[4] and the beam-particle model in two dimension^[5] is used to research the failure process of a steel bar perforating into a RC panel.

For evaluation and designing the blast resistant capability of important buildings, there is need to make investigation for dynamic response of steel bar in reinforced concrete (RC) under blast shock wave load. In this paper, the dynamic response of several reinforcing steel bar in RC, excited by some given shock wave, is theoretically analyzed and numerically simulated to investigate its movement and the damage evolution processes.

2. THEORY ANALYSIS

One-dimensional (1-D) shock wave theory is used to analyze the type model (see Fig.1 and Fig.2). When steel flyer with certain thickness impacts targets at high velocity, a 1-D plane shock wave travels along target and steel flyer respectively, the following formulas are satisfied:

$$P_f = \rho_{of} (-D_f - W)(U_f - W) \quad (1)$$

$$P_t = \rho_{ot} D_t U_t \quad (2)$$

Where P is pressure, ρ_o is initial density, D is shock wave velocity, W is steel flyer velocity, U is particle velocity, subscript f is for steel flyer and t for target. The shock compressional relations are

$$D_f = C_{of} + \lambda_f U_f \quad (3)$$

$$D_t = C_{ot} + \lambda_t U_t \quad (4)$$

The boundary condition is $P_f = P_t$ and $U_f = U_t = U$.

From above equations we obtain

$$U = [B + (B^2 + 4AC)^{1/2}] / 2A \quad (5)$$

Where $A = a\lambda_t + \lambda_f$, $B = (\lambda_f - 1)W - aC_{ot} - C_{of}$, $C = C_{of}W + W^2$, $a = \rho_{ot} / \rho_{of}$. Material parameters are^[6]

$$\rho_{of} = 7.85(10^3 \text{kg/m}^3), C_{of} = 3.574(10^3 \text{m/s}), \lambda_f = 1.920;$$

$$\rho_{ot} = 2.60(10^3 \text{kg/m}^3), C_{ot} = 3.50(10^3 \text{m/s}), \lambda_t = 1.43.$$

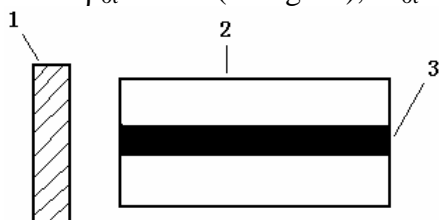


Fig.1: Longitudinal impact

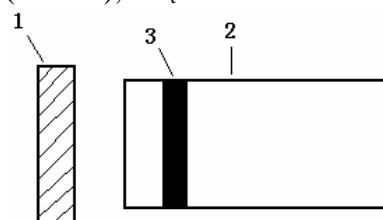


Fig.2: Transverse impact

1. steel flyer, 2. concrete, 3. steel bar

The pressure and velocity of concrete and steel bar for longitudinal impact are listed in Table 1, where subscript s is for steel bar and c is for concrete, $P = P_s - P_c$, $U = U_c - U_s$. On account of transition area between the steel bar and concrete, the actual differential pressure P_a is less than the theoretical one P. When P_a less than the static friction resistance, there is no relative motion occurred(see in Table 1,*). The critical pressure against static friction resistance P_{cr} is about 0.55 GPa^[7].

Table 1: Pressure and velocity of concrete and steel bar for longitudinal impact.

$W(10^3\text{m/s})$	0.05	0.10	0.20	0.30	0.40	0.60	0.80	1.00
$P_s(\text{GPa})$	0.711	1.44	2.96	4.55	6.21	9.77	13.6	17.8
$P_c(\text{GPa})$	0.351	0.713	1.49	2.30	3.19	5.11	7.26	9.66
$P(\text{GPa})$	0.360	0.727	1.47	2.25	3.02	4.66	6.34	8.14
$U_s(10^3\text{m/s})$	0.025	0.05	0.10	0.15	0.20	0.30	0.40	0.50
$U_c(10^3\text{m/s})$	0.038	0.076	0.154	0.231	0.311	0.471	0.634	0.800
$U(10^3\text{m/s})$	*	0.026	0.054	0.081	0.111	0.171	0.234	0.300

For transverse impact, during shock wave transmission(see Fig.2), steel bar and concrete move equidirectionally, after the shock wave removed, the restoring displacement of steel bar is more than the concrete, so a void band between the steel bar and concrete is formed (seen in Fig.3).

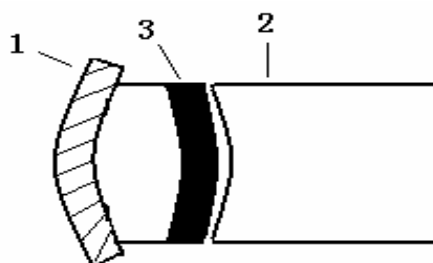


Fig.3: Void band between steel and concrete

3. NUMERICAL ANALYSIS

Dynamic finite element code ANSYS 970/LS-DYNA is used to make numerical analysis for the above mentioned problem. Holmquist's constitutive model ^[2] is used for concrete subjected to large strains, high strain rates and high pressure. The equivalent strength is expressed as a function of the pressure, strain rate, and damage. The pressure is expressed as a function of the volumetric strain and includes the effect of permanent crushing. The damage is accumulated as a function of the plastic volumetric strain, equivalent plastic strain and pressure. The material model type 3 is used for steel bar. This model is suited to model isotropic and kinematic hardening plasticity with the option of including rate effects.

Fig. 4 shows the calculation model, where 1 is steel flyer, 2 is concrete, 3 is steel bar. Four examples are simulated:

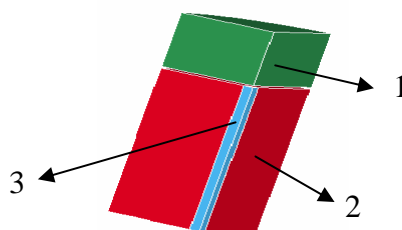


Fig. 4: Calculation model

- (1) The thickness of steel flyer is 15cm. Its impact velocity is $0.04 (10^3 \text{ m/s})$. The results are show in Fig.5 and Fig.6. In this case, the relative motion between the steel bar and concrete is not found.

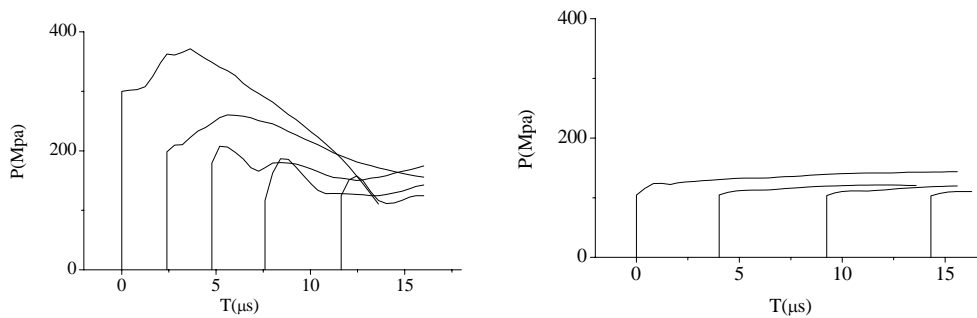


Fig. 5: Pressure curves in steel bar (left) and concrete (right)

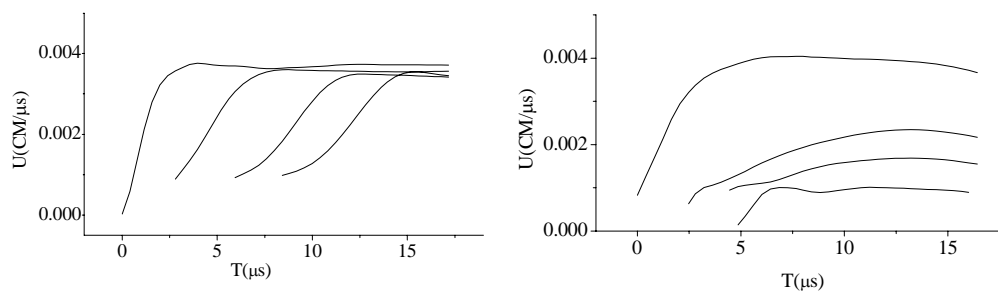


Fig.6: Particle velocity curves in steel bar (left) and concrete (right)

- (2) The thickness of steel flyer is 15cm. Its impact velocity is $0.30 (10^3 \text{ m/s})$. The results are show in Fig.7 and Fig.8. In this case, the relative motion between the steel bar and concrete can be seen in Fig.11.

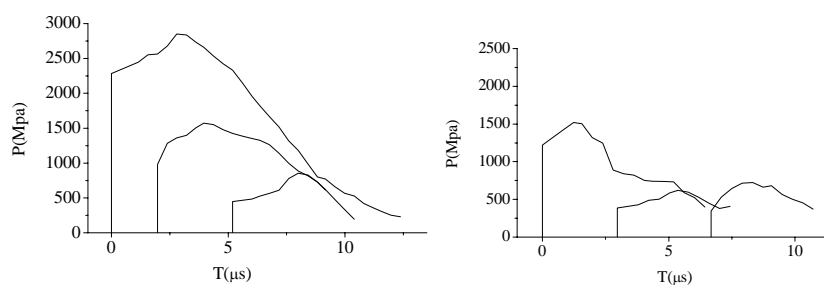


Fig. 7: Pressure curves in steel bar (left) and concrete (right)

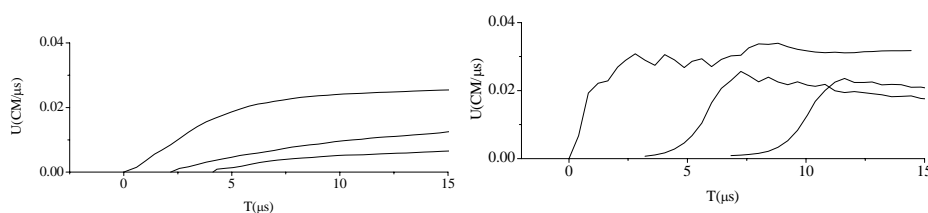


Fig.8: Particle velocity curves in steel bar (left) and concrete (right)

- (3) The thickness of steel flyer is 9 cm. Its impact velocity is $0.30(10^3\text{m/s})$. The results are shown in Fig.9 and Fig.10. In this case, the relative motion between the steel bar and concrete can be seen in Fig.12.

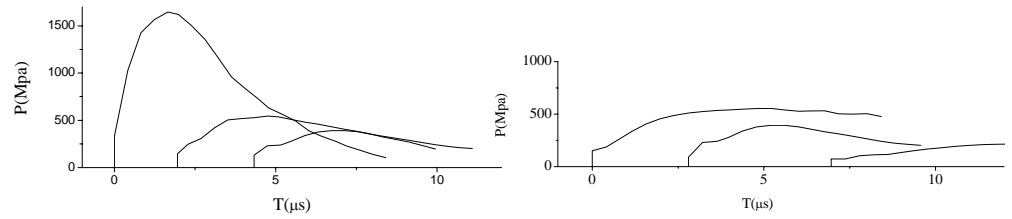


Fig. 9: Pressure curves in steel bar (left) and concrete (right)

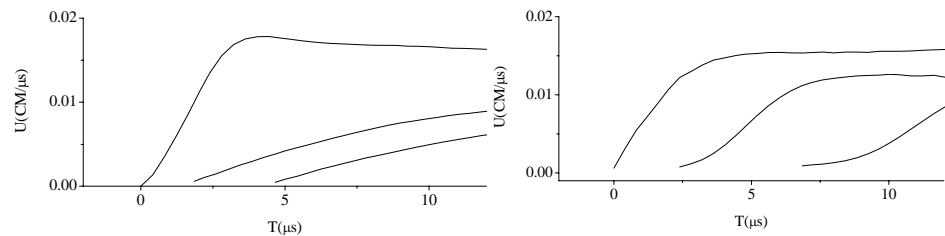


Fig.10: Particle velocity curves in steel bar (left) and concrete (right)

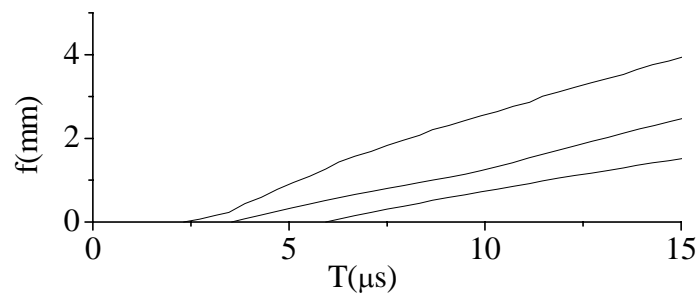


Fig. 11: Relative displacement curves for 15cm steel flyer

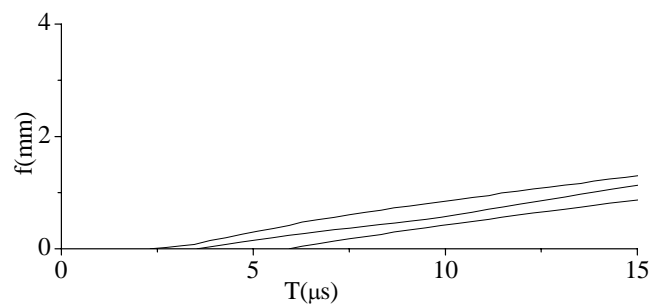


Fig. 12: Relative displacement curves for 9 cm steel flyer

- (4) Fig. 13 is a transverse impact model. The thickness of steel flyer is 5 cm. Its impact velocity is $0.40(10^3\text{m/s})$. A void band under the steel bar can be seen in Fig. 14.

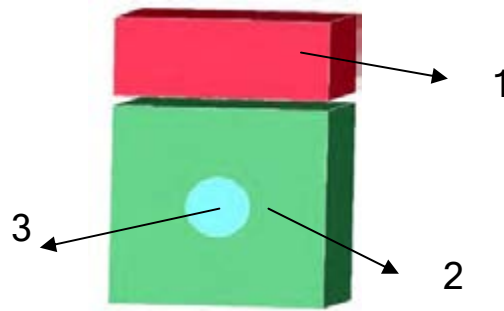


Fig. 13: Transverse impact model.
1. steel flyer, 2. concrete, 3. steel bar

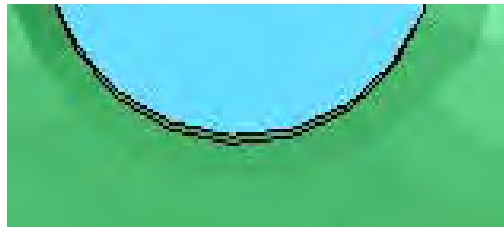


Fig. 14: A void band under the steel bar

1. DISCUSSION

- (1) When loaded by a longitudinal shock wave, the steel bar can be brought a longitudinal relative movement in RC, and a crash zone formed around the steel bar at the same time;
- (2) If the actual differential pressure ΔP_a between the steel bar and concrete is less than the critical pressure which against static friction resistance ΔP_{cr} , there is no relative motion occurred;
- (3) The values obtained from one-dimensional theoretical analysis is more than that from numerical calculation;
- (4) The longer is the shock loading time, the larger is the relative motion between the steel bar and concrete;
- (5) When loaded by a transverse shock wave, some local breaks are formed between the steel bar and concrete;
- (6) The thickness and the longitudinal length of the damage zone above-mentioned are determined by the strength and the acting time of shock wave respectively.

2. REFERENCES

- (1) Cao J. Z., Zhou S. R., Li E. Z., 1998. Effect of constitutive relation of material in numerical computation. *Acta Armamentarii* , 19, 69-72.
- (2) Holmquist T. J., 1992. A computational constitutive model for concrete

- to large strain, high strain rate, and high pressure. 14th International Symposium Ballistics, 591-600.
- (3) Chen E. P., 1994. Simulation of concrete perforation based on a continuum damage model, DE95000544.
 - (4) Wu H. J., Huang F. L., Jin Q. K., Zhang Q. M., 2003. Numerical simulation on perforation of reinforced concrete targets. *Explosion and Shock Waves* 23, 545-550.
 - (5) Zhang D. H., Zhu F. S., Xing J. B., 2005. Application of beam-particle model to the problem of concrete penetration. *Explosion and Shock Waves* 25, 85-89.
 - (6) Yuen S. R., Zhang B. P., 1979. *Explosion and Its Action*. China Industry Press.
 - (7) Li H. L., Han F., 2004. Computation method of shaped-charge jet penetrating concrete targets. *Progress in Safety Science and Technology*, Vol. 4, Science Press, Beijing/New York, 2894-2900.

STATISTICAL STUDY OF LETHALITY RATE FROM ACCIDENTAL BUILDING FAILURE

X. GU¹, Y. LU^{1*}, S. GONG¹
and Y. ZHOU²

¹ Protective Technology Research Centre,
Nanyang Technological University, Singapore

² Defence Science and Technology Agency, Singapore

*Email address: cylu@ntu.edu.sg

ABSTRACT

This study has been conducted in association with the investigation into building failure due to underground explosion induced ground shocks. Previous numerical and experimental studies have shown that strong ground motions induced by large-scale underground explosions have the potential to damage nearby surface buildings. As a probable consequence of severe building damage, especially collapse, the lethality of building occupants is a critical concern for the authorities and the designers. Therefore, the prediction of the possible lethality for building collapse due to ground shocks is required. An important element in the lethality prediction model is a model for the lethality rate in case a building failure occurs. This article summarizes a statistical study in attempt to provide a preliminary probabilistic model for the lethality rate. Because direct evidence of building failure due to blast-induced ground shock is almost none, this study collected cases where rather brittle building failure took place. Such data are relevant because the building failure due to explosive ground shocks is deemed to be of basically a brittle nature. The work presented in this paper includes the description of the database, the classification of the collected data and the preliminary statistical analysis. Subsequently, preliminary probabilistic models for the lethality rate for certain categories of building structures are proposed.

1. INTRODUCTION

Previous numerical and experimental studies have shown that strong ground motions induced by large-scale underground explosions could result in damage to nearby surface buildings. As a probable consequence of severe building damage, especially collapse, the lethality of building occupants can pose a huge negative impact on the society. Therefore, the prediction of occupants' lethality in case of collapse becomes essential while considering the building safety issues and thus, a risk based lethality model is required.

One of the essential information required in the lethality model to predict the lethality at collapse is the expected lethality rate which can be

defined as the ratio of death toll over the total number of building occupants present at the time of the incident. Some previous researches have suggested various lethality rates at building collapse ranging from 10~50% (Kummer 2004). These values are all proposed in deterministic terms. As a matter of fact, the lethality rate largely depends on the damage state and other uncertain factors concerning the integrity of the structure, in addition to those well defined parameters such as the structure type, the number of stories, and the building's function. In other words, there exist large uncertainties in the prediction of lethality due to building collapse. Therefore, a probabilistic lethality rate is considered more appropriate in view of the various uncertainties involved.

In this paper, a simple risk based lethality model to predict the occupants' lethality at building collapse is introduced briefly first. Then, the collection of lethality data and the organization of the database are described. Finally, a probabilistic model for the lethality rate is proposed based on a statistical analysis.

2. THE LETHALITY MODEL

There are a lot of models proposed for the prediction of earthquake casualties. Coburn & Spence (1992) used a four-level injury severity model associated with building collapse. Murkami (1992) proposed an event tree model that includes fatalities caused by building collapse. Recently, the USA Earthquake Loss Estimation Methodology by HAZUS (2003) established an earthquake casualty model using an event tree. Similarly, the event tree concept is applied in the present study. However, due to the fact that the probability of being killed in buildings with low-to-moderate damage is marginal, only the situation where the building is completely damaged and collapsed is considered in the current event tree. Furthermore, only the lethality (not including injury) is concerned here. The simplified event tree is shown in Figure 1.

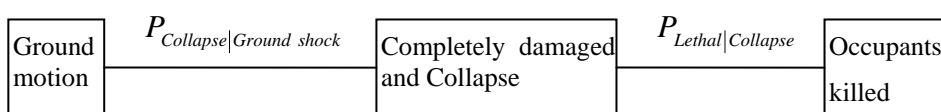


Figure 1 Lethality event tree

According to AC/258 (2002), the Lethality due to an unexpected underground explosion event, $P_{Lethal|Event}$, is defined as the conditional probability of a person

- “being instantaneously killed or mortally injured”
- or
- “receiving injury which pose an immediate life threatening condition if not treated adequately and expeditiously”

if present in a building when hit by the ground shock from an undesired explosion event.

Consequently, from Figure 1, we have

$$P_{Lethal|Event} \approx P_{Lethal|Collapse} \cdot P_{Collapse|Ground_Shock} \quad (1)$$

where, $P_{Lethal|Collapse}$ is the probability of a person falling into the aforementioned lethal situation if present in a building when an undesired collapse event occurs. $P_{Collapse|Ground_Shock}$ is the probability of collapse of a building being hit by an undesired explosion event.

The exact value of $P_{Lethal|Collapse}$ is very difficult to evaluate because the incident, Individual Lethality at Collapse, can never be repeated in a same manner. According to Bernoulli Theorem, the frequency of occurrence of an event converges to the corresponding probability in case of the experiment being repeated for a large number of times. Practically, $P_{Lethal|Collapse}$ can be approximated by the Lethality Rate at Collapse, expressed as $R_{Lethal|Collapse}$, which can be estimated from experience from cases where the number of inhabitants being killed in the collapsed building has been recorded.

Moreover, to estimate the probable death toll, the Lethality Rate of inhabitants in a building when hit by an undesired explosion event, $R_{Lethal|Event}$, is required. In this stage, $P_{Lethal|Event}$ is used to approximate $R_{Lethal|Event}$ as:

$$R_{Lethal|Event} \approx P_{Lethal|Event} \quad (2)$$

Then we have:

$$N_{Lethal} = R_{Lethal|Event} \cdot E \quad (3)$$

where N_{Lethal} is the expected number of lethalties and E is the Exposure expressing the average amount of people expected to be continuously present.

Extracted from a survey of building collapse accidents, $R_{Lethal|Collapse}$ is a percentage (rate) of the number of killed over the number of all inhabitants in a collapsed building. It must be aware that in practice, the lethality rate of an undesired building collapse can never be predicted exactly due to the significant uncertainties involved, such as the random distribution of inhabitants within the building and the random collapse modes. Therefore, a probabilistic lethality rate is considered reasonable to describe this randomness. In the following sections, the efforts which have been made to establish a database of lethality rate at building collapse and to evaluate the probabilistic lethality rate are introduced.

3. THE DATABASE

So far, no report on lethality due to underground explosion induced building collapse has been found from the literature survey conducted by the authors. However, numerous incidents where people are killed by sudden and brittle building collapse due to earthquakes, weather disasters, poor designs and constructions, improper renovations, and so on are reported extensively. On the other hand, according to the previous studies on the characteristics of structural response under blast induced ground shocks (Lu et al. 2001; Ma et al. 2002), it is deemed reasonable to assume that the likely mode of collapse of buildings under strong ground shocks would be generally brittle. Based on this consideration, all those past incidents where sudden and brittle failure of structures occurred, regardless the various structural types, building functions, number of stories, damage states and time of collapse, are pulled together to build up a database concerning the lethality rate due to sudden building collapse. In lieu of more direct information, the statistical results extracted from these cases may be applied to predict the lethality due to building collapse induced by blast induced ground shocks.

It should be mentioned that the definition of collapse of a building structure sometimes can be subjective, especially if the structure does not physically crumble. Considering the fact that the actual physical state of a collapsing structure can never be predicted with certainty as it is by itself a probabilistic matter, the present study adopts the definition of collapse as a state where the structure apparently have lost its integrity or overall stability, which may be signified by large permanent displacements in conjunction with falling structural parts. The variety of actual collapse scenarios satisfying the above definition manifests as a probabilistic phenomenon. This treatment allows the lethality statistics thus derived to be applicable in an analytical procedure involving predicted "collapse" of the building structures.

For cases where only a section of a building structure collapsed while the remaining part apparently remained intact, only the lethality to the persons being present at that collapsed section is considered. This is consistent with the above definition of building collapse.

Most of the reported cases are from newspapers or news websites. The text is usually not precise enough regarding the number of occupants, death toll, structure type and mode of collapse. Despite of these limitations, it is possible to extract directly or indirectly the necessary lethality information for a lot of cases. So far, a total number of 94 individual building collapse cases from all over the world are collected to form the current database. This database contains the following types of information:

- Time and place, when and where the collapse occurs.
The time of collapse is essential information to determine the number of occupants according to the building's function.
- The probable causes of the collapse.
In many cases, the probable causes of the collapse pointed out by authority or police are reported. This information can provide some clues about the mode of collapse and damage state.

- The general information of the collapsed building, including the building's function, structure type, number of stories, and the damage state.

This information can help establish a general picture of the accident. If available, the photograph of the collapsed building is also attached. The building's function, structure type and number of stories are also important criteria for data classification.

- The number of occupants, injury and death.
This is the most essential information regarding the lethality rate. This study focuses on the death toll rather than the number of injury. For a single event, several sources have been traced to verify the number of occupants and death toll.
- Photographs from the site, if available. Some of the pictures are shown in Figure 2 to illustrate some typical modes of collapse.
- Other information including the details of probable causes of the collapse.

Several typical cases from the database are tabulated in Table 1 to illustrate how the database is organized and how one case significantly differs from the others.

Strictly speaking, the collected raw data should be properly classified before a statistical analysis is performed. The possible classification criteria may include the structure type, the number of stories, the building's function, the situation of building before collapse, the cause of collapse, the time of collapse, and the damage state. Restricted by the limited number of the collected cases, it is not feasible to perform such a detailed classification. Nevertheless, based on the limited sample space, a preliminary categorization according to structural types within the database was carried out to establish a rough statistical picture of the collapse induced lethality rate. Other important classification criteria, such as number of stories, will be incorporated in the data processing when the sample space becomes big enough.

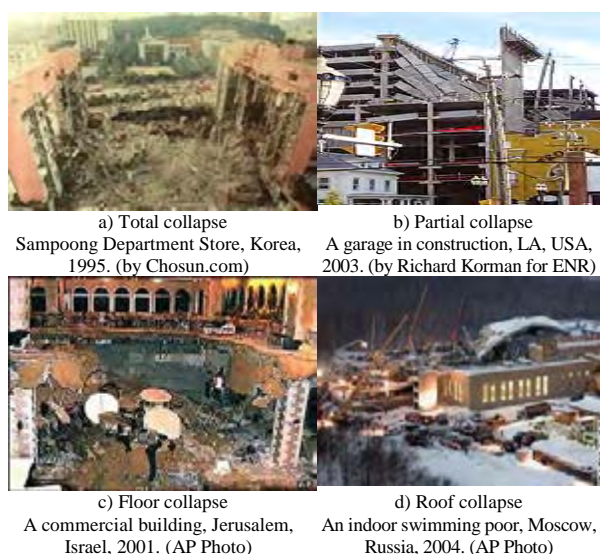


Figure 2 Photographs of some collapsed buildings

Four main structure types are identified from the database as RC (reinforced concrete), BMC (brick, masonry & concrete), BM (brick & masonry), and TM (timber & masonry). Steel structure is not included because few cases of steel structures have been found during the data survey. The first three structural types covers the majority of current buildings and facilities in urban area and thus the lethality rate data of these three categories are combined to illustrate a general statistical property of the lethality due to collapse of engineered structures.

Table 1 Typical cases from the database

No.	Incident Description				Building				Casualty			
	Date	Time	Place	Cause	Nature	Type	Storey	Damage state	Total	Injured	Dead	Lethality
RC-09	29-06-1995	17:50	Seoul South Korea	Overweight and poor D/C	Department Store	RC	5	Complete collapse	1411	910	501	35.5%
RC-20	15-03-1986	11:25	Singapore	Poor D/C	Hotel	RC	6+1	Complete collapse	50	17	33	66%
BMC-05	03-08-1998	night	Bandra, India	Illegally added 3 stories	Residential & commercial	Brick & Concrete	4+3	Complete collapse	59	22	37	62.7%
BMC-07	21-02-1999	night	Beirut, Lebanon	Structural damage during the conflict	Residential	Brick & Concrete	5	Complete collapse	9	7	2	22.2%
BM-01	04-06-1959	6:00	Yingde China	Rainstorm	Residential	Brick & masonry	1-2	Complete collapse	185	46	19	10.3%
BM-40	21-08-2002	23:10	Moscow Russia	Gas explosion	Residential	Brick & masonry	5	Complete collapse	36	12	6	16.7%
TB-01	11-05-1927	night	South Dallas, USA	Gas leakage explosion	Residential	Timber & brick	2	Complete collapse	(47)	41	6	12.8%

4. STATISTICAL ANALYSIS

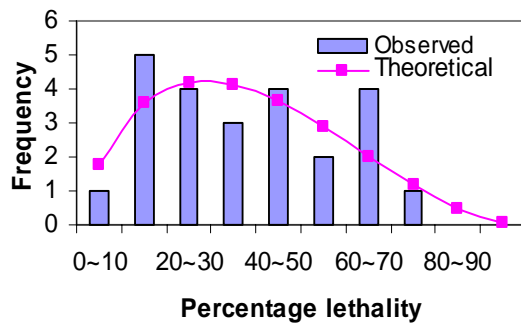
Due to the large uncertainty involved, it is reasonable to predict the collapse-induced lethality in a probabilistic manner. For this purpose, a statistical analysis on the classified database is performed. According to the results from the statistical analysis in Table 2, the lethality rate due to building collapse shows a significant uncertainty as expected. It is found that the probabilistic properties of category RC, BMC and BM are quite similar. Due to prevalence of these three structure types in modern urban area, the probabilistic property of their combination is also evaluated as a general representative of urban buildings. The category TM is treated separately as this structure type is lesser used in modern urban area.

From Table 2, it can be found that category RC, BMC and BM all have a number of samples around 26, which is significantly more than 17, the number of samples in category TM. This also reflects the dominance of the first three structure types. The mean values and COVs of category RC, BMC and BM differ from each other slightly. Normal and Beta distribution are found suitable to describe the probabilistic distribution of the corresponding lethality ratios. The data from the combination of these three categories, representing the main structure types in modern urban area, has a mean value and COV of 0.371 and

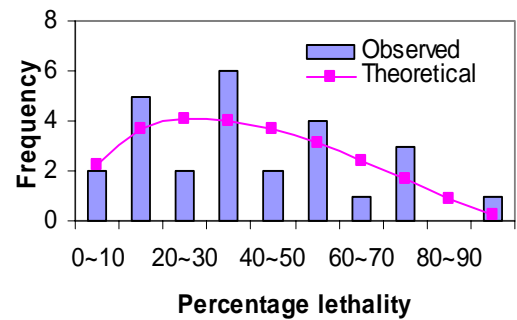
0.547, respectively. This mean value is within the range reported by some other studies (Kummer 2004). Assuming a normal distribution and a probability of being exceeded of 5%, the corresponding lethality rate due to collapse of a modern urban building, i.e. $P_{Lethal|Collapse}$, is 0.705. If the value of $P_{Collapse|Ground_Shock}$ and E is known, say 10% and 100 for instance, $P_{Lethal|Event}$ and N_{Lethal} are equal to 0.0705 and 7 respectively, with a probability of being exceeded of 5% from Equation 1~3. The mean N_{Lethal} would be $3.7 \cong 4$ in this case. For the purpose of illustration, the fitted Beta distribution is plotted in Figure 3, along with the corresponding histogram.

Table 2 Summary of statistics of lethality rate

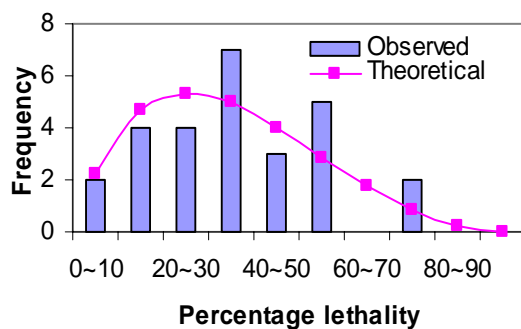
Category	No. of samples	Mean	Cov	Distributions
RC	24	0.376	0.539	Normal, Beta
BMC	26	0.395	0.562	Normal, Beta
BM	27	0.343	0.545	Normal, Beta
RC+BMC+BM	77	0.371	0.547	Normal, Beta
TM	17	0.249	1.055	Lognormal



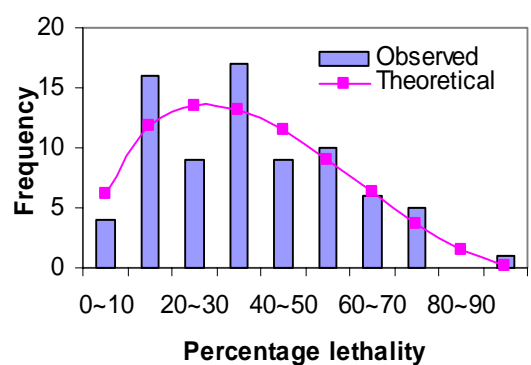
a) Category RC (24 samples)



b) Category BMC (26 samples)



c) Category BM (27 samples)



d) RC+BMC+BM (77 samples)

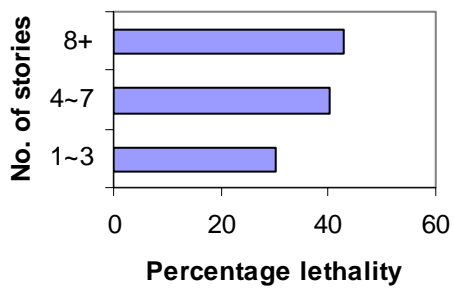
Figure 3 Lethality histograms and fitted Beta distributions

The effect of number of stories on the lethality rate has also been studied. The classification of number of stories applied in this study is generally consistent with that of HAZUS (2003), which are listed as follows:

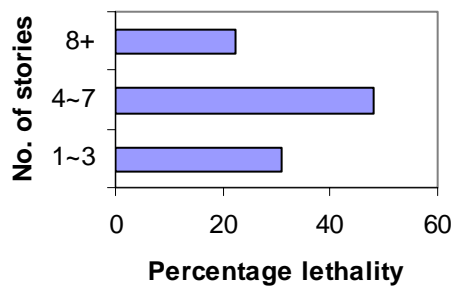
- Low-rise: 1~3 stories
- Mid-rise: 4~7 stories
- High-rise: 8+ stories

Table 3 Effects of number of stories on lethality rates

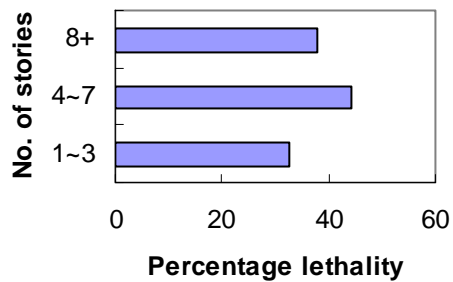
Categories	1~3		4~7		8+	
	No. of samples	Mean value	No. of samples	Mean value	No. of samples	Mean value
RC	8	0.303	10	0.403	6	0.43
BMC	10	0.311	14	0.479	2	0.225
BM	26	0.342	1	0.364	0	-
RC+BMC+BM	44	0.328	25	0.444	8	0.379
TM	17	0.249	0	-	0	-



a) Category RC



b) Category BMC



c) RC+BMC+BM

Figure 4 The effect of number of stories on lethality rate

The mean values of the lethality rates are calculated for different groups of buildings in terms of the number of stories and they are shown in Table 3.

For category RC, there is a general increasing trend of mean lethality rate as the number of stories increases. For categories BMC and BM with much fewer samples of more than 8 stories, the mean lethality rate corresponding to 4~7 stories is also larger than that of 1~3 stories. The result from the combination of categories RC, BMC and BM is similar to categories BMC and BM. Based on these observations, a preliminary conclusion may be drawn that the lethality rate increases with the increase of the number of building stories. This observation echoes the finding from a previous study (Kummer 2004) based on a relative small number of samples. Further data expansion is required to possibly enhance the observation. The effect of number of stories on lethality rate is also illustrated in Figure 4 for categories RC and BMC.

5. CONCLUDING REMARKS

This paper introduces the establishment of a database on the lethality rate due to sudden and brittle building collapse, and the subsequent statistical study on the results. A total number of 94 incidents of sudden building collapse have been collected to form the database. By statistical analysis on the processed data, a probabilistic model of the lethality rate due to sudden building collapse is proposed. It is found that the probabilistic properties of categories RC, BMC and BM are close to each other. These three structure types actually cover a majority of the building structures in a modern urban area. Therefore, they are combined to represent the main structure types in modern urban area. The mean value and COV of lethality rate at building collapse for the combined category are found to be 0.371 and 0.547, respectively.

The dependence of the lethality rate upon the number of building stories has also been examined based on the available database. It can be generally concluded that the mean value of lethality rate at building collapse increases as the number of stories increases.

REFERENCES

- AC/258 (UGSWG) NO (ST) IWP 06-2002, 2002. Lethality Model for Building Inhabitants Exposed to Ground Shock from Accidental Explosions in Underground Ammunition Magazines, First draft. Norwegian Defence Estates Agency, Norway.
- Coburn A. W. and Spence R. J. S., 1992. Factors Determining Human Casualty Levels in Earthquakes: Mortality Prediction in Building Collapse. *Proceeding of 10th WCEE, Madrid, Spain*, 5989~5994.
- HAZUS, 2003. *Multi-Hazard Loss Estimation Methodology: Earthquake Model. Technical Manual*. National Institute of Building Sciences, Washington DC.

- Kummer Peter O., 2004. Lethality/Injury as a Result of Building Collapse, Update dated November 2004 to NATO AC/326 SG 5-UG Storage Custodian Group. Bienz, Kummer & Partner Ltd, Zollikerberg, Switzerland.
- Lu, Y., Hao H. and Ma, G.W., 2002. Experimental investigation of structural response to generalized ground shock excitation. *Experimental Mechanics* 42(3), 261-271.
- Ma, G.W., Hao, H., Lu, Y., and Zhou, Y.X., 2002. Distributed structural damage generated by high-frequency ground motion. *Journal of Structural Engineering*, ASCE, 128(3), 390-399
- Murkami H. O., 1992. A Simulation Model to Estimate Human Loss for Occupants of Collapsed buildings in an Earthquake. *Proceeding of 10 WCEE, Madrid, Spain*, pp. 5969~5974.

SAFETY EVALUATION METHODOLOGY FOR BUILDING CONTENTS SUBJECTED TO EARTHQUAKE LOADING

YUTAKA NAKAMURA⁽¹⁾, MIKA KANEKO⁽²⁾,
HIROSHI KAMBARA⁽³⁾ and KAZUO TAMURA⁽⁴⁾

Institute of Technology, Shimizu Corporation
4-17, Echujima 3-chome, Koto-ku, Tokyo 135-8530, Japan
email address: (1) yutaka.nakamura@shimz.co.jp, (2) mika@shimz.co.jp,
(3) kambara@shimz.co.jp, (4) tamkaz@shimz.co.jp

ABSTRACT

An indoor safety evaluation methodology for buildings subjected to earthquake shaking has been developed that takes into account the risks of overturning or sliding of furniture and other building contents and damage of nonstructural elements. The safety evaluation methodology consists of three main estimation components: an approximate evaluation of the maximum responses of a building subjected to earthquake shaking, estimation of the risks of overturning and sliding of furniture and other contents, and estimation of the significant stages of damage of nonstructural elements. The paper introduces each of the three estimation methods and examples of indoor safety evaluations are shown to demonstrate the validity of the developed method.

1. INTRODUCTION

Overturning or sliding of furniture and other building contents and damage of nonstructural elements due to earthquake shaking may injure building occupants even when the building structural frame does not suffer severe damage. Overturned furniture and damaged nonstructural elements may also become obstacles to evacuation and relief activities following an earthquake. In the study presented here, an indoor safety evaluation method for buildings subjected to earthquake shaking has been developed that takes into account the above-mentioned risks. The flow of the indoor safety evaluation is shown in Figure 1. The developed evaluation methodology consists of the following three main components: (1) an approximate evaluation of the maximum responses of a building subjected to earthquake shaking, (2) estimation of the risks of overturning and sliding of furniture and other contents, and (3) estimation of the significant stages of damage of nonstructural elements. New relationships have been developed that allow the maximum acceleration, velocity and interstory drift of each story of a building to be estimated using only the story number and the PGA (peak ground acceleration) and PGV (peak ground velocity) of the earthquake.

Based upon the estimated maximum responses, the risks of overturning and sliding of specified pieces of furniture and the damage of specified nonstructural elements can be estimated and classified into four levels. The paper introduces each of the three estimation methods and provides examples of indoor safety evaluations to demonstrate the validity of the developed method.

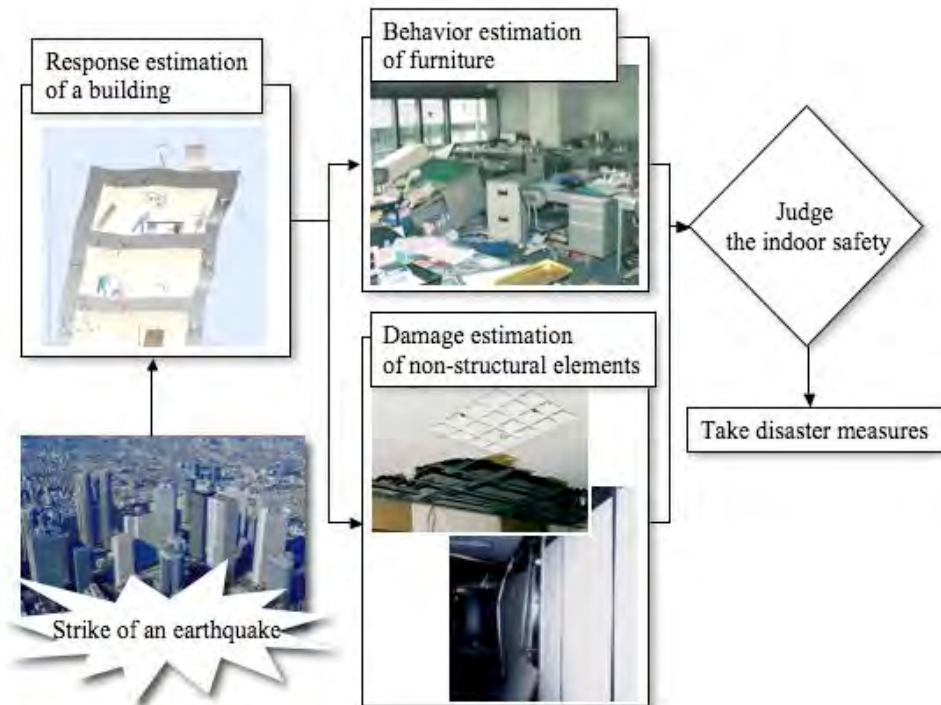


Figure 1: The flow of the indoor safety evaluation

2. DEVELOPED ESTIMATION COMPONENTS

2.1 Approximate evaluation of the maximum responses of a building

New relationships have been developed that allow approximate evaluation of the maximum response of a building to be estimated using only the story number and the PGA and PGV of the earthquake. Since a conventional response analysis requires an analytical model of a building and the time history record or the response spectrum of the earthquake, it is hard for non-engineers to obtain these data and carry out the proper simulation analyses. The developed relationships can be used without expertise, and provide approximate maximum responses with reasonable accuracy for the estimation of the risks of overturning and sliding of furniture and the estimation of the significant stages of damage of nonstructural elements.

A significant number of time-history response analyses have been carried out for the standard building models shown in Table 1 for 1,027 collected earthquake records, the PGA of which are normalized to

100cm/sec². Figure 2 shows the average maximum responses, R (maximum floor acceleration [Acc], velocity [Vel], or story displacement [Dis]) of a 20-story RC building for the same range of earthquake PGA/PGV values. The figure indicates that R ($=Acc$, Vel , or Dis) varies considerably with PGA/PGV even for the same normalized PGA ($=100\text{cm/sec}^2$) and that the evaluations of R should consider the effect of PGA/PGV of the input earthquake.

Table 1: Standard building models

	RC structure	Steel structure
Story number	$N = 5, 10, 15, 25, 30, 40, 50$	
The natural period of 1 st mode	$T=0.07N$	$T=0.10N$
The damping factor of 1 st mode	$h=3\%$	$h=2\%$
Damping factors for higher modes	frequency proportional	
Floor mass	uniform distribution	
Story stiffness	trapezoidal distribution stiffness ratio of 1 st /top story=3.0	

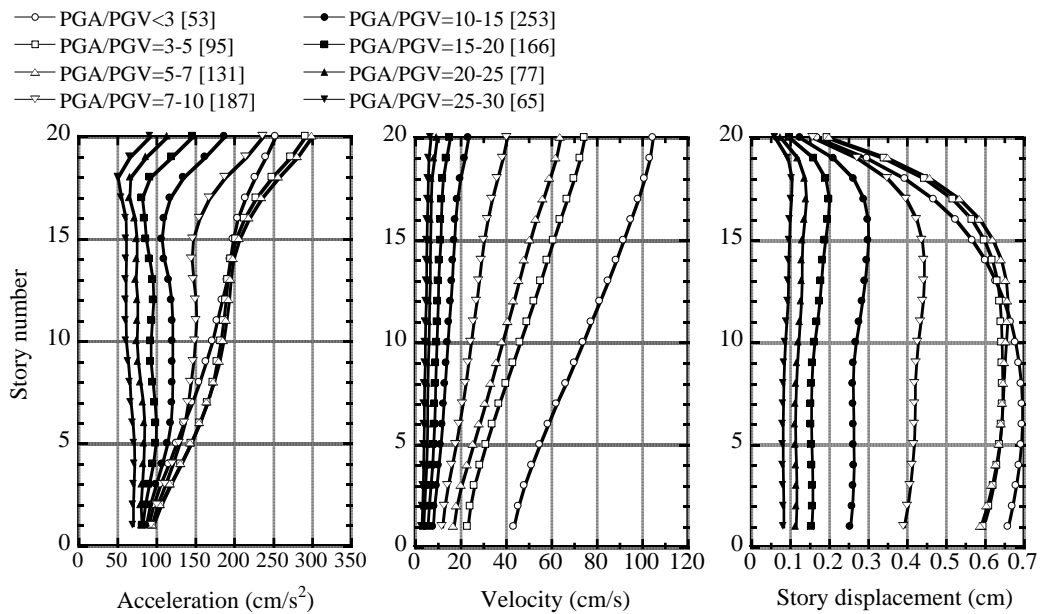


Figure 2: Average maximum responses of a 20-story RC building

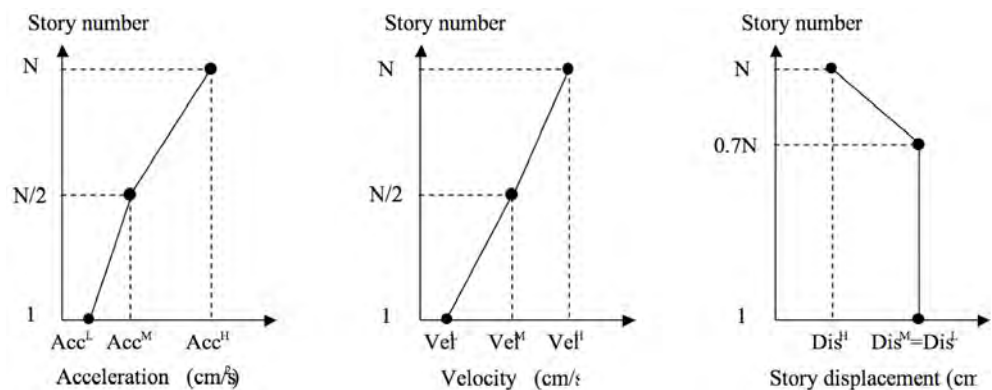


Figure 3: Simplified story-wise distributions of maximum responses

The story-wise distribution of R ($=Acc, Vel,$ or Dis) can be simplified to a piecewise-linear shape represented by two straight lines as shown in Figure 3. The relationships between PGA/PGV and $R^{H,M,L}$, R at the top [H], middle [M] and 1st floor [L], for a RC building with $N=10, 30, 50$ stories are shown in Figure 4. $R^{H,M,L}$ can be expressed by the following formula:

$$R^{H,M,L} = \frac{d}{a(PGA/PGV)^2 + b(PGA/PGV) + c} \cdot f(N) \cdot PGA$$

$$f(N) = \frac{g}{eN + f}$$
(1)

where $f(N)$ is a correction function for the story number, and a, b, c, d, e, f and g are coefficients to be determined based on the results of response analyses such as that shown in Figure 4. Table 2 shows the coefficients for R ($=Acc, Vel,$ or Dis) of RC and steel structures.

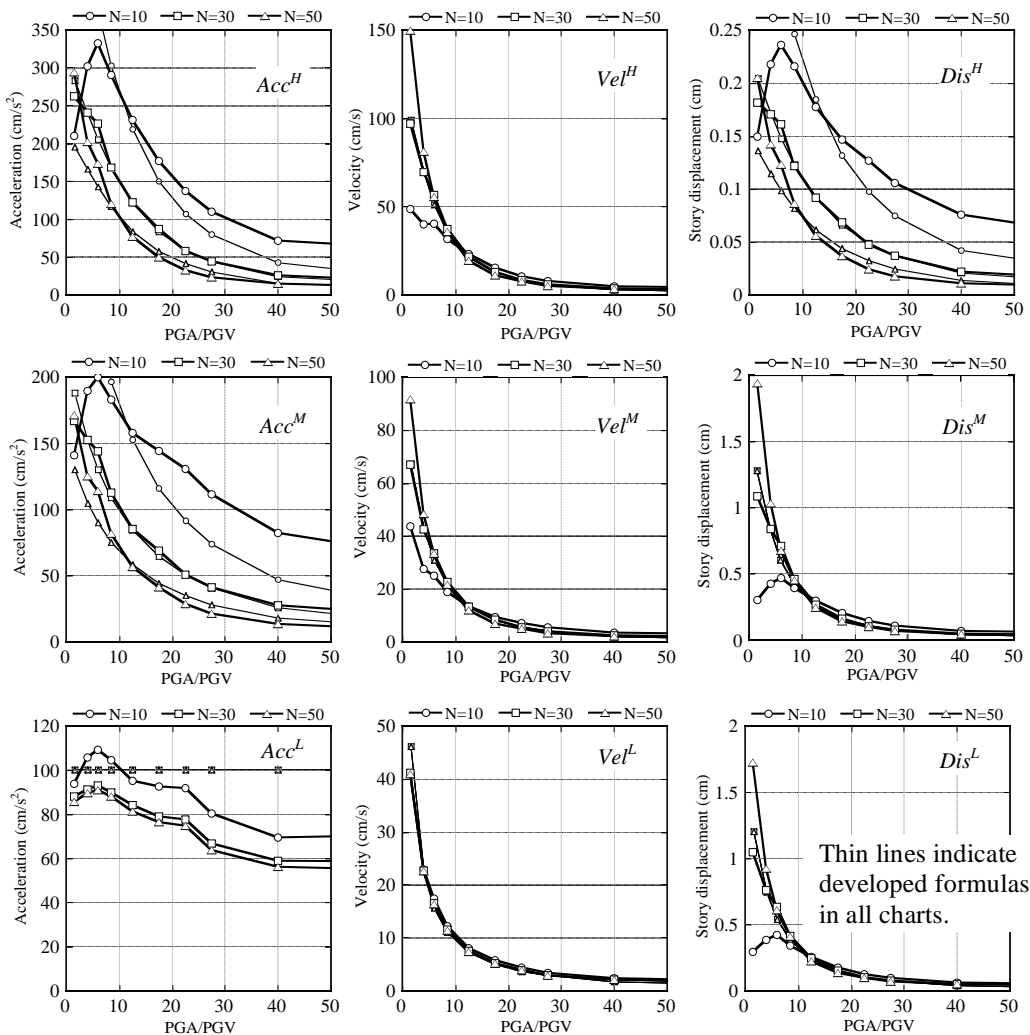


Figure 4: The relationships between PGA/PGV and the average maximum responses at the top, middle and 1st floors for $N=10, 30, 50$ of a RC building

Table 2: Coefficients in equation (1) for RC and steel structure buildings

$R^{H, M, L}$	a	b	c	d	e	f	g
Acc^H	1 (1)	7 (14)	161 (125)	493 (526)	1 (1)	15 (5)	45 (35)
Acc^M	1 (1)	47 (54)	478 (262)	1037 (820)	1 (1)	15 (5)	45 (35)
Acc^L	0 (0)	0 (0)	1 (1)	1 (1)	0 (0)	1 (1)	1 (1)
Vel^H	1 (1)	4 (3)	47 (29)	55 (52)	0 (1)	1 (105)	1 (135)
Vel^M	1 (1)	9 (2)	48 (30)	43 (32)	0 (1)	1 (105)	1 (135)
Vel^L	1 (1)	62 (34)	65 (60)	74 (49)	0 (0)	1 (1)	1 (1)
Dis^H	1 (1)	13 (14)	223 (124)	0.5 (0.7)	1 (1)	10 (5)	40 (35)
Dis^M	1 (1)	8 (10)	49 (22)	0.8 (1.3)	0 (0)	1 (1)	1 (1)
Dis^L	1 (1)	8 (10)	49 (22)	0.8 (1.3)	0 (0)	1 (1)	1 (1)

N.B. Numbers inside parentheses are for steel structure.

2.2 Estimation of risks of overturning and sliding of furniture

The risks of overturning of furniture and other building contents, Q_{or} , can be estimated by the overturning ratios given by (Kaneko, 2003)

$$Q_{or} = \begin{cases} \alpha \cdot \Phi\left(\frac{\ln Acc_f - \lambda_A}{\xi_A}\right) & F_f \leq F_b \\ \alpha \cdot \Phi\left(\frac{\ln Vel_f - \lambda_V}{\xi_V}\right) & F_f > F_b \end{cases} \quad (2)$$

where Acc_f (cm/s^2) and Vel_f (cm/s) are the maximum response acceleration and velocity of the floor, Φ is the probability distribution function of a normal distribution with mean and standard deviation of λ_A or λ_V , and ξ_A or ξ_V , respectively, F_f (Hz) is the equivalent frequency of the floor and F_b (Hz) is the boundary frequency determined by the depth B (cm) and the height H (cm) of a piece of furniture. F_f and F_b are given by

$$F_f = \frac{Acc_f}{2\pi \cdot Vel_f}, \quad F_b = \frac{15.6}{\sqrt{H}(1 + B/H)^{1.5}} \quad (3)$$

In equation (2), α is the slide-resistant coefficient which ranges from 0 to 1 and is determined by considering the ratio B/H and the coefficient of friction μ between the floor and furniture. Table 3 shows λ_A , ξ_A , λ_V , ξ_V and α for

categorized conditions in terms of the furniture and floor types. Figure 5 shows the relationship between Acc_f or Vel_f and Q_{OT} of each type of furniture on Floor B in Table 3. Q_{OT} is classified into four levels as shown in Figure 5.

Table 3: $\lambda_A, \xi_A, \lambda_V, \xi_V$ and α in equation (1) for categorized conditions

type	height of furniture	Lean against wall?	$F_f \leq F_b$		$F_f > F_b$		α		
			λ_A	ξ_A	λ_V	ξ_V	Floor A: $\mu=0.2$ ~ 0.4	Floor B: $\mu=0.4$ ~ 0.6	Floor C: $\mu>0.6$
H1	$H \geq 150cm$	no	5.70	0.34	4.06	0.45	0.8	1.0	1.0
H2		yes	6.11		4.47				
L1	$90cm < H < 150cm$	no	6.34	0.44	4.63	0.63	0.3	0.8	1.0
L2		yes	6.75		5.04				

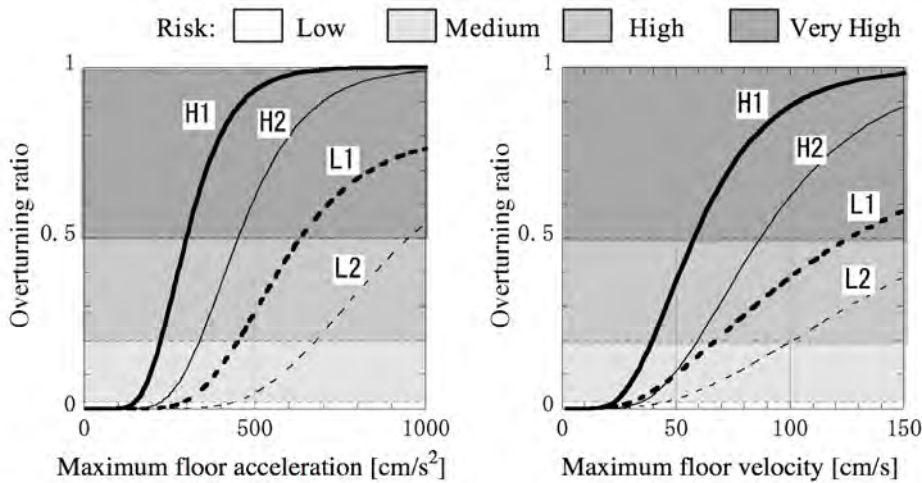


Figure 5: The relationships between the maximum floor responses, Acc_f and Vel_f and the overturning ratios, Q_{OT}

The risks of sliding of furniture and other building contents, Q_{SD} , can be determined by the two indices, namely the probability of sliding, P_S , and the sliding distance, D_s . P_S is given by $1 - \alpha$, and D_s (cm) is estimated by the following formula (Kaneko et al., 1999):

$$D_s = 0.02 \cdot \mu^{-0.3} \cdot F_f^{-0.5} \left(Vel_f - \frac{\mu g}{2\pi F_f} \right)^{1.56} \quad (4)$$

where g denotes the acceleration of gravity. Figure 6 shows the relationship between Vel_f and D_s for three floor types and a roller cabinet with $\mu=0.05$. Q_{SD} is classified into four levels according to the values of P_S and D_s as shown in Figure 7.

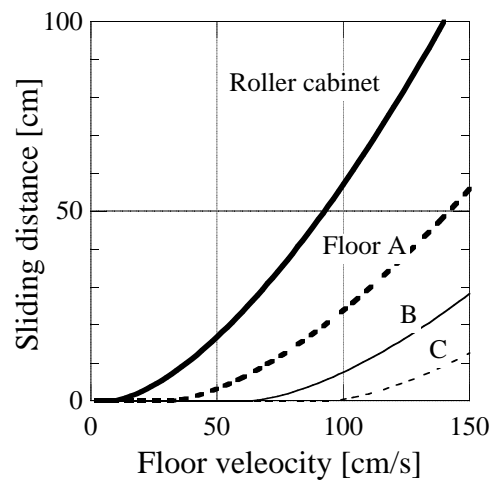


Figure 6: The relationship between floor velocity and sliding distance

Sliding distance (cm)	Probability of sliding $P_s = 1 - \alpha$			
	0	0-0.5	0.5-1	1
$D_s = 0$				
$0 < D_s < 2$				
$2 \leq D_s < 20$				
$20 \leq D_s$				

Figure 7: Risks of sliding determined by probability of sliding and sliding distance

2.3 Estimation of damage of nonstructural elements

Earthquake-resistant capabilities of nonstructural elements are categorized into four classes based on the various published documents of earthquake simulator tests as shown in Table 4. In Table 4, damage of nonstructural elements such as outer and inner walls in classes A, B and C is assumed to be caused by the story drift angle, while damage to ceiling elements in class D is assumed to be caused by the story drift angle and response acceleration. Figure 8 shows fragility characteristics, namely, relationships between the story drift angle and damage level of nonstructural elements in classes A, B and C where damage levels are classified into four levels (Kaneko et al., 2005).

Table 4: Classification of earthquake-resistant capabilities of nonstructural elements

Class	Earthq.-resistant capability	Examples of Nonstructural elements	Damage is caused by
A	High	ALC panel in general, curtain wall framed partition wall, window glass	story drift angle
B	Medium	ALC panel with inserted steel bar, direct-adhered partition wall	
C	Low	tiled wall on RC surface, mortared wall	
D	-	ceiling	story drift angle & response acc.

N.B. ALC= Autoclaved Lightweight aerated Concrete

Class	Story drift angle			
	1/300	1/200	1/100	1/50
A				
B				
C				

Figure 8: Relationships between story drift angle and damage level of nonstructural elements

3. VERIFICATION

The overturning ratios of furniture in a 14-story condominium due to the 2005 West Off Fukuoka Earthquake (March 20, 2005) are estimated by the developed evaluation method and compared to the actual overturning ratios surveyed by questionnaires. Maximum floor responses, Acc_f and Vel_f , of every story are estimated by the developed maximum evaluation formulas with the observed PGA and PGV at the nearest observation point. Figure 9 shows the range of overturning ratios of furniture corresponding to the top, middle and low-story floors along with the results of the survey. The estimated overturning ratios agree well with the observed results, which demonstrates the validity of the developed method.

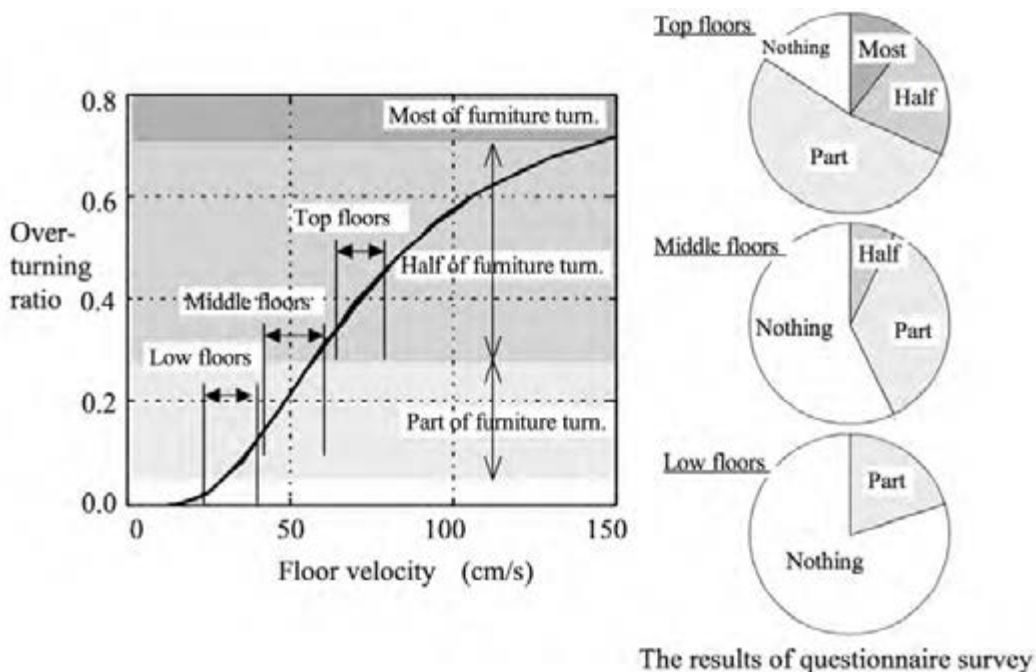


Figure 9: Estimated overturning ratios of furniture with the results of questionnaire survey

Estimated damage levels of selected nonstructural elements due to the Niigata Chuetsu Earthquake (October 26, 2004) are compared to actual observed damage to demonstrate the validity of the developed method. The average maximum story drift angles of a supposed three-story steel building is estimated by the developed maximum evaluation formulas for the observed PGA and PGV in each of the chosen cities in Niigata prefecture. Damage levels of window glass (in class A), ALC panel with inserted steel bar (in class B), tiled wall and mortared wall (in class C) in Nagaoka, Tokamachi, and Ojiya-city are estimated from the estimated responses of the supposed building and the fragility characteristics of the elements specified in Figure 8. Figure 10 shows the estimated damage level of each element in each city along with the comments of observed damage. The estimated damage levels agree well with the actual observed damage, which demonstrates the validity of the developed method.

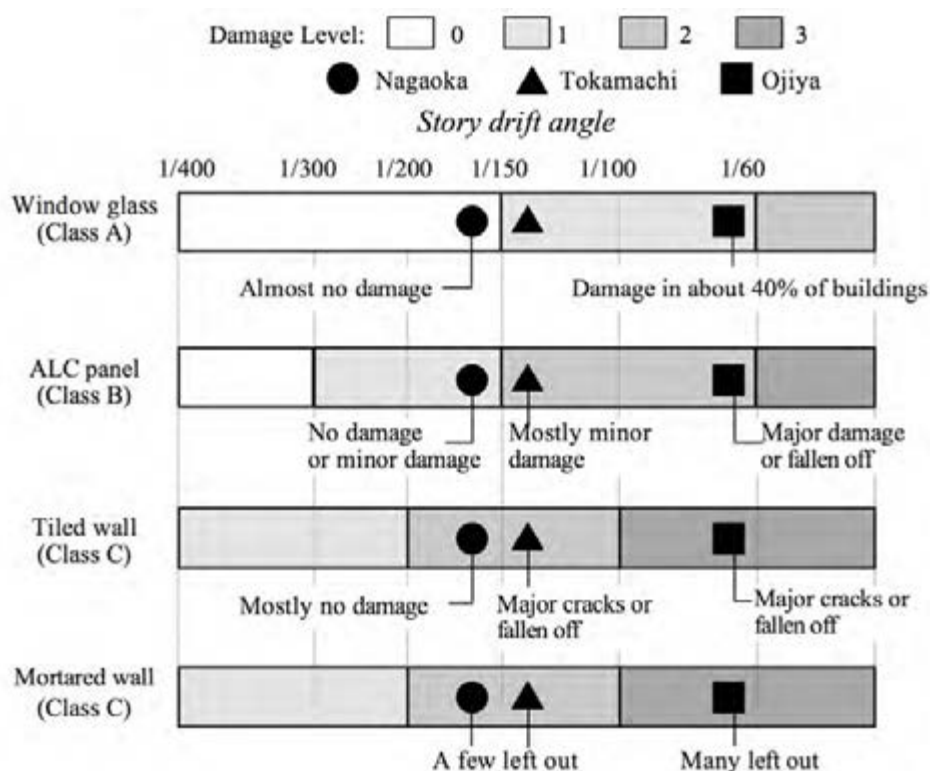


Figure 10: Estimated damage level of four elements in the three cities along with the comments of observed damage

4. CONCLUSIONS

An indoor safety evaluation methodology for buildings subjected to earthquake shaking has been developed that takes into account the risks of overturning or sliding of furniture and other building contents and damage of nonstructural elements. The safety evaluation methodology consists of three main estimation components: an approximate evaluation of the

maximum responses of a building subjected to earthquake shaking, estimation of the risks of overturning and sliding of furniture and other contents, and estimation of the significant stages of damage of nonstructural elements.

The developed response evaluation formulae can estimate the maximum acceleration, velocity and story drift of each story of a building by using only the story number and the PGA and PGV of the earthquake. Based upon the estimated maximum responses, the risks of overturning and sliding of specified pieces of furniture and the damage of specified nonstructural elements can be estimated and classified into four levels. Estimated damage levels of selected nonstructural elements due to the Niigata Chuetsu Earthquake were compared to the actual observed damage to demonstrate the validity of the developed method.

REFERENCES

- Kaneko, M., 2003. Proposal of simple estimation method for overturning ratios of furniture during earthquakes, *Summaries. 2003 Meetings of the Architectural Institute of Japan*, 61-62. (in Japanese) .
- Kaneko, M., Hayashi, Y., and Tamura, K., 1999. Evaluation of sliding displacement of furniture during earthquake: By using revised formula to estimate sliding displacement of furniture. *Summaries. 1999 Meetings of the Architectural Institute of Japan*, 537-538. (in Japanese).
- Kaneko, M., Kambara, H., and Tamura, K., 2005. Seismic performance of non-structural elements based on results of seismic resistant tests. *AIJ Journal of Technology and Design*, No. 21, 39-44. (in Japanese).

ACKNOWLEDGEMENT

The study here has been carried out as part of 'Research project on great earthquake disaster mitigation in big cities' by the Japanese Ministry of Education, Culture, Sports, Science and Technology, and entrusted by National Research Institute for Earth Science and Disaster Prevention.

SAFETY EVALUATION OF SUBMERGED TUNNEL AGAINST BLAST LOAD

MA GUOWEI*, Nanyang Technological University, Singapore
AN XINMEI, Xi'an Jiaotong University, China
LI YONGSHENG, Tongji University, China
cgwma@ntu.edu.sg

ABSTRACT

Submerged tunnel is extremely vulnerable to internal explosion. The design code usually does not take into consideration the blast load effect or oversimplifies the blast load as a constant pressure on the internal walls of tunnel. In the present study, numerical simulation of a submerged tunnel system under blast load caused by high explosive (HE) detonation is presented. The problem is studied by using LS-DYNA, an explicit, 3-D dynamic, nonlinear finite element program. The tunnel damage by different intensity of the blast load is simulated. The pressure- and velocity-time histories of several key points around the donor tunnel are compared. The result is helpful for relative authorities to apply necessary protection measures for submerged tunnel against blast load.

1. INTRODUCTION

Submerged tunnel has been widely used in the recent years. Submerged tunnel can be used in rivers or waterways when it is possible to place the tunnel in the riverbed or seabed. A submerged tunnel may consist of several prefabricated tunnel elements, which are floated to the site; installed one by one; and connected to one another under water in a trench that has been pre-dredged. As construction proceeds, the tunnel is backfilled. The completed tunnel is usually covered with a protective layer over the roof. The history of submerged tunnel practice began in 1910, with the construction of a two-track railroad tunnel across the Detroit River between the United States and Canada (Saveur and Grantz, 1993). After that, fewer than 100 railroad or highway tunnels have been designed worldwide over the past century. The catalog of totally 91 submerged tunnel projects are presented by Grantz (1993). Two basic techniques have been evolved: the steel shell method (commonly used in USA) and the concrete box method (used in Europe) (Hakkaart, 1993). More recently, these techniques have merged in the Far East, Hong Kong and Japan.

The resistance of the submerged tunnel against blast load is an important component of the entire structure's safety. Blast load, as one of the accidental loads should be taken into account in the submerged tunnel design. A recent example is a tunnel in Belgium, located near an industrial area, which has been designed for an internal explosion pressure of 0.4 MPa

(Grantz, 1993). A constant blast pressure is applied on the walls of the tunnel, which, however, may oversimplify explosion induced blast load. Since, the experimental studies with respect to this approach can be very expensive and time-consuming, numerical modeling and simulation of explosion inside a submerged tunnel can play an important role to understand the capability of such tunnels against blast load. A case study by considering a submerged reinforced concrete tunnel is presented in the present paper. The tunnel damage by different intensity of the blast load is simulated. The pressure- and velocity-time histories at different locations on the tunnel wall are compared.

2. ANALYTICAL MODEL

2.1 Description of the Problem

The case study considers a submerged tunnel segment with a length of 40 m along the tunnel axis. The internal explosion occurs at the center of the considered segment. Due to symmetry, only half of the tunnel segment (20 m) is simulated. The bottom of the tunnel is fixed, which assumes that it is sit on the seabed. The cross section of the considered submerged tunnel is shown in Fig 1, which is made of reinforced concrete and integrated with three parallel tunnels. The two side-tunnels are used for main incoming and outgoing traffic lines and the center-tunnel is designed as an operational service tunnel. Points 1-4 are selected at the center of the bottom, top, left, and right walls, respectively, in the donor tunnel of an accidental explosion. Points 5-6 are at the floor 3 meters away from point 1. Load on the walls and damage of the tunnel is simulated by using LSDYNA (LSTC, 2003).

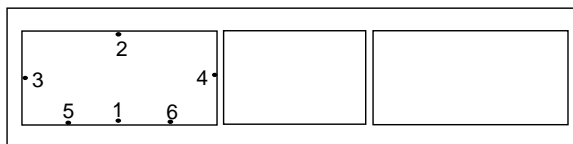


Figure 1: Schematic view of the cross-section of the tunnel

The effect of the water is simplified as a hydrostatic pressure on the external walls of the tunnel. The water-tunnel interaction, however, is not considered. Assuming the water depth above the top of the tunnel is 10 m. Then, the hydrostatic pressure on the top of the tunnel is $1000 \times 9.8 \times 10 = 0.098$ MPa, the pressure on the two sides of the tunnel is $1000 \times 9.8 \times (10 + 9.55/2) = 0.145$ MPa, the hydrostatic pressure on the bottom of the tunnel is 0 since it is assumed to be fixed. The hydrostatic pressure is first applied onto the tunnel until convergence. Blast load is subsequently applied on the inner walls of the donor tunnel.

2.2 Material Model

“Pseudo Tensor Concrete Model”, which is one of most robust material models available for the analysis of concrete structures, is adopted.

This model decouples the volumetric and deviatoric responses; viz. the stress tensor is separated into hydrostatic tensor and deviatoric stress tensor. The hydrostatic tensor changes the concrete volume and the deviatoric one conjugates the distortion or shape deformation. For the hydrostatic tensor, the tabulated compaction equation of state is used and it is linear in internal energy. Pressure variable is defined by

$$p = C(\varepsilon_v) + \gamma T(\varepsilon_v)E \quad (1)$$

in the loading phase, where E is the internal energy per volume, γ is the ratio of the specific heats, ε_v is the volumetric strain and given by the natural logarithm of the relative volume.

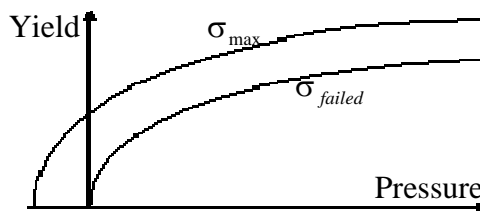


Figure 2: Two-curve concrete strength model

Two curves with respect to the hydrostatic pressure are used to characterize the strength of concrete, which is shown in Fig. 2. The upper curve describes the maximum yield strength of concrete which is defined by

$$\sigma_{\max} = a_0 + \frac{p}{a_1 + a_2 p} \quad (2)$$

the lower curve gives the failure strength which is defined by

$$\sigma_{\text{failed}} = a_{0f} + \frac{p}{a_{1f} + a_2 p} \quad (3)$$

then, the function σ_{yield} which limits the deviatoric stresses is defined as a linear combination of the above described parameters

$$\sigma_{\text{yield}} = \sigma_{\text{failed}} + \eta(\sigma_{\max} - \sigma_{\text{failed}}) \quad (4)$$

where p is the resulted hydrostatic pressure, η is a constant. $\eta = 0.309$ is suggested in the LSDYNA manual (LSTC, 2003) for concrete. The yield surface is mitigating from and σ_{\max} to σ_{failed} .

The effect of reinforcement is simulated by a mixture model. In this model, a reinforcement fraction, f_r , is defined along with properties of the reinforcement material. The bulk modulus, shear modulus, and yield strength are then calculated form a simple mixture rule, e.g., for the bulk modulus,

$$K = (1 - f_r)K_c + f_r K_r \quad (5)$$

where K_c and K_r are the bulk modulus for concrete and the reinforcement material, respectively.

The strain rate effect on the strength of the material is considered by employing a strain rate multiplier. For the mixture model, the strain rate multipliers are obtained from concrete and the reinforcement respectively. Lu and Xu (2004) have given a theoretical model for concrete dynamic strength change with strain rate based on continuum fracture mechanics and

experimental data. The strain rate effect is incorporated by a rate enhancement factor defined as

$$r_c = \frac{3a_1 f_c' r_f + a_2 f_c' r_f^2}{3a_0 a_1 + (1 + a_0 a_2) f_c' r_f} \quad (6)$$

where r_c is the rate enhancement factor at fixed pressure, r_f is the rate enhancement factor for the uniaxial strength, f_c' is the quasi-static compressive strength, and a_i are parameters defining the maximum stress.

The reinforcement dynamic strength change with strain rate is obtained from the equation given by Liu and Owen (1986):

$$\frac{\sigma_d}{\sigma_s} = \lambda \log_{10} \left(\frac{\dot{\epsilon}_d}{\dot{\epsilon}_s} \right) + 1 \quad (7)$$

where σ_d and σ_s are the dynamic and static yield strength; ϵ_d and ϵ_s are the corresponding strain rate, λ is 0.03, ϵ_s is 0.01 for steel.

3. NUMERICAL RESULTS AND DISCUSSIONS

The numerical simulation of the considered submerged tunnel against internal blast load is then simulated. The key parameters, such as the weight of charge (W), vertical distance between the charge and the bottom of the tunnel (D_v), horizontal distance between the charge and the floor center (D_H) are investigated. The damage zone is represented as the area where the plastic strain is above 0.01, shown as red color in the following figures.

3.1 Weight of the Charge (W)

Three cases, i.e. $W=100$ kg, $W=200$ kg, $W=500$ kg are simulated. The damage zone of these three cases is shown in Figure 3. The internal blast induced damage mainly concentrates on the bottom of the tunnel. With the increase of the charge weight, the damage zone is extended to the joint and the ceiling of the tunnel. The ceiling and exterior wall damage may result in disastrous water flood in the tunnel.

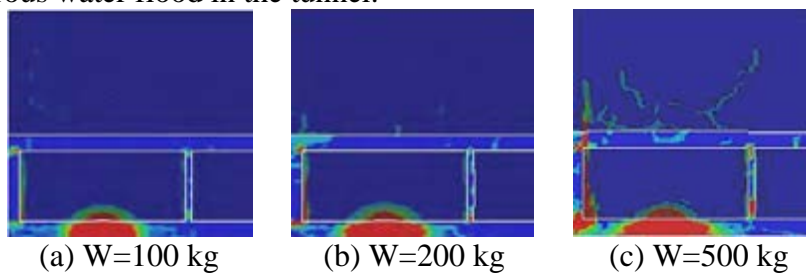


Figure 3: Damage zone with different charge weight

The pressure-time histories of Points 1-4 for these three cases are plotted in Figure 4. It can be seen that the blast-induced pressure is an impulsive load, with a very high peak but a short duration. The peak pressure increases with the charge weight. The peak pressure at point 1 is as high as 145 MPa, which is much higher than those of other points. The simplified uniformly distributed pressure (for example 0.4 MPa) in

submerged tunnel design cannot represent properly the intensity as well as the distribution of the blast load.

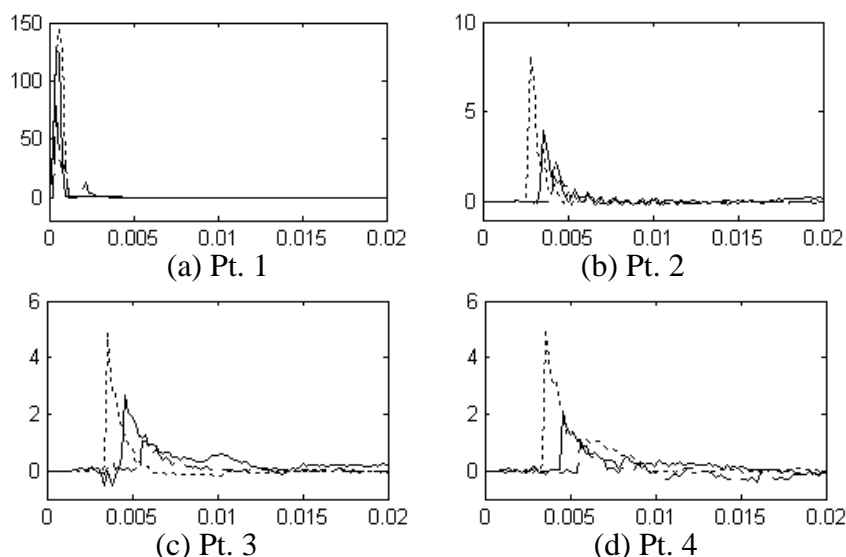


Figure 4: Pressure (MPa) time (s) history of Pt. 1-4 for three cases: $W=100$ kg (dash line), $W=200$ kg (solid line), $W=500$ kg (dot line)

Since PPV (peak particle velocity) is one of the efficient criteria for damage, the velocity time history at points 1-4 for three cases are shown in Figure 5. It is shown again that the PPV increases sharply with the increase of the charge weight and the distribution is significantly uneven.

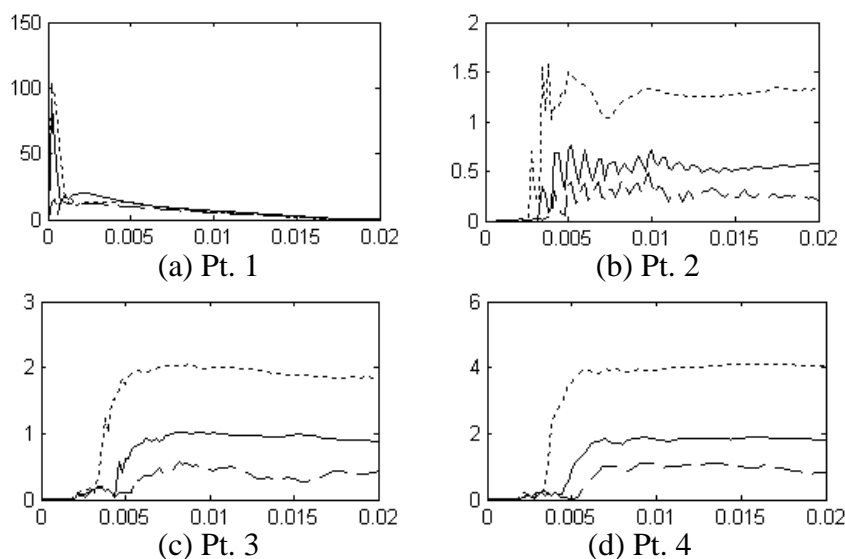


Figure 5: Velocity (m/s) time (s) histories of Pt. 1-4 for three cases: $W=100$ kg (dash line), $W=200$ kg (solid line), $W=500$ kg (dot line)

3.2 Vertical Distance between the Charge and Floor (D_V)

Three cases, i.e. $D_V=0.1$ m, $D_V=0.5$ m, $D_V=1.5$ m are studied to investigate the influence of D_V . The damage zone is shown in Figure 6. When D_V is relatively small (0.1 m), the damage zone is concentrated in a small area right below the charge. When D_V increases to 0.5 m, the damage

zone becomes larger. When the charge is far from the bottom ($D_V=1.5\text{m}$), the damage zone at the bottom decreases, while the damage at the ceiling-exterior wall conner increases.

Pressure-time histories of Pt.1-4 for the three cases are plotted in Figure 7. The maximum peak pressure appears at the bottom of the tunnel and their values are 320 MPa, 144 MPa, 78.3 MPa. The peak pressure of Pt.1 decreases dramatically with the increase of D_V , while the peak pressure of other three points increases with D_V .

Velocity-time histories of Pt.1-4 for three cases are plotted in Figure 8. The maximum velocities appears at the bottom of the tunnel and their values are 98.6 m/s, 88.2 m/s, 7.05m/s respectively for three cases: $D_V=0.1\text{m}$, $D_V=0.5\text{m}$, $D_V=1.5\text{m}$. The velocity at the bottom decreased dramatically with the increase of D_V , while there is only a little increase for the velocities of other places. The damage zone is mainly concentrated at the bottom.

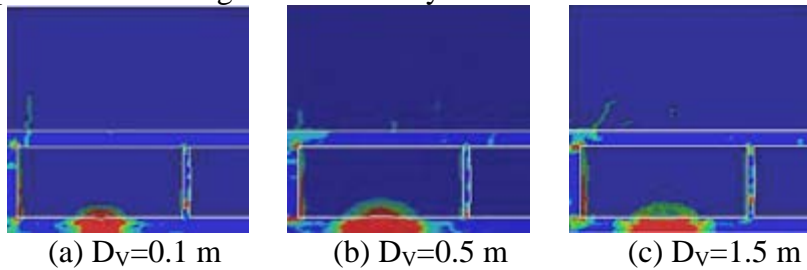


Figure 6: Damage zone in tunnel for three cases

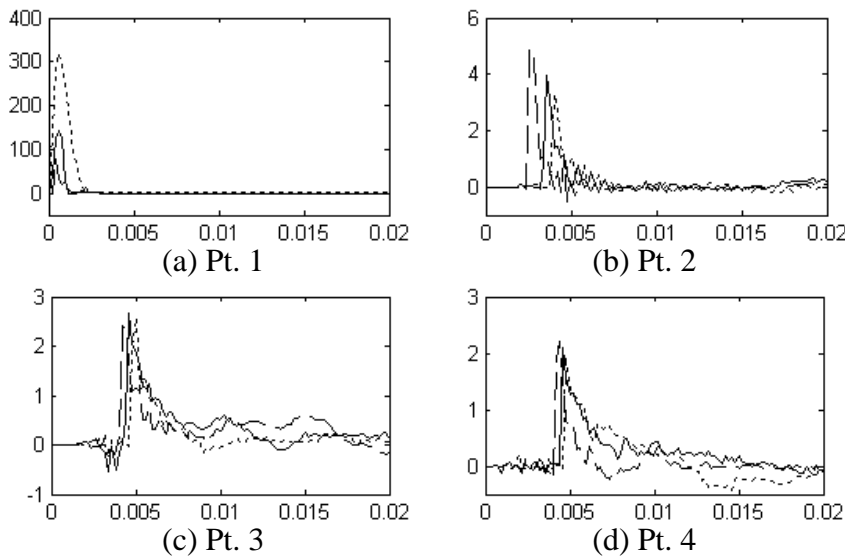
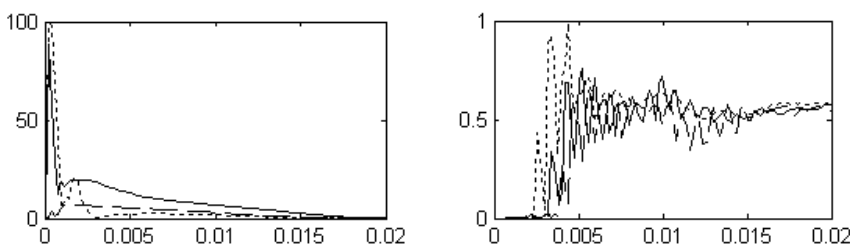


Figure 7: Pressure (MPa) time (s) histories of Pt.1-4 for three cases: $D_V=0.1\text{ m}$ (dot line), $D_V=0.5\text{ m}$ (solid line), $D_V=1.5\text{ m}$ (dash line)



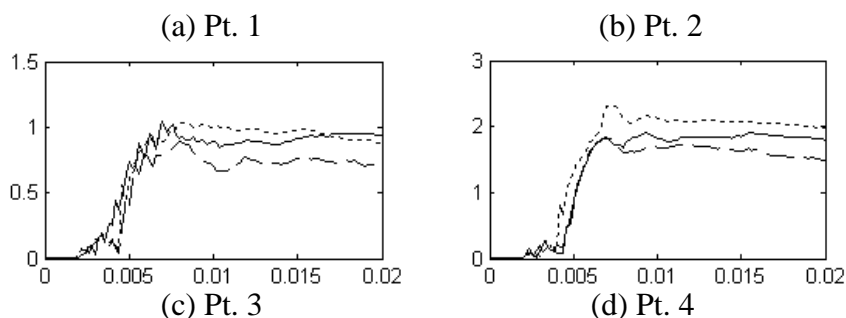


Figure 8: Velocity (m/s) time (s) histories of Pt. 1-4 for three cases: $D_V=0.1m$ (dot line), $D_V=0.5m$ (solid line), $D_V=1.5m$ (dash line)

3.3 Horizontal Distance between the Charge and Floor Center (D_H)

Three cases, i.e. $D_H=-3$ m ('-' means to the left from the center), $D_H=0$ m, and $D_H=+3$ m ('+' means to the right) are studied here. The damage zone corresponding to these three cases are shown in Figure 9. The damage is again mainly concentrated on the floor. When $D_H=\pm 3$ m, the damage in the nearby walls becomes more serious.

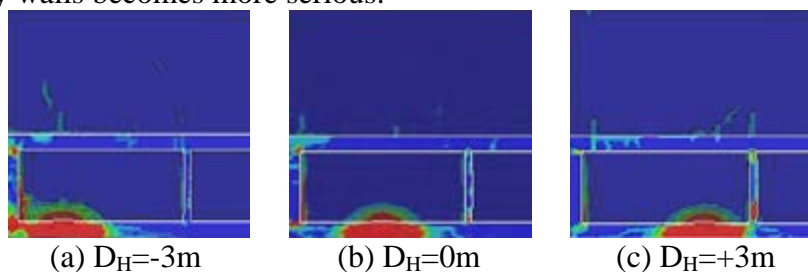


Figure 9: Damage zone in tunnel for three cases

The pressure-time histories of Pt.1 (or 5, 6) –4 are plotted in Figure 10. The maximum peak pressure occurs at the point right below the charge, which is about 150MPa, which is much higher than those of the other three points.

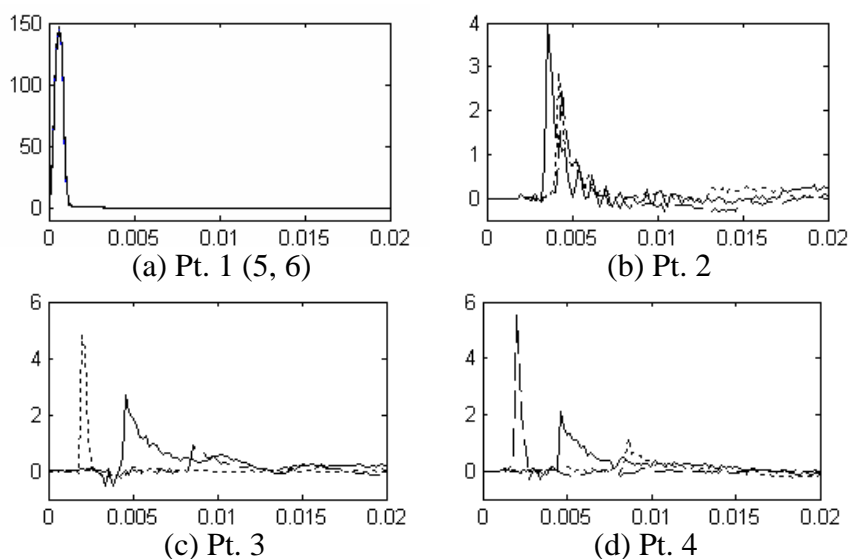


Figure 10: Pressure (MPa) time (s) histories of Pt.1 (or 5, 6) –4 for three cases: $D_H=-3m$ (dash line), $D_H=0m$ (solid line), $D_H=+3m$ (dot line)

Velocity time histories of Pt.1 (or 5, 6) –4 are plotted in Figure 11. The distribution of the velocity around the donor tunnel is again not uniform. The explosion location significantly affects the blast load distribution.

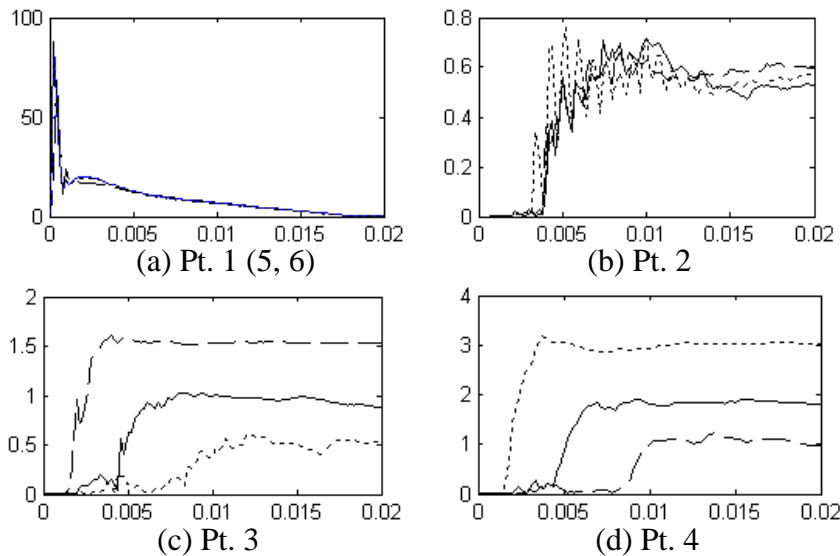


Figure 11: Velocity (m/s) time (s) histories of Pt.1(or 5, 6)-4 for three cases: $D_H = -3m$ (dash line), $D_H = 0m$ (solid line), $D_H = +3m$ (dot line)

4. CONCLUSIONS

In the present paper, numerical simulations of a submerged reinforced concrete tunnel against internal blast load have been carried out. Parametric studies with respect to three key parameters are performed. The tunnel damage induced by different intensity of explosion is simulated. The pressure-and velocity-time histories around the donor tunnel are compared. From this study, following conclusions can be drawn.

- (1) Blast-induced damage in a submerged tunnel is mainly concentrated on the floor but it may spread to ceiling and exterior/interior walls if the explosion is relatively intensive. Under a scale with the equivalent TNT explosive less than 500 kg, the donor tunnel undergoes a certain degree of ceiling damage which may results in disastrous water flood in the donor tunnel. The two parallel tunnels, however, are relative safe without severe damage at the ceiling and the exterior wall.
- (2) Blast-induced pressure is an impulsive load, the peak pressure can be as high as a few hundred MPa but the duration is within a few milliseconds, which is very different from a constant pressure. Maximum peak pressure occurs at the floor bottom of the tunnel, and it is much higher than those of other points. It is oversimplified that the internal blast load is considered as a constant pressure acting on the inner walls of the tunnel.
- (3) It is suggested that the blast load induced by accidental/artificial explosion should be carefully considered in the submerged tunnel design. To prevent severe damage of the submerged tunnel, proper protection measures are required.

REFERENCES

- Grantz W.C., 1993. Chapter 5: Catalog of immersed tunnels, *Tunneling and Underground Space Technology*, Vol. 8, No. 2: 175-263.
- Hakkaart CH. J. A., 1993. Chapter 6: Submerged floating tunnels, *Tunneling and Underground Space Technology*, Vol. 8, No.2: 265-285.
- Liu G.Q. and Owen D.R.J., 1986. Ultimate load behavior of reinforced concrete plates and shells under dynamic transient loading. *International Journal for Numerical Methods in Engineering*, Vol. 22, 189-208.
- LSTC, 2003. LS-DYNA Keyword user's manual, Version 970, Livermore Software Technology Corporation, Livermore, CA.
- Lu Y. and Xu K., 2004. Modeling of dynamic behavior of concrete materials under blast loading, *International Journal of Solids and Structures*, Vol. 41, 131-143.
- Lu Y. Xu K. and Lim H.S., 2003. Numerical simulation of concrete break-up under explosive loading, *Design and Analysis of Protective Structures against Impact/Impulsive/Shock Loads*, pp. 278-286.
- Saveur J. and Grantz W. C., 1993. Chapter 2: Structural design of immersed tunnels, *Tunneling and Underground Space Technology*, Vol. 8, No. 2: 123-139.
- U.S. Department of the Army, 1986. *Fundamentals of Protective Design for Conventional Weapons*, Technical Manual 5-855-1.

FULL-SCALE TESTS OF BLAST DOORS FOR PROTECTION AGAINST EXPLOSION

TAT-SENG LOK and CHEE-HIONG LIM
Protective Technology Research Centre
c/o School of Civil and Environmental Engineering
Nanyang Technological University, Singapore 639798
ctslok@ntu.edu.sg

ABSTRACT

This paper highlights blast doors – these are used to resist the effects of air-blast only – and how these components are tested in full-scale explosion tests. Further, such blast doors may be vulnerable to the effects of fire and fragments. So, secondary tests must be conducted to comply with regulatory authorities. This paper outlines two full-scale explosion tests to assess a number of production blast doors. Testing methodology is described to provide better understanding of the procedure and expectation. Performance of each tested blast door is assessed and survivability is discussed. Detailed outline of the blast doors is presented so that the performance can be compared by designers/engineers who may have conducted similar tests elsewhere.

1. INTRODUCTION

An explosion (e.g. caused by the detonation of high explosives) is essentially a rapid chemical reaction. The consequence of which is the release of a vast quantity of energy in the form of blast wave. Other by-products include heat energy, other gases and traces of unburned products. The most important and damaging component of conventional explosives is the blast wave. If appropriate instrumentation were positioned perpendicular to and facing the detonating source, then a pressure-time history would be recorded. The characteristic of the pressure-time history is a rapid rise in pressure of several bars above atmospheric pressure with a subsequent decay occurring over a short duration, perhaps in the order of a few milliseconds. Thereafter, a negative phase (suction) occurs. This characteristic exposes the violent nature of a chemical process.

Such hazards are often associated with acts of terrorism in mega cities and built-up urban areas but there are other sources of explosions that have similar effects and consequences. For example, explosions derived from a rapid burning process of oil-based products (petroleum refining facility), confined gas (offshore natural gas) and coal/powdery dust (flour, cement and pharmaceutical products).

Pressure generated from an explosion impinges on every object in the path of the expanding gas. The behaviour of the shock front and the effects of explosions are well documented [Baker, 1973; Mays and Smith, 1995]. Thus, engineers need to be aware that the blast loading will cause buildings to deflect, and the response is governed by the flexural stiffness of the combined beam/column joint action and in-filled components. Therefore, it is essential for engineers to design structures or components with due care.

In the past, small-scale tests [Lok and Xiao, 1999] were designed to obtain blast parameters. However, studies showed that size effect has a significant influence on pressure readings and material response. So, full-scale tests [Gould and Higgs, 2000] were considered important, especially in validating blast-resistant glazing, doors and blast valves in buildings and infrastructure systems to ensure that designs are responding to the specific stimulus.

This paper outlines a programme of research and development of blast doors at the Protective Technology Research Centre. As part of the study, full-scale field trials were conducted. Two explosion tests were designed to investigate the performance and response of a number of production blast-resistant doors. The tests were conducted at two separate locations in Australia. A number of secondary studies were also designed to determine the response of “seating” door arrangement. Details of the set-up, types of doors and observation of the performance are presented.

2. FULL-SCALE TEST USING SMALL CHARGE WEIGHT

2.1 Sandwich blast doors

Most blast doors are constructed using a sandwich form. This system promises high strength to weight and high stiffness to weight ratios compared with other structural sections. Sandwich construction is characterised by two flat sheets with a core separating but firmly attached to the sheets, and sandwich blast doors have been used extensively in important buildings and military facilities.

In this test, five different sandwich blast-resistant doors were subjected to an explosion from the detonation of 100 kg of high explosives. Details of the blast doors are summarised in Table 1 and the sandwich doors are shown in Figures 1 to 4.

Figures 1 and 2 are single leaf doors while Figures 3 and 4 are regarded as double-leaf doors. The arrangement of the double-leaf door shown in Figure 3 may be regarded as two single-leaf doors. The doors were installed into standard steel frames with its attendant silicon rubber seal around the perimeter of the rebate. These doors, together with the frame, were manufactured in a high-precision factory and transported to the test site in Australia.

Table 1: Description of blast doors.

No.	Door ID	Description
1	Door #1	Single leaf door – fabricated with horizontal aluminium truss-core [Lok and Cheng, 2000] sections. Core sections span horizontally across the width and door is wrapped in 0.8mm thick mild steel facing sheet.
2	Door #2	Identical construction as Door #1
3	Door #3	Large single-leaf “C” core door – fabricated entirely from mild steel sections. Channel sections use as core, span vertically across the height.
4	Door #4	Double-leaf blast channel-core door – each leaf measures 1075mm wide by 2600mm high. Central mullion built into frame. Doors are effectively single-leaf blast doors. Channel core spans vertically.
5	Door #5	Fabricated exactly as Door #4 but without a central mullion – vertical edge of one door is stiffened and acts as the “central mullion”. Channel sections as core, span vertically across the height.

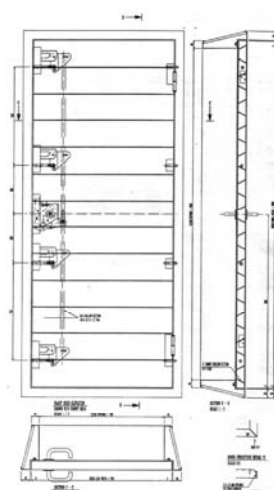


Figure 1: Door #1

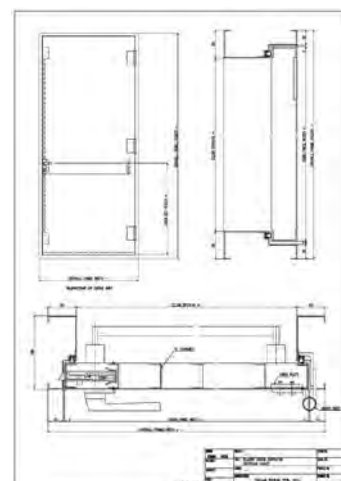


Figure 2: Door #3

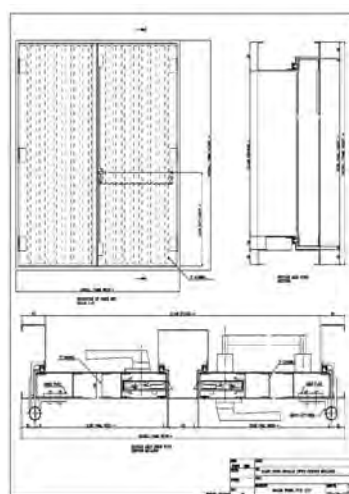


Figure 3: Door #4

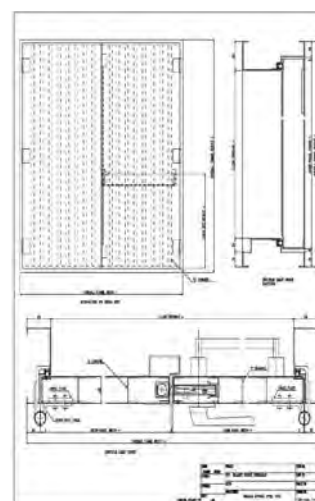
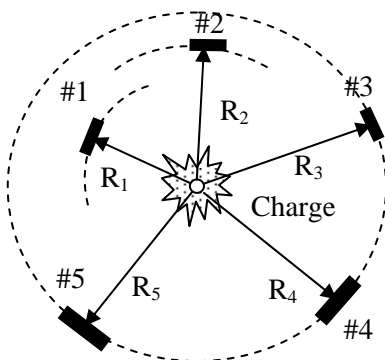


Figure 4: Door #5

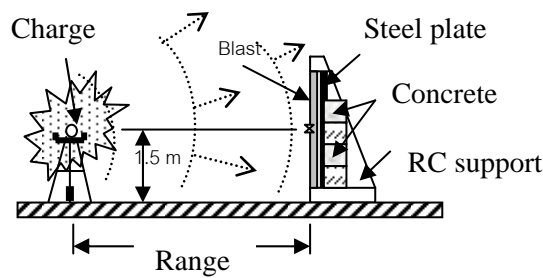
2.2 Test site arrangement

To obtain the designed pressure from the explosion, each door was arranged at the perimeter of circles as shown in Figure 5(a). Five heavily reinforced concrete “open” supports were designed to accommodate the frame/door set. The distance (range) of each door was obtained by estimating the incident and reflected overpressures from the detonation of the 100 kg bare TNT equivalent charge. Estimated overpressures are shown in Table 2. The test was conducted at the Proof and Experimental Establishment in South Australia.

Blast waves flow around rigid objects at relatively high speed. So, depending on the shape of the rigid object, turbulence and eddys form at the leading edge of objects. These flows could interfere with the front and rear face of an open support structure. To prevent the engulfing blast wave from affecting the response, a 25mm thick steel plate was installed at the rear of the supports. This plate was sandwiched between the concrete opening and a stack of four *pendine* concrete blocks – Figure 5(b).



(a) Plan view of site



(b) Elevation of support arrangement

Figure 5: Test arrangement and target layout

Table 2: Estimated and recorded peak blast overpressures

Door No.	Range (R)	Estimated overpressure (kPa)		Measured overpressure (kPa)	
		Incident	Reflected	Incident	Reflected
(1)	(2)	(3)	(4)	(5)	(6)
#1	10.0 m	241	851	---	1406
#2	12.3 m	150	461	---	491
#3	17.9 m	70	178	81	227
#4	17.9 m	70	178	81	302
#5	17.9 m	70	178	81	---

2.3 Explosion testing

Pressure transducers and accelerometers were installed on the reinforced concrete frames and blast doors. One additional pressure transducer was installed to record the side-on free-field incident

overpressure. The data was recorded on personal computers linked by ground cables 300 metres from the site. Figure 6 shows the set-up of the 100 kg of bare PE4 (TNT equivalent) charge prior to detonation. Three hundred and sixty-five sticks of PE4 were arranged in a circle. A single booster with a detonation cord was placed in the middle of the pack.



Figure 6: Arrangement of explosives and relative position of target

2.4 Test Results and performance of blast doors

After the detonation, blast overpressures were successfully recorded on all the instrumentation. The recorded incident overpressure at 17.9 m from the charge is shown in Fig. 7. This recorded incident overpressure was used to check the accuracy of the estimated pressure-time data (70 kPa).

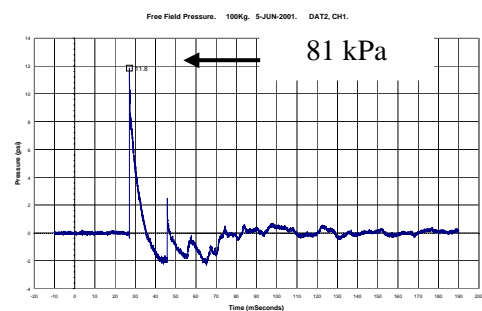


Figure 7: Pressure-time history

The estimated peak free-field overpressure shown in Table 2 underestimated this recorded value by about 14%. Measured normally peak reflected overpressure at Door #1 was 65% higher than the estimated designed pressure. This blast door was positioned closest to the explosive source. At this distance, it would require about 165kg of TNT (equivalent) to yield the same overpressure of 1406 kPa over 11.2 millisecond duration.

Generally, the measured overpressures are of a similar trend as designed values. Although the hinges, shear pins, facing sheet and internal aluminium truss-core units of Door #1 were not damaged, the locking system was torn from the panel. However, the facing sheet was undamaged. This door was positioned closest to the source of the explosion. The measured normally peak reflected overpressure was over 14 bars; which was 65% above the designed overpressure. Figures 8 to 11 show the post-test front view of blast doors #2, #3, #4 (with central mullion) and #5 respectively. All the doors survived the test and the silicon rubber seals around the frame rebate were also intact.



Figure 8: Door #2



Figure 9: Door #3



Figure 10: Door #4



Figure 11: Door #5

3. FULL-SCALE TEST USING LARGE CHARGE WEIGHT

From the previous test, the merits of a “composite” sandwich blast door fabricated from a special extruded hollow aluminium truss-core section were demonstrated. However, the cost of the truss-core aluminium extrusion was high. Consequently, an investigation was undertaken to consider an alternative core-section for the sandwich door with similar strength/stiffness characteristics. An aluminium hollow rectangular core section was selected because this section was generally available. A similar lightweight sandwich blast door panel consisting of steel facing sheets with aluminium hollow rectangular sections as the core was derived. Altogether, five blast doors were fabricated and tested in this second trial, consisting of:

- 3 number lightweight housing shelter blast doors (herein identified as Door #6, Door #7 and Door #8).
- 1 number all-steel blast/ballistic-resistant ammunition storage sliding door (Door #9).

- 1 number all-steel internal “unseated” blast- and fire-resistant doors (Door #10).

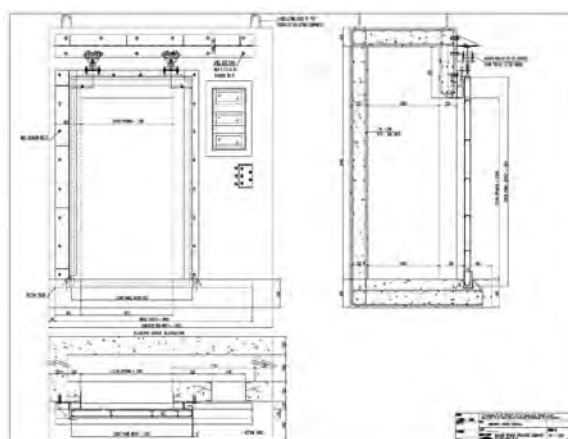
The five blast doors were tested at the Woomera Protected Area in South Australia. To reinforce understanding of structural behaviour of the sandwich system, numerical analyses of these door subjected to the explosive loading was also conducted. The results of the numerical study provided information on the response history and performance of a number of preliminary designs. In the numerical analyses, material non-linearity was included to account for the high-intensity explosive loading.

3.1 Fabrication of blast doors #6, #7 and #8

Three single-leaf doors were fabricated in an identical manner using aluminium rectangular core sections and wrapped with thin mild steel facing sheets. Short lengths (approximate widths of the door opening) of the rectangular section were cut to form the dimension of the door width. Thin steel facing sheets were then glued to the core sections. Various fixtures (e.g. locks, hinges, shear pins) were installed prior to sealing. Overall dimensions of the three doors were 1000mm wide by 2152mm high. The core units were 2.0mm thick extruded aluminium hollow rectangular sections. Thickness of the facing sheets varies with the distance from the centre of the charge. The thicknesses were 1.0mm, 1.5mm and 3.0mm for the doors furthest to the closest point measured from ground zero respectively. Three large reinforced concrete “box” frames with reinforced masonry side/back walls were constructed to house the door. A standard steel door frame was cast in-situ during concreting.

3.2 Details of blast doors #9 and Door #10

Details of two other all-steel blast doors are shown in Figures 12 and 13. In both these doors, a number of glazing component was also tested. For Door #9, three glazing units were built into the reinforced concrete box structure. A single cavity vision panel was installed in Door #10.

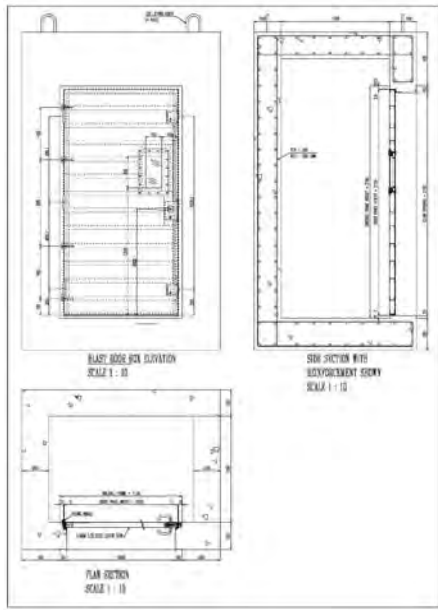


(a) Outline for construction



(b) Set-up at test site

Figure 12 (Door #9) – All-steel sliding blast door (ammo storage)



(a) Outline for construction



(b) Set-up at test site

Figure 13 (Door #10) – All-steel internal “unseated” blast door

Instrumentation of all the blast doors was completed and checked on site. All the five blast doors were subjected to a single detonation from a 5-tonne TNT (equivalent) explosion. The door targets were positioned as shown in Figure 14 to accept the designed air-blast loading. Computed overpressures and positive phase duration were calculated and shown in Table 3. Once the targets were checked, the area was evacuated and all personnel were requested to clear the site until after the detonation. Figure 15 shows an aerial view of the detonation. The fireball was observed at 6 km from ground zero.

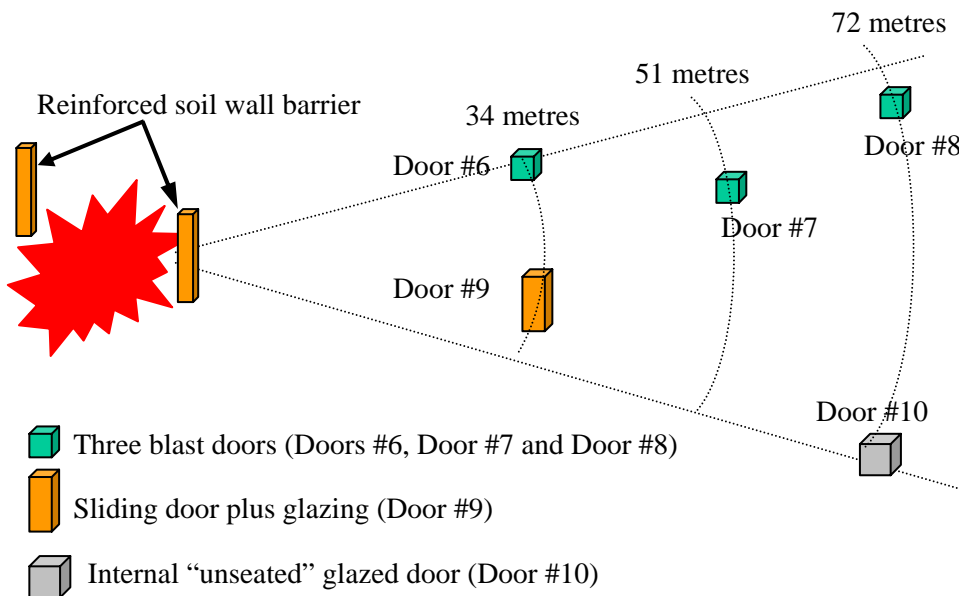


Figure 14: Test site layout of blast door targets

Table 3: Estimated pressure-time values

Pressure loading on	Distance (m)	Normally peak reflected overpressure (bars)	+ve phase duration (milliseconds)
Door #6 & #9	34	10.75	29
Door #7	51	3.36	60
Door #8 & #10	72	1.45	107

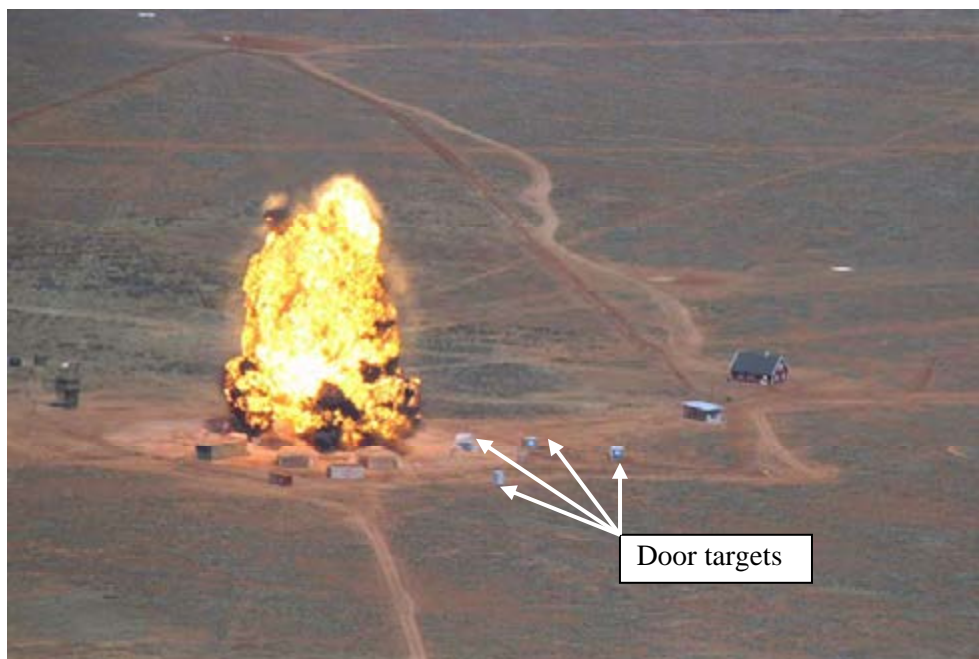


Figure 15: Aerial view of fireball following the detonation

3.3 Results of test

All the blast doors survived the explosion. However, rippling of the facing sheets was clearly observed on Door #6, #7 and #8. Details of the recorded maximum air-blast overpressures and durations are shown in Table 4. It can be seen that all recorded peak reflected overpressures are lower than the estimated blast overpressures shown in Table 4.

Table 4: Recorded peak overpressure and duration

Pressure loading on	Distance (m)	Normally peak reflected overpressure (bars)	+ve phase duration (milliseconds)
Door #6 & #9	34	4.17	25
Door #7	51	1.82	45
Door #8 & #10	72	1.03	50

Although the blast doors were designed to sustain the initial higher estimated peak overpressure, damage was observed to be excessive for Doors #6 and #7. This is due to a number of reasons but the most likely reason was that the doors were improperly fabricated and not manufactured to specification. Due to time constraints, many issues were not resolved

before the doors were transported to and installed in Australia. De-bonding of the surface sheet from the aluminium core was noticeable prior to the test.

4. CONCLUSION

The performance of production blast doors subjected to two full-scale explosion tests has been investigated. Despite the high costs, full-scale blast tests are necessary to identify design faults and to inspire confidence of users. No amount of computer analyses can substitute a full-scale test or the response of the shear pin/locking system. The cost to lives and investment confidence would be higher if faults were not identified or corrected prior to installation of such components in buildings and important facilities in major cities and urban areas. The tests provide a significant learning opportunity to better understand the mechanics of real situations in an explosive environment.

5. ACKNOWLEDGEMENT

The authors wish to acknowledge the financial and other forms of assistance provided by the Defence Science and Technology Agency, Protective Technology Research Centre (NTU), Major Warren Smith and Mr John Carley (from the Proof and Experimental Establishment), Mr Craig Hoing (Chief UK Scientist, Ministry of Defence) and Major Keith Parker (Woomera Protected Area).

REFERENCES

- Baker, W.E., 1973. *Explosions in air*. University of Texas Press, Austin and London.
- Gould, M.J.A, and Higgs, Q., 2000. *UK/Australian 40t donor/acceptor trial housing damage and quantity-distance assessment*. Proc 16th Int. Symp. on Military Aspects of Blast and Shock, Keble College, Oxford, Sept, 201-216.
- Lok, T.S. and Xiao, J.R., 1999. *Steel fibre reinforced concrete panels exposed to air blast loading*. Proc ICE Structs & Bldgs, Vol 134, Nov, 319-331.
- Lok, T.S. and Cheng, Q.H., 2000. *Free vibration of clamped orthotropic sandwich panel*. Jour of Sound and Vibration, Academic Press, Vol 229, No 2, Jan, 311-327.
- Mays, G.C. and Smith, P.D. (Ed.), 1995. *Blast effects on buildings – design of buildings to optimize resistance to blast loading*. Thomas Telford, London, UK.

STUDY ON OPTIMUM DESIGN METHOD FOR PLEASANT OUTDOOR THERMAL ENVIRONMENT USING GENETIC ALGORITHMS (GA) AND COUPLED SIMULATION OF CONVECTION, RADIATION AND CONDUCTION

HONG CHEN, RYOZO OOKA, SHINSUKE KATO
Institute of Industrial Science, University of Tokyo,
4-6-1 Komaba Meguro-ku, Tokyo, Japan
chenhong@iis.u-tokyo.ac.jp

ABSTRACT

A lot of research has recently been conducted into improving outdoor thermal environments in summer. In this paper, (1) an optimum design method with Genetic Algorithm (GA) and coupled simulation of convection, radiation and conduction for comfortable outdoor thermal environments is developed; (2) in order to examine the validity of the proposed optimum design system, apartment block space in an urban area is set as an analysis target and the optimum arrangement of trees is analysed for pleasant outdoor thermal environment design. For the optimum arrangement of trees, two cases which are different in target area are examined to clarify the effect of different target areas (all open space or pedestrian road) on optimization. As a result, the optimum arrangements of trees are given using GA and simulation, and the validity of the optimum design method is confirmed.

1. INTRODUCTION

In recent years, with increasing urbanization, the heat island phenomenon has become significant and a deterioration in the outdoor environment as a result of heat islands and similar phenomena has become a serious problem. In an attempt to improve the outdoor thermal environment in summer, a lot of research has taken place in the fields of urban planning, architectural design, and environmental engineering. The relief effect on the outdoor thermal environment of the arrangement of planting has attracted attention from the point of view of promoting latent-heat evaporation and solar shading (Hagishima et. al., 1999, Yoshida et. al., 2000). However, most of these researches have been concerned with the development of an evaluation method to measure the effect of these techniques on the outdoor thermal environment. An optimum design method for the outdoor thermal environment has not yet been developed sufficiently.

Although appropriate planting arrangements become very important factors in designing a comfortable outdoor thermal environment, these arrangements are actually often made empirically, from the varying standpoints

of conventional planning concepts or landscape design. There is almost no example of research into the optimum design method for a pleasant outdoor thermal environment. On the other hand, for the designer, it would be very useful to develop an optimum design method. However, in order to determine which design is actually "the optimum", it would be necessary to examine the effect of all possible designs. In this case, the potential number of cases to be examined becomes almost impossibly large. Researches into the optimum design method, which sets out to maximise the evaluation function value used as a design target, have reached an early stage in the fields of structural and architectural design (Mitsui et. al., 1994, Okamoto et. al., 1993, Aoki, et. al., 1996) and, recently, researches in optimum design have also been introduced for designing air-conditioning in the environmental engineering field (Kim et. al., 2001). A similar approach is possible for outdoor thermal environmental design. In the present situation, when an improvement of the outdoor thermal environment in summer is urgently required, an optimum design method concerned with the arrangement of planting so as to improve the outdoor thermal environment needs to be developed. However, it could be considered that one of the reasons that these optimizations have never been handled as an engineering problem hitherto is that the engineering design method has not been sufficiently developed. In this research, an optimum design method for planting arrangements to improve the outdoor thermal environment in summer is proposed as the 1st step of research into the outdoor optimum design method. In future, a multiple-object optimum design method incorporating other factors will be examined.

In this research, the authors concentrate on human thermal comfort in an outdoor space; an optimum design method using a coupled simulation of convection, radiation and conduction is examined in connection with planting arrangements for a pleasant outdoor thermal environment. Genetic algorithms (GA) (Kitano et. al., 1993) are used for an inquiry into the optimum solution.

2. OPTIMUM DESIGN SYSTEM

2.1 Composition of Optimum Design System and Optimum Inquiry using Genetic Algorithms

Figure 1 shows a flow-chart of the optimum design system for the outdoor thermal environment using Genetic Algorithm (GA) and coupled simulation of convection, radiation and conduction. This optimum design system is composed of the following three parts: (1) Optimization problem set up by the designer. (2) Numerical analysis of the outdoor thermal environment using

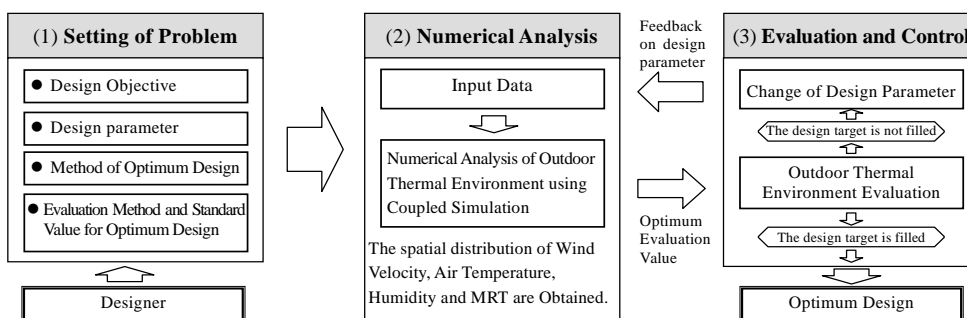


Figure 1 The Composition of the Optimum Design System

coupled simulation of convection and radiation. (3) Evaluation of the optimum solution candidate and control of the optimum inquiry process by GA. Here, in the first part, the design objective and the design element for the optimum design are determined. The optimum design methods, the method for quantifying the outdoor thermal environment and the standard value for selecting the optimum solution candidate are also determined at this stage. In the second part, the spatial distribution of wind velocity, air temperature, humidity and MRT (Mean Radiation Temperature) of a candidate are calculated and the spatial distribution of the optimum evaluation value is calculated from the above results. (In this research, the SET*, New Standard Effective Temperature, which is the comprehensive index of human thermal comfort (Gagge et. al., 1986), is employed.) In the third part, it checks whether the optimum evaluation value of the optimum solution candidate computed in the second part corresponds with the standard value for selecting the optimum solution candidate determined in the first part. When the outdoor thermal environment does not satisfy the design objective, the combination of design variables is changed, and the optimum inquiry is advanced by feeding back this combination of design variables to the second part. Eventually, when the evaluation values of the outdoor thermal environment satisfy the design objective, the feedback is ended at the second part. The value of the design parameter at this time becomes the optimum value.

In this research, the numerical analysis method of outdoor thermal environment which the authors developed is used in the second part (Chen et. al., 2004).

In the third part, the genetic algorithm (GA) is used to select optimum solution candidates and control the optimum inquiry process. In this research, a more efficient Genetic Algorithm called a "Multi-island Genetic Algorithm" is used in this research (Tanese et. al., 1989). Figure 2 shows the concept of multi-island genetic algorithm. The method is a distributed genetic algorithm. The feature of this method is that the population in one generation is divided into several sub-populations, and the genetic operations are performed independently in each sub-population. The exchange of individual information that is called "migration" is generated periodically between sub-populations.

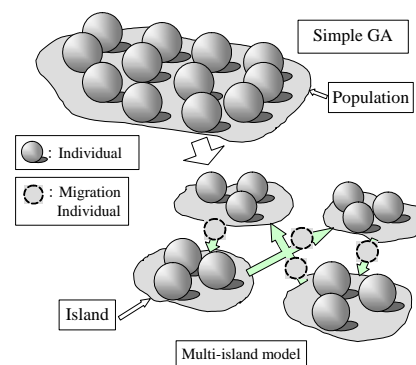


Figure 2 The Concept of Multi-Island Genetic Algorithm

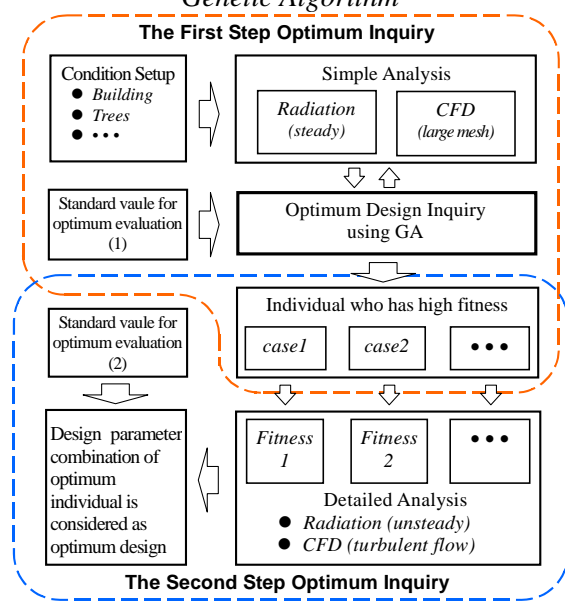


Figure 3 Two-step Type Optimum Design Method

2.2 Two-step type optimum design method

If the detailed coupled simulation of convection, radiation and conduction is performed on all the individuals in the optimum inquiry process described in the foregoing paragraph, the calculation load becomes huge and is unsuitable for a practical design process. Thus, a two-step type optimum design method is used in this research. The two-step type optimum design method is divided into a 1st step inquiry where high-ranking individuals are extracted with a fairly rough calculation and a 2nd step inquiry where the optimum individual is chosen by more detailed analysis from among the group of highest-ranking individuals identified in the 1st step inquiry. Figure 3 shows the flow chart of the two-step type optimum design method.

(1) *1st step inquiry:*

The radiation analysis is performed under steady state conditions. The laminar and isothermal CFD simulation is performed with coarse meshes. From among all the optimum solution candidates, the individual for which the evaluation value exceeds the optimum evaluation standard value becomes the candidate for the 2nd stage inquiry.

(2) *2nd step inquiry:*

The detailed coupled simulation of convection and radiation is performed on the candidate for the 2nd step inquiry. The spatial distribution of air temperature, wind velocity, relative humidity, and MRT are calculated, and the objective function is calculated. In this step, the radiation analysis is performed under unsteady state conditions, and the CFD simulation is performed with small meshes.

(3) Among the candidates analyzed in the 2nd step inquiry, the candidate which has the highest fitness is regarded as the optimum individual, and the design parameter combination of this individual is considered as the optimum design.

3. APPLICATIONS OF THE OPTIMUM DESIGN SYSTEM ON OUTDOOR THERMAL ENVIRONMENTAL DESIGN

3.1 Design Objective

This research sets the optimization problem of the outdoor thermal environment with the optimum arrangement of trees in summer as its design objective. In concrete terms, it investigates the optimum arrangement of trees, where the spatial integration of the spatial distribution of the objective function described later is to be maximized.

3.2 Analysis Target

Figure 4 shows the building block model. The block is composed of the same shaped buildings (20m(L) × 20m(W) × 30m(H)). 15:00 on July 23rd is targeted as the date for analysis. The sun's altitude is 45.1°, the wind direction is south, the wind velocity is 3.0m/s at a height of 74.6m, and the air temperature and relative humidity are set at 31.6°C and 58%. In addition, the number of the trees is fixed at eight in this model. The tree height and tree crown diameter are assumed to be 7m and 5m respectively. In this research, the tree model developed by Yoshida et al. (Yoshida et. al., 2000) is employed for coupled simulation.

3.3 Design Parameter

The position of the tree in the analysis domain is assumed to be a design

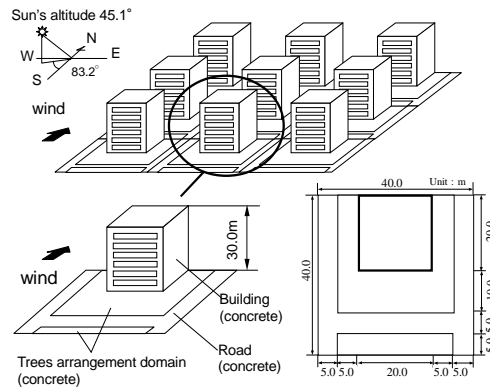


Figure 4 Analysis Target

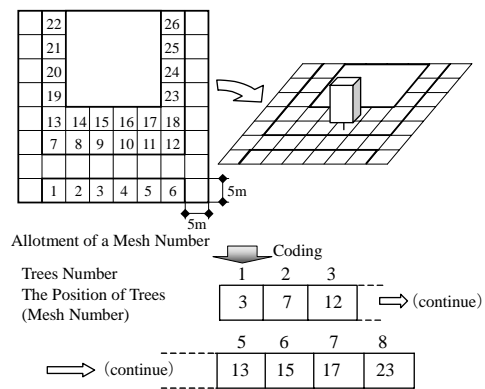


Figure 5 Chromosome's Describing Method

parameter in this research. In practical terms, the number of the mesh in which a tree is positioned among the possible 26 meshes in the analysis domain is assumed to be a design parameter.

3.4 Objective Function

The evaluation of optimization proceeds by the following method. A comparison is performed between the spatial distribution of SET* in the basic case where there are no trees and in the case where eight trees have been arranged. The improvement level of the outdoor thermal environment with the arrangement of trees is evaluated by the decrease in the value of SET*. The objective function (the fitness) is defined by the following equation:

$$F_{total} = \sum \{B_j - D_j\} \tag{1}$$

where, F_{total} is the objective function (fitness), B_j is the value of SET* at point j in the basic case, and D_j is the value of SET* at point j in the case where trees are arranged. In this research, the optimum arrangement of trees that has the maximum value of spatial integration of objective function in the outdoor thermal environment is set as a design objective.

3.5 GA Parameter and Chromosome Description Method

Table 1 shows the GA parameter used in this research. The size of sub-population is 10, the number of islands is 6, and the population size is $10 \times 6=60$. The number of generations is 12, and the total number of individuals analysed in the inquiry process becomes $60 \times 12=720$. The selection used the method of tournament selection, which repeatedly selects the individual with the highest fitness from two or more individuals chosen at random. The rate of a tournament is set as 0.4. The crossover is simple crossover, the rate of crossover is 1.0, and the rate of mutation is 0.02. In addition, the rate of migration and the interval of migration are set at 0.5 and 2 respectively.

Figure 5 shows the chromosome description method. The arrangement problem of trees is becomes the problem of which eight cells should be selected from the 26 cells available for the positioning of trees in the two dimensional plan. One tree is assumed to be a "Unit", and "Tree number" is set respectively. The chromosome is set to a sign row that describes the position of each tree in the row (using the mesh number defined in Figure 5). Usually, the chromosome is described with a binary mark, and a "0" or "1" is written at the appropriate

Table 1 GA Parameters

Size of Sub-Population	10
Number of Islands	6
Population Size	60 (10×6)
Number of Generations	12
Total Individual Size	720 (60×12)
Rate of Migration	0.5
Interval of Migration	2
Rate of Tournament	0.4
Rate of Crossover	1.0
Rate of Mutation	0.02

Table 2 Analysis Case

Case 1-0	Basic case (trees are not arranged)
Case 1-1	The whole outdoor domain is targeted (The horizontal plane at 1.5m height in the analysis domain).
Case 1-2	The road area (human activity domain) is targeted (The horizontal plane at 1.5m height in the pedestrian road).

locus. In this research, the chromosome is defined by each mesh number being changed into a binary mark that is written in the corresponding locus.

3.6 Analysis case

Table 2 shows analysis case. In order to clarify the effect of different target areas (all open space or pedestrian road) for the optimization, the following 3 cases are analysed. (1) case1-0 is the basic case, in which trees are not arranged. (2) case1-1 deals with an entirely open space. In other words, it is evaluated using the sum total of SET* at each point (at 1.5m height) throughout the whole open area. (3) case1-2 applies only to the domain for human activities. Namely, it is evaluated using the sum total of SET* at 1.5m height on the pedestrian road.

3.7 Analysis Procedure

In this research, the analysis procedure shown in Figure 2 is used. The laminar and isothermal CFD analysis is performed with coarse meshes in the 1st step inquiry. In this step, the spatial distribution of air temperature and relative humidity are assumed to be constant throughout the whole analysis space. Among all of the individuals, ten candidates are selected for the 2nd step inquiry. Moreover, the spatial distribution of SET* for the basic case is calculated respectively in two step inquiries and is adopted as the standard value for optimum evaluation at each stage.

4. ANALYTICAL RESULTS AND CONSIDERATIONS

4.1 1st Step Inquiry

Figures 6 and 7 show the optimum inquiry processes of cases1-1 and 1-2 with GA in the 1st step inquiry. The horizontal axis represents the Run Counter of the optimum inquiry process, and the vertical axis is the objective function (SUMSET). As a trend, we can see that the objective function of the individual becomes higher with the optimum inquiry process.

The results of optimum inquiry (up to 5th highest rank) in cases1-1 and 1-2 are shown in Figures 8 and 9. The sun azimuth of Tokyo is west-south-west at 3:00PM on July 23rd and the surface temperature of the building on the west and south sides becomes high. In order to reduce MRT (Mean Radiant Temperature) in both cases, there is a tendency for trees to be arranged on the west and south sides of the building because the sun is located in a south and west direction in the afternoon. The trees are arranged in a rather scattered fashion in the case1-1 that deals with the whole open area. But in contrast to case1-1, in case1-2 that pays attention only to the road area the trees are gathered near the pedestrian road.

4.2 2nd Step Inquiry

The 2nd step inquiry is performed for ten individuals chosen by 1st step inquiry in cases1-1 and 1-2. The optimum individuals chosen by the detailed simulation of convection, radiation, and conduction are shown by the patterns of tree arrangement surrounded by a dotted line in Figures 8 and 9. The thermal environment of the optimum design for cases1-1 and 1-2 are shown in

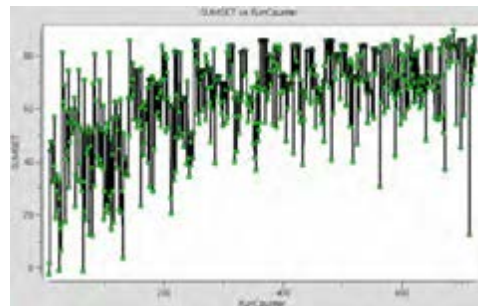


Figure 6 case1-1 The Optimum Inquiry Process

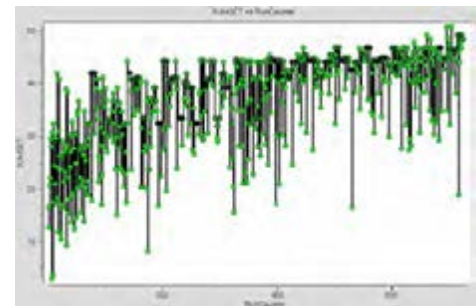


Figure 7 case1-2 The Optimum Inquiry Process

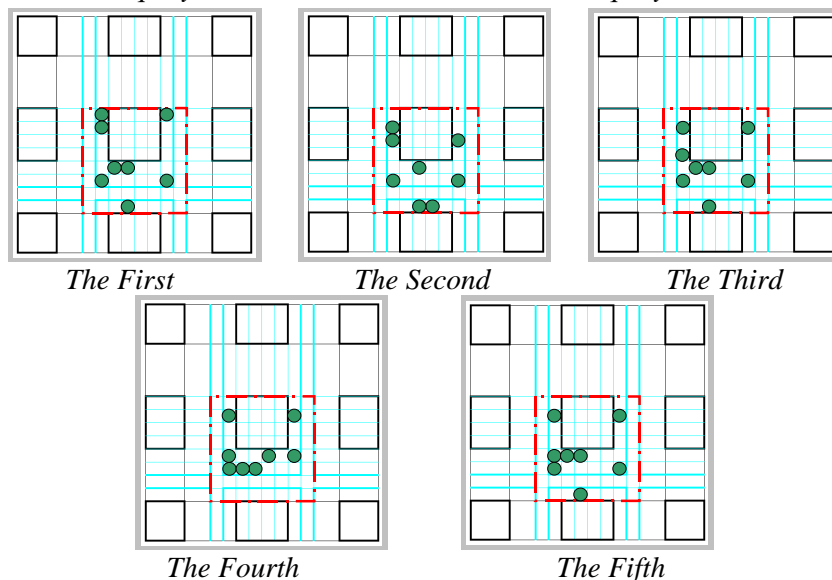


Figure 8 case1-1 The Results of Optimum Inquiry in 1st Step (up to 5th high rank)

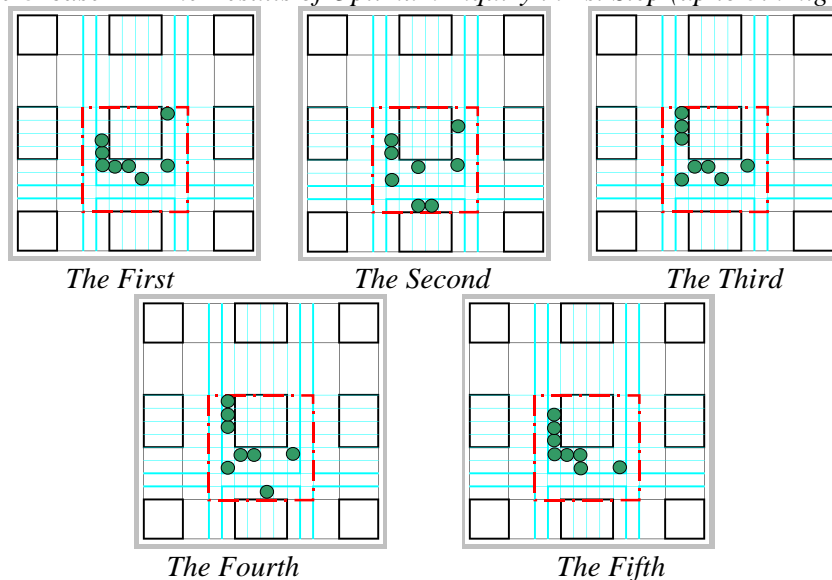


Figure 9 case1-2 The Results of Optimum Inquiry in 1st Step (up to 5th high rank)

Figure 10 and 11. Considering the average value within the analysis domain, the air temperature of case1-1 is about 0.5°C higher than that of case1-2, and along with a higher air temperature, the relative humidity of case1-1 is lower by about 3% than that of case1-2. The wind-velocity scalar value of case1-1 is higher by about 0.04m/s, and MRT of case1-1 is lower by about 0.5°C, than those of case1-2. The average value of SET* at 1.5m height in the whole open area and the road is shown in table 3. Compared with the basic case, SET* decreases in both case1-1 and case1-2, and the outdoor thermal environment relief effect from the arrangement of trees is recognized. Moreover, in case1-1, although average SET* for the whole open area is lower than that of case1-2, average SET* in the road area becomes higher. It is apparent that the difference in target domain has had a significant influence on the result of the optimum inquiry.

In order to reduce MRT, although it might be expected that all trees would be arranged on the south and western sides of a building in the optimum individual, some trees (No. 25 of case1-1, No. 3, 4 and 25 of case1-2) are in fact arranged on the eastern and northern sides of the building in both cases. This is considered to be for the following two reasons. For example, the individual in which trees are arranged like the third place in the 1st step inquiry of case1-2 is similar to two optimum individuals in case1-1 and case1-2. (1) In case1-1, the authors consider the whole open area for the objective function. Although MRT becomes a little higher in the optimum individual (individual of the 4th place in the 1st step inquiry) in case1-1, a circulation flow occurred in the building canyon space because trees are concentrated on the southwest corner in the building canyon, and wind velocity is increased in the building canyon in the optimum individual in case1-1. Moreover, although the tree in No.25 mesh does not shade direct solar radiation, MRT is decreased in the neighboring area of the tree because reflected solar radiation and long wave radiation from the wall are shaded. Therefore, SET* of the individual in the 4th place in the 1st step inquiry becomes low, and this becomes the optimum individual for the 2nd step inquiry. (2) In case1-2, the authors pay attention to the pedestrian road area in the analysis domain for the objective function. Since the sun azimuth at analysis time is in the west-south-west, the road area does not become shaded if trees are arranged in the western and southern sides as in the 2nd place of case1-2 in 1st step inquiry. Moreover, in case1-2, MRT for this optimum individual at the road becomes lower compare with the 3rd place individual in the 1st step inquiry because the reflected radiation and long wave radiation from the neighboring wall are shaded by the trees with mesh numbers 3, 4, and 25. Therefore, the 2nd place individual in the 1st step inquiry becomes the optimum design for case1-2 in the 2nd step inquiry confined to the road area.

5. CONCLUSIONS AND REMARKS

- (1) The optimum design method for the optimum arrangement of buildings and trees with GA and coupled simulation of convection, radiation and conduction for the design on outdoor thermal environment is developed.
- (2) In considering the optimum arrangement of trees, two cases which are different in target area (all open space or pedestrian road) are analysed. Compared with case1-0 (the basic case), the relief effect of trees on the outdoor

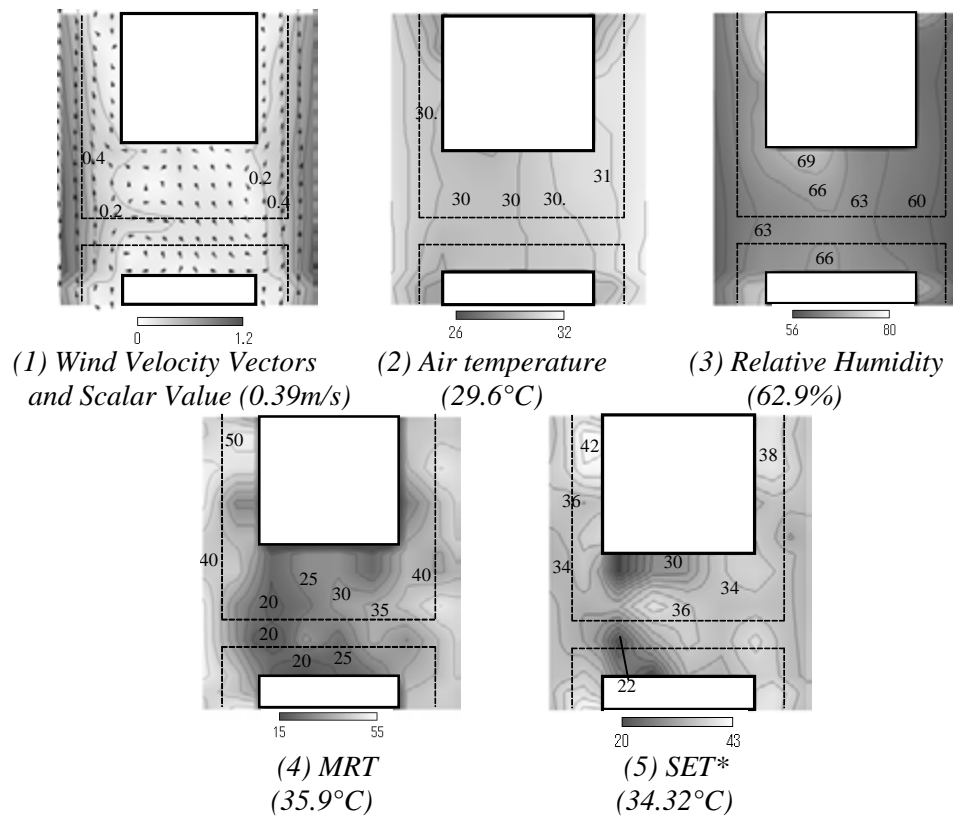


Figure 10 case1-1 The Thermal Environment of the Optimum Design (at 1.5m height)
 (The Horizontal distribution of Physical Quantities in Optimum Evaluation Domain)
 (The value in parentheses is an average value)

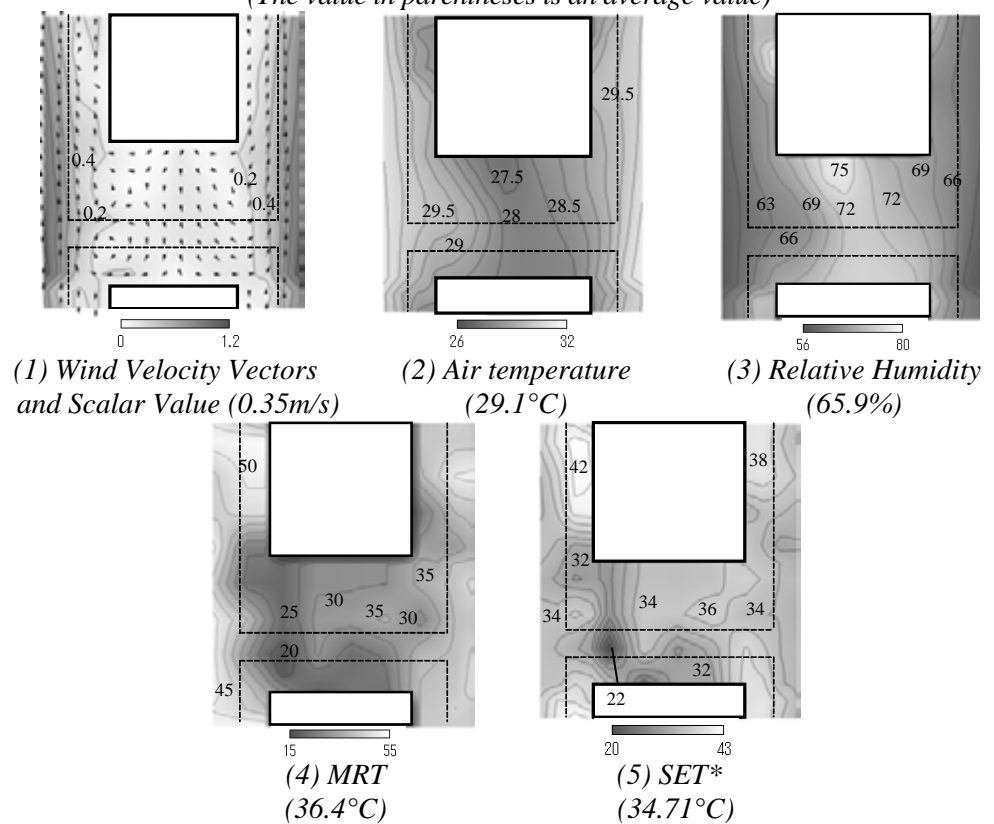


Figure 11 case1-2 The Thermal Environment of the Optimum Design (at 1.5m height)
 (The Horizontal distribution of Physical Quantities in Optimum Evaluation Domain)
 (The value in parentheses is an average value)

outdoor thermal environment is seen from the results of case1-1 and case1-2. In addition, although the average value of SET* in the all open area in case1-2 is higher by about 0.4°C than that in case1-1, the value in pedestrian road in case1-2 is lower by about 0.2°C than that in case1-1. Thus, the optimization of outdoor thermal environment is achieved in accordance with different target areas, and therefore it is considered that the validity of this proposed method for the optimum design can be seen.

(2) A lot of researchers have proposed countermeasures for heat island phenomena in order to realize a healthier outdoor thermal environment. In this context, it is considered that the results of the optimum inquiry method for tree arrangements will be useful in the practical design stage of an urban environment.

REFERENCES

- Aoki, Y., Muraoka, N., 1996. *A method of the facility location by Genetic Algorithm*, J. Archit. Plann. Environ. Eng., AIJ, No.484, 129-135 (in Japanese)
- Chen, H., Ooka, R., Harayama, H., Kato, S., Li, X., 2004. *Study on outdoor thermal environment of apartment block in Shenzhen, China with coupled simulation of convection, radiation and conduction*, Energy and Buildings, pp. 1247-1258
- Gage, A.P., Stolwijk, J.A.J., Nishi, Y., 1986. *A Standard Predictive index of human response to the thermal environment*, AHSRAE Transactions, 92(1), 709-731
- Hagishima, A., Katayama, T., Hayashi, T., Tanimoto, J., 1999. *Numerical analysis on cooling effect of a row of trees in an urban canyon, Part2 Prediction of thermal comfort on streetwith roadside trees*, J. Archit. Plann. Environ. Eng., AIJ, No.525, 83-90 (in Japanese)
- Kim, T., Kato, S., Murakami, S., 2001. *Two Step Optimal Design Method of Indoor Thermal Environment based on CFD Simulation and Genetic Algorithm*, Annual Technical Meeting of Architectural Institute of Japan (D) (2001) 771-772 (in Japanese)
- Kitano, H., 1993. *Genetic Algorithm I*, Industrial books Ltd. (in Japanese)
- Kato, M., Launder, B.E., *The modeling of turbulent flow around stationary and vibrating square cylinders*, Prep. of 9th Symp. on Turbulent shear flow (1993) 10-4-1-6
- Mitsui, K., Tomita, K., Tosaka, N., 1994. *Application of genetic algorithm in structural form analysis*, Annual Technical Meeting of Architectural Institute of Japan (B) (1994) 1211-1212 (in Japanese)
- Okamoto, H., Hatori, M., 1993. *Application of neural network on the optimum arrangement including nonlinear evaluation function*, Annual Technical Meeting of Architectural Institute of Japan (E) (1993) 773-774 (in Japanese)
- Tanese, R., 1989. *Distributed genetic algorithms*, Proc.3rd ICGA, pp. 434-439.
- Yoshida, S., Ooka, R., Mochida, A., Tominaga, Y., Murakami, S., 2000. *Study on Effect of Greening On Outdoor Thermal Environment Using Three Dimensional Plant Canopy Model*, J. Archit. Plann. Environ. Eng., AIJ, No.536, 87-94 (in Japanese)

PREDICTION OF POLLUTANT DISPERSION CAUSED BY AUTOMOTIVE EXHAUST - A COMPARISON BETWEEN FIELD MEASUREMENTS AND WIND TUNNEL DATA -

Takeaki Watanabe¹, Shinsuke Kato², Ryozo Ooka³,
Takeo Takahashi⁴ and Ryohei Kono¹

¹ University of Tokyo, Japan

^{2,3,4} Institute of Industrial Science, University of Tokyo, Japan
wtakeaki@iis.u-tokyo.ac.jp

ABSTRACT

This study aims to contribute to the development of traffic measures that result in less pollution by predicting the distribution of pollutant concentrations caused by automotive exhaust around an intersection in an urban area. An example of the traffic measures is the traffic lights control to reduce the frequency of stop and go at intersections. The study consists of a wind tunnel experiments and field measurements. The studied area is centered on the Ikegami-Shinmachi intersection in Kawasaki-shi, situated in an industrial region in the vicinity of Tokyo. The wind tunnel experiments consist of diffusion tests using point and line sources of tracer gas, and the field measurements include diffusion tests using a point source of tracer gas and measurements of carbon monoxide (CO) and nitrogen monoxide (NO) concentrations. The results of the wind tunnel experiments using point and line sources were also in good agreement with the field measurements. The results indicate that the experimental data obtained in this study is highly reliable in verifying predictions based on computational fluid dynamics.

1. INTRODUCTION

Air pollution from automotive exhaust along major highways has recently been recognized as a problem in large cities. Such pollution is characterized by pollutant concentrations that are several times higher along the highways than in the background urban area. The problem is exacerbated by poor air passage associated with dense use of city space. In order to resolve this problem, precise information on pollutant distribution is required.

This study aims to contribute to the development of traffic measures that result in less pollution by predicting the distribution of pollutant concentrations caused by automotive exhaust around an intersection in an

urban area. An example of the traffic measures is the traffic lights control. Reducing the frequency of stop and go means reducing pollutant generation. The study consists of a wind tunnel experiments and field measurements. The wind tunnel experiments consist of diffusion tests using point and line sources of tracer gas, and the field measurements include diffusion tests using a point source of tracer gas and measurements of carbon monoxide (CO) and nitrogen monoxide (NO) concentrations. The results obtained by the two approaches are then compared. Similar comparative studies were previously performed by Kennedy [1977] and Bachlin [1991].

2. STUDIED AREA

The studied area, shown in Figure 1, is centered on the Ikegami-Shinmachi intersection in Kawasaki-shi, situated in an industrial region in the vicinity of Tokyo. This area is known to have the worst air pollution from automotive exhaust in Japan. A local highway runs in a southwest-northeast direction through the area in parallel with an elevated section of the expressway. A general urban area lies north of the highway with a number of factories to the south. The highway and the expressway are assumed to be the sources of the automotive exhaust.

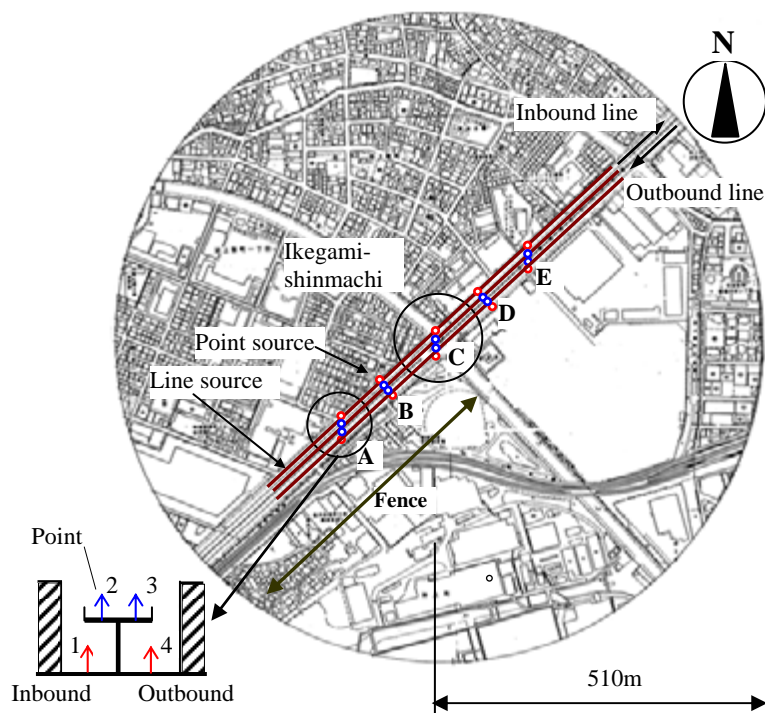


Figure 1: Locations of tracer gas sources in the studied area

3. OUTLINE OF WIND TUNNEL EXPERIMENTS AND FIELD MEASUREMENTS

3.1 Outline of wind tunnel experiments

The experiments were performed using a thermally stratified wind tunnel at the Institute of Industrial Science the University of Tokyo. The

wind tunnel has a cross section of 1.8 m × 2.2 m at the point of measurement and is 16.5 m in length. A 1/600 scale urban model of a circular area defined by a radius of 510 m from the intersection was used for the experiment (Figure 2). On the lower left side of the intersection shown in Figure 1, there is a fence under the elevated expressway, between piers along the centerline of the highway (Figure 3). The fence is intended to remove air pollutants with plants. There are little openings in the fence, which is covered with thickly grown plants. In the model experiment, a fence without openings was installed without considering the effect of concentration reduction by plants. A total hydrocarbon analyzer was used for concentration measurements. The mean wind velocity profile is expressed by $U \propto Z^{1/4}$ at the center of the model installation point. The wind directions used in the experiment include the three dominant directions (south, southwest, and north) and the directions perpendicular to the highway (southeast and northwest). A total of 139 measurement points at a height of 1.8 m (in actual size) were established. Ethylene (C_2H_4) was used as the tracer gas. Point and line sources of tracer gas were used. The point sources were set at five locations (A to E in Figure 1), while four sources were placed at each location (one source on each of the inbound and outbound lines of both the highway and elevated expressway). Gas was exhausted individually for each test. The velocity of exhaust from automobiles is negligible because its effect on the flow field is far less than the effect of the surrounding buildings. Each exhaust opening, situated at road surface level, has a diameter of 6 mm. To minimize the effect of the exhaust velocity, a cover was set 5 mm above the exhaust opening. Figure 4 shows the exhaust openings of the point sources. An air stone with a diameter of 10 mm and a length of 1200 mm was used as a line source, and tracer gas was fed into the source from both ends. When the air stone was used as it was, a large amount of tracer gas flowed out from both ends rather than the central part of the source. Therefore, the air stone was wrapped with plastic tape to adjust the exit area so that the gas would be emitted uniformly from the line source. Line sources were placed at three locations (on the elevated expressway and the inbound and outbound lines of the highway), and gas was exhausted from each source individually. Figure 5 shows the line sources. Atmospheric stability was set to neutral in principle, but both stable and unstable situations were tested only for the wind direction SE.



Figure 2: Wind tunnel model



Figure 3: Fence installed under the elevated expressway

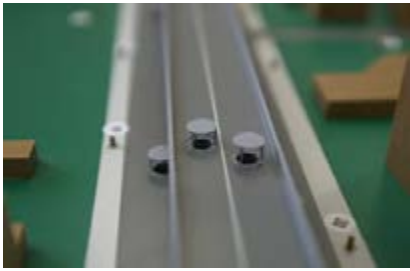


Figure 4: Point sources



Figure 5: Line source

3.2 Outline of field measurements

Field measurements were taken from February 1 to 3, 2005. Measurements were taken at 20-min intervals from 8:45 to 15:05 including every hour on the hour. The measurement points, 17 points in total, are shown in Figure 6. Measurement points 1 and 15 are on a sidewalk of an ordinary road, points 2, 3, and 4 are in a neighboring district, points 5 through 12 are on the sidewalks of the highway, and points 13, 14, 16, and 17 are in a park. The measurement height was 1.5 m above the ground. A tracer gas, sulfur hexafluoride (SF₆), was exhausted from point A or B on a sidewalk of the highway (Figure 6) at a height of 1.5 m. The gas was exhausted at a rate of about 22.4ℓ/min. At each measurement point, polluted air was collected with a suction pump into a 20-ℓ bag and was analyzed with a multi-gas monitor. The CO concentration of the sampled air was measured with a carbon monoxide analyzer and the NO concentration with a nitrogen oxide analyzer. To estimate the emission rates of automotive exhaust, automobiles passing the intersection were videotaped from a pedestrian bridge on the east side of the intersection. The observed automobiles were classified into (1) light and ordinary cars, (2) light and ordinary trucks, (3) large trucks and special vehicles, and (4) buses, and the number of vehicles that passed were determined for each group. The meteorological data used was based on the data observed at an environmental measurement station near the studied area. Atmospheric stability was not measured. Concentrations were measured at ground level along the highway. As discussed later, it was assumed that the effect of emission from the elevated expressway on the ground area was small and that exhaust sources were only on the highway regarding the measurements.

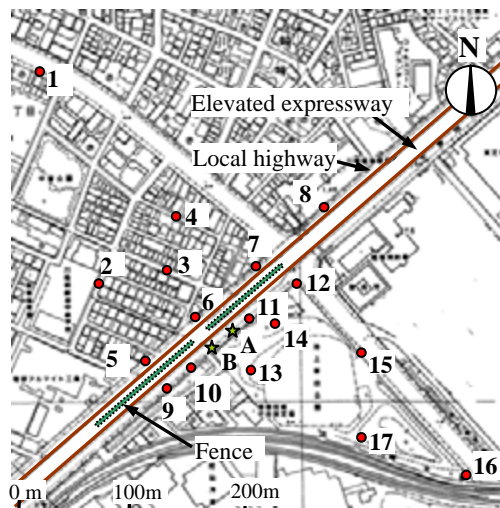


Figure 6: Field measurement and gas emission points

4. RESULTS

4.1 Results of wind tunnel experiments

4.1.1 Distribution of the normalized concentration of exhaust from point sources

For the case of neutral atmospheric stability, measurement results are shown as the normalized concentrations (C_E/C_0). Here, C_E is concentration measured in the wind tunnel experiments, $C_0=Q / (UH^2)$, Q is tracer gas generation rate (=1cc/s), H is the height of the elevated expressway (=1.33 cm), and U is the wind velocity at height H (=0.42 m/s).

1) Wind direction SE; Exhaust opening on the inbound line of the ground-level highway (D1) (Figure 7)

The gas emitted from the exhaust opening was blocked by a medium-rise building located on the leeward side of the opening and was deflected widely along the highway in the lateral directions. A C_E/C_0 value of 0.001 was observed near the intersection, about 100 m away from the opening along the highway. A value of 0.68 was observed in the very vicinity of the exhaust opening, whereas values of 0.04 and 0.01 were observed 40 and



Figure 7: Normalized concentration of gas from an exhaust opening on the ground-level highway (D1; wind direction SE)

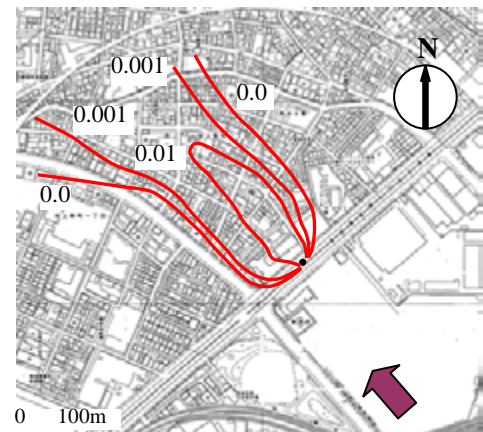


Figure 8: Normalized concentration of gas from an exhaust opening on the elevated highway (D2; wind direction SE)

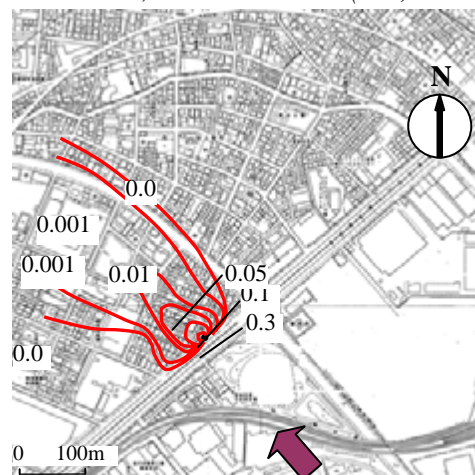


Figure 9: Normalized concentration of gas from an exhaust opening on the ground-level highway (B1; wind direction SE)

150 m leeward of the opening. Attenuation of concentration in the direction was very large.

2) Wind direction SE; Exhaust opening on the inbound line of the elevated expressway (D2) (Figure 8)

Most of the gas exhausted on the expressway diffused upward, and the effect of the gas on the ground level was very small. A C_E/C_0 value of 0.03 was observed 40 m leeward of the exhaust opening, which was greater than the value of 0.02 observed on the sidewalk right beneath the opening. The area with non-dimensional concentrations of 0.001 or more extended as far as 250 m, more extensive than in the case of ground emission (D1).

3) Wind direction SE; Exhaust opening on the inbound line of the ground-level highway (B1) (Figure 9)

The gas emitted from the exhaust opening was influenced by the wake flow of the fence under the expressway and was deflected widely in the lateral directions. A C_E/C_0 value of 0.35 was observed on the sidewalk right next to the opening, and a value of 0.06 at 35 m leeward of the opening. Attenuation of concentration in the leeward direction was very large.

4.1.2 Distribution of the normalized concentrations exhaust from line sources

The distributions of normalized concentrations when line sources were on the ground-level highway and elevated expressway (southeast wind) are shown in Figures 10. When gas was exhausted from the highway, C_E/C_0 values were 0.07 to 0.08 on the leeward-side sidewalk with a fence under the expressway and about 0.07 in an area in front of a wide medium-rise building without a fence under the expressway. The normalized concentrations were rather small at the intersection because of higher wind velocities. The normalized concentrations were 0.05, 0.01, and 0.005 at about 30, 50, and 100 m leeward of the source.

4.2 Field measurements results

4.2.1 Wind directions and velocities over the studied area

Wind directions and velocities observed at the Daishi environmental station during the measurement period are listed in Table 1. The station is located at 2km difference with the intersection. The wind directions during the period were mostly between WNW and NNW.

4.2.2 Emission rates

The traffic volume and emission rates on February 1 are shown in Table 2 as an example. The emission rates were calculated by assuming vehicle velocities of 20 and 50 km/h on the inbound and outbound lines of the highway, respectively, and using emission factors for different vehicle types. Large trucks and special vehicles outnumbered the other types of vehicles, and the traffic volume and emission rates were about the same for the three days.

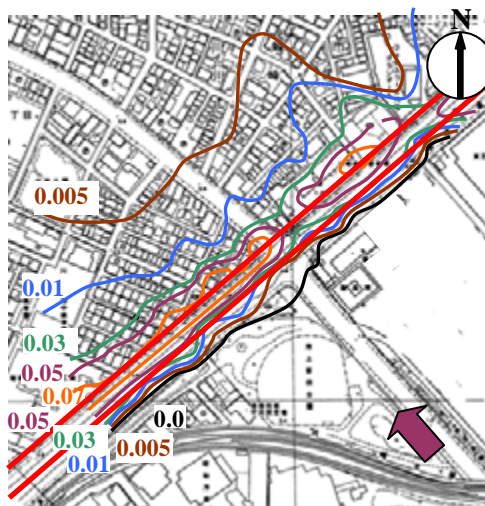


Figure 10: Normalized concentration of gas from line sources on the ground-level highway in wind tunnel experiment (wind direction SE)

Table 1: Wind directions and velocities observed at a height of 16m at Daishi measurement station of the environment bureau of Kawasaki City Office Left : wind velocity (m/s), Right : wind direction

	Weather	9 :00	10 :00	11 :00	13:00	14 :00	15 :00
2/1	Fine	5.7 WSW	4.6 WSW	7.6 WNW	5.9 WNW	5.5 NW	3.3 NNW
2/2	Fine	3.6 WNW	3.7 WSW	3.7 W	2.7 NW	1.9 WNW	0.9 SSE
2/3	Fine	1.7 WNW	1.7 NW	3.8 NW	4.1 NNW	4.5 NW	4.5 N

Table 2: Volume of Traffic and of emission rates of automotive exhaust on the local highway

1) Traffic volume

traffic volume 1 st .Feb. 2005	Light and Ordinary cars	Light and Ordinary Trucks	Large trucks Special vehicles	Bus
9:45~10 : 05	142 (125)	55 (62)	214 (222)	8 (4)
10:45~11 : 05	135 (130)	65 (85)	206 (245)	4 (3)
13:45~14 : 05	178 (145)	63 (60)	192 (195)	5 (2)
14:45~15 : 05	180 (172)	55 (52)	200 (176)	3 (3)

a figure in () : outbound lines

2) Emission rates (g/m ·h)

emission rates 1 st .Feb. 2005	CO		NOx:*	
	Inbound	Outbound	Inbound	Outbound
9:45~10 : 05	3.08	2.11	2.99	2.08
10:45~11 : 05	3.13	2.49	2.89	2.34
13:45~14 : 05	3.22	2.04	2.76	1.85
14:45~15 : 05	3.13	1.97	2.76	1.70

4.2.3 Distribution of the normalized concentrations of SF₆ tracer gas from point sources

The measurement results are given as the normalized concentrations (C_F/C_0). Here, C_F is the concentration measured in the field, and $C_0=Q/(UH^2)$, where Q is the tracer gas generation rate, H is the height of the elevated

expressway (=8 m), and U is wind velocity at height H . Here, H is the height of the elevated expressway as well as the model experiment. The distributions measured at 14:00 on February 1 (wind direction NW, source point A) and 11:00 on February 2 (wind direction W, source point A) are shown in Figures 11 and 12, respectively. In the case of northwest wind (Figure 11), C_F/C_0 values were 0.74 at measurement point 11, which was close to the gas source, 0.14 at point 10, and 0.07 at point 12. The results indicate that the tracer gas dispersed laterally along the fence below the expressway. The gas flowed back windward through gaps in the fence, and a concentration of 0.01 was observed at point 6. C_F/C_0 values were 0.17 (about 1/4 of the concentration near the source) at point 14 (about 15 m leeward from the source), 0.06 (about 1/12 of the concentration near the source) at point 15 (100 m leeward from the source), and 0.02 (1/40 of the concentration near the source) at point 16 (300 m leeward from the source). In the case of west wind (Figure 12), C_F/C_0 values were 1.6 at point 11, which was close to the gas source, 0.23 at point 10, and 0.42 at point 14. Similar to the case of northwest wind, the tracer gas dispersed laterally along the fence below the expressway. A value of 0.02 was observed at point 7, near the intersection. This reflected a flow that bulged toward the north side of the intersection at the leeward end of the fence.

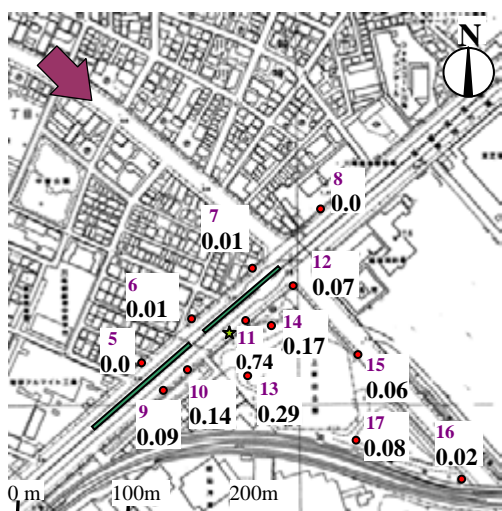


Figure 11: Normalized concentration of tracer gas in case of wind direction = NW, point source=A

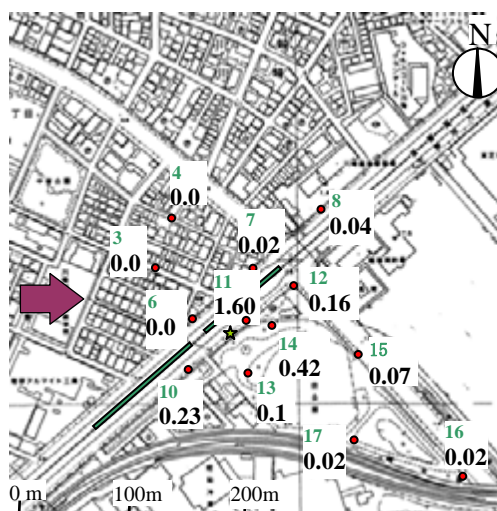


Fig.12. Normalized concentration of tracer gas in case of wind direction = W, point source=A

4.2.4 Distributions of the normalized concentrations of CO and NO

The normalized concentrations of CO and NO (averages for wind direction NW during the measurement period) are shown in Figure 13. The relationship between the normalized concentrations of CO and NO for all wind directions is shown in Figure 14. Using the emission rates estimated in Section 4.2.2, gas generation at distances corresponding to the line sources in the wind tunnel experiment were assumed for the sake of correlation with the experimental results. The amount of NO generation was assumed to be 50% of NO_x generation. Concentration at each point was obtained by deducting background concentration, which was given by

the concentration measured at a windward point sufficiently distant from and unaffected by the highway. Figure 13 shows the presence of high concentration areas near the intersection and under the expressway. The normalized concentrations of CO and NO are close to each other, although there are some discrepancies. Figure 14 also shows good coincidence between non-dimensional CO and NO concentrations. This is probably because emission from the elevated expressway does not affect to the ground level concentration.

4.3 Comparison between the wind tunnel experiment results and field measurements

4.3.1 Point sources

The normalized concentrations shown in Figure 9 (wind tunnel results) and Figure 11 (field measurements) are compared. Because the locations of gas sources and measurement points are different between the wind tunnel experiment and field measurements, there are differences in normalized concentrations near the sources and the westward extent of the wake flow area of the fence. However, similar trends are found in the two figures regarding lateral dispersion of gas toward the intersection side and attenuation of concentration from the source to 100 m leeward.

4.3.2 Line sources

The normalized concentrations shown in Figure 10 (wind tunnel results) and Figure 13 (field measurements) are compared; although the wind directions are different, they are both perpendicular to the main street canyon. The line sources in the wind tunnel experiment had finite lengths, however it is evaluated to be insignificant because the sources were sufficiently long in terms of concentrations observed at the measurement points. A high concentration zone was found only along the highway in the wind tunnel experiments. In the field measurements, C_F/C_0 values were 0.08, 0.04, and around 0.05 at measurement points 6, 11, and 12, respectively. In the wind tunnel experiment, C_E/C_0 values of 0.07 to 0.08 were found on the leeward-side sidewalk with a fence under the expressway. Values around 0.05 were found near the intersection, corresponding to point 12. Thus, the experimental results and the field measurements are in good agreement.

5. CONCLUSIONS

The results of the wind tunnel experiment using point sources of tracer gas showed that the gas dispersed widely in the lateral directions right after emission when there was a building or a fence on the windward or leeward side of the source. The effect of emission from the elevated expressway was much smaller than that from the ground-level highway. CO and NO concentrations were measured and traffic volume was surveyed around the intersection; there was a good agreement between the distributions of non-dimensional concentrations of CO and NO exhausted from the highway.

The results of the wind tunnel experiment using point and line sources were also in good agreement with the field measurements. The results indicate that the experimental data obtained in this study is highly reliable in verifying predictions based on computational fluid dynamics.

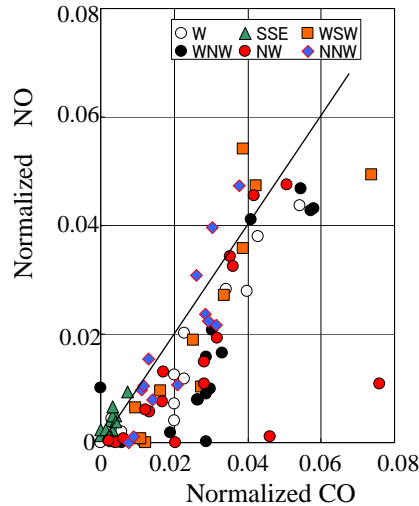
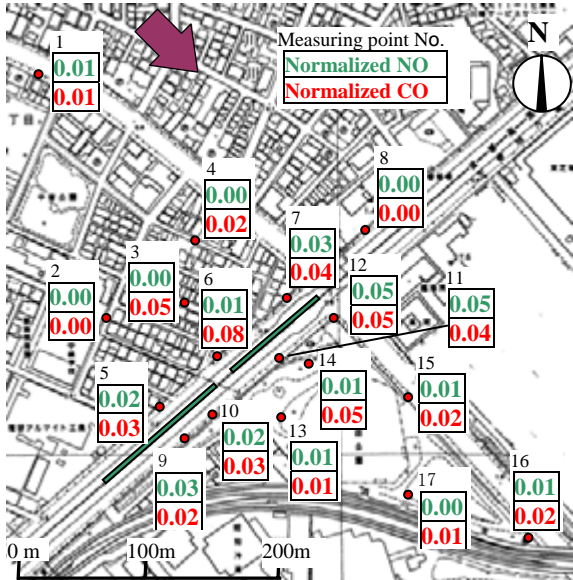


Figure 13: Normalized concentrations of CO, NO in the case of wind direction= NW Fig.14. Comparison of the normalized concentrations of CO and NO

REFARENCES

I. M. Kennedy and J. H. Kent (1977), "Wind tunnel modeling of carbon monoxide dispersal in city streets" Atmospheric Environment, 11, 541-547.

W. Bächlin, W. Theurer and E. J. Plate (1991), "Wind field and dispersion in a built-up area – A comparison between field measurements and wind tunnel data" Atmospheric Environment, 25A, 1135-1142.

LEVELS OF POLYNUCLEAR AROMATIC HYDROCARBONS AND HEAVY METALS IN WATER AND SEDIMENT OF UBEJI CREEK, WARRI RIVER IN NIGER DELTA AREA OF NIGERIA.

OKORO, D., ^{*a}; IKOLO, O. A. ^b

^aDepartment of Chemistry, University of Benin, Benin City, Edo State, Nigeria.

Tel: +234 8033834446; +2348023320809

E-mail: dukeokoro@yahoo.com

^bNational Agency for food and Drug Administration and Control, Central Laboratory, Oshodi, Lagos, Nigeria. Tel: +234 8023089732

E-mail: ikolo111@yahoo.com

ABSTRACT

Polynuclear aromatic hydrocarbons (PNAs) and heavy metals levels in surface water and sediment of Ubeji creek in Warri River were determined and compared with levels observed from Abraka location of Ethiopie River (control). All US EPA 16 listed priority PNAs determined by Gas chromatography using GC – Perkin Elmer Clarius 500, while the heavy metals were determined by Atomic Absorbtion spectrometry using AAS – Perkin Elmer 31,000. Determined levels of Fe, Zn, V, Ni, Pb exceeded standard criteria recommended for surface water by FEPA (1991); ANZECC (1992); US EPA (1996); WHO (1998); DPR (1991) and were in the following decreasing order of magnitude: Fe > Zn > V > Mn > Ni > Pb > Cu > Cr > Cd > Co > Hg. Mecury in surface water (0.001 mg/L) was however higher than interim fresh water guidelines recommended by DPR (1991) and ANZECC (1992). Levels of metals were comparatively higher in the dry season, while levels of PNAs were generally higher in wet season compared to dry season. The high molecular weight PNAs (HPNA) which includes indeno(1, 2, 3, - cd)pyrene, benzo(a) pyrene, benzo(k)fluoranthene, benzo(b)fluoranthene, chysene and pyrene had elevated levels in the water and sediment. The range of value for HPNA for water was 0.0055 – 0.023 mg/L and sediment was 0.437 – 0.938 mg/kg. Chemometric analysis revealed that the heavy metals enter the Warri River via contamination from fossil fuel combustion; storm water runoff / leachate from land fills, refuse dumps, boats / ships, vehicle exhaust and corrosion of galvanized steel structure. The diagnostic concentration ratios of PNAs isomer pair show in water and sediment of the Warri River, that phenanthrene/anthracene < 10; fluoranthene/pyrene > 1; chysene/benzo(a)anthracene < 1, which confirms and permit the conclusion that the PNAs were of pyrogenic origin.

1. INTRODUCTION

Every person alive today carries approximately 250 chemicals within his or her body, some chemicals that did not exist prior to 1945 (UNEP, 1997). This concentration of chemicals within every human being on the face of the earth is called the “body burden”, and it is our common legacy from the processes of development and industrialization. World War II was a catalyst for the transformation from a carbohydrate-based economy to a petrochemical-based economy, as chemical substitutes began to be invented for goods restricted or made available during the war. The economic boom that followed World War II supported the parallel boom in the invention and use of chemicals, many of which are associated with the convenience and flexibility of modern living. These synthetic chemicals find their way into everything – soil, air, water and food. They are in the tissues of plants, animals and people. Although some are naturally occurring, but chemicals like polynuclear aromatic hydrocarbons are mostly manufactured or sometimes by-products of chemical reactions and natural phenomenon (ATSDR, 2004).

In the past decade, several measures have been taken to reduce the input of toxic contaminants into rivers and estuaries, both by treatment of industrial wastewater and by the installation of municipal wastewater treatment plants. There was a reduction in pollutant concentrations in a number of European estuaries in the 1990s (OSPAR., 2000). It is therefore interesting to investigate if this trend is also visible in large fresh water ecosystem like the Ubeji Creek of the Warri River and possibly determine the specific sources of these contaminants. Polynuclear aromatic hydrocarbons (PNAs) are a group of chemicals that are formed during the incomplete combustion of coal, oil, gas, wood, garbage (pyrogenic origin), from emissions of non-combustion derived matter (petrogenic origin) and from the post-depositional transformation of biogenic precursors (diagenetic origin), which generally occur as complex mixtures (Neff, 1979 and Cerniglia *et al*, 1991). In this study, the 16 US EPA priority PNAs listed in table 2 were determined in surface water and sediment of Ubeji creek of the Warri River and Abraka location of the Ethiope River (Control). The investigation also covers the determination of twelve heavy metals including, Fe, Zn, Pb, Mn, Cr, Cu, Ni, Cd, Co, Hg, V and As in the described matrices.

The Warri River and Abraka location of the Ethiope River (control), is located in Delta State of Nigeria, Delta State is one of the thirty-six states that belongs to the Niger Delta geo-political region of the Federal Republic of Nigeria. Warri is a major industrial city with historical background of crude oil exploration, processing and refinery activities at its peak. The Warri River, a tidal fresh water ecosystem, is the recipient of Effluent from all the petroleum and allied industries located in the urban areas of the town.

The sampling points in Ubeji creek of the Warri River are essentially located on latitude N 5⁰ 34.14' and on longitude E 5⁰ 42.25'. The distance between this point and the control (Abraka location of the Ethiope River which is on Latitude N 5⁰ 49.46' and on Longitude E 6⁰ 06.50') is about 58.3 kilometer. Both rivers are flat - floored and they drain into the Atlantic Ocean. They are also prone to flooding, especially during the wet season,

mainly because of the heavy rainfall, high ground water table and the flat - floored valleys (Aweto, 2002). Large stretches, especially the lower reaches of both rivers are permanently water logged.

2. MATERIALS AND METHODS

2.1 MODE OF SAMPLING, HANDLING AND TREATMENT

Samplings for PNAs analysis were carried out in December, 2003; February, 2004; May, 2004 and July, 2004. Composite samples of both water and sediment in Ubeji Creek of Warri River and Abraka location of Ethiope River were collected in the described four months. The water samples for PNAs analysis were collected in a litre amber glass bottle with Teflon - lined screw - cap, 5mL of 1:1 HCL acid was added and cooled to about 4⁰C before it was taken to the laboratory prior to analysis (APHA, 1998), while sediment samples, having being collected in a litre chemically-cleaned glass jars with Teflon-lined screw-cap, were cooled to about 4⁰C, extracted within seven (7) days and extracts analyzed within 40 days. Composite water and sediment samples for heavy metal analysis were collected every month between August, 2003 and July, 2004 from the Ubeji creek of the Warri River. Water samples were collected in a litre polythene bottle that had previously been soaked in concentrated nitric acid for 24 hours and rinsed with de-ionised water, were brought to a PH of less than or equal to 2 with concentrated H₂SO₄ or HNO₃ (Barley and Gardner, 1997) and then stored on ice prior to laboratory analysis, while sediment samples were collected in a clean glass jar, then acidified with 5ml of concentrated HCL acid.

3. ANALYSIS

The water samples for PNAs analysis were extracted with methylene chloride, dried with anhydrous Na₂SO₄ and solvent – exchanged into hexane. Clean-up and fractionation was done using silica gel permeation chromatography. Final extracts after re-concentration using a rotary evaporator was packed in a 2mL GC vials and analysed with a Gas Chromatograph (GC), Perkin-Elmer/Clarius 500. Sediment samples, having being dried with anhydrous Na₂SO₄ were extracted with a mixture of dichloromethane (DCM) and acetone, thereafter solvent-exchanged with hexane. Clean-up and fractionation was similarly done using silica gel permeation chromatography. Final extracts were analysed using the same described GC. Water samples for heavy metal analysis were digested with concentrated HNO₃, (Martin *et al*, 1992) while sediment samples were digested with a mixture of HClO₃, H₂SO₄ and HNO₃ in the ratio of 1:2:2 according to the method described by Soster, *et al.*, (1992). Blank were also prepared in each determinations in the same manner and method using de-ionized water so as to check the accuracy of the method. The filtrate in both matrices were analysed for heavy metals using Flame Atomic Absorption Spectrophotometer, AAS (Perkins Elmer 31,000), and concentrations

calculated from the calibration curve obtained from five dilutions prepared from the standards.

4. CHEMOMETRICS

Multivariate mathematical technique, essentially agglomerative hierarchical clustering technique was employed to reduce the number of variables and detecting relationships between them. Chemometrics is a multivariate mathematical and statistical approach to the analysis and interpretation of analytical data. Hooper and Peters (1989) used multivariate analysis for determining sources of solutes found in wet atmospheric deposition in the United States. Cluster analysis which was used in this study, is a multivariate exploratory method, whose output is a tree-like diagram called dendrogram which shows the various associations of the heavy metals. The % proportion of 2-3 rings PNAs relative to 4, 5-6 rings and Diagnostic concentration ratios of PNAs isomer pairs were used to apportion sources of PNAs input into the Ubeji creek of the Warri River. Statistical treatment of the data obtained were performed using SPSS version 10.00.

5. RESULTS AND DISCUSSION

The results of the mean concentration of polynuclear aromatic hydrocarbons (PNAs) determined in surface water and sediment are presented in Table 1, while the mean concentrations of heavy metals in surface water and sediment of the Ubeji creek are presented in Tables 2 and 3 respectively. The levels of PNAs determined in water and sediment were generally higher in Ubeji creek compared to the levels observed in Abraka location of the Ethiope River (control). 0.3121mg/L observed for Total PNAs in water of the creek was relatively higher than 0.003mg/L recommended for fresh water by ANZECC 1992. Similarly, the total PNAs determined in sediment of the Ubeji creek were in elevated amounts with reference to NOAA (2000) and ANZECC (2000) guidelines for sediment. These elevated levels call for serious pollution concern. The composition of the low molecular weight PNAs (LPNA) in the surface water is less than 20% which suggests a possible pollution from combustion – derived PNAs. Biodegradation and desorption of LPNAs during transport and deposition was a possible mechanism for the PNAs compositional difference in the matrices.

The levels of heavy metals observed in water and sediment of the Ubeji creek were slightly higher than the levels reported in Aladja area of the Warri River in a similar study (Egborge *et al*, 1986). Concentration of lead in surface water of Ubeji creek was observed to be higher than most of the referenced guidelines. Although mercury level was observed to be higher than ANZECC, (1992), it was within the range of the other referenced guidelines. These values were too close for one to accept that all is well. Increased urbanization and industrialization in no distant time may increase the mercury level up to a very deleterious amount. The differences between the amount determined and that of the referenced criteria are shown in

Tables 2 and 3 for further understanding. The selected isomer pairs were used as indices to distinguish between petrogenic and pyrogenic origins for the PNAs. The ratios calculated in water and sediment as shown in Table 4 indicated that the ratio between phenanthrene/anthracene <10 ; fluoranthene/pyrene >1 ; chrysene/benzo (a) anthracene <1 , which confirms and permit the conclusion that the PNAs were of Pyrogenic origin (Colombo *et al.*, 1989). Agglomerative hierarchical clustering technique was used as exploratory multivariate method for the

Table 1: Concentrations of polynuclear aromatic hydrocarbons in water & sediment of Ubeji Creek of the Warri River.

COMPONENTS	Surface Water (mg/L)		Sediment (mg/kg)	
	Mean \pm STDEV	Mean \pm STDEV	Mean \pm STDEV	Mean \pm STDEV
	Ubeji	Abraka	Ubeji	Abraka
Naphthalene	0.0105 \pm 0.013	0.0003 \pm 0.00	0.2995 \pm 0.446	0.0004 \pm 0.00
Acenaphthylene	0.0101 \pm 0.012	0.0006 \pm 0.00	0.6874 \pm 0.542	0.0004 \pm 0.00
Acenaphthene	0.0184 \pm 0.017	0.0001 \pm 0.00	0.9806 \pm 0.321	0.0001 \pm 0.00
Fluorene	0.0125 \pm 0.015	0.0001 \pm 0.00	0.5991 \pm 0.486	ND
Phenanthrene	0.0024 \pm 0.001	ND	0.5119 \pm 0.461	ND
Anthracene	0.0036 \pm 0.0038	ND	0.5245 \pm 0.407	ND
LPNAs	0.0575 \pm 0.062	0.0011 \pm 0.00	3.603 \pm 2.662	0.0009 \pm 0.00
Fluoranthene	0.017 \pm 0.0267	ND	0.5692 \pm 0.276	0.0003 \pm 0.00
Pyrene	0.0273 \pm 0.026	ND	0.9427 \pm 0.468	0.0003 \pm 0.00
Benzo(a)anthracene	0.0438 \pm 0.001	ND	0.7566 \pm 0.590	0.0003 \pm 0.00
Chrysene	0.0456 \pm 0.003	ND	0.4266 \pm 0.463	0.0004 \pm 0.00
Benzo(b)fluoranthene	0.0098 \pm 0.00	ND	0.5124 \pm 0.516	0.0007 \pm 0.00
Benzo(k)fluoranthene	0.0473 \pm 0.007	0.0008 \pm 0.00	0.5122 \pm 0.507	ND
Benzo(a)pyrene	0.0138 \pm 0.0165	ND	1.0320 \pm 0.240	ND
Dibenzo(a,h)anthracene	0.0128 \pm 0.0173	0.0001 \pm 0.00	0.6008 \pm 0.594	0.0003 \pm 0.00
Benzo(g,h,i)perylene	0.0215 \pm 0.0126	ND	0.7688 \pm 0.470	ND
Indeno(1,2,3-cd)pyrene	0.0156 \pm 0.010	0.000205	0.5826 \pm 0.594	ND
HPNAs	0.2545 \pm 0.121	0.0011 \pm 0.00	6.7031 \pm 4.719	0.0023 \pm 0.00
Total PNA	0.3121 \pm 0.207	0.0022 \pm 0.00	9.3595 \pm 2.766	0.0032 \pm 0.00

LPNA--Low Molecular Weight Polynuclear Aromatic Hydrocarbon; HPNA--High Molecular Weight Polynuclear Aromatic Hydrocarbon.

heavy metal data to observe their various associations. The average linkage between groups method used was to see if the heavy metals are grouped in such a way that reflects their association relating to possible source of entry into the aquatic medium. The resultant dendrogram obtained for water and sediment are shown in Figures 1 and 2. In Figure 1, the first cluster made up of nickel and vanadium shows a possible entry via fossil fuel combustion, while the fourth cluster which includes iron and zinc shows a possible entry via construction/metal works and corrosion of galvanized steel structures. Similarly, in figure 2, the second cluster, made up of pb, Cr, As, Cd, and Cu shows possible entry via vehicle exhaust, leachate/runoff.

Table 2: Concentrations of heavy metals in surface water of Ubeji Creek of the Warri River including Referenced Guidelines.

Heavy metals	MEAN ± STDEV	FEPA,1990	DPR,1991	USEPA,1996	ANZECC,1992	WHO,1998
Iron	0,323 ± 0,472	0.3 - 1.0	< 1	0.3	< 0.01	1
Zinc	0,753 ± 0,102	< 1	1	5	0.005-0.05	15
Lead	0,071 ± 0,008	< 1	0.05	0.02	0.001-0.005	NA
Manganese	0,062 ± 0,005	NA	NA	0.05	0.0-0.5	0.05
Chromium	0,066 ± 0,011	< 1	0.03	0.1	NA	0.05
Copper	0,047 ± 0,019	1.0 - 1.5	1.5	1.3	NA	2
Nickel	0,371 ± 0,104	< 1	< 1	NA	0.02	0.02
Cadmium	0,053 ± 0,012	< 1	< 1	0.005	0.0002-0.002	0.05
Cobalt	0,017 ± 0,004	0.5	NA	NA	NA	NA
Mercury	0,0014 ± 0,0009	0.001	0.0001	0.002	0.00005	0.001
Vanadium	0,733 ± 0,216	0.01	0.01	0.019	NA	NA
Arsenic	0,024 ± 0,015	0.05	NA	0.05	0.05	NA

STDEV---Standard Deviation; FEPA---Federal Environmental Protection Agency; DPR---Department of Petroleum Resources; USEPA---United States Environmental Protection Agency; ANZECC---Australian-New Zealand Environment & Conservative Council; WHO---World Health Organization; NA---Not Available;ND---Not Detected.

Table 3: Concentrations of heavy metals in sediment of Ubeji Creek of the Warri River including Referenced Guidelines.

Heavy metals	MEAN ± STDEV	ICSQG,2000	NOAA,2000	SQON,1999	ANZECC,2000
Iron	255.710 ± 57.81	NA	NA	NA	NA
Zinc	46.515 ± 12.715	123	150	620	200
Lead	4.771 ± 1.762	35	46.7	530	50
Manganese	6.708 ± 1.434	NA	460	NA	NA
Chromium	1.079 ± 0.449	37.3	81	NA	< 80
Copper	1.821 ± 0.568	35.7	34	73	65
Nickel	4.884 ± 1.887	NA	20.9	NA	21
Cadmium	0.967 ± 0.214	0.6	1.2	12	1.5
Cobalt	0.705 ± 0.287	NA	NA	NA	NA
Mercury	0.006 ± 0.004	0.17	0.15	10	0.15
Vanadium	9.963 ± 3.895	NA	NA	NA	NA
Arsenic	0.467 ± 0.114	5.9	8.2	55	20

ICSQG---Interim Canadian Sediment Quality Guidelines; NOAA---National Oceanographic & Atmospheric Administration in the United States; SQON---Sediment Quality Objectives in the Netherlands

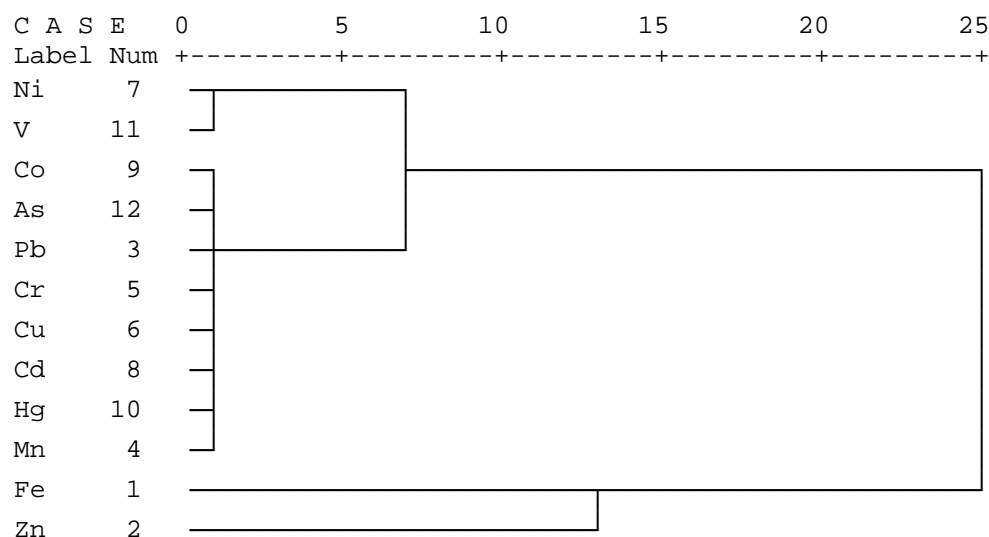


Figure 1: Dendrogram of heavy metals in Water of Ubeji Creek.

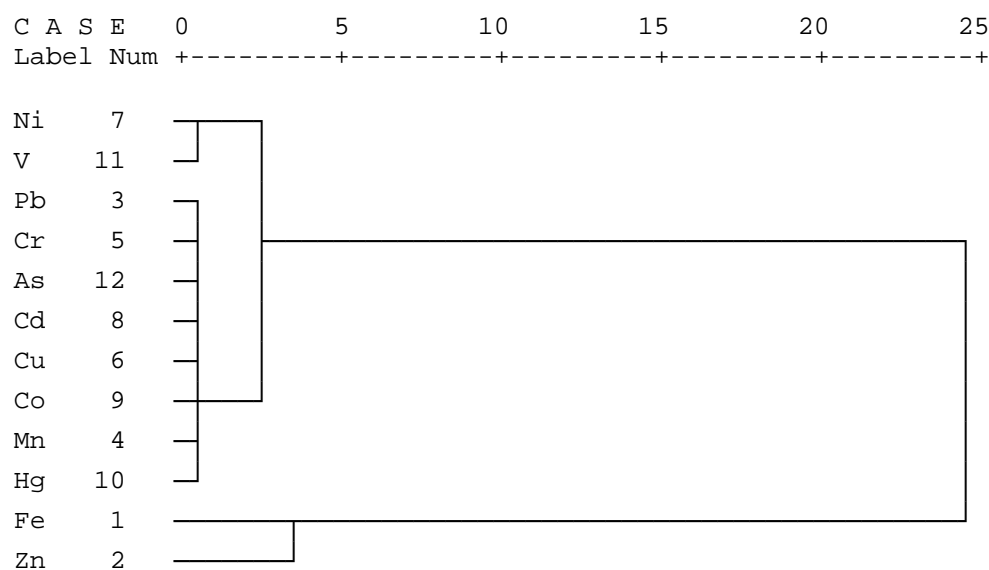


Figure 2: Dendrogram of heavy metals in Sediment of Ogunu Creek.

Table 4: Selected Isomer Pair ratios

Samples	Phen/Anth	Fluo/Pyr	Chry/B[a]A
Water in Ubeji	2.503	1.606	0.961
Sediment in Ubeji	1.62	1.656	0.564

6. CONCLUSION

The relative dominance of the high molecular weight PNAs in all matrices of the Ubeji of creek of the Warri River indicated that the PNAs were predominantly combustion-derived (pyrogenic) as confirmed by the compositional differences and the calculations from the selected isomer pairs. Chemometrics or multivariate analysis revealed that the heavy metals enter the Ubeji creek via contamination from urban and anthropogenic activities being carried into it along with storm water runoff.

REFERENCES

- APHA, (1998). Standard Methods for the Examination of Water and Wastewater, 20th edition Publishers: American Public Health Association; American Water Works Association; Water Environment Federation.
- ATSDR, 1995. Toxicological Profile for polycyclic aromatic hydrocarbons (PAHs): US Department of Health and Human Services. Public Health Service, Agency for Toxic Substances and Disease Registry, Division of Toxicology, Atlanta, GA. pp 23.
- Aweto, A., (2002). Outline geography of Urhoboland, *Oxford University Press, Ibadan, Nigeria*. pp. 2-4.
- Barley, G. E., and Gardner, D., 1977. Sampling and Storage of natural waters for trace metal analysis. *Intro. Journ. Environ.* 11: 745 – 746 pp.
- Cerniglia, C. E., and Heitkamp, M. A., 1991. Microbial Degradation of polycyclic aromatic hydrocarbons (PAH) in the aquatic environment, *Baltelle Press, Columbus, Ohio* . 32pp.
- Colombo, J. C., Pelletier, E., Brochu, C., and Khalil, M., 1989. Determination of Hydrocarbon sources using n-alkane and polyaromatic hydrocarbon distribution indexes. Case study: Rio de La Plata Estuary, *Argentina. Environ. Sci. Technol.* 23: 888-894.
- Egborge, A. B. M., and Benka-Coket, J., (1986) Water Quality Index: Application in the Warri River, *Nigeria. Environ. Poll. Science*. B.12: 27-40.
- Hooper, R. P., and Peters, N. E., 1989. "Use of Multivariate analysis for determining sources of solutes found in wet atmospheric deposition in the United States. "*Environ. Sci. Technol.* 23: 1263-1265.
- Martin, T. D., Brockhoff, C. A., Creed, J. T. and Long, S. E., 1992. Determination of metals and trace elements in water and wastewater by inductively coupled plasma – atomic emission spectrometry. *I.C.P. News t t r*, 18(3): 147-169.
- Neff, J. M., 1979. Polycyclic aromatic hydrocarbons in the aquatic environment. *Applied science Publ. Ltd., London*. 262pp.

- OSPAS, 2000. Water Quality status Report 2000 for the North-East Atlantic Report. Oslo and Paris Commission for protection of the marine environment of the North-East Atlantic London, England.
- Soster, D. A., Harvey, D. T., Troska, M. R. and Gromms, T. 1992. The effect of Turbificid oligochaetes on the uptake of Zinc by Lake Erie sediments. *Hydrobiologica*. 248: 249-258.
- UNEP, 1997. Reference method for Marine Pollution Studies, No 31-39.

DEVELOPMENT OF NEW ENVIRONMENTAL INDICES FOR URBAN SUSTAINABILITY

RYOZO OOKA, YOSHIHUMI YASUOKA, JUNICHI SUSAKI,
TAKAHIRO ENDO, YOICHI KAWAMOTO
Institute of Industrial Science, The University of Tokyo, Tokyo, Japan
HIDENOBU NAKAI, MADOKA NAKASHIMA, REI TAKADA
Tokyo Electric Power Company
MASAHIRO SETOJIMA, MANABU FUNAHASHI
Kokusai Kogyo Co. LTD.
KEIICHI OKADA
Shimizu Corporation
ooka@iis.u-tokyo.ac.jp

ABSTRACT

In this research, the comprehensive assessment indices that becomes the indicator of the plan for a sustainable city is developed (Environmental Indices for Urban Sustainability: EIUS). Various indices that evaluated urban environment have been developed in order to solve the urban problem including a so-called environmental pollution issue since 1970's in many countries of the world, especially by OECD. These are the indices that evaluate mainly the environmental qualities such urban air quality or various services supported by the administration inside the city. However, the environmental load such as CO₂ emissions that the city activity exerts on the larger area or the global environment cannot be neglected with the rise of the consideration of global environmental problems in recent years. In this paper, at first stage, the several items which represent the environmental quality inside the city (Health, Services, Safety, etc.) and the environmental load outside the city (Energy consumption, Resources consumption, Environmental pollution, etc.) are selected. Then, these items are combined in order to construct the comprehensive assessment indices (EIUS) which consider both the environmental quality and the environmental load in and outside the city. Furthermore, these indices are applied for 11 government ordinance specification cities in Japan. The applicability of these indices is estimated and the sustainability of these 11 cities is examined.

1. Introduction

In Asia, there is a strong tendency for population and functionality to converge in cities. The economic development in many countries is creating a problem of runaway urbanization (the megacity problem). These megacities lag in the creation of urban infrastructure and safety measures, as well as environmental, educational, and other measures. This is causing services for city residents to decline, making environmental pollution and

other issues an everyday occurrence, and causing the appearance of slums and other problems in some areas. Meanwhile, however, the over-concentration of functions in the cities is causing its own problems; the areas around cities are becoming depopulated wastelands.

In addition, the rapid expansion of urban functions is increasing the flow of pollutants (such as sulfur oxides and carbon dioxide) into the air and seas, which is polluting the global atmosphere and coastal seas. It is highly likely that this situation will create critical environmental issues on a global scale in the future.

The present research is developing an index to comprehensively assess urban environments, to serve as a guideline for planning sustainable cities. Many indices have been created in many countries to assess urban environments, starting with the OECD in the 1970s. These indices were used to assess the environment inside the city, in order to resolve such urban issues as urban pollution. But as awareness of global environmental issues has increased over the past few years, it has become impossible to ignore the impact that urban activities themselves have on the global environment. The present paper identifies measures that specify the quality of life inside the city and environmental impact (load) outside the city at the municipal-government level, and reconstructs an urban-environment index taking both aspects into account. It also applies this index to Tokyo and 11 government ordinance specification cities, considers the appropriateness of the measures used within the index, and compares the sustainability of Tokyo and the 11 government ordinance specification cities.

2. Basic Concept of Creating an Index to Assist Urban Environments

The present research is developing an index to comprehensively assess urban environments, to serve as a guideline for planning sustainable cities. This is thus an assessment of cities; but in order to assess an urban environment, it is first necessary to define just what we mean by "city." While the definition of "city" is argued by a great many scholars and people in the field, here the authors define a city as a region under the jurisdiction of a municipal government. The reason the authors define it thusly is because most environmental measures for cities are carried out at the municipal level, and so assessing at the municipal level simplifies our work. The areas inside and outside the city for the urban environmental index mentioned above are defined as follows: the region within the municipality is inside the city, and other areas are outside it.

The following points were also taken into account in the creation of this assessment index.

- (1) **Consistency** When assessing urban environments, it is vital to collect detailed data for each city. But the more data one has, the more complex it becomes to handle, and the more difficult to assess. Consequently, it is important to summarize data to a certain extent, and create a comprehensive index.
- (2) **Generality** There is great disparity among the set of urban areas called "cities." For example, in Japan we have cities ranging in population from more than 8 million in Tokyo (in its 23 wards), to cities

with fewer than 50,000 people. There are also major differences in their population makeup, industrial structure, climatic conditions, and economic conditions, among others. It is thus necessary to create an index that is general and fair for all cities; this requires some sort of standardization, such as showing figures in per-capita units.

- (3) **Comprehensiveness** As can be seen in check systems used for environmental impact assessment, checks of the impacts and effects of policies must encompass an extremely broad range of phenomena. Put simply, it is necessary to prepare a set of individual elements that are well balanced, and put together with the consistency mentioned in item (1).
- (4) **Representativeness** Environmental monitoring and the like must be representative. In other words, measurements of environmental elements are not representative if they change depending on when or where in an area they are taken. For example, the location that air pollution or noise is measured has a great impact on the results. In such cases, it is necessary to create clear rules for measurement, and investigate geographical and temporal representativeness.
- (5) **Intuitiveness** An index of urban environments should not used solely by researchers, government officials, and other experts; it should also facilitate dialog with city residents. Consequently, the index must be intuitiveness understandable by residents; it should jibe with their live experiences and sensibilities.
- (6) **Ease of Measurement** No matter how elaborate of an index of urban environments one creates, it is unusable if one cannot obtain the data making it up. The data used to calculate the index must be easy to obtain, and the method to calculate it must be simple.

3. Overview of a Comprehensive Assessment Index for Urban Environments

In order to assess the environment of a city, it is necessary to assess both its good and bad aspects. The reason people live concentrated in a city in the first place is to reap some sort of benefit. If urban environments are assessed in ignorance of this aspect, one is led to the extreme argument that not having cities is best for the environment. We have thus built an index that assesses both the pros and cons of cities. To put this another way, the authors evaluate both the benefits gained by residents living inside the city, and the impact on the environment surrounding it. The authors call these aspects as Quality of Life inside City and Environmental Load Outside City, and define them as follows.

(1) Quality of Life inside City

Table 1 shows examples of each of the elements making up the Quality of Life inside City aspect. The environment inside the city can be divided into three major categories: (1) environment and public health; (2) functions and services; and (3) safety and security.

(1) Environment and public health: This is an index of level of public health, hygiene, and natural richness available to city residents. The percentage of greenery is used as a measure of the richness of the natural environment. The authors believe this is both relatively easy to measure, and representative. Concentration of air pollutants is an intuitive index of the air environment. It is difficult to create indices for soil and water quality, because the conditions of soil and water pollution are highly localized, and the measurements taken will depend greatly on where they are made. Consequently, the authors represent these by numbers of patients of communicable diseases. The authors use sewerage connection rate to represent public health.

Table 1. Index of Quality of Life Inside City

Major Category	Minor Category	Assessment Index	Weight [%]		Score				
			Minor	AI	1	2	3	4	5
Q1 Environment/ public health	Natural environment	Greenery [%]	30	100	-10	-20	-30	-45	45-
	Air	SO ₂ concentration [ppm]	30	50	0.007-	-0.007	-0.005	-0.003	-0.001
		NOX concentration [ppm]		50	0.07-	-0.07	-0.05	-0.03	-0.01
	Public health	Number of communicable disease infexions/1,000 people	40	50	1.0-	-1.0	-0.7	-0.5	-0.3
Sewerage connection [%]		50		-60	-70	-80	-90	90-	
Q2 Public Functions / Services	Administration	Population growth [%]	20	50	-0.3	-0.1	-0.1	-0.3	0.3 -
		Fiscal index		50	-0.6	-0.7	-0.8	-0.9	0.9-
	Habitation	Total housing floor space per capita	20	40	-27	-32	-36	-40	40 -
		Electrification		30	-80	-85	-90	-95	95-
		Internet access		30	-60	-70	-80	-90	90-
	Education	Library books per capita	10	40	-1.2	-1.6	-2.0	-2.4	2.4-
		Elementary-school teachers/1,000 people		30	-2.4	-2.5	-2.6	-2.7	2.7-
		Preschools/kindergardens /1,000 people		30	-0.08	-0.09	-0.1	-0.11	0.11-
	Commerce	Retail stores/1,000 people	10	100	-6	-8	-10	-12	12-
	Traffic	Total road length per capita	20	50	-2	-2.5	-3	-3.5	3.5-
		Public transport burden		50	-10	-20	-30	-40	40-
	Welfare	Welfare facilities/1,000 people	20	50	-0.25	-0.3	-0.35	-0.4	0.4-
		City park area per capita		50	-4	-7	-10	-14	14-
Q3 Safety/ Security	Earthquakes	Existing buildings without adequate earthquake-proofing	20	100	-	-	-	-	-
	Fire	Fires/1,000 people/year	20	50	0.56-	-0.56	-0.48	-0.40	-0.32
		Fire fighters/1,000 people		50	-0.7	-0.9	-1.1	-1.3	1.3-
	Storm /Flood	Victims/total rainfall upon damage per year	20	100	-	-	-	-	-
	Crime/ accidents	Crimes/1,000 people	40	30	40-	-40	-35	-30	-25
		Traffic accidents/1,000 people		20	9-	-9	-8	-7	-6
Police boxes/stations/ 100,000 people		20		-4	-5	-6	-7	7-	
Hospital beds/10,000 people		30		-10	-13	-16	-19	19-	

(2) Functions and services: This is an index of the cultural and social benefits reaped by city residents. It indicates that the higher the population growth rate, the greater the attraction of this aspect. Additionally, the higher a city's fiscal index, the sounder the state of its economy. Sub-category "housing functions" indicates the richness of the living environment. An element of culture and education is number of elementary-school teachers.

Although there are no great differences in this area between municipalities in Japan, it should serve as an index of social maturity when expanded to cities throughout Asia. Another minor category is transportation. In this minor category, public-transportation utilization responds directly to supply, and is a measure of the degree to which public transportation has been created. Meanwhile, road area and traffic volumes should be used to express convenience of road utilization, but detailed calculations of traffic volumes are not conducted on a nationwide scale. It has thus been substituted for another index here.

(3) Safety and security: As the name suggests, this is an index of the safety and security with which residents can live in the city. The number of out-of-code buildings is used as a measure of earthquake and fire safety, but figures on this are not currently kept in Japan. A simple measurement and estimation method and database are needed for buildings at risk of collapsing in an earthquake, or in the event of a fire, spreading a fire. It is also difficult to evaluate flood danger. The level of flooding in urban areas greatly depends on the sewerage treatment capacity, and other factors are also large. Hazard maps are needed for this aspect.

Environmental Load Outside City

Table 1 shows examples of each of the elements making up the Environmental Load Outside City aspect. The major categories are: (1) energy consumption; (2) resources and materials; and (3) the greater-area environment.

(1) Energy consumption: This is an investigation of total energy consumption through the evaluation of primary energy (heat) in relation to total energy. The lower the total energy consumption, the more sustainable the city is deemed to be. Thus, the authors do not example individual efforts to conserve energy here.

(2) Resources and materials: This index is represented by water usage and the amount of waste. The lower the level of waste, the more sustainable the city is deemed to be. Thus, the authors do not example individual efforts to conserve resources here.

(3) Greater-area environment: Unlike the environmental and public health used in the previous section (Quality of Life inside City), this is a measure of the degree to which the city contributes to environmental pollution outside the city, and to the global environment. Since there will probably be a large difference between the amount of pollution imported by the city and the amount exported out of the city, this can be represented by the amount of pollution produced inside the city. The calculation of pollution generation includes all pollution produced by urban activities, rather than just pollution produced inside the city. For example, with regard to electric power consumption, air pollution produced by a thermal power plant located far from the city is included. Additionally, waste that is sent outside the city for treatment is included in the greater-area environment, as it contributes to the environmental impact (load) outside the city.

Each item was also weighted in order to create a comprehensive index. Weighting should be changed according to the circumstances of each city. Tables 1 and 2 show sample weighting and scores used for the present

report. The scores were assigned as follows: for each evaluation index, quality of life and environmental load were each given three points, and the total was normalized to a maximum of 5 points. If the levels of both quality of life and environmental load were improving, the score would be high; if they were worsening, the score would be low. It should be noted here that a high score for environmental load indicates a low level of environmental impact. Furthermore, the items for the major categories (Q 1–3 and L 1–3) have a maximum score of 5 points, in accordance with the weighting shown in Tables 1 and 2. In the table a dash (–) indicates all municipalities do not keep such data, and the data could not be obtained. Consequently, these items were eliminated from the present scoring. The collection of this data will be a future task.

Table 2. Index of Environmental Load Outside City

Major Category	Minor Category	Assessment Indices	Weight [%]		Score				
			Minor	AI	1	2	3	4	5
L1 Energy	Electricity	Electricity usage [MJ/person/year]	50	100	8000-	-8000	-7000	-6000	-5000
		City gas usage [MJ/person/year]	50	100	30-	-30	-20	-15	-10
	Propane gas usage [MJ/person/year]	-		-	-	-	-	-	
	Others	Kerosene usage [MJ/person/year]	-	-	-	-	-	-	-
L2 Resources/ Resources	Water Resources	Tap-water usage [tons/person/year]	40	100	135-	-135	-125	-115	-105
	Waste	Household waste [tons/person/year]	60	50	600-	-600	-500	-400	-300
		Industrial waste [tons/person/year]		50	5-	-5	-4	-3.5	-3
L3 Environment over wide area	Air	CO ₂ emissions [tons/person/year]	100	100	15-	-15	-10	-7	-3
		NO _x emissions per capita		-	-	-	-	-	-
		SO _x emissions per capita		-	-	-	-	-	-
	Others	Waste within system not treated per capita	-	-	-	-	-	-	-

4. Results of Calculation

Fig. 1 shows the index of urban environments scoring results for Tokyo and the 11 government ordinance specification cities in radar charts. Two designated major cities – Saitama and Shizuoka – recently merged, and the area of the city changed; for this reason, they do not yet have prepared data, and thus were excluded from the scoring. The larger the area occupied by the city inside the hexagonal radar chart, the higher its level of environmental performance.

Sapporo's score was high for Q1 (environment and public health). This is due to the high proportion of the city area covered by greenery. The score for L1 (energy) is also high. The present estimate excludes kerosene usage; Sapporo is located in a frigid area, and kerosene usage (for heating) is high. Thus, it is believed that if kerosene usage were added to the estimate, Sapporo's score in this area would fall.

As with Sapporo, Sendai scored highly in Q1 (environment and public health). In terms of load, it also scored highly for L1 (energy). As with Sapporo, this is likely due to the fact that kerosene usage is not counted in

the estimate. The score for L2 (resources) is also high. This is due to the lower generation of household and industrial waste than other cities.

Chiba's score for Q3 (safety) is low. This is due to the relatively high crime rate there, and the low number of hospital beds per capita. In terms of low, the scores for L1 and L2 were low. This is probably due to the fact that Chiba consumes a large amount of energy and produces large quantities of CO₂, because it is an industrial city.

Tokyo (the 23 wards) had low scores for Q3 (safety) and L1 (energy). In terms of energy usage, the electricity consumption per capita is high. This is probably due to the concentration of economic activity in Tokyo.

Kawasaki had low scores for Q3 (safety), L1 (energy), and L3 (greater-area environment). This is because, like Chiba, Kawasaki has the characteristics of an industrial city.

Yokohama's score for Q1 (environment and public health) is low. The reason for the low score for Q1 (environment and public health) in particular is due to the poor state of air pollution. Overall, environmental-load scores were high.

Nagoya had low scores for Q3 (safety) and L1 (energy). This is also due to its characteristics as an industrial city.

Kyoto had low scores for Q3 (safety) and L2 (resources and materials).

As with other industrial cities, Osaka had overall low scores for environmental load. Its score for L1 (energy), however, was high in comparison with other industrial cities. This indicates that Osaka's industrial structure is moving from heavy industries to information-intensive industries.

Kobe's scores for Q1 (environment and public health) and Q2 (functions) were high.

Hiroshima's characteristics are similar to those of Kobe, but its scores were low for L2 (resources and materials) and L3 (greater-area environment), resembling an industrial city.

Fukuoka also has characteristics of an industrial city.

Kitakyushu also has characteristics of an industrial city. In this case, however, it had relatively high scores for Q1 (environment and public health) and Q2 (functions) for an industrial city.

5. Conclusions

The authors have developed a comprehensive environmental assessment index for sustainable cities. This has required assessments from the perspectives of both quality of life in the city and the environmental load of the city. This index was also applied to Tokyo and the 11 government ordinance specification cities. This has shown the environmental performance and features of each city. In the future, the authors will work to obtain a fuller set of data, and expand the assessments to smaller cities in Japan and to cities in Asia.

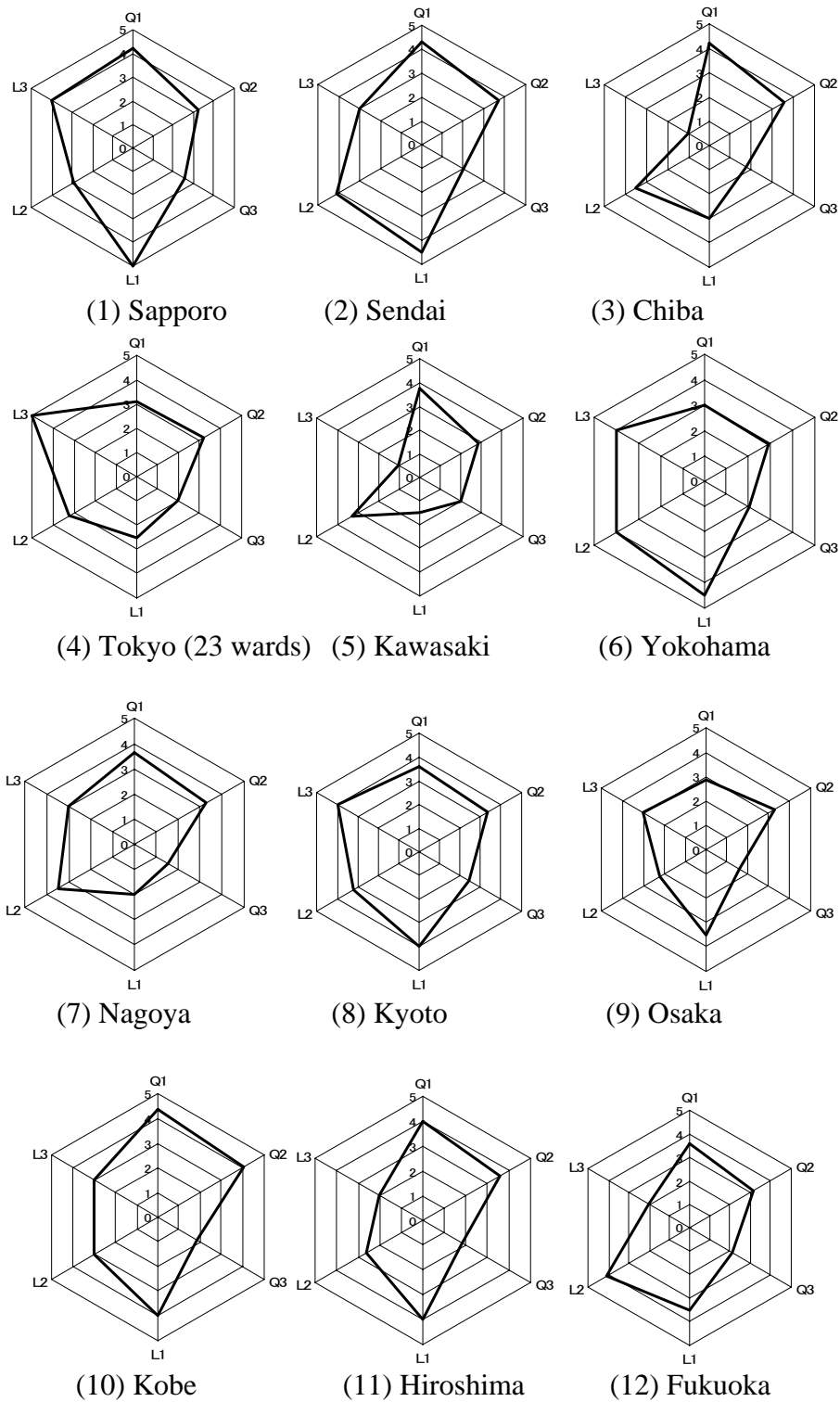


Figure 1. Comprehensive Assessment Indices for Environments of Tokyo and 11 government ordinance specification cities

EXTRACTION OF PARAMETERS FROM REMOTE SENSING DATA FOR ENVIRONMENTAL INDICES FOR URBAN SUSTAINABILITY

Junichi Susaki, Ryozo Ooka, Yoshihumi Yasuoka, Takahiro Endo, Yo-ichi Kawamoto; Institute Industrial Science, University of Tokyo, Tokyo, Japan
Hidenobu Nakai, Madoka Nakashima, Rei Takada
Tokyo Electric Power Company
Masahiro Setojima, Manabu Funahashi; Kokusai Kogyo Co. LTD.
Keiichi Okada; Shimizu Corporation
susaki@iis.u-tokyo.ac.jp

ABSTRACT

Asian mega cities have continued to expand, and accordingly, various problems, e.g. social, economical and environmental problems, have been widely recognized in Asia. Especially, environmental issues caused by Asian mega cities will affect not only the areas within mega cities but also the whole area of Asian countries because the effects will be widely propagated by atmospheric or marine transportation. Authors have conducted researches related to comprehensive assessment indices for urban sustainability, named as Environmental Indices for Urban Sustainability (EIUS). In the framework of EIUS, both the environmental quality and the environmental load are focused on. An urban sustainability will be evaluated based on the scores for all categories of EIUS (Ooka, et. al, 2005).

Most of the environmental data used in EIUS are collected from statistical data and those are restricted to point-based data. If area-based data such as vegetation distribution or urban area distribution are required, remotely sensed technique is quite useful. Remote sensing data also has an advantage to compare the parameters of different cities by the same criteria. In the present research, the applicability of remote sensing data to extract area-based environmental data for EIUS was examined. Landsat Thematic Mapper (TM) and Enhanced Thematic Mapper Plus (ETM+) images, observed in 1990s and 2000s, were used to extract vegetation index, albedo and land surface temperature. Urban areas of Bangkok in 1990s and 2000s were extracted from such parameters. Based on the acquired results, the methodology will be improved and applied to extract urban areas in other Asian mega cities.

1. INTRODUCTION

Environmental issues caused by Asian mega cities have been recognized to be monitored and assessed in an effective manner. While some statistics of mega cities have been reported to date, a systematic

assessment is still lacking. Authors have developed comprehensive assessment indices for urban sustainability, named as Environmental Indices for Urban Sustainability (EIUS). The EIUS is based on the framework of comprehensive assessment system for building environmental efficiency (CASBEE). The CASBEE was developed for assessment of the efficiency surrounding a building. In Section 2, EIUS as well as CASBEE are described. Considering implementation of EIUS, data accessibility is quite a difficult issue. Therefore, we examined the feasibility of application of satellite remote sensing data.

2. FRAMEWORK OF EUIS

2.1 CONCEPT OF EUIS

In the field of architecture where mass resources and energy are consumed, “sustainability” has been one of the most important keywords. Development of techniques and polices for sustainability is quite indispensable. CASBEE aims to promote proactive decisions in terms of environmental effects caused by construction and management of buildings. Therefore, CASBEE focuses on environmental functions of buildings (CASBEE Manual 1, 2003). In CASBEE, “Virtual boundary” is assumed to discriminate a space inside boundary from a space outside boundary, shown in Figure 1. The space inside boundary refers to the quality of the space mainly provided by the building. This is called as “Environmental quality”. On the other hand, the flow from the inside to the outside of boundary can be regarded as a negative load to the environment. This is called as “Environmental load”. BEE (Building Environment Efficiency) can be defined as the ratio of “Environmental quality” to “Environmental load”. Such a simple index can represent both quality and environmental load of a building, and enables the comparison between different buildings.

This framework of CASBEE can be applied for environmental indices for urban sustainability, or EIUS. Table 1 shows EUIS framework. In the EUIS, there are two types of categories such as “Quality life of inside city” and “Environmental load”. Each category has hierarchical structure consisted of the first classification and the second classification items. Assessments based on BEE and a radar chart are available in the framework of EIUS. Such an evaluation enables a comparison between many cities for the analysis of urbanization.

Table 1 also represents the results of data availability in Bangkok. Authors have contacted ministries and departments of Thailand, and examined data availability. The “Source” in Table 1 means ministries and departments of Thailand which can provide the data. Gray column shows the data were not available. In the case of Bangkok, it was found that most of data required in the current framework are available.

2.2 DIFFUCULTIES IN DATA COLLECTION FOR EUIS

Even though data collection was successfully conducted in Bangkok, it is not expected to obtain as much data as in other mega cities. Therefore, the data items should be flexibly changed in accordance with the real data accessibility. Simultaneously, we have to consider the data source independent of statistical data collected by organization in different countries. Another reason for the necessity of another data source is to apply the same criteria for data collection. While the statistics are useful for the national analysis, non-unified criteria for the statistics will make an international comparison difficult.

Remote sensing has a strong advantage for such problems. Satellite remote sensing can observe land, ocean and atmosphere from the space. In most of applications, remote sensing data are converted into physical parameters or indices. The quantitative and qualitative analysis based on the same criteria can be implemented by using remote sensing data. Moreover, most of remote sensing data are processed as images, and such area-based data are quite effective to grasp urbanization. Another advantage of remote sensing data is periodical observation. We have different types of earth observation satellite and sensors. High resolution data such as Landsat Thematic Mapper (TM) and Enhanced Thematic Mapper Plus (ETM+) has 16-day periods. Optical sensor data are easily contaminated by atmospheric effects, e.g. clouds or aerosols. While we cannot expect many images with good quality through a year, such periodical observation enables the analysis of temporal environmental change.

3. FEASIBILITY OF DATA COLLECTION BY REMOTE SENSING

While EIUS mainly deals with various statistics, remote sensing has a potential to be one of the most effective data sources for EIUS. In the framework of EIUS, authors examined the feasibility of data collection by remote sensing.

In terms of spatial resolution of remote sensing data, very high resolution data, e.g. 1 m-spatial resolution data, are available, and those data can provide the detailed spatial data. However, because of the expensive data cost, we focus on the usage of high resolution data such as TM and ETM+. Those costs are relatively reasonable. Moreover, many Landsat TM/ETM+ images are available free of charge through the Internet (Global Land Cover Facility). Such services are quite useful for the analysis conducted in the present research, i.e. quantitative analysis of temporal change of urban area. As a result, Landsat TM/ETM+ images were used for the analysis in the present research. Especially, those images were used for the extraction of urban areas. As parameters describing urbanization, three parameters were selected, i.e. Normalized Difference Vegetation Index (NDVI), albedo and land surface temperature (LST). In the following subsection, methods to derive parameters are described. Most of the constant values in the following equations are shown in literatures such as (Chander and Markham, 2003) (Landsat 7 Science Data Users Handbook).

3.1 PARAMETERS OBTAINED FROM REMOTE SENSING

3.1.1 NDVI

NDVI has been widely recognized as useful for the studies of the land biosphere characteristics and dynamics at regional to global scales. NDVI has more sensitivity to chlorophyll and less contamination by atmospheric water vapor. NDVI is obtained through calculation of reflectances of the red and near infrared (NIR), expressed as Equation (1).

$$NDVI = \frac{\rho_{NIR} - \rho_{RED}}{\rho_{NIR} + \rho_{RED}} \quad (1)$$

where ρ_{RED} and ρ_{NIR} denote reflectances at red band and NIR band, respectively. For Landsat TM/ETM+, band 3 and 4 are used.

3.1.2 ALBEDO

Land surface albedo is a physical parameter that describes the optical reflectance of the land surface. Albedo is commonly defined as the reflectance of a surface integrated with respect to both wavelength and angle. Land surface broadband albedo is the fraction of incident (shortwave) solar radiation reflected in all directions by the land surface. Examples of the albedo applications include global and regional climatic models for computing the surface energy balance, and ecological models. In the present research, Liang conversion model was used to estimate albedo. The procedure to estimate albedo from DN value is described in the below (Chander and Markham, 2003). Firstly, DN value was converted into radiance L by Equation (2). Then, radiance was converted into reflectance by Equation (3).

$$L_{\lambda} = (L_{max,\lambda} - L_{min,\lambda})/255 * DN + L_{min,\lambda} \quad (2)$$

$$\rho_{\lambda} = \frac{\pi \cdot L_{\lambda} \cdot d^2}{E_{\lambda} \cdot \cos \theta} \quad (3)$$

where $L_{min,\lambda}$ and $L_{max,\lambda}$ are the spectral radiances for band λ at digital numbers 0 and 255, ρ_{λ} unitless planetary reflectance, L_{λ} spectral radiance at the sensor's aperture, d earth-sun distance in astronomical units, E_{λ} mean solar exoatmospheric irradiances, θ solar zenith angle in degrees. Finally, broadband albedo was estimated by applying Liang model for Landsat ETM+, expressed as Equation (4) (Liang, 2000).

$$\alpha_{VIS} = 0.443\rho_1 + 0.317\rho_2 + 0.240\rho_3$$

$$\alpha_{NIR} = 0.693\rho_4 + 0.212\rho_5 + 0.116\rho_7 - 0.003$$

$$\alpha_{SW} = 0.356\rho_1 + 0.130\rho_3 + 0.373\rho_4 + 0.085\rho_5 + 0.072\rho_7 - 0.0018$$

(4)

where α_{VIS} , α_{NIR} and α_{SW} denote VIS albedo (0.4 – 0.7 μm), NIR albedo (0.7 – 2.5 μm) and SW albedo (0.25 – 2.5 μm) for ETM+, respectively. Hereafter they are mentioned as “VIS albedo”, “NIR albedo” and “SW albedo”, respectively. ρ_n denotes reflectance of band n . In Liang, 2000, there is no model for Landsat TM. Therefore, Equation (4) was also applied for the estimation of albedo of Landsat TM.

3.1.3 Temperature

Thermal band data (band 6) from Landsat TM/ETM+ can also be converted from spectral radiance to effective at-satellite temperature (Chander and Markham, 2003). The conversion formula is described as Equation (5).

$$T = \frac{K_2}{\ln\left(\frac{K_1}{L_\lambda} + 1\right)} \quad (5)$$

where T denote effective at-satellite temperature in Kelvin, K_1 , calibration constant 1 in $W/(m^2*sr*\mu\text{m})$, K_2 calibration constant 2 in Kelvin, L_λ spectral radiance at the sensor’s aperture. The effective at-satellite temperature values T are referenced to a black body. Therefore, corrections for spectral emissivity ε are necessary. Equation (6) represents the emissivity correction to derive land surface temperature (LST) S_t .

$$S_t = \frac{T}{1 + (\lambda \times T / \rho) \ln \varepsilon} \quad (6)$$

where λ is wavelength of emitted radiance ($\lambda = 11.5 \mu\text{m}$), $\rho = h \times c / \sigma$ ($1.438 \times 10^{-2} \text{ m K}$), $\sigma =$ Boltzman constant ($1.38 \times 10^{-23} \text{ J/K}$), $h =$ Planck’s constant ($6.626 \times 10^{-34} \text{ J s}$), and $c =$ velocity of light ($2.998 \times 10^8 \text{ m/s}$) (Weng *et al.*, 2004). Emissivity ε can be estimated in many ways. In the present research, a methodology reported in (Li *et al.*, 2004) is selected. Emissivity ε is expressed as Equation (7).

$$\varepsilon = f_v \varepsilon_v + (1 - f_v) \varepsilon_s \quad (7)$$

where ε_v and ε_s denote emissivity of vegetation and soil, respectively. f_v denotes fractional cover of vegetation (0 – 1). ε_v and ε_s were assumed as 0.985 and 0.978. Fractional cover f_v can be expressed as Equation (8) (Choudhury *et al.*, 1994)

$$f_v = 1 - \left(\frac{NDVI_{\max} - NDVI}{NDVI_{\max} - NDVI_{\min}} \right)^a \quad (8)$$

where $NDVI_{\max}$ is the NDVI for complete vegetation cover, and $NDVI_{\min}$ is the NDVI for bare soil. In the present paper, $NDVI_{\max}$ and $NDVI_{\min}$ were assigned as 0.94 and 0.0, respectively. The coefficient a is a function of leaf orientation distribution with the canopy. In the present research, a was assumed as 0.6 for the application.

3.2 EXTRACTION OF URBAN AREAS

In most of applications of remote sensing data, parameters extracted from remote sensing data or original DN data are used for the classification to produce thematic map. Our purpose is to extract urban areas from remote sensing images. In usual classification, statistical classifiers have been applied. Such classifiers have severe shortcoming that they classify on pixel-basis, which tend to produce patch-like classification results. Therefore, classifiers based on image processing techniques have been examined. Recently, a software eCognition has been popular as an effective classification tool (eCognition). It classifies based on segmentation technique, and eCognition was used to extract urban areas in this research.

3.3 CASE STUDY: BANGKOK

In the present research, Bangkok was selected as a case study because we completed data collection of Bangkok regarding EIUS. The purpose is to examine the possibility to extract effective parameters related to environmental assessment in EIUS. As an effective parameter, urban area was selected. Both Landsat TM images in 1990s and ETM+ images in 2000s were obtained from Web site (Global Land Cover Facility). Two images of path 129, row 50 and path 129, row 51 were merged as a mosaic image. The observed dates are listed in Table 2.

Figure 2 shows a flow of extraction of urban areas from Landsat TM/ETM images. From original DN values of band 1 to 5 and band 7, NDVI and albedos were estimated. And, LST was estimated from a thermal band data, i.e. band 6 data. These sets of parameters were calculated for TM images in 1990s and ETM+ images in 2000s. Firstly, urban areas in 1990s were extracted. eCognition was used for the segmentation and classification of urban areas. After urban areas in 1990s were estimated, the areas were used as a mask layer for ETM+ images. And then, urban areas since 2000s were extracted. Figure 3 represents the results of urban areas extracted from Landsat TM/ETM+.

4 DISCUSSIONS

Figure 3 represents remote sensing can produce area-based information about urbanization. However, the methodology described in Figure 2 and the results shown in Figure 3 are preliminary. The results obtained in the present research should be examined from various viewpoints, and some improvements are required. Authors examined combinations of several parameters, i.e. NDVI, albedo (VIS, NIR and SW) and LST. Among those combinations, the combination of VIS albedo and LST was found to be effective for the extraction of urban areas. However, these combinations should be examined more.

The methodology to mask urban areas in 1990s needs discussions. In the beginning, authors extracted urban areas in 1990s from parameters in 1990s and urban areas in 2000s from parameters in 2000s, separately. However, the urban areas in 2000s were smaller than the urban areas in 1990s. The shrink of the extracted urban areas may be caused by different atmospheric conditions and different observation seasons. It is quite difficult that a perfect atmospheric correction is implemented because of lack of sufficient data related to atmospheric. On the other hand, authors assumed that the urban areas in 1990s will be urban areas even in 2000s. The methodology to use the masking is based on such an assumption. However, such assumption should be examined by referring to the existing thematic map. Validation of extracted urban areas and application of the methodology for other Asian mega cities will be examined in future.

5 CONCLUSIONS

In the present paper, authors report the framework of EIUS and feasibility of application of remote sensing data for EIUS. EIUS has a potential to enable the comparison of sustainability of Asian mega cities. However, implementation of EIUS may have difficulty to collect data, mainly statistics. Even though statistics are collected from mega cities, non-unified criteria make the comparison between mega cities difficult. Therefore, a feasibility to apply remote sensing data was examined. Remote sensing enables the acquisition of area-based data, which is effective for understanding urbanization, and the comparison between many mega cities under the same criteria. In the present research, NDVI, albedo and LST were derived from Landsat TM/ ETM+ images obtained in 1990s and 2000s. Finally, urban areas in 1990s and 2000s were extracted, and it was found that remote sensing has a potential to be used for EIUS. The methodology utilized in the framework of EIUS should be examined.

REFERENCES

- CASBEE Manual 1, 2003. *Institute for Building Environment and Energy Conservation (IBEC)* (in Japanese)
- Chander, G. and Markham, B., 2003. Revised Landsat-5 TM Radiometric Calibration Procedures and Postcalibration Dynamic Ranges, *IEEE Transactions on Geoscience and Remote Sensing*, Vol. 41, No. 11, pp.

2674-2677

Choudhury, B. J., Ahmed, N. U., Idso, S. B., Reginato, R. J., and Daughtry, C. S. T., 1994. Relations between evaporation coefficients and vegetation indices studied by model simulation, *Remote Sensing of Environment*, vol. 50 pp. 1-17

eCognition, available at <http://www.definiens-imaging.com/>

Global Land Cover Facility. Earth Science Data Interface, available at <http://glcfapp.umiacs.umd.edu:8080/esdi/index.jsp>

Landsat 7 Science Data Users Handbook, available at http://ltpwww.gsfc.nasa.gov/IAS/handbook/handbook_htmls/chapter11/chapter11.html

Li, F. Jackson, T. J., Kustas, W. P., Schmugge, J., French, A. N., Cosh, M. H. and Bindlish, R., 2004 Deriving land surface temperature from Landsat 5 and 7 during SMEX02/SMACEX, *Remote Sensing of Environment*, vol. 92, pp. 521-534

Liang, S., 2000. Narrowband to broadband conversions of land surface albedo I - Algorithms, *Remote Sensing of Environment*, vol. 76, pp. 213-238

Liang, S., 2003. A direct algorithm for estimating land surface broadband albedos from MODIS imagery, *IEEE Transaction on Geoscience and Remote Sensing*, vol. 41, pp. 136-145

Ooka, R., Yasuoka, Y., Susaki, J., Endo, T., Kawamoto, Y., Nakai, H., Nakashima, M., Takada, R., Setojima, M., Funahashi, M. and Okada, K., 2005. Development of new environmental indices for urban sustainability, *Proceeding of the Fourth International Symposium on New Technologies for Urban Safety of Mega Cities in Asia*

Weng, Qihao., Lu, D. and Schubring, J., 2004. Estimation of land surface temperature-vegetation abundance relationship for urban heat island studies, *Remote Sensing of Environment*, vol. 89, pp. 467-483

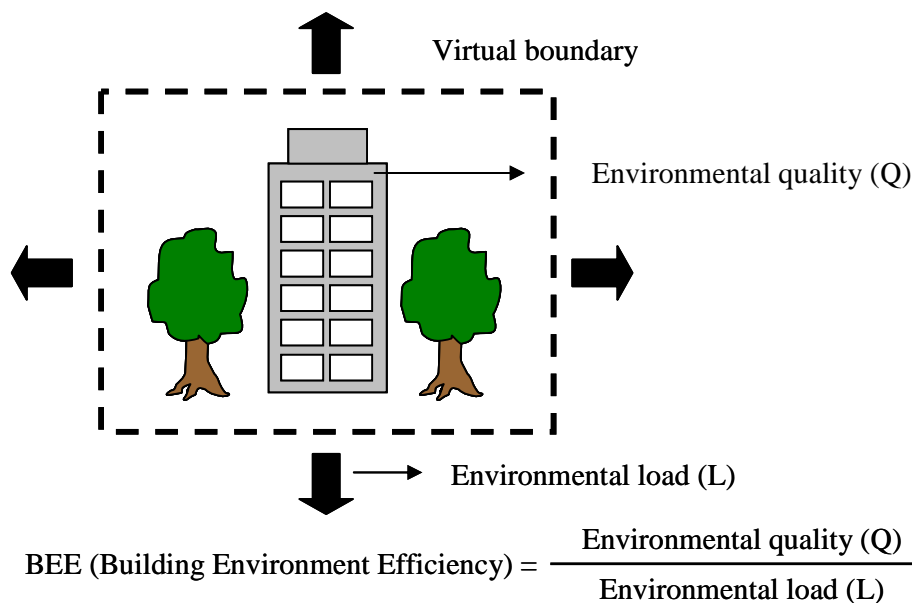


Figure 1: Basic concept of CASBEE. BEE (Building Environment Efficiency) can be defined as the ratio of “Environmental quality” to “Environmental load” (CASBEE Manual 1, 2003).

Table 1: Framework of EUIS and results of data collection in Bangkok. Gray column represents data were not available in Bangkok.

Quality of Life Inside City				
First Classification	Second Classification	Third Classification	Source	
Environment/ Public Health	Degree of nature	Ratio of vegetation coverage		
	Sanitary conditions	Cases of grievances against pollution		PCD
		Distribution ratio of sewerage (%)		BMA
		Air pollution concentration along main roads		PCD
		Cases of oxidase smog		---
		Ratio of patients of breathing diseases		MPH/BMA(DMS)
		Ratio of patients of infectious diseases		MPH/BMA(DMS)
		SO ₂ Density (ppm)		PCD
		NO _x Density (ppm)		PCD
		SPM Density (mg/m ³)		PCD
Public Function/ Public Services	Administration	Growth rate of population (%)	NSO	
		Financial capability index	NSO	

	Habitation	Floor space of houses (m ² /one person)		---
		Ratio of electrified areas		---
		Ratio of persons equipped with information devices		---
	Education	Ratio of graduates studying in elementary schools		BMA/NSO
		the number of teacher at primary school (the number/1,000persons)		BMA/NSO
		the number of the library volumes (the number/one persons)		BMA/NSO
		the number of Infant school (the number/1,000persons)		BMA/NSO
	Commerce	Retail stores(the number/1,000persons)		---
	Traffic	Length of roads/Passing transport		PWD
		Modal share of public transport(%)		OTP
	Welfare	Areas of urban parks (m ² /person)		BMA
		Medical welfare facilities (the number/one person)		DLP/SSO
Safty/ Security	Earthquake	Ratio of non-earthquake-proof houses (%)	---	

	Fire	Fire occurrences (the number/1,000perons/one year)		BMA (DPS)
		Ratio of non-fire-proof houses (%)		---
		Rescue operation persons of fire station (the number/1000persons)		---
	Storm and flood damage	the number of disasters /the volume of rainfalls (the ratio/one year)		DDPM
	Crime/Accident	Criminal offenses (the number/1000persons/one year)		Royal Thai Police
		Traffic accidents (the number/one person/one year)		Royal Thai Police
Field policemen (the number/1,000persons)			Royal Thai Police	
	Beds of sickness (the number/1,000persons)		MPH/BMA(DMS)	

Environmental Load				
First Classification	Second Classification	Third Classification	Source	
Energy	Electricity	Consumption of electricity (kWh/one person/one year)	MEA	
	Gas	Consumption of city gas (MJ/one person/one year)	---	
		Consumption of propane gas (kg/one person/one year)		PTT/PTIT
		Consumption of kerosene (t/one person/one year)		EPPD
Resources	Water Resources	Water use (m ³ /one person/one year)	MWA	
	Waste	Household refuse (kg/one person/one year)		BMA
		Industrial wastes (ton/one person/one year)		DIW
Environment over wide area	Atmosphere	CO ₂ Emission Volume (ton/one person/one year)	DAEDE	
		SO ₂ Emission Volume (ton/one person/one year)	DAEDE	
		NO _x Emission Volume (ton/one person/one year)	DAEDE	
		SPM Emission Volume (ton/one person/one year)	DAEDE	

Remarks;

BMA: Bangkok Metropolitan Administration
 DAEDE: Department of Alternative Energy Development and Efficiency
 DDPM: Department of Disaster Prevention and Mitigation
 DDS: Department of Drainage and Sewerage
 DEQP: Department of Environmental Quality Promotion
 DIW: Department of Industrial Works
 DLP: Department of Labour Protection and Welfare
 DMS: Department of Medical Services
 DPS: Disaster Prevention Subdivision
 DPT: Department of Public Works, Town and Country
 EPPD: Energy Policy and Planning Office
 MEA: Metropolitan Electricity Authority
 MPH: Ministry of Public Health
 MWA: Metropolitan Waterworks Authority
 NSO: National Statistical Office
 OTP: Office of Transport and Traffic Policy and Planning
 PCD: Pollution Control Department
 PTIT: Petroleum Institute of Thailand
 PTT: PTT Public Company Limited
 PWD: Public Works Department
 SSO: Social Security Office

Table 2: TM/ETM+ images used for the analysis. These images were obtained from Web site (Global Land Cover Facility) (Landsat 7 Science Data Users Handbook).

Path/Row	129/50	129/51
TM	1994/Oct/25	1994/Oct/25
ETM+	2000/Nov/02	2002/Jan/08

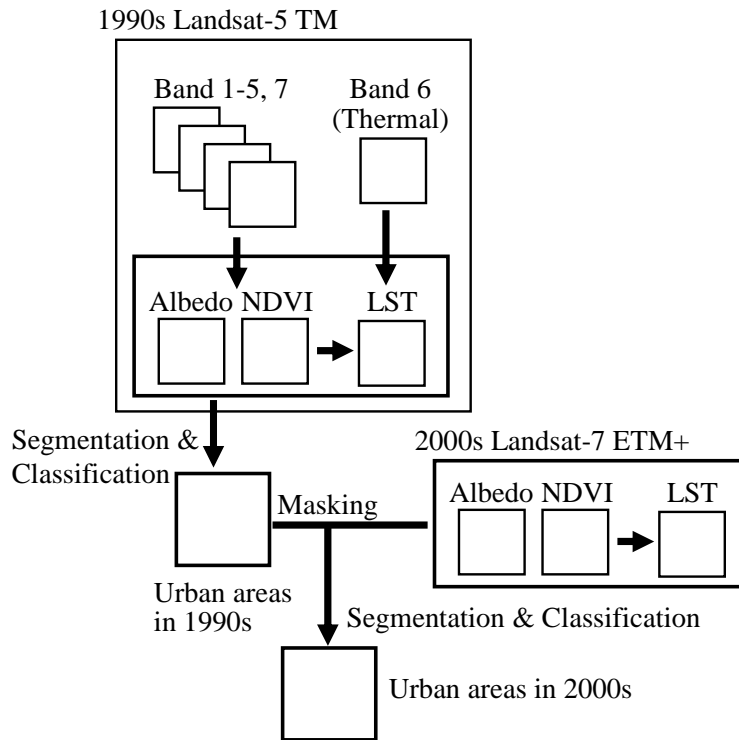


Figure 2: Flow of extraction of urban areas from Landsat TM and ETM+ images

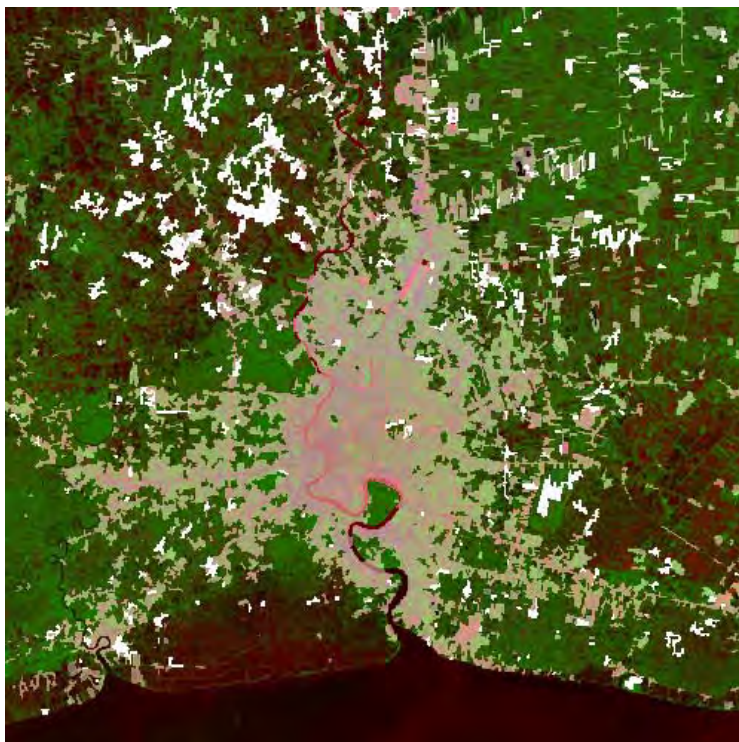


Figure 3: Urban areas of Bangkok, Thailand in 1990s and 2000s extracted from Landsat TM/ETM+ images. A base map is a composite of VIS albedo (red), NDVI (green) and LST (blue) of Landsat ETM+ in 2000s. Gray and white areas represent urban areas since 1990s and urban areas since 2000s, respectively.

ENVIRONMENTAL IMPACT ASSESSMENT OF HEAVY METALS ON FISHES AND CRUSTACEANS IN OGUNU CREEK, WARRI RIVER IN NIGER DELTA AREA OF NIGERIA.

OKORO, D.,^{*a}; OSAKWE, J.^b

^aDepartment of Chemistry, University of Benin, Benin City, Edo State,
Nigeria.

Tel: +234 8033834446; +2348023320809

E-mail: dukeokoro@yahoo.com

^bMail – In Oilfield & Labouratory Services Limited, Plot 5, 38th Street,
DDPA, Effurun, Delta State, Nigeria. Tel: +234 8032718214

E-mail: osakwejo@yahoo.com

ABSTRACT

*Water, sediment and some selected faunae were sampled monthly in Ogunu creek of Warri River between August, 2003 and July, 2004. The samples were analyzed for twelve heavy metals including iron, zinc, lead, manganese, chromium, copper, nickel, cadmium, cobalt, mercury, vanadium, and arsenic. Analytical results were compared to data available in the literature and standard criteria recommended by FEPA, WHO, and ANZECC. Concentration Factor (CF) and Biotic – sediment Accumulator Factor (BSAF) were used to establish connections between the heavy metals concentrations in the organisms and the surrounding environment. Very strong correlations were found to exist between the pairs of iron:zinc and vanadium:nickel, which along with other factors revealed possible contamination due to increased anthropogenic activities and urbanization. The results observed in this study indicated that heavy metals were present in elevated levels as reflected in their bioaccumulation in *Chrysichthys nigrodigitatus*, *Drepane africana*, *Palaemon hastatus* and *Uca pugilator*.*

1. INTRODUCTION

Fishes and macro invertebrates obtained from the Ogonu creek of the Warri River enter the local markets indiscriminately via local anglers and Fishermen, which are being consumed daily by humans. The creek is host to industrial activities from petroleum and allied companies including the residential and industrial area of a mother oil company. This research work was aimed at carrying out an investigative study on the pollution level of the Ogonu Creek of the Warri River with the objective directed towards obtaining current information about the surface water quality, sediment quality and levels of twelve heavy metals in selected fishes and crustaceans in the Ogonu creek of the Warri River.

When heavy metals are taken up by an organism, a fraction of it is metabolized and utilized for its physiological needs (e.g. energy supply, growth, reproduction) or accumulated in some tissues, and a part, which cannot be utilized, is released into the environment. The concentration of a substance in an organism is the result of the difference between the amount of the substance taken in and that released into the environment.

The comparison between the contaminations of an aquatic organism in relation to that of the water in which it lives is commonly quantified by the ratio between the concentration of the pollutant in the organism (related to the wet weight) and that in the water. It is the value of this ratio that we have referred to in this paper as concentration factor (CF). This same ratio was referred to as Biological accumulator factor (BAF) by William *et al.* (1999), where it was used to calculate the accumulation of polychlorobiphenyls (PCBs) in phytoplankton, zooplankton and zebra mussel (*Dreissena polymorpha*) in relation to PCB concentration in the water.

Because sediment seems to be the most important source of pollutants for benthic species, the pollutant concentration in the organism is compared with that in the sediment, instead of with the concentration in the water. This relationship is quantified by the "Biotic-sediment accumulator factor" (BSAF); which is the ratio between the pollutant concentration in the organism and that in the surrounding sediments. This factor was also successfully adopted by Song and Breslin (1998) for heavy metals concentrations in an amphipod (*Diporeia spp.*; formally classified as *Pantoporeira hoyi*) from Lake Ontario. All water and sediment sampling was carried out between August, 2003 and July, 2004. The selected faunae essentially, fishes and crustacean species were all obtained fresh and alive from local anglers and fishermen from the mouth of the Ogonu Creek. The points where water and sediment samples were taken are on Latitude N 50 31.80' and Longitude E 50 42.46'.

2. SAMPLE HANDLING AND TREATMENT

Composite water samples were collected every month from described points in Ubeji creek of the Warri River in 1-litre polythene bottles that had previously been soaked in concentrated nitric acid for 24 hours and rinsed

with de-ionised water (APHA, 1998). Composite sediment samples were collected monthly with the aid of a Van Veen Grab Sampler, stored on ice in a one-litre chemically-cleaned glass jars with Teflon-lined screw-cap, until the sample could be frozen. All samples were frozen upon returning to the lab for analysis. The selected faunae, after obtaining them, were rapped up with aluminium foil and kept in ice before proceeding to the laboratory. *Drepane africana* (spade fish) were classified as pelagic (living and swimming in the open river) with average weight of 54.04g, *Chrysichthys nigrodigitatus* (cat fish) were classified as benthopelagic (live near or at the bottom sediment and feeds mainly on benthic organism) according to Marshall and Merrett (1997) with average weight of 96.85g. *Paelemon hastatus* (white shrimp) and *Uca pugilator* (fiddler crab) were classified as Benthos with average weight of 30.24g and 17.56g respectively (Ajayi *et al.*, 1986).

3. ANALYSIS

Water samples were digested with concentrated HNO₃ in a Pyrex conical flask (Martin *et al.*, 1992). The resulting solution after digestion was cooled and filtered through a Whatman filter paper No. 42 into a volumetric flask and made up to 100 mL mark with de-ionized water. A blank was also prepared in the same manner and method using de-ionized water. 100 mg/L stock standards for the various metals were prepared using standards and the concentrated 30% HNO₃. Sediment samples having been air-dried overnight were sieved with a 22 mm sieve aperture. 1.00g of the samples were weighed into a 100mL Pyrex conical flask and was digested with 15mL of a mixture of the following concentrated acid until dense white fumes occur in a fume hood. Mixture of acids, Sulphuric acid: Nitric acid: Perchloric acid were in the ratio 2:2:1. All digested filtrate in water and sediment were analyzed with Flame Atomic Absorption Spectrophotometer (Perkin-Elmer AAS 31,000) according to a modification of the method described by Soster, *et al.* (1992). For all the selected faunae, once whole body of organism was macerated, 5.00g of homogenous blend was weighed into a pyrex conical flask and 15 mL of a mixture of three concentrated acids, perchloric, nitric and sulphuric acid in the ratio of 1:2:2, was used to digest sample for 2-3 hours until brown fumes ceased to evolve (Bursell, 1975). The content of the flask after digestion was filtered through a whatman GFK glass filter and solution made up to 100 mL mark with de-ionized water and kept in a heavy metal polythene bottle ready for AAS analysis.

4. RESULTS AND DISCUSSIONS

The descriptive statistics of all data obtained including Mean, Maximum, Minimum, Standard deviation along with correlation matrix were calculated using the software Kyplot version 2.0 for windows at 95% confidence level. The results of the mean concentrations of the determined heavy metals in all the described matrices of the Ogunu Creek of the Warri River are presented

in Table 1. Correlation matrix of the metals in water and sediment of the creek are shown on Tables 2 and 3, while the calculated Concentration Factor (CF) and the Biotic-Sediment Accumulator Factor for the described faunae are respectively presented in Tables 4 and 5.

Table 1: Concentrations of heavy metals in surface water, sediment and selected faunae of Ogunu Creek of the Warri River.

Heavy Metals	Mean \pm STDEV					
	Water (mg/L)	Sed.(mg/kg)	<i>D. africana</i> (mg/kg)	<i>C. nigrodigitatus</i> (mg/kg)	<i>P. hastatus</i> (mg/kg)	<i>U. pugilator</i> (mg/kg)
Iron	0,596 \pm 0,514	236.50 \pm 94.61	8.621 \pm 1.818	12.170 \pm 3.057	15.004 \pm 5.652	16.133 \pm 5.323
Zinc	0,891 \pm 0,235	50.164 \pm 11.389	5.734 \pm 1.345	15.629 \pm 7.082	22.906 \pm 7.142	28.088 \pm 7.487
Lead	0,055 \pm 0,005	3.929 \pm 1.406	0.757 \pm 0.257	1.67 \pm 0.836	1.247 \pm 0.094	3.374 \pm 1.368
Manganese	0,064 \pm 0,014	8.222 \pm 2.712	1.603 \pm 0.155	2.226 \pm 0.576	5.254 \pm 2.526	12.673 \pm 4.558
Chromium	0,060 \pm 0,009	0.965 \pm 0.485	0.083 \pm 0.005	0.113 \pm 0.031	0.466 \pm 0.398	0.874 \pm 0.543
Copper	0,030 \pm 0,021	1.758 \pm 0.443	0.302 \pm 0.156	0.549 \pm 0.090	0.766 \pm 0.185	3.978 \pm 1.587
Nickel	0,301 \pm 0,110	4.613 \pm 2.014	1.569 \pm 0.454	4.194 \pm 1.626	6.210 \pm 1.966	7.827 \pm 1.753
Cadmium	0,049 \pm 0,014	0.697 \pm 0.183	0.412 \pm 0.158	0.598 \pm 0.137	0.805 \pm 0.150	0.949 \pm 0.137
Cobalt	0,027 \pm 0,013	0.870 \pm 0.437	0.063 \pm 0.008	0.084 0.012	0.108 \pm 0.022	0.134 \pm 0.030
Mercury	0,001 \pm 0,001	0.007 \pm 0.001	0.003 \pm 0.00	0.005 \pm 0.004	0.011 \pm 0.005	0.021 \pm 0.013
Vanadium	0,589 \pm 0,226	9.342 \pm 4.046	3.153 \pm 0.921	8.398 \pm 2.267	12.137 \pm 3.673	15.592 \pm 3.545
Arsenic	0,044 \pm 0,005	0.623 \pm 0.215	0.035 \pm 0.009	0.198 \pm 0.129	0.381 \pm 0.208	0.898 \pm 0.201

Sed.—Sediment; STDEV ---Standard Deviation

Table 2: Correlation matrix of heavy metals in surface water of Ogunu Creek of the Warri River.

	Fe	Zn	Pb	Mn	Cr	Cu	Ni	Cd	Co	Hg	V	As
Fe	1											
Zn	0.943	1										
Pb	0.890	0.955	1									
Mn	0.759	0.790	0.861	1								
Cr	0.246	0.238	0.125	0.212	1							
Cu	0.648	0.804	0.890	0.732	0.056	1						
Ni	0.519	0.479	0.589	0.474	0.274	0.598	1					
Cd	0.501	0.373	0.451	0.204	0.232	0.315	0.653	1				
Co	0.753	0.811	0.864	0.643	0.327	0.788	0.606	0.716	1			
Hg	0.915	0.898	0.878	0.640	0.253	0.768	0.714	0.614	0.803	1		
V	0.506	0.459	0.565	0.424	0.257	0.558	0.991	0.690	0.588	0.710	1	
As	0.751	0.846	0.856	0.772	0.082	0.676	0.285	0.193	0.709	0.633	0.248	1

The determined levels of Fe, Pb, Mn, Cr, Ni, Cd, Co, and V exceeded standard criteria recommended for surface water by FEPA (1991); WHO (1998); and ANZECC (1992). Lead has a mean value of 0.056 ± 0.005 mg/L in surface water of the creek. This amount in drinking water could substitute for calcium and be included in bones, which may affect the skeletal systems of children. The presence of elevated heavy metal levels in the waters of the

creek indicated that the water may be unsuitable for drinking. The levels of heavy metals in the matrices were observed to be in the following order of magnitude: sediment > crustacean > fish > water. Nickel has its mean value for surface water in the described creek of Warri River as 0.301 ± 0.110 mg/L which was within the range of values reported for streams in Colombia, PA (Turchi – Dooley *et al.*, 2001). The observed values were however higher than most reported local and international standard water quality guidelines. Nickel has a very strong correlation with vanadium as observed from the correlation coefficient in water and sediment of the creek (Correlation coefficient > 0.9). Further investigation in both matrices revealed that their ratio was in V: Ni (2:1). This was an indication that they were probably from petroleum related sources.

Table 3: Correlation matrix of heavy metals in sediment of Ogonu Creek of the Warri River.

	Fe	Zn	Pb	Mn	Cr	Cu	Ni	Cd	Co	Hg	V	As
Fe	1											
Zn	0.821	1										
Pb	0.872	0.856	1									
Mn	0.798	0.944	0.937	1								
Cr	0.761	0.966	0.836	0.894	1							
Cu	0.979	0.810	0.853	0.787	0.769	1						
Ni	0.747	0.959	0.814	0.919	0.946	0.777	1					
Cd	0.874	0.948	0.862	0.928	0.893	0.866	0.905	1				
Co	0.446	0.811	0.695	0.805	0.878	0.491	0.868	0.677	1			
Hg	0.937	0.780	0.757	0.713	0.759	0.953	0.738	0.848	0.438	1		
V	0.704	0.949	0.791	0.917	0.935	0.737	0.997	0.895	0.882	0.706	1	
As	0.688	0.875	0.723	0.831	0.889	0.747	0.931	0.894	0.779	0.742	0.932	1

Aquatic sediments are principally derived from weathering processes, with major transportation from terrestrial sources under high runoff from storms and floods. In addition, discharges from urban, and industrial activities are potential sources of particulates. Anthropogenic contaminants, including heavy metals and nutrient elements are associated with particulate and dissolved inputs to natural waters like the Ogonu Creek of the Warri River. Iron had one of the highest concentrations and the observed values for fish samples were well above the ones reported for fish samples in Rima River, Sokoto, Nigeria (Abdulrahman *et al.*, 2004). The observed values for zinc in fish samples of the Ogonu Creek were within the values reported for fishes in the Lagos Lagoon (Tomori, 2004) and Cooks River, Australia (Gupta, 1997). The observed mean value of zinc in *Uca pugilator* of the Ogonu Creek was in agreement with mean value reported for same specie of crab in Degema District of Rivers Sate, Nigeria (Ogbonda, 1992). These values were however, below allowable limits of Australian New Zealand Food Authority (ANZFA, 1992). Cadmium had elevated levels in all fish samples of the Creek when compared to allowable limits of ANZFA (1992). The observed values were in agreement with those recorded in previous studies conducted for fish samples in Warri River (Nwajei, *et al*, 2004). The levels of cadmium observed for crustaceans in the Creek were relatively high

when compared with reported levels in crustaceans of Forcados River (Ndiokwere and Eloke, 2001). Mercury had a range of 0.003 – 0.021 mg/kg in all selected faunae tested. These values were low compared to ANZFA (1992) allowable limits and the levels reported in fish samples of Cooks River, Australia (Gupta, 1997), but were higher than the value recommended for fish by Tennessee Water Quality (1998). The CF and BSAF in all metals for the selected faunae were in the following order of magnitude: *Uca pugilator* > *Palaemon hastatus* > *Chrysichthys nigrodigitatus* > *Drepane africana*. The crustaceans including fiddler crab and the white shrimp exhibited higher bioaccumulation potentials compared to the fishes. However, bioaccumulation was stronger in benthopelagic catfish compared to the pelagic spade fish as observed in Tables 4 and 5.

Table 4: Concentration Factors (CF) of described Faunae of Ogonu Creek of the Warri River.

Metals	<i>D.africana</i>	<i>C.nigrodigitatus</i>	<i>P.hastatus</i>	<i>U.pugilator</i>
Iron	0.04	0.05	0.06	0.07
Zinc	0.11	0.31	0.46	0.56
Lead	0.19	0.43	0.32	0.86
Manganese	0.19	0.27	0.64	1.54
Chromium	0.09	0.12	0.48	0.91
Copper	0.17	0.31	0.44	2.26
Nickel	0.34	0.91	1.35	1.70
Cadmium	0.59	0.86	1.15	1.36
Cobalt	0.07	0.10	0.12	0.15
Mercury	0.43	0.71	1.57	3.00
Vanadium	0.34	0.90	1.30	1.67
Arsenic	0.06	0.32	0.61	1.44

Table 5: Biotic-Sediment Accumulator Factor (BSAF) of described Faunae of Ogonu Creek of the Warri River.

Metals	<i>D.africana</i>	<i>C.nigrodigitatus</i>	<i>P.hastatus</i>	<i>U.pugilator</i>
Iron	14.44	20.43	25.19	27.09
Zinc	6.44	17.55	25.72	31.54
Lead	13.83	30.42	22.71	61.46
Manganese	25.05	34.78	82.09	198.02
Chromium	1.38	1.88	7.77	14.57
Copper	10.03	18.24	25.45	132.16
Nickel	5.21	13.92	20.6	25.97
Cadmium	8.48	12.31	16.56	19.53
Cobalt	2.37	3.16	4.06	5.04
Mercury	2.73	4.55	10	19.09
Vanadium	5.35	14.25	20.6	26.46
Arsenic	0.8	4.52	8.7	20.5

5. CONCLUSION

Heavy metals investigation produced significant results that revealed much unusual characteristics in the quality of water, sediment and faunae of the Ogonu creek of the Warri River. *Uca pugilator*, *Palaemon hastatus* and *chrysiichthys nigrodigotatus* bioaccumulated heavy metals in the creek, indicating that they are good indicators for biomonitoring of pollution of aquatic environment.

REFERENCE

- Abdulrahman, F. W., and Tsafe, A. I., 2004. Trace metals Composition in Fishes from Sokoto Ruma River. Published in: 27th Int'l Conf. of the Chemical Society of Nigeria. pp 219-223.
- Ajayi, T. O., Ukpe, E. T., Ssentongo, G. W., 1986. Marine Fishery Resources of Nigeria: A review of exploited Fish stocks. Chapter 6 page 3.
- APHA, 1998. Standard Methods for the Examination of Water and Wastewater, 20th edition Publishers: American Public Health Association; American Water Works Association; Water Environment Federation.
- Burrell, D. C., (1975). Atomic spectrometric analysis of heavy metal pollutant in water. Ann Arbor Science publishers, Inc., Ann Arbor, Michigan.
- Gupta, L., 1997. Environmental Health Assessment of Fish and Oyster from the Cooks River – heavy metals and organochlorine pesticides CSAH public health unit. Technical Report . 4pp.
- Marshall, N. B., and Merrett, N. R., 1977. The existence of a benthopelagic fauna in the deep-sea, in A voyage of Discovery, George Deacon 70th Anniversary Volume, edited by M. V. Angel, pp. 483-497, Pergamon Press, Oxford.
- Martin, T. D., Brockhoff, C. A., Creed, J. T., and Long, S. E., 1992. Determination of metals and trace elements in water and wastewater by inductively coupled plasma – atomic emission spectrometry. *I.C.P. News t t r*, 18(3): 147-169.
- Ndiokwere, C. L., and Elope, F. O., 2001. Environmental Impact Assesment of Petroleum exploitation on fish and mollusks in the Niger Delta Forcados River as a case study. Msc thesis.
- Nwajei, G. E., and Okrija, B. O., 2004. Cadmium, Chromium, Lead and Zinc Concentrahoria in fishes, Earthworm and soil from Warri River, Nigeria. Published in: 7th International conference of the Chemical Society of Nigeria pp. 155-158.
- Ogbonda, C., 1992. Bioaccumulation of Heavy metals in mollusks and crustaceans in Mangrove Area of River State. M. Phil thesis. University of Benin, Nigeria.
- Song, K. H., and Breselin, V. T., 1998. Accumulation of contaminant metals in the amphipod *Diporeia Spp*. In Western Lake Ontario. *J. Great Lakes Res.*, 24: 949-961.

- Soster, D. A., Harvey, D. T., Troska, M. R., and Gromms, T., 1992. The effect of Turbificid oligocheates on the uptake of Zinc by Lake Erie sediments. *Hydrobiologica*. 248: 249-258.
- Tomori, W. B., Aiyesanmi, A. F., and Obijola, O. A., 2004. Heavymetal quality Assessment of Marine Fishes of Lagos Lagoon. Published in 27th Int'l Conf. of Chemical Society of Nigeria pp 252-256.
- Turchi-Dooley, S., and Wallace, J., 2001. A preliminary study on Trophic level Analysis for Heavy Metals in Aquatic Macroinvertebrates in two streams in Columbia, PA.
- William, E. J., Manchester-Neesvig, J. B., Agrell, C., and Armstrong, D. E., 1991. Influence of ortho-substitution homologous group on polychlorobiphenyl bioaccumulation factors and fugacity ratios in plankton and Zebra mussels (*Dreissena polymorpha*). *Environ. Toxicol. Chem.*, 18: 1380-1389.

FLOOD FORECAST AND FLOOD CONTROL STRUCTURES OPERATION FOR FLOOD CONTROL OF HA NOI CITY

Tran Thuc, Nguyen Xuan Hien, Dang Quang Thinh, Huynh Thi Lan Huong
Institute of Meteorology and Hydrology, Vietnam
thuc@netnam.vn

ABSTRACT

The Red River system, with a catchment area of about 143,000 km², is the biggest river system in North Vietnam. There are three main river tributaries, namely, Da River, Thao River and Lo River. The river basin is affected mainly by flood, inundation and storm surge. Flood protection system in the area includes river and sea dyke, flood regulation by reservoirs, flood diversion and detention.

Numerical models were applied for flood forecast for the Red River system, especially for Ha Noi, the capital of the country. The objective is to improve the forecast accuracy and forecasting lead time, and to provide a tool for the operation of flood control structures. Rainfall-runoff model is used for headwater computation and forecast, and hydrodynamic model is applied for flood routing in the river network downstream. Two models were applied for the Red River System; namely: (i) Hydrological Modeling System (HMS) and HECRAS; and (ii) MIKE-11 system. HMS and HECRAS models give very good results in rainfall-runoff computations, flood routing, and flood control structure operation. However, the models do not have module for error updating, a crucial module for flood forecasting. It is then cannot be applied in real time flood forecast. The MIKE-11 model, with separate modules for rainfall-runoff, flood routing, reservoir and other structures operation, especially module for automatic error update. The model is then applied for the Red River flood forecast.

The models were used for real-time flood forecast for the flood seasons of 2003 and 2004. Results are found very satisfactory. The model system is, therefore, recommended for operational real-time flood forecast.

Introduction

Two model systems are applied for rainfall-runoff and hydrodynamic computation and forecast for the Red River system, North Vietnam. They are: (1) HMS and HECRAS models; and (2) MIKE-11 system.

The HMS and HECRAS give good results in rainfall - runoff, hydrodynamic, reservoir operation and flood control structures operations. However, the models do not have error updating module - a very important module for forecasting, therefore, the model cannot be used for operational flood forecast.

The MIKE-11 model system has the advantage that it has separate modules for rainfall-runoff, flood routing, reservoir and other structures operation, especially module for automatic error update. The model is then applied for the Red River flood forecast.

NAM model is a lumped parameters rainfall-runoff model. It is based on a system of vertical tanks and linear storage. Each sub catchment is treated as one unit.

Governing equations for unsteady 1-D open channel flow in the river system, used in the Mike-11 model, are as follows:

Continuity equation:

$$dt - \rho \left(Q + \frac{\partial Q}{\partial x} dx \right) dt = \rho dA dx = \rho \frac{\partial Q}{\partial t} dx dt$$

in which: $\frac{\partial Q}{\partial t} = \frac{\partial A}{\partial t}$ and $\frac{\partial Q}{\partial t} - B \frac{\partial h}{\partial t} = 0$

Momentum equation:

$$\frac{\Delta M}{\Delta t} = \frac{\Delta(M.U)}{\Delta x} + \frac{\Delta P}{\Delta x} - \frac{F_f}{\Delta x} + \frac{F_g}{\Delta x} \quad (2)$$

where: momentum: $M = \rho h b U$, momentum flux: $M_f = \rho h b U U$,

pressure term: $P = \frac{1}{2} \rho g b h^2$, friction term: $F = \Delta x b \frac{\rho g U^2}{C^2}$,

gravity term: $P = \rho g A S$.

The governing equations are solved by implicit 6-point numerical scheme (Bott - Inoescu).

FLOOD FORECAST FOR THE RED RIVER SYSTEM

Model Calibration and Verification

NAM model is applied for headwater hydrological forecast. The Da, Thao, Lo, Cau, Thuong and Luc Nam Rivers are subdivided into 6, 8, 8, 1, 1, and 1 sub-catchments, respectively. The headwater computational scheme is shown in Fig.1.

Six-hour rainfall data at stations in the river basin in 2001 and 2003 are used for model calibration and verification, respectively. Results of model calibration and verification are shown in Table 1.

Table 1: Results of rainfall-runoff model calibration and verification

Sub Catchment	Station	Nash Sutcliffe Coefficient	
		Calibration	Verification
Da River	Ta Bu	78%	75%
Thao River	Phu Tho	81%	79%
Lo River	Vu Quang	78%	78%
Cau River	Thai Nguyen	77%	76%
Thuong River	Cau Son	80%	81%
Luc Nam River	Chu	71%	75%

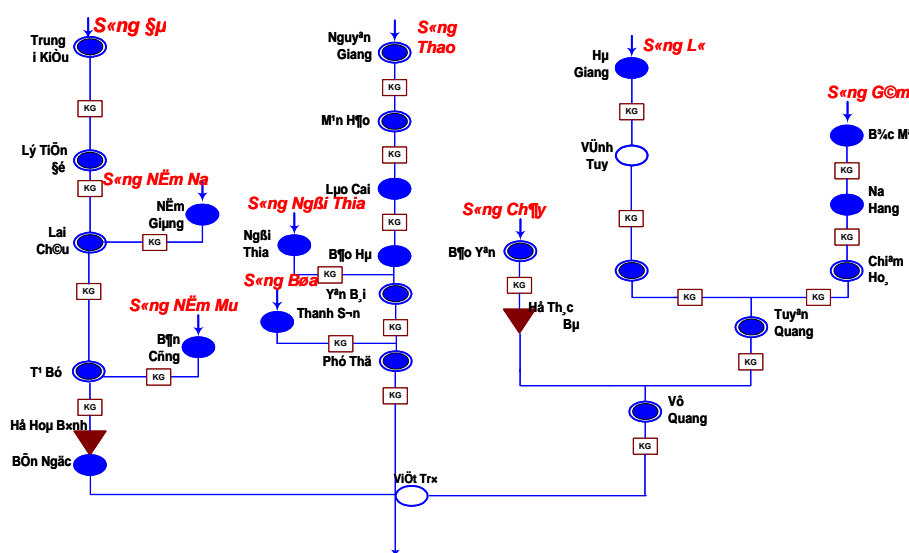


Fig. 1: Headwater Computational Scheme

MIKE-11 model is applied for flood forecast and flood control structures operation for the Red River system. Rivers in the scheme includes: Da, Thao, Lo, Hong, Cau, Thuong, Luc Nam, Duong, Thai Binh, Kinh Thay, Kinh Mon, Lai Vu, Gua, Da Bach, Moi, Mia, Luoc, Lach Tray, Hoa, Tra Ly, Dao, and Day river.

The river system consists of 25 main rivers, divided into 52 river reaches with 792 river cross-sections. In which, Da River has one reach with 51 cross-sections, Thao River has one reach with 27 cross-sections, Lo River has two reaches with 19 cross-sections, Red River has 8 reaches with 156 cross-sections, Thai Binh River has 5 reaches with 44 cross-sections, Luoc River has one reach with 34 cross-sections, Duong River has one reach with 31 cross-sections. Flood control structures in the Red River system such as: Hoa Binh dam, Day River flood diversion structure, Tam Thanh, Lap Thach, Luong Phu - Quang Oai flood detention areas are

presented in the scheme of computation. Operational procedure of flood control structures is presented in model and scheme of computation is shown in Fig. 2.

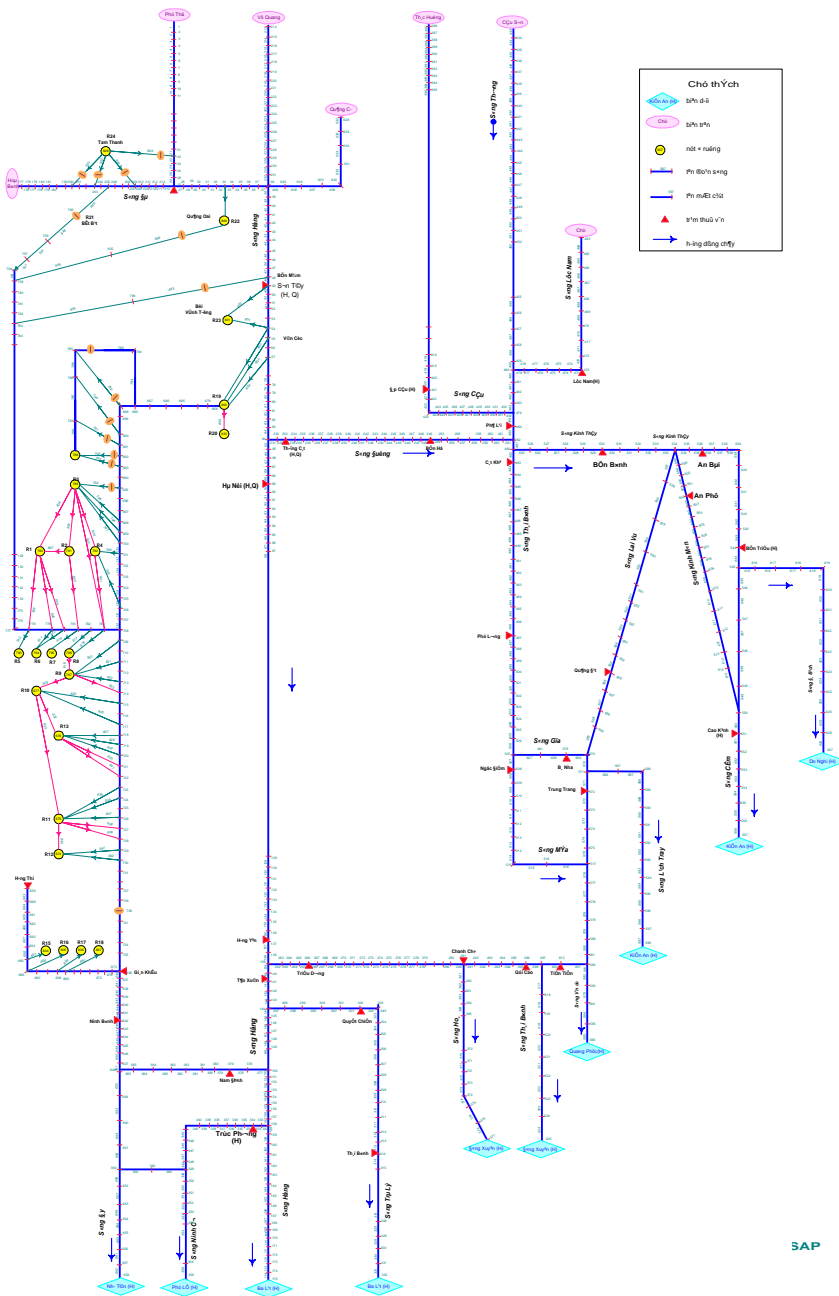


Fig. 2: Downstream Flood Routing Computational Scheme

Upstream boundaries are hourly discharges at 6 hydro-stations: Hoa Binh, Yen Bai, Phu Ninh, Thac Bui, Cau Son and Chu. Downstream boundaries are tidal water level at hydro-stations: Nhu Tan, Truc Phuong, Ba Lat, Dinh Cu, Dong Xuyen, Quang Phuc, Kien An, Cua Cam, and Don Son.

Water level/discharge data at hydrological stations in 1996 and 2000 are used for model calibration and verification, respectively. Results of model calibration and verification are shown in Table 2. It is found that the computed results are in good agreement with observed data.

Table 2: Results of hydrodynamic model calibration and verification

No	Station	Model Calibration		Model Verification	
		Efficiency (%)	Absolute Error (m)	Efficiency (%)	Absolute Error (m)
1	Trung Ha	98	0.00	96	0.30
2	Viet Tri	98	0.10	97	0.36
3	Son Tay	98	0.12	95	0.48
4	Ha Noi	98	0.22	95	0.34
5	Thuong Cat	97	0.17	97	0.34
6	Luc Nam	97	0.04	96	0.16
7	Phu Lang Thuong	90	0.04	98	0.03
8	Pha Lai	96	0.10	97	0.06
9	Cat Khe	89	0.10	94	0.15
10	Phu Luog	92	0.29	93	0.39
11	Ben Binh	91	0.01	95	0.35
12	Cao Kenh	95	0.05	97	0.03
13	Don Son	95	0.15	91	0.04
14	An Phu	89	0.04	83	0.43
15	Quang Dat	91	0.02	91	0.01
16	Ba Nha	78	0.16	79	0.06
17	Trung Trang	87	0.02	76	0.13
18	Ben Ho	82	0.10	92	0.32

Results of Operational Flood Forecasts

Operational flood forecasts are conducted for flood season of 2003 and 2004. Flood forecast are done for all computational nodes of the model, in which more attention are focused for importation locations in the river system, i.e. Ha Noi, Thuong Cat, Pha Lai, Son Tay and Hung Yen.

Results of Headwater Flood Forecast

Forecasts are carried out for water level at Yen Bai, Tuyen Quang and flow to Hoa Binh reservoir. Forecast time is 24 hours. Totally, there are 92 bulletins are issued. Accuracy of flood forecast is 83%.

Results of Flood Forecast for Downstream

Forecasts are done for 24 hours, 36 hours and 48 hours. Results of flood forecast for downstream location are shown in Table 3. It is found that the accuracy of flood forecast using the model system is acceptable for

operational flood forecast for the Red River system. It is comparable with conventional method currently used in the river basin.

Table 3: Results flood forecast for Ha Noi and Pha Lai stations

Station	Flood season in 2003		Flood season in 2004	
	Ha Noi	Pha Lai	Ha Noi	Pha Lai
No of 24-hour forecast	29	29	46	46
No of accurate forecast	25	19	37	35
Confidential level	86 %	66 %	81 %	76 %
Min error	0 cm	1 cm	0 cm	1 cm
Max error	56 cm	148 cm	64 cm	35 cm
No of 36-hour forecast	29	28	46	46
No of accurate forecast	20	17	33	31
Confidential level	69 %	61 %	71,7 %	67,4 %
Min error	0 cm	1 cm	0 cm	1 cm
Max error	77 cm	163 cm	117 cm	43 cm
No of 48-hour forecast	28		45	
No of accurate forecast	20		32	
Confidential level	71 %		71,1 %	
Min error	0 cm		0 cm	
Max error	137 cm		175 cm	

CONCLUSIONS

MIKE-11 model system has special modules in which flood forecasting module has updating function that evaluate and eliminate deviations between observed and simulated discharges/water levels in the hindcast period to improve the accuracy of the model results in the forecast period. Moreover, the model also has reservoir operation and flood control structure operation functions. Thus, MIKE-11 system can be applied for purpose of operational hydrological forecast for the Red River system. Results of operational forecast are found satisfactory.

Experience has been gained in applying the model for operational forecast. In the coming time, development and enhancement of model will be conducted to improve forecast accuracy.

REFERENCES

1. Hydro-meteorological Service of Viet Nam, *Hydrological data in 2003, 2004*.
2. *Tran Thuc*, Report of Operational Flood Forecast in Flood Season 2003 and 2004.
3. *MIKE-11 User's Manual, 2003*.
4. *HEC-RAS User's Manual, 2003*.
5. *HEC-HMS User's Manual, 2003*.

FLOOD CONTROL INVESTIGATION OF HAD YAI CITY, SOUTHERN THAILAND

TAWATCHAI TINGSANCHALI
Professor, School of Civil Engineering,
Asian Institute of Technology, Thailand
Email Address: tawatch@ait.ac.th

AKAPOB TEERAORANIT
Former graduate student, School of Civil Engineering,
Asian Institute of Technology, Thailand
Email Address: akapob@hotmail.com

ABSTRACT

Had Yai City in Songkhla province situates in the Utaphao river basin in Southern Thailand. Rapid development of the city obstructs the natural waterways and decreases the flood drainage capacity from the city to Songkhla Lake. Four major floodings occurred in Had Yai in 1942, 1969, 1988 and 2000 resulting in enormous damages to the city. Utaphao river basin has a total drainage area 2305 km². Khlong Utaphao is the main river in the basin and drains water from Had Yai city to Songkhla lake. The length of Khlong Utaphao is about 112 km. The estimated drainage capacity is 420 m³/s. Floods in the Utaphao river basin are influenced by northeast monsoon. The average annual rainfall in the basin is approximately 1800 mm. In November 2000, the largest flood ever occurred and caused severe damages to 11 Provinces including Had Yai. 2,200,000 people were affected by the flood and 8,300 people were evacuated. 59 people and 1,600,000 live stocks were killed and 269,230 ha of farmlands were damaged. The total damage is estimated about one billion US dollars. It is required to find flood control measures for Had Yai.

The flood in October to December 2000 is selected for calibration of MIKE-11 model. The verification of the hydrodynamic model is done for 1988 flood. Compared to the observed data, the results of model calibration and verification are satisfactory. The effects of three proposed flood control schemes are investigated by considering the flood in 2000 namely; scheme 1) shortcut channel, scheme 2) flood diversion channels and scheme 3) shortcut plus flood diversion channels. The shortcut channel is found to reduce water level just enough to eliminate flooding at Had Yai. For the two flood diversion channels, they have large effect on flood level and duration at Had Yai. The combination of diversion channels and shortcut channel yields only a little better result compared to the case of diversion channels only. Recommendations on flood control measures are given.

1. INTRODUCTION

Had Yai city in Songkhla province situates in the lower part of Utaphao river basin and is the meeting point of many canals. Rapid development causes Had Yai to be one of the important city and center for business and tourism in southern region of Thailand. This development obstructs the natural waterway and cannot conveniently drain water to Thale Sap Songkhla lake. Because of its geographical location Had Yai is very prone to flood because all the runoffs in the river basin combine together in the city. Utaphao river basin has a total drainage area 2,305 km². Khlong Utaphao is the main river in the basin and drains water from Amphoe Sadao to Amphoe Had Yai city before it drains into Thale Sap Songkhla (Songkhla lake). The length of Khlong Utaphao is about 112 km. General topography of Utaphao river basin is low lying plain which has high mountains at the upstream and slope to downstream area. The eastern and western areas are mountainous and plateau. The estimated drainage capacity is 420 m³/s or 36.3 million m³/day. The depth of Khlong Utaphao is 2 to 12 meters and has the average width is about 40 meters. Tidal effects in Songkhla lake cause flood in Utaphao river basin. The average maximum water level in Songkhla lake is 0.60 m. msl or more in November to December. The average minimum water level is 0.25 m. msl or less in June to August. The lake water level normally varies from -0.25 to +0.25 m. msl and does not affect to drainage system of Khlong Utaphao. The heaviest rainfall is in November and the minimum rainfall is February. The average annual rainfall in the basin is approximately 1800 mm (NESDB, 2001).

Floodings in the Utaphao river basin, as well as in southern region of Thailand, are generally caused by heavy rainfalls which resulted from cyclones or low pressures centers developed in the Gulf of Thailand. Changing economic, demographic and physical conditions have greatly increased flood occurrence. Economic growth and growing populations have caused increasing frequency and severity of flood disaster in the basin because of changing in land use. Unregulated town and country development, invasion of natural waterway and the green area cause land use changes. Rapid development, such as construction of building, trespasses the green area and decrease catchment area which result flood in Utaphao river basin. Human interventions such as roads can also cause floods because they obstruct the natural water way. (Kasetsart University, 2002).

The lake major floods in Utaphao river basin such as in November 1988, November 1991 to January 1992 and November 2000, caused enormous losses. In November 2000, the largest flood ever occurred and caused severe damages to 11 Provinces including Had Yai. 2,200,000 people were affected by the flood and 8,300 people were evacuated. 59 people and 1,600,000 live stocks were killed and 269,230 ha of farmlands were damaged. The total damage was estimated to be about one billion US dollars. The estimated flood depth in Had Yai city is 2-3 meters as shown in Figure 1. It is required to find flood control measures for Had Yai (Prince Songkhla University, 2002).



Figure 1: Areal photo of flooding in Had Yai City in November 2000

2. FLOOD MODELING IN UTAPHAO RIVER BASIN

2.1 Model setup

Flood modeling in Utaphao river basin is performed using MIKE11 model (DHI and AIT, 1996). The model setup consists of rainfall runoff model and hydrodynamic model. The rainfall-runoff model NAM embedded in MIKE-11 generates lateral inflows from various sub-basins to the main river. Utaphao river basin can be divided into 13 sub-basins. The rainfall in each sub-basin was calculated by using Thiessen Polygon method. For hydrodynamic model there are 27 river cross-sections located along Utaphao, the main river. All the surveyed cross sections were input into MIKE 11 cross section data base. The upstream model boundary is the computed discharge by NAM model from rainfall at station X-172. The downstream boundary is the observed water levels at X-194 in Songkhla lake.

2.2 Model calibration

The model is calibrated and verified by recent data set in this study. The Manning roughness number along Utaphao river is varied from 20 to 30 $\text{m}^{1/3}/\text{s}$. The calibrated relative resistance range from 1 to 50. The storage width ranges from 20 m to 4,000 m. The value of the calibrated resistance factor is from 0.5 to 1. The calibration results of water levels X-44 are shown Figure 2. The simulated water levels from the model are compared with the observed water levels for station X-44. The simulated water level for station X-44 shows a good agreement with the observed water level

especially at peak values. The time to peak and rising limb simulated hydrograph at station X-44 agree with the observed value. However, the falling limb recesses quite slow for station X-44. The calibration results of discharge at X-44 are shown Figure 2. The shape of simulated hydrograph is quite the same as the shape of observed hydrograph. The rising limb and the falling limb of the simulated hydrograph have good agreement with the observed one. The peak value of simulated discharge at X-44 is quite different but the time to peak is the same as the observed data. The efficiency index of model is quite high (0.87 for water level and 0.93 for discharge). The correlation coefficients of water level and discharge at station X-44, are 0.94 and 0.97 respectively.

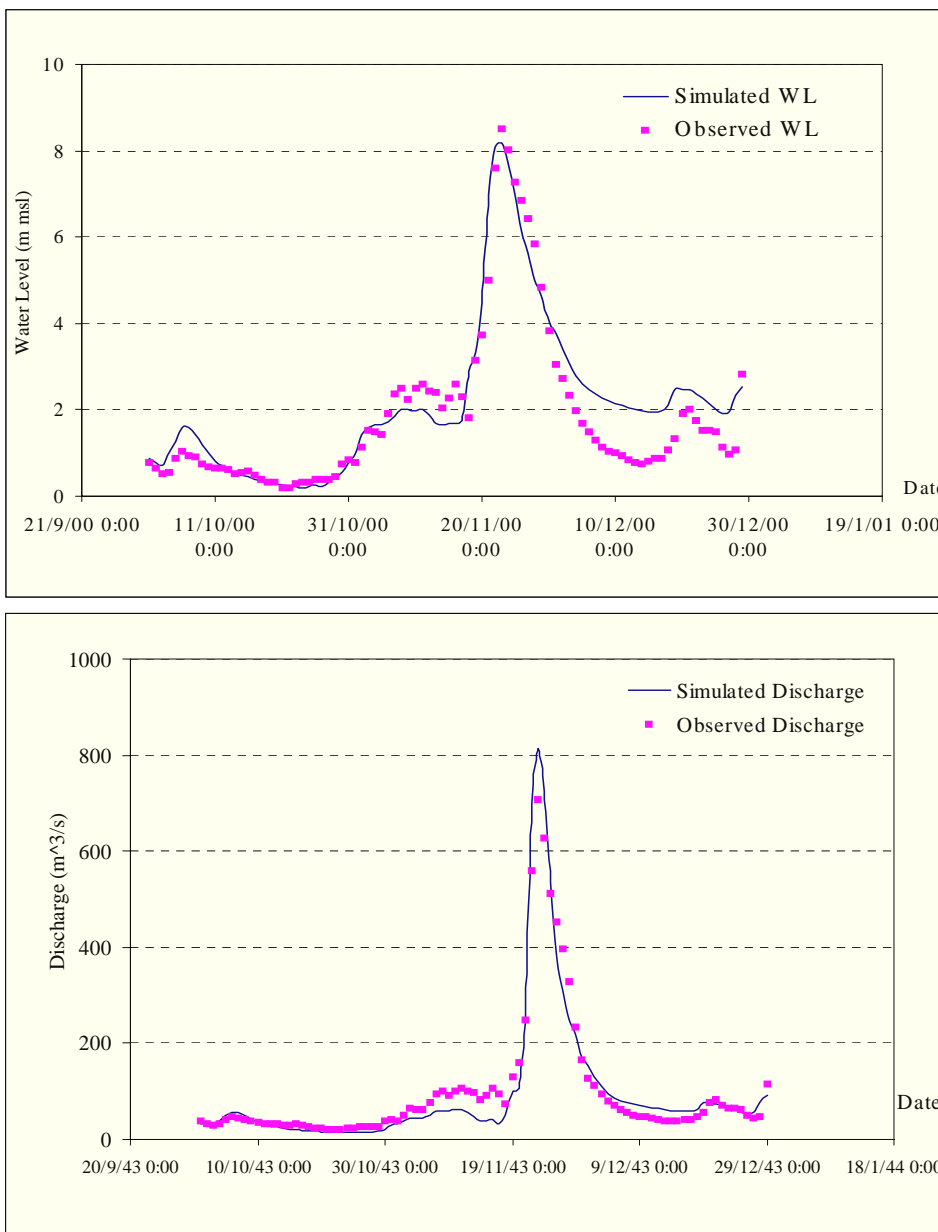


Figure 2: Calibration results of water level and discharge at station X-44

2.3 Model verification

The verification of the calibrated hydrodynamic model is done in the flood year of 1988 at station X-44. The period of verification is from October to December. The results of simulated daily water levels and discharges obtained from the model in this verification are shown in Figure 3. The simulated water levels obtained from the model verify that the model gives a good result for flood peak values and timing to peaks, but the simulated hydrograph does not well fitted to the observed hydrograph. The simulated discharge hydrograph at X-44 has good agreement with the observed hydrograph for the flood peak value, timing to peak as well as the rising limb and the falling limb. The efficiency index of model is quite high (0.77 for water level and 0.83 for discharge). The correlation coefficients in water level and discharge are between 0.95 and 0.92 respectively for X-44.

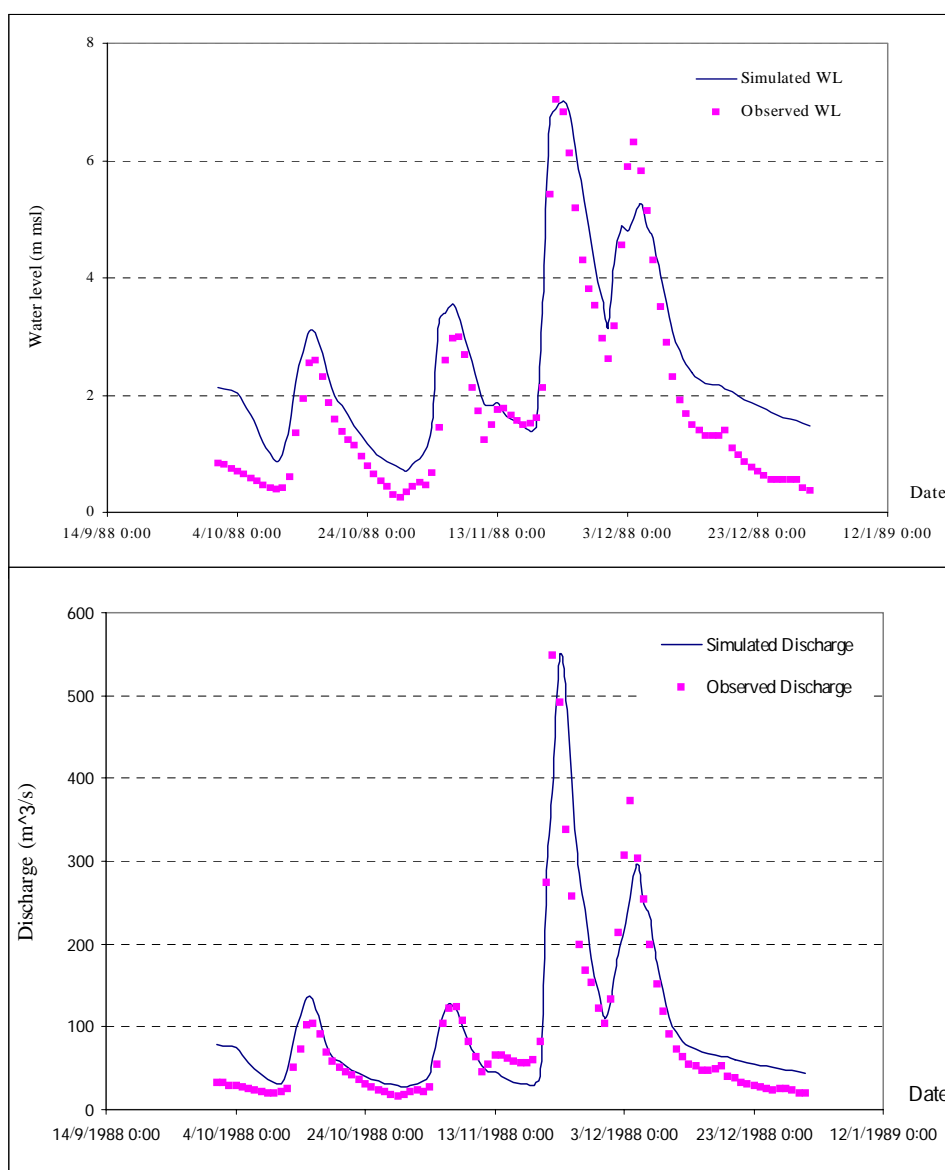


Figure 3: Verification results of water level and discharge at station X-44

3. PROPOSED FLOOD CONTROL MEASURES

The effects of proposed flood control measures are investigated by using flood situation in November 2000. There are three schemes of proposed flood control measures as shown in Table 1. The proposed flood control measures are shown in Figure 4. The general channel cross sections of short cut and diversion channel is shown in Figure 5 and the details of them are shown in Table 2. The model setup and result of each scheme can be described as following:

Table 1: Components of Structural Measures in Each Scheme.

Scheme	Structural Measures	
	Shortcut Channel (C1)	Diversion Channel (D1 and D3)
I	x	-
II	-	x
III	x	x

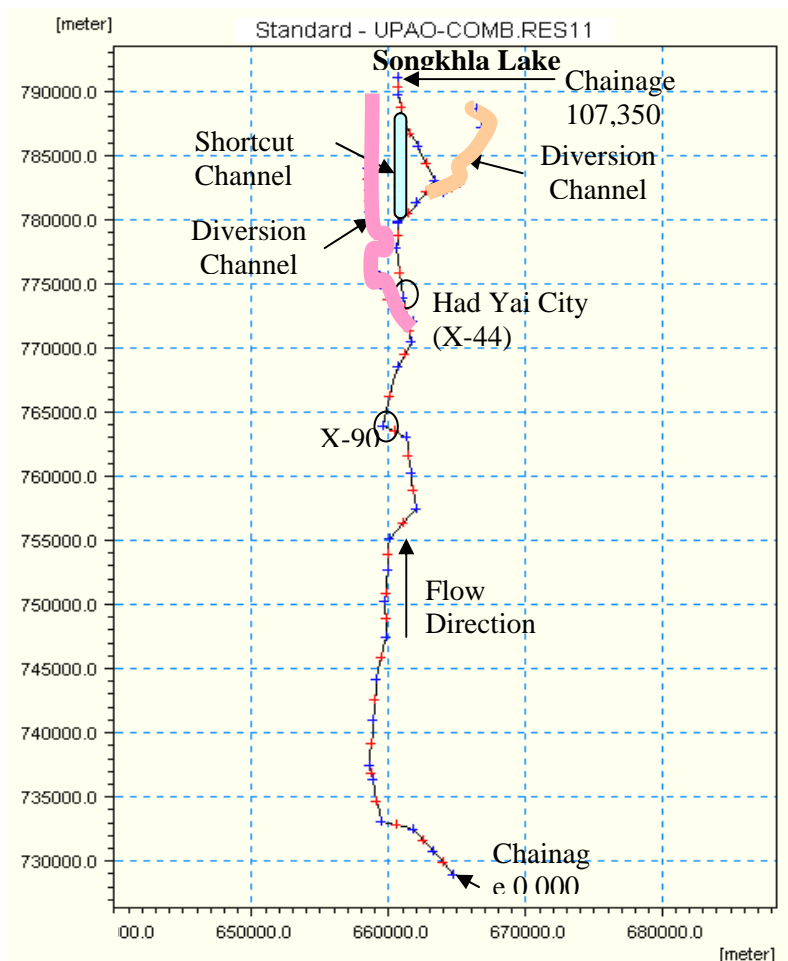


Figure 4: Model configuration of Utaphao river for the proposed flood control measures

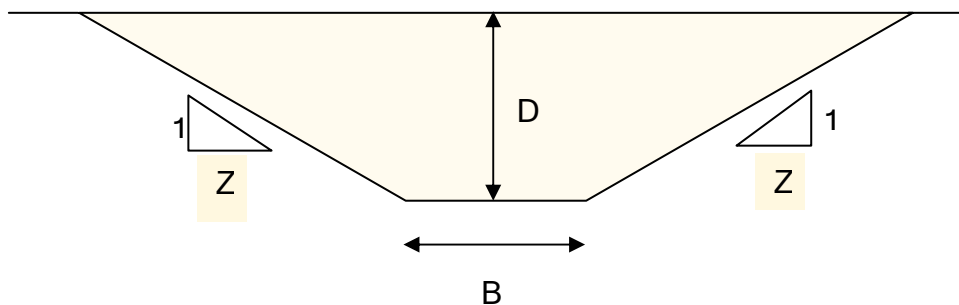


Figure 5: General cross section of short cut and diversion channels

Table 2: The dimensions of cross sections of short cut and diversion channel

Channel	Station to Station		A (mP ^{2P})	n	Bed Slope S	B (m)	D (m)	Side Slope (Z)
C1	0+000	7+765	372	0.025	1:15,800	50	6	2
*D1	0+000	14+460	372	0.025	1:8000	50	6	2
*D1	14+460	21+343.718	216	0.018	1:4000	24	6	2
*D3	0+000	3+600	220.5	0.025	1:10,000	40	4.5	2
*D3	3+600	6+700	184.5	0.025	1:10,000	32	4.5	2
*D3	6+700	8+200	130.5	0.025	1:10,000	20	4.5	2

(* Royal Irrigation Department, Thailand)

3.1 Flood control scheme I

This scheme consists of shortcut channel (C1) between station 90+890 and station 103+850 along Utophao river. The length of shortcut channel is 7.765 km. The longitudinal slope of shortcut channel is about 1:15,800. The Manning number of the channel has been assumed to be 40 m^{1/3}/s and the side slope is 1:2. The results of this scheme are shown in Figure 6 for water levels at station X-44.

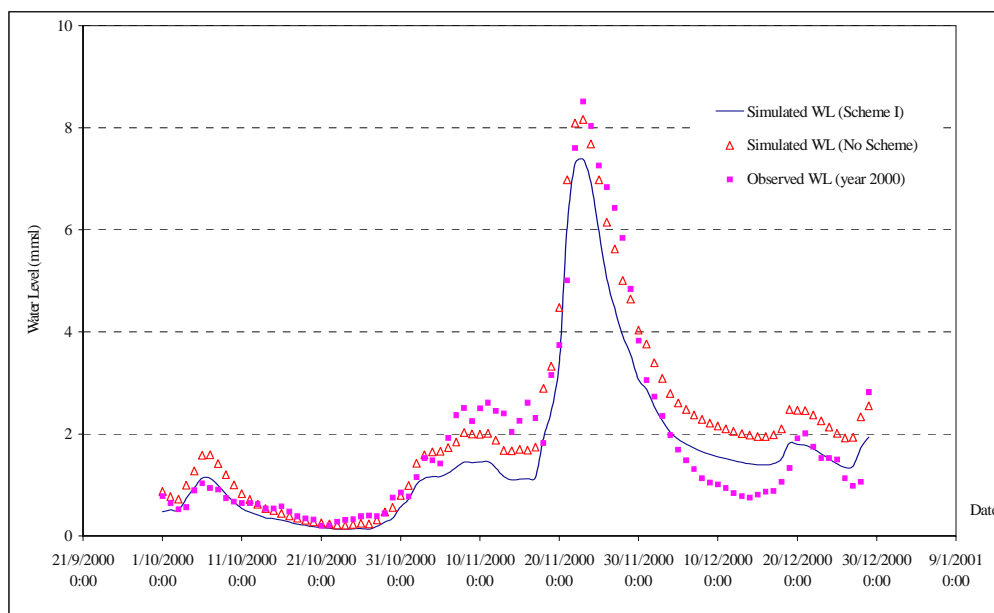


Figure 6: Comparison of simulated and water level at station X-44 , flood control scheme I

The shortcut channel does not have much effect to station X-90 (upstream from station X-44) in term of flood volume and duration of flood because it is far from the shortcut channel. The simulated water level at X-44 is 7.38 m msl and the water level change of station X-44 is about decreasing -0.79 m compared to without any flood control measures. The shortcut channel has effect on water level at X-44. The simulated maximum water level is just at the bank level, so there is no flooding at this station.

3.2 Flood control scheme II

The purpose of this scheme is to study the effect of diversion channels, proposed by Royal Irrigation Department. The model consists of two diversion channel namely: D1 and D3 as shown in Figure 4. Alignment of diversion channel, D1, is on the west of Had Yai city and reach from Utaphao river upstream the gauging station X-44 to Songkhla lake. The length of the channel is 21.343 km. Another diversion channel, D3, is on the east and extends from Utaphao river downstream Had Yai city to Songkhla lake. The length of D3 is 8.2 km. The result of this scheme is shown in Figure 7 for water level at station X-44.

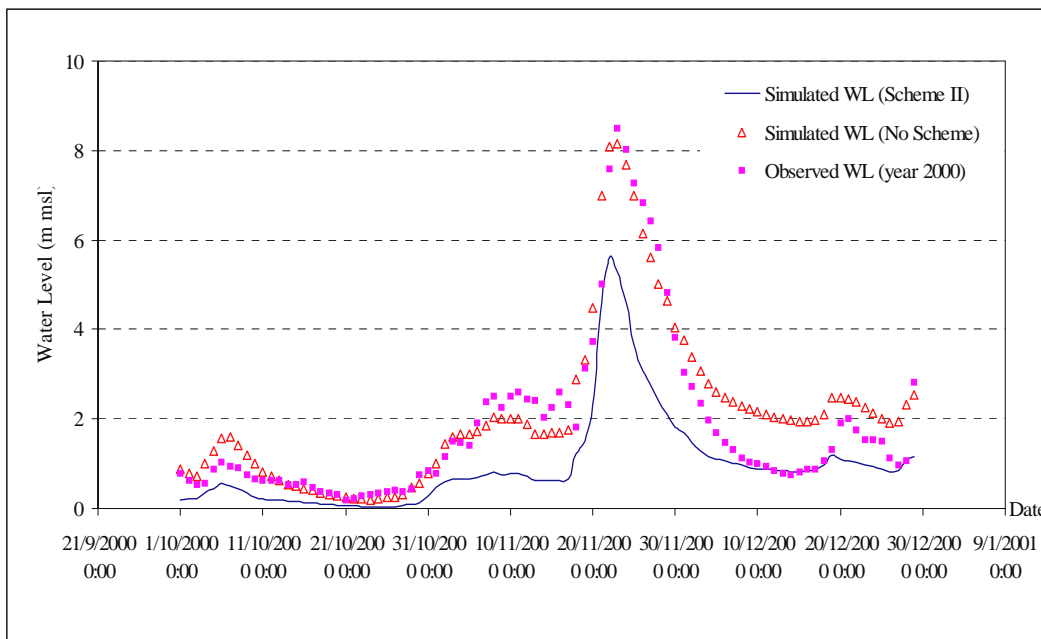


Figure 7: Comparison of simulated and water levels at station X-44, flood control scheme II

The simulated water level X-44 is 5.6 m msl. Water level change of X-44 is decreased by -2.57 m, which is lower than the bank level, compared to the case without flood control measures. The purpose of diversion channel is for flood protection to Had Yai city so there is large effect on the water level at station X-44.

3.3 Flood control scheme III

Scheme I and scheme II are combined that consists of shortcut channel (C1) and diversion channels (D1 and D3) as shown in Figure 4. The detail of each channel is the same as described earlier. The result of this scheme is shown in Figure 8 for the water levels at station X-44. The simulated maximum water level at X-44 is 5.04 m msl. The water level at station X-44 is decreased by 3.13 m, which is lower than the bank level, compared to without flood control measures.

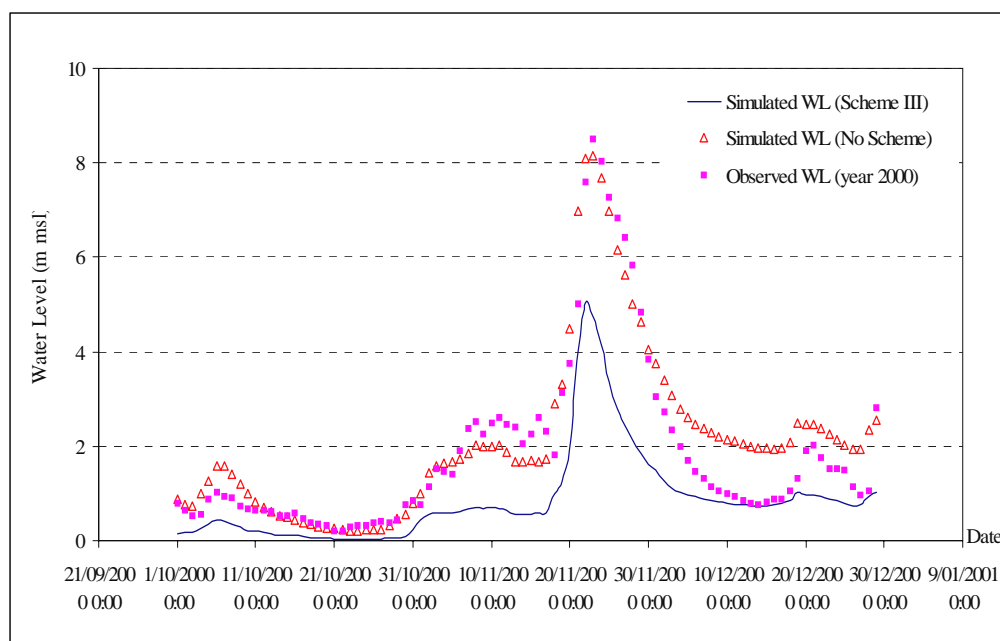


Figure 8: Comparison of simulated and water levels at station X-44, flood control scheme III

4. RESULTS AND DISCUSSIONS

It can be seen that each scheme can reduce flood damages. For scheme I, the shortcut channel, has larger effect on water level at X-44 (Had Yai city). The shortcut channel can reduce the maximum water level at X-44 by -0.79 m compared to without flood control measures. The shortcut channel results in better drainage water from Utaphao river to Songkhla lake. Utaphao river can drain water to Songkhla lake faster than without flood control measures. In this scheme, the shortcut channel, C1, alone can get rid of flooding at Had Yai city (X-44). For Scheme II, the maximum water level at X-44 is reduced by -2.57 m compared to without flood control measures. The reason of the reduction of water depth at X-44 is D1 works as an interceptor of local inflow or side flow from sub-basins and drain the sideflow or local inflow to Songkhla lake directly. Another reason is that some of the runoff from upstream is diverted from Utaphao river so the maximum water level at Had Yai city (X-44) is reduced and causes no flood in the city. For the diversion channel, D3, it is located downstream of Had Yai city. The effect of D3 is less than D1 and it can help in decreasing flood

discharge and reduction of flood period in Had Yai city (X-44). Scheme III, is a combination of the diversion channels (D1 and D3) and the shortcut channel, C1. For scheme III, the maximum water level at X-44 is reduced by 3.13 m compared to without flood control measures. The reason of the reduction of water level at X-44 is the same as in scheme II but there is an additional support from the shortcut channel to quickly drain water to Songkhla lake.

5. CONCLUSIONS AND RECOMMENDATION

Three schemes of flood control measures for Utaphao river basin are proposed for Had Yai city. Scheme I consists of a shortcut channel (C1). Scheme II consists of two diversion channels namely D1 and D3. Scheme III is the combination of Scheme I and Scheme II. It consists of the shortcut channel (C1) and two diversion channels, D1 and D3. The flood control measures can reduce flood water level at Had Yai city at station X-44 by – 0.786 m, –2.566 m and –3.126 m respectively. There is very little effect by these structural measures on water levels for station X-90 located upstream of Had Yai city.

The shortcut channel will not pass through the residential areas, its cross section is nearly the same as the diversion channels but its distance is shorter. The construction cost of the shortcut will be likely less than the diversion channels. The shortcut alone would be sufficient to protect flood at Had Yai at a lower cost. Therefore the shortcut should be recommended for the flood control scheme of Had Yai. The study on effects of the flood control schemes in terms of environmental and socio-economic in Utaphao river basin should be done to evaluate the feasibility of the project.

REFERENCES

- DHI and AIT, 1996. *Flood Modeling Programme in Thailand: Flood modeling in Utaphao River Basin: Summary report*. Asian Institute of Technology, Bangkok, Thailand.
- Kasetsart University, 2002. *Study and Analysis for Development of Master Plan for Flood Management and Environmental Impact, Utaphao River Basin, Songkhla Province*. Kasetsart University, Bangkok, Thailand. (in Thai)
- NESDB (Office of National Economic and Social Development Board), 2001. *Flood Protection Plan for Utaphao River Basin, Hat Yai District, Songkhla Province*. Office of National Economic and Social Development Board, Songkhla, Thailand. (in Thai)
- Prince of Songkhla University, 2002. *Seminar Report for Prevention and Solving Flooding Problems in Hat Yai city*. Research and Development Office, Prince of Songkhla University, Songkhla, Thailand. (in Thai)

DEVELOPMENT OF POSSIBLE TSUNAMI EXPOSURE ESTIMATION MODULE FOR TSUNAMI DISASTER RESPONSE

Masasuke TAKASHIMA, JSPS research fellow
Institute of Industrial Science, The University of Tokyo, JAPAN
takashim@iis.u-tokyo.ac.jp

Shunichi KOSHIMURA, Associate Professor
Disaster Control Research Center, School of Engineering, Tohoku Univ.
koshimura@tsunami2.civil.tohoku.ac.jp

Kimiro MEGURO, Professor
Institute of Industrial Science, The University of Tokyo, JAPAN
meguro@iis.u-tokyo.ac.jp

ABSTRACT

In Indian Ocean Tsunami Disaster, Dec. 26, 2004, it was more than one month after the event occurred that the overview of the damage situation in the affected countries was revealed. It is indispensable, especially in the large scale disaster, to know the big picture of damage situation such as possible affected area, affected population in early stage for effective deployment of limited resources under the international coordination among various donor countries and NPOs.

To address above-mentioned needs, our research group is developing an information system to support tsunami warning, disaster response and relief. When a tsunami occurred anywhere in the world, this WebGIS-based system estimates and publishes various kinds of possible damage situation information such as, tsunami arrival time, maximum tsunami height, severely affected area, affected population (Possible Tsunami Exposure; PTE) due to the tsunami in the early stage.

In this paper, we report the development of PTE estimation module in the system. In this module, PTE is estimated in 30'' by 30'' grid from maximum tsunami height based on numerical simulation, population data and elevation data along the coast line. Landscan provided from Oak Ridge National Laboratory and STRM30 provided from NASA are basically used as global population and topological data. Using the module, we estimated PTE of Indian Ocean Tsunami Disaster, Dec. 26, 2004 and that of another tsunami which hit northern Sumatora in Mar. 28, 2005. The relationship between PTE and actual damage in each affected countries was examined. As a result, it was confirmed that the estimated PTE is consistent with reported damage and that the module could assess the PTE due to the event with enough accuracy to get the big picture of the event.

1. INTRODUCTION

In case of large scale disaster, it tends to require lots of time and resources to grasp total damage situation. In Indian Ocean Tsunami Disaster, Dec. 26, 2004, huge tsunami swept Indian Ocean rim countries such as Indonesia, Sri Lanka, India and Thailand as shown in Figure 1. 169,752 dead and 127,294 missing were reported as of Feb. 22, 2004. It took more than one month after the event occurred that the overview of the damage situation in the affected countries was revealed.

Delay of grasping damage situation leads delay and inefficiency of response and relief activities by affected countries, donor countries and NPOs. So, it is required to identify severely damaged areas in very early stage and then concentrate limited resources on those areas for getting detailed damage situation efficiently. In such first stage screening, grasping big picture of total damage is important rather than pursuing precise number. Especially, it tends to require more time for most of developing countries to grasp damage situation because of lack of disaster information and communication system and because of high vulnerability against natural disasters which cause larger damage with same extreme natural force compared with developed countries.

PTE estimation module we introduce in this paper is developed for screening severely damaged area. This module is applicable to tsunami disaster which occurred anywhere in the world with recent development of tsunami simulation technology and global demographic and topographic database. All of these global database used in the module are available in public domain. This global applicability is an advantage of the module in applying it to the tsunami disaster which occurred in developing countries. In case of tsunami, the module receives maximum tsunami height simulated by tsunami researchers and calculates PTE in reasonable time. As a result, possible total affected population, affected population by countries and by regions and possible severely affected area can be published via Web-GIS.

Such information will help stakeholder countries and organizations to recognize the significance of the event and to know which country or area should be prioritized in relief activity. Sharing common view against the situation among the stakeholders will lead efficient coordination.

In this paper, the PTE estimation process and data required in the process are described in chapter 2. Then, application of the module to Indian Ocean Tsunami Disaster, Dec. 26, 2004 and another tsunami which hit northern Sumatra in Mar. 28, 2005 is introduced and it is shown that the estimated PTE is consistent with reported damage and that the module could assess the PTE due to the event with enough accuracy to get the big picture of the event in chapter 3. Chapter 4 is concluding remarks.

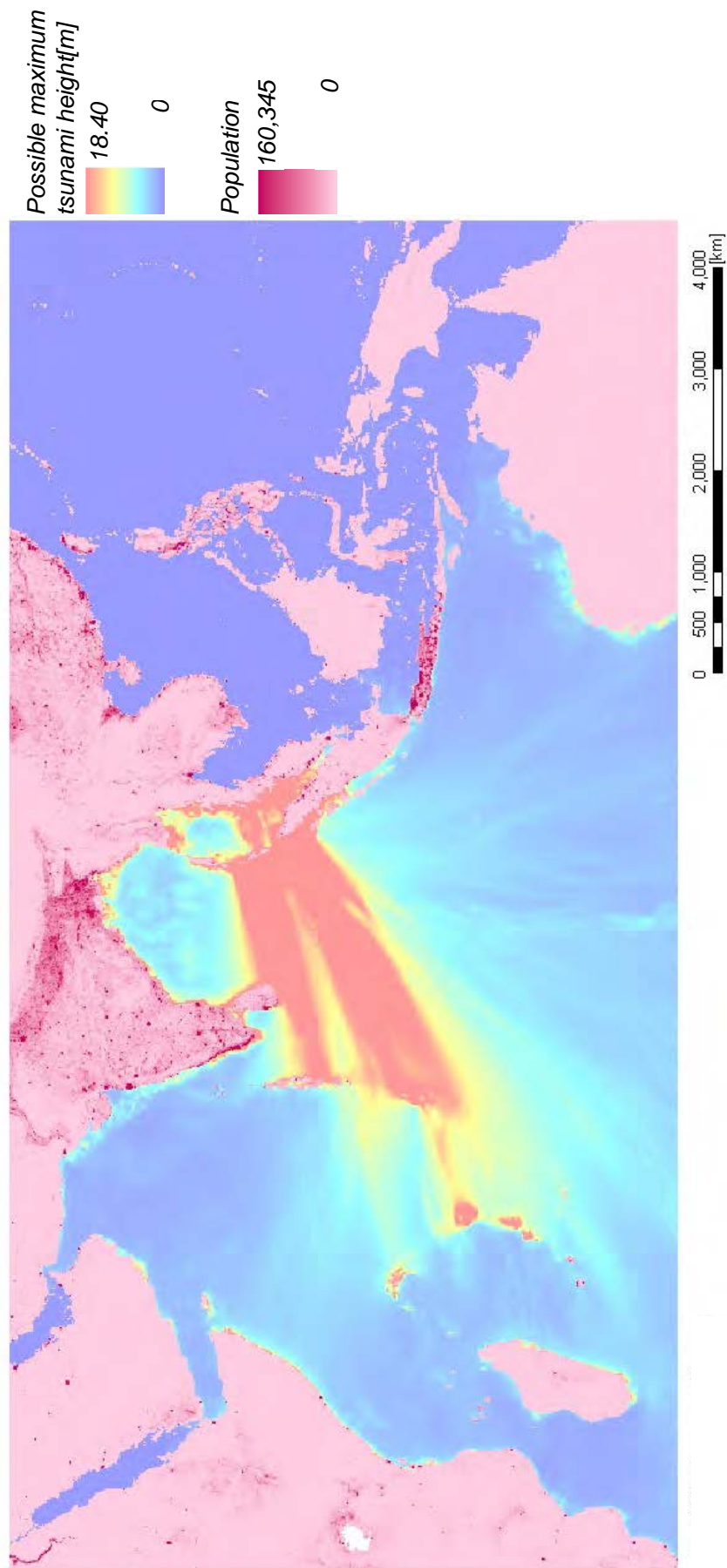


Figure 1 : Possible maximum tsunami height of Indian Ocean tsunami ,Dec. 23, 2004 simulated by S. Koshimura, Tohoku Univ. (2' grid) and Population distribution of Indian Ocean rim countries based on LandScan2003, Oak Ridge National Laboratory (30'' grid) (LandScan Global Population Database. Oak Ridge, TN: Oak Ridge National Laboratory. Available at [http://www.ornl.gov/gist/.](http://www.ornl.gov/gist/))

2. PTE ESTIMATION MODULE

In this module, PTE is estimated in the process shown in Figure 2. The module was developed on ArcGIS. Input data are maximum tsunami height (MTH), population distribution and DEM. Output is PTE by MTH and by region or country.

2.1 Data required in the module

2.1.1 *Maximum tsunami height (MTH)*

Any data provided in ArcGIS grid or ASCII format can be used. Basically, MTH must be provided by numerical simulation from tsunami researchers. In our research group, MTH can be calculated on the basis of global bathymetry data provided in 2' grid by National Geophysical Data Center wherever tsunami occurs in the world.

2.1.2 *Population*

Any data provided in ArcGIS grid or ASCII format can be used. Landsat provided from Oak Ridge National Laboratory is used as global population data with default setting (Figure 1). It is provided in 30" grid. Landsat data is not census based data. Reported total population within a political boundary is allocated in each grid considering land use, proximity to the major road, slope, and night-time city light. So, Landsat should be used to know gross configuration of population. If census based statistics in similar spatial resolution is available in the target region, it will lead more precise result.

2.1.3 *DEM*

Any data provided in ArcGIS grid or ASCII format can be used. STRM30 provided from NASA is used as global topological data with default setting. It is provided in 30" grid.

2.2 PTE estimation process

At first stage, coastal population grid and coastal MTH grid is extracted. Then, coastal population grid at elevation less than 30m is extracted by using DEM grid to avoid overestimate of coastal population which a tsunami can affect. Then, coastal population grid at elevation less than 30m is assigned to nearest coastal MTH grid. Finally, coastal population exposed to a certain MTH in a certain region is calculated.

In this process, whole population in 30" grid along shoreline is included in PTE without considering local topography. 30" is approximately 900m in low latitude area. So, this module may overestimate PTE in case that coastal area is mountainous or may underestimate PTE in case that there is large flat plane next to shoreline. How far a tsunami come to inland depends on local coastal topography. The process to evaluate coastal population which a tsunami can affect should be reviewed for further study.

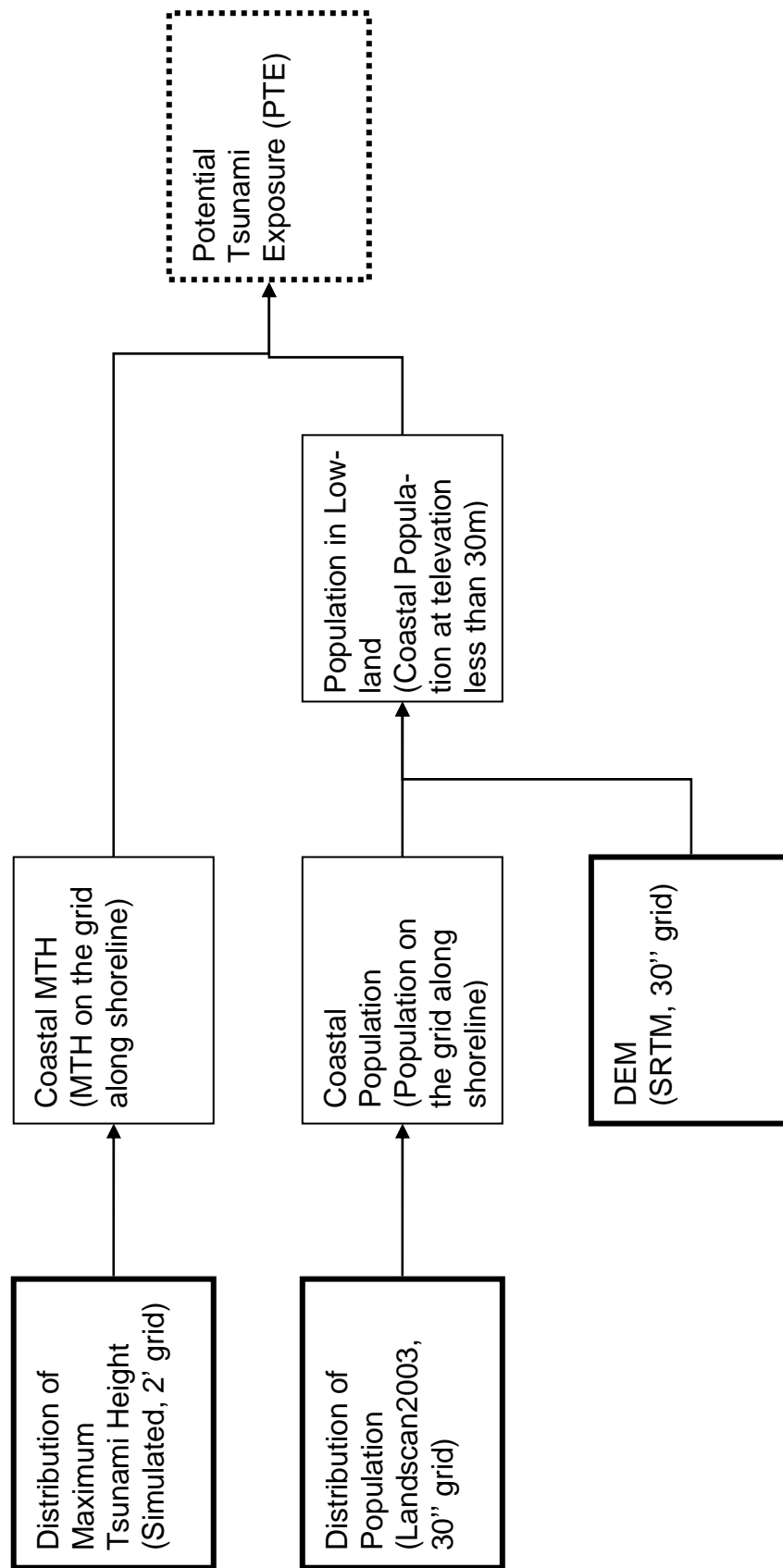


Figure 2: Potential tsunami exposure (PTE) estimation process flow

3. ESTIMATION OF PTE IN ACTUAL TSUNAMI DISASTERS

3.1 PTE of Indian Ocean tsunami disaster, Dec. 26, 2004

PTE of Indian Ocean Tsunami Disaster (M9.0), Dec. 26, 2004 was estimated with PTE estimation module introduced in previous chapter. The result is shown in Table 1. Indonesia had largest coastal population in lowlands. It can be seen that Indonesia had larger PTE for MTH larger than 5m compared with other countries. On the other hand, India and Sri Lanka had larger PTE for MTH which ranges from 2m to 5m. As a whole, Indonesia had largest PTE among the affected 11 countries and India, Sri Lanka and Thailand followed. Compared with other countries, PTE of these four countries were apparently dominant.

Reported number of dead and missing as of Feb. 22, 2005 (CNN) is shown at the bottom of Table 1. Indonesia had largest number of dead and missing (236,169) and Sri Lanka (35,672), India (16,416) and Thailand (8,388) followed at that time. These numbers corresponded to 13.3%, 3%, 0.4% and 6.4% of PTE for MTH larger than 1m in each country, respectively. This result shows the vulnerability of Indonesia against tsunami is higher than other three countries.

It can be said that countries which had larger PTE tend to have larger number of dead and missing. And also, it can be seen that dead and missing in a country got larger sharply when the country had PTE for MTH larger than 7m. Dead and missing was very limited when there is no PTE for MTH larger than 7m.

3.2 PTE of tsunami disaster in Mar. 28, 2004

In Mar. 28, 2004, another large earthquake (M8.7) and tsunami occurred along the Sunda trench and hit northern Sumatra. Although the magnitude was considerably large and the source area was adjacent to that of the previous event, the damage was very limited. Indonesia had several hundred dead and missing. No damage was reported in other countries which were affected in the previous event.

We also applied the module to estimate the PTE of the event. As a result, it was clarified that only Indonesia had moderate PTE compared with the previous event. No country had PTE for MTH larger than 7m. It was confirmed the module could assess the PTE due to the event with enough accuracy to get the big picture of the event and within reasonable calculation time.

As a result of above-mentioned application, it can be said that PTE estimated by the module is reflecting actual damage situation as a whole. This result supports that PTE estimation module we developed can be used to get a big picture of tsunami disaster.

Table 1 : Cumulative possible tsunami exposure due to Indian ocean tsunami disaster Dec. 26, 2004, by maximum tsunami height for Indian Ocean rim countries

Maximum Tsunami Height[m]	Indonesia	India	Thailand	Sri Lanka	Myanmar	Malaysia	Bangladesh	Maldives	Somalia	Kenya	Tanzania	Seychelles	Australia	Total
0	8,178,490	6,923,301	898,902	1,188,898	1,305,493	1,347,390	2,370,781	328,164	420,947	552,882	1,092,660	19,173	75,347	24,702,428
1	1,775,482	4,403,036	130,425	1,188,898	950,480	369,769	1,451,794	328,164	387,148	520,322	1,025,921	17,299	245	12,548,983
2	446,557	1,947,329	130,421	1,070,477	252,752	307,918	403,176	268,382	245,536	224,134	330,940	8,947	0	5,636,569
3	156,750	953,828	108,485	586,008	65,303	19,080	133,810	139,998	1,412	360	2,893	0	0	2,167,927
4	93,604	149,938	41,285	159,962	5,343	0	2,743	0	6	0	0	0	0	452,881
5	67,139	45,711	18,954	79,274	1,780	0	1,790	0	0	0	0	0	0	214,648
6	56,793	19,786	9,780	35,612	23	0	98	0	0	0	0	0	0	122,092
7	49,279	8,266	8,366	17,854	0	0	0	0	0	0	0	0	0	83,765
8	39,563	6,626	4,168	2,022	0	0	0	0	0	0	0	0	0	52,379
9	32,203	4,048	4,039	1,345	0	0	0	0	0	0	0	0	0	41,635
10	18,596	2,826	2,430	493	0	0	0	0	0	0	0	0	0	24,345
11	10,821	1,878	15	346	0	0	0	0	0	0	0	0	0	13,060
12	10,200	444	13	0	0	0	0	0	0	0	0	0	0	10,657
13	7,024	100	0	0	0	0	0	0	0	0	0	0	0	7,124
14	6,878	100	0	0	0	0	0	0	0	0	0	0	0	6,978
15	319	100	0	0	0	0	0	0	0	0	0	0	0	419
16	173	100	0	0	0	0	0	0	0	0	0	0	0	273
17	0	100	0	0	0	0	0	0	0	0	0	0	0	100
18	0	92	0	0	0	0	0	0	0	0	0	0	0	92
19	0	92	0	0	0	0	0	0	0	0	0	0	0	92
death	122,232	10,776	5,395	30,974	59	68	2	82	150	1	10	3	0	169,752
missing	113,937	5,640	2,993	4,698	0	0	0	26	0	0	0	0	0	127,294
death +missing	236,169	16,416	8,388	35,672	59	68	2	108	150	1	10	3	0	297,046

4. CONCLUSION

In this study, we developed PTE estimation module which is applicable globally. Then, we applied the module to Indian Ocean Tsunami Disaster, Dec. 26, 2004 and another tsunami which hit northern Sumatora in Mar. 28, 2005 to calculate the PTE of both events. As a result of examination of relationship between estimated PTE and actual damage, it is shown that the estimated PTE is consistent with reported damage and that the module could assess the PTE due to the event with enough accuracy to get the big picture of the event.

The module we introduced in this paper can be used not only in emergency response but also in risk analysis for possible tsunami disasters in future by preparing simulated MTH of future tsunami scenario as input data. To prepare for future tsunami disaster, risk evaluation against possible scenario is indispensable. But, the target area get larger, it is almost impossible to conduct detailed risk assessment for all target area. Since our module can provide gross configuration of risk due to future scenario, we can concentrate our resources on the high risk area for detailed assessment.

As mentioned in chapter 2, in the PTE estimation process, whole population in 30" grid along shoreline is included in PTE without considering local topography. How far a tsunami come to inland depends on local coastal topography. The process to evaluate coastal population which a tsunami can affect should be reviewed for further study.

REFERENCES

- Dobson, J. E., E. A. Bright, P. R. Coleman, R.C. Durfee, B. A. Worley. 2000. "LandScan: A Global Population Database for Estimating Populations at Risk," Photogrammetric Engineering & Remote Sensing Vol. 66, No. 7, July 2000, pp. 849-857.
- NASA(2000) : SRTM (Shuttle Radar Topography Mission) ,<http://www2.jpl.nasa.gov/srtm/>
- National Geophysical Data Center (2005) : 2-Minute Gridded Global Relief Data,<http://www.ngdc.noaa.gov/mgg/fliers/01mgg04.html>

CREATING AN INTEGRATED WATER GEODATABASE FOR ENVIRONMENTAL RISK MANAGEMENT

AKIYUKI KAWASAKI, YUICHI SATO and SATORU SADOHARA
Graduate School of Environment and Information Sciences,
Yokohama National University, JAPAN
akiyuki@arc.ynu.ac.jp

ABSTRACT

Considering urban environmental problems requires investigating water resource availability and supply, especially in relation to human activity. An integrated water geodatabase for environmental risk management was created in this study to visually and interactively understand water supply and circulation. The geodatabase covers from upstream ecosystems in mountain and forest regions, to middle and downstream areas primarily marked by human activity such as agricultural areas, and urban areas with artificial water supply systems (pipes, drainage canals, etc.). Underground water was not considered at this moment.

Integrated water database have not been well understood in Japan due to vertically divided water authorities and lack of suitable tools for integration. ESRI ArcGIS and ArcHydro technologies were utilized to build the geodatabase by digitizing paper maps of waterworks, sewage systems (storm and sanitary), and irrigation canals (industrial and agricultural) of individual municipal administrations. Attribute data was then included like flow direction, water quantity and some quality data, junction types, as well as natural surface water flow in each watershed calculated with a Digital Elevation Model.

The geodatabase was built for both the main water network in Kanagawa Prefecture (macro level) and for the local water network in Isehara City (micro level), and the connectivity between the macro and micro levels was databased.

By using this geodatabase, the impact of human activity on water quality and quantity can be clarified by investigating the change of water quality and quantity flowing through areas with a specific land use (residential, agricultural, industrial, etc.) in urban areas. As a conclusion, environmental risk management in urban area using the geodatabase and future works are described.

1. INTRODUCTION

Since the last half of the 20th century, species extinction and destruction of ecosystems have increased rapidly due to a swift increase in

population, and use of toxic chemicals, etc. Especially, preservation of bio/eco-systems in Asia is critically important.

Yokohama National University has started “Environmental Risk Management for Bio/Eco-systems” as a 21st Center of Excellence program by MEXT (the Japanese Ministry of Education, Culture, Sports, Science, and Technology) since 2002. Our program has the following goals:

- Collect and analyze the environmental risk of terrestrial and aquatic bio/eco-systems in East Asia by investigating relationships between ecosystems and human activity (like using toxic chemicals).
- Establish bio/eco environmental risk assessment methods and develop concepts and ideas for risk management.
- Build networks among related domestic/international organizations, and prepare easy data-retrieve system not only for researchers, but also for government and the general public.

In order to consider “Management”, not an individual (traditional) research approach but a multidisciplinary integrated approach is necessary to understand the mechanism of complicated bio/eco-systems. In this study, an integrated water geodatabase was built for both the main water network in Kanagawa Prefecture as a proto-type of macro level, and for the local water network in Isehara City as a micro level, since Kanagawa Prefecture, including Isehara City is a common research field in our COE program.

Integrated exhaustive water geodatabase is an important infrastructure for environmental managements, but it does not exist in Japan due to vertically divided water authorities and lack of suitable tools for integration.

Water is the key of integration of multidisciplinary research, because it moves chemicals from upstream where ecosystems in mountain and forest regions, through middle and downstream areas primarily marked by human activity such as agricultural areas, and urban areas with artificial water supply systems (pipes, drainage canals, etc.), to the ocean. Through the

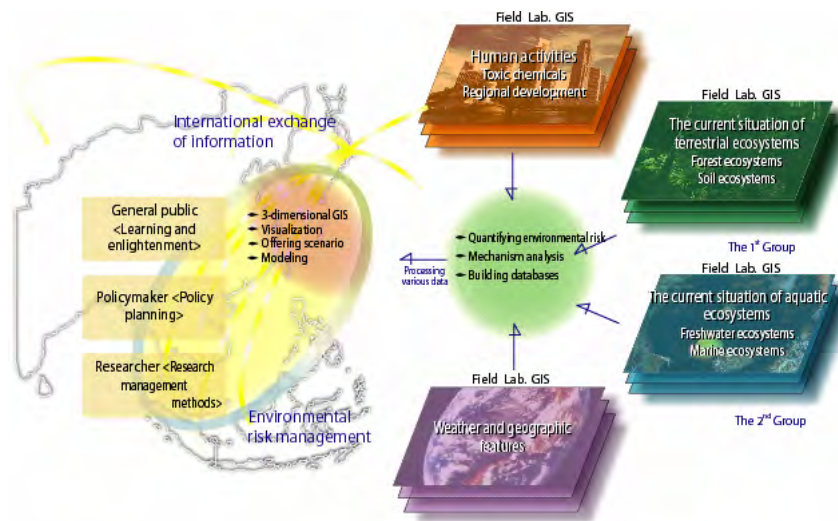


Figure 1: Framework of our COE program: “Environmental Risk Management for Bio/Eco-Systems”

water flow, many researchers could join it. Their research interest and data could be combined with water flow.

Additionally, by building water database, not only the effect from human activity to natural ecosystems, but also the effect from ecosystem to human activity could be understood through the water, because water flow circulate inside the basin.

2. Integrated Water Geodatabase.

2.1 Water map resources

Integrated water geodatabase for environmental risk management. have not been well understood in Japan due to vertically divided water authorities and lack of suitable tools for integration. ESRI ArcGIS and ArcHydro technologies were utilized to build the model by digitizing paper maps of waterworks, sewage systems (storm and sanitary), and irrigation canals (industrial and agricultural) of individual municipal administrations. Attribute data was then included like flow direction, water quantity and some quality data, junction types, as well as natural surface water flow in each watershed calculated with a Digital Elevation Model. Underground water is not considered at this moment. The list of water map and data resources for our geodatabase is shown table 1 and table 2.

2.2 Kanagawa Prefecture macro-level

In order to understand the whole water system in Kanagawa Prefecture, the water comes from outside Kanagawa Prefecture has to be considered. As shown at Figure 2, more than 1/4 surface of Mt. Fuji is included in Sagami-river basin and Sakawa-river basin, where are the main

Table 1: Data resources (Kanagawa Prefecture macro map)

Name	Area	Scale	Publish Date	Data Resource
Water utility map	Kanagawa Prefecture	1:100000	2001/04	Dept. of planning, Kanagawa Pref.
Water management block map	Kanagawa Prefecture	1:100000	2002/04	Dept. of environment and agriculture, Kanagawa Pref.
Water quality gaging map	Kanagawa Prefecture	1:100000	2002/04	Dept. of environment and agriculture, Kanagawa Pref.
River, harbor, coastal map	Kanagawa Prefecture	1:100000	2003/03	Kanagawa Prefecture.
Sagami-river preserve map	Sagami-river basin	1:50000	2005/04	Office of preservation, Kanagawa Pref.
Sagami-river facilities map	Sagami-river basin	1:100000	2001/04	Office of preservation, Kanagawa Pref.
Sakawa-river basin sewer map	Sakawa-river basin	1:25000	2003/02	Office of sewer preservation, Kanagawa Pref.
Sakawa-river Mho dam map	Sakawa-river basin	1:50000	1996/03	Business management agency, Kanagawa Pref.

Table 2: Data resources (Isehara City and Yokohama City micro map)

Name	Area	Scale	Publish Date	Data Resource
Urban planning map	Isehara City	1:15000	2004/03	Dept. of urban planning, Isehara City
River basin map	Isehara City	1:15000	2002/11	Isehara City
Public sewer planning map (Sanitary)	Isehara City	1:15000	2003/03	Dept. of sewer, Isehara City
Public sewer planning map (Storm)	Isehara City	1:15000	2003/03	Dept. of sewer, Isehara City
Agricultural irrigation and spring map	Isehara City	1:10000	2005/06	Dept. of agriculture, Isehara City
Water works map	Yokohama City	1:30000	2004/04	Dept. of sewer, Yokohama City
River map	Yokohama City	1:30000	2004/12	Division of river, Dept. of sewer, Yokohama City
River planning map	Yokohama City	1:30000	2004/10	Division of river, Dept. of sewer, Yokohama City
Public sewer planning map	Yokohama City	1:30000	2005/03	Bureau of environment creation, Yokohama City

drinking water resources for Kanagawa-Prefecture (2,415km², 8.5 million populations).

Figure 3 shows waterworks map from Kanagawa prefecture, sewage systems map (storm and sanitary) from Kanagawa sewage foundation, Kanagawa Prefecture, are digitized to create integrated water utility network database in Kanagawa Prefecture. Artificial water supply systems (pipes, drainage canals, etc.) are maintained in whole Kanagawa Prefecture in order to distribute drinking water from Mt. Fuji and Sakawa-river basin and Sagami-river basin to almost the entire citizen in Kanagawa Prefecture. Mainly center and east part of Kanagawa Prefecture has highly urbanized landuse. Especially, City of Yokohama, Japan's 2nd largest city (3.5 million populations) is 100% rely on the water carried thought artificial pipes from Sakawa-river and Sagami-river.



Figure 2: More than 1/4 surface of Mt. Fuji is included in Sagami-river basin and Sakawa-river basin



Figure 3: Main artificial water supply systems (pipes, drainage canals, etc.) in Kanagawa Prefecture

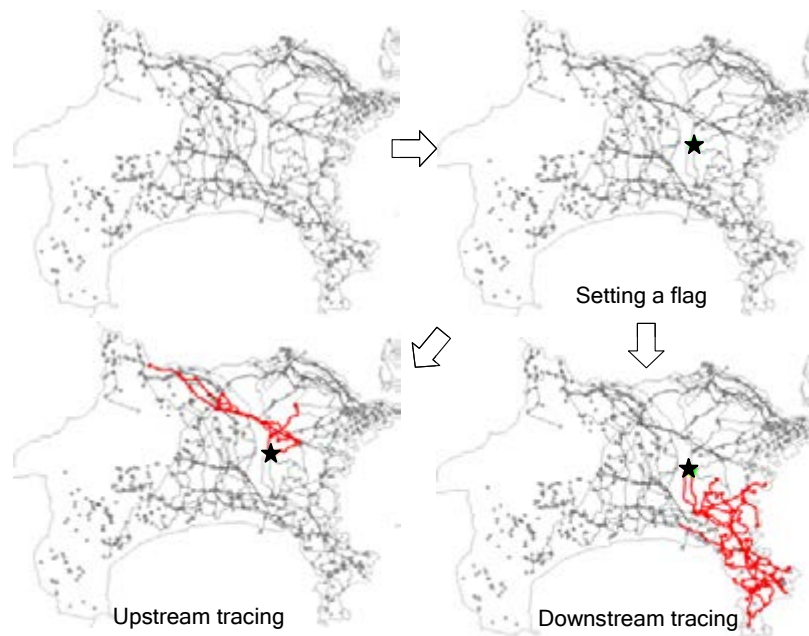


Figure 4: An example of network tracing from a point to upstream or downstream through Kanagawa waterworks database.

In this geodatabase, attribute data was then included like flow direction, water quantity and some quality data, junction types, as well as natural surface water flow in each watershed calculated with a Digital Elevation Model. Thus, the attribute on the network could be traced interactively. Figure 4 shows an example of networking tracing from a point to upstream or downstream through Kanagawa waterworks database.

Therefore, this database could be utilized for the specifying the point sources of pollution and the effected area of a point on the network. Additionally, each connection point on the network, called “node” such as pumping, water purification plant, can be behave as a bulb, so many kind of simulation (e.g. Find common ancestors, Find connected, Find loops, Find disconnected, Find path upstream, Find path, Trace downstream, Find upstream accumulation, Trace upstream) could be used.

2.2 Isehara City micro-level

Isehara City is most suitable to understand local water circulation and watershed environment in Kanagawa Prefecture, since almost all of city area is included in one large watershed from Mt. Oyama (1,251m), and has the diversity of landuse in small city area (55km²) as Figure 5 shows. Sewage systems map (storm and sanitary) from Isehara Sewer Foundation, agricultural irrigation canals, spring waters and weirs map from Dept. of Agriculture, Isehara City, and the results our field work, are digitized to create integrated water utility network database in whole city area (Figure 6).

Detailed (mainly 1:2500 based) waterworks, sewer (sewage and storm), irrigation water (agriculture and industrial), spring water, drainage area, are in a geodatabase. This geodatabase can be considered as an integrated whole rather than as a set of separate data layers using ArcHydro

technologies. It allows us to support behavioral modeling because the ArcHydro concept all features in the database are uniquely labeled hydro features. It is a powerful idea to think about water flow.

The creation of an integrated database, instead of a collection of data layers, is a key accomplishment of this geodatabase design, providing a stronger foundation for building water resources application in GIS has previously existed.

How water resources agencies subdivide a given landscape into drainage units (watershed) may vary significantly from one agency to



Figure 5: Artificial water supply systems and natural surface



Figure 6: Extraction of agricultural Irrigation from 1:2500 terrain maps

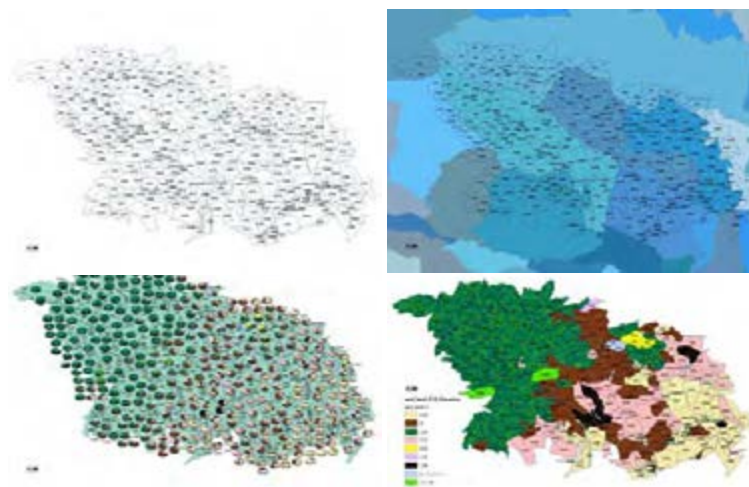


Figure 7: A consideration of the area of drainage units (watershed) using 25m DEM and drainage area map by Dept. of Sewer, Isehara City.

another or even within the same agency when different kinds of analyses are undertaken. All of these watershed delineations serve legitimate but different purposes. There are an infinite number of ways to subdivide the landscape into watersheds, and no unique way serves all purposes.

Therefore, we are considering the area of drainage units (watershed) using 25m DEM and drainage area map by Dept. of Sewer, Isehara City. We have to establish the size and methodologies the drainage units (watershed) using GIS for the “Environmental risk management for bio/ecosystems”.

3. Future Works

3.1 Integration with COE geodatabase collected by many scientists

As a future work, we will integrate this water database into COE integrated geodatabase. 18 faculties and 14 post doctoral fellows from many research fields such as natural sciences, social sciences, agriculture and engineering, are joined our COE program. Many of them convert their field survey data and research results into integrated geodatabase (Kawasaki et al., 2005). PRTR [Pollutant Release and Transfer Register] factories and companies, dioxin risk assessment for water creatures, fagaceae [buna-rin] forest, soil from various depths, and so forth are databased in a common GIS format by our COE researchers for data sharing and further overlay analysis.

By this integration, water network database is used to connect the research results by COE researchers from upstream ecosystems in mountain and forest regions, to middle and downstream areas primarily marked by human activity such as agricultural areas, and urban areas. It will exceed the difference of not only spatial field but also their specialized research field. This will become a starting point of multidisciplinary environmental

the introduction, we have to go from personnel at an authority to another personnel at another authority all around large Kanagawa Prefecture. Through our experience, we would like to create a “Stake holder map for water resource management in Kanagawa Prefecture” as not spatial-drawn (traditional) map but schematic map (Figure 10). GIS and relational database management technologies are utilized to create this schematic map. Almost all of the data and information, and human connectivity related water resources management between authorities including personnel at authorities, researchers, NPO, etc., could be relationally databased using spatial information as a “key”. Building the stakeholder map in Kanagawa Prefecture is still underway.

4. Conclusions

An integrated water geodatabase for environmental risk management was created in this study to visually and interactively understand water supply and circulation. The geodatabase covers from upstream ecosystems in mountain and forest regions, to middle and downstream areas primarily marked by human activity such as agricultural areas, and urban areas with artificial water supply systems, though underground water was not considered at this moment. The geodatabase was built for both the main water network in Kanagawa Prefecture (macro level) and for the local water network in Isehara City (micro level).

This database using ArcHydro technologies provides an elegant tracing capability – the ability to trace upstream or downstream across drainage areas, so we can determine the region of hydrologic influence of any location on the landscape. Also, we can determine watershed properties, such as average precipitation or runoff, and accumulate them going down stream so that we can estimate the flow in streams and rivers. At the use of this database using ArcHydro technologies continues to grow, further hydrologic analysis and modeling capabilities will become available.

ACKNOWLEDGEMENT

Special thanks to SADOHARA & YOSHIDA laboratory’s Water-team members for their dedicated work to this study: Ms. ASANO Mayuko, Mr. FANG Ji, Mr. INOUE Yusuke, Mr. IZUMI Masahiko, Mr. SUZUKI Wataru, Mr. TERAHATA Yuki, Mr. YOSHIDA Kohei, Mr. YOSHIDA Sho, Ms. WANG Dongzhi, and Mr. YAERMAIMATI Tawaikuli.

This work is contribution to the 21st Century Center of Excellence Program: “Environmental Risk Management for Bio/Eco-systems” (Leader: Prof. URANO Kohei, YNU) by MEXT (the Ministry of Education, Culture, Sports, Science, and Technology).

REFERENCES

- Arctur, D., and Zeiler, M., 2004. *Designing Geodatabases –Case Studies in GIS Data Modeling*. ESRI Press, California, USA.
- Kawasaki, A., Suzuki, W., Park Y. J., Sadohara, S., and Urano, K., 2005, *Development of a Spatial Data Sharing System supporting Multidisciplinary Environmental Research at a University - Forming a World-class Center of Excellence for “Environmental Risk Management for Bio/Eco-systems” No. 1 -*, Theory and Applications of GIS, Vol.13, No.1, pp.83-89 (Japanese).
- Maidment, R. D., 2002. *ArchHydro: GIS for Water Resources*. ESRI Press, California, USA.
- Yokohama National University, 2005. *21st century COE program “Environmental Risk Management for Bio/Eco-systems” web site*.
<http://www.bio-eco.eis.ynu.ac.jp/>
- Zeiler, M., 2002. *Modeling Our World –The ESRI Guide to Geodatabase design* . ESRI Press, California, USA.

ENVIRONMENTAL ASSESSMENT OF URBAN UNDERGROUND INFRASTRUCTURE

NIKOLAI BOBYLEV
United Nations University, Tokyo, Japan
bobylev@hq.unu.edu

ABSTRACT

The paper will discuss application of two forms of environmental assessment for urban underground infrastructure appraisal: environmental impact assessment and strategic environmental assessment. Environmental decision-making and multi-criteria analysis methods will be studied. Some data and analysis on city of Tokyo urban underground infrastructure state-of-the-art, sustainability, and vulnerability will be given.

1. INTRODUCTION

According to the United Nations Population Division, in July 2005, the world gained 6.5 billion inhabitants; almost half of them are living in urban areas. As 95 percent of population growth occurs in developing world, 10 new megacities will appear in developing countries by 2010. Asian megacities have the highest population density: up to almost 400 people per hectare in Mumbai, India. These facts indicate places where urban problems are concentrated, and where major challenges for researches and developers exist. Development of sustainable urban underground infrastructure is one of those challenges. Integrated development of urban underground facilities can contribute towards improvement of transport accessibility, air quality, noise level reduction, and, overall, increase safety, reliability, and environmental quality in densely populated and built urban areas.

2. URBAN UNDERGROUND INFRASTRUCTURE

Conduits, storages, and transport systems has the longest history of being a part of urban underground infrastructure (UUI). Urbanization and advancements in construction technologies in the 20th century facilitated development of a widespread UUI, which provides many services, in downtown areas in particular. Well developed infrastructure includes public and private transport facilities, storages, energy supply utilities, retail, commercial, community services, civil defense and emergency rescue facilities.

2.1 State-of-the-art

UUI has a huge potential for assisting cities to develop in a sustainable way. However, components of UUI are quite complicated structures, which require to be built using careful long-term planning and modern sophisticated construction technologies. Decisions on development or redevelopment of UUI are never straightforward, they always involve many conflicting criteria which must be taken into consideration, many stakeholders are involved and many tradeoffs have to be made.

One of the significant obstacles in new UUI development is congestion of underground space beneath urban areas, and megacities in particular. UUI as cities themselves, was evolving historically, thus valuable underground space at the depth of 5-10 meters has been already occupied by outdated, old infrastructure, which has difficulty to comply with requirements of growing metropolises. This old infrastructure has been in permanent, continuous operation, and its maintenance, modernisation, renovation, and redevelopment associates with many difficulties such as suspension of vital urban services (e.g. utility supply, transport).

Megacity of Tokyo, with a population of 35 million people (United Nations Population Division, 2004) has a significant volume of UUI. Taking these facts into account, it is appropriate to refer to experience of the Tokyo central area in historical development of underground space.

UUI at the Iidabashi station in Tokyo is a good example of congested underground space and disintegrated networks of different functional purposes (Figure 1). Here underground space is filled with 4 subway lines, electric power lines, gas pipes, communication lines, water supply pipes, sewer conduits. Figure 2 illustrates and table 1 indicates density of utility networks under major roads of central Tokyo. Table 2 shows typical distribution of public utilities in a street cross-section.



Figure 1: Dense UUI under Iidabashi station, Tokyo (source: Ministry of construction of Japan; ITA).

Table 1: Length of utility networks under major roads in central Tokyo (from Deep underground utilization law and its benefits, Matsumoto, 2005).

Utility	Total length, km	Length per 1 km of road, km
Telecommunication	2737	17.0
Electricity	1498	9.3
Gas	326	2.0
Water network	367	2.3
Drainage	311	1.9

Table 2: Distribution of public utilities in a street cross-section in Tokyo (data obtained from Tokyo Metropolitan Government).

Depth, m	Part of a street, under which utilities are located	
	Pavement	Road
0-3	Electricity, gas, water, sewer, cables. Air conditioning facilities of the adjacent buildings.	Electricity, gas, water, sewer, cables. Shopping malls, motor ways, parking facilities.
3-5	Shopping malls, motor ways, parking facilities, metro stations. Electricity, gas, water, sewer, cables.	
6-10	Motor ways, metro stations and train tracks. Sewerage collector, cables.	
10-30	Motor ways, metro stations and train tracks. Sewerage collector, specialized tunnels, cables.	

Some Tokyo areas have quite up-to date UUI, those areas tightly connected with good modern redeveloped above-ground environment. Effective city planning that utilises multi-level approach with separation of different transport streams was implemented in Shinjuku area.

Although some complexes of UUI are being created on an advanced technological and design level, Tokyo UUI can not be considered as a sustainable one, because of disintegration and many weak points in a chain of inter-connected facilities.

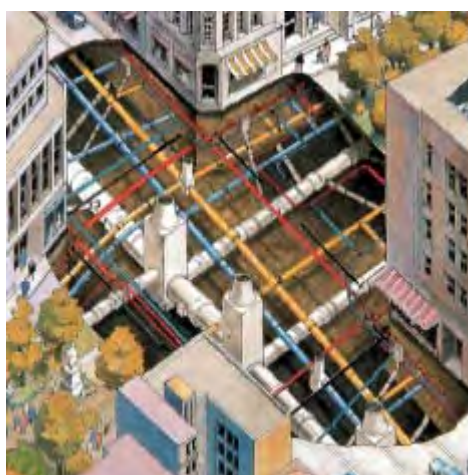


Figure 2: Dense city utility lines appear to be a hindrance for new UUI development (source: ITA).

2.2 Sustainability and vulnerability issues

Sustainable development is a development that meets the needs of the present generation without compromising the ability of future generations to meet their needs (Brundtland Commission, 1987). Breheny (1990) defined urban sustainability as the achievement of urban development aspirations, subject to the condition that the natural and man-made stock of resources are not so depleted that the long term future is jeopardized. Following above definitions the role of UUI in urban sustainability can be viewed from at least two points: UUI helps to archive urban development aspirations, and urban underground space is a valuable natural nonrenewable resource. Taking this two considerations into account it is natural to conclude that careful assessment is needed before making decisions on utilizing urban underground space.

Sustainability of UUI can't be considered apart from city's sustainability as a whole. Regarding UUI it is appropriate to consider its contribution, positive as well as negative to sustainability of urban territory. Main positive contribution of UUI is provided by opportunities for development at high environmental standards, negative contribution is related to bad planning and design of UUI. Environmental assessment is an instrument for linking UUI development plan with the sustainability concept. The present paper limits sustainability considerations to one of its three pillars: environmental one. Methods which fall under broad definition of sustainability appraisal are used for integrating two remaining pillars: economy and society.

Vulnerability analysis in regard to UUI can be considered as two problems (1) city vulnerability and contribution of UUI to this characteristic of a city, and (2) vulnerability of UUI.

Considering the first problem, city's vulnerability, UUI could increase it, as well as decrease. UUI can contribute towards decreasing city's vulnerability by creating an extra layer of facilities, doubling functions of some systems and creating emergency response facilities. UUI is a vital part of urban system, so failure to provide its services will increase city's vulnerability.

The second problem, vulnerability of UUI can be studied by considering natural and artificial disasters, to which UUI could be exposed. Those disasters include natural (earthquakes, floods, unfavorable atmospheric conditions), and artificial ones (terror attacks, fires, equipment failures, construction failures). Vulnerability considerations are limited in the present paper to external for UUI factors (It is assumed that UUI is reliable, i.e. provides the services for which it was designed).

3. ENVIRONMENTAL ASSESSMENT

Environmental assessment (EA) is a process of determining, forecasting, valuating, and elaborating solutions for mitigation of impacts on the environment. Environmental impact assessment (EIA) and strategic environmental assessment (SEA) are specific tools of EA and environmental

decision-making (EDM), which has a developed methodology and legal base in most developed countries and international organizations concerned.

3.1 Environmental decision-making

Much of what falls under the collective heading of EDM can be classified as efforts to identify and quantify environmental risks, and to set priorities and implement policies for managing those risks (Andrews and Valverde, 2004). The application of assessment methods generally entails the use of science and professional judgment. Collectively, these methods and judgments are used to group development options into defined categories. In this way, decision making provides a framework that facilitates the formulation and framing of strategic management options. There is much that risks analysts can learn about speaking scientific “truth” to political “power,” starting with an appreciation that neither truth nor power are absolutes in the real world of EDM (Price, 1965). Typical models of decision processes acknowledge three distinct stages of analysis: identification of the need to make a decision, developing alternative choices, and selecting a preferred choice (Janssen, 1992).

3.2 Scale of consideration

EIA and SEA considering environmental impacts at a different level: EIA is dealing with projects (e.g. a particular underground facility), and objects of SEA are policies, plans, and programs (PPP) (e.g. strategy for underground space development in a megacity). Figure 3 shows application of EA procedures and methods depending on the scale of proposed UI development.

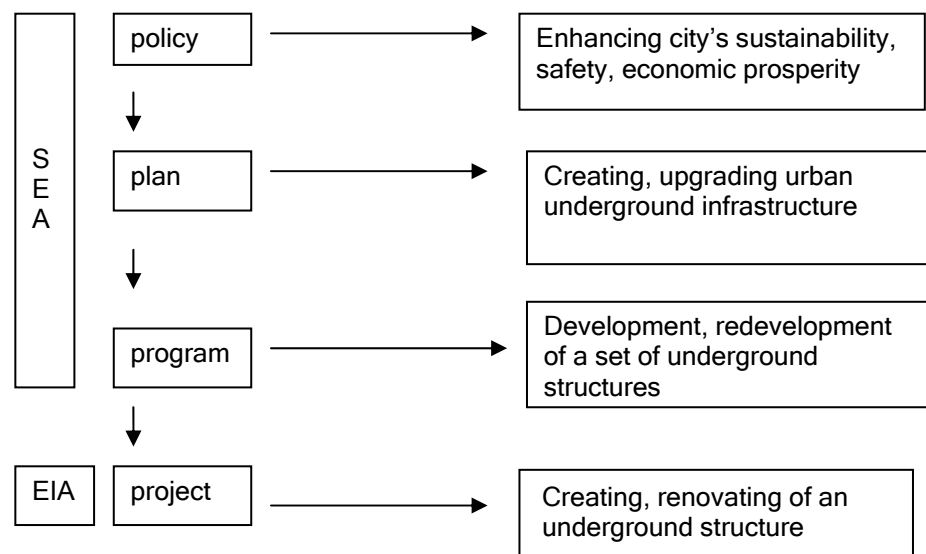


Figure 3: Different scales of EA methods application

3.3 Environmental impact assessment

EIA is a process of examining the environmental consequences of development projects in advance of decision-making. EIA normally starts when feasibility studies for a particular development are in place. EIA is a process, thus it should be extended throughout and be integrated with the project planning and decision-making, so that necessary amendments can be done in planning and design to mitigate negative environmental impacts. Project approval stage is a climax of the EIA process, when the decision to be or not to be has to be made. However, permission to go ahead with a development project does not mean end of EIA process; project follow-up, monitoring of impacts, and implementation of mitigation measures are very important.

EIA process generally consists of the following steps:

- Screening – identification if considered project requires EIA;
- Scoping – identification which impacts needed to be addressed;
- Establishment of environmental baseline;
- Development of alternatives;
- Impacts evaluation;
- Proposing impacts mitigation and monitoring measures;
- Presenting findings and discussion of the results with stakeholders involved, including public.

EIA is required for most of the underground structures – components of UUI. Main adverse environmental impacts take place during underground structure construction period.

3.4 Strategic environmental assessment

SEA is a relatively new tool of EDM which was largely developed in 1990s. Partidario and Clark (2000) define SEA as a systematic on-going process for evaluating, at the earliest stage of decision-making, the environmental quality and consequences of alternative visions and development intentions incorporated in PPPs, ensuring full integration of relevant biophysical, economic, social and political considerations. Generally, as it is seen from the above definition, SEA incorporates a broad array of issues. The following definition appears to be more suitable for achievement of SEA which is focused on environmental issues: SEA is a process of evaluating the environmental impacts of PPPs at a strategic level to ensure environmentally sound decision-making.

SEA considerations should be embedded in a process of PPP elaboration as early as possible. This means that environmental experts are taking part in a PPP elaboration and facilitate the process on a par with other experts, rather than evaluate already taken decisions. SEA is dealing with much broader scope of multidisciplinary information than EIA. Outcome of SEA is a broad brush indication about magnitude of environmental impacts most likely to be, rather than predictions of quantifiable environmental values.

SEA process generally embraces the following considerations:

- Identification of the strategic action objective;
- Incorporation of sustainability issues;
- Identification of targets and indicators;
- Establishment of environmental baseline;
- Development of alternatives;
- Impacts evaluation;
- Impacts mitigation and monitoring.

SEA, analyzing conflicts between different objectives of PPPs, aimed to show explicitly trade-offs that should be made while selecting alternative for UUI development.

4. CONDUCTING ENVIRONMENTAL ASSESSMENT OF UUI

The range of methods that can be used for EA of UUI embraces a wide variety, from experts' workshops and public involvement to usage of computer models and scenarios building. Let's mention some important methods: aggregation, checklists, cost-benefit analysis (CBA), Delphi surveys, geographic information systems (GIS), life cycle assessment (LCA), matrices, multi-criteria analysis (MCA), overlapping maps, scenario development. MCA (this term is equal to multi-criteria decision analysis) techniques are applicable to a very broad range of issues where decisions are needed to handle complex situations involving alternative options evaluated along several conflicting criteria.

Some recent works on EA (European Commission 5th Framework projects PROSPECTS (2004) and SUSTOOLS (2003)) explore integrative approach, combining CBA and MCA. Those combinatory techniques provide opportunities for obtaining assessment based on substantial volume of quantitative information, however for strategic UUI development PPPs this kind of detailed data is unavailable in many cases. Stand alone MCA is currently seen as the most appropriate method for UUI EA, since it's basic ability to be implemented doesn't depend on information availability.

4.1 Multi-criteria analysis

MCA is a method of decision analysis, that involves the use of scoring and weighting systems based on criteria, in order to test and compare the impacts of alternatives. MCA is not a method that provides the 'right' solution of a complex problem, simply because no such solution exists. Alternatively, MCA helps stakeholders to effectively handle complex decisions in which the level of conflict between criteria is beyond intuitive solutions. In addition, MCA has reliable tools for detecting and mitigation conflicts and disagreements between stakeholders upon criteria prioritizing (Belton and Stewart, 2002). MCA methods can be divided according to an aggregation rule into two broad categories: multi-attribute value theory methods and outranking methods (Holland, et al., 2004).

Multi-attribute value theory methods are aiming at associating a unique number (value) representing the overall strength of each alternative if all criteria are taken into account. Weights in this method play the role of scaling factors in the sense that they relate scores in one criterion, to the scores of all other criteria. This means that by assigning weights of relative importance, stakeholders implicitly determine how much units in one criterion they are willing to give up, in order to improve the performance of another criterion by one unit.

Outranking methods proceed to a pairwise comparison of alternatives in each single criterion in order to first determine partial binary relations denoting the evidence that 'an alternative *a* is at least as good as alternative *b*'.

Both methods, multi-attribute value methods and outranking methods are suitable for the assessment of UUI; however the author finds outranking methods more accurate because of technique of pairwise comparison.

Table 3 shows a step-wise procedure of MCA methods and its relation to EA of UUI.

Table 3: A summary of MCA process with respect to EA of UUI.

MCA steps	Comment for EA of UUI
Establishment of the decision context	Identification of assessment object (what exact components of UUI needed to be assessed): <ul style="list-style-type: none"> • piecemeal/integral assessment? • how many assessments should be conducted? • what are the constrains?
Identification of the options to be assessed	Identification/development of alternative options (e.g. variations of design solutions, or even alternative types of infrastructure)
Identification of criteria	Development of a set of multi-disciplinary criteria, and composing them in a hierarchy structure
Weighting – assigning weights for each of the criteria	Identification of priorities at all the levels of the hierarchy structure (e.g. which impacts are more important: on atmosphere or litosphere?)
Scoring – assessment of expected performance of each option against criteria	Comparison of impacts form different PPPs, or project options
Combining the weights and scores	Technique depends on particular MCA method
Results examination	Examination of different alternatives performance in terms of environmental impacts
Sensitivity analysis	Results reliability check

MCA process, shown in table 3 is likely to involve substantial iteration, with feedbacks to earlier steps. Good quality MCA should be done with many iterations, which allow identifying crucial points for decision-

making and explicitly addressing them in subsequent considerations (Dodgson et al., 2000).

MCA can be built up from any level of quantification, though better quality of data is available, more reliable results of assessment will be obtained. Requirements for information quantification differ from EA scale. Sadler (2002) suggested that in most cases of SEA qualitative information on the basis of expert judgment is sufficient. EIA normally has higher level of quantification than SEA, Therivel (2002) suggested that quantification should be considered where effects are already close to a threshold. Share of qualitative information is usually more than a half in input data for UUI EA. Thus, there is a substantial uncertainty in MCA, namely it arises from input data accuracy, composition of a hierarchy structure, scores, and weights assignation. Sensitivity analysis addresses those uncertainties and appears to be a vital element for MCA.

Sensitivity analysis seeks to assess the extent to which the overall attractiveness and hence ranking of strategies changes as plausible changes are made to key input assumptions, reflecting the degree of uncertainty that might surround them. The output from such investigations of sensitivity would be a deeper understanding of how vulnerable any particular package of measures might be to changes in key input assumptions. A response to high levels of sensitivity might involve search for more detailed information or diminishing the uncertainty surrounding a particular input, or re-designing of the alternatives set to seek to make it less susceptible.

Going beyond sensitivity tests, there are a number of other approaches to uncertainty (expected utility theory, real options approach) (Dixit and Pindyck 1994). For most UUI EAs sensitivity analysis is sufficient tool to assure accuracy and truthfulness of MCA results.

5. CONCLUSION

Population growth, urbanization, and aspiration for improving life standards and the environmental quality in urban areas motivate the development of UUI. Development and redevelopment of UUI in megacities central areas is a pressing problem. The UUI development has both beneficial and adverse environmental impacts. The contribution of well planned and designed UUI to megacity sustainability is significant, although UUI is vulnerable to natural and technogenic disasters. EA is an effective tool for achieving better quality of UUI performance. The EDM for UUI applications utilizes different EA methods and depends on a scale of proposed development: EIA at a project level and SEA for PPPs. MCA is an effective tool of decision analysis, applicable for EIA and SEA.

EA is a relatively new area of science; experience in EA of UUI is very exiguous yet. Given the need for UUI development in megacities, future research is needed in the area of environmental impacts of UUI and its potential contribution towards megacity sustainability.

ACNOWLEGEMENTS

Author would like to acknowledge the contribution of the following organizations, which provided opportunities for conducting research: Japan Society for Promotion of Science; United Nations University; University of Tokyo.

REFERENCES

- Andrews, C.J., Valverde, A.L.J., JR, 2004. Analysis in support of the environmental decision-making. *Comparative Risk Assessment and Environmental Decision Making*, Kluwer.
- Belton, V., Stewart, T. J., 2002. *Multiple Criteria Decision Analysis: An integrated approach*. Kluwer Academic Publishers, Dordrecht.
- Breheny, M. 1990. Strategic Planning and Urban Sustainability. *Proceedings of the 1990 Town and Country Planning Association Annual Conference*. TCPA, London.
- Dixit, A.K., Pindyck, R.S., 1994. *Investment under Uncertainty*. Princeton University Press, Princeton.
- Dodgson, J., Spackman, M., Pearman, A.D., Phillips, L.D., 2000. *Multi-Criteria Analysis: a Manual*. Department of the Environment, Transport and the Regions, London.
- Holland, M. et al., 2004. Tools for sustainability Development and application of an integrated framework.
- Janssen, R. 1992. *Multiobjective Decision Support for Environmental Management*. Kluwer Academic Publishers, Dordrecht.
- Levett-Therivel Sustainability Consultants, 2002. *Draft Guidance on the Strategic Environmental Assessment Directives: Proposals for practical guidance on applying Directive 2001/42/EC "on the assessment of the effects of certain plans and programmes on the environment" to land use and spatial plans in England*.
- Matsumoto, R., 2005. Deep underground utilization law and its benefits. *Proceedings of the World Tunnel Congress 2005 "Underground space use – Analysis of the Past and Lessons for the Future"*, Istanbul.
- Minken, H. et al. 2003. Deliverables of PROSPECTS Project. Institute of Transport Economics. Oslo.
- Partidario, M.R., Clark, R., eds., 2000. *Perspectives on Strategic Environmental Assessment*. Lewis Publishers.
- Price, D.K. 1965. The spectrum from truth to power. *The Scientific Estate*. Belknap Press, Cambridge.
- Sadler, B., McCabe M., eds., 2002. *UNEP Environmental Impact Assessment Training Resources Manual, Second Edition*. UNEP, Geneva.

INTERACTIVE STRUCTURAL DYNAMICS LEARNING KIT

Ashutosh Kumar & B. Rajesh Babu

M.Tech in Computer Aided Structural Engineering

IIIT Hyderabad

India

and

Ramancharla Pradeep Kumar

Earthquake Engineering Research Centre

IIIT Hyderabad

India

e-mail: ramancharla@iiit.ac.in

ABSTRACT

Natural disasters like earthquake, landslide, flood, drought, cyclone, forest fire, volcanic eruption are quite common in different parts of the globe. These natural disasters lead to the loss of life, property damage and socio-economic disruption. Earthquakes are one of the worst among the natural disasters. Seismic zonation map given in IS 1893:2002 shows that India is highly vulnerable for earthquake and over 60% of India is prone to moderate to major earthquakes. During past century, India has witnessed more than 650 earthquakes of magnitude greater than 5 and during past 15 years, 6 earthquakes of magnitude over 6.

From recent earthquakes, it is very well understood that lack of awareness is one of the contributing factors for huge casualty losses. In order to increase the awareness about the effects of earthquakes among professionals involved in construction, it is necessary to make them understand the concepts of structural dynamics and earthquake engineering. For this, we have developed a software tool called Interactive Structural Dynamics Learning Kit (ISDLK) for explaining structural dynamics in a simple manner. For convenience in explaining the concepts, we divided the tool into six modules. Each module contains few experiments with good G.U.I. In these modules, user can input the value and he/she can find the desired results with explanation using graphical diagram. At the end of sixth module, user can understand the complete dynamic behavior of a structure. ISDLK aims to help students, architects and design professional in understanding structural dynamics.

1. INTRODUCTION

According to latest seismic zonation map given in IS: 1893: 2002, more than 60% of India is prone to earthquakes. Metropolitan cities like Delhi, Calcutta, Mumbai, Chennai, Ahmedabad etc., lie in zone III or above.

If we look at past 15 years, India has witnessed 6 moderate earthquakes causing around 40,000 casualties and innumerable property loss. This loss is caused mainly due to collapse of structures. Hence, it is very important to built capacity in professionals for ensuring earthquake resistant constructions.

Earthquake engineering education in India though started early, it has not picked up to the extent what is required at present (NPEEE 2003). This is clearly evident from the damages during previous earthquakes. The main drawback for this is that average civil engineer in the country is not getting enough formal training in the concepts of structural dynamics and earthquake engineering during his undergraduate training period. The reason is that in most of the universities, these topics are not incorporated into the curriculum. Even during post-graduate training, very few institutes are emphasizing on earthquake engineering. Because of the fast growth in multi-storied constructions in urban areas of the country, there is a strong need for incorporating structural dynamics/earthquake engineering studies into the curriculum.

Contrarily, even if we incorporate these topics into curriculum, we do not have sufficient trained faculty to teach these topics. Hence there is a very urgent need for us to develop manpower in this field. To address this issue, we developed Interactive Structural Dynamics Learning Kit (ISDLK), where a faculty with some knowledge on structural engineering can be able to learn by himself the fundamentals of structural dynamics. This virtual laboratory will introduce the user, the concepts of structural dynamics in very lucid way. User can interact with the experiments using GUI developed on Visual Basic platform.

2. ISDLK MODULES

It is necessary to design and construct earthquake resistant dwellings in the seismic prone zones. Normally houses are built to withstand vertical load only and as a result they collapse when subjected to horizontal forces produced by earthquake waves. For understanding of behavior of lateral load, we should have better understanding of structural dynamics. For easy understanding of structural dynamics, we have divided the tool in six different modules. Name of different module as listed below

- 1) Simple oscillator
- 2) Single degree of freedom system
- 3) Response due to arbitrary force
- 4) Response spectrum
- 5) Multi degree of freedom system
- 6) Vibration control

2.1 Module 1: Simple oscillator

In this module, basic concepts of simple oscillator are explained. Initially, an example of simple pendulum is taken and the basic terminology *i.e.*, what is initial displacement, initial velocity, natural frequency and time period are explained. Each of these terms is illustrated by giving an example, where user can enter his value and observe the behavior of structure for his input. At the end, two experiments are illustrated *i.e.*, i) simple oscillator and ii) mass and spring.

2.1.1 Experiment 1: Simple oscillator

In this experiment, user will input the desired displacement and upon inputting that he/she can see the pendulum vibrating at a given initial displacement and adjacent to it a dynamic plot will appear showing the time history of oscillator. User can pause the oscillation and check the displacement at any given time instant. Figure 1 shows illustration of experiment 1.

2.1.2 Experiment 2: Mass and spring

This experiment gives the option for entering initial displacement and initial velocity to initiate free vibration in a mass and spring system. After setting the input parameters, user can see the influence of initial conditions in the adjacent plot showing the time history of the system. User can experiment by setting one parameter zero and varying other to check the system response.

2.2 Module 2: Single degree of freedom system

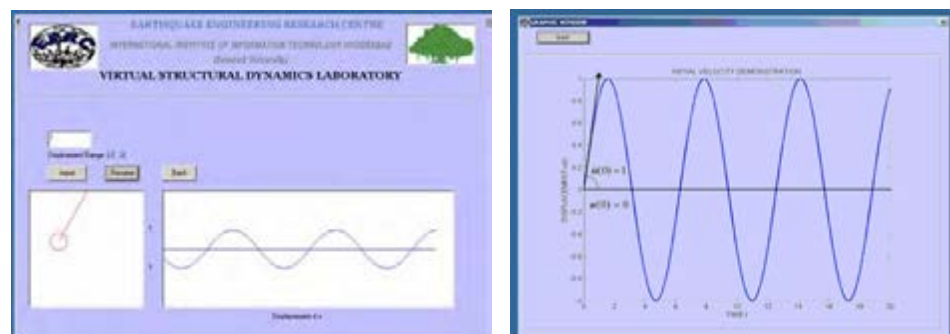


Figure 1: Initial displacement and initial velocity

In this module, basic concepts of a single degree of freedom system are introduced. It explains initially the procedure to obtain the dynamic equilibrium equation and later it's various forms with respect to presence and absence of forcing function and natural damping. This module is also presenting two experiments *i.e.*, i) mass, spring and damping system and ii) response generator for linear systems.

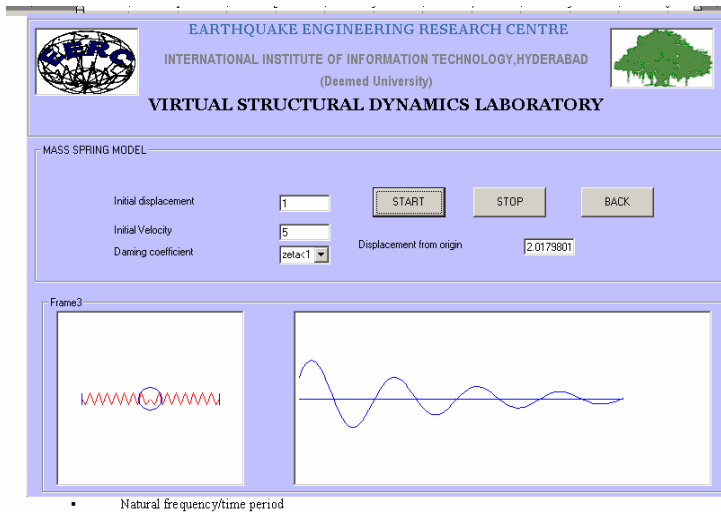


Figure 2: Experiment showing effect of damping

2.2.1 Experiment 3: Mass, spring and damping

In this experiment, user has option to input the desired displacement, velocity and damping. Upon inputting that he/she can see the vibration of mass and adjacent to it a dynamic plot showing the time history of the

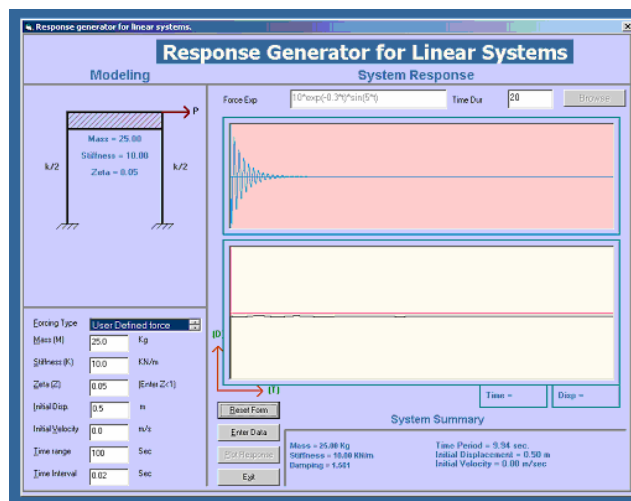


Figure 3: Response generator for linear oscillator

system. In this plot, user can see the influence of damping on the vibration amplitude. Response of the system will decay exponentially and the same can be seen in experiment.

2.2.2 Experiment 4: Response generator for linear systems

This experiment introduces user the concept of damped forced vibration. This is a convenient experiment to find out the response of linear single degree of freedom system for a given mass, stiffness and damping for a given force. Force can be any arbitrary force or an earthquake force. Figure

4 shows the snapshot of experiment 4. From this figure, it is clear that we can see the input force and output response of the system simultaneously. User can experiment by changing the parameters and observing the response. Under special cases, user can verify free and undamped vibrations also. In this experiment the following cases are possible *viz.*, a) free undamped vibrations, b) free damped vibrations, c) forced undamped vibrations and d) forced damped vibrations.

2.3 Module 3: Response due to arbitrary force

In many practical situations the dynamic excitation is neither harmonic nor periodic. Thus we are interested in studying the dynamic response of SDF to excitations varying arbitrarily with time. A general procedure is developed to analyze the response of an SDF system subjected to force varying with time. This module has subdivided into three sub module. i) response due to unit impulse ii) response due to rectangular impulse iii) response due to half cycle.

2.3.1 Experiment 5: drawing response for arbitrary force

User has four options to choose from different condition. Clicking on the option button he/she will get the desire result related to impact of unit impulse and step force

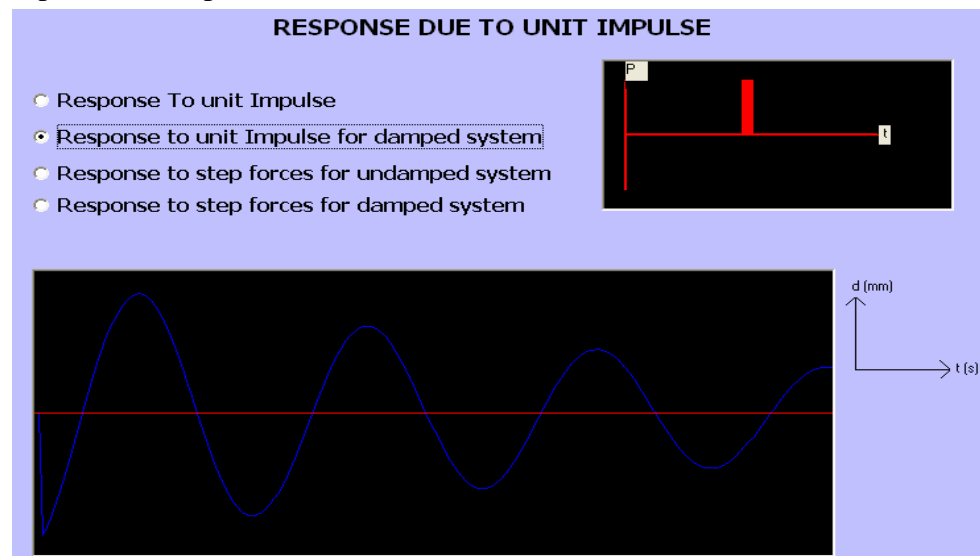


Figure 4: Response due to unit impulse for damped system

2.3.2 Experiment 6: drawing response due to Rectangular Force

The normalized deformation depends only on t_d/T_n , the ratio of pulse duration to natural vibration period of the system, not separately on t_d or T_n . The nature of the response is seen to vary greatly by changing just the duration t_d of the pulse. However no matter how long the duration, the dynamic response is not close to the static solution, because the force is

suddenly applied. User can view the different condition for t_d/T_n and find the response history.

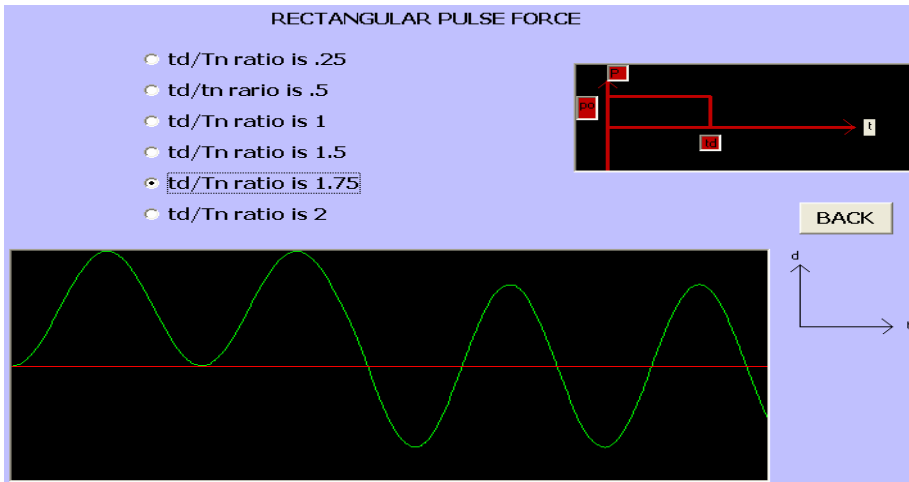


Figure 5: Response due to Rectangular pulse force

2.2.3 Experiment 7: drawing response due to Half Cycle Sine Pulse Force

The normalized deformation depends only on t_d/T_n , the ratio of pulse duration to natural vibration period of the system, not separately on t_d or T_n . The nature of the response is seen to vary greatly by changing just the duration t_d of the pulse. However no matter how long the duration, the dynamic response is not close to the static solution, because the force is suddenly applied. User can view the different condition for t_d/T_n and find the response history.

2.4 Module 4: Response spectrum

Engineers to quantify the effect of an earthquake often use response spectra. Response spectrum is a plot between time period and maximum response of a linear single degree of freedom system oscillator. In this module, response spectrum concept is explained by showing some oscillators with different mass and stiffness properties but same natural period. It is explained here that the maximum response of a single degree of freedom system oscillator to a given earthquake ground motion depends on natural period and damping only.

2.4.1 Experiment 8: Spectrum generator for a given earthquake record

This experiment generates response spectrum for a given component of earthquake record. Here user can input the earthquake record, desired response (i.e., displacement, velocity or acceleration), frequency range of response and damping. Then, oscillator corresponding to each frequency will be subjected to the earthquake motion and maximum response is stored. All such stored maximum responses are plotted with respect to their natural frequency to form response spectrum. At the end, few examples problems

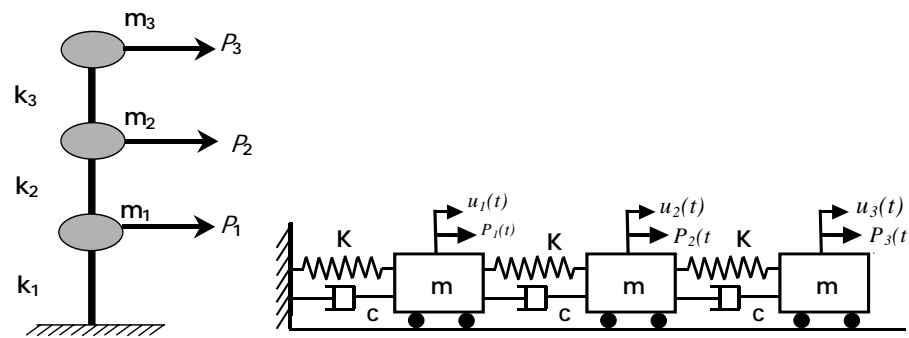


Figure 6: Lumped mass idealization of three-story building

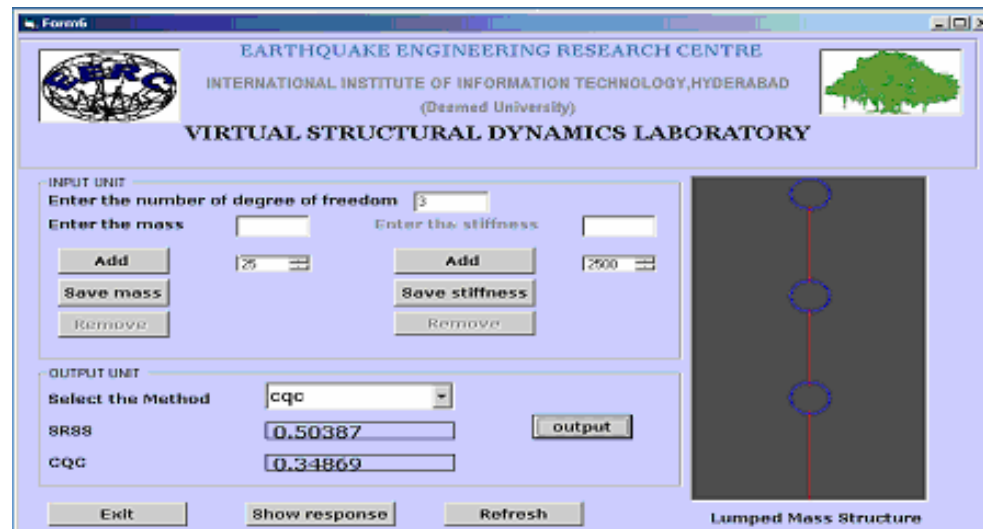


Figure 7: Modal analysis tool

are also given to explain the procedure how to use response spectrum plot (and tripartite plot also).

2.5 Module 5: Multi-degree of freedom system

If the systems have more than one degree of freedom (as shown in fig. 6) the motion is more complex and the vibratory motion is considered to possess as many separate harmonic motions as there are degrees of freedom. Procedure to develop characteristic equation and solution for eigen values and eigen vectors is explained by keeping mathematics minimal. In this module, two experiments are there to explain i) modal analysis and ii) interpretation of mode shape.

2.5.1 Experiment 8: Modal analysis tool

In this experiment, modal analysis can be performed for n degree of freedom system. Initially user has to select number of degrees of freedom and then enter the mass and stiffness parameters corresponding the each floor. Then program calculates natural frequencies and mode shapes of the system. For each natural frequency, program calculates the maximum response from already generated response spectrum. After finding out maximum, it multiplies the quantity with mode shape to give maximum response at each floor level. And then these values are multiplied with participation factor to

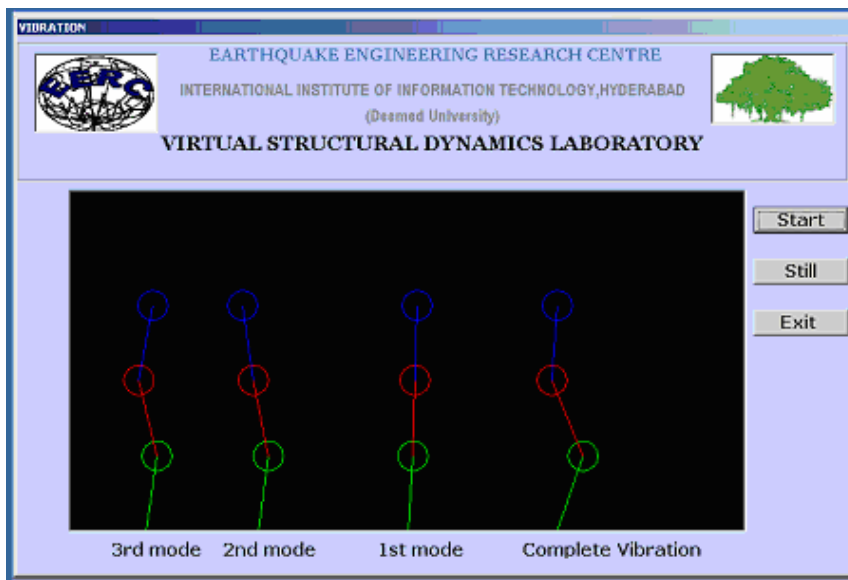


Figure 8: Demonstration of mode shapes

give participation that mode in total response. Similarly, the maximum response is calculated for other frequencies also. Finally, these values are combined using appropriate modal combination rule. In this experiment, two modal combination methods are explained *i.e.*, a) Square root of sum of squares (SRSS) and b) Complete quadratic combination (CQC).

2.5.2 Experiment 7: Interpretation of mode shape

This experiment is especially developed to explain the user the concept of mode shape and contribution of each mode in the total response. Three mode shapes are considered in this example. Three participation factors corresponding to each mode shape are used. User is tempted to vary these participation factors and check the effect of each mode on the total response. A snap shot of the same is shown in the figure 8.

2.6 Module 6: Vibration control

Structural control of building is very much needed for earthquake resistant design. Structural control techniques can be broadly classified into two types namely passive control and active control. With reference to buildings in passive control methods special members are added to the structure. The strength and stiffness characteristics of these members depend on the level of structural response experienced by them.

In active control methods, ground motion and structural response are measured through sensors, called seismometers. These inputs are fed to a computer which calculates forces required to be applied through special members to modify the building response to the desired level. These special members are called active control devices.

This module contains the description about vibration control and different methods of vibration control. It contains one experiment for finding the response of structure due to tuned mass damper.

2.6.1 Experiment 11: Time History Analysis of by Tuned Mass Damper

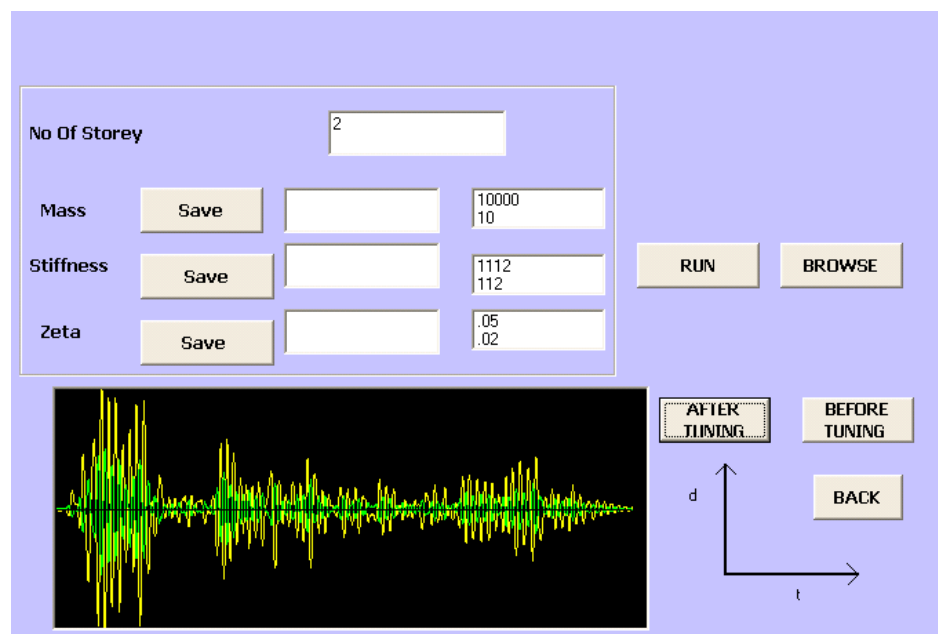


Figure 9: Experiment for Tuned Mass Damper

In this experiment, Tuned mass Damper analysis can be performed for n degree of freedom system. Initially user has to select number of degrees of freedom and then enter the mass, stiffness and damping parameters corresponding the each floor. Then program calculates the time history analysis for given earthquake record. Graphs has plotted for the structure before the tuning and after the tuning effect.

3. CONCLUSIONS

In order to increase the awareness about the effects of earthquakes among professionals involved in construction, it is necessary to make them understand the concepts of structural dynamics and earthquake engineering. To address this issue, we have developed a software tool named Interactive Structural Dynamics Learning Kit. This is an easy tool for users to understand structural dynamics. Mathematics is kept very minimal in explaining the concepts. Total 9 experiments are used to explain the fundamentals of structural dynamics. User is tempted to experiment with the parameters and understands the influence of various parameters on the total response.

REFERENCES

National Programme on Earthquake Engineering Education, A ministry of HRD (GoI) initiative, March 2003.

Evangelos Petroutrisos, 2002. *Mastering Visual Basic 6.0*, B.P.B. Publishers, New Delhi.

Anil K.Chopra, Dynamics of Structures theory & Application to Earthquake Engineering, Prentice Hall of India, New Delhi 1996.

THE GREAT SUMATRA-ANDAMAN ISLANDS EARTHQUAKE ($M_w = 9.0$) OF 26 DECEMBER 2004: POTENTIAL VULNERABILITY OF BUILDINGS AND INFRASTRUCTURES IN REMOTE METROPOLITAN AREAS

KAZI REZAUL KARIM AND TSO-CHIEN PAN

Protective Technology Research Centre, School of Civil and Environmental Engineering, Nanyang Technological University, Singapore
crkkazi@ntu.edu.sg

ABSTRACT

Resulting from the rapid economic growth and development, many high-rise buildings and complex infrastructure systems have been constructed in South-East Asia. The main active seismic sources that generate numerous earthquakes in the region are the Sumatra fault and the Sumatra subduction zone. During the past 30 years, the high-rise buildings in the major metropolitan areas of the South-East Asian region have reportedly felt the tremors from many medium to large earthquakes in Sumatra. Although there has not been any seismic damage observed so far in this region, the seismic performance of buildings to larger and closer Sumatra earthquakes has yet to be investigated. In this paper, the Sumatra-Andaman Islands earthquake, damages, public responses, and the earthquake ground motions recorded in Singapore are reported. Discussions on the local seismic hazard in this region are also presented. The recent Sumatra-Andaman Islands earthquake of 26 December 2004 has given another fresh reminder of the potential seismic hazards and vulnerability of buildings and infrastructures in the region. It caused severe damage and a massive loss of life in the region, where earthquake-resistant design is not specifically required. The observations on the damages, public responses and the ground motions recorded in Singapore due to the recent Sumatra-Andaman Islands earthquake support the continued monitoring and research in the low seismicity zones.

1. INTRODUCTION

The massive undersea earthquake ($M_w = 9.0$) of 26 December 2004 occurred off the north-west coast of Sumatra, Indonesia as depicted in Figure 1. It caused tsunamis around the Indian Ocean with a global death toll approaching 290,000 (as of 22 March 2005), making it the deadliest tsunami ever recorded. The epicenter of the earthquake was 908 km north-northwest

from Singapore. The main tremors and a series of aftershocks from the recent earthquake were also reportedly felt in several areas of Singapore. A local newspaper reported that the areas where the tremors were felt are Tanjong Rhu, Marine Parade, Toa Payoh, Siglap and Meyer Road (*Today*, 27 December 2004). At these locations, the tremors caused no damage.

Singapore is located in a low seismicity region of Sunda plate, where the Sumatra fault and the Sumatra subduction zone, are located more than 350 km away. While earthquakes have never posed any real problems for Singapore, previous large earthquakes have induced tremors felt in Singapore (Pan, 1995; Pan and Sun, 1996; Pan, 1997; Pan *et. al.*, 2001). It is therefore reasonable to postulate that larger and closer earthquakes in Sumatra might result in higher, or even damaging, ground motions on the Malay Peninsula. This is further accentuated when coupled with the fact that earthquake-resistant design has yet to be specifically required in the current regional building codes. In this paper, the Sumatra-Andaman Islands earthquake, damages, public responses, and the earthquake ground motions recorded in Singapore are reported. Discussions on the local seismic hazard in this region are also presented.

2. THE GREAT SUMATRA-ANDAMAN ISLANDS EARTHQUAKE OF 26 DECEMBER 2004

2.1 Main Shock

The Sumatra-Andaman Islands earthquake occurred in Banda Aceh (off the West Coast of Northern Sumatra), Indonesia, on 26 December 2004, at 00:58:53 UTC (26 December 2004, 08:58:53 Singapore Time). According to the USGS National Earthquake Information Center (NEIC), the epicenter of the earthquake was located at 3.298° N and 95.778° E, under the Indian Ocean, off the west coast of Banda Aceh in Northern Sumatra Island. The epicenter was about 250 km south-southeast of Banda Aceh, Sumatra, and 908 km of south-southwest of Singapore, as shown in Figure 1. The focal depth (30 km) was reported to be shallow. The tremors from the earthquake were reportedly felt with intensity VIII at Banda Aceh and V at Medan, Sumatra and II to IV in parts of Bangladesh, India, Malaysia, Maldives, Myanmar, Singapore, Sri Lanka and Thailand.

2.2 Aftershocks

Preliminary locations of larger aftershocks following the megathrust earthquake show that approximately 1200 km of the plate boundary slipped as a result of the earthquake. Aftershocks are distributed along much of the shallow plate boundary between northern Sumatra (approximately 3° N) to near Andaman Island (at about 14° N) as shown in Figure 1. The main shock of the earthquake on 26 December 2004 was followed by many aftershocks. Following the main shock, aftershocks were collected from the Incorporated Research Institutions for Seismology (IRIS). Occurring

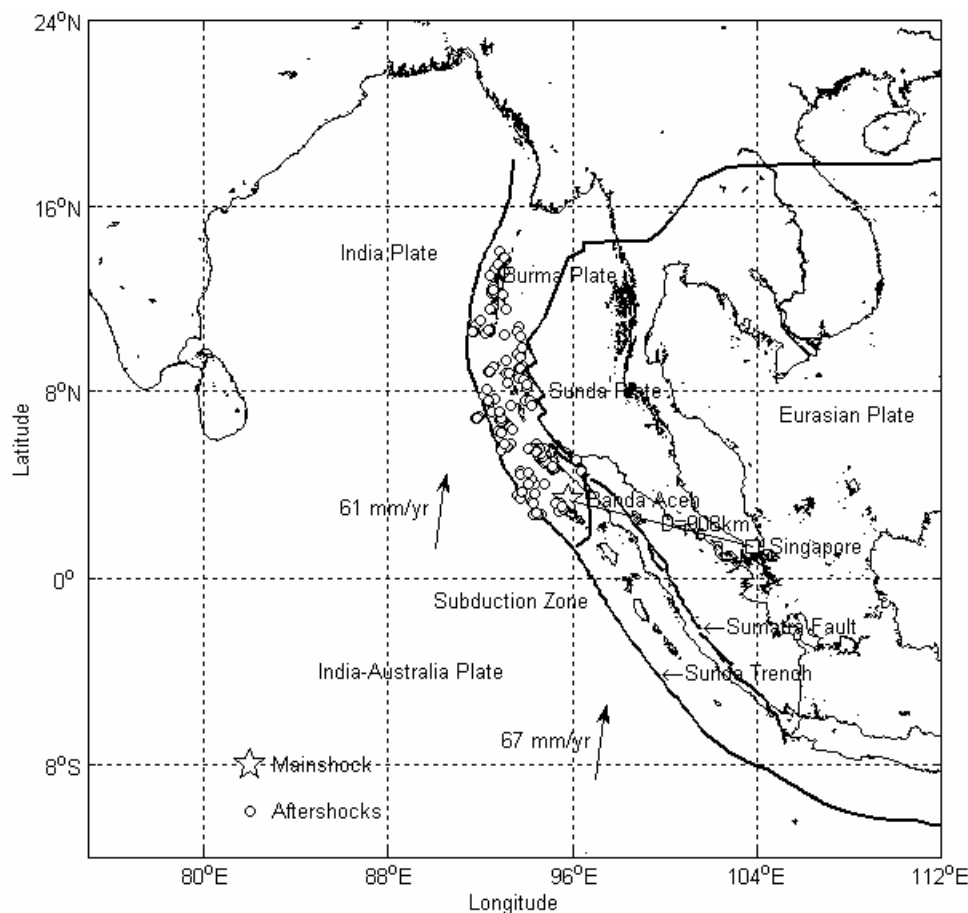


Figure 1: Epicentral locations of main shock and major aftershocks ($M \geq 5.0$) of the Sumatra-Andaman Islands earthquake of 26 December 2004

between 26 December 2004 and 1 January 2005, there were about 145 aftershocks with minimum magnitudes of about 5.0. Figure 1 shows the epicentral locations of the large aftershocks. By comparison with other large megathrust earthquakes, the width of the causative fault-rupture was likely over one-hundred km. From the size of the earthquake, it is likely that the average displacement on the fault plane was about fifteen meters (IRIS). The sea floor overlying the thrust fault would have been uplifted by several meters as a result of the earthquake.

2.3 Tectonic Summary

There was a great tsunami reported following the tsunamigenic subduction earthquake with sudden deformation of seabed. The devastating megathrust earthquake of 26 December 2004 occurred on the interface of the India and Burma plates and was caused by the release of stresses that had developed as the India plate subducts beneath the overriding Burma plate. The India plate begins its descent into the mantle at the Sunda trench, which lies to the west of the earthquake's epicenter. The trench is the surface expression of the plate interface between the Australia and India plates, situated to the southwest of the trench, and the Burma and Sunda plates, situated to the northeast. In the region of the earthquake, the India plate

moves toward the northeast at a rate of about 60 mm/year relative to the Burma plate. This results in an oblique convergence at the Sunda trench. The oblique motion is partitioned into thrust-faulting which occurs on the plate-interface that involves slip directed perpendicular to the trench, and strike-slip faulting which occurs several hundred kilometers to the east of the trench and involves slip directed parallel to the trench. The 26 December 2004 earthquake occurred as the result of thrust-faulting.

2.4 Damages in Banda Aceh and Other Areas

While an official assessment report has to be made, there has been reportedly widespread damage to residential buildings, commercial buildings, military buildings, religious buildings and infrastructural facilities. Most of the buildings damaged were non-engineered, traditional wooden and masonry structures. Engineered infrastructural facilities that experienced severe damage include railway tracks and bridges. Sumatra's northern Aceh province is situated about 150 km north of the epicenter of the magnitude 9.0 earthquake. In the Aceh province, distinction between the structures damaged by the earthquake ground shaking directly or the resultant tsunami cannot yet be clearly made.

Infrastructural facilities that experienced damage due to the earthquake and tsunami include railway tracks, roads and bridges. They include overturning of railway tracks in Colombo and Telwatte, Sri Lanka, complete collapse of several spans of a bridge in India, failure due to subsidence of a bridge in Indonesia, and damage induced on a road in Banda Aceh. In Indonesia, *The Jakarta Post* (4 January 2005) reported that a diesel-fired power plant was destroyed by the earthquake. In Kalpakkam, India, a nuclear power plant was shut down before waves spread into that region. According to the *Asian Age* (27 December 2004), "the second unit of the atomic power station was shut down after sea water entered its plant but the key installation was declared safe".

In Thailand, the local Phuket International Airport was suspended for operations due to failures of the control tower and communication systems and also flooding of the runway. In Indonesia, the local Iskandar Muda Airport in Aceh was also closed (*The Jakarta Post*, 27 December 2004), where the airport operator PT Angkasa Pura II secretary Kasmin Kamil was quoted, "Our control tower and communication system are damaged, and the runway is submerged". Most of the residential buildings that were destroyed are non-engineered structures. The types of damage included collapse and cracking of masonry walls and collapse of wooden frames that support the roof. A common phenomenon was 'sliding' failure of roof tiles due to insufficient attachment to the roof frame. However, in Kuala Lumpur, Malaysia, *The Star* (27 December 2004) reported damage caused by the earthquake on an engineered residential structure, which was a reinforced concrete building.

2.5 Socio-Economic Responses to Asian Crisis

As a result of the tsunami, many countries around the Indian Ocean in Asia experienced casualties and damage. On 31 December 2004, Singapore's Prime Minister called for an urgent meeting of the Association of South-East Asian Nations (ASEAN) leaders. The meeting was held on 5 January 2005 in Jakarta, Indonesia. Attending this meeting were leaders from China, Japan, India, Australia, the United States and European Union. Also attending are representatives from the United Nations, World Bank, Asian Development Bank and World Health Organization. The meeting of the ASEAN leaders is to coordinate the relief efforts for the victims of the tsunami and also to outline the management of the donations pledged by countries and worldwide. To date (5 January 2005) aid pledges from around the world is nearing US\$4 billion.

The Prime Minister of Malaysia, Datuk Seri Abdullah Badawi, announced that Malaysia will appeal to the Organization of Islamic Conference (OIC) countries to aid the children in Aceh made orphans by the tragedy. Also, the government has set aside RM50 million to aid the fishing community that was devastated by the tsunami (*The Star*, 5 January 2005). Associate Professor Hoe I. Ling of University of Columbia has urged Malaysia to carry out a seismic hazard study to promote earthquake awareness and preparedness (*The Star*, 4 January 2004). The framework for the proposed study includes estimating the worst-case scenario earthquake, evaluating the integrity of existing building, soil response assessment, risk assessment and instrumentation of selected buildings.

The Republic of Singapore Air force mobilized pilots for ferrying food, water, clothes and relief crew to inaccessible places. Singapore Armed Forces landing ships stocked with engineering equipment, transport vehicles and 196 personnel set off for Sumatra on 4 January 2005. The City Harvest Community Services sent a team to Banda Aceh to support the existing Indonesian and Swedish doctors in the hospital. The team also brought with it 15 tones of food, drinks and medicine.

2.6 Seismic Instrumentation and Recorded Ground Motions in Singapore

In 1996, the Meteorological Services of Singapore (MSS) installed a network of seismic stations, which consists of two down-hole arrays (BES and KAP) of strong-motion stations and five teleseismic stations (BTDF, FTC, NTU, PTK and SJA). The two down-hole arrays are located on the Kallang formation of Quaternary deposits. The main station, located in the Bukit Timah nature reserve and denoted as BTDF, is a Global Seismic Network (GSN) station, which is equipped with a comprehensive set of sensors to record ground tremors continuously. BTDF is located on a rock outcrop site. The recorded ground motion time histories are transmitted to the MSS headquarters to be processed and analyzed.

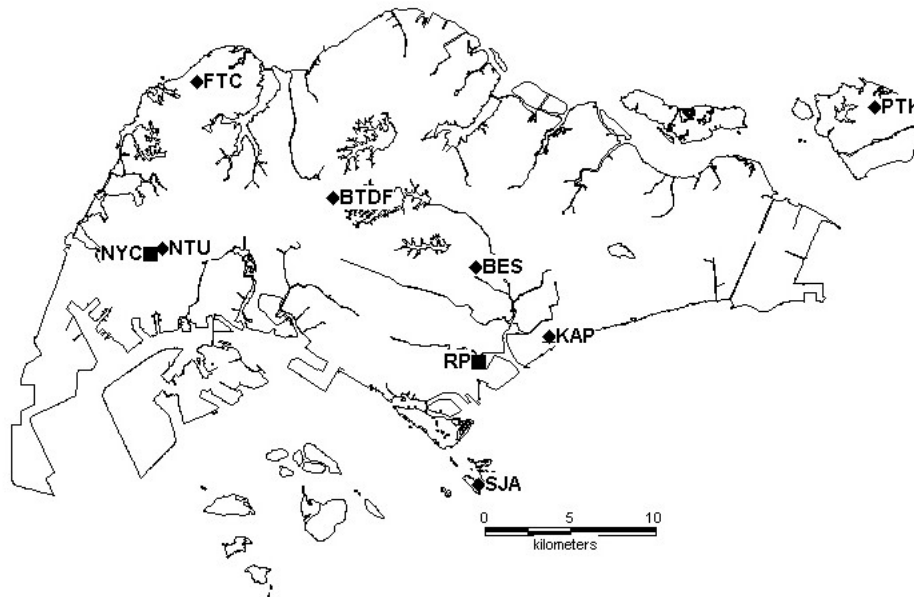


Figure 2: Seismic stations in Singapore (SAFER Array)

The Nanyang Technological University (NTU) has also installed two additional seismic stations, one inside the campus (denoted as NYC) and the other in the basement of a high-rise office building in the central business district (denoted as RP). The NYC station is located on a firm residual soil site, and the building in which the RP station is located sits on rigid caissons. The seven MSS and two NTU stations form an array called the Singapore Array for Earthquake Response (SAFER). The locations of the SAFER array stations are depicted in Figure 2.

The two NTU stations (NYC and RP) and four of the MSS stations (BES, BTDF, NTU, and PTK) were triggered during the Sumatra-Andaman Islands earthquake. Ground motions from the main shock ($M_w = 9.0$) on 26 December 2004 (00:58:53 UTC) and one major aftershock ($M_w = 7.5$) later the same day (04:21:26 UTC) were successfully recorded. The epicenters of the main shock and large aftershocks are shown in Figure 1. Baseline-corrected accelerations of the recorded ground motions at different MSS seismic stations due to the main shock are shown in Figure 3. Table 1 summarizes the peak ground acceleration (PGA), peak ground velocity (PGV), and peak ground displacement (PGD) of each component of ground motion recorded at each seismic station due to the main shock.

3. DISCUSSIONS

Although the magnitude of the Sumatra-Andaman Islands earthquake is larger ($M_w=9.0$) compared to the ones of the previously felt events, however, it induced less ground shaking and structural response than expected both in Kuala Lumpur and Singapore. This could be explained from the distribution of aftershocks as depicted in Figure 1. It suggests that the rupture plane extended from the Simeuleue Island. The epicenter was

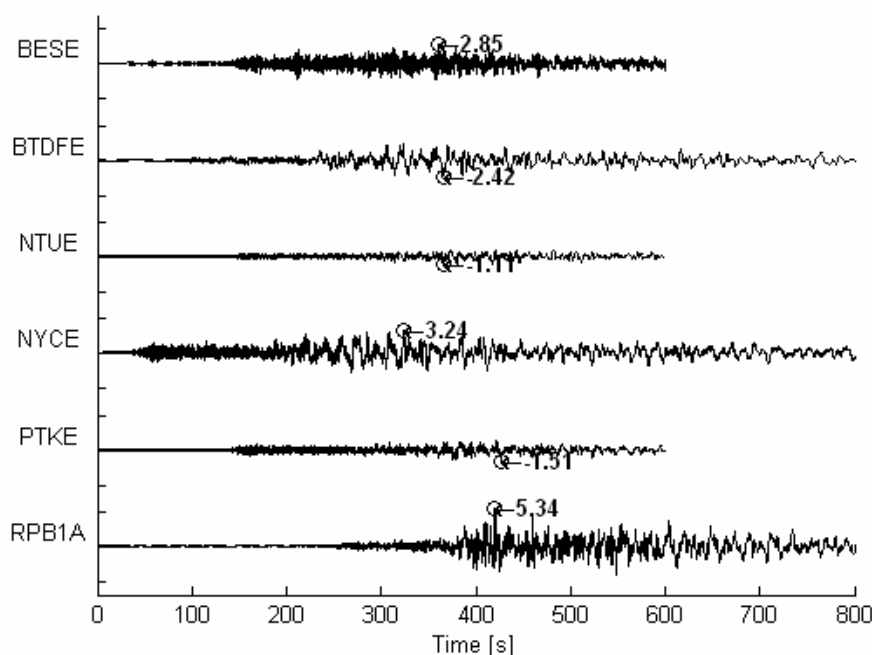


Figure 3(a): Baseline-corrected acceleration (EW component) in mm/s^2 of the main shock (2004/12/26 00:58:53 UTC) of the Sumatra-Andaman Islands earthquake, recorded in Singapore

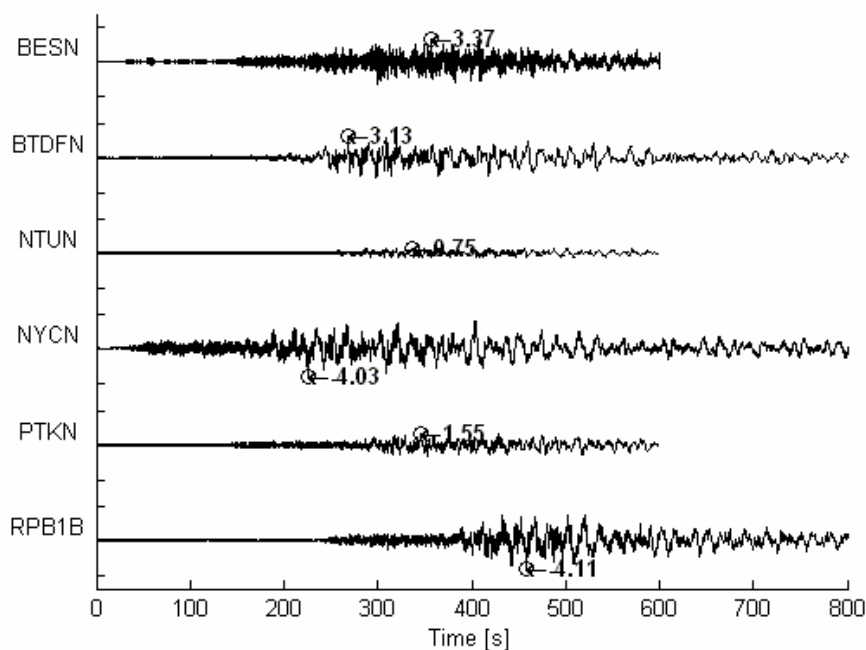


Figure 3(b): Baseline-corrected acceleration (NS component) in mm/s^2 of the main shock (2004/12/26 00:58:53 UTC) of the Sumatra-Andaman Islands earthquake, recorded in Singapore

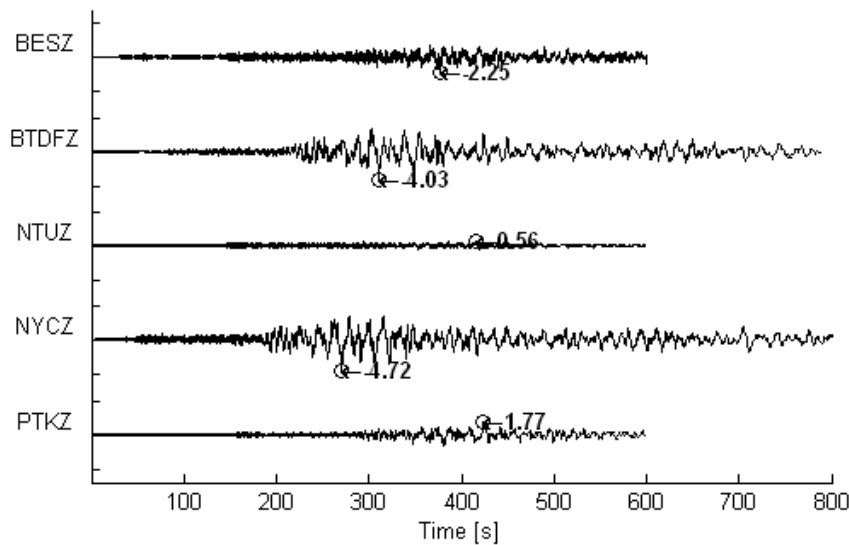


Figure 3(c): Baseline-corrected acceleration (UD component) in mm/s^2 of the main shock (2004/12/26 00:58:53 UTC) of the Sumatra-Andaman Islands earthquake, recorded in Singapore

located beneath the Simeuleue Island and the rupture may have initiated beneath the island, and propagated in a northeast direction. That probably explains why the ground shaking in Banda Aceh ($R=250$ km, MMI VI-VIII, estimated $\text{PGA}=70\text{-}100$ cm/s^2 , estimated $\text{PGV}=8$ cm/s) was stronger than that in the cities located southeast of the epicenter, such as Medan ($R=300$ km, MMI IV-V). Compared to these cities closer to the epicenter, distance from the epicenter is the most probable reason why the tremor was felt less in Kuala Lumpur ($R=650$ km) and Singapore ($R=908$ km). Therefore, the intensity of the ground shaking in the region was smaller than that would be expected from such a giant earthquake.

As more tall buildings are present in Singapore today and the number of felt events is increasing recently, the possibility is not remote that such far-field ground motions can induce larger response of buildings. Firstly, as compared to the Sumatra-Andaman Islands earthquake, the smaller but closer Bengkulu earthquake (Pan *et. al.*, 2001) has led to: (a) more widespread tremors felt, and (b) larger far-field PGAs induced. Secondly, it has been noted that the Bengkulu earthquake was not really the maximum credible earthquake that may occur in Sumatra (Sun and Pan, 1995). Sun and Pan (1995) found that the moment magnitude of an earthquake with a 10% probability of being exceeded in 50 years in Sumatra region was 8.5.

Therefore, the possible effects of very large earthquakes in the subduction zone or on the Sumatra fault with an epicenter closer to Singapore than the Sumatra-Andaman Islands or Bengkulu earthquake can occur. Hence, the effects of these large earthquakes on the high-rise buildings in Singapore and Malay Peninsula need to be investigated further.

Table 1: Summary of the ground motion parameters recorded in Singapore due to the Sumatra-Andaman Islands earthquake

Event date and time [UTC]	Stn	Comp	Parameter		
			PGA [mm/s ²]	PGV [mm/s]	PGD [mm]
26 December 2004 00:58:53	BES	EW	2.80	1.97	4.69
		NS	3.36	2.73	6.44
		UD	2.24	2.66	6.53
	BTDF	EW	2.42	4.26	14.36
		NS	3.13	5.10	17.50
		UD	4.02	6.97	19.41
	NTU	EW	1.10	1.26	3.35
		NS	0.74	1.29	3.26
		UD	0.55	0.72	1.53
	NYC	EW	3.24	6.09	13.92
		NS	4.02	6.96	19.25
		UD	4.72	7.67	21.25
	PTK	EW	1.50	2.09	4.44
		NS	1.55	2.90	6.43
		UD	1.70	2.59	6.99
RP	B1A	5.34	5.49	16.92	
	B1B	4.10	6.78	20.21	

4. CONCLUDING REMARKS

In this paper, the Sumatra-Andaman Islands earthquake, damages, public responses, and the earthquake ground motions recorded in Singapore are reported. Discussions on the local seismic hazard in this region are also presented. The recent Sumatra-Andaman Islands earthquake of 26 December 2004 has given another fresh reminder of the potential seismic hazards and vulnerability of buildings and infrastructures in the region. It caused severe damage and a massive loss of life in the region, where earthquake-resistant design is not specifically required. The observations on the damages, public responses and the ground motions recorded in Singapore due to the recent Sumatra-Andaman Islands earthquake support the continued monitoring and research in the low seismicity zones.

5. ACKNOWLEDGMENTS

The authors would like to thank Mr. K. K. Mah of the Meteorological Services of Singapore, National Environment Agency, Prof. J. M. W. Brownjohn of the Department of Civil Engineering, University of Plymouth, UK, Mr. C. L. Lim, Mr. X. T. You, and Mr. C. L. Leong of the Nanyang Technological University. Without their help, this work would not have been possible. The public responses in Indonesia, Singapore and Malaysia were taken from major newspapers in each country. They are *The Jakarta Post* (Indonesia), *The Straits Times* (Singapore), *The New Strait Times*, and *The Star* (Malaysia).

REFERENCES

- Pan, T.-C., 1995. When the doorbell rings – a case of building response to a long distance earthquake. *Earthquake Engineering and Structural Dynamics* 24, 1343-1353.
- Pan, T.-C., and Sun, J., 1996. Historical earthquakes felt in Singapore. *Bulleting of the Seismological Society of America* 86, 1173-1178.
- Pan, T.-C., 1997. Site-dependent building response in Singapore. *Earthquake Spectra* 13(3), 475-488.
- Pan, T.-C., Megawati, K., Brownjohn, J. M. W., and Lee, C. L., 2001. The Bengkulu, Southern Sumatra, earthquake of 4 June 2000 ($M_w = 7.7$): Another warning to remote metropolitan areas. *Seismological Research Letter* 72(2), 171-185.
- Sun, J., and Pan, T.-C., 1995. The probability of very large earthquakes in Sumatra. *Bulleting of the Seismological Society of America* 85, 1226-1231.

EMERGENCY ROUTING ALGORITHM BASED ON THE 3D-GIS

ZHU Qing¹, LI Yuan¹, TOR Yam Khoon²

¹LIESMARS, Wuhan University, P.R.China

zhuq66@263.net; liyuan@lmars.whu.edu.cn

²School of Civil & Environmental Engineering, NTU, Singapore

cyktor@ntu.edu.sg

ABSTRACT

An increasing number of disasters (such as fire, collapse, poison gas leakage, bombing, etc.) are reported frequently with huge losses of life and asset both on the surface and underground in mega cities. The high population density and complicated urban environment often make rescue work difficult due to the absence of powerful and emergency response tools, which consider multi-dimensional uncertainties and dynamic factors, to aid in the disaster risk management and decision making. The advent of 3D-GIS technology provides new perspective for such emergency rescue and attracts a lot of attention in the last several years. This paper introduces an emergency routing algorithm which deals with the multi-dimensional information (DEM, texture, graph, symbol, simulation results).

Based on the 3D-GIS, it is possible to calculate the shortest vehicle evacuation route, in full 3D environment, during emergency situation. The focus of this paper is on 3D “route mining”, i.e. to extract the crucial and meaningful “clues” for emergency vehicle routing in a 3D city landscape, and to improve the conventional 2D shortest path algorithm by considering the information provided by the 3D emergency “clues” into 3D dynamic network and “weights” of road segment. The model was constructed and tested in 3DGISTM software using a case study of Wuhan, China.

1. INTRODUCTION

Modern city now gradually extends in the third dimension, both upwards and downwards (Zlatanova, 1999). With all kinds of natural and man-made factors, an increasing number of disasters, such as fire, collapse, poison gas leakage, bombing, etc., are reported frequently with huge losses of life and asset both on the surface (road flyover, multi-storey building) and underground (tunnel, subway station) in mega cities. Such disasters occurring in areas of high population density and complicated urban environment often make rescue work more difficult due to the absence of powerful and emergency response tools, which consider multi-dimensional uncertainties and related dynamic factors, to aid in the disaster risk management and decision making.

The advent of 3D-GIS technology provides new perspective for such emergency rescue and attracts a lot of attention in the last several years. 3D-GIS has promised to manage as well as to intuitively visualize multi-dimensional data (DEM, texture, graph, symbol, simulation results). For example, it is possible to depict in three dimensional spaces, the vertically disjointed structure (overpass or underpass), realistic terrain environment, building and its surrounding circumstance. It is also possible to simulation traffic flow and human behavior in a complex urban system. These are beyond the ability of the traditional 2D GIS. 3D objects presented as 2D projections in GIS may loose some of their properties (Texture, graphic, height, etc) and spatial relationships to other objects (Miller and Shaw, 2001).

Researches on emergency routing problem, in 3D environment, attracts diverse interests, such as needs and requirements analysis, methodology development, data collection and management, data integration and mining, data visualization, positioning and navigation. Pollitt et al (1995; 1996) developed a network-based vehicle routing algorithm in 3D environment, which considers static impedances (road segment length in 3D dimension, gradient, and different routing speed) and dynamic impedances (turn, lane changes) with the use of Dijkstra algorithm. Laakso (2002) discusses the use of 3D navigation map in routing/wayfinding. Through analyzing the spatial knowledge, i.e. landmark knowledge, routing knowledge, survey knowledge, vis-a-vis 2D and 3D map, he indicates the importance of landmark in 3D environment for navigation in a city environment. Slavick et al (2005) demonstrate the utility of 3D visualization to meet military and homeland security needs for event-related data in an intuitive display. Through the description of Tactical Operations Center (TOC) 3D program, it shows the importance of the use of 3D models, military symbology, and homeland security symbology in a 3D navigable environment. Kwan and Lee (2005) proposed a navigable network which integrates 2D transportation network and multi-level structure to support 3D emergency response system. Their work emphasizes the integration of intelligent transportation system (ITS) and intelligent building system (IBS) into an emergency routing system. Nanda (2004) utilizes 3D positional information to provide more efficient and reliable routing. He proposes a new hierarchical, zone-based 3D routing algorithm that uses multi-path routing in 3D. Another important extension of 3D application in emergency routing is 3D web-base GIS with the use of 3D visualization function, such as flythrough (Held et al., 2004).

However, real 3D emergency routing algorithm, which has ability to integrate both multi-dimensional and dynamic emergency “clues” into 3D environment, is still limited. One reason is that, much attention were spent on 3D modeling and visualization in 3D-GIS and yet to embark on the analysis of the multi-dimensional information in 3D-GIS, for instance route mining. Another reason is that, emergency simulation of human behavior, traffic dynamic change, hazard proliferation, and many others are studied in

2D or 2½D space to get emergency “clue”. Shortest routes are also calculated in 2D space, basing on fully intersected, planar network (Miller and Shaw, 2001). For real 3D emergency routing algorithm, the crucial multi-dimensional and dynamic emergency information, the knowledge of emergency situation, and shortest path algorithm, should be integrated in a 3D-GIS platform.

In this paper, the idea of a multi-dimensional and dynamic emergency “clue” is illustrated as well as its special function in efficient vehicle routing. The shortcomings of traditional planar network in emergency situation will be discussed next. Finally, a 3D dynamic network, which improves the conventional 2D shortest path algorithm by considering the multi-dimensional information (DEM, texture, graph, symbol, and simulation results) and emergency “clue” is outlined. The model was constructed and tested in 3DGISTM software using a case study of Wuhan, China.

2. EMERGENCY “CLUE” AND 2D NETWORK

Emergency vehicle routing problem is very complicated and dynamic in real disaster situation. Take earthquake for example, it may break traffic system (flyover etc.) directly; destroy buildings around the road network and thus cause traffic congestion. It may also bring flood - which block traffic in some lowlands – as well as fire which further threaten human life and make people panic and flee away from building to road surface. All of the above knowledge is known as emergency “clues”. They are both multi-dimension and dynamics, and bring great challenges to the development of emergency vehicle routing algorithms. Emergency clues have great potentials to avoid unnecessary incident and direct vehicle to get to the destination safer and faster. With the use of emergency “clues”, our traditional routing problem can be extended to suit real emergency cases better. In 3D-GIS environment, multi-dimensional data (including 3D network) are available; however, the problem lies in how to “mine” the important emergency clues and integrate them to improve the efficiency of current route mining algorithm in real emergency situation.

Our traditional vehicle routing approach has been adapted from static and deterministic algorithm to dynamic and stochastic algorithm (Eklund et al., 1996; Gendreau et al., 1996; Lu, 2001; Guo et al., 2002; Bent and Hentenryck, 2004) with the appearance of complicated transportation phenomena (such as turn restriction, multi-lane, lane changing) in many applications. Although many improved strategies such as lane-based (Cova and Johnson, 2003), non-planar network model (Fohl et al., 1996), dynamic segmentation approach, case-based, knowledge-based method (Liu et al., 1994; Ginty and Smyth, 2001) and hierarchical representation (Hock and Srikanthan, 2000) can improve the efficiency of routing in dynamic and stochastic environment, they are all implemented in 2D environment with the support of 2D planar or 2D non-planar network based on graph theory. Furthermore, when the road network of the city is very complicated and

dense which is typical in mega city, it will take too long for the algorithm to find the shortest path (Liu et al., 1994).

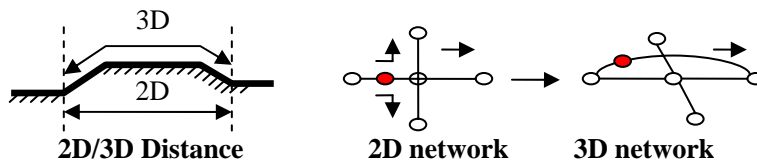


Figure 1: 2D/3D road network

Incorporating 3D information allows more accurate understanding of potential vehicle conflicts in real-time. 3D network overcomes the problem made by 2D planar at least from two aspects: first, it can measure the true distance across sloping or hilly terrain; second, it can represent 3D structures such as overpasses or underpasses (Figure 1). For complex spatial analysis, like emergency routing, 3D network has the potential to detect incident made by multi-dimensional damage. In this paper, in response to real 3D environment and quick response for emergency, 3D dynamic network is constructed for better represent the real situation (under/overpass, gradient, the location of potential incident, etc) of road network. Next, based on 3D dynamic network, Dijkstra algorithm is developed to find “shortest” routes in the 3D emergency environment with the use of emergency “clue” from 3D-GIS.

3. 3D DYNAMIC NETWORK

In traditional planar node-arc graph, the underlying assumption is that spatial data is stored and referenced in a 2D coordinate system. In contrast, a 3D system allows the z -coordinate to be represented as a geometric property and as such, features are represented in their true geometric form (Pollitt, 1995). Furthermore, 3D dynamic network needs some special function to deal with the specific requests for emergency vehicle routing in disaster situation. Firstly, emergency vehicle is in moving condition and tracked by on-board GPS in real time. If the network structure is changed by any sudden incidents, it needs to recalculate the routes from current vehicle point (new start point) to the original destination (original end point). Second, sudden incident may break the transportation network, and this situation should be reflected timely in an updated network structure. These two needs call for dynamic transportation network with abilities to depict the dynamic events (location of vehicle location, incident location and disaster location). Lastly, for quick and flexible response, the events can be reflected directly on the transportation network. The user must be able to select point in the road structure or structure near road network to effect the change or instruction, and the algorithm will determine and display the appropriate path.

There are several methods to construct basic 3D network in 3D-GIS. In 3D environment, it possible to construct 3D transportation network

intuitively on DEM-based road surface, which reflects the real situation of traffic network, including under/overpass, slope, incident point, vehicle location and destination point, etc. With the support of map “snap” function, it is possible to add events (vehicle point, incident point, disaster point) to the basic 3D network to form a dynamic emergency network.

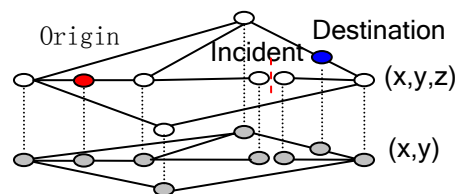


Figure 2: 3D emergency dynamic transportation network

3D dynamic network is presented by the standard notation $N = \{V, E, W\}$ ($G = \{V, E\}$, $W = \{w(v_i, v_j)\}$), where the nodes V correspond to intersection, turning point, origin, incident point, and destination; arc E connecting nodes represent road segmentation; weight W shows the ability of arc connectivity. In 3D dynamic network, the potential $D(v)$ is a changing value, which represents the time to travel to a node at the time the node is being scanned. Corresponding to some special operation in 3D dynamic network, the following symbols are given:

- N – the number of nodes ($|V|$)
- M – the number of arcs ($|E|$)
- $D(v)$ - the current potential (travel time) of nodes
- $S(v)$ - the current status tag of nodes
- PutVex($G, v, value$)- put the vertex v in graph G and give its value
- InsertVex(G, v)- insert vertex v in graph G
- DeleteVex (G, v)- delete the vertex v in graph G
- DeleteArc (G, v, w)- delete the arc from vertex v to w in graph G

From planar network to 3D network, the ambiguity situation of under/overpass in 2D graph can be eliminated. Similarly, from static network to dynamic network, real-time information about vehicle, disaster point, and incident location can be directly considered into routing process. However, for quick response, a better way to improve routing efficiency through optimizing the 3D dynamic network and reduce the research space is still necessary. In different cases, the optimization result is diverse and poses special strategies to “intelligently” optimize the 3D network. More specifically, knowledge (“clue”) indicate to the shortest path algorithm where it should search and where it should not (Liu, Choo et al., 1994). Start point (S) and destination point (D) make basic 3D network add only one vertex each, however, every incident point adds two vertexes on the network segment and break the segment between the two vertexes. The next step is to eliminate the hanging points (vertexes) of the network “tree” till optimization result (the degree of each vertex $d(v) \geq 2$) is achieved. Take Figure 3 as example, after optimization, the unnecessary vertexes are eliminated and the total numbers of vertexes are reduced greatly.

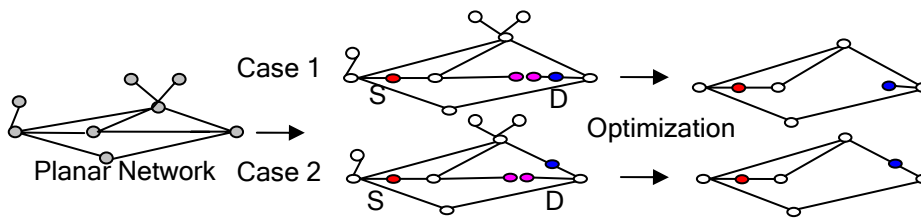


Figure 3: Optimization of 3D dynamic transportation network

In short, the process of 3D dynamic routing is composed by two parts: the building and optimization of 3D network; and using algorithm to find the shortest path, as follows:

- Putvex(G,v, value) in 3D environment
- building basic 3D network
- InsertVex(G, v_i), InsertVex(G, v_s), InsertVex(G, v_d) ∈ V
- building dynamic 3D network
- (v_i: incident point, v_s: start point, v_d: destination point)
- DeleteVex(G, v(i)) and DeleteArc (G, v(i), v(i))
- eliminate hanging points → optimization
- Node labeling and Dijkstra algorithm → find the shortest path

4. EMERGENCY ROUTING ALOGRITHM

For well-connected network, Dijkstra's algorithm implementation have a lower computational complex (Liu et al., 1994; Pollitt, 1995; Eklund et al., 1996; Zhan and Noon, 1998), and therefore commonly used in many dynamic and stochastic vehicle routing cases. In 3D network, an important characteristics of the implementation of Dijkstra algorithm lies in the determination of “weights” for each arc. Sophisticated routing algorithms can base route selection on multiple metrics, combining them in a single (hybrid) metric. In 3D-GIS, the following metrics are to be considered to suit emergency cases well: segment length (the distance between the points in 3D), gradient impedance, travel speed, volume (vehicles per minute, vehicles per hour), and vehicle type, level of service (LOS), etc. For quick emergency response and management, “time” as unique metrics has been commonly used in many routing cases. Basically, traveling time is determined by travel distance and travel speed. In real 3D environment, travel distance is usually unchanged and shaped by urban landscape; however, travel speed is not constant and difficult to be denoted in a single value due to complex transportation phenomenon and traffic rule. Usually, vehicle will travel slower on steeper slope, lesser lanes, and larger number of traffic light controls, etc. As a result, it specially requests a measure to combine those multiple criteria into one “weight” to determine vehicle speed.

$$\text{Distance} = \sqrt{\Delta x^2 + \Delta y^2 + \Delta z^2} \tag{1}$$

$$\text{Speed} = \text{Standard speed} * \text{Weights} \tag{2}$$

$$\text{Time} = \frac{\text{Distance}}{\text{Speed}} \tag{3}$$

$$\text{Gradient} = 100 * \frac{\Delta z}{\sqrt{\Delta x^2 + \Delta y^2}} \tag{4}$$

$$\text{Weights} = \sum_{i=1}^n \text{score}_i * \text{weight}_i \tag{5}$$

Distance: the 3D distance of two nodes in real world

Speed: the vehicle speed in different transportation condition

Time: the time taken to travel between two nodes

Gradient: slope between two nodes

Weights: the summation of the product of score and weight of the contributing criteria or factors

The methodology which seemed to be well suited to support the decision making process in selecting the “best” alternative from a number of feasible alternatives under the presence of multiple choice criteria and diverse criterion priorities was MCE (Pettit and Pullar, 1999). For each arc, the MCE matrix is used to determine its weights for vehicle travel speed in real emergency situation. In this paper, we just give an example of using MCE matrix to score and weight for the three major factors (Table 1). For different cases, the choice of factors, score, and weight can be different.

Table 1: Example MCE matrix to determine speed weights

Factors	Weights		
	Grade	Score _i	Weight _i
Gradient	-5% ~ 5%	1	0.2
	>5% or <-5%	0.6	
Lane number	1 ~ 2	1	0.3
	>2	1.5	
Light control number	1	1	0.5
	>1	0.5	

In Short, an important issue of using Dijkstra algorithm in 3D emergency environment is to determine the “connectivity” or “weight” of each road segment in a multi-dimensional environment. MCE method provides a framework to decide the speed weights through synthesizing potential factors in road network system. Corresponding to the above MCE matrix, the process of “weights” determination for each arc is illustrated as follows:

Optimize 3D dynamic network

Initial Standard Speed

Calculate 3D distance of each road segment: 3D_Distance(V,W)

Calculate 3D_Gradient(v,w), Num_Lane(v,w), Num_Control(v,w)

Score 3D_Gradient(v,w), Num_Lane(v,w), Num_Control(v,w)

Calculate speed weights
 Calculate Arc_Length(v,w)

Next, we use a case study done in Wuhan, China, to show the results of emergency routing algorithm in 3D-GIS. The software adopted is 3DGISTM; the system provides two kinds of view: global view and navigation view (Figure 4). The incidents points (from Incident 1 to Incident 4) are inputted on-screen using cursor and 3D dynamic network optimization process will be followed. Different from traditional routing algorithm, the proposed emergency routing algorithm will be able to avoid unnecessary road segment as well as consider multi-dimensional information, such as slope, traffic control and lane numbers. In 3D-GIS environment, building with texture, landscape, traffic signal, etc., can be added into routing system to improve the quality of routing visualization.

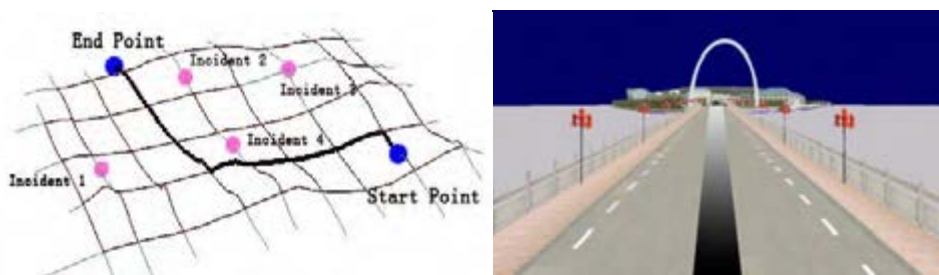


Figure 4: Results of emergency routing in 3D-GIS

5. CONCLUSION

Disasters in urban region often present multi-dimensional and dynamic characteristics. Though many researchers have developed all kinds of techniques to visualize 3D landscape, to locate incident with the use of GPS or mobile GIS and to simulate disaster phenomena with the support of dynamic model in 3D-GIS environment, most of shortest path algorithms are still conducted with a 2D GIS with the adoption of 2D road network and without consideration of multi-dimensional and dynamic emergency “clues” and knowledge. In this paper, we propose an emergency routing algorithm based on the 3D-GIS, and emphasize on the construction and optimization of 3D dynamic network, and the way to determine multi-dimensional weights for road segment. It has been found that 3D dynamic network has the potential to depict real traffic system (over/underpass) and its dynamic relationship with emergency “clues”. The number of nodes and arcs in a 3D dynamic network can be greatly reduced, thus improves the efficiency and effectiveness for emergency routing. MCE method is used to evaluate the overall weights for travel speed in each road segment. It considers multi-dimensional and dynamic factors in real vehicle routing process. In 3DGISTM, through inputting of 3D dynamic incident and considering of multi-dimensional road “connectivity”, Dijkstra algorithm can be improved to implement in our 3D emergency routing practice. 3D visualization of the emergency routing results (Global and Navigation Model), improves the

understanding for emergency situation and efficiency of disaster management.

The performance of emergency routing largely depends on how well emergency-related characteristics are arranged into algorithm. The work in this paper only gives a general description on the development of emergency routing algorithm based on the 3D-GIS. In the next stage, the proposed emergency routing algorithm is to improve the scalability of 3D dynamic network, to include a number of other emergency “clues” (such as traffic congestion, flood, etc.), to measure the true distance and the impedance over 3D curved surface for travel, to automatically extract incident point on 3D dynamic network. More heuristic strategies are also to be explored to improve the computation speed of Dijkstra algorithm in 3D environment.

REFERENCES

- Bent, R. W. and Hentenryck, P. V., 2004. Scenario-based planning for partially dynamic vehicle routing with stochastic customers. *Operations Research*, Volume 52 (6), 977-987.
- Cova, T. J. and Johnson, J. P., 2003. A network flow model for lane-based evacuation routing. *Transportation Research* 37: 579-604.
- Eklund, P. W., Kirkby, S., and Pollitt, S., 1996. A dynamic multi-source Dijkstra's Algorithms for vehicle routing. *Australian and New Zealand Conference on Intelligent Information Systems*: IEEE Press, 329-333.
- Fohl, P., Curtin, K. M., Goodchild, M. F., and Church, R. L., 1996. A Non-Planar, Lane-Based Navigable Data Model for ITS. In: *Proceedings, Seventh International Symposium on Spatial Data Handling*, Delft, August 12-16 (M. J. Kraak and M. Molenaar, eds.).
- Gendreau, M., Laporte, G., and Seguin, R., 1996. Stochastic Vehicle Routing. *European Journal of Operational Research* 88(3-12).
- Ginty, L. M. and Smyth, B., 2001. Collaborative Case-based Reasoning application in personalised route planning. *the Fourth International Conference on Case-Based Reasoning (ICCBR)*. 362-376.
- Guo, Y., Xie, B., and Guo, Q., 2002. Overview of Stochastic Vehicle Routing Problem. *Journal of Southwest Jiaotong University* 10(2).
- Held, G., Abdul-Rahman, A., and Zlatanova, S., 2004. Web 3D GIS for Urban Environments. *Proceedings of the International Symposium and Exhibition on Geoinformation 2004 (ISG2004)*, 21-23 September, Kuala Lumpur, Malaysia, CDROM, 12 p.
- Hock, Q. K. and Srikanthan, T., 2000. A hierarchical representation of roadway networks. *7th World Congress on Intelligent Transportation Systems*.
- Kwan, M.-P. and Lee, J., 2005. Emergency response after 9/11: the potential of real-time 3D GIS for quick emergency response in micro-spatial environments. *Computers, Environment and Urban Systems* 29: 93-113.
- Laakso, K., 2002. Evaluating the use of navigable three-dimensional maps

- in mobile devices. Master's thesis, Helsinki University of Technology, Helsinki, November 2002.
- Liu, B., Choo, S.-H., Long, S.-M., Lee, S.-C., Poon, F.-P., and Tan, H.-H., 1994. Integrating Case-Based Reasoning, Knowledge-Based Approach and Dijkstra Algorithm for Route Finding. *Proceedings of the Conference on Artificial Intelligence Applications*, pp.149-155.
- Lu, X., 2001. Dynamic and stochastic routing optimization: algorithm development and analysis. Ph.D., Civil Engineering, 2001. 139 pp. Adviser: Amelia C. Regan.
- Miller, H. J. and Shaw, S.-L., 2001. GIS-T Data Models. *Geographic Information Systems for Transportation: Principles and Applications*, Oxford University Press: 480PP.
- Nanda, S. and Gray, R. S., 2004. Spatial multipath location aided ad hoc routing. *Proceedings.13th International Conference on Computer Communications and Networks (IEEE Cat.no.04EX969)* 2004, pg.544-544.
- Pettit, C. and Pullar, D., 1999. An integrated planning tool based upon multiple criteria evaluation of spatial information. *Computers. Environment and Urban Systems* 23: 339-357.
- Pollitt, S., 1995. A 3-D spatial information system for emergency routing in Okayama city. Honours Thesis, 1995 Department of Computer Science, University of Adelaide, November 1995.
- Slavick, D., Christopher, Moore, 2005. 3D Visualization Bolsters Homeland Security.<http://www.geointelmag.com/geointelligence/article/articleDetail.jsp?id=162588>.
- Zhan, F. B. and Noon, C. E., 1998. Shortest Path Algorithms: An Evaluation using Real Road Networks. *Transportation Science* 32(1): 65-73.
- Zlatanova, S., 1999. An alternative for a 3D GIS. *Proceedings of the International symposium and exhibition on Modern information and GPS technology-aspects and implications of their application*, 11-12 November, Sofia, Bulgaria, pp.221-231.

APPLICATION OF A COUPLED SIMULATION METHOD FOR PREDICTING FIRE SPREAD IN A MODELED URBAN AREA

TAIFENG JIANG

Graduate School, the University of Tokyo, Japan

HONG HUANG, RYOZO OOKA

Institute of Industrial Science, the University of Tokyo, Japan

tfjiang@iis.u-tokyo.ac.jp

ABSTRACT

Research into fire spread dynamics in built-up districts under certain meteorological conditions is of critical importance to fire safety issues. The objective of this paper is to apply an approached coupled simulation method for the prediction of urban fire growth and spread by combining a one-dimensional wood pyrolysis model, gaseous combustion model, with computational fluid dynamics (CFD) method. In this research, the application of the coupled method is conducted on basis of a CFD code and divided into four sequential steps, which is also elaborated in this paper. As well, the calculation over a modeled urban area under certain assumed meteorological condition has been carried out to analyze the feasibility of the method. The simulation results illustrate detailed temperature and concentration distribution as well as the heat transfer characteristics on the wall surface via both convection and radiation. The phenomena of fire spread within the objective domain are also reproduced.

1. INTRODUCTION

Fire is arguably one of the most complex phenomena, embracing as it does in many cases subsonic chemical reaction flows, fluid dynamics, combustion, kinetics, radiation, and multi-phase flow (Novozhilov, 2001). Companying with the revolutionary progress in CFD modeling and radical improvements in computation capacity over the last several decades, simulations of the fire dynamic have advanced significantly in terms of the algorithms for combustion physics and mathematical modeling across almost all respects related to fire phenomena. In order to minimize the life and property loss caused by fire accidents, especially large scale fires occur in urban districts with dense populations and building, the simulation of fire behavior is of great interest and critical importance to fire safety issues. As early as the 1950s, researches into fire had been already developed as a science. However, because of its complexity, fire simulations were still a long way off and required great effort. Di Blasi (1993) developed a

theoretical model to study the effect of gas flow on the spreading flames, while Quintiere (1981) proposed a semi-empirical method. In terms of the essential importance of burning wood and other cellulosic materials, Kung (1972) has made significant contribution in developing a wood pyrolysis model. Recently, the CFD method was also undertaken for a temporal study of flame propagation and fire growth in indoor fires in order to closer approximate reality. Yan (1996) has analyzed flame propagation over surface lining material in an indoor corner fire by means of CFD. Three-dimensional transient turbulent gas flow, combustion, heat transfer, and pyrolysis of a charring material were all taken into consideration. However, that study is still in its preliminary stage, and restricted to compartmental fires.

This paper aims to extend the simulation of fire growth and spread from indoor scale to urban districts, which are apparently larger in scale and complexity of geometrical configuration. In this research, a one-dimensional wood pyrolysis model is proposed to be utilized and coupled with a CFD code. The method is introduced and as well a trial case in a modeled urban area is carried out.

2. URBAN FIRE SPREAD MECHANISM

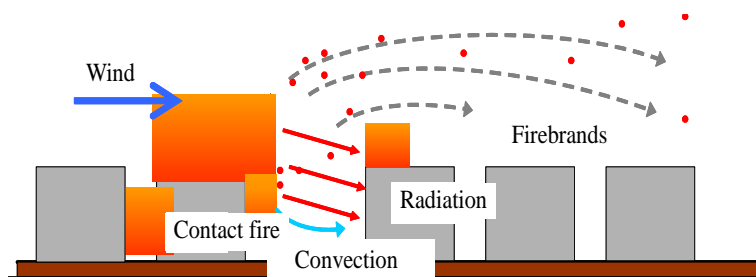


Figure 1: Illustration of urban fire spread

The mechanism for urban fire spread phenomena can be roughly divided into four sequential stages as follows (Novozhilov, 2001):

1). Heating up: The building blocks' surface temperature increases as it receives the incident net radiative heat flux and convective, conductive heat flux transferred by fluid flow from an upwind high temperature region.

2). Ignition: As it continues to be heated, once the surface temperature exceeds the material's critical temperature for pyrolysis, ignition occurs. In this stage, the surface material is converted to gaseous volatiles and residual char.

3). Fire growth and spread: After ignition, the combustion of material and gaseous volatiles produces a thermal plume and exports thermal energy feedback to the surfaces of contiguous and nearby blocks. Moreover, the firebrands bringing high energy will potentially contribute to great increase of surface temperature at their landing areas. If the surface temperature reaches up to the critical temperature of pyrolysis, combustion begins. Therefore, the fire zone expands. The schematic is shown in figure 1 (Otake, 2004).

4). Decay: At this stage, since all volatile fuel is consumed, the fire gradually goes extinct.

3. DESCRIPTION OF THE MATHEMATICAL MODEL

3.1 CFD model

Both the density and temperature in the fire flame experience extreme fluctuations. Therefore, the assumption of the incompressible fluid (Boussinesq approximation) doesn't stand up, thus the plume must be considered as the compressible fluid. For this solution, the Favre-averaged (Favre, 1969) process is introduced for the mass, momentum, enthalpy, and gas species transport. Moreover, a modified k-ε model, proposed by El Tahry (1983) for compressible reciprocating engine flows, is employed.

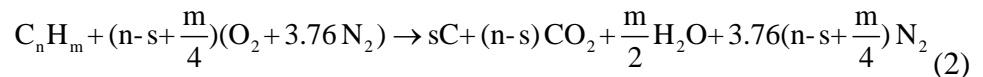
3.2 Gaseous combustion model

Burning reaction in the gaseous phase is modeled by employing the eddy break-up model (Magunussen, 1976) here, which has already been in widespread used in fire modeling. The reaction rate is determined by the slower of the turbulence dissipation rates for either the fuel or oxygen:

$$\bar{w}_f = -\bar{\tau}(e/k) \min(A\tilde{Y}_f, A\tilde{Y}_{O_2}/i) \quad (1)$$

Where, A – constant, 4.0; i – stoichiometric ratio of O₂ to fuel; Y – mass fraction.

In this paper, propane is chosen as the representative gaseous volatile as generally treated in the other researches. The following chemical reaction is assumed (Novozhilov, 1996):



S is a parameter to define the amount of soot produced. A non-zero value results in some of the carbon remaining as soot, with a consequent reaction to CO₂. The value of s can be determined from the soot conversion factor which is chosen from experimental data; for example, 2% for propane (Yan, 1996). The soot concentration is determined from the species equation and treated as a gas-phase species.

Radiation is solved in parallel with the governing equations. The absorption and emission of gas and soot are considered. Scattering is omitted due to the small diameter of the soot. The effect on radiation intensity is represented by the following radiation transport equation:

$$\frac{dI}{ds} = -(k_g + k_s)I + \frac{\sigma}{\pi}(k_g + k_s)T^4 \quad (3)$$

where I – radiation intensity in the direction of the solid angle Ω, W/sr; s – transfer distance of the radiation flux, m; k_g, k_s – absorption coefficients for gas and soot.

The calculations for k_g and k_s are based on equation (4), which is proposed by Novozhilov (2001):

$$k_g = 0.28 \exp\left(-\frac{T}{1135}\right) \quad k_s = 1264 f_v T \quad (4)$$

3.3 Wood pyrolysis modeling

In this research, the walls of building blocks are assumed to be wooden slabs with a constant depth of 0.20m. It is because wooden apartment still remain in widespread use by residents in modern-day Japan.

Wood pyrolysis contains varieties of phenomena related to transient conduction, incident radiation, variable properties, Arrhenius decomposition, and heat of reaction. A pyrolysis model by Kung (1972), based on partial differential equation, is employed as a simplified description of these phenomena. As described above, heat received on surfaces penetrates into the interior virgin wood along a direction normal to the surface. When the temperature in any element reaches pyrolysis temperature, ignition occurs. The decomposition rate is controlled by the Arrhenius reaction (7).

$$\frac{\partial(\rho h)}{\partial t} = \frac{\partial}{\partial x} \left(\lambda \frac{\partial T}{\partial x} \right) + \dot{q}_{0x} \quad (5) \quad \dot{q}_{0x} = -\frac{\partial \rho}{\partial t} Q_{pyro} + S_x \quad (6)$$

$$\frac{\partial \rho}{\partial t} = -\rho_w a A_0 \exp\left(-\frac{E}{RT}\right) \quad (7) \quad a = (\rho - \rho_c) / (\rho_w - \rho_c) \quad (8)$$

$$\lambda = a \lambda_w + (1 - a) \lambda_c \quad (9) \quad C_p = a C_{pw} + (1 - a) C_{pc} \quad (10)$$

Here, Q_{pyro} – heat of pyrolysis, J/kg; S – hear source in local element except pyrolysis heat release, W/m³; subscripts w and c denote virgin wood and char respectively. Detail properties can be referred to table 1 (Kudou, 1999).

In this modeling, three assumptions are adopted additionally:

- 1) Ignition temperature in considered as constant value.
- 2) All volatiles escape to the surface as propane and soon after are consumed in pyrolysis.
- 3) Pyrolysis converts the material from virgin wood to char, while residual char will not pyrolyze further.

Table 1: Material properties used.

Parameter	Unit	Value
Wood Density: ρ_w	[kg/m ³]	525.0
Wood Heat Conductivity: λ_w	[W/m/k]	0.11
Specific Heat of Wood : C_{pw}	[J/kg/k]	1300.0
Wall Thickness : σ_w	m	0.15
Char Density: ρ_c	[kg/m ³]	191.0
Char Heat conductivity : λ_c	[W/m/k]	0.07

Specific Heat of Char : C_{pc}	[J/kg/k]	1000.0
Pyrolysis Temperature : T_{pyro}	K	623.0
Reaction heat of Pyrolysis : Q_{pyro}	[J/kg]	1.8×10^6
Activation Energy : E	[J/mol]	1.04×10^5
Pre-exponential factor A_0	1/s	4.33×10^6

4. DESCRIPTION OF COUPLED SIMULATION METHOD

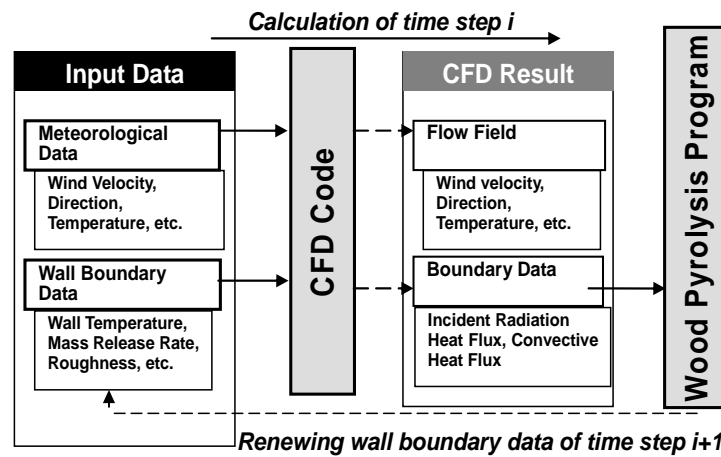


Figure 2: Algorithm of the proposed coupled simulation method

In this research, an alternative calculation is utilized for the coupled simulation. The approach is so called semi-unsteady method since CFD simulation is carried out in steady status, while wood pyrolysis in unsteady.

The calculation for each time step consists of four distinct processes.

1). First, meteorological conditions, wall temperatures, mass flux at wall et al, are read into the CFD code as initial data.

2). Steady CFD simulation is employed via a CFD code to obtain flow specifications including gas velocity, temperature, species concentration, radiant and convective heat flux to building surfaces, and surface temperatures.

3). Radiant and convective heat flux data at building surfaces are read from the CFD results and then input into the wood pyrolysis program. Calculation covers all meshes on the building surfaces as well as the interior elements arranged along the normal line according to each surface mesh. Updated surface temperatures, heat flux, propane release rates for the next time step are prepared.

4). CFD simulation for the next time step is carried out by using the boundary conditions updated by the newest data obtained from the pyrolysis routine.

In terms of such proposed semi-unsteady prediction, the time stream is divided into time steps with constant interval. Here, for example, if the time interval is set in 10 seconds, time step $i+1$ means 10 seconds later from time step i .

5. OUTLINE OF COMPUTATION

To specify the validation of the coupled simulation method, prediction of the fire spread with a modeled urban area was carried out. The details of the calculation are described as follows.

5.1 Calculation domain configuration

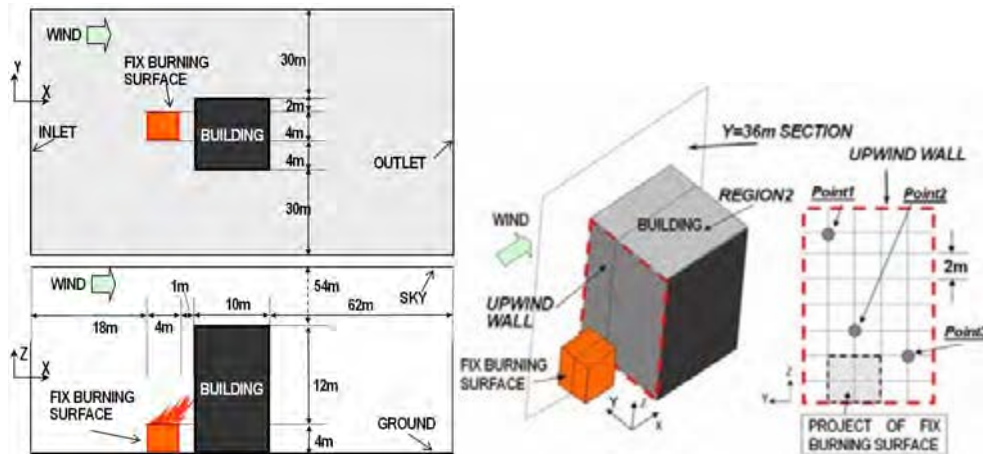


Figure3: Geometrical configuration of the modeled urban area

The whole calculation domain covers a dimension of 95m(X) × 70m(Y) × 70m(Z), in which one block in upwind location with a scale of 4m(X) × 4m(Y) × 4m(Z) is defined as fix burning surface (fire source), exhibiting a constant heat release. The block in bigger size (10m(X) × 10m(Y) × 16m(Z)) is positioned 1.0 m downstream from fire source and is treated as the prediction objective. The mesh system is in unstructured form, with a total number of 140,669. For better prediction accuracy, extruded mesh is created with a size of about 0.2m adjacent to block's surface.

For convenience of the following examination to simulation results, one Y=36m section in X-Z plane and three check points on the upwind wall of building block are defined, which can be referred to figure 3.

From previous investigations, in the case of wooden apartment fires, the average surface heat release rate is generally 1.5MW/m². From equation (23)(Hayashi, 2002), the surface heat release rate can be converted into the mass release rate of propane.

$$V=AQ/(\rho_{C3H8} \times Q_{C3H8}) \quad (23)$$

Where, A – area, m²; Q – average surface heat release rate, 1.5 MW/m²; ρ_{C3H8} – density of propane, 1.9kg/m³; Q_{C3H8} – heat of combustion of propane, 4.646×10⁷J/kg; V– presumed propane mass release rate, m³/s.

Hereby, the boundary condition of the fix burning surface is defined as inlet, with a constant concentration 1.0 of propane, and fix velocity along normal direction $U_{normal}=0.017$ m/s.

5.2 Boundary settings

Table 2: Boundary conditions.

Inlet	$U=2.0\text{m/s}$, $V=W=0.0$, $T=293.0\text{K}$ $k=1.5 \times (I \times U)^{2.0}$, $I=0.1$ $\epsilon=C_{\mu}k^{3/2}/L$, $L=1.0\text{m}$, $C_{\mu}=0.09$
Sky, Side-boundary	Free slip wall
Wall	Generalized log law
Burning surface	$U_{\text{normal}}=0.017\text{m/s}$, $T=623.0\text{K}$

The settings for each boundary are referred to table 2.

The principle of discretization is obtained by utilizing first-order upwind scheme for convection term, while second-order central scheme for rest terms. The pressure and velocity coupling in CFD prediction is achieved by utilizing the SIMPLE algorithm. The program of wood pyrolysis is solved in full implicit method

CFD simulation is performed on the commercial code STAR-CD (Version 3.24). For the coupled method solution, the time interval between each time step is fixed at 10 seconds and totally 110 time steps calculation has been carried out. The time intervals set for implicit solution of wood pyrolysis is 0.1s.

For reasonable solution accuracy, a strict convergence criterion for residual is specified as 10^{-4} .

6. RESULT DISCUSSION

Simulation results created by supposed couple method are discussed in this part. From the investigation, feasibility of the approach to fire spread simulation for a modeled urban area is examined.

6.1 Temperature distribution

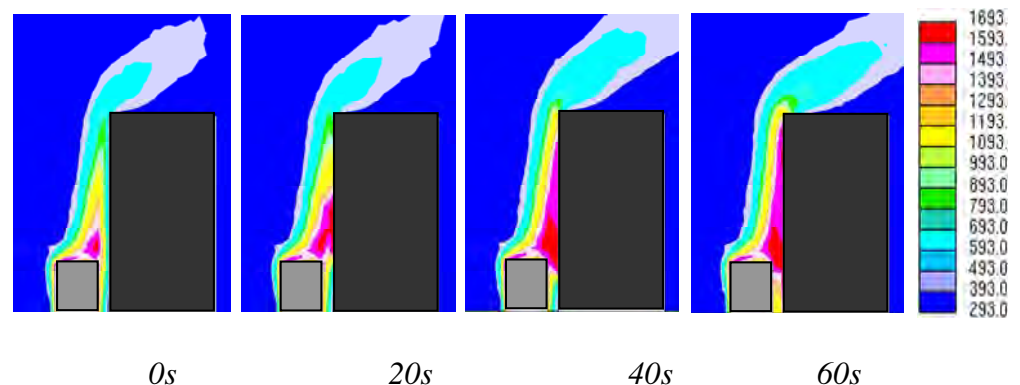


Figure4: Temperature distribution at each time step in the Y=36m section (K)

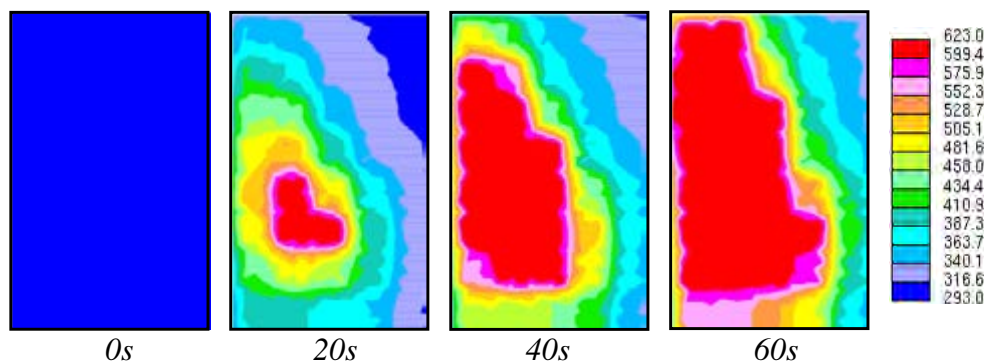


Figure 5: Temperature distribution in the upwind wall (K)

The $Y=36\text{m}$ vertical section locates in the $X\text{-}Z$ plane along the center-line of the fire source. The temperature distributions of this section at specified time step are demonstrated in figure 4. While figure 5 shows the temperature change of the upwind wall of the building block at the same time step.

At initial stage (time = 0s), gaseous propane runs out from the fire source (fix burning source) and starts to combust immediately, thus to heat up the local air where reaction occurs. The air with extremely high temperature, appearing as fire flame, climbs up by buoyancy driven force and is suppressed and inclines to leeward region from effect of urban wind and hence embraces the upwind wall of the building block locating at the downstream area. Observing the contour figure, the temperature of the core part of flame is as high as over 1693K. Moreover, large part of the windward side and rooftop of the building are found to be covered with hot air with the temperature of over 800K. Hence, significant heat flux given from fire flame to this region can be estimated.

Examining the surface temperature change from figure 5, the fire growth in the upwind wall of the building block can be observed apparently. From 20s, the area adjacent to flame exhausted from fix burn surface has appeared began to be burning. Moreover, an expected expansion of the burning area has been reproduced from the result at 40s and 60s in Figure 5. At 40s, about 30% of the upwind wall reaches pyrolysis stage, while at 60s nearly half of the wall can be found burning.

Since material of the upwind wall began to pyrolyze and thus release propane, combustion reaction occurs at the region near to the wall. In figure 4, the temperature distribution from 20s changes as fire flame has been exhausted from the block surface in downstream area. The high temperature areas specified by red color increase gradually as time go on. At time step equals to 60s, in lower part of the gap between the two buildings, flame with high temperature air can be observed

From this discussion, the fire spread behaviors are considered to be reproduced.

6.2 Profiles at the check points

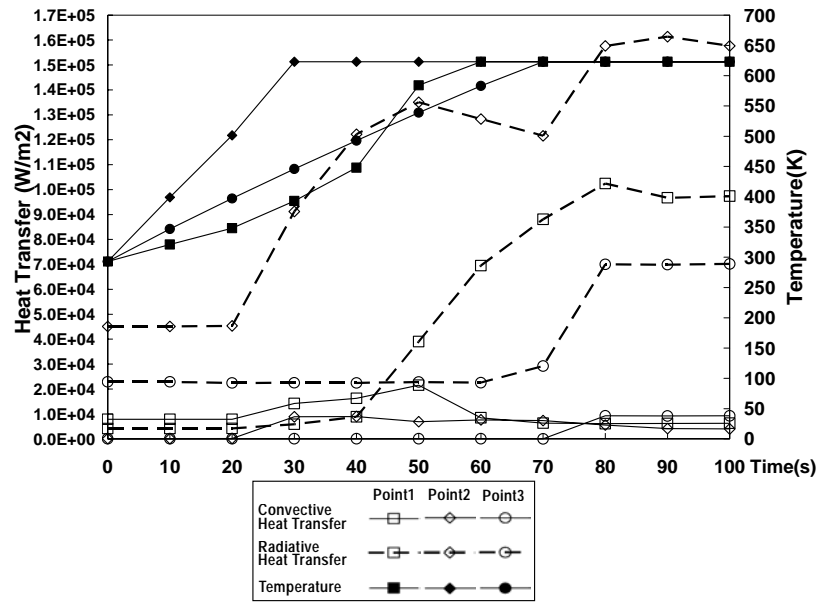


Figure 6: Heat flux and surface temperature profiles at each check point.

Figure 6 illustrates the comparison of incident radiation, convective heat flux obtained in the three check points at each time step, as well as the surface temperature profile. The definition of each check point can be referred to figure 3.

Point 2 is located straightly behind the exhausting flame from fix burning surface, which results into reasonable highest heat flux get among the three points. At 20s, the heat flux obtained at point 2 is shown an intensive increase; it is because the flame begins to be exhausted from its adjacent area at this time step. Therefore, the surface temperature of point 2 climbs up quickly and reaches the pyrolysis temperature, thus ignition occurs in local area at 30s. The location of point 1 and point 3 are not right into the area embraced by flame from the fire source, the temperature change much slower than point 1.

In addition, for each check point, the incident radiation flux can be found far greater than the convective heat transfer. In case of point 1, radiation flux get various in range of $4.5 \times 10^4 \sim 1.6 \times 10^5 \text{ W/m}^2$, while the convective heat flux is averagely one order smaller than it. Therefore, radiation flux given from fire source can be considered as the critical factor to cause fire spread between the buildings.

7. CONCLUSION

In this research, a coupled method is supposed for the fire spread simulation within urban district. In this approach, a combination of CFD model, combustion model, radiation model, and wood pyrolysis model, is considered. The feasibility of the method is examined by conducting validation simulation over a modeled urban area. From the prediction results, a detailed temperature distribution, either at the surface or in fluid flow, and

any other parameter data can be obtained, which proves urban fire and its spread behaviors to be reproduced.

To discuss the prediction accuracy of the coupled method in this urban fire spread simulation, a comparison between the simulation results and fire tunnel experimental data or other investigation result of the real accidents are taken into consideration in future research work.

REFERENCES

- B. F. Magunussen, 1976, On mathematical modeling of turbulent combustion with special emphasis on soot formation and combustion, *Proceedings 16th Symposium (International) on Combustion*, 719-729.
- Di Blasi, 1993, Modeling and simulation of combustion process of charring and non-charring solid fuels, *Prog. Energy Combust Sci*, 71-104.
- EI Tahry, 1983, k- ϵ Equation for Compressible Reciprocating Engine Flows, *AIAA, J. Energy*, 345-353.
- Favre, A., 1969, Problem of hydrodynamics and continuum mechanics, *Soc. Indust. Appl. Mech.*, 231-266.
- H. C. Kung, 1972, A Mathematical Model of Wood Pyrolysis, *Combust. Flame*, 185-195.
- H. Otake, 2004, Simulation of flames and thermal plume in urban fire under windy condition, *J. of Industrial Science Research, University of Tokyo*, 11-16.
- Quintiere, J. G., 1981, A simplified theory for generalizing results from a radiant panel rate of flame spread apparatus, *Fire Mater.*, 5.
- V. Novozhilov, B. Moghtaderi, D. F. Fletcher and J. H. Kent, 1996, Computational fluid dynamics modeling of wood combustion, *Fire Safety Journal*, 69-84.
- V. Novozhilov, 2001, Computational fluid dynamics modeling of compartment fires, *Prog. Energy Combust Sci*, 611-666.
- Y.Kudou, H.Hayasaka, 1999, Internal temperature distribution and combustion characteristics of wood, *The 36th national heat transfer symposium (in Japanese)*
- Y.Hayashi, Y. Ohmiya, 2002, Study on flames and thermal plumes induced by fires under windy condition. *The 17th national symposium on wind engineering (in Japanese)*, 173-184
- Yan, Z. H., 1996, CFD experimental studies of room fire growth on wall lining materials, *Fire safety journal*, 201-238.

PREDICTION OF URBAN HEAT ISLAND IN TOKYO METROPOLITAN AREA IN 2020

YOICHI KAWAMOTO¹ and RYOZO OOKA²

¹ Graduate School of Engineering, the University of Tokyo, Japan

² Institute of Industrial Science, the University of Tokyo, Japan
kwmt@iis.u-tokyo.ac.jp

ABSTRACT

In large cities in Japan, as exemplified by Tokyo, temperature increases in summer due to urbanization, i.e. the urban heat island effect, are becoming very serious. If no countermeasures are taken, it is likely that urban heat islands will become ever more serious and prediction of the effect of future urbanization on urban heat islands is necessary. On the other hand, three-dimensional meteorological meso-scale models are often used to determine the mechanisms of urban heat islands. However it is necessary to represent the properties of building canopies precisely in order to analyze the spatial and temporal distribution of temperature in urban environments. Therefore, in this paper, the urban thermal environment in the Tokyo metropolitan area is analyzed and predicted by means of a meteorological meso-scale model based on the Mellor-Yamada model level 2.5 with incorporation of an urban canopy model. In order to predict the state of the Tokyo metropolitan area in 2020, firstly the authors estimate the total floor space based on the projected population. For analysis with a meteorological meso-scale model incorporating an urban canopy model, details of the building conditions such as building density or building size will have to be estimated. In the analysis targeted on the present (in 1997) Tokyo metropolitan area, detailed data is provided with GIS (Geographic Information System) data prepared by the Tokyo Metropolitan Government. On the other hand, for the analyses targeted on the future (in 2020), there is no detailed data. Therefore, in this paper, five types of future urban compositions are assumed. These five cases targeted on the future and one targeted on the present are analyzed and evaluated. The case studies show that different building conditions, despite having the same total floor space, will affect the thermal environment differently.

1. INTRODUCTION

In large cities in Japan, as exemplified by Tokyo, urban heat islands have become very serious problems. If no countermeasures are taken, it is likely that urban heat islands will become ever more serious and prediction of the effect of future urbanization on urban heat islands is necessary. Therefore, in this paper, the urban thermal environment in the Tokyo metropolitan area is analyzed and predicted by means of a meteorological meso-scale model based on the Mellor-Yamada model level 2.5 (Mellor and

Yamada, 1982) with incorporation of an urban canopy model (Ooka, 2004). In order to predict the state of the Tokyo metropolitan area in 2020, firstly the authors estimate the total floor space based on the projected population. For analysis with a meteorological meso-scale model incorporating an urban canopy model, details of the building conditions such as building density or building size will have to be estimated. However, such future conditions are not very apparent. Thus, the authors estimate the building conditions in 2020 from the present building conditions and the prediction of the total floor space increase in 2020.

2. OUTLINE OF FUTURE PREDICTION

It is predicted that the population in Tokyo's 23 wards will increase until 2010 as a reflection of the population concentration in the center of the city in recent years, and gradually decrease afterwards (Figure 1, solid line). The total floor space in these 23 wards is predicted based on this population transition. Ikaga (2000) has predicted that the floor space per person will increase by 4 square meters for residential use and also by 4 square meters for non-residential use from 1997 to 2020 in Japan (Figure 2). The authors applied these prediction results to Tokyo's 23 wards (Figure 1, dotted line).

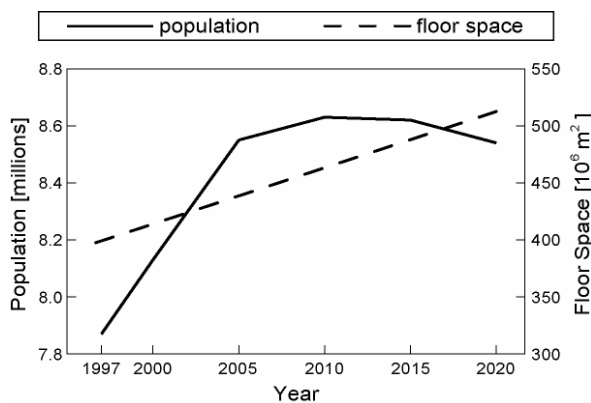


Figure 1: Projected population and floor space in Tokyo's 23 wards

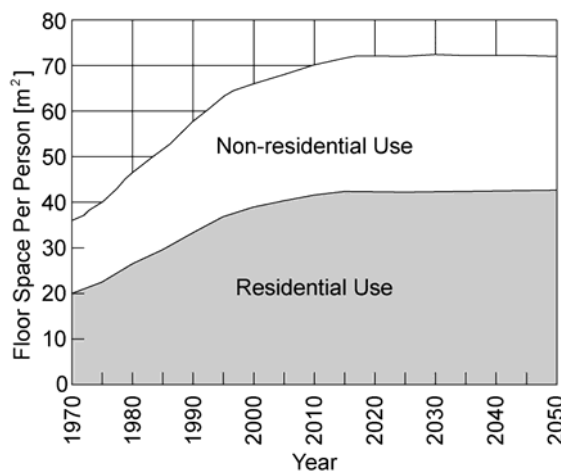


Figure 2: Prediction of floor space per person in Japan (Ikaga, 2000)

In this paper, the thermal environment in the Tokyo metropolitan area is analyzed with a meteorological meso-scale model incorporating an urban canopy model. Therefore, the buildings' compositions have to be estimated. In the analysis targeted on the present (in 1997) Tokyo metropolitan area, detailed data, e.g. building area, floor space, building height, building use and land use, is provided with GIS (Geographic Information System) data prepared by the Tokyo Metropolitan Government. On the other hand, for the analyses targeted on the future (in 2020), there is no detailed data. Therefore, the urban composition in the Tokyo metropolitan area in 2020 has to be supposed. In this paper, the following five types of future urban compositions are assumed. Figure 3 shows the concepts for each case.

Case 0: Present

The building compositions expressed using GIS data prepared in 1997.

Case 1: Becoming multistory

The height of all buildings in Tokyo's 23 wards increases according to the increase in the total floor space.

Case 2: Overcrowded

The building area of all buildings in Tokyo's 23 wards increases and other land use decreases according to the increase in the total floor space.

Case 3: Inner city concentration

Buildings in the center of Tokyo only become overcrowded, while buildings in other areas of Tokyo remain unchanged from present conditions.

Case 4: Towards uniformity

The size and density of buildings are assumed to be uniform throughout Tokyo's 23 wards.

Case 5: More high-rise and ground greening

The building area taken up by all buildings in Tokyo's 23 wards is halved and the height they become very high to reflect the increase in the total floor space. Released land is greened.

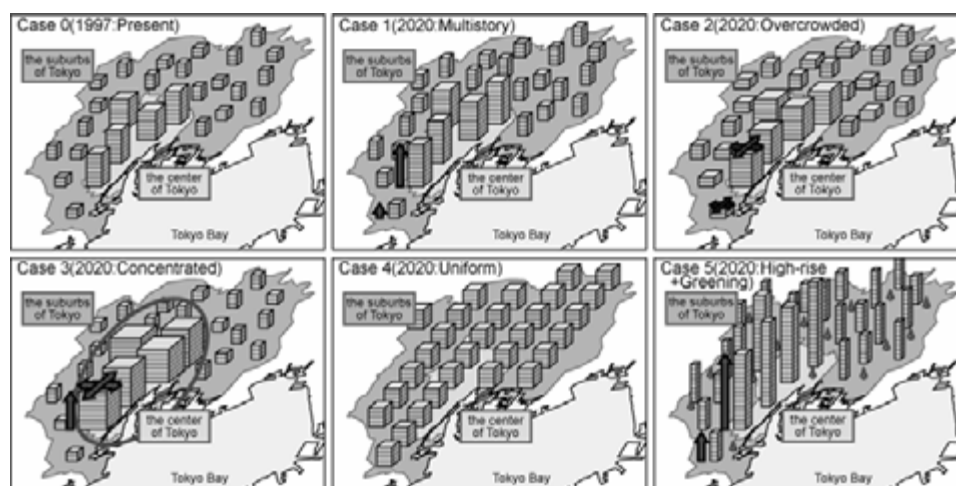


Figure 3: Concept of case study

3. SIMULATION MODEL

In the meso-scale analysis, which was originally developed to predict the climate above the surface boundary layer, a one-dimensional heat balance model is usually used for the ground boundary conditions. In this conventional model, a roughness parameter is employed in order to present the effect of the building complex. As the vertical grid size adjacent to the ground surface must be made several times larger than the roughness length in the conventional model, physical phenomena within the surface layer cannot be estimated. Furthermore, the definition of surface temperature is rather vague in the conventional model because its relationship with ground, roof and wall surface temperatures is unclear. Therefore, it is necessary to include the effect of the urban canopy precisely in order to analyze the thermal environment at pedestrian level in an urban area. On the other hand, the one-dimensional urban canopy model is also typically used to analyze urban thermal environments (Kondo, 1998) (Ashie, 1999). Although this model can easily predict the thermal environment at pedestrian level, it is not empowered to consider the effect of local climate due to the assumption of a horizontally homogeneous flow and temperature field. Thus, the authors have developed a new meteorological meso-scale model based on the Mellor-Yamada model level 2.5 incorporating an urban canopy model (Ooka, 2004).

The following five factors relating to the building complex are incorporated into the meteorological meso-scale model; (1) wind reduction by the building complex, (2) production of turbulence by the building complex, (3) solar radiation heat transfer inside and outside of the building complex, (4) long-wave radiation heat transfer inside and outside of the building complex, and (5) sensible and latent heat transfer from the building surface. Four factors related to the plant canopy are also incorporated into the meteorological meso-scale model; (1) wind reduction by the plant canopy, (2) production of turbulence by the plant canopy, (3) solar radiation absorption by the plant canopy, and (4) transpiration from the plant canopy. Figure 4 shows the concept figure of meteorological meso-scale model incorporating the urban canopy model.

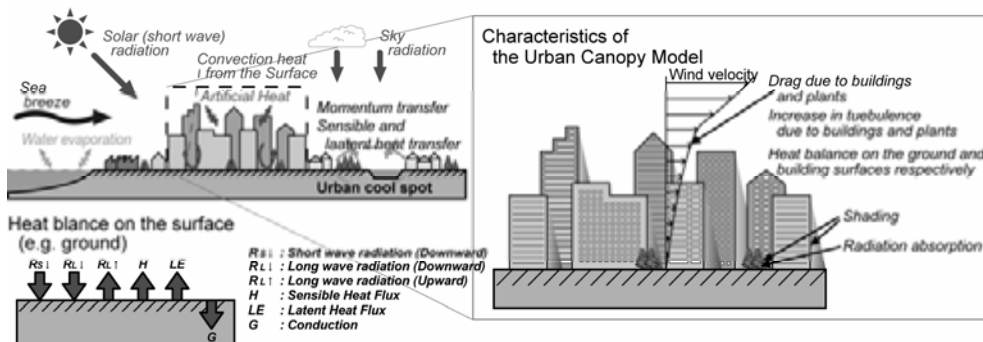


Figure 4: Concept figure of meteorological meso-scale model incorporating the urban canopy model

4. OUTLINE OF ANALYSIS

4.1. Analysis domain

Figure 5 illustrates the analysis domain, which covers 480 km (east-west) \times 400 km (south-north) \times 9.6 km (vertical direction). The whole analysis domain (Grid 1) is nested into three sub-domains; Grid 2, Grid 3 and Grid 4 as illustrated in Figure 5. Table 1 also summarizes the size and grid discrimination of each domain.

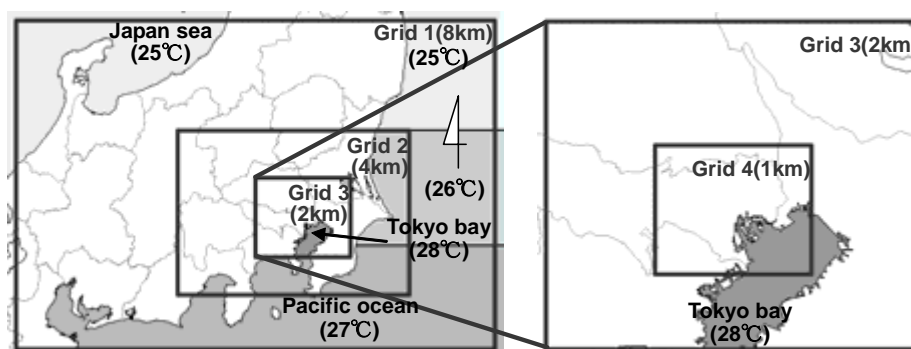


Figure 5: Analysis domain

Table 1: Analysis domains and grid arrangements

	Computational Domain [km] (x \times y \times z)	Grid Number	Horizontal Grid Size [km]
Grid 1	480 \times 400 \times 9.6	60 \times 50 \times 49	8
Grid 2	232 \times 200 \times 9.6	58 \times 50 \times 49	4
Grid 3	96 \times 96 \times 9.6	48 \times 48 \times 49	2
Grid 4	40 \times 40 \times 9.6	40 \times 40 \times 49	1

4.2. Meteorological Meso-scale Model

The Mellor-Yamada model level 2.5 is employed for meteorological meso-scale analysis in this paper. The urban canopy model described above is incorporated into this analysis.

4.3. Analysis Condition

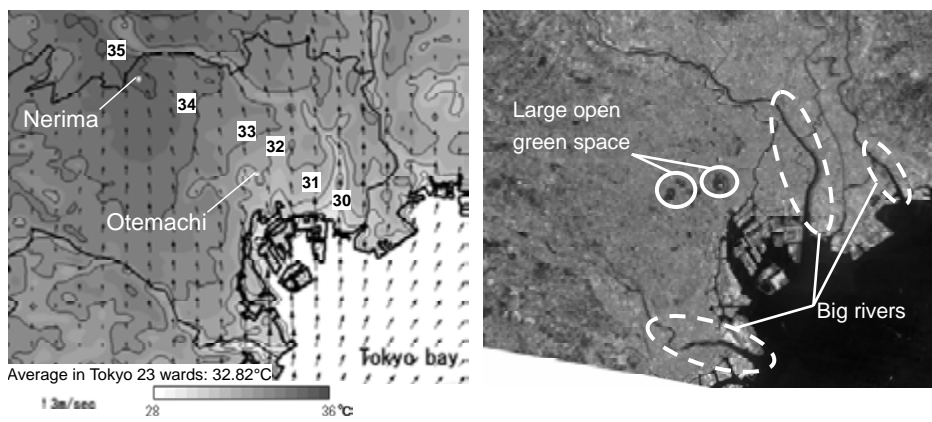
In this paper, analysis is conducted for the thermal environment on July 24th, which represents a typical summer meteorological situation. The simulations are started from 6:00 a.m. on July 23rd, and time integration is performed for 42 hours. The initial wind direction and velocity are set southerly 2.0 m/s at a height of 9.6 km from the ground surface in the whole computational domain. Here, the ground surface is classified into 10 types of land-use, and surface parameters, such as albedo, roughness length Z_0 , heat capacity, and moisture availability β are set individually following the land-use conditions.

Table 2: Surface parameter

Land Use	Moisture availability	Albedo	Roughness length [m]
Rice paddy	0.5	0.20	0.05
Farming	0.3	0.10	0.01
Orchard	0.3	0.20	0.05
Forest	0.3	0.15	0.05
Park	0.3	0.10	0.01
Vacant land	0.3	0.20	0.01
Buildings	0.0	0.10	0.05
Paved Road	0.0	0.10	0.01
Other land	0.0	0.10	0.01
Water site	1.0	0.03	0.001

5. RESULTS AND DISCUSSION

Figure 6 shows the horizontal distribution of air temperature and wind velocity of the analytical results of case 0 (present) at a height of 2 meters above the ground surface. The time is set as 13:00 hours. The domain for the evaluation is Grid 4; which has a horizontal mesh size of 1 km. In addition, an aerial photograph of the Tokyo metropolitan area, covering the same domain as the analytical domain Grid 4, is also shown. In the analytical results, the sea breeze blowing in from Tokyo bay can be represented. In terms of the air temperature distribution, the temperature rise in the northwest of Tokyo is represented, whereas conversely, the air temperature decrease near big rivers and large open green spaces is represented too. Such a tendency shows good agreement with observation data on a typical summer's day by AMeDAS (Automated Meteorological Data Acquisition System), as recorded by the Japan Meteorological Agency. Figure 7 shows a comparison of air temperature of analysis and observation.



a) Wind velocity and temperature
(July 24th 13:00, 2m height)

b) Aerial photograph

Figure 6: Analytical result and aerial photograph (Grid4)

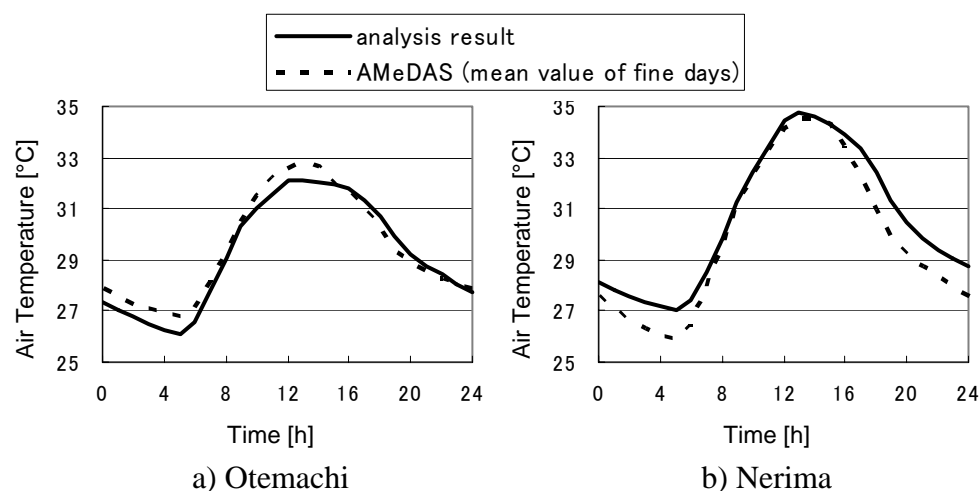


Figure 7: Comparison of air temperature of analysis result and AMeDAS observation data

Figure 8 shows the air temperature differences between the analytical results of Cases 1-5 in 2020 and Case 0, as the present situation. In Case 1, which assumes more multistory buildings, as the buildings are higher, the sky view factor from ground level is reduced and short- and long-wave radiation directed at the ground is further interrupted by the buildings. As a result, the air temperature in Case 1 decreases throughout the whole area compared with that in Case 0. In Case 2, the overcrowded scenario, the air temperature rises in the whole area due to decreased wind velocity near the ground surface because of the increase in resistance from buildings. In Case 3 where buildings are concentrated in the center, there are two large domains where the air temperature increases and decreases. In the center of Tokyo, the concentration area, the air temperature decreases by 2.5°C at most at 13:00 hours compared with the present situation. However, the temperature rises on the leeward side, and this high temperature range extends as far as Saitama Prefecture. In Case 4, with buildings arranged uniformly throughout Tokyo's 23 wards, the air temperature rises in the center of Tokyo, but on the other side, it decreases in other districts. As a result, the overall difference in temperature is small. In Case 5, which features a transition to high-rises and ground greening, the air temperature at ground level falls significantly because of the greater radiation interruption by the plant canopies.

6. CONCLUSIONS

- 1) The total floor space in Tokyo's 23 wards in 2020 has been predicted based on population projections.
- 2) Case studies into the progress of the heat island phenomenon in 2020 were conducted.
- 3) The case studies show that different building conditions, despite having the same total floor space, will affect the thermal environment differently.

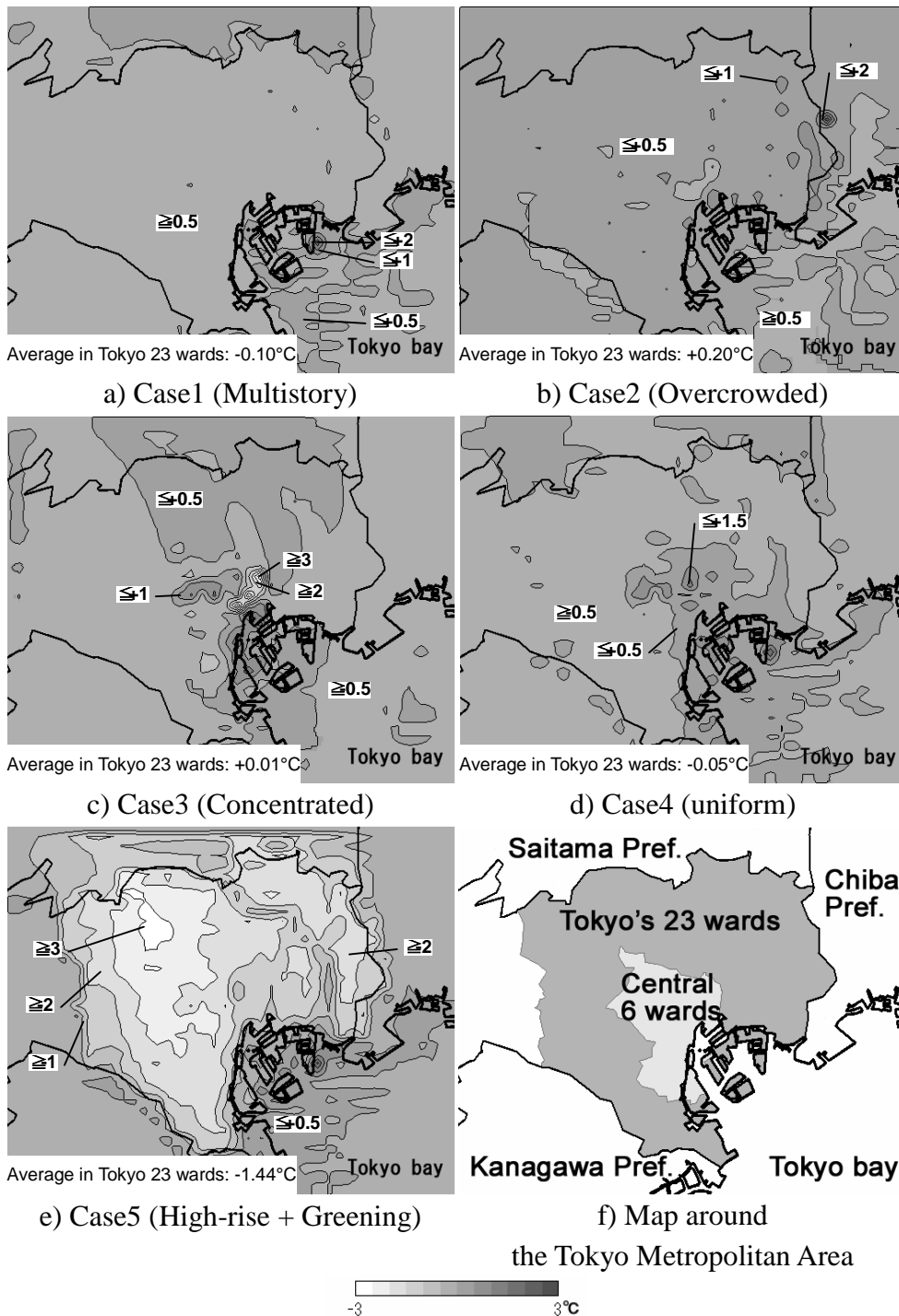


Figure 8: Distribution of temperature change (July 24th 13:00, 2m height)

REFERENCES

- Ashie, Y., V. T. Ca and T. Asaeda, 1999, Building canopy model for the analysis of urban climate, *Journal of Wind Engineering and Industrial Aerodynamics*, Vol. 81, 237-248
- George L. Mellor and Tetsuji Yamada, 1982, Development of a Turbulence Closure Model for Geophysical Fluid Problems, *Reviews of Geophysics and Space Physics*, Vol.20, No.4, 851-875

- Ikaga, T., Murakami, S., Kato, S. and Shiraishi, Y., 2000, Estimation of CO₂ emission associated with building construction and operation till 2050 in Japan, *Journal of Architecture, Planning and Environmental Engineering*, NO.535, 53-58
- Kondo, H. and F. Liu, 1998, A study on the urban thermal environment obtained through one-dimensional urban canopy model, *Journal of Japan Society of Atmospheric Environment*, 33 (3), 179-192
- Ooka, R., Harayama, K., Murakami, S. and Kondo, H., 2004, Study on Urban Heat Islands in Tokyo Metropolitan Area Using a Meteorological Mesoscale Model Incorporating an Urban Canopy Model, *The 5th Symposium on the Urban Environment*, 9.15

OPTIMAL DESIGN OF SMOKE CONTROL SYSTEM IN ROOM FIRE USING CFD AND GENETIC ALGORITHMS

HONG HUANG, RYOZO OOKA, SHINSUKE KATO, HONG CHEN
Institute of Industrial Science, The University of Tokyo, Japan
hhong@iis.u-tokyo.ac.jp

ABSTRACT

In fire-prevention designs for buildings, the major concerns are ensuring safe evacuation in the event of a fire and preventing the fire from spreading. On the other hand, improving the degree of design freedom and reducing costs are also expected. In recent years, research into the optimal design in the fields of building construction and building environments has apparently increased. It is thought that a similar optimization approach could also be applied to building designs for fire prevention. In this research, the vestibule pressurization smoke control system in an office room is optimized using a coupled approach of Computational Fluid Dynamics (CFD) and Genetic Algorithms (GA). The design parameters include the locations and sizes of the smoke extraction, and the air supply vents are selected using GA to maximize the airflow rate through the doorway of the vestibule, which would ensure that the smoke does not escape to the vestibule during evacuation. The fire-driven flow characteristics are simulated by the Fire Dynamics Simulator (FDS) (developed by the National Institute for Standards and Technology (NIST)) which is based on the fundamental conservation of heat, momentum and mass using a Large Eddy Simulation (LES) method.

1. INTRODUCTION

Preventing smoke from entering a stair shaft is very important in smoke control design. One approach is by pressurizing the stair shaft or the vestibule adjacent to the stair shaft with outdoor air. Thus, there are basically two types of pressurized smoke-control systems. One is a stair pressurization system, the other a vestibule pressurization system. While the stair pressurization system is common in the United States and Canada, the vestibule pressurization system is now popular in Japan. In this study, the vestibule pressurization system will be discussed. For the system, the air supply rate necessary to maintain a sufficient pressure differential is usually determined using a zone model (Matsushita et al., 1998) or some simplified calculation method (Kujime et al., 2000). However, it is difficult to specify a detailed design of the system, for example, the sizes and locations of the air supply vents, using these methods. Therefore, the possibility exists that smoke may flow into the vestibule or stairwell in local areas even if the necessary air supply rate is satisfied. With the rapid developments made in computational fluid dynamics (CFD), it is now possible to analyze the three-dimensional distribution of velocity, temperature, pressure and so on.

CFD affords us a fine tool to analyze the aforementioned problem. Meanwhile, there is no doubt that an optimized design for a smoke control system is expected.

In recent years, research into optimal designs in the fields of building construction and building environments has apparently increased. A coupled approach using Computational Fluid Dynamics (CFD) and Genetic Algorithms (GA) has been attempted in HVAC design (Kato et al., 2004) and outdoor thermal environment design (Chen et al., 2004). It is thought that a similar optimization approach could also be applied to building designs for fire prevention. In this research, the smoke control system for an office room is optimized with a coupled approach using Computational Fluid Dynamics (CFD) and Genetic Algorithms (GA).

2. OPTIMIZATION SYSTEM COUPLING GA AND CFD FOR SMOKE CONTROL SYSTEM DESIGN

2.1 Optimization system

The optimization system coupling GA and CFD for smoke control design, which is based on a feedback system (Kim et al., 2002, Chen et al., 2004), is shown in Fig. 1. This system is comprised of three parts: A. Setting optimal problem; B. CFD analysis of fire dynamics, C: Evaluation of smoke control system and optimal process control. In part A, the design objective and design parameters are determined. Meanwhile, the optimization method and the evaluation method for optimal design are determined. In part B, CFD analysis is conducted to provide spatial and temporary distribution of the variables of interest of fire evolution. In part C, if the optimum solution satisfies the design objective, the results are obtained. If it doesn't satisfy the design objective, the design parameters will be selected by GA and fed back to the CFD analysis for the next evaluation. The feedback loop will continue until the optimum solution satisfies the design objective.

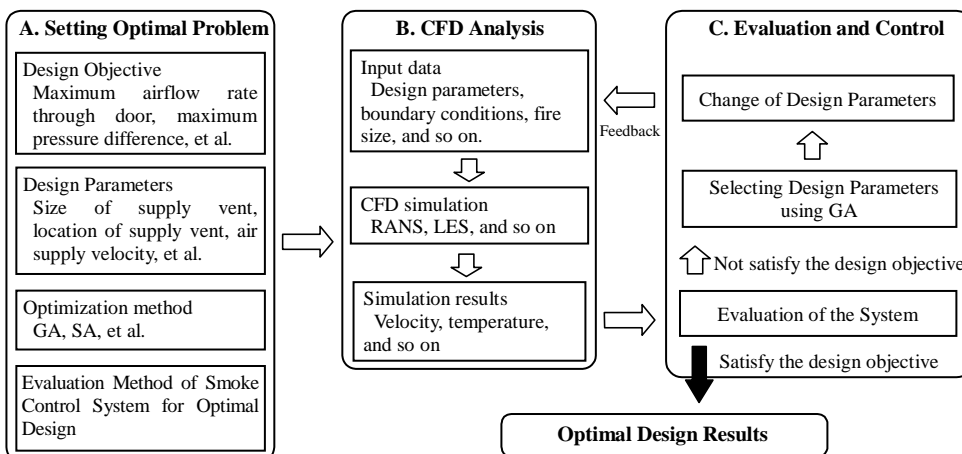


Figure 1. Optimal design system coupling GA and CFD for smoke control design

2.2 Two-step optimal design process

In generally, the feedback loop in Fig. 1 will be one thousand or more. If a detailed CFD analysis is conducted in every loop, it will impose a high computational load, as well as take much time. In this study, a two-step optimization process is used (Kim et al., 2002; Chen et al., 2004) to reduce the calculation load and time taken to find the optimal solution. Fig. 2 shows

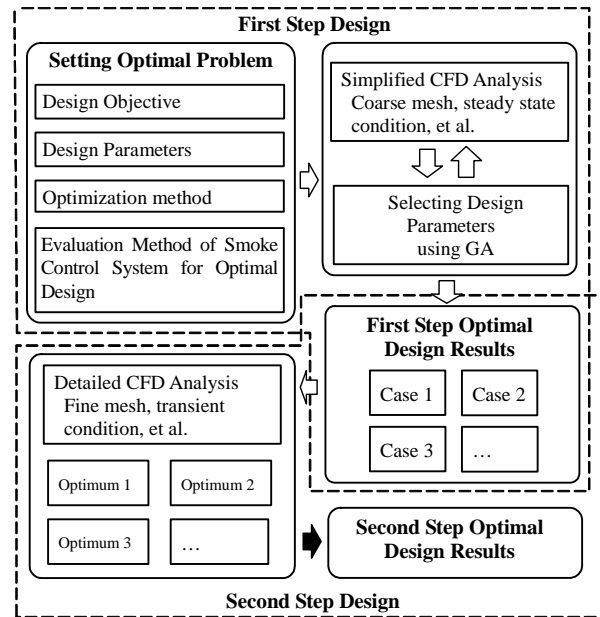


Figure 2. Two step optimal design method

the process. In the first-step design, a simplified CFD analysis using a coarse mesh is conducted out of consideration for the calculation load. The high ranking solutions from the first step optimal design results will be selected as candidates for the second step design. In the second step design, a detailed CFD analysis using a fine mesh is conducted only for the high rank solutions. Finally, the optimum solution is obtained.

2.3 CFD simulation

CFD modeling has been successfully applied to various fire safety problems, and its role in fire research is steadily increasing as the models progressively become more robust and sophisticated, and validation studies render them more reliable (Novozhilov, 2001). CFD models are naturally classified based on the methods by which they treat turbulence phenomena. The two major groups may be identified as Reynolds Averaged Navier-Stokes (RANS) models and Large Eddy Simulation (LES) models. In this study, the fire-driven flow characteristics are simulated by the Fire Dynamics Simulator (FDS) (developed by the National Institute for Standards and Technology (NIST)) which is based on the fundamental conservation of heat, momentum and mass using a LES method (McGrattan et al., 2004). FDS is now a well-used tool for solving practical fire problems in fire protection engineering and in the study of fundamental fire dynamics and combustion.

3. APPLICATION OF THE OPTIMAL DESIGN SYSTEM ON VESTIBULE PRESSURIZATION SYSTEM DESIGN

3.1 Design object

The design object is shown in Fig. 3. This is a simplified office building with 10 stories. The office is of length 10 m, width 10 m and height 2.5 m, and an adjacent corridor is of length 8.0 m, width 3.0 m and height

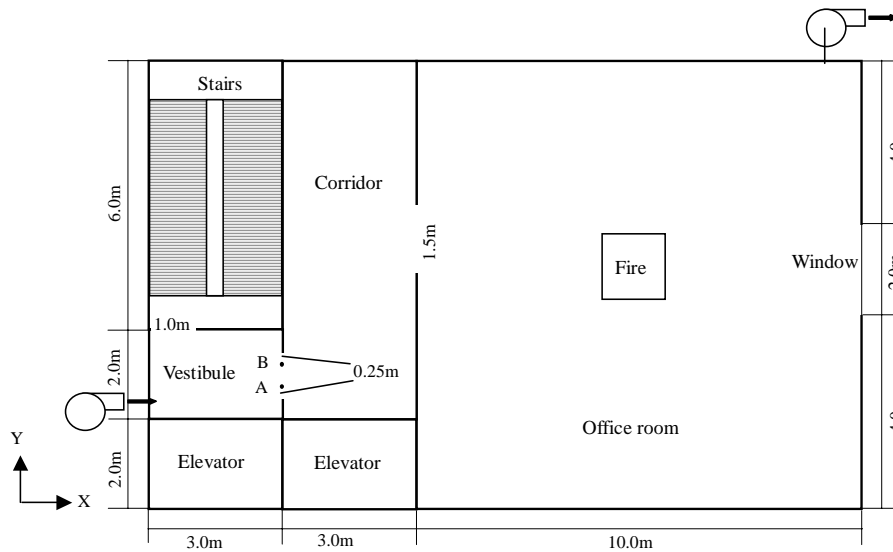


Figure 3. The design object

2.5 m. The office has a doorway of width 1.5 m and height 2.0 m opening into the corridor. A vestibule, which has two doorways opening to the corridor and the stairs, is provided. The heights of the doorways are 2.0 m. The smoke control system consists of smoke extraction from the office and a pressurization process through the vestibule. The vestibule is pressurized with outdoor air using a supply air fan to prevent smoke from entering the vestibule and the stairwell.

3.2 Design objective

As has already been mentioned, the air supply rate necessary to maintain a sufficient pressure differential is usually determined using the zone model (Matsushita et al., 1998) or some simplified calculation method (Kujime et al., 2000). However, it is difficult to specify a detailed design of the system, for example, the sizes and locations of the air supply vents, using these methods. Therefore, the possibility exists that the smoke may flow into the vestibule or stairwell in local areas even if the necessary air supply rate is satisfied. In this study, the average airflow rate through the doorway between the vestibule and the corridor during the evacuation time is selected as the design objective. The design parameters are selected using GA to maximize the airflow rate during evacuation, which would ensure that the smoke does not escape to the vestibule. That is, at the same time, no backward wind occurs through the doorway.

3.3 Design parameters

The air supply rate is set at a constant $4.17 \text{ m}^3/\text{s}$ based on the calculations of Kujime et al. (2000) and Matsushita et al. (1998). Usually, air is also supplied from the elevator shaft, but the airflow from the elevator is assumed to be zero for simplicity because such air is minimal compared to that from the vestibule. Patterns of smoke extraction vents and air supply vents are shown in Figs. 4-6. The locations and sizes are changed. In the

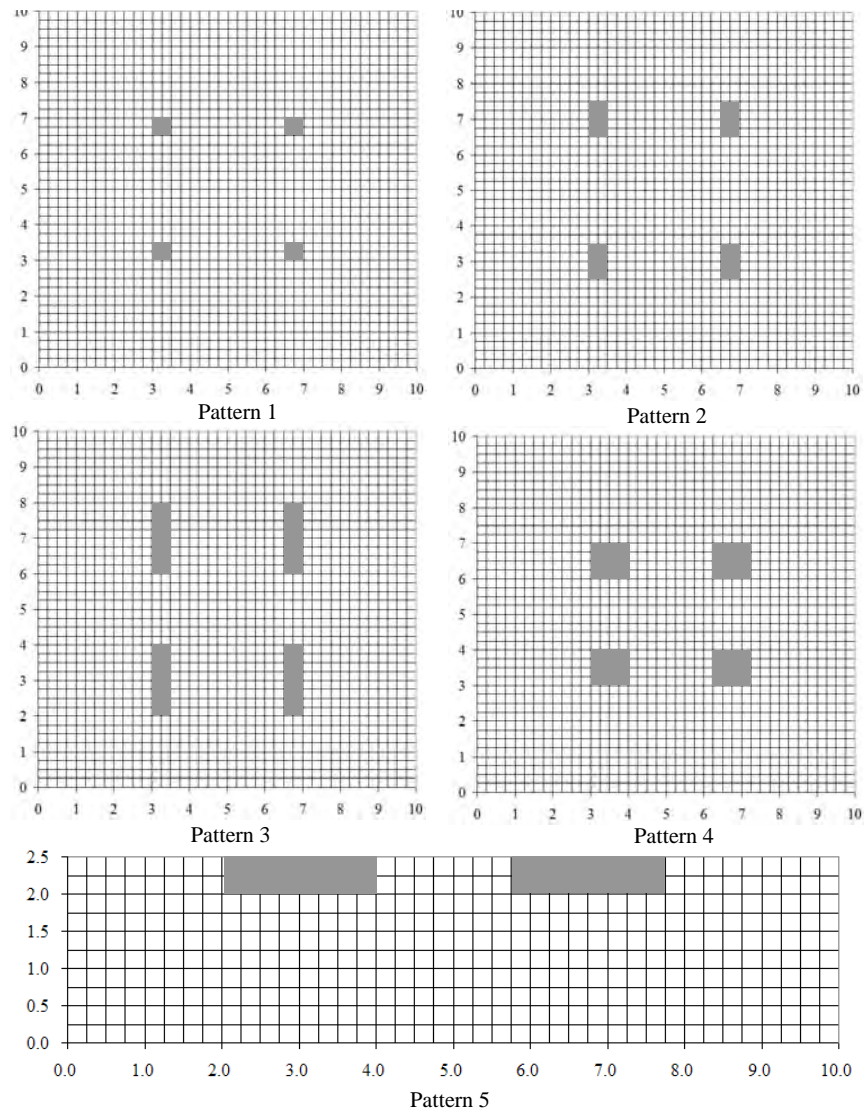


Figure 4. Patterns of smoke extraction vents

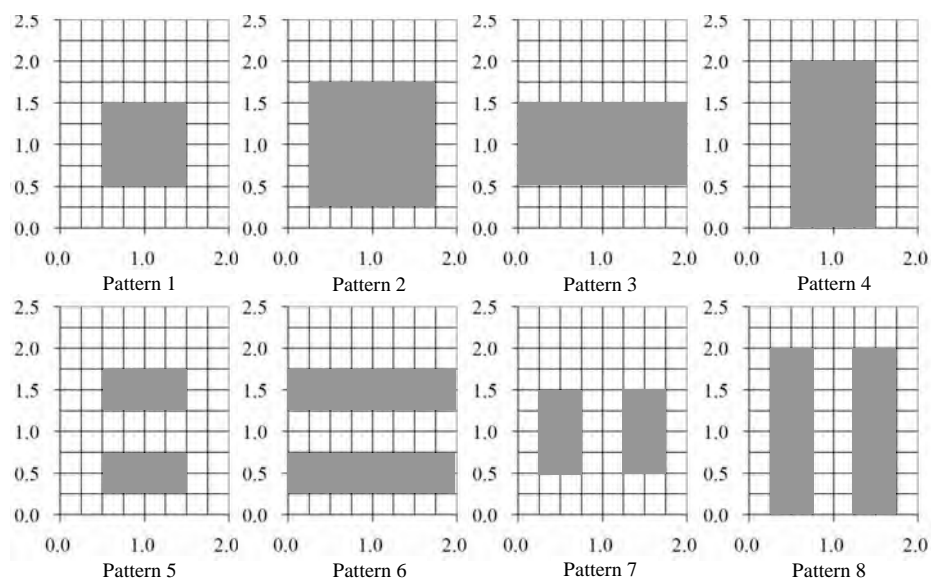


Figure 5. Patterns of air supply vents (facing the doorway and side wall)

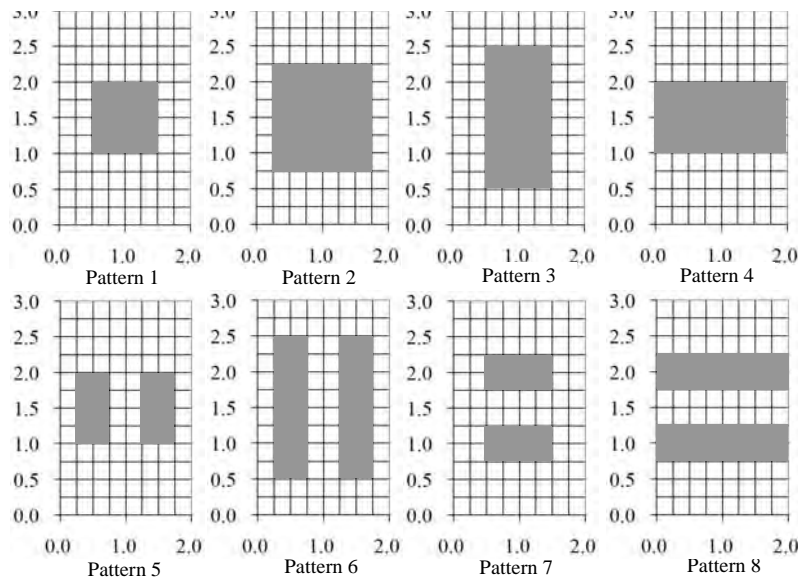


Figure 6. Patterns of air supply vents (ceiling)

vestibule, the vents are assumed to be a combination of vents in the ceiling, the straight wall facing the doorway or the side wall adjacent to the stairs.

3.4 Fire scenario

The fire scenario is important in smoke control system design. The following fire scenario is assumed here. The fire size is set to be 1.0 m × 1.0 m in the middle of the office. The fire was quantified by assuming a fast t^2 fire. That is, $Q = at^2$. This assumption is reasonable for an office. A and the maximum heat release rate are set to be 0.015 and 500 kW respectively (Ikehata et al., 2004). The smoke control system starts 20 minutes after the fire starts. The window is also assumed to be open 20 minutes later. Smoke extraction will stop if the temperature of the smoke entering the duct is higher than 280°C. The doorway adjacent to the stairs in the vestibule is open.

3.5 Evacuation time

Evacuation generally consists of three stages: burning room evacuation, burning story evacuation and whole building evacuation. The evacuation time for this office building is calculated based on the fundamental theory of evacuation (Tanaka, 1993). The result is shown in Fig. 7. The evacuation time for the fire story is 48.5 s, and for the whole building is 208.5 s.

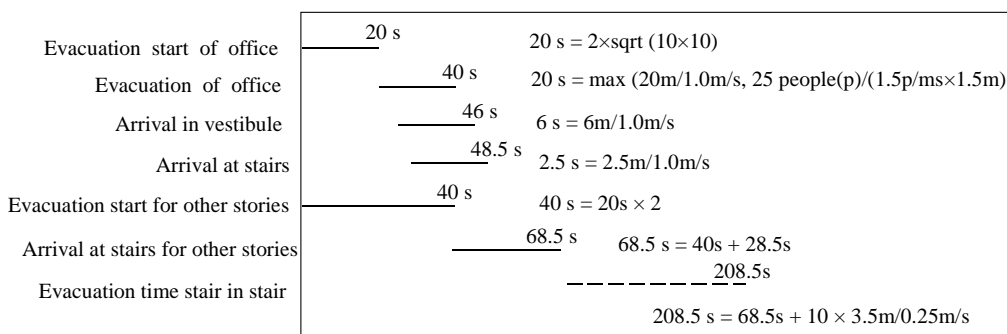


Figure 7. Calculation of evacuation time

Table 1. Setting the multi-island GA

Size of Sub-Population	10
Number of Islands	5
Number of Generations	20
Total Individual Size	1000 (10×5×20)
Rate of Crossover	0.5
Rate of Mutation	0.02
Rate of Migration	0.5
Rate of Tournament	0.4
Interval of Migration	4

3.6 GA method

Genetic algorithms (GA) are used to select the optimum solution candidates, and control of the optimum inquiry process. GA is a method which solves the optimization problem by imitating the organic evolutionary process. Here, the optimum solution candidate, which is called an “Individual”, is considered to be a living entity. As with organic evolution, the individual’s information is described by the sign row called “Chromosome”, and matches the individual and the chromosome one to one. GA performs the genetic operations – such as the selection, crossover, and mutations – on the chromosome of each individual, and the fitness (objective function) of each individual is calculated to evaluate them. The individual with the highest fitness value among all the inquired individuals becomes the optimum individual (Chen et al., 2004).

Moreover, a more efficient Genetic Algorithm, which is called the “Multi-island Genetic Algorithm”, is used in this research. The method is a distributed genetic algorithm. The feature of this method is that the population in one generation is divided into several sub-populations, and the genetic operations are performed independently in each sub-population. An exchange of individual information called “migration” is performed periodically between sub-populations. Therefore, the procedure for GA operations in this research is actually performed as follows. First, the initial population (the first generation) is determined randomly as an initial value. Next, fitness is calculated respectively using FDS simulation. Individuals with the highest ranking fitness are selected from the entire population based on the selection rate set by the designer. The GA operations such as simple crossover or mutation are performed at random for selected individuals according to the crossover rate or mutation rate that has been set. The offspring (individuals) of the next generation are produced by the above operations, and these operations are repeated. During multi-island GA, the exchange between individuals – called migration – is performed between each island based on a migration interval. Each island of migration is decided at random, and individuals are exchanged between predetermined islands according to the migration rate. The above process is repeated, and the optimum inquiry is performed for the number of generations set by the designer. The parameters in this study are shown in Table 1.

4. RESULTS

4.1 First step selection

The curve of GA selection in the first step by multi-island GA and CFD are shown in Figure 8. It can be seen that the maximum airflow through the doorway converges at about 2.5 m³/s. Some values higher than 2.5 m³/s are shown, but these

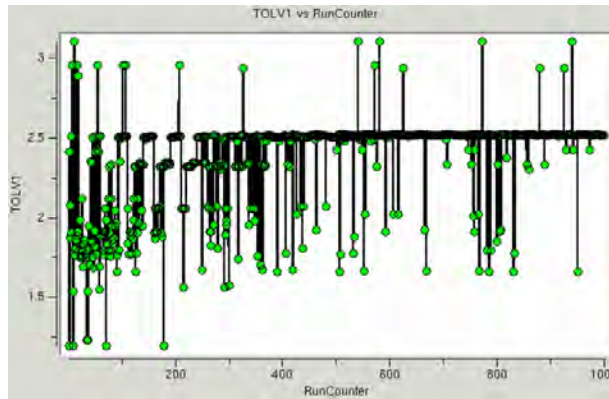


Figure 8. Curve of GA selection

Table 2. Results of the two-step selection

		Case	1	2	3	4	5	6
First step	Extraction		4	4	2	3	3	1
	Vestibule ceiling		5	-	-	-	5	5
	Vestibule straight		-	4	4	4	-	-
	Vestibule lateral		-	-	-	-	-	-
	Total air flow (m ³ /s)		2.525	2.516	2.512	2.510	2.508	2.504
Second step	Total air flow (m ³ /s)		2.482	Penalty	Penalty	Penalty	2.442	2.449

also exhibit a backward flow through the doorway. The results of the top six cases are shown in Table 2. The best one is the combination of pattern 4 (see Fig. 4) for the smoke extraction vent and pattern 5 (see Fig. 6) at the vestibule ceiling for the pressurization vent. The top six cases in the first step are selected for a detailed CFD analysis using a fine mesh in the second step.

4.2 Second step selection

The results of the detailed CFD analysis in the second step are also shown in Table 2. It is found that a backward flow exists through the

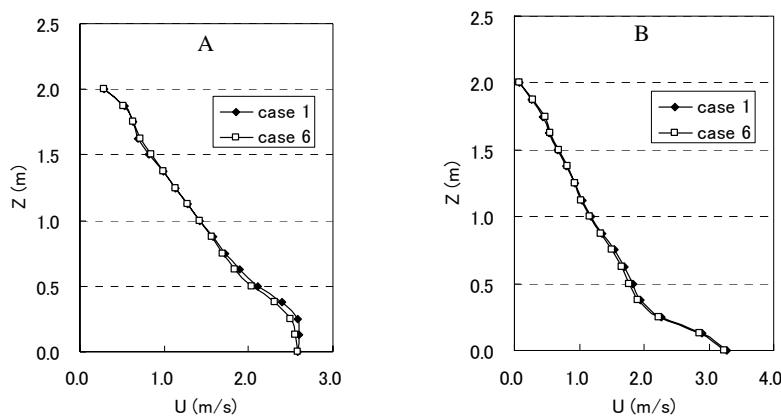


Figure 9. X-axis velocity at site A and B in the vertical direction

doorway near the bottom in Cases 2, 3 and 4, and consequently these cases are exempted. The final top three cases are Cases 1, 6 and 5. The maximum airflow through the doorway of the vestibule is $2.482 \text{ m}^3/\text{s}$. Because the total air supply rate is $4.17 \text{ m}^3/\text{s}$, it is clear that some air flows to the stairwell through the open doorway adjacent to the stairs. Figures 8 and 9 show the X-axis velocity at site A and B (see Fig. 3) for Cases 1 and 6. The velocity at the lower part is higher than the higher part because the air is supplied from the ceiling. Some tendencies can be found that for extraction vents, the square pattern is better than rectangular; for pressurization vents, ceiling vents are better. The results are a little different from the first step due to the influence of the grid resolution. But the 2-step selection method used here is still an effective approach for determining the optimal design bearing in mind the computational costs.

5. CONCLUSIONS

In this research, the vestibule pressurized smoke-control system in an office is optimized with a coupled approach using Computational Fluid Dynamics (CFD) and Genetic Algorithms (GA). The 2-step selection approach is used here. The result of the second step is a little different from the first step due to the influence of the grid resolution. However, the 2-step selection method used here is still an effective approach for determining the optimal design bearing in mind the computational costs.

Fire inevitably involves many uncertainties, such as, the site of the fire, whether the window is open or not, and so on. The optimal design should have considerable reliability in cases where such uncertainties exist. Therefore, a reliable optimal design based on a reliability analysis will be performed in future work.

REFERENCES

- Chen, H., Ooka, R. and Kato, S., 2003. Study on design methods for pleasant outdoor thermal environment using Genetic Algorithms (GA) and coupled simulation of convection, radiation and conduction, Optimum arrangement of trees for design of pleasant outdoor thermal environment, *J. Archi. Plann. Environ. Eng. AIJ*, 576, 65-71.
- Kato, S. and Lee, J. H., 2004. Optimization of hybrid air-conditioning system with natural ventilation by GA and CFD, *25th AIVC Conference, Ventilation and Retrofitting*.
- Kim, T., Kato, S. and Murakami, S., 2001. Two step optimal design method of indoor thermal environment based on CFD simulation and Genetic Algorithm, *Summaries of Technical Papers of Annual Meeting Architectural Institute of Japan*, D2, 771-772.
- Kim, T., Kato, S. and Murakami, S., 2002. Optimal design method of indoor thermal environment based on CFD simulation and Genetic Algorithm, Part 1, Development of prototype of optimal design method, *Transactions of the Society of Heating, Air-Conditioning and Sanitary Engineers of Japan*, 84, 53-60.
- Kujime, M., Matsushita, T. and Tanaka, T., 2000. Hand Calculation method

- for air supply rates in vestibule pressurization smoke control system, *J. Archi. Plann. Environ. Eng. AIJ*, 511, 1-8.
- Ikehata, Y., 2004. Design fires for means of egress in office buildings, *Summaries of Technical Papers of Annual Meeting Architectural Institute of Japan*, A-2, 113-114.
- Matsushita, T., Kujime, M., Takano, K., Kanatani, Y. and Tanaka, T., 1998. Calculation method of air supply rate in vestibule pressurization smoke control system for office building, Part 3: Calculation by computer model of smoke movement prediction. *Summaries of Technical Papers of Annual Meeting Architectural Institute of Japan*, 167-168.
- McGrattan, K. and Forney, G., 2004. Fire Dynamics Simulation (version 4) User's Guide, National Institute of Standards and Technology.
- Novolzhilov, V., 2001. Computational fluid dynamics modelling of compartment fires, *Progress in energy and combustion science*, 27, 611-666.
- Tanaka, T., 1993. Fundamental of building fire safety engineering, Building Center of Japan.

STUDY ON THERMAL EVALUATION OF HOT OUTDOOR ENVIRONMENT USING 2-NODE MODEL AND PHS MODEL

SHINSUKE SAWASAKI¹, RYOZO OOKA²,
TOMONORI SAKOI³ and KAZUYO TSUZUKI³

¹ Graduate School of Engineering, The University of Tokyo, Japan

² Institute of Industrial Science, The University of Tokyo, Japan

³ National Institute of Advanced Industrial Science and Technology, Japan

sawasaki@iis.u-tokyo.ac.jp

ABSTRACT

There is extended potential for serious mishaps like “Heat Disorder” arising in the harsh hot outdoor environment during summer. An appropriate thermal index is required in order to evaluate the risk of such accidents. There are two major human thermal regulation models, i.e. the 2-Node Model (2NM) in SET and Predicted Heat Strain Model (PHS Model) for evaluation of the thermal environment. However, these models were developed for the indoor or labor environment, and it is not clear whether these are applicable to Japanese people in a hot outdoor environment. Furthermore, there are no popular indices with which to evaluate tolerance or safety. The purpose of this study is the development of an index for hot outdoor environment. For the initial investigation, subject experiments are performed in a laboratory to better comprehend the physiological response of the human body to heat. The results are compared with the computed values from the 2NM and PHS Model. The computed core temperatures of both models accommodate the experimental values in all cases. As for skin temperature and water evaporation, the computed values from 2NM accommodate the experimental values in resting cases, while the PHS Model value accommodates the experimental values from exercise on a treadmill. Furthermore, the applicability of these models to hot outdoor thermal environment is considered.*

1. INTRODUCTION

There is extended potential for serious mishaps like “Heat Disorder” arising in the harsh hot outdoor environment during summer. An

appropriate thermal index is required in order to evaluate the risk of such accidents. There are two major human thermal regulation models, i.e. the 2-Node Model (2NM) in SET* and Predicted Heat Strain Model (PHS Model) for evaluation of the thermal environment. However, these models are developed for the indoor environment, and it is not clear whether these are applicable to Japanese people in a hot outdoor environment. Furthermore, there are no popular indices with which to evaluate tolerance or safety.

The purpose of this study is the development of an index for hot outdoor environment. For the initial investigation, subject experiments are performed in a laboratory to better comprehend the physiological response of the human body to heat. The results are compared with the computed values from the 2NM and PHS Model.

2. Subject Experiment

2.1. Outline

Fig. 1 shows the setup for the experiment, while Table 1 presents an outline of the subject experiment. This experiment is performed in a test chamber whose air temperature and relative humidity can be arbitrarily controlled. The subject persons rested for over 60 minutes in an anterior room, then remained for 60 minutes (or 30 minutes) in the test chamber. During the test-chamber period, all physiological factors were measured and declarations of psychological factors were accepted.



Figure 1: Setup for the Subject Experiment

Table 1: Outline of Subject Experiment

Time	From 29 November to 20 December 2004
Place	Ultimate Environment Test Chamber, I.I.S., The University of Tokyo
Subject	University students (5 men and 4 women in healthy condition)
Case	4 cases per subject

2.2. Measurement Factors

Table 2 presents the measurement factors. Core temperature is measured as the tympanic temperature using infrared radiation. Mean skin temperature is calculated from 8 skin temperature sensors on the forehead, right back, left upper chest, right upper arm, left lower arm, left hand, right anterior thigh and left calf by weight averaging based on ISO 9886. Water evaporation is calculated from the change of weight determined by an accurate weight scale.

Table 2: Measurement Factors

	Factor	Equipment	Place	Interval
Environmental factors	Air temperature	Thermocouple thermometer	0.7, 1.1 & 1.7 meters above floor	1 min.
	Wall temperature		4 wall surfaces, 16 points	
	Relative humidity	Assman psychrometer	1.1 meters above floor	
	Air velocity	Hot-wire anemometer	1.1 meters above floor	
Physiological factors	Core temperature	Infrared clinical thermometer	Tympanic membrane	5 min.
	Skin temperature	Thermocouple thermometer	8 points	1 min.
	Evaporative rate	Accurate weight scale	–	5 min.
Psychological factors	Personal thermal state	Declarations of him/herself	–	5 min.
	Personal comfort state			
	Personal tolerance			

2.3. Experimental Conditions

Table 6 shows the conditions of each case. Case 0 is the standard case, and Cases 1, 2 and 3 are those that evaluate the effect of activity, air temperature and relative humidity respectively. In Case 2, the subjects walk on a treadmill at a speed of 0.9 [m/s] (equivalent of 2.0 met), but stop for about 20 seconds when mounting the weight scale. The same prepared clothes are worn, namely a white tee shirt and white short pants. For the safety of the subjects, the experimental span for Case 1 was shortened to 30 minutes.

Table 6: Experimental Conditions

Case		0	1	2	3
Experimental conditions	Air Temperature [$^{\circ}\text{C}$]	35.7	35.7	39.4	35.7
	MRT [$^{\circ}\text{C}$]	35.7	35.7	39.4	35.7
	Relative humidity [%]	46.4	46.4	51.9	72.5
	Air Velocity [m/s]	0.16			
Subject conditions	Metabolic rate [met]	1.0 (at rest)	1.9 (treadmill)	1.0 (at rest)	1.0 (at rest)
	Clothing Insulation [clo]	0.3			
SET* [$^{\circ}\text{C}$]		34.0	33.4	39.2	38.3

3. Experimental Results

3.1. Transitions in Core Temperatures

Fig. 2 shows the transitions of core temperature. The value of each case is the average for all subjects, and the vertical lines on the locus of Case 0 indicate the standard deviations. In all cases, the core temperature rose by about 0.5°C in the first 15 minutes, and then tended to stabilize. The standard deviation was about 0.2°C .

3.2. Transitions in Mean Skin Temperatures

Fig. 3 shows the transactions of mean skin temperatures. In all cases, the mean skin temperature rose by about 2.0°C in the first 10 minutes. In Cases 0, 2 and 3 under low metabolism, the mean skin temperature kept on rising slowly. On the other hand, it began to decrease after a peak at 15 minutes in Case 1 under high metabolism. The standard deviation was about 0.6°C .

3.3. Cumulative Water Evaporation

Fig. 4 shows the amount of weight reduction, i.e. the cumulative amount of water evaporation. It increases linearly in all cases. And the gradient in Case 1 is more than twice those of the other cases. The standard deviation was about $0.03 [\text{kg}/\text{m}^2]$ after 60 minutes.

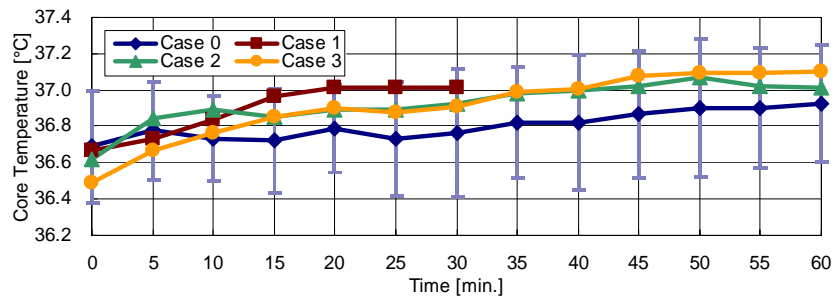


Figure 2: Transitions of Core Temperatures

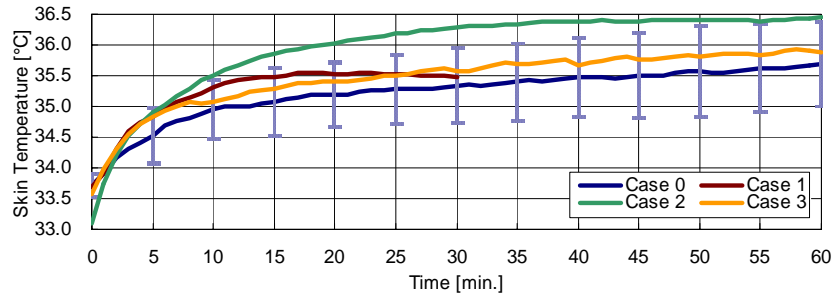


Figure 3: Transitions of Skin Temperatures

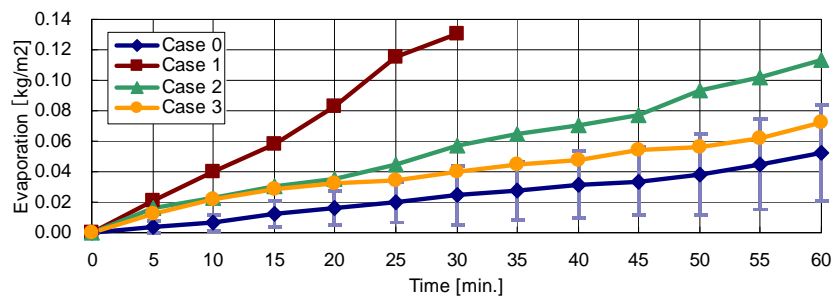


Figure 4: Cumulative Water Evaporation

4. Comparison between the Experimental and Computed Values

4.1. Outline of 2-node model

The 2-Node Model (2NM) was proposed by A. P. Gagge et al. for the calculation of SET* and so on. 2NM assumes that the human body is composed of two nodes, i.e. a central core and a skin shell, and calculates the thermal balance respectively. The physiological response of sweating is also built into this model, which might be more relevant in a hot environment. Thus 2NM is thought to be a reliable model for hot environment. However, 2NM was developed for indoor environments, and it is not clear whether it can be applied to hot outdoor environment.

4.2. Outline of Predicted Heat Strain Model

Predicted Heat Strain Model (PHS Model) was proposed by J. Malchaire et al. for evaluation of hot labor environments, and is being discussed for incorporation in revisions to ISO 7933. The PHS Model predicts transitions in core temperatures with consideration of the required evaporative rate to maintain a steady thermal equilibrium, the response characteristic of evaporation, and thermal storage of the skin. Even though the PHS Model is developed based on a large number of subject experiments, it is aimed at labor conditions. Additionally, it is not clear whether a model developed in Europe can be applied to Japanese people in hot outdoor urban environments because of the differences in evaporative characteristics, physical attributes and climate.

4.3. Computational Conditions

Table 7 presents the preset values for both models. Concerning the PHS Model, two cases are computed on the basis of correspondence to 2NM, i.e. PHS Model (33.7) and PHS Model (34.1). Other conditions are in accordance with the experimental conditions presented in Table 6.

Table 7: Computational Conditions

	2NM	PHS (33.7)	PHS (34.1)
Weight	70 [kg]		
Surface area	1.8 [m ²]		
Initial core temperature	36.8 [°C]		
Initial skin temperature	33.7 [°C]		34.1 [°C]
Convective heat transfer coefficient	Seated: $h_c = 3.1 (0 < V_{air} < 0.2)$ Treadmill: $h_c = 6.5 V_{treadmill}^{0.39}$	Maximal value of: $h_c = 2.38 (T_{sk} - T_a)^{0.25}$ $h_c = 3.5 + 5.2 V_{air}$ $h_c = 8.7 V_{air}^{0.6}$	

5. Comparison Results

5.1. Comparison of Core Temperatures

Figs. 5 to 8 present a comparison of the core temperatures in each case respectively. Along with Section 3, the experimental values of each

case are the average of all subjects, and the standard deviations are indicated as vertical lines on the experimental locus. Even though the computed value for 2NM is about 0.2°C higher than for the PHS Model after 60 minutes in Cases 2 and 3, both models follow approximately the same excursion and correspond well to experimental values in all cases.

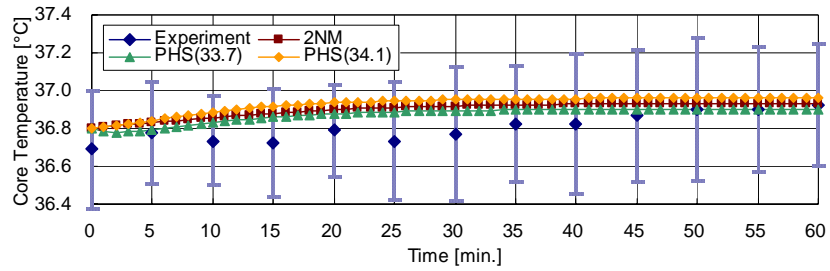


Figure 5: Comparison of Core Temperature (Case 0)

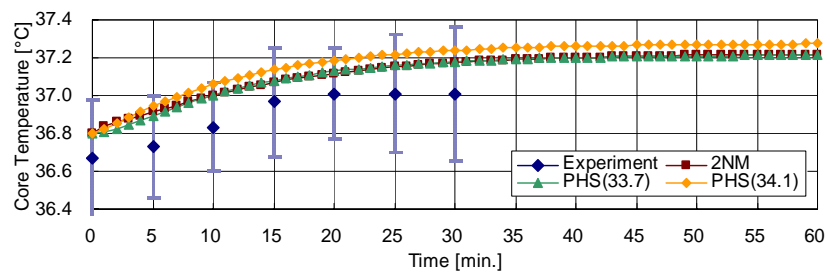


Figure 6: Comparison of Core Temperature (Case 1)

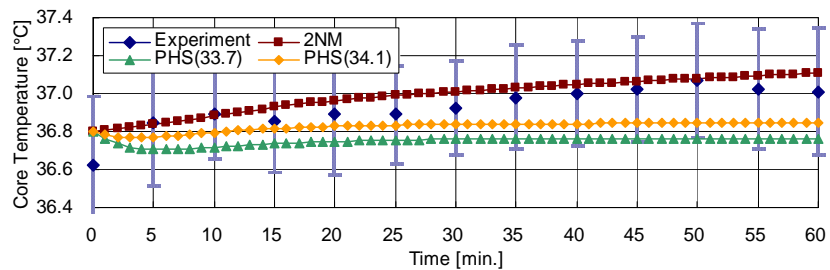


Figure 7: Comparison of Core Temperature (Case 2)

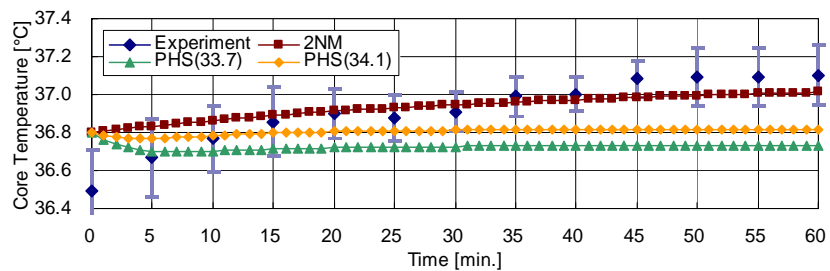


Figure 8: Comparison of Core Temperature (Case 3)

5.2. Comparison of Skin Temperature

Figs. 9 to 12 present a comparison of skin temperatures in each case respectively. The computed value for 2NM is about 1.2°C higher than for the PHS Model after 60 minutes. In Cases 0, 2 and 3 under low metabolism, 2NM corresponds well with the experimental values. However, 2NM does not concur well with the experimental values in Case 1 under high metabolism.

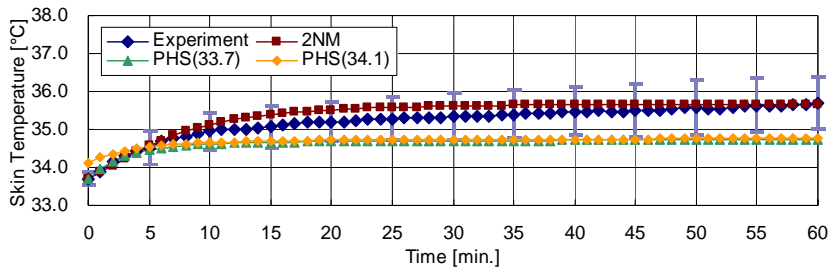


Figure 9: Comparison of Skin Temperature (Case 0)

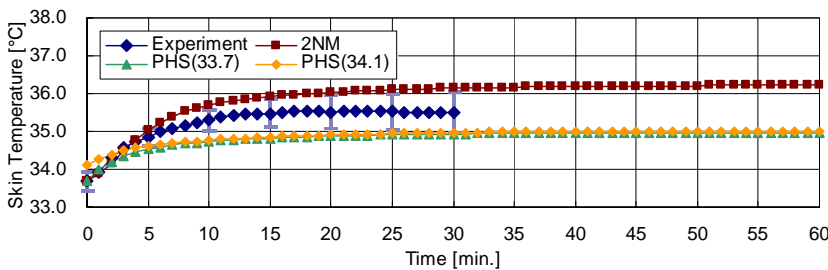


Figure 10: Comparison of Skin Temperature (Case 1)

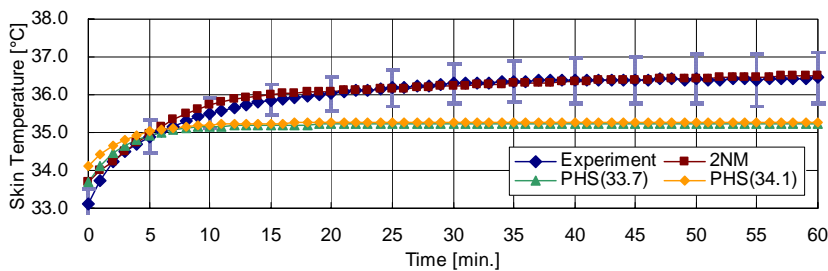


Figure 11: Comparison of Skin Temperature (Case 2)

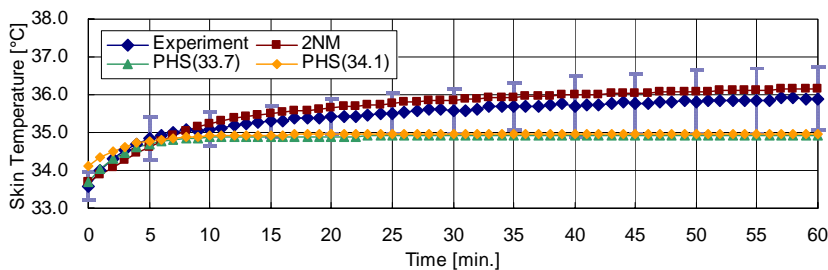


Figure 12: Comparison of Skin Temperature (Case 3)

5.3. Comparison of Cumulative Water Evaporation

Figs. 13 to 16 present a comparison of cumulative water evaporation in each case respectively. In all cases, the values for the PHS Model are 0.2 [kg/m²] greater than for 2NM after 60 minutes. In Cases 0, 2 and 3 under low metabolism, 2NM corresponds well with the experimental values. On the other hand, the PHS Model corresponds well with the experimental values in Case 1 under high metabolism.

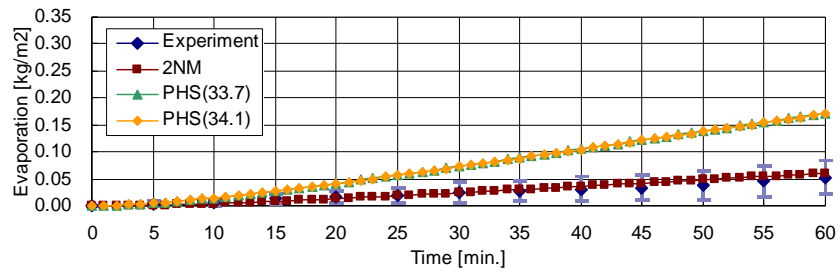


Figure 13: Comparison of Cumulative Water Evaporation (Case 0)

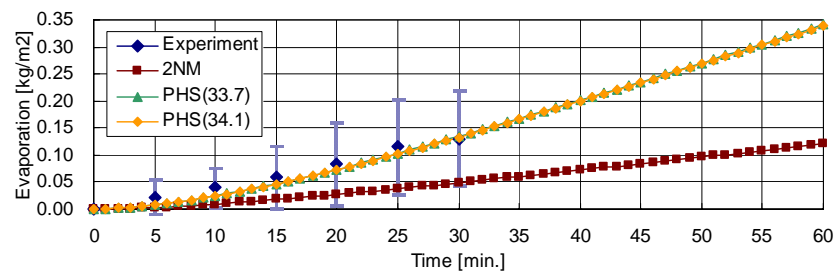


Figure 14: Comparison of Cumulative Water Evaporation (Case 1)

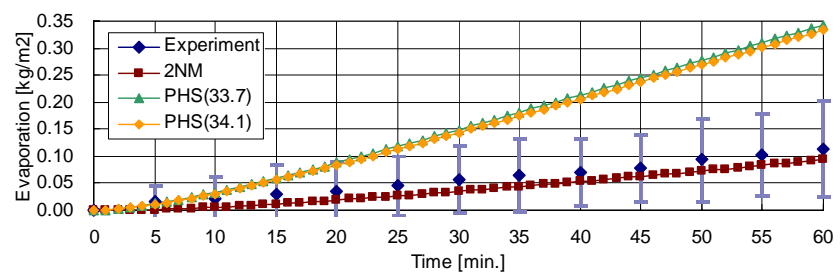


Figure 15: Comparison of Cumulative Water Evaporation (Case 2)

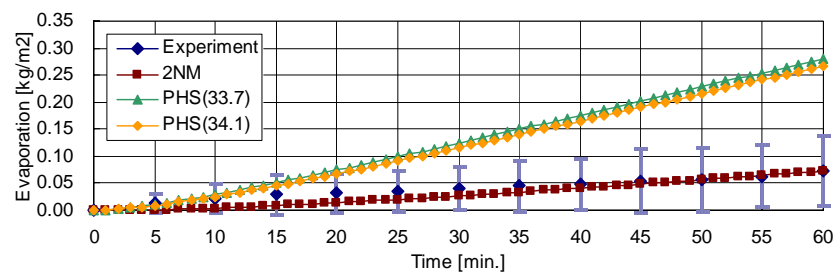


Figure 16: Comparison of Cumulative Water Evaporation (Case 3)

6. Concluding Remarks

Subject experiments were performed in a laboratory to better comprehend the physiological response of the human body to heat. The experimental conditions are in the following ranges; $35.7 < T_a < 39.4 [^{\circ}\text{C}]$, $35.7 < \text{MRT} < 39.4 [^{\circ}\text{C}]$, $46.4 < \text{RH} < 72.5 [\%]$, $\text{VEL} < 0.16 [\text{m/s}]$, $1.0 < \text{MET} < 1.9 [\text{met}]$, and $\text{CLO} = 0.3 [\text{clo}]$.

Then experimental values of the core temperature, skin temperature and cumulative water evaporation were compared with the computed values for the 2NM and PHS Model. The core temperature for both models follows approximately the same excursion and corresponds well with the experimental values in all cases. The skin temperature for 2NM is higher than for the PHS Model in all cases. In low metabolic cases, 2NM corresponds well with the experimental values. On the other hand, 2NM does not concur well with the experimental values in the high metabolic case. Cumulative water evaporation for the PHS Model is greater than for 2NM in all cases. In low metabolic cases, 2NM corresponds well with the experimental values. Conversely, the PHS Model corresponds well with the experimental values in the high metabolic case.

On the whole, 2NM corresponds well with experimental values in low metabolic cases, while the PHS Model corresponds well with experimental values in high metabolic case. Hereafter, the following points should be considered for development of a physiological model for hot outdoor environments; Modification of the evaporative model for 2NM under high metabolic conditions or apportionment between the 2NM and PHS Model.

REFERENCES

- A. P. Gagge et al., 1971, *An Effective Temperature Scale Based on A Simple Model of Human Physiological Regulatory Response*, ASHRAE Transactions Vol.77, pp.247-262
- A. P. Gagge et al., 1986, *A Standard Predictive Index of Human Response to The Thermal Environment*, ASHRAE Transactions, Vol. 92-1, pp.709-731
- ISO 7933, 2004, *Ergonomics of the thermal environment – Analytical determination and interpretation of heat stress using calculation of the predicted heat strain*, International Organization for Standardization
- ISO 9886, 2004, *Ergonomics – Evaluation of Thermal Strain by Physiological Measurements*, International Organization for Standardization
- A. P. R. Fobelets and A. P. Gagge, 1988, *Rationalization of The Effective Temperature ET^* , as A Measure of The Enthalpy of The Human Indoor Environment*, ASHRAE Transactions Vol.94-1, pp.12-31
- J. Malchaire et al., 2001, *Development and Validation of the Predicted Heat Strain Model*, British Occupational Hygiene Society, The Annals of Occupational Hygiene, Vol.45, No.2, pp.123-135

GEOINFORMATICS AND PUBLIC DOMAIN SYSTEM MODEL ON THAILAND MEGA PROTOTYPE SAFTY

Assoc.Prof. Dr. Hansa Vathananukij
Faculty of Engineering, Kasetsart University,
50Paholyothin, BKK10900, Thailand
E-mail: fenghsv@ku.ac.th ,
URL: <http://gis.eng.ku.ac.th>

ABSTRACT

Geoinformatics of MODES/Terra 500 resolution contained five multi-spectral bands, performed good correlation with mean monthly hydro-informatics, was one of a rather modern high frequency earth observation imageries. Thus has been assimilated and assessment to mega multi-purpose prototype in Thailand. Together with essential hydroinformatics from GAME-T data mining did play much important role with consequential interest through renowned soil and water public domain system model.

Pasak river reach is one of the new enormous regimes with complex purpose and rapidly population enlargement in Thailand, that could digest in term of geo-informatics database such as topography, land cover and river system etc., through three series in dry circumstance of MODES/Terra imageries. Spatial analysis on best correlation of band3, band5 and band6, of MODES/Terra were distinguished to classify, transfer and verify in both regulated and unregulated methodology upon soil and water public domain system model.

Data analysis interface has been modified by data analysis programming and data access approached on access basic standard query language. This appropriate model calibrations and verifications, admissible ensued on high percentage of correlation efficiency and affirmable best arbitrated on mega scale-mild slope potentiality together with un-implied in either continual or sufficient hydroinformatics investigation. Consequence of assessment could illustrate risk and safety potentiality quantity on the prototype area.

Keywords: Geoinformatics, Hydroinformatics, Public Domain System, Data Analysis Program, Standard Query Language, MODIS/Terra, SWAT

1. INTRODUCTION

Whereas the Chaophraya regime has been regional characterized by monsoon, spatial and intensive heavy rainfall, increased mean rainfall intensity attitude as rainfall variations with plenitude could cause both flash and sluggish floods, landslide and debris flow. Pasak river basin is one of mega tributary drainage area that comes upon the lower Chaophraya areas of Thailand which rapidly increased population in recent year.

While most popular water resource models that have been employed in Thailand were costly licensed, SWAT(Soil and water assessment tools) model, could inundated simulation which major caused of water-related extreme event, was attempted to structure, verify and renown an innovative public domain revolutionize to geoinformatic system model as SWAT, SWAT/GIS.

500 resolution of MODES/Terra was a rather modern high frequency satellite imagery which contained five multi-spectral bands, did perform good correlation with hydro-informatics system played much important role to surface and water assessment.

2. PROTOTYPE AREA

A feather shaped of Pasak basin, 16,292 square kilometers surface area with 350 kilometers length and 45 kilometers width was selected as mega prototype domain. Thus basin has been one of the dense population, covered area of seven provinces which are Loei, Petchaboon, Lopburi, Saraburi, Nakornratchasima, Chaiyaphum, and Phranakorn-sriayuthaya as illustrated in figure 1. Principal topography is hilly feature, mountainous enclosure and a few flatness while Petchaboon terrain compassed on upper part and flood plain at lower part merged to the Chaophraya main river at Phranakorn-sriayuthaya province. Open channel regime flows from north to south with shorten east to west tributaries.

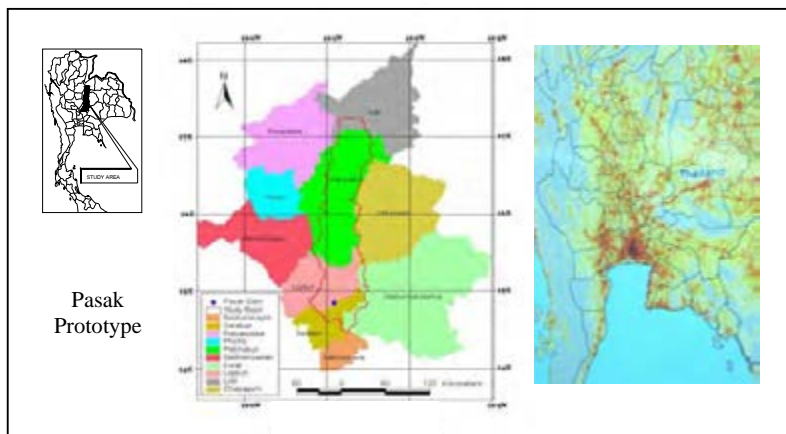


Figure 1: Prototype area

3. SPATIAL ASSESSMENT

While innovative geoinformatics technology is widely spread through academic area, high frequency of MODIS/Terra earth observation satellite is one of them with selected multi-spectral bands 3, 4, 5, 6 and 7. Dry season in year 2003, resulted high reflectance relations, were intentional selected extent, geo-coded studios specify on both geoinformatics and hydro-informatics database system over beneficially regulated mega area of north-central plain Pasak prototype. Assessment consequence on basin delineation and digital elevation model were illustrated in figure 2.

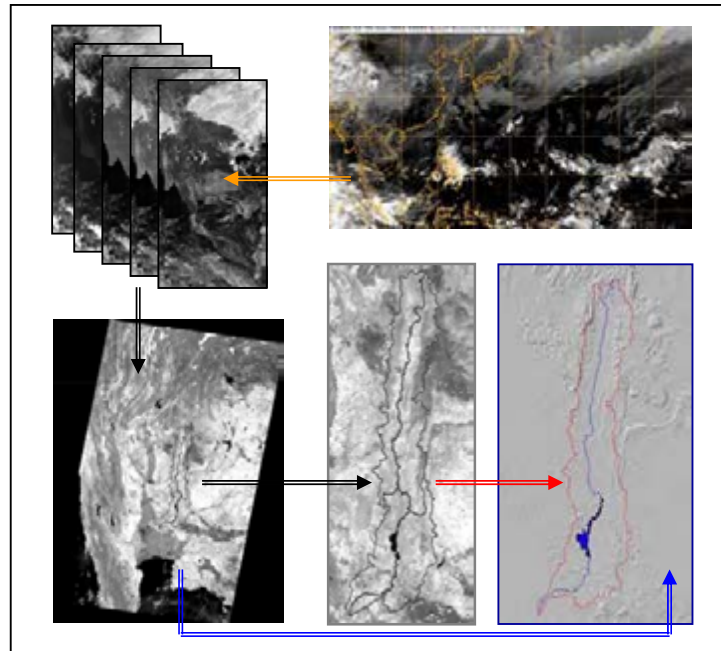


Figure2: Basin delineation and DEM

This prototype has been aligned further studiosness in both supervised and unsupervised assessments, for monitoring updated circumstance of digital information system scenario such as topography, soil, land covers, streams and etc., as shown in figure 3.

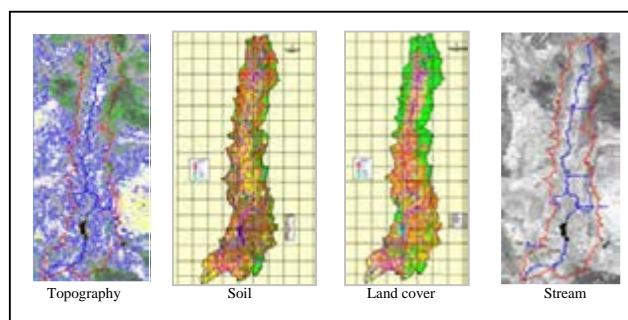


Figure3: Geoinformatic system

4. PUBLIC DOMAIN SYSTEM MODEL AND ASSESSMENT

The Soil and Water Assessment Tool (SWAT) model is continuation long term effort of non-point source pollution modeling. This continuous time model designed either to simulate continuous event, long time periods with of agricultural management effect and could apply to large and small watersheds. The most current geo-informatics data available were initial input in the model that could digest in term of digital database such as topography, soils, land cover and river system which basely employed on water balance equation as follows:

$$SW_t = SW + \sum (R_i - Q_i - ET_i - P_i - QR_i) \quad (1)$$

$$Q = \frac{(R - 0.2s)^2}{R + 0.8s}, R > 0.2s \quad (2)$$

where

$$Q = 0.0, R \leq 0.2s \quad (3)$$

and

$$s = 254 \left(\frac{100}{CN} - 1 \right) \quad (4)$$

Geoinformatics and hydrologic information has been approached convert for model utilization. Investigated precipitation from 14 stations, weather information 5 stations together with actual surface stream flow from 8 stations were selected for model calibration and verification as shown in figure 4.

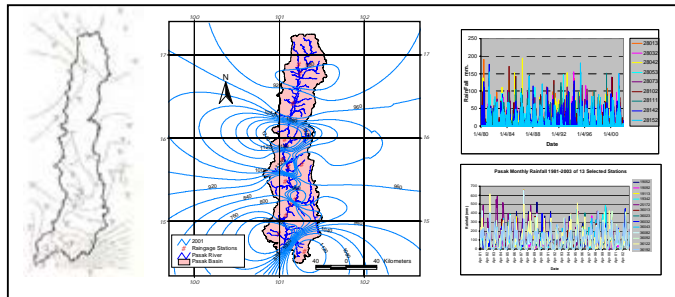


Figure4: Hydroinformatic system

Model was calibrated, verified and monitored on surface stream flow. Confine prototype which was divided into 86 hydrologic respond units/ eight sub-basins with data analysis program interface as shown in figure 5.

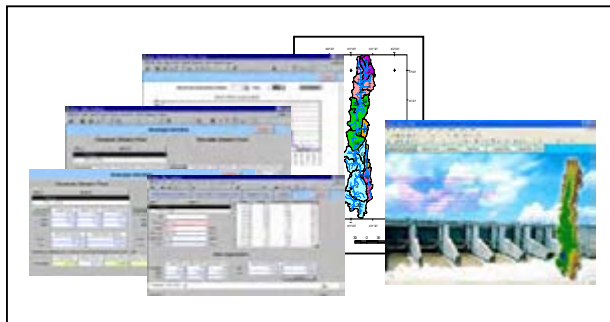


Figure5: Data analysis program

5. CONCLUSIONS:

SWAT model has been affirmable best arbitrated on Thailand mega scale-mild slope potentiality with perfectly runoff analyses results as in correlation coefficients of figure 6. Consequent intricacy from SWAT model, MODIS/Terra spatial supervised classification and sufficient hydroinformatic system have been combined into geoinformatic summation polygon of potential area and could illustrate risk and safety potentiality quantity on the mega prototype area for urban expansion, dry season agriculture and sluggish flood as illustrated in figure 7 and table 1.

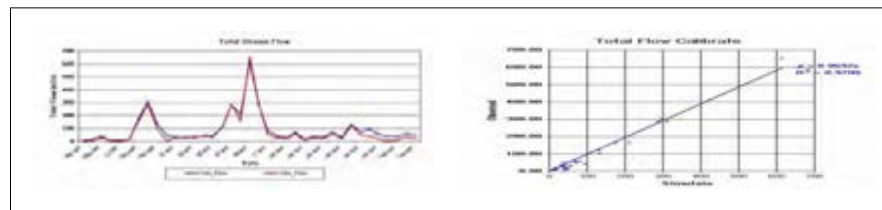


Figure6: Correlation analysis

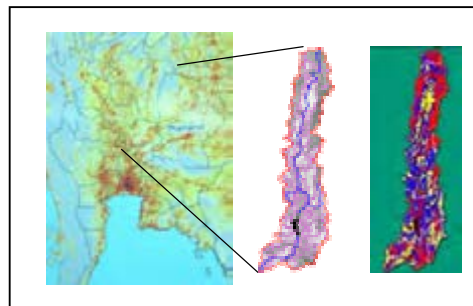


Figure 7: Risk and safety potentiality

Table 1: Provincial Potential Area

Province	Potential areas sq.km.
Loei	120.5
Petchaboon	2,900.0
Lopburi	1,200.0
Saraburi	565.0

6. ACKNOWLEDGEMENT:

This research has been continuously supported by RM-GIS Center, Faculty of Engineering, Kasetsart University, National Research Council of Thailand and Geoinformatics and Space Technology Development Agency since 2003.

REFERENCES

- Arnold, J.G.Williams, R.Srinivansan, K.W.King and R.H.Griggs., 1995
SWAT – Soil and Water Assessment Tool Draft Users Manual, USDA
– ARS, Temple, TX Arnold, J.G. R.Srinivansan, R.S.
- Hansa V.1998., *River Engineering*. Physics Center CO.LTD., 120 p.
- Hansa V, Kittipong T., 2002. *Thailand Tributaries Relativity Assessment through Geoinformatic System and SWAT Modelling*. Proceedings International Workshop on GAME-T and Hydro-meteorological Studies in Thailand and Southeast Asia, Chiengrai, Thailand. Pp.62-68
- Hansa V., 2003. *Geographic Information System/Geoinformatic System*. Physics Center CO.LTD., 151 p.
- Hansa V., Thitikorn P., 2003. *Design Flood Application through Geoinformatic System and AutoCAD Land Development Desktop Model*. Proceedings International Forth Regional Symposium on Infrastructure Development in Civil Engineering, Bangkok, Thailand. pp.1087-1093
- Hansa V. 2003., *Public Domain Model (SWAT/GIS) Development on Nan River Basin*. Proceedings International Symposium on the Climate System of Asian Monsoon and its Interaction with Society, Khon Khaen, Thailand. pp.15-23
- Hansa V. 2004., *Geographic Information System / Geoinformatics System*. Physics Center CO.LTD., 150 p.
- Hansa V. 2004., *Portentous Flood Exposition on Geoinformatic System*. Proceedings International Symposium on Water Resource and Its Variability in Asia in the 21stCentury, Epochal, Tsukuba, Ibaraki, Japan. pp.25-28.
- Hansa V. 2004., *Sustention Models for Water Resource Management*. 2nd APHW Conference jointly with 1st AOGS Annual Meeting, Suntec International Convention and Exhibition Center, Singapore. Volume II pp.668-676
- Hansa V., 2005. *Geoinformatic Public Domain Model on Upper Ping River*. Proceedings Interdisciplinary Workshop on Multi-scale Governance of Forests, Village and Water in the Upper Ping River Basin, Northern Thailand Lotus Pang Suan Kaew Hotlel, Chiang Mai.
- Hansa V., 2005. *Near Real Time MODIS/TERRA on Hydro-informatics for Agriculture in Thailand*. Proceedings International Seminar on Near Real Time Agriculture Activity Monitoring Using Multi-Temporal MODIS Earth Observation Satellite Data: Faculty of Engineering, Kasetsart University, Bangkok, Thailand. pp.10-22
- Muttiah, P.M. Allen.1999., *Continental Scale Simulation of the Hydrologic Balance*. J. American Water Res. Ass., 35(5). pp.1037 – 1050.
- Michael F.G., 1998. *GIS and environmental modelling*. Fort Collins. GIS World Books, 486 p.
- Sloto, R.A., Crouse M.Y., 1996. *HYSEP: A Computer program for stream flow hydrograph Separation and analysis*. U.S.Geological Ecological Survey Water-Resources Investigations Rept 96-404. 46 p.
- Steven T. B., 1998. *Brush/Water yield feasibility studies, Blackland Research and Extension Center*. 720 E. Blackland Rd., Temple, Texas.

PATH FINDING IN 2-LAYER 1-IRS TOPOLOGIES FOR REAL-TIME EVACUATION SYSTEMS

CHEN PO-HAN (cphchen@ntu.edu.sg), FENG FENG (feng0009@ntu.edu.sg), HSU WEN JING(hsu@ntu.edu.sg), DUH BEEN-LIRN(mblduh@ntu.edu.sg).
Nanyang Technological University, Singapore.

ABSTRACT

Some previous research (Chen and Feng, 2005) has introduced 1-Interval Routing Scheme (1-IRS) techniques from computer network routing to inside-building shortest Euclidean path finding. 1-IRS topologies, which frequently appear in indoor areas like campus and commercial buildings, have been analyzed in that research and static 1-IRS algorithms have been improved into dynamic 1-IRS algorithms. In that research, a general procedure has been given in order to combine Dijkstra's shortest path finding algorithm with 1-IRS information of individual Element Classes (EC) to compute the shortest path between any two locations in a large complex network.

From our observation, the complex networks with certain properties can be given 2-layer 1-IRS information, with which shortest paths can be found without Dijkstra's shortest path algorithm involved at all. This article introduces the concept of 2-layer 1-IRS and then identifies the properties, with which certain complex topologies can use 2-layer 1-IRS technique to find shortest paths.

With the findings of our research, Dijkstra's shortest path algorithm can be totally replaced with the 2-layer 1-IRS technique in the complex networks with certain properties. With the routing information provided by the intervals, new functions like real-time digital guide can be added to the real-time evacuation system in addition to its application on optimal path finding.

1. INTRODUCTION

The emergency evacuation system under our research is a mobile and wearable computing system, which supports location-aware computing, and offers services that are relevant to the mobile user's current location (Beadle and Harper, etc. 1997). Mobile user's outdoor location can be given by GPS. And by now, some commercial location trackers have been able to give indoor location information with a wireless network, like IEEE 802.11 Wi-Fi wireless LAN. Nowadays, the average accuracy of this type of location tracker can be up to 3-5 cm. Under this accuracy level of the location

trackers, some location-aware algorithms can be implemented on the real-time systems, like the one under our research. After a building's indoor area, especially passageways and staircases, is abstracted to be a mini transportation network in certain way, the shortest path from the mobile user's current location to any location in the network can be given by certain algorithms. Dijkstra's shortest path algorithm (Dijkstra, 1959) is the classic one, which can be used for the networks in any topologies. But for some special topologies, other algorithms can be applied independently from any Dijkstra's thoughts. Interval routing schemes (IRS) in computer network routing are in this category and is the main topic of this paper. Some research (Chen and Feng, 2005) has introduced the routing concept popular in computer networks into Euclidean shortest path finding. This article is trying to extend that research from 1-IRS dynamic algorithm to 2-layer 1-IRS dynamic algorithm.

2. PREVIOUS WORK

With certain abstraction method, a large indoor area can be converted into a transportation network. All the networks used in this article are abstracted with the method, with which all passageways and staircases are represented by their middle lines or approximate middle lines (Chen and Feng, 2005). These connected lines look like transportation rails and to a large degree resemble the regular walk ways people may follow when roaming the building.

Some topologies of the networks abstracted with above method, which appears frequently inside modern buildings, have been identified and they are called Element Classes (EC) (Chen and Feng, 2005). They are trees, rings, 2D and 3D grids. For the shortest path finding with an EC, a routing technique, named Interval Routing Scheme (IRS) can be applied instead of Dijkstra's shortest path finding algorithm.

IRS has been discussed in a number of research articles, which have been summarized (Gavoille, 2000). Actually interval routing scheme is based on representing the routing table of a computer network stored at each node in a compact manner. In this method, each node is assigned a distinct label from the set $\{1, 2, \dots, n\}$. Arcs are bi-directional and are labeled with one or several subintervals of the interval $[1..n]$ so that for any node v the intervals associated with outgoing edges from v are pair-wise disjoint and their union covers $[1..n]$. When a message with destination v arrives at node u , the message is forwarded on the unique outgoing edge labeled with an interval containing the label of v .

In most cases, $[1..n]$ is the cyclic interval, i.e., all subintervals are understood to wrap around. Such a scheme is called a circular interval routing scheme (CIRS). Variants of the scheme include linear interval routing schemes (LIRS), in which $[1..n]$ is viewed as a linear interval; k -interval routing schemes, in which edges can be labeled with at most k

intervals (k-IRS). An interval routing scheme for which all messages are routed along shortest paths is called an optimal scheme.

Some highly regular networks, such as 2D grids and 3D grids (alias meshes), admit optimal 1-LIRS (Leeuwen, and Tan, 1987). Trees and rings admit optimal 1-CIRS (Santoro and Khatib, 1985). In a computer network, the message source and target are two static computers, whose locations are assumed not changed in the network. So the routing tables like IRS intervals are filled according to the network hops and they can only be used to determine the optimal route between any two static computers. A research (Chen and Feng, 2005) found that the topologies like grids, trees and rings also frequently appear inside modern buildings. In order to provide real-time shortest path finding and road guide functions for an evacuation system (Chen and Feng, 2005), the usage of 1-IRS technique were extended from routing for two static nodes to any two dynamic (mobile) nodes. And the IRS intervals for all static (dummy) nodes are filled according to the Euclidean distance of the arcs instead of hop numbers. In addition to 1-IRS dynamic algorithms developed, a systematic method of calculating optimal paths in complex networks, which consist of multiple connected EC, were introduced as well (Chen and Feng, 2005). This method combines 1-IRS and Dijkstra's algorithm, and can be applied to any topologies. In our research we are discussing another series of topologies, which are composed of multiple EC connected in a certain way. This series of topologies also appear frequently. Multiple layer 1-IRS, especially 2-layer 1-IRS technique is introduced and applied on this series of topologies without any Dijkstra's algorithm involved.

3. 2-LAYER 1-IRS TOPOLOGIES

In 1-layer dynamic 1-IRS algorithms (Chen and Feng, 2005), all static nodes in the EC (a tree, a ring or a grid) are labeled from one, and each arc are given an appropriate interval (Leeuwen, and Tan, 1987, Santoro and Khatib, 1985). After the labeling of the nodes and arcs, the network can be input to the algorithms. The source node represents the location of the mobile roamer, and the target node the destination the roamer request the shortest path for. So the source and target nodes are deemed as dynamic, which are determined in real time. A dynamic node's location is simplified to be adjacent to two and only two static nodes, which are called Gating Nodes (GN). When the distance to each GN is determined, a dynamic node's location is determined and can be input to the algorithms. 1-layer dynamic 1-IRS algorithms were developed for 1-layer 1-IRS topologies (EC), which are trees, rings and grids. Hereafter, we define the 2-layer 1-IRS topologies with the following properties:

- i) A 2-layer 1-IRS topology consists of multiple connected EC.
- ii) One of the EC is deemed as first-layer EC (FLEC). And all other EC are deemed as second-layer EC (SLEC).
- iii) Each SLEC intersects with FLEC with one and only one node, which is called Crossing Node (CN) of the SLEC to the FLEC. This

node can be a dummy node or any dynamic node in FLEC and SLEC.

- iv) All SLEC are connected with FLEC only by CN. There are no other connections between SLEC. Each node belongs to a SLEC or the FLEC. Each arc belongs to a SLEC or the FLEC.

The topologies with above properties are defined as 2-layer 1-IRS topologies and after the node and arc labeling introduced in the next section, the network of this series of topologies can be input to the 2-layer 1-IRS procedure introduced later.

4. 2-LAYER 1-IRS LABELING

Within each EC, the nodes and arcs are labeled with appropriate methods (Leeuwen, and Tan, 1987, Santoro and Khatib, 1985). Thereafter, each static node is given an EC identity number (ECID). The static nodes within the same EC have the same ECID.

According to the properties of 2-layer 1-IRS topologies, each SLEC are connected with FLEC only by one CN. This CN can be a static or dynamic node of the SLEC and FLEC. As a static node can be deemed as a special dynamic node, the consideration of only dynamic cases is enough for our purpose. So let CN be a dynamic node of the SLEC and a dynamic node of the FLEC. The distance of the CN to its two GN in SLEC and the distance to its two GN in FLEC are recorded.

5. 2-LAYER 1-IRS PROCEDURE

After above node and arc labeling, the network can be input to the 2-layer 1-IRS algorithm, which is based on the dynamic 1-IRS algorithms. A systematic flowchart is used to demonstrate this algorithm in Figure 1.

If s and t have the same ECID, their GN and distance to GN are recorded. With this information and 1-IRS labeling already done, the 1-IRS dynamic algorithms (Chen and Feng, 2005) can find the shortest path. According to the property of 1-IRS topologies, this path is the shortest path.

If one among s and t are located in FLEC, and the other is located in SLEC. The shortest path is composed of 2 parts. One is in FLEC and the other part is in the SLEC. These two parts are connected at the CN of the SLEC to the FLEC. The part in FLEC is the path from the dynamic node (s or t) to the CN and is calculated by the 1-IRS dynamic algorithms with FLEC's 1-IRS interval information. The part in SLEC is the path from another dynamic node (s or t) to the CN and is calculated by the 1-IRS dynamic algorithms with SLEC's 1-IRS interval information.

If s and t are located in different SLEC, the shortest path is composed of 3 parts. One is in FLEC and the other 2 parts in the source and target SLEC respectively. The 2 parts in SLEC are calculated by the 1-IRS dynamic algorithms with each SLEC's 1-IRS interval information. The part in FLEC is the path between the CN of the two SLEC and is calculated by the 1-IRS dynamic algorithms with FLEC's 1-IRS interval information. The overall shortest path is these 3 paths connected by two CN.

In the next section, an example is given to illustrate this procedure.

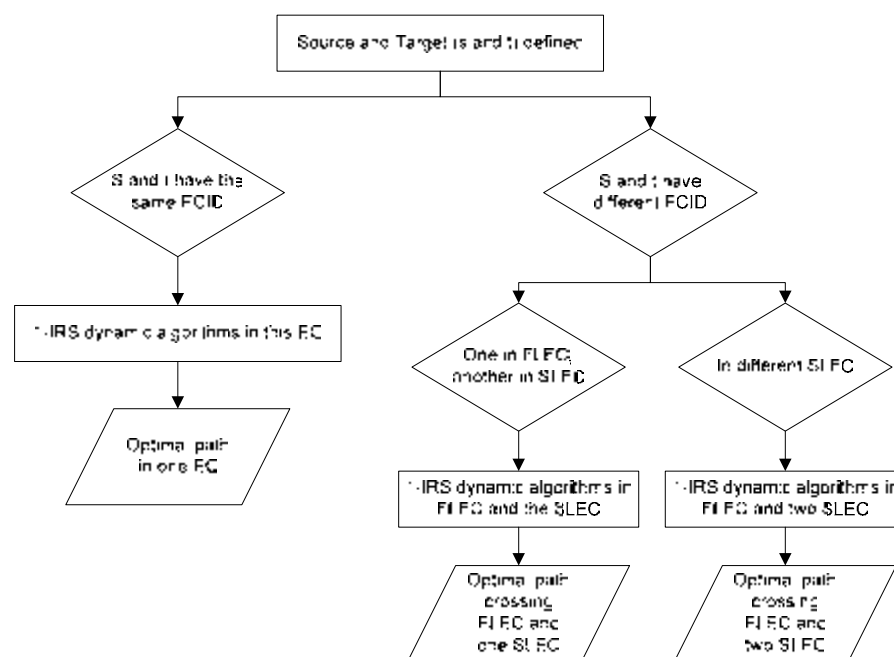


Figure 1: 2-layer 1-IRS procedure

6. AN EXAMPLE TO ILLUSTRATOR THE PROCEDURE

To illustrate the procedure in the previous section, we take network of N1-B3 and N1.1-B3 of Nanyang Technological University for example.

The passageway topology of N1-B3 is a 2x3 2D grid; the N1.1-B3 a 2x2 grid. They are connected by a straight passageway. The network is shown in Figure 2. A and B are the dynamic nodes representing the passageway's two ends.

Segment AB can be deemed as a simple tree, which is an EC. N1.1-B3 and N1-B3 are EC as well. If segment AB is treated as the FLEC and two grids as SLEC, we find that the network has all properties of 2-layer 1-IRS topologies. So we can apply the 2-layer 1-IRS procedure to find the shortest path between any two dynamic nodes on the network rails.

We call the SLEC with A as the CN EC1, and the SLEC with B as the CN EC2. After the node and arc labeling, the IRS interval information is as in Figure 3.

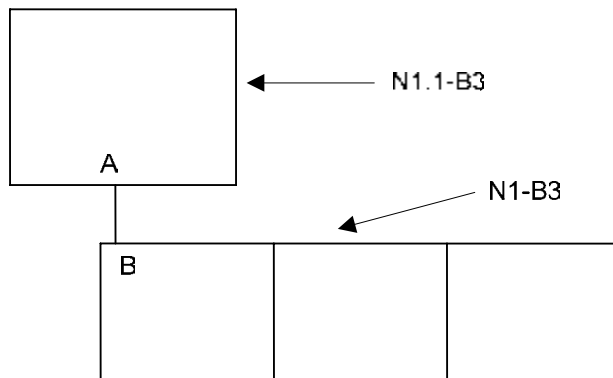


Figure 2: Example network topology

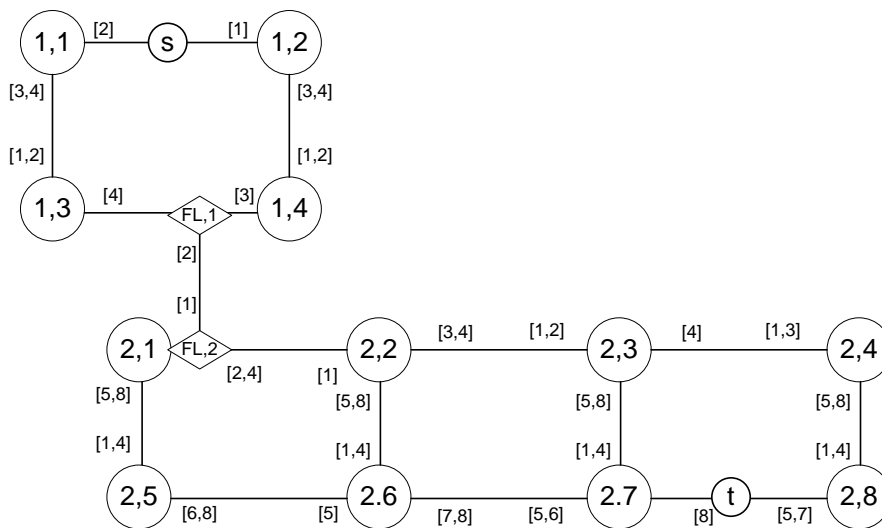


Figure3: 2-lay 1-IRS labelling

The label of a node contains the EC number followed by a 1-IRS node label. The FLEC is labeled as FL, which contains only two nodes. The interval for each arc is only effective within it's own EC and has nothing to do outside of it. If s and t are located in the way shown in Figure 3, the GN information of s and t are tested first. As GN of s (node (1,1) and (1,2)) are located in EC1, and GN of t (node (2,7) and (2,8)), s and t in different SLEC. Then the first part of the path is from s to the CN of EC1, which is node (FL,1). This part can be calculated by dynamic 1-IRS algorithm directly with the IRS interval information in EC1. The second part of the path is from t to the CN of EC2, which is node (FL,2). This part can be calculated by dynamic 1-IRS algorithm directly with the IRS interval information in EC2. The final part of the path is from EC1's CN to EC2's CN. This part

can be calculated by dynamic 1-IRS algorithm directly with the IRS interval information in FLEC. The final path is got by adding these 3 parts together. With the properties of the 2-layer 1-IRS topologies, this path is guaranteed to be the shortest path from s to t.

When s and t are located in one SLEC and the FLEC respectively, it's just a degenerate case of the above situation. And the procedure can be applied in a similar way.

And also note that, the node label includes two parts, the first one is the ECID and the second one is the id with the EC. A node has a first layer id, which is ECID here, and a second layer id, which is the labeling within the SLEC it's located in. That's where the term "2-layer" comes from.

7. CONCLUSION AND FUTURE WORK

In this research, the properties of 2-layer 1-IRS topologies are discussed. As this series of topologies appear frequently inside modern buildings, a systematic procedure on the basis of dynamic 1-IRS algorithms are developed to solve the shortest path finding problem. This procedure is a more effective alternative for Dijkstra's algorithm for 2-layer 1-IRS topologies in terms of computation complexity. Additionally, it can provide some other application potentials than Dijkstra's algorithm, such as real-time road guide and real-time road mark in virtual reality systems.

Computer networks and buildings' internal topologies often take similar high regular topologies. The reason may be that they are both artificial products of human minds, which prefer orderliness, standardization and easiness of reproduction. Due to the characteristics of computer networks, a variety of routing techniques have been applied very early. IRS has been applied to Euclidean networks recently. This research is an extension of this application from dynamic 1-IRS to 2-layer IRS technique. It's very likely that k-IRS can also be extended to 2 or more than 2 layer situations to deal with shortest path finding problem for more complex networks.

REFERENCES

- Beadle, H., Harper, B., Maguire, G. Jr., and Judge, J., 1997. Location aware mobile computing. In *Proc. ICT '97 (IEEE/IEE Int. Conf. on Telecomm.)*, Melbourne, Australia.
- Chen P. H. & Feng F., 2005. Path finding for real-time evacuation systems for large indoor areas. *22nd International Symposium on Automation and Robotics in Construction (ISARC 2005)*.
- Dijkstra E.W., 1959. A note on two problems in connection with graphs. *Numerische Mathematic*,1:269-71.

Gavoille, C., 2000. A survey on interval routing. *Theoretical Computer Science*, 245, 217-253.

Leeuwen, Van J., Tan, R. B., 1987. Interval routing. *The Computer Journal*, 30, 298-307.

Santoro, N., Khatib, R., 1985. Labeling and implicit routing in networks. *The Computer Journal*, 28, 5-8.

ASSESSMENT OF ADVERSE EFFECTS TO UTILITIES CAUSED BY MASS EXCAVATION

KONG GUANGYA, YANG WENYI, XIAO YI
Tiandi Science and Technology Co. Ltd, China
DR JEFFREY WANG
Tritech Consultants Pte Ltd, Singapore
e-mail: tritech@tritech.com.sg

ABSTRACT

It is always a critical problem for the designers and engineers to have accurate assessment of the status of the utilities, especially those settlement-sensitive utilities, namely the water mains and sewer lines around the excavation area. However, all those utilities are buried in 2 to 4m deep below the ground level and the actual conditions of the pipes and joints can not be easily inspected and assessed. When the settlement and differential settlement reach to some critical values, the sewer line and water mains will burst out due to the failure of pipe and joints and cause an unexpected failure of excavation. In addition, it is not possible to carry out the mass excavation to the same depth of the whole station box. The excavation depths are expected to be uneven and hence the induced ground settlement around the station box is not uniform even if the soil conditions are the same. As such, the differential settlement of the diverted water pipes is critical.

A back-analysis method is proposed focusing on the actual stress condition of the water pipes induced by the differential settlement along the pipe and advises in time to the engineers the status of the utility. The assessment is based on the actual settlement readings from the deep settlement markers along the pipes. The stress inside the pipes can be estimated solely on the basis of monitoring data without the additional information of excavation and soil conditions.

1. GENERAL

It is always a critical problem for the designers and engineers to assess the status of the utilities, especially those settlement-sensitive utilities, namely the water mains and sewer lines around the excavation area. However, normally those utilities are buried in 2 to 4m deep below the ground level and the actual conditions of the pipes, and joints can not be easily inspected and assessed. When the settlement and differential settlement reach to some

critical values, the sewer line and water mains will burst out due to uneven settlement caused by mass excavation.

Practically it is not possible to carry out various 2-D or 3-D analysis for the purpose of predicting the utility settlement profiles for unlimited possible excavation schemes. It is of importance to assess the actual conditions of the water pipes at every case. One of the practices is to impose a very stringent criteria of settlement and differential settlement, which can cover all the worst condition. However, this will inevitably cause the great difficulties and increase unnecessary cost, hence is considered insensible.

Back-analysis method introduced here focuses on the actual stress condition of the pipes induced by the differential settlement along the pipe and advises in time to the engineers the status of the utility. The differential settlement of the pipes can be obtained by installing the deep settlement markers and the back-analysis can be carried out at the time required. Hence the actual excavation scheme could be modified by the early planing, re-schedule as well as control of the progress of the work at any time according to the monitoring results of settlement along the pipes.

2 METHODOLOGY

As shown in Fig.1, the water pipe will deform as the ground settles. Assume settlements of pipes at points A, B, C be δ_A , δ_B , and δ_C respectively. For any type of deformed pipes, the general differential equation of the elastic curve is

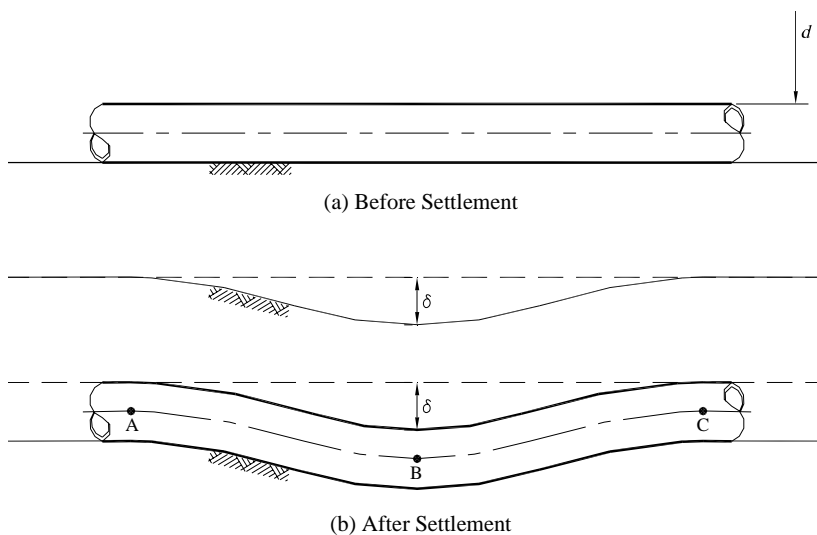


FIG. 1 UTILITY SETTLEMENT DUE TO GROUND MOVEMENT.

$$EI \frac{d^2y}{dx^2} = M \tag{1}$$

where

- M — bending moment of pipes;
- E — elastic modulus of the pipe;
- I — moment of inertia;
- y — settlement of pipe in respect to original location.

Assuming that total n numbers of deep settlement markers are installed to monitor the settlement of pipe, the deformed curve of pipes can be estimated on the basis of settlement readings at any time.

As shown in Fig.2, the deformed curve of pipes can be described as:

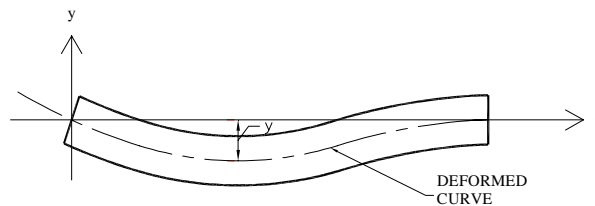


FIG. 2 DEFORMED BEAM AND THE COORDINATION SYSTEM.

$$y = y_0 + A_1x + A_2x^2 + \dots + A_nx^n \tag{2}$$

where x is the distance to reference point;

y is the settlement of pipes at x in respect to the original level.

At the point (x_i, y_i) , the monitored settlement is δ_i , namely $y_i = \delta_i$.

Substituting (x_i, δ_i) into Eq. (2), we have

$$\varphi_m(x) = \prod_{i=1}^m (x - x_i) \tag{3}$$

and

$$a_j = \prod_{i \neq j} (x_j - x_i) \quad (1 \leq j \leq m) \tag{4}$$

then

$$l_j(x) = \frac{\varphi_m(x)}{(x - x_j) \cdot a_j} \quad (1 \leq j \leq m) \tag{5}$$

and

$$y = \sum_{j=1}^m \delta_j \cdot l_j(x)$$

$$\begin{aligned}
 &= \sum_{j=1}^m \delta_j \cdot \frac{\prod_{i=1}^m (x - x_i)}{(x - x_j) \cdot a_j} \\
 &= \varphi_m(x) \cdot \sum_{j=1}^m \frac{\delta_j}{(x - x_j) \cdot a_j}
 \end{aligned}
 \tag{6}$$

The induced bending stress inside the pipe can be obtained from the followings

$$\begin{aligned}
 \sigma_{b\max} &= \frac{M}{\pi R^2 t} \\
 &= \frac{1}{\pi R^2 t} \cdot EI \frac{d^2 y}{dx^2} \\
 &= \frac{1}{\pi R^2 t} \cdot E \pi R^3 t \frac{d^2 y}{dx^2} \\
 &= ER \frac{d^2 y}{dx^2}
 \end{aligned}
 \tag{10}$$

The pipes may be subjected to internal pressure (Fig.3) and the correspondent tensile stress inside the pipes can be expressed as

$$\begin{aligned}
 \sigma_1 &= 0 \text{ (along pipe direction)} \\
 \sigma_2 = \sigma_t &= \frac{qR}{t}
 \end{aligned}
 \tag{11}$$

where σ_t is the tensile stress induced by internal pressure.

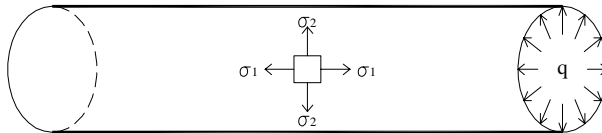


FIG. 3 INTERNAL PRESSURE OF WATER PIPE.

Under the combination effects of bending stress and tensile stress induce by deflection and internal pressure of pipe respectively, the failure criteria of pipe could be written as

$$\sigma_{b \max}^2 + \sigma_t^2 + \sigma_{b \max} \sigma_t = \sigma_y^2 \quad (12)$$

where σ_y — yield stress of pipe.

3 CASE STUDIES

Two cases studies are presented here to show the application of back-analysis method for assessment of water mains near mass excavation. One case is the assessment of stress level of water main at the particular date and the other is under worst settlement readings during the course of excavation. The project site is the construction of Serangoon Station box, north east line, Singapore. The station box requires mass excavation upto 22 to 25m below existing ground level. Water mains and sewer lines have been diverted as utility verges around the station box. The close distance of the utility verge to the soldier piles retaining wall is less than 1m. The diameters of water pipes range from 150mm to 800mm. As confirmed by the Authority of PUB, Singapore, the connections of water pipes are socket-type for those with max. 300 mm diameter and welded-type for those with more than 300 mm diameter. All materials of water pipes are composed of steel.

Due to the close proximity of the diverted utility verge, the mass excavation at Serangoon Station is expected to cause ground settlement with a magnitude up to 80 mm to 100 mm. This settlement of ground will inevitably cause the settlement of the utilities around. In addition, it is not possible to carry out the mass excavation to the same depth of the whole station box. The excavation depths are expected to be uneven and hence the induced ground settlement around the station box is not uniform even if the soil conditions are the same. As such, the differential settlement of the diverted water pipes is very critical.

The above described back-analysis method has been used for the assessment of the water pipes at Serangoon Station since the start of the excavation. The results of assessment has been submitted to Authorities and provided a fundamental and in-time information to the relevant parties. Meanwhile, the conclusions of the assessment have been verified through out the project.

3.1 Case 1- Assessment of stress level of water pipes for a particular date

A few of deep settlement markers have been installed along the utilities verges around Serangoon Station. The readings of settlement markers along the utility verge on the particular date is shown in Fig.4 and listed in Table 1.

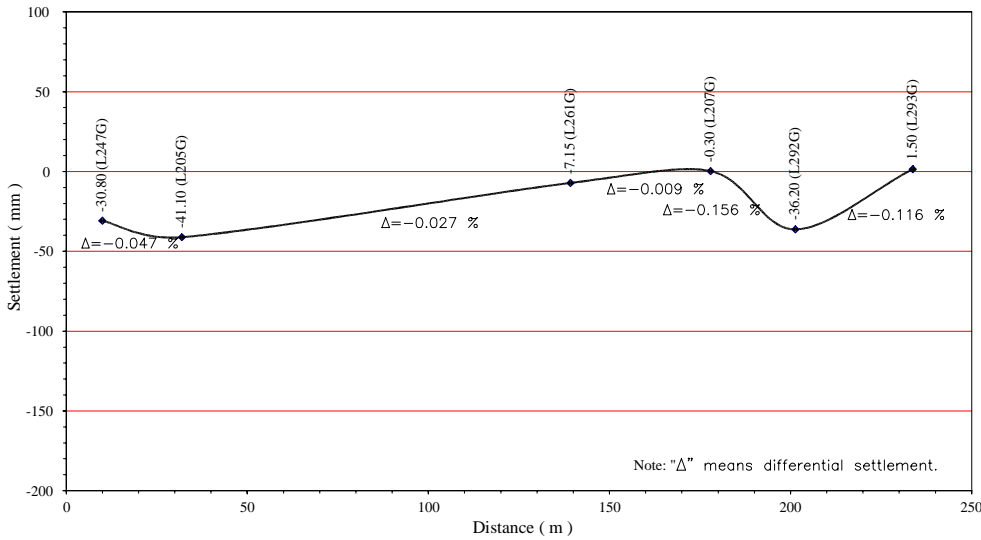


FIG. 4 SETTLEMENT PROFILE OF UTILITIES AT SERANGOON STATION.

Table 1 Monitoring Reading of Settlement Markers along utility verge on 27/8/1998 at Serangoon Station

No.	Utility Settlement Markers	Distance to L247 (G)	Monitored Settlement as per 27/8/1998
1	L 247 (G)	0.0 m	-30.80 mm
2	L 205 (G)	22.0 m	-41.10 mm
3	L 261 (G)	92.4 m	-7.15 mm
4	L 207 (G)	131.1 m	0.30 mm
5	L 292 (G)	154.6 m	-36.20 mm
6	L 293 (G)	186.9 m	1.50 mm
		x_i	δ_i

As described above, we can get the following on the basis of the above readings:

$$\begin{aligned} \sigma_{b_{\max}} &= ER \frac{d^2 y}{dx^2} \\ &= ER(7.2 * 10^{-10} x^3 - 1.8 * 10^{-7} x^2 + 1.22 * 10^{-5} x - 1.86 * 10^{-4}) \end{aligned} \tag{16}$$

The stress states inside the water pipes at Serangoon Station can be checked accordingly. The results of stress checking are listed in Table 2.

Table 2 Estimation of Stresses inside Water Pipes due to the excavation at Serangoon Station (as per 27/8/98)

Nominal Diameter of Pipes	External Diameter of Pipes	Thickness of pipe	Yield Strength Of Pipes	Maximum Internal Water Pressure	Elastic Modulus of Pipe	Induced Maximum Bending Stress
mm	mm	mm	N/mm ²	N/mm ²	kN/mm ²	N/mm ²
800(Steel)	825.9	8.0	275	1.2	205	5.46
700(Steel)	667.2	6.3	275	1.2	205	4.41
300(Ductile Iron)	326.0	7.2	420	1.2	205	2.16
150(Ductile Iron)	170.0	6.3	420	1.2	205	1.12

(Cont.)

Nominal Diameter of Pipes	Induced Maximum Tension Stress	Mises Combined Stress	Remarks
mm	N/mm ²	N/mm ²	
800(Steel)	61.94	64.85	O.K
700(Steel)	63.54	65.86	O.K
300(Ductile Iron)	27.17	28.31	O.K
150(Ductile Iron)	16.19	16.78	O.K

The results of assessment indicate that the maximum bending stress induced by the uneven settlement inside water pipe is only 5.46 N/mm², which are only 2% of allowable stress. The combined stress with consideration of settlement and internal water pressure is 63.5 N/mm², which is very much less than the allowable yield stress of 225 N/mm² and 420 N/mm² respectively. Hence, the actual stress conditions of the water pipes at Serangoon Station are judged to be safe with the monitored settlement. As matter of fact, no special action was taken after this conclusion was drawn and there was no abnormal phenomenon or burst out of water pipes observed.

3.2 Case 2- Estimation of stresses inside water pipes under the worst condition ($\delta_{max} = 100$ mm)

The worst case refers to the condition that due to the uneven excavation, the differential settlement reaches to the maximum values, which could occur. Table 3 is the assumed worst condition along the utility verge at Serangoon Station.

Table 3 Predicted Worst Condition of Settlement along Utility Verge at Serangoon Station

No.	Utility Settlement Markers	Distance to L247 (G)	Expected Maximum Settlement
1	L 247 (G)	0.0 m	0.00 mm
2	L 205 (G)	22.0 m	-100.00 mm
3	L 261 (G)	92.4 m	0.00 mm
4	L 207 (G)	131.1 m	-100.00 mm
5	L 292 (G)	154.6 m	0.00 mm
6	L 293 (G)	186.9 m	-100.00 mm
		x_i	δ_i

Similarly, we can get

$$y = 1.84 * 10^{-10} x^5 - 8.6 * 10^{-8} x^4 + 1.39 * 10^{-5} x^3 - 8.95 * 10^{-4} x^2 + 1.84 * 10^{-2} x \tag{17}$$

and

$$\sigma_{b\max} = ER(3.68 * 10^{-9} x^3 - 1.03 * 10^{-6} x^2 + 8.34 * 10^{-5} x - 1.79 * 10^{-3}) \tag{18}$$

The results of stress assessment are shown in Table 4.

From the above analysis, it can be concluded that under the predicted worst combination of utility settlement, i.e., maximum settlement of utilities reaches 100 mm, the induced stress due to bending and internal pressure is about 30% of the yield strength, which is still acceptable.

4 CONCLUSIONS

The back-analysis method makes use of the monitoring data from the settlement markers along the utility line. The stress inside the pipes can be estimated solely on the basis of monitoring data without the additional information of excavation and soil conditions. This method has been applied to Serangoon and Woodleigh Stations during the period of construction and it has been proven to be very effective and reliable.

Table 4 Estimation of Stresses inside Water Pipes due to the Excavation at Serangoon Station (Predicted Worst Conditions)

Nominal Diameter of Pipes	External Diameter of Pipes	Thickness of pipe	Yield Strength Of Pipes	Maximum Internal Water Pressure	Elastic Modulus of Pipe	Induced Maximum Bending Stress
mm	mm	mm	N/mm2	N/mm2	kN/mm2	N/mm2
800(Steel)	825.9	8.0	275	1.2	205	23.11
700(Steel)	667.2	6.3	275	1.2	205	18.67

300(Ductile Iron)	326.0	7.2	420	1.2	205	9.12
150(Ductile Iron)	170.0	6.3	420	1.2	205	4.76

(cont.)

Nominal Diameter of Pipes	Induced Maximum Tension Stress	Mises Combined Stress	Remarks
mm	N/mm ²	N/mm ²	
800(Steel)	61.94	76.17	O.K
700(Steel)	63.54	74.65	O.K
300(Ductile Iron)	27.17	32.70	O.K
150(Ductile Iron)	16.19	19.02	O.K

REFERENCES

REFERENCES

Land Transport Authority Singapore, 1996. *North East Line - Contract 704, Design Criteria*. Unpublished report, Singapore

Skempton, A. W., Mac Donald, D. H., 1956. *The Allowable Settlement of Buildings*, Proc ICE, Part III, 5, 727-784.

Burland, J. B., Wroth, C. P., 1974. *Settlements of Buildings and Associate Damage SOA Review*, Conference on Settlement of Structures, Cambridge, 611-654, Pentech Press, London.

ASSESSMENT OF BUILDING DISTORTION AND MOVEMENT AROUND THE EXCAVATION BOX

YANG WENYI, KONG GUANGYA
Tiandi Science and Technology Co. Ltd, China
DR JEFFREY WANG
Tritech Consultants Pte Ltd, Singapore
e-mail: tritech@tritech.com.sg

ABSTRACT

One of the problems associated with the ground settlement due to mass excavation is the impact to the adjacent building. The commonly used method to estimate the induced strains is the Deep Beam Model as recommended by Burland, J.B et al. (1974). When buildings on the shallow foundation affected by a settlement trough are assumed to follow the deformed ground at the foundation level. However, the buildings on piles will not deform with the same settlement profile of ground. It is difficult to use the deep beam method to estimate the distortion and tensile strains. Even though it is possible to assume that the settlement of the pile heads is equal to the settlement at certain depth of the piles, the accuracy and reliability of the estimated values is greatly influenced by the excavation depth, pile length as well as the distance of the piles to the excavation

The deep beam method has been extended to the piled foundation to assess the building deformation with consideration of details of excavation and strutting system, soil conditions and the distance. The application of the extended deep beam method indicates that the predicted values are in good agreement with the measured values. The conclusion drawn by the extended deep beam method, i.e. the buildings are basically safe during all the stages of construction, is verified by the facts of observation and monitoring for the buildings.

1. GENERAL

The commonly used method to estimate the induced strains is the Deep Beam Model as recommended by Burland, J.B et al. (1974). The building can be idealized as a beam with span L and height H deforming under central point load to give a maximum deflection δ . The height H is taken as the height from foundation level to the caves. The roof of the building is usually ignored. When buildings on the shallow foundation affected by a settlement trough are assumed to follow the deformed ground at the foundation level.

However, the buildings on piles will not deform with the same settlement profile of ground. It is difficult to use the deep beam method to estimate the distortion and tensile strains. Even though it is possible to assume that the settlement of the pile heads is equal to the settlement at certain depth of the piles, the accuracy and reliability of the estimated values is greatly influenced by the excavation depth, pile length as well as the distance of the piles to the excavation.

The following section will concentrate on the development of the method to estimate the distortion and tensile strains of buildings on piled foundation.

2 DEEP BEAM MODEL METHOD

As shown in Fig. 1, the building is supported by shallow foundation and the height of the building is H , length of building L (L_h in hogging zone and L_s in sagging zone). Then the bending strain ε_b and the diagonal strain ε_d can be expressed as recommended by Burland, J.B et al (1974).

$$\varepsilon_b = \frac{\frac{\delta}{L}}{\left(\frac{L}{12t} + \frac{3I}{2tLH} \frac{E}{G}\right)} \quad (1)$$

$$\varepsilon_d = \frac{\frac{\delta}{L}}{\left(1 + \frac{HL^2}{18I} \frac{G}{E}\right)} \quad (2)$$

where H is the height of the building;

$\frac{E}{G}$ is the relation between Young's modulus and shear modulus of the building;

L is the length of the considered building span;

I is the second moment of the equivalent beam height of the building at the respective zone: in sagging zone $I = H^3/12$ and in hogging zone $I = H^3/3$;

t is the furthest distance from the neutral axis to the edge of the equivalent beam at the respective zone: $t = H/2$ in sagging zone and $t = H$ in hogging zone;

δ is the maximum relative settlement at the considered span

$\frac{\delta}{L}$ is the ratio between the maximum relative settlement at the considered span and the length of this span.

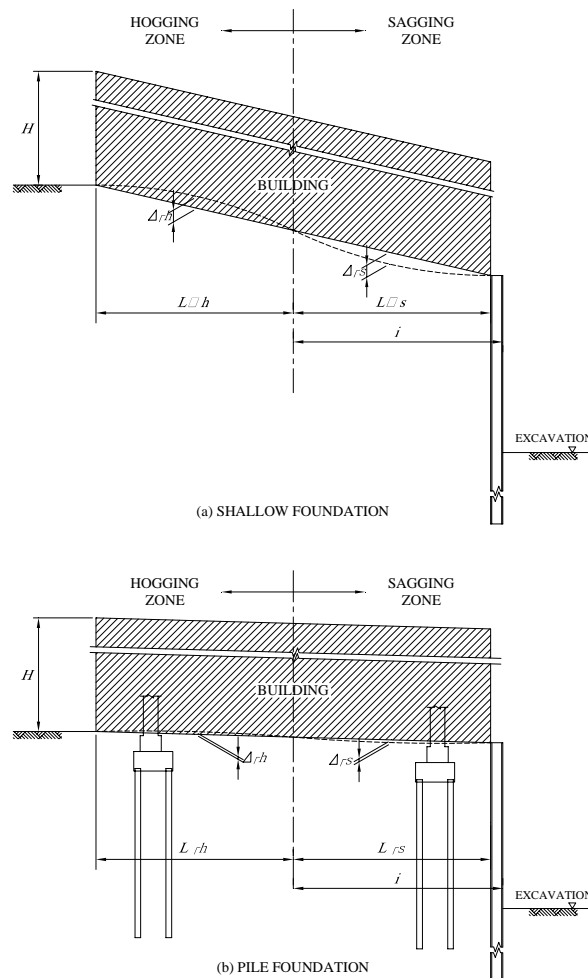


FIG. 1 GENERAL CASE OF A BUILDING AFFECTED BY A SETTLEMENT TROUGH.

The average horizontal strains ϵ_h for the respective sub-span (sagging and hogging) can be calculated by determining the horizontal movements at either end of a building span and the span length as below:

$$\epsilon_h = \frac{\delta_{h2} - \delta_{h1}}{y_2 - y_1} \tag{3}$$

where

δ_{h1} is the horizontal displacement at the beginning of the span;

δ_{h2} is the horizontal displacement at the end of the span;

y_1 is the distance from centre line to the beginning of a span;

y_2 is the distance from centre line to the end of a span.

The total horizontal strains can be estimated from the summation of the above two components:

$$\varepsilon_{bt} = \varepsilon_h + \varepsilon_b \quad (4)$$

Diagonal (shear) strains can be determined by making use of a Mohr's circle of astrain. If a tensile horizontal strain ε_h is induced in the building, a compressive strain of $-0.3 \varepsilon_h$ will be resulted in vertical direction (assuming Poisson's ratio of 0.3). With two points on the Mohr's circle ($\varepsilon_h, \varepsilon_d$) and ($-0.3 \varepsilon_h, -\varepsilon_d$), the circle can be obtained. The total diagonal strain ε_{dt} due to diagonal distortion can be calculated as:

$$\varepsilon_{dt} = 0.35\varepsilon_h + [(0.65\varepsilon_h)^2 + \varepsilon_d^2]^{0.5} \quad (5)$$

3 EXTENSION OF DEEP BEAM MODEL METHOD

As observed in most cases, the settlement of piled foundation due to excavation is mainly attributed to two parts, namely the settlement of pile toe and the settlement due to deflection of the piles.

$$\delta_{pi} = \delta_{toe} + \delta_{def} \quad (6)$$

where δ_{pi} is the total settlement of pile head (i) due to adjacent excavation;

δ_{toe} is the settlement of soil at the level of pile toe;

δ_{def} is the settlement of pile head caused by the horizontal displacement of foundation piles.

In case that the toe level of piled foundation is lower than the excavation level, δ_{toe} will be negligible. In case that the toe level of the piled foundation is higher than the excavation level, the settlement of pile toes can be estimated by proportion the ground settlement of soil according to the ratios of the pile length and the excavation depth.

It is difficult to estimate the pile head settlement due the horizontal deflection of piles induced by adjacent excavation. However, the elongation of the piles is negligible in comparison of the pile deflection. The pile head settlement can be reasonably assumed to be equal to the maximum deflection of piles caused by adjacent excavation.

$$\delta_{toe} = \delta_v \frac{H - L}{H} \quad (7)$$

and

$$\delta_{def} = \rho_{pile} \quad (8)$$

Where δ_v is the settlement of soil at the ground level of the considered pile location.

H is the excavation depth,

L is the length of pile,

ρ_{pile} is the maximum deflection of pile caused by excavation.

The pile head settlement at every location of piles could be estimated based on the method proposed by H. G. Poulos et al (1980), which takes into consideration of details of excavation, bracing and soil condition. After obtaining the settlement of pile head (i), the distortion and tensile strain of the buildings can be assessed by using Deep-Beam Method accordingly.

4 CASE STUDY ASSESSMENT OF POSSIBLE DAMAGES TO HDB BLOCKS AT SERANGOON STATION, NEL, SINGAPORE

In an urban environment such as Singapore, land available for infrastructure development is continually decreasing. As a result, more infrastructure are constructed underground. The construction of such underground space often entails excavating below existing grade down to depths of 20m or even more.

Serangoon MRT Station forms part of North East Line (NEL) in Singapore. The construction of the station box involved up to 25m deep mass excavation, braced by soldier piled retaining wall.

There are a few of HDB Blocks located at close proximity of Serangoon Station Box. Those adjacent buildings may be affected by the excavation work nearby. Instruments like building and column settlement markers, tape extensometers and tiltmeters were installed monitored continuously during the process of excavation.

As shown in Fig.2, HDB Blocks 412 and 413 are resting on the H pile foundation as indicated in Figs 3 and 4. Since the toe levels of the H piles are below the excavation level for concourse area, the settlement of pile toe due to excavation is negligible. The settlements of the Building Blk 412 and 413 have been predicted according to the method described above.

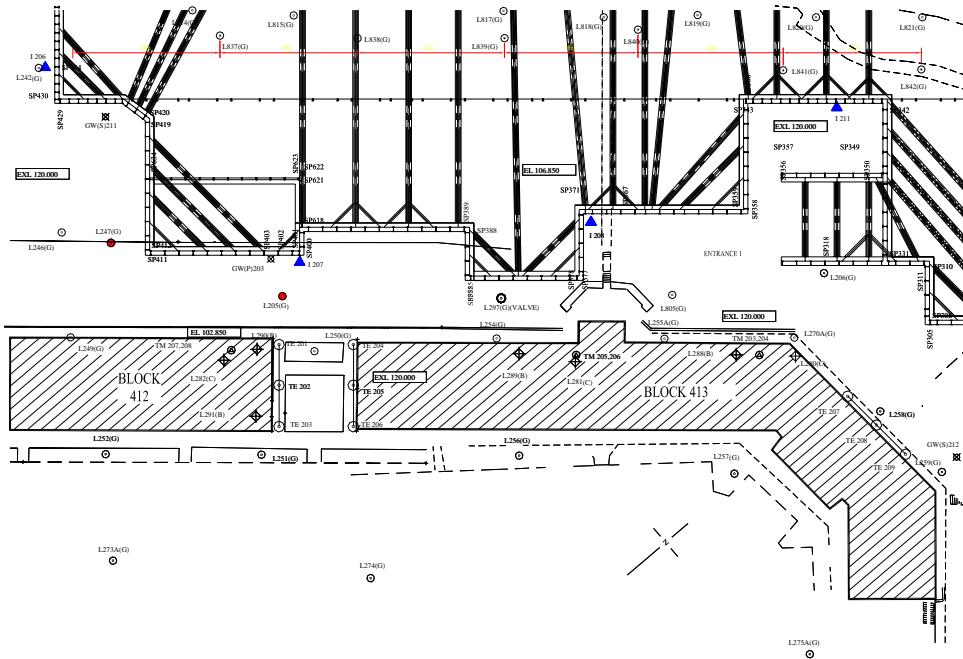


FIG. 2 HDB BUILDINGS AND RELEVANT INSTRUMENTS NEAR SERANGOON STATION

Table 1 is the comparison between the predicted building distortion by extended Deep Beam Method and the measured values. The distance of the building to the excavation, the stiffness of the soldier piles retaining wall, the spacing of the struts and the soil conditions are considered according to the method described above.

Table 1 Comparison between the Predicted and Measured Deformation of HDB Buildings at Serangoon Station

Buildings	Items	Instrument	Maximum Values	
			Measured	Predicted
BLK 412	Tensile Deformation	TE201-TE202	0.65mm	1.23mm
		TE202-TE203	1.32mm	1.12mm
	Inclination	TM207	0.03arc	0.01arc
		TM208	0.01arc	0.01arc
	Settlement	L290(B), L291(B), L282(C)	6.0mm	7.74mm
BLK 413	Tensile Deformation	TE204-TE205	0.9mm	1.27mm
		TE205-TE206	1.44mm	1.09mm
	Inclination	TM205	0.02arc	0.01arc
		TM206	0.03arc	0.01arc
	Settlement	L280(C), L281(C), L288(B), L289(B)	5.0mm	9.0mm

The results of comparison are satisfactory in view that the magnitudes of predicted and measured values are about the same. The predicted values are in good agreement with the measured values and the conclusion drawn by the prediction, i.e. the buildings are basically safe during all the stages of construction, is verified by the facts of observation and monitoring for the buildings.

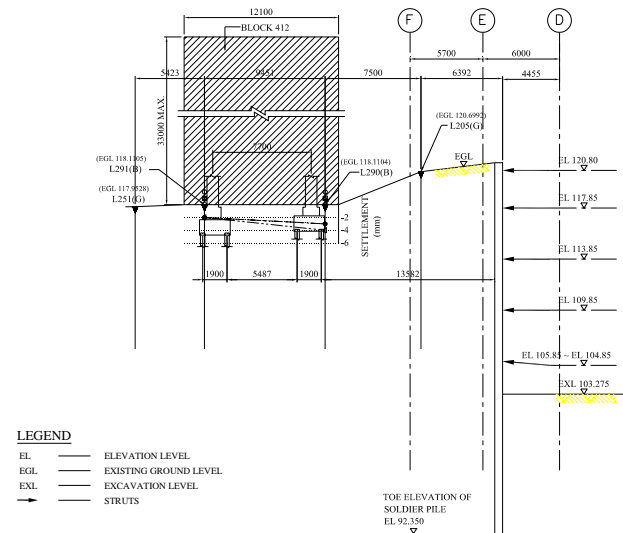


FIG. 3 TYPICAL SECTION OF BLOCK 412 IN RELATION TO EXCAVATION.

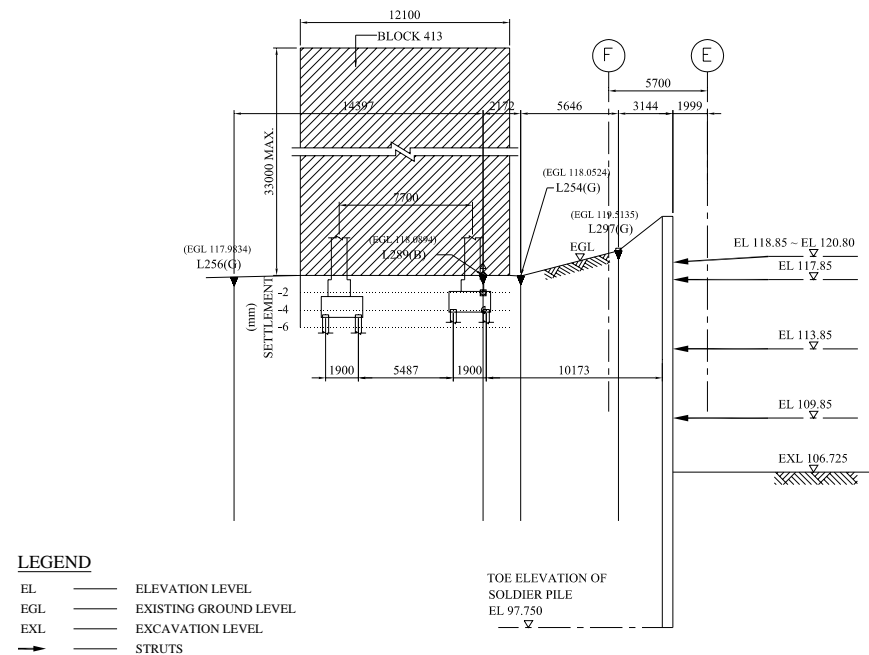


FIG. 4 TYPICAL SECTION OF BLOCK 413 IN RELATION TO EXCAVATION.

5 CONCLUSIONS

The deep beam method has been extended to the piled foundation to assess the building deformation with consideration of details of excavation and strutting system, soil conditions and the distance. The application of the extended deep beam method indicates that the predicted values are in good agreement with the measured values. The conclusion drawn by the extended deep beam method, i.e. the buildings are basically safe during all the stages of construction, is verified by the facts of observation and monitoring for the buildings.

REFERENCES

- Burland, J. B. and Wroth, C. P., 1974. *Settlements of Buildings and Associate Damage SOA Review*, Conference on Settlement of Structures, Cambridge, 611-654. Pentech Press, London.
- Peck Ralph. B, 1969. *Deep Excavations and Tunneling in Soft Ground*. State-of-Art Report. 7th ICSMF, Mexico City, Vol. 1, 156-167.
- Poulos, H. G., 1980. *Pile Foundation Analysis and Design*. John Wiley & Sons, New York.

UBIQUITOUS REAL TIME MONITORING AND ALERT APPLIED TO EXCAVATION WORKS

GUAN HONG TAN, YE KONG POH, MAX STRINGER
SysEng (S) Pte Ltd, SINGAPORE
syseng@singnet.com.sg

JAMES MW BROWNJOHN
UNIVERSITY OF SHEFFIELD, UNITED KINGDOM,
James.brownjohn@sheffield.ac.uk

ABSTRACT

As cities expand to Mega cities, new higher buildings, additional roads, expanded highway bridges and underground structures will be built to increase land utilization and transportation capacities. These trends increase the demand for the Ubiquitous Real Time Monitoring and Alert Systems of adjacent buildings and infrastructures to minimize the construction risks and insurance costs. In modern cities, the infrastructures for the Internet and Wire-less communications have more extensive coverage due to the consumer demands for Mobile phones and Internet access. Today Mobile Internet is already a reality for users to access information anytime and anywhere, a ubiquitous environment, such as news, share prices, games and emails. By leveraging this Mobile Internet infrastructure, sensors in any excavation work can be integrated into a Ubiquitous Real Time Monitoring and Alert system for monitoring structural and soil movements. With the shortening of construction schedules, work progresses continuously for 24 hours a day and 7 days a week. Hence the monitoring has to also follow with continuous Real Time Monitoring and Alert. With the Mobile Internet, the users can then have these mission-critical information deliver to their personal mobile devices such as Mobile Phones and Pocket PCs. Today wire-less networks are already common in businesses and homes to provide a ubiquitous experience, making this technology more acceptable to the more traditional construction industry. This ubiquitous information demand will fully automate the monitoring and alert systems to send the right information, to the right location, to right person to make the right decision for any actions to be taken. The paper will discuss the integrated multi-discipline system approach and the challenges in implementing an outdoor full-scale Ubiquitous sensor network used in the monitoring struts in excavation site.

Keywords: Ubiquitous Real Time Monitoring Alert M2M Wireless GPRS

1. INTRODUCTION

The transformation of cities to Mega cities will pose new challenges as old building will be replaced with new higher buildings, roads will be expanded with more highway bridges, and underground structures will be built to increase land utilization and transportation capacities. In all modern cities, the Internet and Wire-less communications infrastructures have more extensive coverage. This forms the basis to provide Ubiquitous Real Time Monitoring and Alert systems, as the same public infrastructure will now carry mission critical data from sensor to the end user mobile devices instantly. Today Mobile Internet is already a reality for user to access information anytime and anywhere globally, a ubiquitous environment, such as news, stock prices, games and emails. With the shortening of construction schedules, work progresses continuously for 24 hours a day and 7 days a week. Hence the monitoring has to also follow with continuous Real Time Monitoring and Alert. With the Mobile Internet, the users can then have these mission-critical information deliver to their personal mobile devices such as Mobile Phones and Pocket PCs. Wire-less networks are already common in businesses and homes to provide a Ubiquitous experience. This will fully automate the monitoring and alert system to send the right information to the right person to make the right decision for any actions to be taken. To provide the user with Ubiquitous environment, the whole information chain must be examine such that the entire information flow challenges can be analyzed from the sensor information until they reach the user mobile devices, for the sensor data upload and data download via wire-less means.

2. REAL TIME MONITORING AND ALERT SYSTEM

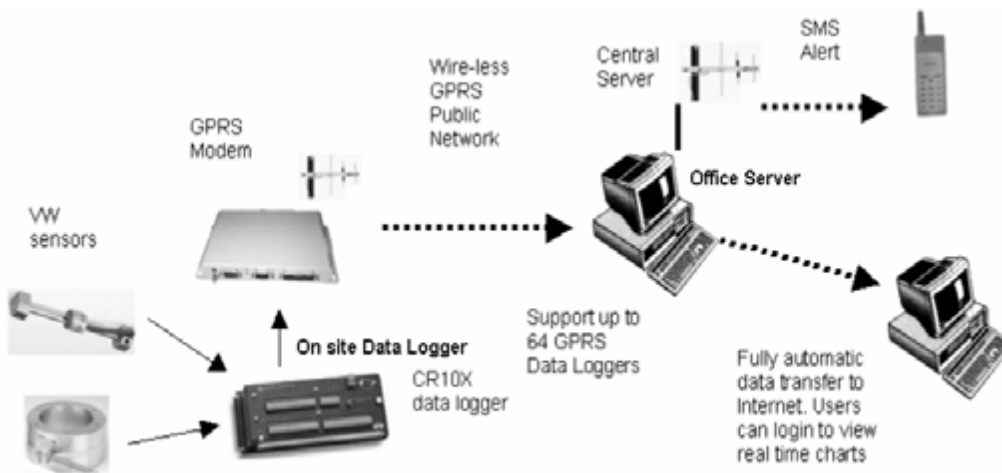


Fig 1. A typical Real Time Monitoring and Alert System

Vibrating Wire Strain Gages (VWSG) are installed at the struts to measure the strut forces. Data loggers are used for collecting VWSG data from construction sites continuously at every 10 minutes intervals and upload to a website. The Geotechnical and Structural designers require the data for analyzing the behavior of the construction sequence and system. The data from the same VSWG sensors from sites can now be shared. The site staff now can make real time judgment during the excavation process, where the reaction time is very short for remedial action. Figure 1 shows the Real Time Monitoring and Alert system described by Tan (2004) using Machine-to-Machine (M2M) technologies. In this system, a wire-less General Packet Radio Service (GPRS) modem is used to transmit the data from the data logger to the central server. GPRS is used as an always-connected wire-less communication system. In this system, the monitoring and alert response time is in the order of minutes time scale. Real time is only meaningful when the actual sensor readings are taken and then send to the end-users in minutes. Today, many real time systems narrowly define the time from when the data of the office computer is sending out to various end-users and it neglects the time delay, which could be in hours, when the VWSG sensor data uploads to central server.

The GPRS data speed is 32,000 bps, which is very much faster than the GSM of 9,600 bps. This makes it suitable for wire-less real time monitoring and alert systems. The cost for using GPRS network depends on the amount of data transfer. The data logger is always connected to the central server. Data can be transmitted between the logger and server immediately when the last channel of sensor is measured. Hence, there is no connection time delay. The information can then be access by multiple users through the Internet. Through the use of Infocomm Technologies (IT) and Internet technologies in instrumentation and monitoring, engineers and decision makers could access to the data from their desktops or notebooks from anywhere in the world as mentioned by Alaghebandian (2003) and Radulescu (2003).

3. THE CHALLENGES OF REAL TIME MONITOING AND ALERT SYSTEM

With Real Time Monitoring, the sensor data streams into the central server system at a high data rate. Traditional manual monitoring and alert system will experience user information overload if a manual EXCEL spreadsheet based system is used. The computer system will slow down and manually the user cannot cope up with the high data rate. Hence a fully automated information flow system is a solution to overcome such a challenge.

In a Real Time Monitoring site in a excavation site, the Real Time Monitoring and Alert system monitors 810 Vibrating Wire Strain Gage (VW SG) and 44 Load Cells readings every 10 minutes. Two VW SGs monitor a strut with its individual temperature sensor and the Load Cell has 4 VW SGs and 1 Temperature sensor. Hence there is a total of 810 VW+ 810T + 44 x 4 VWSG + 44 T = 1,840 sensor readings per 10 minute measurement cycle. The data rate is then $1840 \times 6 \times 24 = 264,960$ data points per day. In an

EXCEL spreadsheet system, the system will be overloaded. One solution to overcome EXCEL limitations is to use a more efficient software development platform such as C.

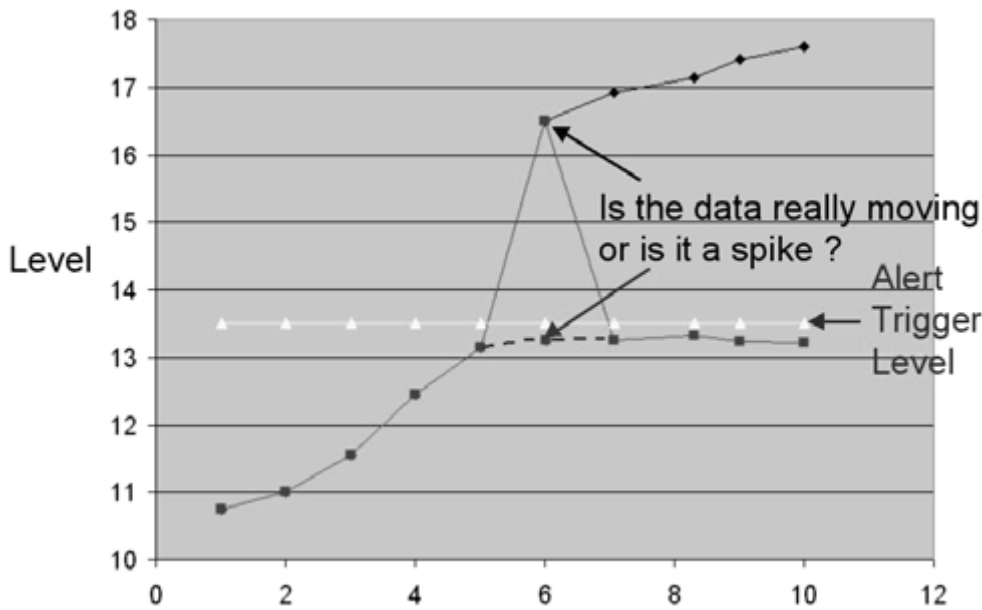


Fig 2. Sensor Level movements in time sequence

At high-volume data rate in the real time system, any sensor noise or intermittent failure will cause unnecessary alerts. Fig 2 shows sensor level movements in time sequence. In Real Time Monitoring system, when the sensor level exceeds the Alert Trigger Level, SMS will be sent out. However, if the sensor data only exceeds this threshold only once, it is most likely that this sensor reading contains false readings caused by noise. But on the other hand, if the sensor readings maintain above the Alert Trigger limit, then the sensor reading must trigger an SMS alert. With a manual system, the amount of data is insufficient and slow to provide a re-confirmation within minutes that there is a trigger alert as the manual data collection and analysis cycle time is usually in the order of hours. There is a need for a Monitoring System Design Strategy to overcome false alert and prevent user overload. In a manual system where the readings are done twice per day, there will be 3,680 readings per day. A 0.1% false reading means 4 false alerts. For the same 0.1% false readings in 264,960 real time data, it will mean 265 false readings, which are unacceptable for Quality data. Using a Real time monitoring and alert system will improve the Quality standards of the instrument service provider, as the user will have higher quality expectation in the whole process of sensor installation, cabling, grounding, system setup, commissioning and monitoring.

A monitoring system deployed by the authors were used in an excavation site over 18 months and had 143,078,400 VWSG data collected. The total false alert readings over that period was 1,203 and they were mainly in the

initial stage of familiarization by the contractor. This works out to be 8 false readings per million readings as a Data Quality index. As the sensors and electronics are used in outdoor environment, noise is a perpetual problem causing false SMS alerts. Noise can cause the sensor readings to increase or decrease from their actual values. Hence the alert levels have upper and lower bounds assigned to each sensor.

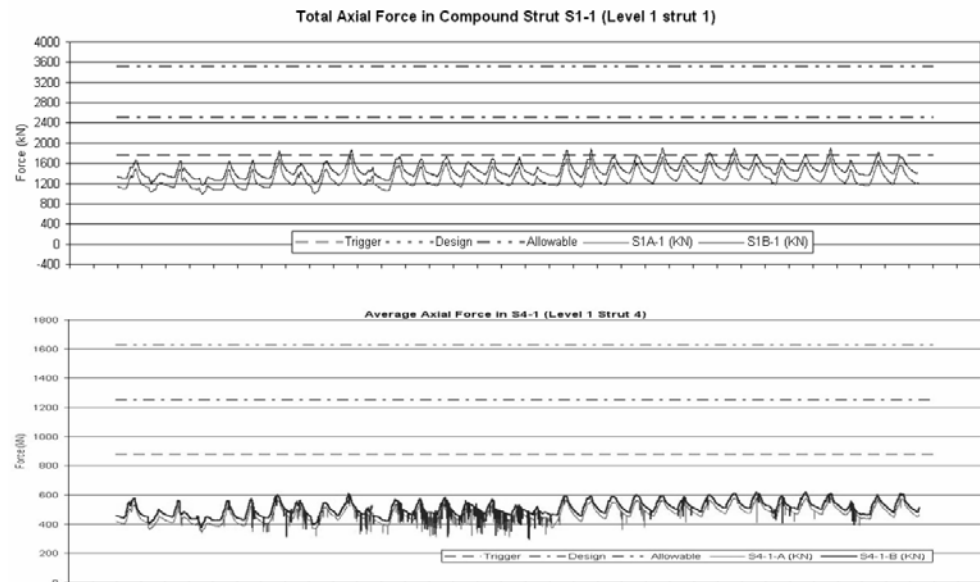


Fig 3. Strut forces time series readings over days

Field results of Fig 3 from a site show that the VWSG readings for strut at Level 1 strut 1 have very clean readings while for those strut at Level 1 Strut 4 shows noisy VWSG readings. By compressing the time scale, these strut force readings have now been interpreted as a waveform for signal analysis where the rules of digital signal processing come into consideration. Traditionally when the user takes only a few reading per day, such time series information is not available for analysis.

At every 10 minutes, the sensor readings stream to a central server in continuous. If there is a trigger event as shown in Fig 4. The system will send SMS alerts, but that point which exceeds the trigger value might be a true reading or a false trigger caused by noise. After that trigger and if the next measurement cycle exceeds the trigger limit, then the site engineers take it with more attention. However if the next cycle, the sensor readings drop, then it is classified as a false trigger. Various smart alert algorithms can be used but however the choice is always by the end users.

By integrating the sensors into the Ubiquitous environment, it requires a cross-disciplinary engineering team, which has to understand each other's objectives, constraints, risks and maintenance effort in the system. The engineering skills from the domain expertise of Structural and Geotechnical, Electronics, Communications and Software to design and maintain the system through out the entire life span of the project.

4. UBIQUITOUS ENVIRONMENT FOR DELIVERING DATA INTO THE HANDS OF THE END USERS

In Fig 1, the users receive SMS text alerts on their mobile phones and they require a PC connected to the Internet to view and analyze the sensor historical trend. Fig 4 shows the SMS Alert text message while the time chart data is taken from a PC website screen shot. By linking the server data to the new generation of Mobile phones and Pocket PCs, which have larger graphical displays, the sensor charts can now be delivered as shown in Fig 5. Both mobile devices are growing tremendously and this platform makes it easier for the sensor data to be delivered in the Ubiquitous environment on the same unit.

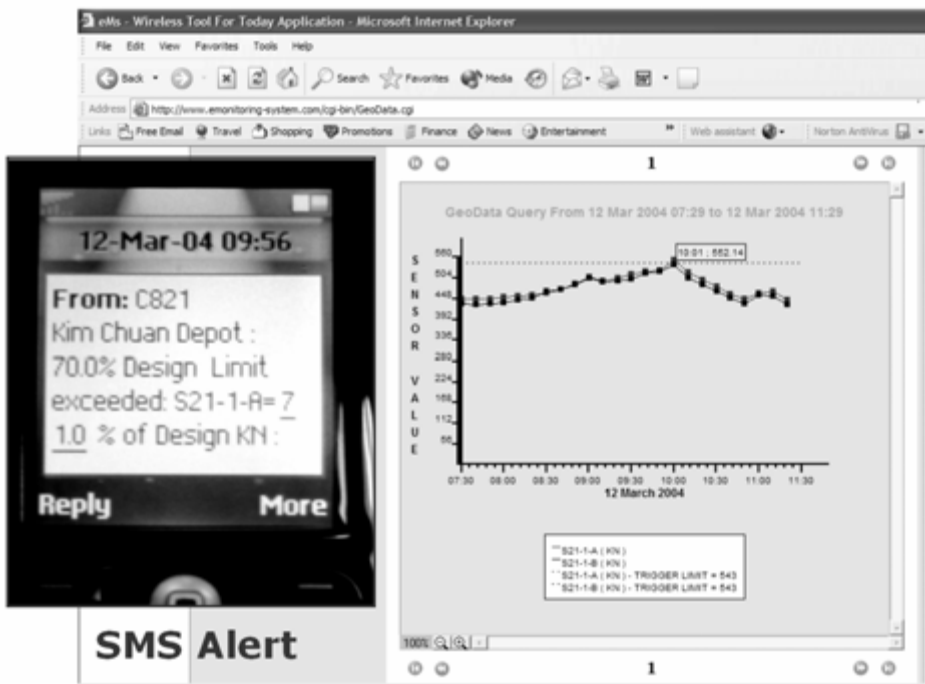


Fig 4 SMS Alert on a mobile phone and screen shot of a PC Internet Web interface



Fig 5 Crack sensor time chart displayed on an Ericsson Mobile phone and a HP iPAQ Pocket PC

5. BENEFITS OF UBIQUITOUS REAL TIME MONITORING AND ALERT SYSTEM

The main advantage of the Ubiquitous Real Time Monitoring and Alert system is obviously the Real Time alert where the site staff gets urgent data instantly when sensors exceed their limits. The other benefit is to provide the users and designers the actual on-site forces acting on the struts when construction works progresses. This increases the productivity of the Geotechnical consultants by having their verification of the design via the Internet instead of visiting the site, which could be hours drive away. The data is also shared with multiple users and this makes collaborative work easier across the globe. This brings the important site data into the hands of the users via wire-less communication technologies of Mobile Internet, hence reducing the unproductive time of traveling to site to retrieve data or requiring a PC for data access. It also helps to raise the Data Quality standards as it impose new challenges to provide Reliable Data timely to all stake holders of the project.

6. CONCLUSION

Data Loggers have been used in monitoring systems for many years, especially for projects, which required continuous monitoring. They are mainly used for design verification, monitoring, investigation works and research. Using M2M technologies of wireless communications, Mobile Internet devices and services, these monitoring systems have evolved into a Ubiquitous Real Time Monitoring and Alert systems, where the information are needed in a matter of minutes rather than hours at any time and anywhere. Using available proven technologies, Mission Critical Real Time Monitoring and Alert systems are used to monitor and deliver information from the sensor until the end users in minutes. When the sensor readings exceed their predefined limits, the system automatically sends SMS alerts to multiple users within minutes. The Ubiquitous system delivers the important information onto the mobile devices of the users. This compression of the total delivery time, from the remote site sensor to the user, is useful to inform site problems immediately for critical projects so that preventive actions can be mobilize faster. It gives users more reaction time to organize, to investigate and to prevent collapses or failures rather than having data to confirm that the site had problems. With the wider acceptance of Mobile Internet technologies by the consumer sector, the relevant technologies have become easily accessible for wider deployment in the civil engineering sector. This forms a new cluster of Ubiquitous mission critical monitoring and real time alert systems based upon the M2M technologies.

REFERENCES

Tan G.H. Ng T.G. and Brownjohn, J. ,2004. Real Time Monitoring and Alerts Systems for Civil Engineering Applications using Machine-to-Machine Technologies, *International Conference on Structural and Foundation Failures*, 2 – 4 August 2004.

Alaghebandian, A., Abe, M. and Fujino, Y.,2003. An Internet Orientated Platform for Structural Health Monitoring, *Proceedings of First International Conference on Structural Health Monitoring and Intelligent Infrastructure*, 13-15 November 2003, Tokyo, Japan, pp. 339-344.

Radulescu, D.C., Radulescu, C. and Sereci, A.M. ,2003 Structural health monitoring 24/7 broadcasting system, *Proceedings of First International Conference on Structural Health Monitoring and Intelligent Infrastructure* 13-15 November 2003, Tokyo, Japan, pp. 971-976

COMPUTATIONAL FLUID DYNAMICS SIMULATION OF THERMAL BEHAVIOR UNDER WORKING WATER SCREENS IN A TUNNEL

DR. REIKO AMANO

The University of Tokyo Visiting Professor

Kajima Corporation, Tokyo, Japan

amanor@iis.u-tokyo.ac.jp

DR. HITOSHI KURIOKA, OSAMU IMAZEKI

Kajima Corporation, Tokyo, Japan

ABSTRACT

Recently, research using Computational Fluid Dynamics (CFD) on the flow fields and temperature fields of various fire phenomena has been progressing. CFD is a practical analysis tool for most fire phenomena. In this research, both actual experiments using a 1/2 scale tunnel and numerical analysis by CFD were carried out in a tunnel, and both sets of results were compared. The fire experiments were performed using the 1/2 scale tunnel equipped with water screens.

CFD analysis of the fire field, when water screens are activated, was carried out using measured heat release rates. When the water screens are working, the inside of the tunnel is sectioned by the water screens. The heat flow generated from a fire source is cut off by the water screens, and circulates around the inside of the section.

1. INTRODUCTION

Since heat and smoke caused by a fire rapidly permeate the whole of an enclosed underground space, in general, it is necessary to partition a fire zone in order to prevent any occupants from being overwhelmed by heat and smoke when taking refuge. We have proposed a water screen partitioning technology (hereafter referred to as WS) which can cut off the flame and smoke using water screens made by spraying water from sprinkler heads arranged in a line at certain intervals on the ceiling of the partitioned boundary. It may well be that this will be applied as one of the new fire prevention technologies for deep tunnels.

In order to estimate the efficiency of the fire prevention section with the WS, fire experiments using a 1/2 scale tunnel model have been carried out for the understanding of thermal behavior in any closed underground space. The experiments are excellent so far as the grasp of physical phenomena is concerned. However, there are environmental problems in carrying out the experiments as well as high labor and material cost.

Furthermore, studies on the effects of such various factors as the variation in tunnel shape, the direction and shape of a fire source and any ventilation system are restricted by cost and time. Therefore, in the experiments using this water sprinkling system there are many factors that are difficult to measure. Also, it is often difficult to conduct flow visualization tests for understanding the behavior of thermal flow.

On the other hand, the numerical simulations carried out by the computational fluid dynamics (hereafter referred to as CFD) can rapidly and quite universally grasp the behavior in the fire field caused by changes in the conditions. CFD is a useful tool for solving the problems in experiments due to the fact that the flow visualization can be made using computer graphics. Recently, studies¹⁾⁻³⁾ on the application of CFD to fire phenomena have been developed and it is now in the stage of practical use in the research and development field. Kawabata et al. reported on an investigation into a tunnel fire simulation using a turbulent model LFS. With regard to the LFS code with a water drop model built-in in the case of water sprinkling equipment working, the Building and Fire Research Laboratory belonging to the National Institute of Standards and Technology (NIST) of the Department of Commerce in U.S.A developed a fire dynamic simulator (hereafter referred to as FDS)⁴⁾.

This study aims at confirming the practicality of the CFD when water sprinkling equipment such as WS is activated. This paper reports on the comparison between the results of the fire experiments and the FDS simulation results.

2. EXPERIMENT METHOD⁵⁾

2.1 Road Tunnel Model

The experiments were carried out in a large space facility with a height of 25m, a breadth of 25m and a length of 120m. A 1/2 scale box type model of a submerged tunnel of the first AA class in the Road Standards was used in the experiments. This model is 2.7m high, 5.4m broad and 18.2m long. The model was placed in close vicinity to the wall of the large experimental facility. Partitioned boundaries were installed near both openings of the model. Water sprinkler heads used for the WS were fitted to the ceiling in two lines at an interval of about 1.6m. 5~6 heads were installed in each line at intervals of 1.0m in a zigzag pattern.

2.2 Establishment of the Fire Source

The heat release rate (Q model) was established at 1.5MW by taking into account the reduced scale ratio of the model for the fire source⁶⁾ under the assumption of 7m for a spatial height of the actual tunnel and large-sized automobiles such as vans (corresponding to 15MW).

Altogether, 23.3l n-heptane mixed with 5% toluene for visualization was burnt over a 10 minutes period on a circular plate (diameter of 1000mm × height of 200mm) placed on the floor at the center of the model.

2.3 Measurements

The temperature in the vicinity of the ceiling was measured at intervals of 5 sec using sheath K type thermocouples with a diameter of 1.6mm. Fig.2-1 shows the experiment model as well as the installation positions No.1~No.16 for the thermocouples. The thermocouples were installed at points 50mm under the ceiling at intervals of 1.0m along the center of the model in the longitudinal direction.

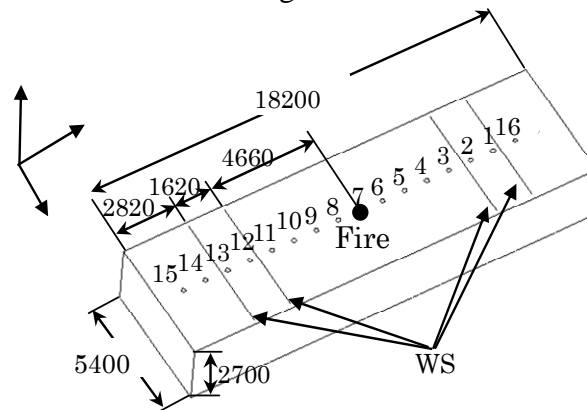


Fig.2-1 Model used for the experiments

2.4 Experiment Cases

Experiments subjected to the simulation were carried out in case 1 (where the WS was not activated) and case 2 (where the WS was activated). As shown in Fig.2-1, the fire source was placed right under the thermocouple No.7. The WS were arranged in two lines at places 4.66m and 6.28m away from the fire source in a zigzag pattern. The specifications of the WS are as follows:

The number of sprinkler heads on one side: 11, Flow volume: 10l/min (total for both sides 220l/min), Spraying angle: 170~180°, Mean diameter of Sauter: 200 μm

2.5 Heat Release Rate

From the weight decrease value per unit time and the theoretical unit calorific value for the fuel, obtained from the measurement of the weight of combustibles as well as the amount of water that had dropped into the plate using a load cell located under the plate, the heat release rate was obtained by equation (2-1). It is assumed that during a burning period the evaporation of the water is restrained by a film of the fuel (n-heptane).

$$Q = q \left(\frac{\Delta G}{\Delta t} - w \right) \quad (2-1)$$

Where Q: Heat release rate [kW], q: Unit calorific value [kJ/kg], $\Delta G/\Delta t$: Quantity of weight decrease of fuel per unit time [kg/s], w: Increased water volume caused by the water spraying equipment [kg/s]

By using this heat release rate, a simulation of a fire's behavior was carried out. Fig.2-2 illustrates the time variation in the heat release rate. In case 1 where the WS is not activated, the value for the heat release rate reaches 1000kW in about 120sec and attains to the maximum value in 300sec. In case 2 where the WS was activated after 90sec, the heat release rate showed almost constant values about 180sec after the water was sprayed.

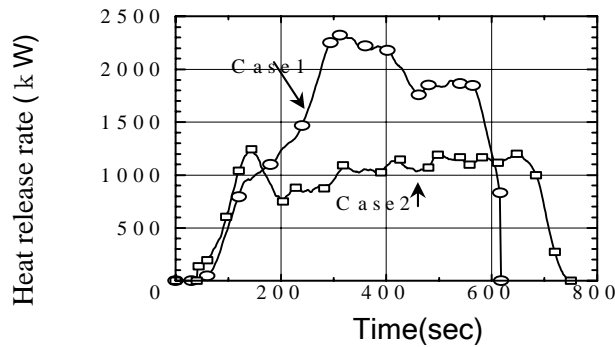


Fig.2-2 Time variation in heat release rate

3. NUMERICAL SIMULATIONS

Numerical simulations were carried out by giving the same conditions to the experimental facility and the heat release rate. The characteristics of the FDS used for the computations are described below.

3.1 Dominant Equation and Discrete

A physical phenomenon is dominated by 5 equations: conservation of mass, conservation of chemical species, conservation of momentum (Navier-Stokes), conservation of energy and equation of state.

3.2 Physical Model

A LES made by the standard Smagorinsky model is used for dealing with turbulence phenomena in the FDS. The correspondence of the heat transfer rate to the material diffusion coefficient of chemical types and turbulent viscous coefficient is expressed as a 0 equation model using the Prandtl number Pr and Schmidt number Sc .

In the simulations, the Smagorinsky constant, the Prandtl number and the Schmidt number were set to be $C_s=0.2$, $Pr=0.5$ and $Sc=0.5$ respectively. The combustion model is a mixture fraction model which burns in an instant when fuel meets with oxygen. Therefore, this model is made so that fuel and oxygen can not exist simultaneously. Furthermore, with consideration to the heat radiation, a radiation transportation equation for a medium radiating absorbed heat is to be solved using a finite volume method. As for the drops of water sprayed from the WS, the combination of the Rosin-Rammler distribution and a logarithmic normal distribution is used for the particle size distribution. The effects of the waterdrops on the thermal flow are considered as the external force term f of the Navier-Stokes equation. The water which drops on the floor is eliminated from the

computation domain. Further details of the physical model can be referred to in the theory manual attached to the FDS⁴⁾.

3.3 Computation Conditions

(a) Partitioning of the Grid

The computation domain is a box type space with the same dimensions as those for the 1/2 scale experiment model. It has a height of 2.7m, a breadth of 5.4m and a length of 18.2m. The numbers of cells for the equally spaced orthogonal grid are 36 in a vertical direction, 36 in a sectional direction and 108 in a longitudinal direction. There are 139968 grid cells in all.

(b) Initial Condition and Boundary Condition

As the initial condition in the whole domain, the speed was set to be 0m/s and the temperature was set at 14°C that is equivalent to the value for the experiments. N-heptane was used as fuel for the fire source which was set at the floor center in the same manner as that in the experiments. The shape of the fire source with the same area as that for the experiments was formed to be a square because the orthogonal grid was used. In respect of the heat release rate, the value obtained from the experiments was used. The heat release rate was linearly interpolated at intervals of 60sec. The speed boundary condition for the wall was set to be a half-slip and the temperature boundary condition was insulated. As for the condition of the entrance of the tunnel, the boundary pressure fluctuation at the air exhaust boundary was established to be zero and the atmospheric release condition assuming the space at infinity being zero was applied to the air supply boundary.

(c) Condition of the WS

The values for the volume of water flowing from the WS, its working pressure and the Sauter averaged particle size were set to be equivalent to those for the experiments. The WS was activated 90sec after the start of combustion in the same manner as that for the experiments.

4. CONCLUSIONS AND EXAMINATIONS

In this paper, it was investigated whether or not the FDS has reached the stage of practical use as a tool for estimating fire performance. The value measured in the model experiments and the value computed by the FDS were compared with each other using the moving average value obtained from 15 points; first 7 points and last 7 points for each.

4.1 Simulations in the case of the WS not being activated

(a) Temperature Behavior of the Ceiling near the Fire Source

Fig.4-1 illustrates the temperatures measured in the vicinity of the ceiling near by the fire source. No.6, No.7 and No.8 in the figure correspond to the number of the thermocouple installed in the tunnel model shown in

Fig.2-2. The measurement point No.7 is located right above the fire source and No.8 as well as No.9 is 1m away from No.7. The temperature at No.6 is higher than at No.7 in the range from about 160sec up to 450sec. It can be thought that the flame inclines toward No.6. This is so due to the fact that the model was installed close to the wall of the experiment facility, a difference occurred in the amount of the air flowing in from both openings of the tunnel model. An inclination of the flame was observed in the experiments. On the other hand, in the computation the flame does not incline due to the same condition of both openings of the tunnel.

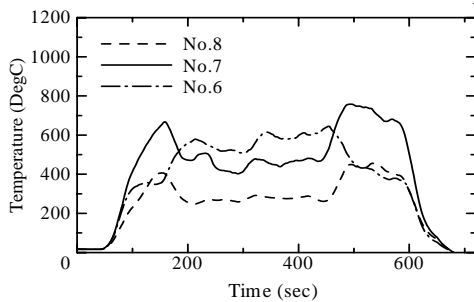


Fig.4-1 Variation in the measured temperature in the vicinity of the ceiling near the fire source (in the case of the WS not being activated)

Fig.4-2 illustrates the variation in the temperature measured at No.7 just above the flame (Exp in the figure) and computed temperature (FDS). It can be seen in the time variation in the computed temperature that an increase in the temperature is caused by the heat release rate given and that it reaches the maximum value at about 300sec. Then, the temperature falls at about 600sec. The computation results simulate quite well the actual measurement results in the time range up to 160sec at which the flame inclines. The measured temperature is lower than the computed temperature after about 160sec because the flame inclines.

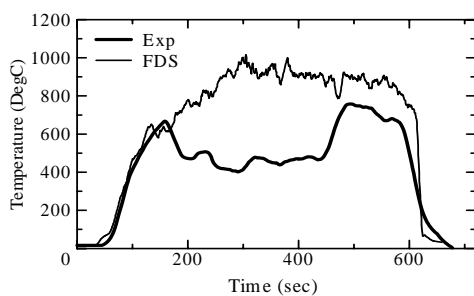


Fig.4-2 Variation in the measured temperature and the computed temperature (No.7) (in the case of the WS not being activated)

(b) Behavior of the Ceiling Temperature at the WS Installation Side

Fig.4-3 shows the changes in the measured temperature and the computed one at No.5 located 2m away from the fire source. Figs.4-4 and 4-5 illustrate the variation in the measured temperature and the computed one at No.3 and No.16 respectively. No.3 is located at a place before the WS installation position (on the fire source side) and No.16 is on the opening side that is beyond the WS position. Compared with the measured temperature, the computed temperature is slightly higher, but almost the same behavior is discernible in both temperatures.

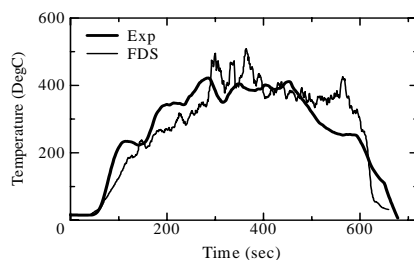


Fig4-3 Variation in the measured temperature and the computed temperature (No.5) (in the case of the WS not being activated)

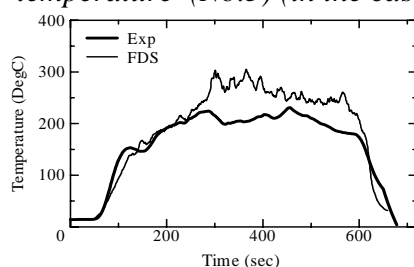


Fig.4-4 Variation in the measured temperature and the computed temperature (No.3) (in the case of the WS not being activated)

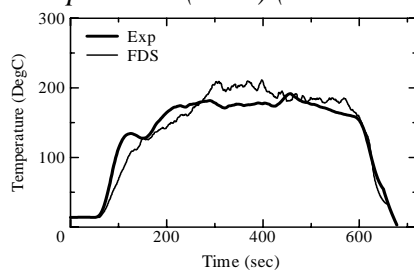


Fig.4-5 Variation in the measured temperature and the computed temperature (No.16) (in the case of the WS not being activated)

4.2 Simulation in the case of the WS working

(a) Behavior of the Temperature at the Ceiling near the Fire Source

Fig.4-6 illustrates the variation in the measured temperature in the proximity of the ceiling near the fire source. The temperatures at No.6 and No.8 both of which are 1m away from the fire source are lower than at No.7 located right above the fire source. The temperature behavior at No.6 is almost equal to that at No.8. It can be judged from this that the flame developed vertically in a different manner from that in the case of the WS not being activated. Fig.4-7 shows the change in the measured temperature and the computed one obtained at No.7 just above the fire source. The computed result simulated quite well the measured result.

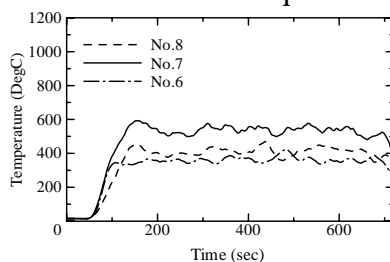


Fig.4-6 Variation in the measured temperature in the vicinity of the ceiling near the fire source (in the case of the WS being activated)

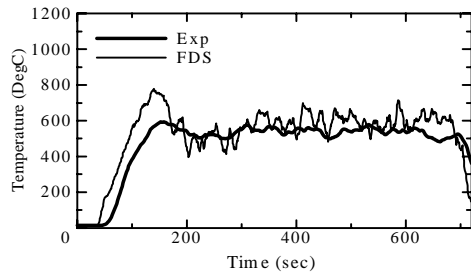


Fig.4-7 Variation in the measured temperature and the computed temperature (No.7) (in the case of the WS being activated)

(b) Behavior of the Temperature at the Ceiling on the WS installation Side

Fig.4-8 illustrates the variation in the measured temperature and the computed one at No.5 located 2m away from the fire source. The behavior of the computed temperature simulates well that of the measured temperature. Figs.4-9 and 4-10 show the changes in the measured temperatures and the computed ones at No.3 located on the near side of the WS (on the fire source side) and at No.16 located beyond the WS (on the opening side) respectively. At any measurement point, the computed temperature simulates quite well the behavior of the measured temperature. The whole behavior of the computed results obtained using the thermocouples arranged in the front and rear of the WS at No.3 and No.16 correspond very well to the behavior of the measured results. It is clear from this that the behavior of the waterdrops as well as the amount of heat and the momentum which are exchanged between flow fields are well understood.

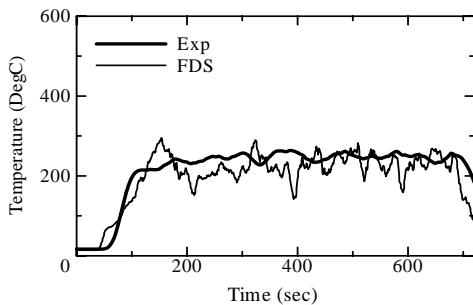


Fig.4-8 Variation in the measured temperature and the computed temperature (No.5) (in the case of the WS being activated)

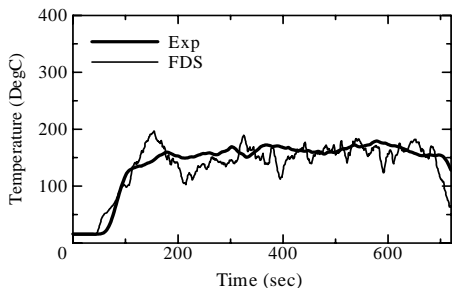


Fig.4-9 Variation in the measured temperature and the computed temperature (No.3) (in the case of the WS being activated)

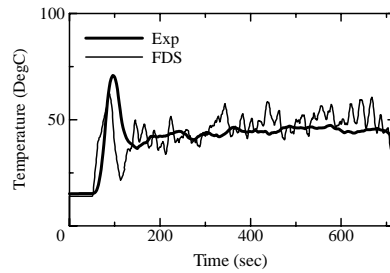


Fig.4-10 Variation in the measured temperature and the computed temperature (No.16) (in the case of the WS being activated)

4.3 Visualization of Flow and Temperature

Fig.4-11 shows the vector of the air flowing from the fire source position through the opening of the tunnel when the WS is not activated. The flow vector in the case of the WS working is shown in Fig.4-12. The vector figure indicates the resultant sum vector values for the flow speed in directions X,Y and Z. Both figures show the results obtained from the visualization of the central cross-section composed of a sectional direction and a vertical direction.

(a) Results in the case of the WS not being activated

When the WS is not operated, fire plumes generated from the fire source reach the ceiling surface and form a high temperature layer as a ceiling jet, which flows out through the upper part of the opening. Furthermore, the air flowing into the tunnel through the lower part of the opening is caught in the fire plumes in the vicinity of the fire source, and a large convective flow is formed. As a result, it can be seen that a thermal profile with a high temperature layer in the upper part and a low temperature in the lower part has been produced.

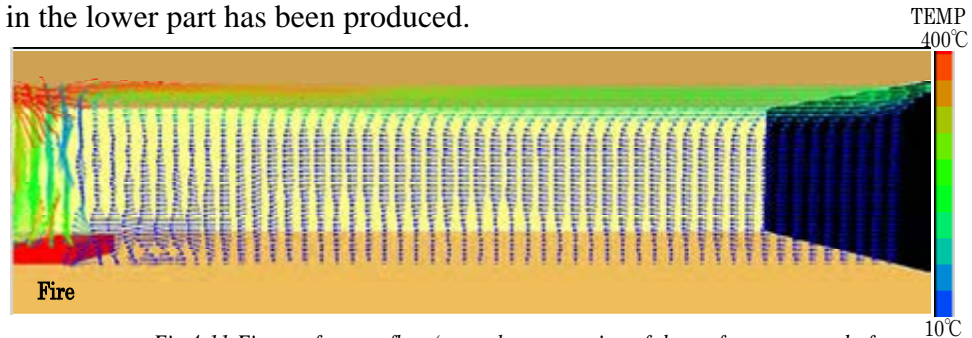


Fig.4-11 Figure of vector flow (central cross-section of the surface composed of longitudinal and vertical directions) (in the case of the WS not being activated)

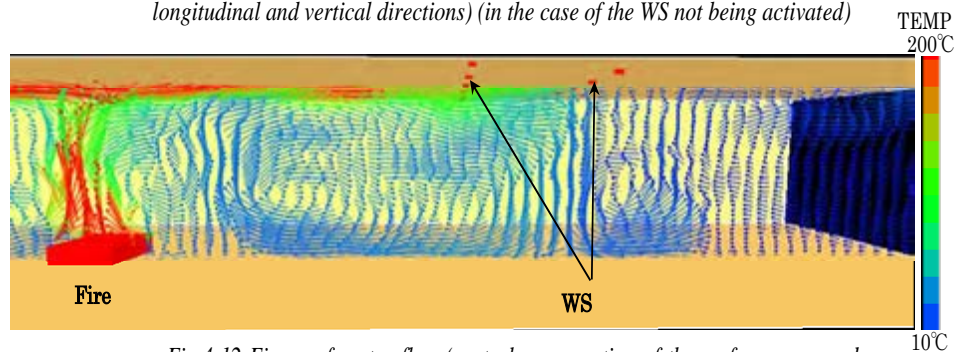


Fig.4-12 Figure of vector flow (central cross-section of the surface composed of longitudinal and vertical directions) (in the case of the WS being activated)

(b) Results in the case of the WS working

Fig.4-12 in respect to the flow vector clarifies the following characteristics. Namely, at the WS installation point on the fire source side the air flow thrusts through the WS, but at the WS installation point on the opening side the flow is controlled to run from the upper part to the lower part and the longitudinal flow is cut off. Two large convective flows are produced with the WS on the opening side as a boundary. When the WS works, the flow of the high temperature layer in the upper part of the space partitioned by the WS is isolated. Then, the direction of the flow changes toward the floor due to the water sprinkling from the WS and a circulating flow running toward the fire source is again formed. As a result, it can easily be understood that the WS plays an important role in the partitioning system.

5. CONCLUSIONS

The following items have been obtained by comparing the experiment results with the computation results from the FDS.

- (a) In the case of the WS not being activated, since the boundary condition was not faithfully simulated, the computation result with regard to the temperature at the center of the fire source obtained using the FDS showed a higher value. The temperature distribution behavior of the whole space was simulated with accuracy.
- (b) In case of the WS working, the temperature distribution behavior of the whole space was simulated with very high accuracy.
- (c) In the case of the WS working, the formulation of the partitioning was simulated.
- (d) In the case of the WS working, it can be estimated that the ceiling jet is intercepted due to the partitioning and that a circulating flow is formed in the partitioned space.

There are few reports on the estimation of thermal behavior based on the partitioning with water sprinkling equipment such as water screens using the CFD. In this study, computational results obtained from the CFD showed a favorable conformity to the measured values. Although conditions for experiments are often limited, in numerical simulations various phenomena can be studied comparatively with ease. It can be judged that the FDS will be effective for the narrowing down of experiment cases in advance and for the estimation of the behavior which can not be obtained in experiments under the restriction of costs and environmental matters.

REFERENCES

- 1) Kohyo Satoh, K.T. Yang : Simulations of Swirling Fires controlled Self-generated Entrainment Flows, Fire Safety Science Proceedings of the fifth International Symposium, 1997
- 2) W.K. Chow, N.K. Fong : Numerical Simulation on Cooling of the Fire-induced Airflow by Sprinkler Water Sprays, Fire Safety Journal 17, 1991
- 3) William Mell, McGattan KB, Borm HR : Large Eddy Simulation of Fire-Driven Flows, ASMEHTD Vol.304, National Heat Transfer Conference Vol.2, 1995
- 4) Kevin B. McGrattan et al : Fire Dynamics Simulator (Version 3) Technical Reference Guide, <http://www.bfrl.nist.gov/>
- 5) Reiko Amano et al : Water Screen Fire Disaster Prevention System in Underground Space, 6th Asia-Oceania Symposium on Fire Science and Technology, 2004
- 6) G.Su, J.G. Quintiere, N.Schultz : Physical Scaling of Fire Suppression By Water Mist, Proceeding of 2001 ASME International Mechanical Engineering Congress and Exposition November 11-16, 2001, HTD-Vol.369-4, MECE2001/HTD-24238

PLANNING OF EMERGENCY RESCUE ROUTES AFTER STRONG EARTHQUAKES

CHIN-HSUN YEH¹, WEI-CHANG CHEN², WEN-YU JEAN¹ and
LAP-LOI CHUNG¹

¹Research Fellow, ²Assistant Research Fellow
National Center for Research on Earthquake Engineering, Taiwan
chyeh@ncree.org.tw, wcchen@ncree.org.tw, wychien@ncree.org.tw and
chung@ncree.org.tw

ABSTRACT

Buildings, bridges, buried pipelines and so on are vulnerable in strong earthquakes. The damages of these infra-structures may interrupt the rescue routes and reduce the effectiveness of live-saving efforts. The main purpose of this study is to provide a systematic way to plan emergency routes for the rescue vehicles immediately after strong earthquakes in the metropolitan areas. It is expected to minimize the mean travel-time or to maximize the mean speed of rescue vehicles. To achieve the goal, several significant nodes of the road-network in each district are identified first based on the quantities of neighboring populations, the capacities of neighboring hospitals and fire stations, the accessibility of the selected nodes, and so on. Seismic performance index (SPI) of each road segment has been defined in this study according to the width and the design speed of the road segment, and the damage-state probabilities of bridges or elevated-highways which are either on the road, pass-over the road or parallel to the road. In short, the SPI is intended to reflect the mean velocity of rescue vehicles on the road segment immediately after strong earthquakes. The damage assessment of infra-structures considering the ground excitation intensity and ground failure extent can be carried out by applying software such as Taiwan Earthquake Loss Estimation System, which is developed by the National Center for Research on Earthquake Engineering, Taiwan. Based on the results of seismic scenario simulation, the emergency rescue routes connecting all the significant nodes in each district are then selected by the shortest path algorithm using mean travel-time as the cost. It is noted that an analyzable road-network must be constructed before applying Dijkstra algorithm to identify the minimum travel-time routes. In this paper, Taipei City serves as the pilot study region and the emergency rescue routes of different priorities in Taipei City have been identified.

Keywords: emergency rescue routes, seismic scenario simulation, shortest path problem

1. BACKGROUND

Since Taiwan is located in seismic active region and has many active faults, as shown in Figure 1, in the past decades, several devastating

earthquakes, such as the 1999 Chi-Chi earthquake in Taiwan, have caused serious losses and casualties, especially in the metropolitan areas. In view of the fact that highway systems play important roles in economy and emergency responses; however, some of the components in the highway systems, such as tunnels, bridges and elevated-roads, are vulnerable in strong earthquakes. Once some of the components or the neighboring buildings/pipelines are damaged, they may block the roads and significantly interrupt the functionality of highway systems, such as convenient communications, shipment of rescue and medical resources, etc. Therefore, it is important to plan emergency rescue routes in advance based on considerations of seismic safety and transportation rapidity.

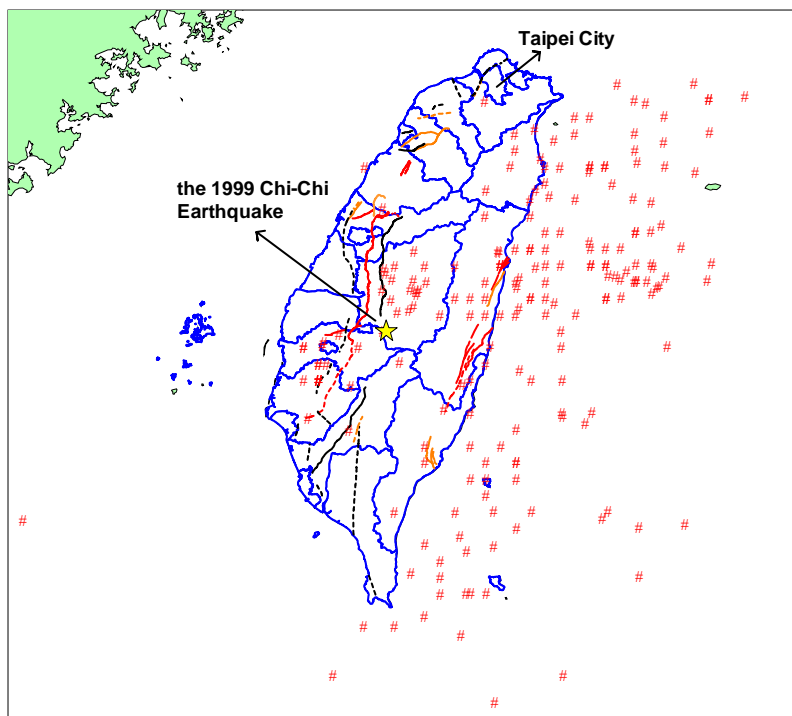


Fig. 1 Distribution of the historical seismic events with magnitude exceed 6.0 and the active faults in Taiwan

Figure 2 shows the flow chart which is used in this study to plan emergency rescue routes. The detail procedures will be explained step by step in the succeeding sections. Taipei City, not only the capital but also one of the economic centers in Taiwan, is chosen as the pilot study region to examine the feasibility of proposed planning scheme.

2. DATA COLLECTION AND PROCESSING

There are many factors that can influence the effectiveness of life-saving efforts immediately after earthquakes. It is necessary to collect the entire related database and to identify some of the important factors and characteristics in the database which can be used in planning emergency rescue routes. In this study we collected and processed database of administration boundaries, river basins, populations, highway transportation

systems, schools, hospitals, fire stations, and so on. Some of the data were collected from Taipei City government or other resources. Some of the data were investigated in field, if the existing database could not be found. All the data were stored in GIS format so that the spatial distribution and inter-relationship of objects could be visually displayed and analyzed.

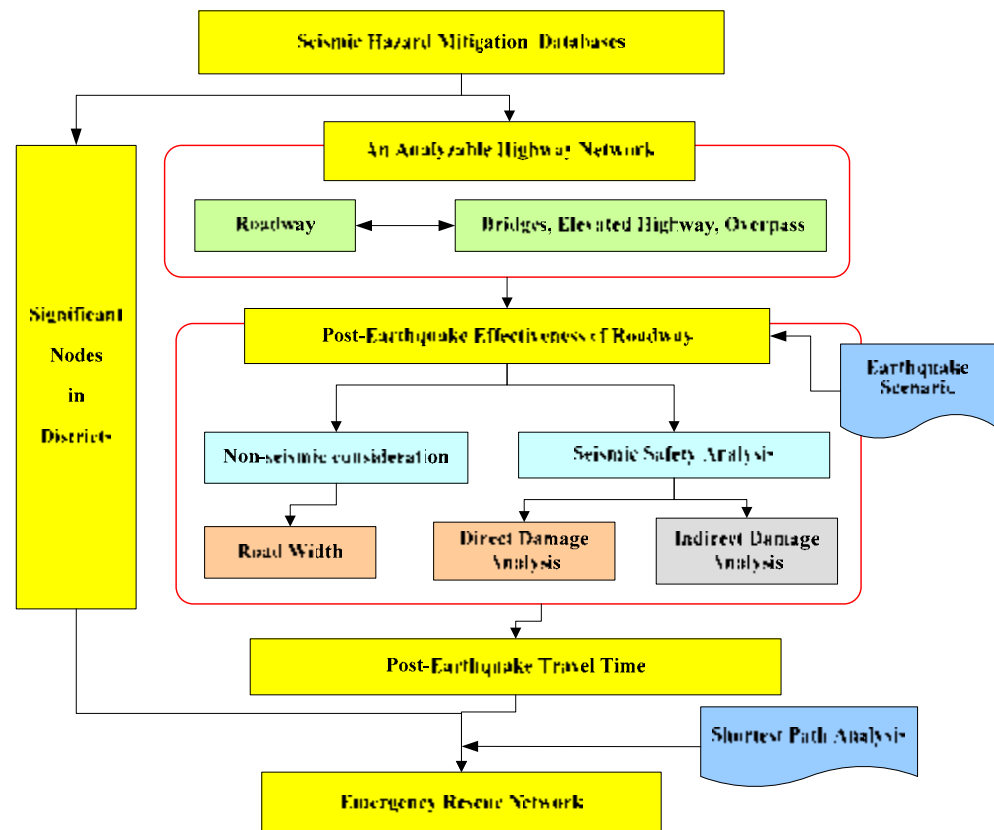


Fig.2 Flow chart of planning emergency rescue routes in metropolitan area

2.1 Establishment of Analyzable Road-Network

Generally speaking, a highway system should be transformed into a logical network, which is composed of links and nodes, before it can be recognized or analyzed by digital computers. A link represents a road segment, while a node represents an intersection of several road segments. Some of the links represent bridges or elevated highways, which may be damaged or even collapsed under strong excitations. These links should be identified and their seismic design parameters used in damage assessment should be associated with them.

Most of the links in a highway system are not influenced by other links in case of damage or collapse. However, some of the links may be over passed by other links (e.g. bridges or overpasses) or adjacent to other links (e.g. ramps or elevated roadways). The aforementioned three types of inter-relationships of links are demonstrated in Figure 3 and are denoted as normal type, overpass type and adjacent type, respectively. The attributes of each link includes information of one-way/two-way, number of lanes or width of the link, overpass or adjacent elevated link ID if they exists, design speed or speed limit of the link, and so on.

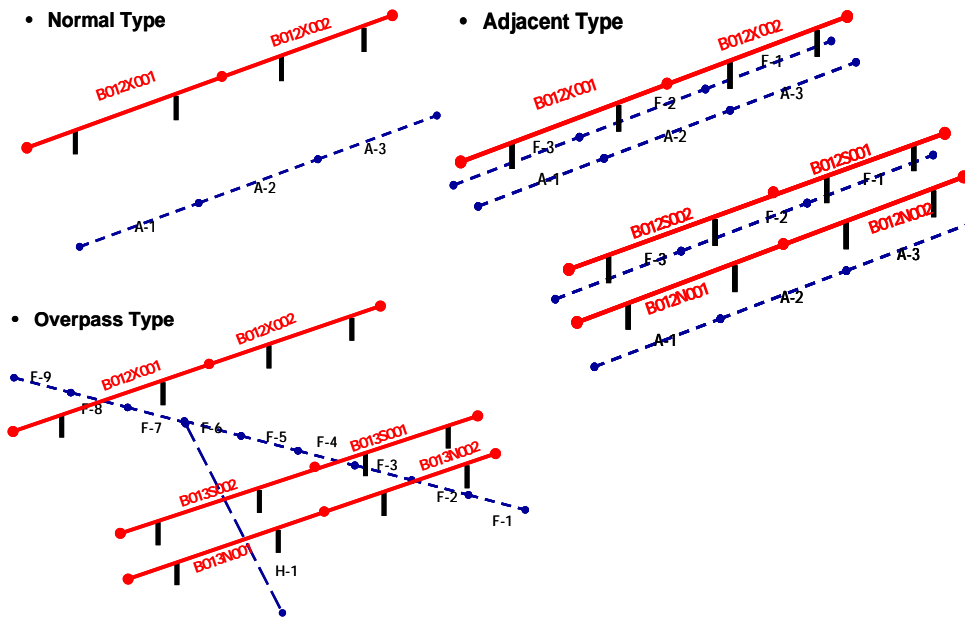


Fig. 3 Three relationships between transportation components, i.e., (1) normal (2) adjacent (3) overpass

2.2 Selection of Significant Nodes in Each District

In this study, the planning of emergency rescue routes in metropolitan areas can be roughly divided into three steps. The first step is to choose several significant nodes in each district. These nodes represent the most important or convenient places to access in the district when disasters occur. The second step is to build an inner-district network connecting the significant nodes in each district; and the final step is to complete the inter-district network connecting the entire set of significant nodes. Therefore, it is essential to select significant nodes in each district.

Since there are thousands of nodes in Taipei City, it is difficult to select the significant nodes based solely on intuition or experience. Hence, a significance index I_r was proposed to evaluate the accessibility and rescue capacity of each node based on the quantities of neighboring populations, hospitals, schools and fire stations, and the widths of roads connected to the node. The significance index I_r ranges between 0 and 1 and is defined as follows.

$$I_r = 0.3R_w + 0.2R_h + 0.2R_f + 0.1R_s + 0.2R_v$$

where R_w is a factor reflecting the number of roads connected to the nodes; R_h is a factor reflecting the number of beds in hospitals within a specified region; R_f is a factor reflecting the number of firefighters within a specified region; R_s is a factor reflecting the shelter spaces within a specified region; and R_v is a factor reflecting the number of populations within a specified region. All the factors are scaled to range between 0 and 1; and the specified region is a circular buffer region with 500-meter radius.

3.1 Non-Seismic Effect

If the width of link is large enough, not only it will not be blocked by fallen buildings or damage pipelines, but also it may provide a reserved lane for rescue vehicles. Therefore, it is reasonable to assign C_e a larger value for links with more than two lanes on each side. On the other hand, every link has its design speed; and there might be more traffic on wider links. So, the C_e can not increase unlimitedly. In this study, C_e is set to 1 when there is one lane on each side of the link. The C_e is set to 1.1 or 1.2 depending on the number of lanes on each side of link is two or larger than two, respectively.

3.2 Seismic Safety Performance of Links

Assume the expected rescue vehicle speed on a link after strong earthquakes is proportion to the seismic safety performance of the link. In other words, if the link is seismic designed or it will not be blocked out by other damage links, not only it is safe to drive after strong earthquakes, but also the design vehicle speed of the link can be ensured. Since the impact of an earthquake can not be predicted accurately beforehand, the seismic safety performance of links should be evaluated in a probabilistic sense. In this study, the seismic safety performance of the link is expressed as a function of damage-state-probabilities of the link itself and the neighboring links which may influence the link when damaged or collapsed. The speed modification factor I_p in Eq. (1) can be expressed as follow:

$$I_p = F_s \cdot F_o \cdot F_a \cdot F_b \quad (2)$$

where F_s indicates the success probability of the link itself. The term success means that vehicles can pass through the link. If there is some probability that the link will fail after strong earthquakes, the expected speed is reduced and assumed to be proportional with the success probability. Similarly, the factors F_o , F_a and F_b are the success probability to be influenced by the overpass link, the adjacent link and the neighboring buildings/pipelines, respectively.

All the ground motion intensity estimates, soil liquefaction potential and settlement estimates, and the damage-state-probabilities of roads, bridges, overpasses and elevated highways, etc are evaluated by using TELES. There are five damage states defined for bridges and elevated roads, i.e., none (d_1), slight damage (d_2), moderate damage (d_3), extensive damage (d_4) and complete damage (d_5). The probability in each damage state is denoted by p_1 , p_2 , p_3 , p_4 and p_5 , respectively. The success probability of the link itself F_s can be evaluated as

$$F_s = \sum_{i=1}^5 p_i \cdot s_i \quad (3)$$

where s_i is the success probability given specific damage state d_i of the link. Eq. (3) is one of the applications of total probability theorem.

Similarly, the success probabilities due to indirect effects of overpass and adjacent link damages are expressed as follows:

$$F_o = \sum_{i=1}^5 p_i \cdot o_i$$

$$F_a = \sum_{i=1}^5 p_i \cdot a_i$$

where o_i and a_i are the conditional success probabilities that vehicles can pass through the link given the overpass link and the adjacent link, respectively, being in damage state d_i . The values of coefficients s_i , o_i and a_i are given subjectively and listed in Table 1. Due to lack of information, F_b is set to 1 temporarily. The seismic safety performance and the expected rescue vehicle speed of the links in Taipei City are shown in Figures 5 and 6, respectively, based on the assumption that peak ground acceleration (PGA) equals 0.23g everywhere.

Table 1 Conditional success probabilities in various damage states

classification	d_1	d_2	d_3	d_4	d_5
s_i (road)	1.0	1.0	0.9	0.8	0.7
s_i (bridge)	1.0	1.0	0.6	0.3	0.0
o_i (overpass bridge)	1.0	1.0	0.8	0.5	0.2
o_i (pedestrian overpass)	1.0	1.0	1.0	0.9	0.8
a_i (adjacent highway)	1.0	1.0	0.9	0.8	0.7

4. PLANNING OF EMERGENCY RESCUE ROUTES

As explained previously, significant nodes in each district were selected first. The expected rescue vehicle speed on each link was evaluated by using Eq. (2), and the expected travel time on each link could be obtained accordingly. The shortest (travel time) path connecting each pair of significant nodes could be identified by using the Dijkstra (1959) algorithm, e.g., the inner-district rescue routes in Daan are shown in Fig. 7.

The next step was to select rescue routes connecting significant nodes in different districts. Since there were more than one significant node in each district, it was necessary to identify the shortest paths for all possible combinations of significant nodes and to select the rank-one path with minimum travel time. When the rank-one rescue routes had been identified, they were removed from the road-network temporarily. Using a similar approach in finding the rank-one rescue routes, rank-two rescue routes were obtained. In turn, the rank-one and rank-two rescue routes were removed from the road-network temporarily to find rank-three rescue routes.

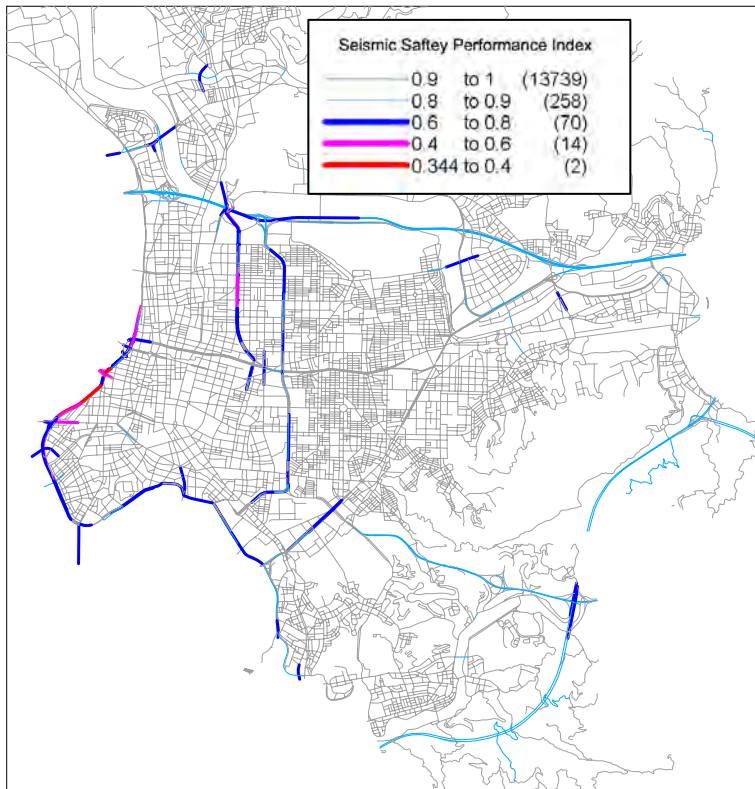


Fig. 5 Seismic safety performance of links in Taipei City

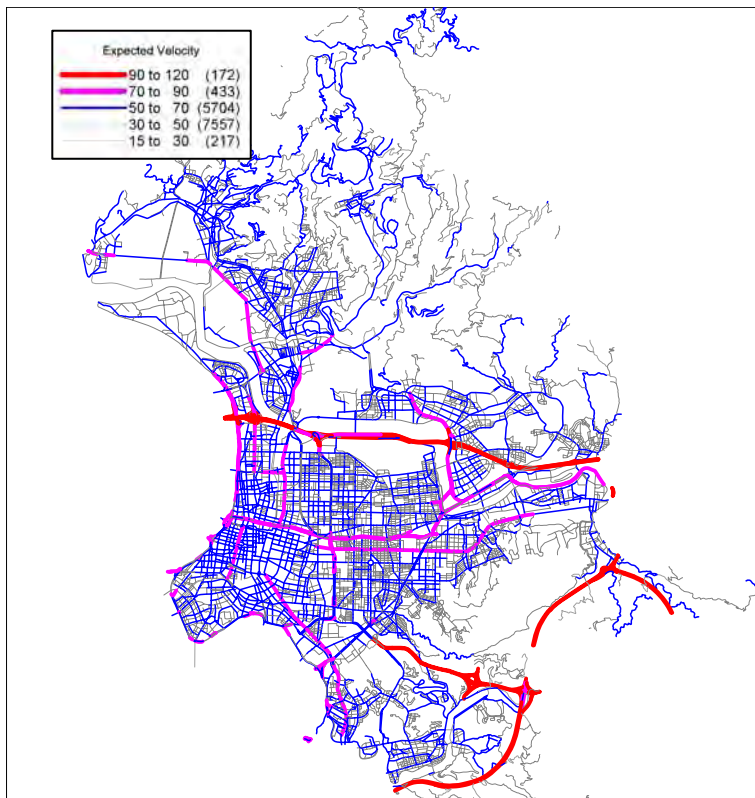


Fig. 6 Expected vehicle speed of links after earthquakes in Taipei City



Fig. 7 The rescue route of Daan district in Taipei City

Through this approach, it is guaranteed that no rescue routes will overlap with each other. After comprehensive network analysis and parameter sensitivity study, there were 615 links served as inner-district rescue routes, 461 links as the rank-one rescue routes, and 1,057 links as the rank-two or rank-three rescue routes. The inner- and inter-district rescue routes in Taipei City are shown in Figure 8.

5. CONCLUDING REMARKS

In order to evaluate the seismic performance of transportation systems and to plan the optimal rescue routes in a metropolitan area, a systematic approach, which includes GIS data processing, seismic hazard analysis, structural damage assessment and shortest-path network analysis, has been proposed and demonstrated in this paper. Using the proposed method, the emergency rescue routes are classified into three priorities and no overlap among each rescue route. The proposed approach to select rescue routes is based on the link width as well as the seismic safety performance of the link and its neighboring links. So, it is expected that the selected rescue routes will perform better in strong earthquakes and the approach can be easily applied in other metropolitan areas.

6. REFERENCES

Dijkstra, E.W., 1959. "A Note on Two Problems in Connection with Graphs," *Numerische Mathematik*, vol. 1, pp. 269-271.

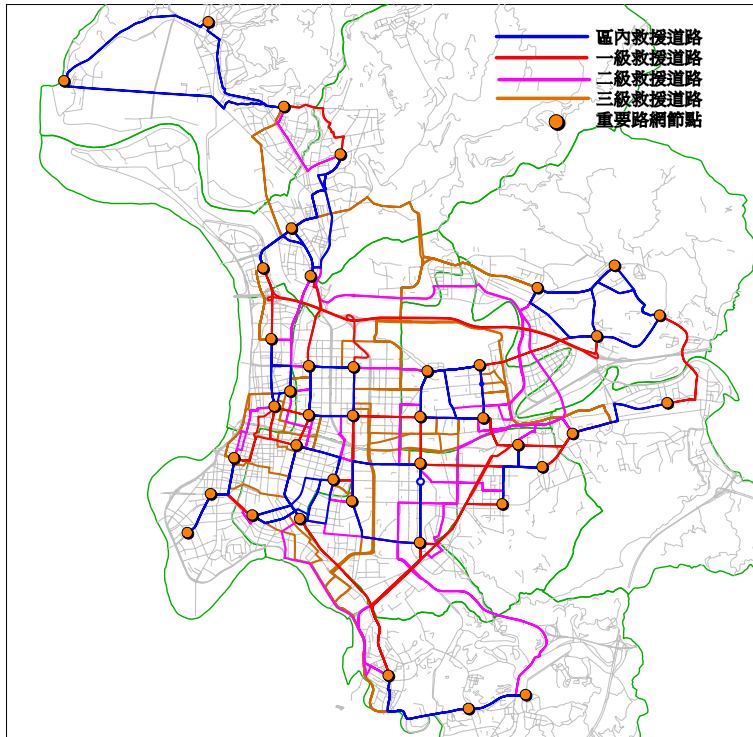


Fig. 8 The inter-district rescue routes in Taipei City

AUTHOR INDEX

A	
AKAPOB TEERAORANIT	471
AKIYUKI KAWASAKI	489
ALIREZA ANDALIB	153
AN XINMEI	389
ASHUTOSH KUMAR	509
ATSUSHI YOKOZAWA	69
B	
B ARCH, MSIA	163
BING LI	267, 341
BRIAN CAVILL	293
B. RAJESH BABU	509
C	
CHEE LEONG LIM	333
CHEE-HIONG LIM	399
CHEN PO-HAN	585
CHIEN-MEI LEE	173
CHIN-HSUN YEH	629
D	
DANG QUANG THINH	465
DUH BEEN-LIRN	585
DUSHMANTA DUTTA	203
E	
EMA KATO	69
F	
FANG YEA SAEN	163
FENG FENG	585
G	
GUAN HONG TAN	611
G. F. SU	31
H	
HAICHENG RONG	341
HANSA VATHANANUKIJ	579
HIDENOBU NAKAI	439, 447
HIROSHI KAMBARA	379
HIROSHI YOKOTA	69
HISASHI KANADA	129
HITOSHI KURIOKA	619
HO CHOI	323
HONG CHEN	409, 559
HONG HUANG	539, 559
HSU WEN JING	585
HUAN SHI	361
HUANG FENGLI	361
HUYNH THI LAN HUONG	465
I	
IKOLO, O. A.	429
J	
JAMES MW BROWNJOHN	611
JEFFREY WANG	593, 603
JIANG GUOPING	361
JITBODEE KHUNTHONGKAEW	147
JUNICHI SUSAKI	439, 447
K	
KAZI REZAUL KARIM	519
KAZUO TAMURA	379
KAZUYO TSUZAKI	569
KEIICHI OKADA	439, 447
KIMIRO MEGURO	9, 119, 193, 213, 231, 481
KONG GUANGYA	593, 603
KUMAR NEERAJ JHA	221
KUO-SHUH FAN	173, 183
L	
LANCHAO JIANG	109
LAP-LOI CHUNG	629
LI YONGSHENG	389
LI YUAN	529
LIU ZHIHANG	361
M	
MA GUOWEI	389
MADOKA NAKASHIMA	439, 447
MANABU FUNAHASHI	439, 447
MASAHIRO SETOJIMA	439, 447
MASANORI ITO	241
MASASUKE TAKASHIMA	481
MAX STRINGER	611
MD. REZAUL ISLAM	283
MEHEDI AHMED ANSARY	283
MIHO YOSHIMURA	213
MIKA KANEKO	379
MIN-CHENG TENG	173, 183
MITSUYOSHI TSUNEKUNI	51
N	
NAOKI TAKESHITA	79

NASROLLAHZADEH NESHELI	9, 231
NAVARATNARAJAH SATHIPARAN	9, 231
NGUYEN XUAN HIEN	465
NIKOLAI BOBYLEY	499

O

OKORO, D.	429, 457
ONKAR DIKSHIT	89
OSAKWE, J.	457
OSAMU IMAZEKI	619

P

PAKAWAT SANCHAROEN	249
PAOLA MAYORCA	9, 231
PENNUNG WARNITCHAI	41
PHAN HUU DUY QUOC	99
PITISAN KRAMMART	147
P. J. BARUAH	3

R

RAKTIPONG SAHAMITMOGKOL	139
RAMANCHARLA PRADEEP KUMAR	351, 509
RAMESH GURAGAIN	9, 231
RAVI SINHA	303
REI TAKADA	439, 447
REIKO AMANO	619
RI GAO	109
ROHAN KUMAR GUNARATNA	1
RYOHEI KONO	419
RYOZO OOKA	409, 419, 439, 447, 539, 549, 559, 569

S

S FAISAL HASHMI	89
SANJAYA KUMAR PATRO	303
SATORU SADOHARA	489
SHARIF MOTAWEF	153
SHIH-CHIEN HUANG	183
SHINICHIRO OKAZAKI	61
SHINSUKE KATO	409, 419, 559
SHINSUKE SAWASAKI	569
SHINYA KONDO	193
SHUNICHI KOSHIMURA	481
SHYAM SUNDER REDDY T.	351
SOMNUK TANGTERMSIRIKUL	147
SUDHIR MISRA	89, 221
S. GONG	369

T

TAIFENG JIANG	539
TAKEAKI WATANABE	419

TAKEO TAKAHASHI	419
TAKETO UOMOTO	51, 61, 129, 241, 249, 257
TAN XIANGQIAN	361
TAT-SENG LOK	399
TAWATCHAI TINGSANCHALI	471
TEDDY BOEN	19
TOMONORI SAKOI	569
TOR YAM KHOON	529
TOSHIHARU KISHI	99, 139
TRAN THUC	465
TSO-CHIEN PAN	267, 277, 333, 341, 519
TSUGIO NISHIMURA	51
T. ENDO	3, 439, 447
T. NEMOTO	3

W

WEI-CHANG CHEN	629
WEIGUO YANG	109
WEN-YU JEAN	629
WORAKANCHANA KAWIN	119
W. C. FAN	31
W. TAKEUCHI	3

X

XIANJIE XU	109
XIAO YI	593
XIN ZHANG	277
X. GU	369

Y

YANG WENYI	593, 603
YE KONG POH	611
YOICHI KAWAMOTO	439, 447, 549
YOSHIAKI NAKANO	323
YOSHIFUMI YASUOKA	3, 439, 447
YOSHIKAZU AKIRA	69
YOSHITAKA KATO	51, 79, 241
YUICHI SATO	489
YUKIHIRO ISHIKAWA	129
YUTAKA NAKAMURA	379
Y. LU	313, 369
Y. ZHOU	369

Z

ZHU QING	529
Z. WANG	313